ELECTRONIC AND OPTICAL PROPERTIES OF SEMICONDUCTOR NANOSTRUCTURES

A THESIS
SUBMITTED TO THE MATERIALS SCIENCE DEPARTMENT OF THE
UNIVERSITY OF PATRAS IN PARTIAL FULFILMENT
OF THE REQUIREMENTS FOR THE DEGREE OF
DOCTOR OF PHILOSOPHY

BY

ZAIPING ZENG

MATERIALS SCIENCE DEPARTMENT
UNIVERSITY OF PATRAS
GREECE

NOVEMBER, 2014

Advisory committee

Associate Professor Sotirios Baskoutas (supervisor)
Materials Science Department, University of Patras, Greece

Professor Andreas F. Terzis
Department of Physics, University of Patras, Greece

Professor Gabriel Bester
Department of Chemistry, University of Hamburg, Germany

Examination committee

Associate Professor Sotirios Baskoutas
Materials Science Department, University of Patras, Greece

Professor Andreas F. Terzis
Department of Physics, University of Patras, Greece

Professor Gabriel Bester
Department of Chemistry, University of Hamburg, Germany

Associate Professor Emmanuel Paspalakis
Materials Science Department, University of Patras, Greece

Assistant Professor Iosif Galanakis
Materials Science Department, University of Patras, Greece

Assistant Professor Ioannis Koutselas
Materials Science Department, University of Patras, Greece

Associate Professor Alexandros Vanakaras
Materials Science Department, University of Patras, Greece

Examination date: 7:00 PM, 10 November 2014.

Abstract

The goal of this Thesis is to study the electronic and optical properties of semiconductor nanostructures by employing different theories. The work present in this Thesis is divided into three parts.

Part I is devoted to the effective-mass theory and its several applications. A general description of the effective mass theory and several ways of solving the effective-mass Schrödinger equation with an emphasis on the potential morphing method are given in the first chapter. In the following few chapters, we apply these theories in many realistic systems for the study of many properties. They include: i) the binding energy of hydrogentic donor impurity in semiconductor quantum dots under the influence of static electric field and/or magnetic field, ii) the linear and nonlinear optical properties associated with intraband transitions in semiconductor quantum dots, core shell quantum dots and quantum-dot-quantum-ring systems.

Part II is devoted to the pseudopotential theory and its several applications. The background theories primarily regarding to the empirical pseudopotential method and configuration interaction approach are described in the first chapter. In the following few chapters, we employ these theories for the study of the electronic and optical properties of many nanostructures of group II-VI materials. The optical properties studied herein include the band gap, Stokes shift, exciton fine structure, optical polarization and absorption spectra.

Part III is devoted to the appendix, where twelve published papers are presented.

Keyword(s): Semiconductor nanostructures, Effective mass approximation, Binding energy, Linear and nonlinear optical properties, Pseudopotential theory, Configuration interaction

Περίληψη

Στόχος της παρούσας διατριβής είναι η μελέτη των ηλεκτρονικών και οπτικών ιδιοτήτων νανοδομών ημιαγωγών κάνοντας χρήση κατάλληλων υπολογιστικών μεθόδων και τεχνικών. Η διατριβή χωρίζεται σε τρία μέρη.

Το πρώτο μέρος εστιάζει στην θεωρία της ενεργούς μάζας (Effective-mass Theory) και τις εφαρμογές της. Στο πρώτο κεφάλαιο παρουσιάζεται το απαραίτητο θεωρητικό υπόβαθρο και δίνεται μία συνοπτική περιγραφή των συνηθέστερων μεθόδων επίλυσης της μονοηλεκτρονιακής εξίσωσης του Schrödinger,δίνοντας ιδιαίτερη έμφαση στην μέθοδο μορφοποίησης δυναμικού (Potential Morphing Method). Στα επόμενα κεφάλαια του πρώτου μέρους οι τεχνικές και μέθοδοι που περιγράφηκαν χρησιμοποιούνται για την μελέτη κρίσιμων ιδιοτήτων και παραμέτρων σε νανοσυστήματα ημιαγωγών. Μεταξύ αυτών είναι: i) η ενέργεια δέσμευσης υδρογονοειδών προσμίξεων τύπου δότη υπό την επίδραση στατικού ηλεκτρικού ή/και μαγνητικού πεδίου, ii) γραμμικές και μη γραμμικές οπτικές ιδιότητες που συνδέονται με intraband μεταβάσεις εντός ζώνης σε κβαντικές τελείες ημιαγωγών, κβαντικές τελείες με δομή πυρήνα-φλοιού και σε μεικτά συστήματα κβαντικής τελείας – κβαντικού δακτυλίου.

Το δεύτερο μέρος εστιάζει στην θεωρία των ψευδοδυνάμικών και τις εφαρμογές της. Αρχικά παρουσιάζεται το απαραίτητο θεωρητικό υπόβαθρο της μεθόδου εμπειρικών ψευδοδυναμικών (Empirical Pseudopotential Method) καθώς επίσης και της μεθόδου αλληλεπίδρασης διαμορφώσεων (Configuration Interaction). Στην συνέχεια, οι προαναφερθείσες τεχνικές εφαρμόζονται στην μελέτη των ηλεκτρονικών και οπτικών ιδιοτήτων σε μία πληθώρα νανοδομών ημιαγωγών II-VI. Μεταξύ των ιδιοτήτων αυτών είναι: το ενεργειακό χάσμα, η μετατόπιση Stokes, η λεπτή δομή των εξιτονίων, η οπτική πόλωση και τα φάσματα απορρόφησης.

Το τρίτο μέρος της διατριβής περιλαμβάνει το παράρτημα, στο οποίο παρατίθενται οι δώδεκα δημοσιευμένες εργασίες.

Λέξεις Κλειδιά: Νανοδομές ημιαγωγών, Προσέγγιση ενεργούς μάζας, Ενέργεια δέσμευσης, Γραμμικές και μη γραμμικές οπτικές ιδιότητες, Μέθοδος ψευδοδυναμικών, Αλληλεπίδραση διαμορφώσεων.

To my parents and my brother

Preface

This Thesis is submitted to the Materials Science Department of University of Patras, as a partial fulfillment of the requirements to the degree of Doctor of Philosophy. The work presented was carried out in the academic years 2011-2014 under the supervision of Prof. Sotirios Baskoutas and in collaboration with many professors and researchers both in-house and abroad.

Present semiconductor physics appears to the physics of reduced dimensionality, such as quasi-two dimensional quantum wells, quasi-one dimensional quantum wires, and quasi-zero dimensional quantum dots. These structures build a bridge between the traditional macroscopic condensed matter systems and the microscopic objects, such as atoms, exhibiting extraordinary physical properties. The work of the Thesis is devoted to the study of electronic and optical properties of these structures. Two types of theories, i.e., effective mass theory and pseudopotential theory, are employed. Various properties, such as i) binding energy of hydrogenic impurity, ii) linear and nonlinear optical properties associated with the intraband transition, iii) exciton states and related properties, are covered throughout the thesis.

The Thesis is composed of three parts, i.e., I) effective-mass theory part, II) pseudopoential theory part, III) appendix part. The first chapter of parts I and II is given to the description of the background theory that employed in the following few chapters, where the applications of the theory in the realistic systems are performed. Part III presents the twelve published papers carried out during my PhD.

Zaiping Zeng
Patras, 2014

Acknowledgement

After three-years staying in Greece, I have been substantially improved both physically and mentally, both in the realm of science and in the aspect of socialization. This is, to certain extent, due to the healthy Greek food and the amazing climate in the region nearby Mediterranean sea. The majority of the reasons could be attributed to the people who I met, who I learned from, who I worked with, and who helped me out of the difficulties. Those people are the ones I would like to acknowledge herein.

First and foremost, the utmost gratitude should go to my supervisor Prof. Sotirios Baskoutas. It is him who gave me the opportunity to work in a field I really like, offered excellent financial support and tried the best to take good care of me in the past three years. It is him who gave me the freedom, the guidance, and most importantly the trust for selecting and executing each project. It is also him who is always ready for offering suggestions and helps in any aspect whenever I need. He is a person who had given strong influence on my scientific and personal development. I always appreciate what he did for me and he is surely at a position nearby my parents' in my heart.

I would like to thank the other two members of the advisory committee, Prof. Andreas F. Terzis and Prof. Gabriel Bester. It is Prof. Terzis who initially introduced this position to me and offered many valuable suggestions on improving the quality of the manuscripts later on. It is Prof. Bester who gave me the opportunity to work with one of the best methods for electronic calculations, empirical pseudopotential method, and afterwards offered plenty of constructive advices on improving the quality of the manuscripts.

Special thanks must be given to Dr. Christos S. Garoufalis, who is my friend, my collaborator, and most likely my "elder brother". For the time being, I still remember in my mind the first lesson for Linux operating system, the first lesson for Vim, the first lesson for Gabedit, Avogadro, Gimp, Opendx and Gaussview, the first lesson for Orca, Firefly, Gaussion, Turbomole, Quantum Espresso and Crystal. There were so many first "kick" he has given to me which opened many doors of many fields in my mind and made me be aware that there is another way of doing work. The improvement of my writing skills of scientific papers, my programming (from Fortran to Scilab) and scripting (from Bash, Sed, AWK to recently Python) abilities is certainly related with his comments.

Many thanks go to the faculty and staff members in the Materials Science Department who taught or helped me, or from whom I learned: Prof. Demetri Photinos, Prof. Vainos Nikolaos, Prof. Nikolaos Bouropoulos, Prof. Emmanuel Paspalakis, Prof. Iosif Galanakis, Prof. Spyros Yannopoulos, Prof. Michael Sigalas, Prof. Konstantine Galiotis, Prof. Ioannis Koutselas, Prof. Alexandros Vanakaras, Mrs. Kapsali-Economopoulou Penelope, Mrs. Skaperda Maria, Mrs. Elena Serpi, Mr. Stavros Zogas.

I strongly appreciate the invaluable support from my friend Elena Giorgia Sotiropoulos. Finally, I would like to thank my parents and my younger brother for their continual support, understanding and encouragement.

List of papers

I **Zaiping Zeng**, Christos S. Garoufalis, Sotirios Baskoutas, Andreas F. Terzis
Tuning the binding energy of surface impurities in cylindrical GaAs/AlGaAs quantum dots by a tilted magnetic field
Journal of Applied Physics **112**, 064326 (2012).

II **Zaiping Zeng**, Christos S. Garoufalis, Sotirios Baskoutas, Andreas F. Terzis
Stark effect of donor binding energy in a self-assembled GaAs quantum dot subjected to a tilted electric field
Physics Letters A **376**, 2712 (2012).

III **Zaiping Zeng**, Christos S. Garoufalis, Sotirios Baskoutas
Combination effects of tilted electric and magnetic fields on donor binding energy in a GaAs/AlGaAs cylindrical quantum dot
Journal of Physics D: Applied Physics **45**, 23102 (2012).

IV Sotirios Baskoutas, **Zaiping Zeng**, Christos S. Garoufalis, Gabriel Bester
Tuning of the optical emission polarization of ZnO nanorods by an applied hydrostatic pressure
The Journal of Physical Chemistry C **116**, 26592 (2012).

V Yashar Azizian-Kalandaragh, Ali Khodayari, **Zaiping Zeng**, Christos S. Garoufalis, Sotirios Baskoutas, Lionel Cervera Gontard
Strong quantum confinement effects in SnS nanocrystals produced by ultrasound-assisted method
Journal of Nanoparticle Research **15**, 1388 (2013).

VI **Zaiping Zeng**, Emmanuel Paspalakis, Christos S. Garoufalis, Andreas F. Terzis, Sotirios Baskoutas
Optical susceptibilities in singly charged ZnO colloidal quantum dots embedded in different dielectric matrices
Journal of Applied Physics **113**, 054303 (2013).

VII **Zaiping Zeng**, Christos S. Garoufalis, Sotirios Baskoutas, Gabriel Bester
Electronic and optical properties of ZnO quantum dots under hydrostatic pressure
Physical Review B **87**, 125302 (2013).

VIII **Zaiping Zeng**, Christos S. Garoufalis, Andreas F. Terzis, Sotirios Baskoutas
Linear and nonlinear optical properties of ZnO/ZnS and ZnS/ZnO core shell quantum dots: Effects of shell thickness, impurities and dielectric

environments
Journal of Applied Physics **114**, 023510 (2013).

IX **Zaiping Zeng**, George Gorgolis, Christos S. Garoufalis, Sotirios Baskoutas
Competition effects of electric and magnetic fields on impurity binding energy in a disc-shaped quantum dot in the presence of pressure and temperature
Science of Advanced Materials **6**, 586 (2014).

X **Zaiping Zeng**, Christos S. Garoufalis, Sotirios Baskoutas
New insights in the excitonic emission of ZnS colloidal quantum dots
The Journal of Physical Chemistry C **118**, 10502 (2014).

XI **Zaiping Zeng**, Christos S. Garoufalis, Sotirios Baskoutas
Linear and nonlinear optical susceptibilities in a laterally coupled quantum-dot-quantum-ring system
Physics Letters A **378**, 2713 (2014).

XII **Zaiping Zeng**, Alexia Petoni, Christos S. Garoufalis, Sotirios Baskoutas, Gabriel Bester
Near-band-edge exciton polarization change in ZnO nanowires
Physical Chemistry Chemical Physics (2015), DOI: 10.1039/C4CP04551C.

XIII **Zaiping Zeng**, Christos S. Garoufalis, Sotirios Baskoutas, Gabriel Bester
Excitonic fine-structure splitting in high-symmetry ZnO colloidal quantum dots
Under preparation

XIV **Zaiping Zeng**, Christos S. Garoufalis, Sotirios Baskoutas, Gabriel Bester
Exciton fine structure in non-polar and polar ZnO nanowires: Effects of quantum confinement, growth direction and atomistic asymmetry
Under preparation

XV **Zaiping Zeng**, Christos S. Garoufalis, Sotirios Baskoutas, Gabriel Bester
Excitonic optical properties of wurtzite ZnS quantum dots under pressure
Under preparation

Papers not included in the Thesis:

- Sotirios Baskoutas, **Zaiping Zeng**, Christos S. Garoufalis, Gabriel Bester
  Tuning of the optical emission polarization of ZnO nanorods by an applied hydrostatic pressure
  The Journal of Physical Chemistry C **116**, 26592 (2012).

- Yashar Azizian-Kalandaragh, Ali Khodayari, **Zaiping Zeng**, Christos S. Garoufalis, Sotirios Baskoutas, Lionel Cervera Gontard
  Strong quantum confinement effects in SnS nanocrystals produced by ultrasound-assisted method
  Journal of Nanoparticle Research **15**, 1388 (2013).

- **Zaiping Zeng**, Christos S. Garoufalis, Sotirios Baskoutas, Gabriel Bester
  Excitonic fine-structure splitting in high-symmetry ZnO colloidal quantum dots
  Under preparation

- **Zaiping Zeng**, Christos S. Garoufalis, Sotirios Baskoutas, Gabriel Bester
  Exciton fine structure in non-polar and polar ZnO nanowires: Effects of quantum confinement, growth direction and atomistic asymmetry
  Under preparation

- **Zaiping Zeng**, Christos S. Garoufalis, Sotirios Baskoutas, Gabriel Bester
  Excitonic optical properties of wurtzite ZnS quantum dots under pressure
  Under preparation

Contents

Part I

Effective-mass Theory

1

Background Theory

This chapter is devoted to the description of the background theory employed in the following few chapters, including the envelope function approximation, effective mass approximation and many numerical methods for solving the single-band effective-mass Schrödinger equation emphasizing on the potential morphing method.

Contents

1.1 Envelope function approximation

In an attempt to give a general description of the envelope function approximation, we consider an electron which experiences a non-periodic potential. The corresponding Schrödinger equation is given by

$$[\hat{H} + U(\mathbf{r})]\psi(\mathbf{r}) = \varepsilon\psi(\mathbf{r}), \tag{1.1}$$

where $\hat{H}$ is the single-electron Hamiltonian, $U(\mathbf{r})$ is the non-periodic potential, $\psi(\mathbf{r})$ is the eigenfunction and ε is the corresponding eigenenergy. To solve this equation, it is often convenient to write the wave function $\psi(\mathbf{r})$ as a linear combination of the Bloch states:

$$\psi(\mathbf{r}) = \sum_{k\nu} c_{k\nu}\phi_{k\nu}(\mathbf{r}), \tag{1.2}$$

Inserting the expression (1.2) into equation (1.1) and keeping in mind that the Bloch states $\phi_{k\nu}(\mathbf{r})$ are the eigenstates of the single-electron Hamiltonian $\hat{H}$ with the corresponding eigenenergies $\varepsilon_{k\nu}$, one can derive the following equations for the coefficients $c_{k\nu}$:

$$\varepsilon_{k\nu}c_{k\nu} + \sum_{k'\nu'} U_{k\nu,k'\nu'}c_{k'\nu'} = \varepsilon c_{k\nu}, \tag{1.3}$$

where

$$U_{k\nu,k'\nu'} = \langle\phi_{k\nu}(\mathbf{r})|U(\mathbf{r})|\phi_{k'\nu'}(\mathbf{r})\rangle \tag{1.4}$$

are the matrix elements of the non-periodic potential $U(\mathbf{r})$ within the Bloch basis $\phi_{k\nu}$. Considering

$$\phi_{k\nu}(\mathbf{r}) = u_{k\nu}(\mathbf{r})e^{i\mathbf{k}\cdot\mathbf{r}}, \tag{1.5}$$

where $u_{k\nu}(\mathbf{r})$ is a periodic function, the expression (1.4) can be written as

$$U_{k\nu,k'\nu'} = \sum_{\mathbf{G}} F_{\mathbf{k}\nu,\mathbf{k}'\nu'}(\mathbf{G})\tilde{U}_{\mathbf{q}}, \tag{1.6}$$

with

$$F_{\mathbf{k}\nu,\mathbf{k}'\nu'}(\mathbf{G}) = \int u^*_{\mathbf{k}\nu}(\mathbf{r})u_{\mathbf{k}'\nu'}(\mathbf{r})e^{-i\mathbf{G}\cdot\mathbf{r}}d^3r, \tag{1.7}$$

and

$$\tilde{U}_{\mathbf{q}} = \frac{1}{\Omega}\int U(\mathbf{r})e^{i\mathbf{q}\cdot\mathbf{r}}d^3r, \tag{1.8}$$

where Ω is the volume of the crystal, $\mathbf{G}$ is the lattice vector in the reciprocal space, $\mathbf{q} = \mathbf{k} - \mathbf{k}' - \mathbf{G}$. The expression in equation (1.8) is essentially the Fourier transform of the potential $U(\mathbf{r})$. If $U(\mathbf{r})$ varies slowly on the atomic scale, its Fourier transform will

only contribute for $\mathbf{q}$ in the vicinity of $\mathbf{q}=0$, i.e., $\mathbf{q}=\mathbf{k}-\mathbf{k}^{'}-\mathbf{G}\rightarrow 0$. In this condition, equation (1.7) could be given as

$$F_{\mathbf{k}\nu,\mathbf{k}'\nu'}(\mathbf{G})\approx\delta_{\nu\nu'}\delta(\mathbf{G}). \tag{1.9}$$

In the above equation, we used the orthonormality properties of the Bloch states. Employing the equation (1.9) in equation (1.6), one can get

$$U_{k\nu,k'\nu'}\approx U_{\mathbf{k}-\mathbf{k}'}\delta_{\nu\nu'}. \tag{1.10}$$

This covers the key result of the envelope function approximation: if the non-periodic potential is a slowly varying potential, its matrix elements within the Bloch basis are diagonal with respect to the band index ν and are given by its Fourier transform $\tilde{U}$ at $\mathbf{k}-\mathbf{k}^{'}$. This suggests that all the interband coupling terms ($\nu\neq\nu^{'}$) are zero and for intraband transitions ($\nu=\nu^{'}$) the form of the Bloch functions $u_{\mathbf{k}\nu}$ is irrelevant. Inserting the above approximated matrix elements into equation (1.3), we have

$$\varepsilon_{k\nu}c_{k\nu}+\sum_{\mathbf{k}^{'}}U_{\mathbf{k}-\mathbf{k}'}c_{\mathbf{k}'\nu}=\varepsilon c_{\mathbf{k}\nu}. \tag{1.11}$$

Considering the fact that all the interband coupling terms are vanished, the linear combination of the Bloch states in equation (1.2) can be simplified as

$$\psi_{\nu}(\mathbf{r})=\sum_{k}c_{k\nu}\phi_{k\nu}(\mathbf{r}). \tag{1.12}$$

In the limit of a vanishing potential $U(\mathbf{r})\rightarrow 0$, the solution of equation (1.11) could be

$$c_{\mathbf{k}\nu}=\delta_{\mathbf{k}-\mathbf{k}_0},\quad \varepsilon=\varepsilon_{\mathbf{k}_0\nu}. \tag{1.13}$$

In the presence of a non-zero potential $U(\mathbf{r})$, the wave function ψ_{ν} will also involve $\mathbf{k}$ values different from the reference wavevector $\mathbf{k}_0$. However, due to the slowly varying nature of the perturbation, corresponding to a sharp-peak structure of its Fourier transform $\tilde{U}$, the corresponding solution $c_{\mathbf{k}\nu}$ will be strongly peaked around the reference wavevector $\mathbf{k}_0$. Thus, it is convenient to perform to inverse Fourier transform of the eigenvalue equation (1.11) with respect to the relative wavevector $\Delta\mathbf{k}=\mathbf{k}-\mathbf{k}_0$. By denoting with

$$\bar{\psi}_{\mathbf{k}_0\nu}(\mathbf{r})=\frac{1}{\sqrt{\Omega}}\sum_{\mathbf{k}}c_{\mathbf{k}\nu}e^{i\Delta\mathbf{k}\cdot\mathbf{r}}, \tag{1.14}$$

the inverse Fourier transform of the coefficients $c_{\mathbf{k}\nu}$ with respect to $\Delta\mathbf{k}$, and applying the same inverse Fourier transform to equation (1.11), we get the following Schrödinger-like

equation for the effective wave function as detailed in equation (1.14):

$$\varepsilon_\nu(\mathbf{k}-i\nabla_r)\bar{\psi}_{\mathbf{k}_0\nu}(\mathbf{r})+U(\mathbf{r})\bar{\psi}_{\mathbf{k}_0\nu}(\mathbf{r})=\varepsilon\bar{\psi}_{\mathbf{k}_0\nu}(\mathbf{r}), \tag{1.15}$$

where $\varepsilon_\nu(\mathbf{k}-i\nabla_r)$ denotes the operatorial version ($\triangle\mathbf{k}\rightarrow-i\nabla_\mathbf{r}$) of the crystal band structure $\varepsilon_{\mathbf{k}\nu}\equiv\varepsilon_\nu(\mathbf{k}_0+\Delta\mathbf{k})$.

Compared to the original Schrödinger equation (1.1), the above effective equation involves only the potential $U(\mathbf{r})$ Consequently, it is possible to solve the original problem in equation (1.1) by solving an extremely simplified Schrödinger-like equation involving only the potential $U(\mathbf{r})$.

Let us now come to the link between the original wave function ψ and the effective wave function $\bar{\psi}$ detailed in equation (1.14). More specifically, by inserting the explicit form of the Bloch states into the linear combination (equation 1.12) and taking into account that $u_{\mathbf{k}\nu}(\mathbf{r})$ is a slowly varying function of the wavevector $\mathbf{k}$, the latter may be taken out of the sum and evaluated in $\mathbf{k}_0$:

$$\psi_{\mathbf{k}_0\nu}(\mathbf{r})=\sum_\mathbf{k}c_{\mathbf{k}\nu}e^{i\mathbf{k}\cdot\mathbf{r}}u_{\mathbf{k}\nu}(\mathbf{r})\approx(\sum_\mathbf{k}c_{\mathbf{k}\nu}e^{i\triangle\mathbf{k}\cdot\mathbf{r}})\phi_{\mathbf{k}_0\nu}(\mathbf{r}). \tag{1.16}$$

Taking into account that the quality in parenthesis is just proportional to the effective wave function $\bar{\psi}$, we finally get

$$\psi_{\mathbf{k}_0\nu}(\mathbf{r})\approx\sqrt{\Omega}\bar{\psi}_{\mathbf{k}_0\nu}(\mathbf{r})\phi_{\mathbf{k}_0\nu}(\mathbf{r}). \tag{1.17}$$

This is the fundamental result of the envelope-function approximation: for any given band ν and reference wavevector $\mathbf{k}_0$, the corresponding global wave function ψ is simply given by the original Bloch function ϕ multiplied by the slowly varying effective wave function $\bar{\psi}$, called envelope function, the latter is obtained by solving the effective Schrödinger equation, also referred to as envelope function equation.

1.2 Effective-mass approximation

In the conditions that (i) the conduction band minimum (CBM) or the valence band maximum (VBM) is at the Γ point of the Brillouin zone, e.g., $\mathbf{k}_0=0$ and (ii) the constant energy surface is spherical so that

$$\varepsilon_\nu(\mathbf{k})=\varepsilon_\nu(0)+\frac{\hbar^2k^2}{2m^*}, \tag{1.18}$$

the envelope function equation can be written as

$$[-\frac{\hbar^2}{2m^*}\nabla^2 + U(\mathbf{r})]\bar{\psi}(\mathbf{r}) = \varepsilon\bar{\psi}(\mathbf{r}), \tag{1.19}$$

where we set $\varepsilon_\nu(0) = 0$. After making a comparison between equations (1.1) and (1.19), it is found that the effect of the periodic potential $V(\mathbf{r})$ is included in the effective mass m^*. In the other words, for an electron (or a hole) near by the CBM (or VBM), its movement is like the movement of a particle with mass $m = m^*$. Therefore, the above mentioned theory is often called as effective-mass approximation.

1.3 Solutions to effective-mass Schrödinger equation

As mentioned before, the eigenvalue problem given in equation (1.1) is significantly simplified by employing the effective-mass approximation, which leads to another eigenvalue problem detailed in equation (1.19). It has been generally accepted that this eigenvalue problem, for most of the physical systems, can not be solved exactly. Therefore, numerical techniques have been employed in order to solve this problem. Hereafter, we give a general overview of the most widely used numerical methods, such as perturbation theory, variational method, matrix diagonalization method et al. and point out the corresponding disadvantages. In the following step, we describe a powerful method, that is, potential morphing method, which is developed for the quantum-mechanical determination of the eigenstates and eigenvalues of a particle in a potential of general shape.

1.3.1 Perturbation theory

Perturbation theory can be used when the Hamiltonian of a system can be written as

$$\hat{H} = \hat{H}_0 + \hat{H}', \tag{1.20}$$

where $\hat{H}_0$ is the Hamiltonian of a system with well-known eigenvalues E_{0n} and eigenfunctions ψ_{0n} which is usually called as unperturbed system, and $\hat{H}'$ represents a *perturbation*, which is required to be significantly small in comparison to $\hat{H}_0$. In this case, if we know the solution to the system described by $\hat{H}_0$, we can use the perturbation theory to get the approximate solution of a system described by $\hat{H}$. To illustrate the perturbation theory, we restrict our attention on a simple case where the energy levels of the unperturbed

system are not degenerate. We assume that the eigenvalues and eigenfunctions of $\hat{H}$ can be expanded as a series whose terms are of zeroth, first, etc., order in $\hat{H}^{'}$. This can be done in a more efficient way if we re-write equation (1.20) as

$$\hat{H} = \hat{H}_0 + \lambda \hat{H}^{'}, \tag{1.21}$$

where λ is a constant and generally assumed to be small. By this way, the series for the eigenvalue E_n and eigenfunction ψ_n can be written as

$$\begin{aligned} E_n &= E_{0n} + \lambda E_{1n} + \lambda^2 E_{2n} + ... \\ \psi_n &= \psi_{0n} + \lambda \psi_{1n} + \lambda^2 \psi_{2n} + ... \end{aligned} \tag{1.22}$$

In the above expressions, the terms independent on the parameter λ are the zeroth order terms, while that contains λ is the first order term, and so forth. Substituting these expressions into the following Schrödinger equation

$$\hat{H}\psi_n = E_n \psi_n, \tag{1.23}$$

we get

$$\begin{aligned} &(\hat{H}_0 + \lambda \hat{H}^{'})(\psi_{0n} + \lambda \psi_{1n} + \lambda^2 \psi_{2n} + ...) \\ &= (E_{0n} + \lambda E_{1n} + \lambda^2 E_{2n} + ...)(\psi_{0n} + \lambda \psi_{1n} + \lambda^2 \psi_{2n} + ...) \end{aligned} \tag{1.24}$$

If we expand the above equation and compare both sides of the equation with regarding to the terms having the same power of λ, we can obtain

$$\hat{H}_0 \psi_{0n} = E_{0n} \psi_{0n}, \tag{1.25}$$

$$\hat{H}^{'} \psi_{0n} + \hat{H}_0 \psi_{1n} = E_{0n} \psi_{1n} + E_{1n} \psi_{0n}, \tag{1.26}$$

$$\hat{H}^{'} \psi_{1n} + \hat{H}_0 \psi_{2n} = E_{0n} \psi_{2n} + E_{1n} \psi_{1n} + E_{2n} \psi_{0n}. \tag{1.27}$$

If we consider that ψ_{1n} can be expressed as a linear combination of the basis of the unperturbed eigenfunctions ψ_{0k}:

$$\psi_{1n} = \sum_k a_{nk} \psi_{0k}. \tag{1.28}$$

Substituting the above expression into (1.26), we obtain

$$(\hat{H}^{'} - E_{1n})\psi_{0n} = \sum_k a_{nk}(E_{0n} - E_{0k})\psi_{0k}, \tag{1.29}$$

where we have used the expression (1.25). Multiplying the both sides of (1.29) by ψ_{0n}^* and make an integration over all space, and using the fact that $\langle\psi_{0n}|\psi_{0m}\rangle = \delta_{nm}$, we can get

$$E_{1n} = \hat{H}'_{nn}, \tag{1.30}$$

where

$$\hat{H}'_{nn} = \langle 0n|\hat{H}'|0n\rangle. \tag{1.31}$$

The above expression is the first-order energy correction which is just the expectation value of the perturbation operator. We now move our attention to the calculation of the first-order correction to the eigenfunction. This can be done by multiplying both sides of (1.29) by ψ_{0m}^* (where $m{\neq}n$) and integrate over all space. Through this way, we can get

$$a_{nm} = \frac{\hat{H}'_{mn}}{E_{0n} - E_{0m}} \quad (m{\neq}n), \tag{1.32}$$

where $\hat{H}'_{mn} = \langle 0m|\hat{H}'|0n\rangle$ is the matrix element. Therefore, the wave function ψ_n in (1.23) becomes

$$\psi_n = (1 + a_{nn})\psi_{0n} + \sum_{k\neq n} \frac{\hat{H}'_{kn}}{E_{0n} - E_{0k}}\psi_{0k} + ... \tag{1.33}$$

The above expression can be significantly simplified by setting $a_{nn} = 0$ but without the loss of generality,[1] which leads to the following expression of the wave function ψ_n (up to the first-order correction)

$$\psi_n = \psi_{0n} + \sum_{k\neq n} \frac{\hat{H}'_{kn}}{E_{0n} - E_{0k}}\psi_{0k}. \tag{1.34}$$

We now proceed to consider the second-order corrections. Following a similar way as we did previously for the first-order corrections, we write ψ_{2n} as a linear combination of the wave functions of the unperturbed system:

$$\psi_{2n} = \sum_k b_{nk}\psi_{0k}. \tag{1.35}$$

Substituting this expression into (1.27) and making some rearrangements, it is not difficult to obtain the following expression:

$$\sum_k b_{nk}(E_{0k} - E_{0n})\psi_{0k} + \sum_k a_{nk}(\hat{H}' - E_{1n})\psi_{0k} = E_{2n}\psi_{0n}. \tag{1.36}$$

Multiplying both sides of (1.36) by ψ_{0n}^* and making an integrating over all space, we have

$$E_{2n} = \sum_{k \neq n} a_{nk} \hat{H}_{nk}. \tag{1.37}$$

Considering the expression (1.32) and the fact that $\hat{H}$ is Hermitian operator which means that $\hat{H}'_{kn} = \hat{H}'^*_{nk}$, (1.37) becomes

$$E_{2n} = \sum_{k \neq n} \frac{|\hat{H}'_{kn}|^2}{E_{0n} - E_{0k}}. \tag{1.38}$$

This expression is the second-order correction of the eigenenergy of the perturbed system. Normally, we could also proceed with the calculation of the second-order correction in the eigenfunction and even up to higher-order corrections. However, the expressions become significantly complicated. Thus, it often stops the correction of the wave function at the first order, otherwise, it would be better to search some other methods for solving the problem.[1]

If one or more of the eigenenergies from expression (1.34) (or (1.38)) are degenerate, which means one or more E_{0k} equals to E_{0n}, one of the denominators $(E_{0n} - E_{0k})$ in (1.34) (or (1.38)) would be zero. This would result in an infinite value in the series. Therefore, a developed perturbation theory for the degenerate systems is often needed. Since we are only interested on the general idea of the perturbation theory and its limitations rather than the applications of this type of theory in real systems, a detailed explanation for the extended perturbation theory for the degenerate systems will not be further covered in the Thesis. However, the ones who have special interests can find it in Refs. [1, 2]. As mentioned previously, the perturbation theory could be useful for the cases that the perturbation is sufficiently small in comparison to the unperturbed system. However, practically, most of the cases we want to study do not satisfy this condition. Moreover, The convergence problem is also in connection with this type of theory.

1.3.2 Ritz variational method

Anthoer method which is widely used to solve the Schrödinger equation is the variational method. The key point of this method is to have a good initial guess to the form of the ground-state eigenfunction corresponding to a given system. Let us consider that ψ_{trial} to be the trial wave function of a system under consideration described by operator $\hat{H}$. This function typically contains a set of parameters α_i $(i = 1, 2, ..., n$, where n is the total

number of the parameters). That is:

$$\psi_{trial} = \psi_{trial}(\alpha_1, \alpha_2, ..., \alpha_n), \tag{1.39}$$

where these parameters are often called as "variational parameters". Employing the trial wave function ψ_{trial} which is assumed to be not normalized, the expectation value $\langle \hat{H} \rangle$ can be given by

$$\langle \hat{H} \rangle(\alpha_1, \alpha_2, ..., \alpha_n) = \frac{\int \psi^*_{trial} \hat{H} \psi_{trial} d\tau}{\int \psi^*_{trial} \psi_{trial} d\tau}. \tag{1.40}$$

The ground-state energy of the system under consideration E_0 can be obtained by minimizing the above equation with respect to the variational parameters, which is

$$E_0 = \min_{\alpha_1, \alpha_2, ..., \alpha_n} \langle \hat{H} \rangle. \tag{1.41}$$

As discussed before, the variational method depends significantly on the trial wave function. The choice of the trail wave function affects strongly the accuracy of the results.

1.3.3 Matrix diagonalization method

Another one of the most popular methods for the solution of the Schrödinger equation is the matrix diagonalization method. Within this method, the eigenfunction $\widetilde{\psi}$ of the system under investigation can be expanded as

$$\widetilde{\psi} = \sum_{i=1}^{N} c_i |\phi_i\rangle, \tag{1.42}$$

where $\{|\phi_i\rangle\}$ is a fixed set of N basis functions. We assume that the basis functions are real and orthonormal, that is,

$$\langle \phi_i | \phi_j \rangle = \langle \phi_j | \phi_i \rangle = \delta_{ij}. \tag{1.43}$$

The matrix representation of the Hamiltonian operator $\hat{H}$ by using the basis functions $\{|\phi_i\rangle\}$ can be written as

$$\mathbf{H}_{ij} = \langle \phi_i | \hat{H} | \phi_j \rangle, \tag{1.44}$$

Since the eigenfunction $\widetilde{\psi}$ is normalized, we can get

$$\langle \widetilde{\psi} | \widetilde{\psi} \rangle = \sum_{ij} c_i c_j \langle \phi_i | \phi_j \rangle = \sum_i c_i^2 = 1. \tag{1.45}$$

The expectation value $\langle \hat{H} \rangle$, which is a function of the coefficients c_i $(i = 1, ..., N)$, is

$$\langle \hat{H} \rangle = \sum_{ij} c_i \langle \phi_i | \hat{H} | \phi_j \rangle c_j = \sum_{ij} c_i c_j \mathbf{H}_{ij}. \tag{1.46}$$

The problem for us is to find a set of parameters c_i^0 $(i = 1, ..., N)$ so that the expectation value $\langle \hat{H} \rangle$ is a minimum. This can be solved by the *Lagrange's method of undetermined multipliers*. We firstly construct a function

$$\begin{aligned} \ell(c_1, c_2, ..., c_N, E) &= \langle \widetilde{\psi} | \hat{H} | \widetilde{\psi} \rangle - E(\langle \widetilde{\psi} | \widetilde{\psi} \rangle - 1) \\ &= \sum_{ij} c_i c_j H_{ij} - E(\sum_i c_i^2 - 1), \end{aligned} \tag{1.47}$$

where E is the eigenenergy. Considering (1.45), it is easy to find out that we have only added zero to the rightmost side of (1.46). Therefore, the minimum values of both $\langle \hat{H} \rangle$ and ℓ should occur at the same values of the coefficients c_i^0 $(i = 1, ..., N)$. If we arbitrarily choose $c_1, c_2, ..., c_{N-1}$ as independent and c_N is determined by the normalization condition (1.45), then we have

$$\frac{\partial \ell}{\partial c_k} = 0, \quad k = 1, 2, ..., N - 1, \tag{1.48}$$

but $\partial \ell / \partial c_N$ is not necessarily zero. We now choose the multiplier E so that $\partial \ell / \partial c_N = 0$ does equal zero. Consequently, for all c_i $(i = 1, 2, ..., N)$, we have

$$\frac{\partial \ell}{\partial c_k} = 0, \quad k = 1, 2, ..., N. \tag{1.49}$$

Using (1.47), we can further develop (1.49) into

$$\frac{\partial \ell}{\partial c_k} = 0 = \sum_j c_j H_{kj} + \sum_i c_i H_{ik} - 2E c_k. \tag{1.50}$$

Since $\hat{H}$ is Hermitian, i.e., $\mathbf{H}_{ij} = \mathbf{H}_{ji}$, we have

$$\sum_j \mathbf{H}_{ij} c_j - E c_i = 0. \tag{1.51}$$

If we introduce a column vector $\mathbf{c}$ with element c_i, the above expression can be written in matrix notation as

$$\mathbf{H}\mathbf{c} = E\mathbf{c}. \tag{1.52}$$

This is the standard eigenvalue problem which can be solved by diagonalizing the matrix $\mathbf{H}$. Instead of finding just one eigenvalue E and the corresponding coefficients, we actually

have found N solutions, which are E_α ($\alpha = 0, 1, ..., N-1$) for the eigenenergies with $E_0 \leq E_1 \leq ... \leq E_{N-1}$ and c_i^α for the expansion coefficients. The lowest eigenvalue E_0 is the best approximation to the ground state energy of the system under consideration within the truncated Hilbert space $\{|\phi_i\rangle, i = 1, 2, ..., N\}$.

As pointed out by Rieth et al.,[3] the problems involved in the matrix diagonalization method are: (i) if the selected basis functions $|\phi_i\rangle$ do not well represent the physical properties of the system under consideration, the number of the basis functions N has to be so large that the dimension of the $N \times N$ Hamiltonian matrix $\mathbf{H}_{ij}$ can be extremely large. Numerically solving directly the problem becomes highly unstable and hence numerically ill-suited;[4] (ii) in some cases, the discrete basis set $\{|\phi_i\rangle, i = 1, 2, ..., N\}$ is not complete since there are continuum components which are necessary. If we do need these continuum components in the expansion, then the matrix diagonalization method is no longer applicable. A typical example can be found in Ref. 5 with regarding the calculation of the quadratic Zeeman effect for the hydrogen atom in strong white dwarf or neutron star magnetic fields.

1.3.4 Potential morphing method

Potential morphing method is a robust method developed by Rieth, Schommers and Baskoutas.[3] In an attempt to describe the potential morphing method, we consider that a particle with mass m moves in an arbitrary potential v_S. Here, the subscript S donates the system under consideration. The time-independent Schrödinger equation in this case can be written as

$$\{-\frac{\hbar^2}{2m}\bigtriangledown^2 + v_S(\mathbf{r})\}\psi_S(\mathbf{r}) = E_S\psi_S(\mathbf{r}), \tag{1.53}$$

where $\hbar$ is the Planck constant divided by 2π, E_S and $\psi_S(\mathbf{r})$ are the eigenvalue and eigenfunction of the system S, respectively, and $\mathbf{r}$ is the position vector. In order to employ potential morphing method to solve equation (1.53), we need a reference system (donated by R) with well-known potential v_R, eigenvalues E_R and eigenfunction ψ_R, which satisfy the following time-independent Schrödinger equation:

$$\{-\frac{\hbar^2}{2m}\bigtriangledown^2 + v_R(\mathbf{r})\}\psi_R(\mathbf{r}) = E_R\psi_R(\mathbf{r}). \tag{1.54}$$

The essential point of potential morphing method is that the transition from the reference system R to the system under consideration S can be performed by means of the time-dependent Schrödinger equation:

$$i\hbar\frac{\partial\psi(\mathbf{r},t)}{\partial t} = \{-\frac{\hbar^2}{2m}\bigtriangledown^2 + v_t(\mathbf{r})\}\psi(\mathbf{r},t), \tag{1.55}$$

where

$$v_t(\mathbf{r}) = \sigma(t)v_S(\mathbf{r}) + [1-\sigma(t)]v_R(\mathbf{r}), \tag{1.56}$$

with $\sigma(t)$ having the following property

$$\sigma(t) = \begin{cases} 0, & t \leq t_a \\ 1, & t \geq t_b \end{cases}, \tag{1.57}$$

where t_a is the morphing starting moment, t_b is the morphing ending moment, for time $t_a < t < t_b$, the function $\sigma(t)$ may have any shape but should vary monotonically with respect to time t. This property of $\sigma(t)$ enables the form of the wave function $\psi(\mathbf{r},t)$ to be the following,

$$\begin{cases} \psi(\mathbf{r},t) = \psi_R(\mathbf{r},t) = C_R \exp(-\frac{iE_R t}{\hbar})\psi(\mathbf{r}) & \textbf{if} \quad t \leq t_a \\ \psi(\mathbf{r},t) = \psi_S(\mathbf{r},t) = C_S \exp(-\frac{iE_S t}{\hbar})\psi(\mathbf{r}) & \textbf{if} \quad t \geq t_b \end{cases}, \tag{1.58}$$

We divide the time interval $t_b - t_a$ into N parts and the time step can be defined as $\Delta t = (t_b - t_a)/N$. If the value N is sufficiently large so that Δt can be sufficiently small, the perturbation to the wave function from time to time can be required as significantly small. Following this idea, if we integrate both sides of (1.55) with respect to time t for $t \in [t_a, t_1]$, we get

$$\psi(\mathbf{r},t_1) - \psi(\mathbf{r},t_a) = \frac{1}{i\hbar}\int_{t_a}^{t_1} \{-\frac{\hbar^2}{2m}\nabla^2 + v_t(\mathbf{r})\}\psi(\mathbf{r},t)dt, \tag{1.59}$$

where $t_1 = t_a + \Delta t$. By considering the fact that $\psi(\mathbf{r},t_a) = \psi_R(\mathbf{r},t_a)$ which is well-known as required previously, the wave function after the first time step can be written as

$$\psi(\mathbf{r},t_1) = \psi_R(\mathbf{r},t_a) + \delta\psi^1 \tag{1.60}$$

with the perturbation $\delta\psi^1(\mathbf{r})$ being

$$\delta\psi^1(\mathbf{r}) = \frac{1}{i\hbar}\int_{t_a}^{t_1} \{-\frac{\hbar^2}{2m}\nabla^2 + v_t(\mathbf{r})\}\psi(\mathbf{r},t)dt. \tag{1.61}$$

From the above expression, we can see that if the time step Δt can be chosen as sufficiently small, the numerical integration can be realized with any degree of freedom. After knowing $\psi(\mathbf{r},t_1)$, we can follow a similar procedure and proceed with the second time step, the third time step and so on and so forth. After finishing all the time steps, the wave function $\psi(\mathbf{r},t_N)$ is

$$\psi(\mathbf{r},t_N) = \psi_R(\mathbf{r},t_a) + \sum_{i=1}^{N}\delta\psi^i(\mathbf{r}) \quad . \tag{1.62}$$

If one takes a look at (1.58), it is not difficult to find out that the wave function of the system S $\psi_S(\mathbf{r}) = \psi(\mathbf{r}, t_N)$. The corresponding eigenvalue is given by

$$E_S = \int \psi_S^*(\mathbf{r})\{-\frac{\hbar^2}{2m}\nabla^2 + v_s(\mathbf{r})\}\psi_S(\mathbf{r})d\mathbf{r}. \tag{1.63}$$

It should be noted that: (i) the wave functions of the system S are automatically orthogonal and normalized to be unity providing that their counterparts of the system R have the same properties; (ii) the choice of the reference system does not affect the final results because the potential morphing method needs only a known reference system to start the morphing process and finally to give the eigenfunctions and eigenvalues for the unknown system, independently on the choice of the initial reference system. In general, potential morphing method is a powerful method which can be used for the determination of the eigenvalues and eigenfunctions of a system with any arbitrary shape of potential. In comparison to the other methods we discussed previously, the advantages of this method is very obvious. In the following chapters of this part of the Thesis, we would like to employ the potential morphing method in the framework of the effective-mass approximation for the studies of the shallow donor impurity-related properties and optical nonlinearities in several semiconductor nanostructures.

2

Stark effect of donor binding energy in a self-assembled GaAs quantum dot subjected to an electric field

*In this chapter, the donor binding energy distribution with respect to the dopant positions in self-assembled GaAs/AlGaAs quantum dots in the presence of a tilted electric field is studied. It is found that there is a critical line in a doping plane, corresponding to zero Stark shift of the donor binding energy. At low electric fields, our work reveals that Stark shift of an on-center donor binding energy is a purely quadratic function of the electric field strength, irrespective of quantum dot dimensions and field orientations. This scaling law permits us to indirectly estimate the impurity polarizability in a self-assembled quantum dot. The results presented herein are published in Physics Letters A **376**, 2712 (2012).*

Contents

2.1 Introduction

Doping semiconductor quantum dots (QDs) allows tuning many properties for tailoring quantum devices and it provides further means to control their performance.[6] Moreover, donors have already been used in some elegant quantum computing proposals that draw upon the vast expertise of the semiconductor device industry.[7] Therefore, the binding energy of impurities confined in semiconductor QDs has been extensively studied using different numerical methods and several confining potential shapes.[8–12] In all these reports, only a few impurity positions (on the growth direction or along the radial direction) are considered. Furthermore, application of an external electric field induces the carriers distribution polarization and shifts the energy states. These effects considerably change the energy spectrum of the carriers, which may be used to control and modulate the intensity output of devices. Consequently, this makes the external electric field an effective tool for studying the physical properties of semiconductor nanostructures, both from theoretical and practical points of view. It is well known that when an electric field is applied in a semiconductor QD in which the carriers (electron or hole) are confined in all three directions, the quantum-confined Stark effect appears. Due to this effect, the symmetry of the electron probability density distributions at zero electric field breaks and the maximum of the electron probability density moves away from the QD center to the opposite direction of the applied field. Consequently, the donor binding energy corresponding to the doping positions which are located opposite to applied field direction exhibits blue shift. Conversely, red shift takes place if the doping positions are distributed along the field direction. Are there any doping positions in the QD at which the donor binding energy keeps invariant (zero shift) under the influence of an applied electric field?

On the other hand, quantum-confined Stark effect on the exciton energy in a semiconductor self-assembled QD has been extensively investigated,[13–18] indicating that a shift of the excitonic peak in absorption or photoluminescence (PL) spectra, for small electric field F, has the form $\delta E(F) = E(F{\neq}0) - E(F = 0){\approx}\alpha^X F - \beta^X F^2$, where α^X and β^X are, respectively, the components of the permanent dipole moment and the polarizability. Especially, if the symmetry of the problem rules out a preferential direction, the Stark shift is an even function of F and the expansion begins with the polarizability term ($\alpha^X{=}0$). As is well known, the donor impurity behaves like an exciton with infinite hole effective mass. Therefore, a question which naturally arises is the following: what is the relation connecting the Stark shift of the donor binding energy with the applied electric field in a self-assembled semiconductor QD ?

To put a quantitative answer to the questions addressed before, in this chapter, we performed detailed theoretical investigations on the donor binding energy distributions

with respect to the dopant positions in a self-assembled GaAs/AlGaAs QD, considering the effect of an applied tilted electric field. The numerical approach we used is potential morphing method[3] (see also Chapter 1) in the framework of effective-mass approximation.

2.2 Theoretical model

It is well-known that the self-assembled QDs are quasi-two dimensional structures which strongly confine the carriers (electron or hole) in the growth direction, while the lateral confinement is typically softer. Due to this fact, GaAs/AlGaAs QDs with cylindrical shape are adopted for our model calculations (see Fig. 2.1). The parameter L referred to the dot height is responsible for the QD growth-direction (z-axial direction) quantum confinement. Whereas the parameter R referred to the dot radius is responsible for the QD lateral quantum confinement.

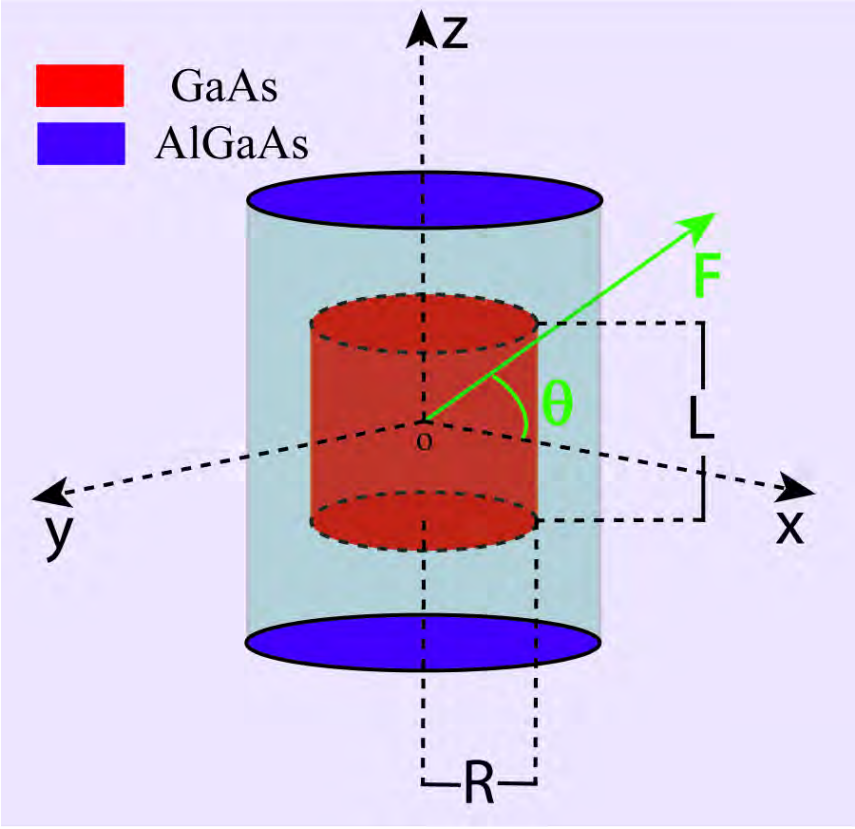

Figure 2.1: Schematic representation of the self-assembled GaAs/AlGaAs QD under investigation with the dot height L and the radius R in the presence of an electric field F applied parallel to the xoz plane making an angle θ relative to the x axis.

In the framework of the effective-mass approximation, a shallow donor impurity embedded in a self-assembled QD is modeled by the Hamiltonian

$$\hat{H} = \hat{p}\frac{1}{2m_e^*}\hat{p} + V(\vec{r}) + V_F(\vec{r}) - \frac{e^2}{\varepsilon|\vec{r} - \vec{r_i}|}, \tag{2.1}$$

where m_e^* is the electron effective mass, $V(\vec{r})$ is the electron confinement potential, which is assumed to zero insider the QD and V_0 outside the QD (V_0 is the conduction band discontinuity). $V_F(\vec{r})$ is the electrostatic potential induced by the tiled electric field applied parallel to the xoz plane making an angle θ relative to the x axis (see Fig. 2.1), which is given by

$$V_F(\vec{r}) = eF(x\cos\theta + z\sin\theta), \tag{2.2}$$

where e is the absolute value of the electron charge, F is the magnitude of the applied electric field. The last term of Eq. (2.1) represents the Coulomb interaction between the electron and the shallow donor impurity which is located at $r_i = (x_i, y_i, z_i)$ and ε is the static dielectric constant. It should noted here that due to the symmetry consideration, the dopant positions considered in the present calculations are distributed in the xoz plane ($y_i = 0$).

The ground-sate donor binding energy is defined as the difference between the ground-state energies of the free electron and that of the donor, which is the following

$$E_b = E_0 - \widetilde{E}, \tag{2.3}$$

where $\widetilde{E}$ is the energy which corresponds to the Hamiltonian in Eq. (2.1) and E_0 is the energy without Coulomb interaction (absence of the last term in Eq. (2.1)). In order to obtain the ground state energy of the electron (E_0) and the donor ($\widetilde{E}$) as well as corresponding wave functions, PMM, which has been described in the previous chapter, is employed. In the present numerical calculations, the usual three-dimensional (3D) harmonic oscillator is taken as a reference system and its ground state wave function is selected as the initial wave function (Φ_R). The interaction potential corresponding to the ground-state energy of the electron (E_0) is

$$v_S^e = V(\vec{r}) + V_F(\vec{r}). \tag{2.4}$$

Whereas, the interaction potential corresponding to the ground-state energy of the donor ($\widetilde{E}$) is

$$v_S^d = V(\vec{r}) + V_F(\vec{r}) - \frac{e^2}{\varepsilon|\vec{r} - \vec{r_i}|}. \tag{2.5}$$

To further understand the electric field effect on the donor binding energy in a semiconductor QD, the Stark shift of the donor binding energy is defined as the difference between the

binding energy of a donor impurity at electric field $F \neq 0$ (a finite electric field) and its binding energy at $F = 0$ (zero electric field), which can be given by

$$\delta E_b = E_b(F \neq 0, \theta) - E_b(F = 0, \theta). \tag{2.6}$$

The negative Stark shift of the donor binding energy ($\delta E_b < 0$) means essentially the electric field effect makes the donor binding energy "red shift". Conversely, the "blue shift"of the donor binding energy takes place if the Stark shift of the donor binding energy is positive ($\Delta E_b > 0$).

2.3 Results and discussion

Before presenting the numerical results obtained from our model calculations, it is deserved to discuss the validity of the effective mass approximation in small systems. As mentioned by several authors,[12,19,20] validity of effective mass approximation in semiconductor QD depends on the range of the Bloch function wave vectors necessary to construct the envelope wave function for the dot. This range has to be much smaller than the width of the Brillouin zone. For GaAs QD, the effective mass approximation is valid for the case of dot size larger than $2 - 3$ nm.[12] To insure the validity, the sizes of the QDs in our calculations are much larger than the aforementioned critical dot size value. The physical parameters used in our calculations are $\varepsilon = 12.4$ and $V_0 = 228$ meV. As verified by Li and Xia,[21] the effective-mass mismatch has considerable influence on the high excited states but it only weakly affects the ground-state donor binding energy and the low excited states. Thus, in our calculations, a position independent electron effective mass ($m_e^* = 0.0667 m_0$) is used as a reasonable approximation. These parameters are suitable for GaAs/Al_xGa_{1-x}As heterostructures with aluminum concentration $x \approx 0.3$. First of all, in an effort to obtain a quantitative understanding of the dependence of donor binding energy on the dopant positions in the presence of an applied electric field, we create suitable contour plots (Fig. 2.2) of the Stark shift of the donor binding energy ($\delta E_b = E_b(F \neq 0) - E_b(F = 0)$) for various dopant positions in a cylindrical GaAs QD with different dot configurations. The field strength is $F = 50$ kV/cm and tilted angle $\theta = 45°$. It is interesting to find from Fig. 2.2 that for any dot configuration, there is a critical line determined by $\delta E_b = 0$. The doping region above the critical line satisfying $\delta E_b < 0$ represents the red shift of the donor binding energy and the doping area below the critical line described by $\delta E_b > 0$ shows the blue shift of the donor binding energy. By observing these plots, it is found that the critical line exhibits two distinct features. One is horizontal displacement (shift to left/right-hand side) and the other one is planar rotation. Although both of them are due to the applied electric field effect, their behaviour is differently influenced by the QD

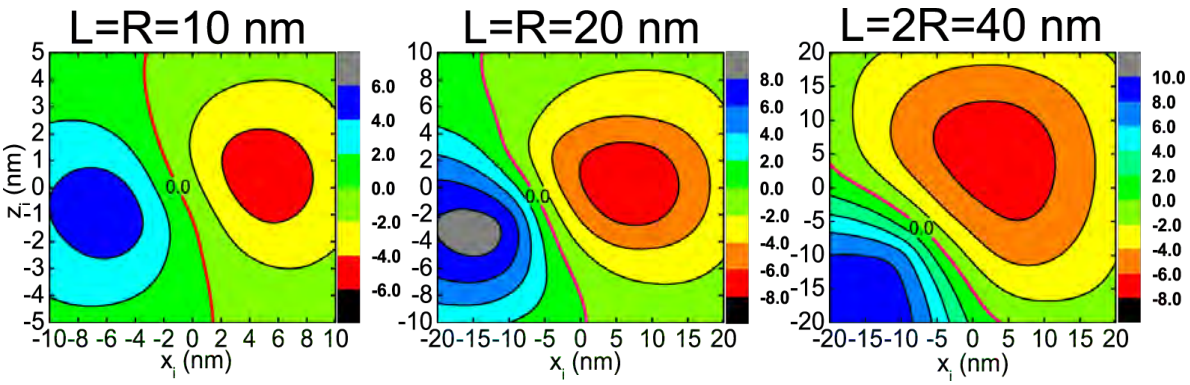

Figure 2.2: Contour plots of the Stark shift of the donor binding energy (in unit of meV) for various dopant positions distributed in xoz plane of a GaAs/$Al_{0.3}Ga_{0.7}$As cylindrical QD with different dot configurations subjected to an uniform electric field ($F = 50$ kV/cm, $\theta = 45°$).

geometric characteristics, such as dot sizes and aspect ratios ($\rho = L/R$). As is observed in Fig. 2.2, for a specific QD aspect ratio (i.e. $\rho = 1$), the critical line appears to show a left-hand displacement and simultaneously a counterclockwise planar rotation as the dot size increases (see the first two plots). Whereas, if the QD aspect ratio increases (see the last two plots of Fig. 2.2), a right-hand displacement of the critical line takes place and simultaneously the counterclockwise planar rotation is significantly more intense. Especially, for a weak-confinement cylindrical QD with aspect ratio $\rho = 2$ (see the last plot of Fig. 2.2), the area corresponding to the "red" shift of the donor binding energy is dominant. The critical line is displaced far from the center of the doping plane and preferably rotated to be perpendicular to the field direction. These novel behaviour is attributed to the competition effects between the applied electric field and geometric confinement.

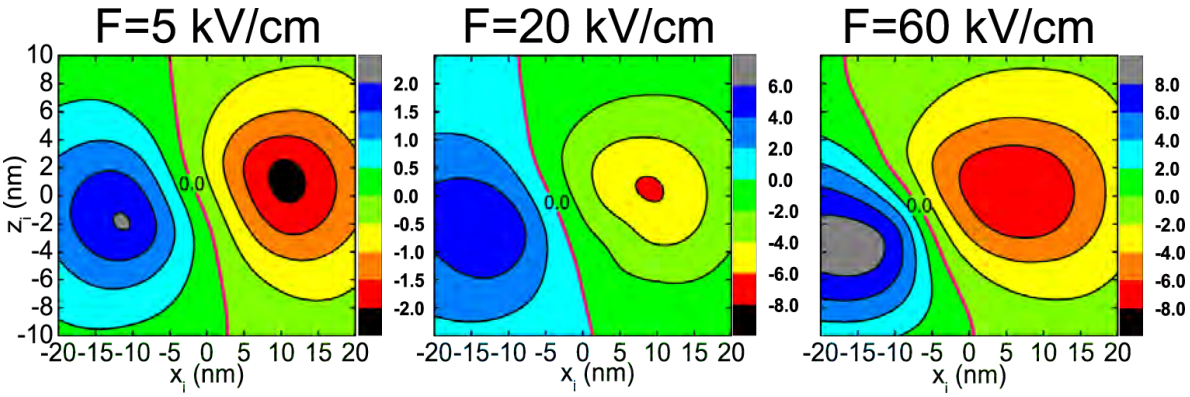

Figure 2.3: Contour plots of the Stark shift of the donor binding energy (in unit of meV) for various dopant positions distributed in xoz plane of a GaAs/$Al_{0.3}Ga_{0.7}$As cylindrical QD with dot height $L = 20$ nm and radius $R = 20$ nm, considering different electric field magnitudes at tilted angle $\theta = 45°$.

For a self-assembled cylindrical QD with aspect ratio $\rho = 1$ and radius $R = 20$ nm, we have also displayed the contour plots of Stark shift of the donor binding energy for various dopant positions in Fig. 2.3, in which different field strengths ($\theta = 45°$) are considered. As expected, the critical line corresponding to zero shift of the donor binding energy appears in any field strength configuration. Generally, the enhancement of the applied field causes the enlargement of the doping area corresponding to the red shift of the donor binding energy. Particularly, it is found that the increase of the field strength practically has negligible influence on the translational displacement of the critical line. Conversely, it has a significant effect on the planar rotation. As can be seen from Fig. 2.3, the counterclockwise rotation of the critical line is significantly enhanced as the field strength increases.

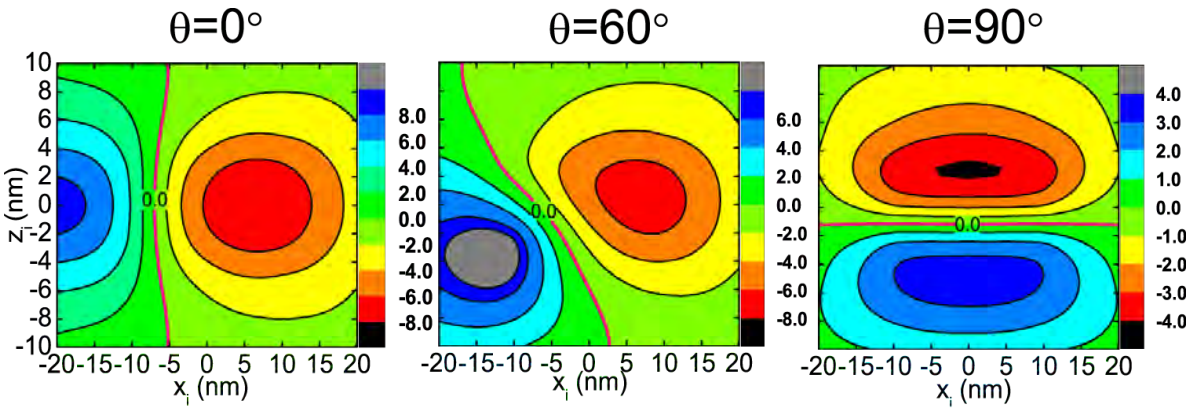

Figure 2.4: Contour plots of the Stark shift of the donor binding energy (in unit of meV) for various dopant positions distributed in xoz plane of a GaAs/$Al_{0.3}Ga_{0.7}As$ cylindrical QD with dot height $L = 20$ nm and radius $R = 20$ nm, considering different electric field orientations with strength $F = 50$ kV/cm.

In accordance to the previous reports about the tilted electric field effect on the electron[22] and magnetoexciton states,[23] the applied field orientation also significantly affects the electron and excitonic properties. At this point, one may expect that the relative orientation of the applied field may also has considerable effect on the Stark shift of the donor binding energy. To check this assumption, in Fig. 2.4, we displayed several contour plots of the Stark shift of the donor binding energy for various dopant positions in the same QD configuration as in Fig. 2.4, considering different field orientations. As is observed, the critical line determined by $\delta E_b = 0$ appears for any field orientation. Variation of the field orientation from the in-plane direction ($\vec{F} \| \vec{x}$) to the growth direction ($\vec{F} \| \vec{z}$) leads to the shrinking of the doping area corresponding to the red shift of the donor binding energy. It is also found from Fig. 2.4 that increasing the titled angle turns out to shift the critical line to the right-hand side of the doping plane and simultaneously leads to a

counterclockwise planar rotation. Especially, when the field is applied along the growth direction (see the last plot of Fig. 2.4), the Stark shift of the donor binding energy exhibits obviously axially symmetric distributions (with respect to $x_i = 0$ axis) in the doping plane. Moreover, the critical line corresponding to the zero shift of the donor binding energy is distributed apparently perpendicular to the field direction and vertically but slightly displaced from the center of the doping plane.

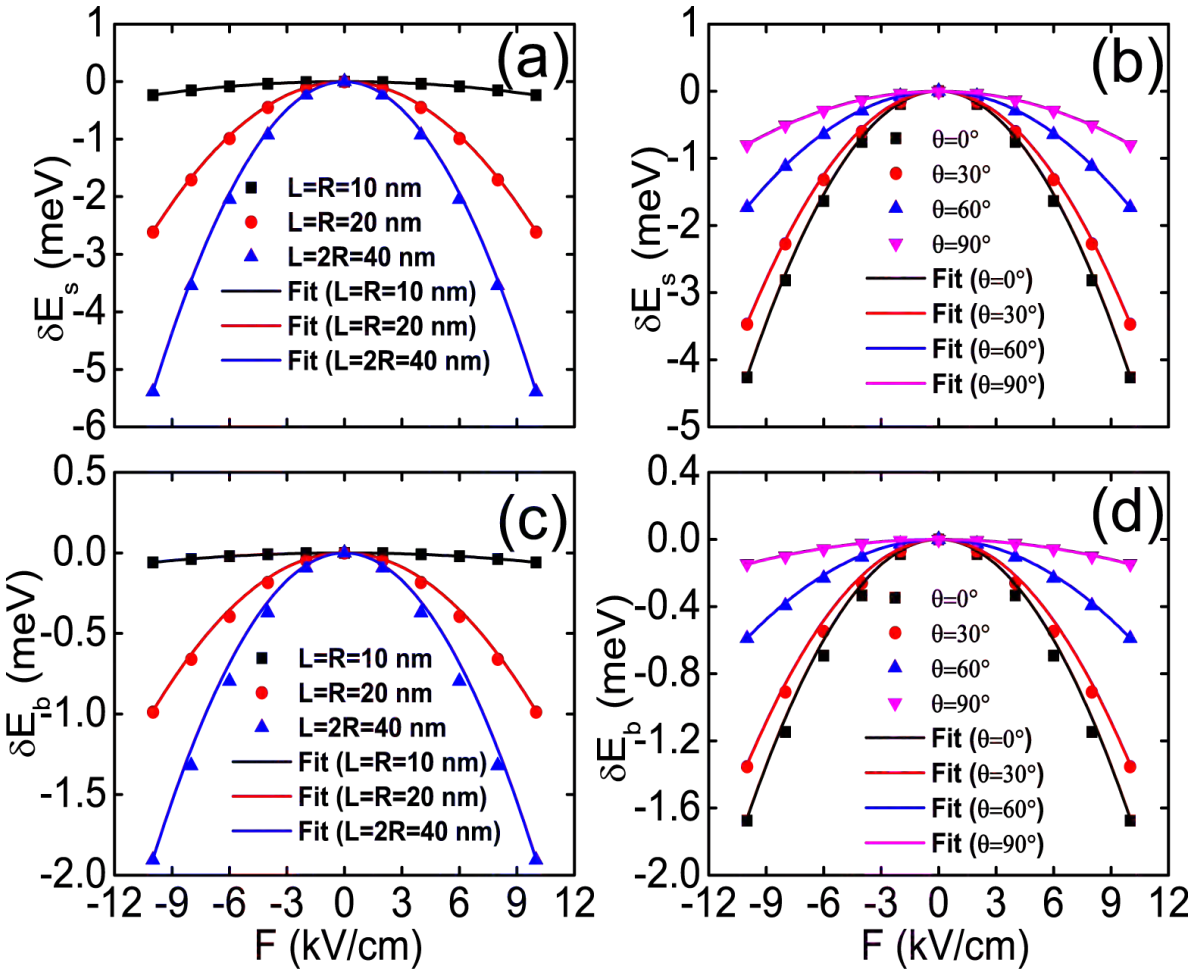

Figure 2.5: Variation of the ground-state electron subband energy δE_s ((a) and (b)) and Stark shift of binding energy of an on-center donor impurity δE_b ((c) and (d)) in a self-assembled GaAs/$Al_{0.3}Ga_{0.7}$As QD as a function of the electric field strength (symbols). In each figure, each solid line represents a fit to a purely quadratic field dependence of the energy variation ($\delta E_i = E_i(F \neq 0) - E_i(F = 0) \approx -\beta^i F^2$ ($i = s$ or b)). (a) and (c) are for different QD configurations and $\theta = 45°$, while (b) and (d) are for different field orientations and $L = R = 20$ nm, respectively.

Finally, in order to examine whether the aforementioned relation for the field dependence of the Stark shift of the exciton energy is also valid for the Stark shift of the donor binding

energy, we firstly present in Fig. 2.5(a) and (b) the change of the ground-state electron subband energy δE_s ($\delta E_s(F) = E_s(F{\neq}0) - E_s(F = 0)$, where E_s is the ground state electron subband energy) as a function of the applied field strength in a self-assembled GaAs QD, considering different QD configurations (Fig. 2.5(a)) and field orientations (Fig. 2.5(b)). As can be seen from Fig. 2.5(a) and (b), δE_s decreases quadratically with the applied electric field, irrespective of the QD dimensions and the applied field orientations. This finding is in excellent agreement with a general quantum mechanical theorem[24] which states that the ground-state energy is a concave function of any parameter that enters linearly in the Hamiltonian. This is a quite general result, which does not depend on the model Hamiltonian used.

Table 2.1: Theoretical values of β^s and β^b (in unit of $meV \cdot cm^2 \cdot kV^{-2}$) obtained from the fits in Fig. 2.5(a) and (c), respectively.

QD Configurations	β^s	β^b
$L = R = 10$ nm	$(2.34{\pm}0.003){\times}10^{-3}$	$(0.59{\pm}0.002){\times}10^{-3}$
$L = R = 20$ nm	$(26.1{\pm}0.17){\times}10^{-3}$	$(9.8{\pm}0.15){\times}10^{-3}$
$L = 2R = 40$ nm	$(53.87{\pm}0.4){\times}10^{-3}$	$(19.03{\pm}0.42){\times}10^{-3}$

Table 2.2: Theoretical values of β^s and β^b (in unit of $meV \cdot cm^2 \cdot kV^{-2}$) obtained from the fits in Fig. 2.5(b) and (d), respectively.

Tilted angle	β^s	β^b
$\theta = 0°$	$(42.52{\pm}0.402){\times}10^{-3}$	$(16.62{\pm}0.37){\times}10^{-3}$
$\theta = 30°$	$(34.62{\pm}0.263){\times}10^{-3}$	$(13.43{\pm}0.24){\times}10^{-3}$
$\theta = 60°$	$(17.26{\pm}0.081){\times}10^{-3}$	$(5.89{\pm}0.07){\times}10^{-3}$
$\theta = 90°$	$(7.94{\pm}0.016){\times}10^{-3}$	$(1.48{\pm}0.02){\times}10^{-3}$

To understand qualitatively the donor binding energy variation under the influence of an applied electric field, we also investigated, in Fig. 2.5(c) and (d), the Stark shift of the binding energy corresponding to an on-center donor impurity as a function of the field strength for different QD dimensions (Fig. 2.5(c)) and electric field orientations (Fig. 2.5(d)). In general, donor's intrinsic dipole moment becomes orientated by the applied electric field, irrespective of dopant positions in a self-assembled QD. Due to an additional separation of the electron and ionized donor impurity (e^-/D^+), the induced dipole moment

will also interact with the applied electric field. In total, this results in a change of the donor binding energy as $\delta E_b \approx \alpha^D F - \beta^D F^2$, where the coefficients α^D and β^D donate impurity permanent dipole moment and impurity polarizability, respectively. As can be seen from Fig. 2.5(c) and (d), it is interesting to find that δE_b decreases (red shift) quadratically with the applied electric field for any dot configuration and field orientation. This therefore suggests the absence of a permanent dipole moment in each case considered. This result is in good agreement with the symmetry consideration which states that any system with an inversion symmetry does not have a permanent dipole moment ($\alpha^D = 0$). On the other hand, the fits in Fig. 2.5(c) and (d) also suggest a good way to estimate the impurity poloarizability. As indicated in Tables. 2.1 and 2.2 (see the third column), the impurity polarizability is in order of $10^{-3} meV \cdot cm^2 \cdot kV^{-2}$, which is comparable with its exciton counterpart as shown in the previous literature.[17,18] After making a comparison between β^s and β^b listed in Tables. 2.1 and 2.2, it is easy to find that both coefficients are similarly affected by the QD dimensions or the field orientations. Increase of QD dimension results in significantly increase in the two coefficients, while tilting the electric field from the lateral direction to the growth direction turns out to decrease both of them. This is a good reflection of the competition effects between the quantum confinement and applied electric field. More specially, comparing to δE_s, it is found that the applied electric field effect on δE_b is less effective (β^s is much larger than β^b in each case). This is because of the Coulomb attraction between the electron and the donor impurity which inhibits the displacement of the electron probability density far from the impurity center.

2.4 Brief summary

To summarize, we have studied the Stark shift of the donor binding energy distributions with respect to the dopant positions in a self-assembled GaAs/$Al_{0.3}Ga_{0.7}As$ QD subjected to an applied electric field. The electric field is tilted from the QD growth direction. It is found that there is a critical line in the doping plane corresponding to the zero shift of the donor binding energy. The doping area above the critical line shows the red shift of the donor binding energy and that below the critical line represents the blue shift. The position of the critical line is strongly affected by the QD size, its aspect ratio and the strength and orientation of the applied electric field. Our results also indicate that the variation of the ground-state electron subband energy and the Stark shift of an on-center donor binding energy, for small electric field (0-10 kV/cm in our calculations), are purely quadratic functions of the field strength, irrespective of the QD configurations and the field orientations. More specially, it is found that comparing to the variation of the ground-state electron subband energy under the influence of the applied electric field, the applied field

effect on the Stark shift of the on-center donor binding energy is less effective. We believe that the results presented here can be useful for design and application of some commonly used δ-doped self-assembled GaAs/AlGaAs QD based optoelectronic devices. We also hope that our results can stimulate forthcoming theoretical and experimental investigations in this attracting research area.

3

Tuning the binding energy of surface impurities in cylindrical GaAs/AlGaAs quantum dots by a tilted magnetic field

In this chapter, the effect of a tilted magnetic field on the binding energy of surface impurities in GaAs/AlGaAs cylindrical quantum dots is studied by using the potential morphing method in the framework of the effective-mass approximation. It is found that contrary to what was expected based on the existing literature for growth-direction magnetic fields, the presence of a tilted field does not always contribute positively to the binding energy of surface impurities. The shape (aspect ratio) and size of the cylindrical quantum dot as well as the dopant positions at the quantum dot surface play an important role. Furthermore, we find that decrease of the quantum dot size can reduce the sensitivity of the variation of the donor binding energy with respect to the field strength (orientation) but it can not change its general behaviour. The results presented herein are published in Journal of Applied Physics ***112****, 064326 (2012).*

Contents

3.1 Introduction

Rapid advance in material growth technology lead to a renewed interest in studies of semiconductor nanostructures subjected to a tilted magnetic field directed at an angle with respect to the growth direction.[25–29] Since the pioneering works of Stern[30] and Maan,[31] subband-Landau-level coupling effect,[32] electron[33–35] and impurity states,[36,37] quantum hall effect,[38] exciton binding energy and excitonic absorption[29,39] in a semiconductor quantum well (QW) structure in the presence of a tilted magnetic field have been investigated theoretically in the past three decades. These studies revealed that the titled magnetic field influences dramatically the electronic and optical properties in a semiconductor QW structure, as it has also been shown by relative experimental works.[27,28,40–44] From the theoretical point of view, the presence of a tilted magnetic field, breaks the cylindrical symmetry and the variables in the Schrödinger equation can not be fully separated (the only exception seems to be the special case of parabolic potential[31]). To solve this problem, variational and perturbation methods have been used. It is well known that the variational method is highly dependent on the trial wavefunctions, while the perturbation method is a reliable method only if the magnetic field is weak enough so that its effect can be viewed as an external perturbation.

Investigations of hydrogenic impurity in the above setup are of particular relevance, since the presence of the hydrogenic impurity influences greatly the electronic mobility and optical properties. Up to now, only few reports concerning the study of the effect of a tilted magnetic field on the donor impurity states in low dimensional semiconductor nanostructures have been published. Kasapoglu et al.[36] investigated variationally the binding energy of a shallow donor impurity located at the center of GaAs/AlGaAs QW under the influence of a tilted magnetic field by making a coordinate transform. Their results show that the donor binding energy is a *nonmonotonic* function of the tilted angle (the orientation of the magnetic field). On the contrary, the findings of Redliński and Jankó,[37] who also used a variational procedure, show that the binding energy of a donor impurity located at the center of the rectangular CdTe/MgCdTe QW is a *monotonic* function of the tilted angle. More recently, Monozon and Schmelcher[29] developed an analytical approach to the problem of the fundamental and exciton magnetoelectroabsorption in a narrow QW. For comparison purpose, the ground-state binding energy of a donor impurity located at the center of the CdTe/MgCdTe QW in the presence of a tilted magnetic field has been calculated by using the analytical approach. Their results show that the donor binding energy is a monotonic function of the tilted angle of the magnetic field, which is in agreement with that reported in Ref. 37. In their report, as an approximation, the electron-impurity Coulomb interaction has been neglected and the carrier confinement

potential is assumed to be infinite (infinite-depth QW). However, the impurity related properties[37,45,46] and the optical band gap[47,48] in semiconductor nanostructures are also highly dependent on the barrier height (or indirectly on the host matrix). From then on, no further investigations were involved with the study of the donor impurity states in a semiconductor QW subjected to a tilted magnetic field. Moreover, in spite of considerable progress in the investigations on the tilted magnetic field effect in a semiconductor QW, no studies have been involved investigating the tilted magnetic field effect in a semiconductor quantum dot (QD).

In this chapter, we employ the potential morphing method (PMM)[3,47–53] in the framework of effective-mass approximation (EMA) in order to investigate the effect of a tilted magnetic field on the donor binding energy in GaAs/AlGaAs semiconductor QDs. In our calculations, for simplicity, the difference of the electron effective mass between the dot material and the barrier material, the dielectric mismatch and the conduction band nonparabolicy have been neglected.[37] On the other hand, according to the presently accepted mechanisms of doping, the behaviour of surface impurities in semiconductor nanocrystals prepared at relatively low temperature plays a crucial role during the incorporation process (the success in doping nanocrystals depends on the possibility of the impurity to be absorbed on the nanocrystals surface and to stay there a time long enough to be incorporated during the growth process).[54–56] Although there are many investigations on the on-center impurity in semiconductor QDs, studies with impurities located at off-center positions are much less.[12,57,58] Especially, to our best knowledge, there are no reports in the literature, within the framework of EMA, concerning to the detailed investigations of the surface impurities binding energy in semiconductor QDs subjected to a tilted magnetic field. In the present Chapter, theoretical predictions about the behaviour of the magnetic and angle shift of the binding energy of the surface impurities under the influence of a tilted magnetic field in a cylindrical GaAs/AlGaAs QD are reported.

3.2 General theory

In the framework of EMA, a shallow donor impurity embedded in a cylindrical QD is modeled by the Hamiltonian

$$\hat{H} = (\hat{p} + \frac{e}{c}\vec{A}(\vec{r}))\frac{1}{2m_e^*}(\hat{p} + \frac{e}{c}\vec{A}(\vec{r})) + V(\vec{r}) - \frac{e^2}{4\pi\varepsilon|\vec{r} - \vec{r_i}|}. \tag{3.1}$$

The first term of the Hamiltonian is the operator for the Kinetic energy of a delocalized conduction electron (where e is the absolute value of the electron charge, c is the speed

of the light in vacuum, m_e^* is the electron effective mass) in the presence of the tilted magnetic field $\vec{B} = B(\cos\theta, 0, \sin\theta)$ which is parallel to the xoz plane with an angle θ to the x-axial direction. In the previous theoretical treatment[36,37] of the tilted magnetic field effect in a semiconductor QW, the asymmetric gauge ($\vec{A}(\vec{r}) = B(0, x\sin\theta - z\cos\theta, 0)$) was adopted in order to simplify the numerical calculations. However, PMM which is developed to solve the time independent Schrödinger equation for any arbitrary interaction potential offers us more flexibility to choose the gauge. For the magnetic field $\vec{B}$ considered in the present paper, the commonly used cylindrical gauge is employed in our calculations and the vector potential in the cylindrical gauge is

$$\vec{A}(\vec{r}) = \frac{1}{2}\vec{B}\times\vec{r} = \frac{1}{2}B(-y\sin\theta, -(z\cos\theta - x\sin\theta), y\cos\theta). \tag{3.2}$$

Substituting Eq. (3.2) into Hamiltonian (3.1), the operator for the Kinetic energy of the electron under the influence of a tilted magnetic field $\vec{B}$ (the first term of Hamiltonian (3.1)) is the following

$$\hat{H}_{Kin} = \hat{p}\frac{1}{2m_e^*}\hat{p} + \frac{eB}{2m_e^*c}(\cos\theta\hat{l}_x + \sin\theta\hat{l}_z) + \frac{e^2B^2}{8m_e^*c^2}[y^2 + (z\cos\theta - x\sin\theta)^2], \tag{3.3}$$

where $\hat{l}_i$ $(i = x, z)$ is the i-component of the angular momentum operator ($\hat{l}_x = y\hat{p}_z - z\hat{p}_y$, $\hat{l}_z = x\hat{p}_y - y\hat{p}_x$). The second term of Eq. (3.3) represents the interaction between the magnetic field $\vec{B}$ and the orbital angular momentum $\vec{l}$ ($\vec{B}\cdot\vec{l} = B_x\hat{l}_x + B_y\hat{l}_y + B_z\hat{l}_z$, here $B_y = 0$). The third term of Eq. (3.1),

$$V_B(\vec{r}) = \frac{e^2B^2}{8m_e^*c^2}[y^2 + (z\cos\theta - x\sin\theta)^2], \tag{3.4}$$

is the magnetic field induced confinement potential. For in-plane magnetic field ($\theta = 0°$), the magnetic field induced confinement potential is $V_B(\vec{r}) = \frac{e^2B^2}{8m_e^*c^2}(y^2 + z^2)$, which is in yoz plane; while for growth-direction magnetic field ($\theta = 90°$), $V_B(\vec{r}) = \frac{e^2B^2}{8m_e^*c^2}(x^2 + y^2)$, which is in xoy plane. Furthermore, for any $B\neq0$ and $\theta\neq0°$ (or 90°), the magnetic field induced confinement potential $V_B(\vec{r})$ takes the form of Eq. (3.4), which is in both yoz plane (contributed from the transverse component of the magnetic field $B_x = Bcos\theta$) and xoy plane (contributed from the longitudinal component of the magnetic field $B_z = Bsin\theta$).

$V(\vec{r})$ in Eq. (3.1) is the step-like electron confinement potential, which is assumed to be zero inside the QD and V_0 outside the dot. The third part of the Eq. (3.1) is the Coulomb interaction between the electron and the shallow donor impurity which is located at $\vec{r}_i = (x_i, y_i, z_i)$, and ε is the static dielectric constant. In order to obtain the ground state of the Hamiltonian (3.1), we are using the PMM following the procedure outlined in

Chapter 1. The ground-state donor binding energy is represented as the following

$$E_b = E_0 - \widetilde{E}, \tag{3.5}$$

where $\widetilde{E}$ is the energy which corresponds to the Hamiltonian in Eq. (3.1) and E_0 is the energy without Coulomb interaction (absence of the third term in Eq. (3.1)). The magnetic shift of the donor binding energy is defined as the difference between the binding energy of a donor impurity at magnetic field $B{\neq}0$ and its binding energy at magnetic field $B = 0$ for a fixed tilted angle θ, which is given by[29]

$$\delta E_b = E_b(B{\neq}0, \theta) - E_b(B = 0, \theta). \tag{3.6}$$

Similarly, the angle shift of the donor binding energy is defined as the difference between the binding energy of a donor impurity at angle $\theta{\neq}0^\circ$ and its binding energy at angle $\theta = 0^\circ$ is the following[29]

$$\Delta E_b = E_b(B, \theta{\neq}0^\circ) - E_b(B, \theta = 0^\circ). \tag{3.7}$$

3.3 Results and discussion

In the following, we will discuss the influence of the QD geometric characteristics (such as dot size and height-to-radius aspect ratio), impurities positions (on-surface or on-center) and magnetic field intensities and orientations on the donor binding energy in a cylindrical QD characterized by the dot radius R and dot height L. Our calculations are based on a typical GaAs cylindrical QD, surrounded by larger band gap material $Al_{0.3}Ga_{0.7}As$ in both the radial and z-axis directions. All the parameters used in our calculations are the same as in Ref. 50. The cartesian coordinates of the on-center, top and side impurities, which are considered in the present calculations, are (0,0,0), (0,0,$\frac{L}{2}$) and (R,0,0), respectively.

As a first step towards studying the effect of a tilted magnetic field on the binding energy of surface impurities in cylindrical GaAs/$Al_{0.3}Ga_{0.7}As$ QDs, we performed calculations for the magnetic shift of the donor binding energy of surface impurities δE_b (top and side impurities) as a function of the magnetic field strength B (see Figs. 3.1(a) and (b)). This procedure was repeated for height-to-radius aspect ratios $\rho = \frac{L}{R} = 0.5$, 1.0 and 2.0, while the dot's radius was set to $R = 20$ nm. As reported in previous investigations,[59] for a cylindrical QD subjected to the growth direction magnetic field, the binding energy of on-edge impurity (corresponding to the top impurity in our calculations) is totally insensitive to the increase of the magnetic field strength. However, for a tilted magnetic field (for instance, $\theta = 45^\circ$), the binding energy of top impurity, as indicated in Fig. 3.1 ,

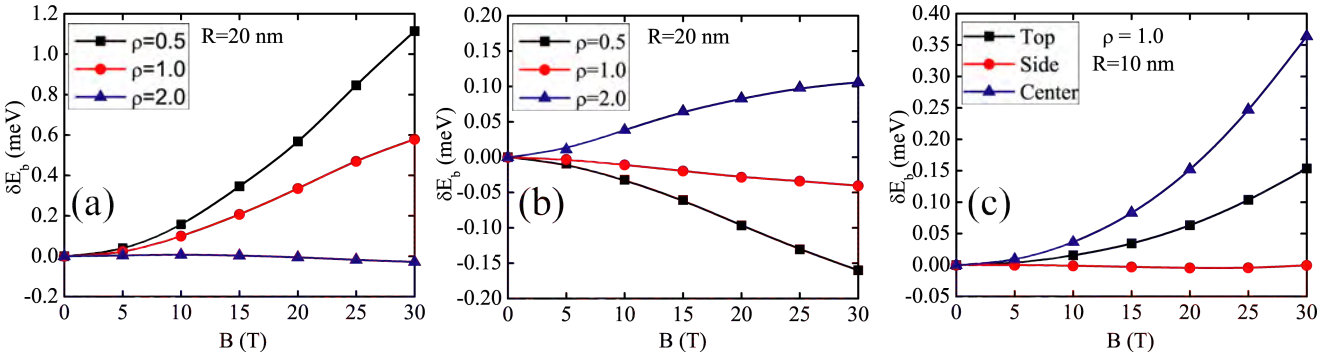

Figure 3.1: Magnetic shift of the donor binding energy δE_b as a function of magnetic field B with tilted angle $\theta = 45°$. (a) is for different aspect ratios ($R = 20$ nm) and top impurity; (b) is for different aspect ratios ($R = 20$ nm) but side impurity; (c) is for different impurity positions (top, side and center) but for radius $R = 10$ nm and aspect ratio $\rho = 1$.

is very sensitive to the magnetic field and δE_b increases dramatically with increasing the magnetic field for a disc-shaped QD (i. e., $\rho = 0.5$). However, as the aspect ratio increases this sensitivity declines and δE_b even becomes negative for the rod-shaped QD ($\rho = 2.0$). On the other hand, for the case of side impurity, the behaviour of δE_b is found to be quite different. For a disc-shaped QD ($\rho = 0.5$), as shown in Fig. 3.1(b) δE_b is negative and it keeps decreasing dramatically with increasing the magnetic field strength. When the aspect ratio goes up to $\rho = 1$, δE_b is also negative as the field increases, but the sensitivity of the donor binding energy with respect to the field strength is reduced. However, if the aspect ratio keeps increasing and a rod-shaped QD is produced, the enhancement of the magnetic field results in a positive δE_b, which is in contrast to the case of top impurity.

In an effort to explain these novel behaviour of the binding energy of surface impurities and understand the underlying physics, we have created suitable 3D contour plots of the electron probability density (first column of Fig. 3.2), as well as isosurfaces of the electron probability density differences (the last three columns of Fig. 3.2) in impurity-free QDs with different aspect ratios and magnetic fields (strength and orientation). In particular, each density difference plot has been produced by subtracting the zero field density from the density which corresponds to a specific field strength and orientation. This subtraction leads to positive (blue) and negative (red) density areas which indicate the charge movement due to the presence of the magnetic field. As a result, the red surfaces correspond to charge depletion areas, while the blue surfaces correspond to charge accumulation areas. For the creations of these 3D contour plots, the Gabedit graphical program[60] was used. By observing these figures, two distinct trends can be identified. The presence of the magnetic field makes the electron probability density shrink towards the center of the dot and also elongates along the applied field direction. The geometric characteristics of the dot (aspect ratio) have a different influence on these two trends. The shrinking due to the magnetic field induced confinement is not significantly affected by the variation of the

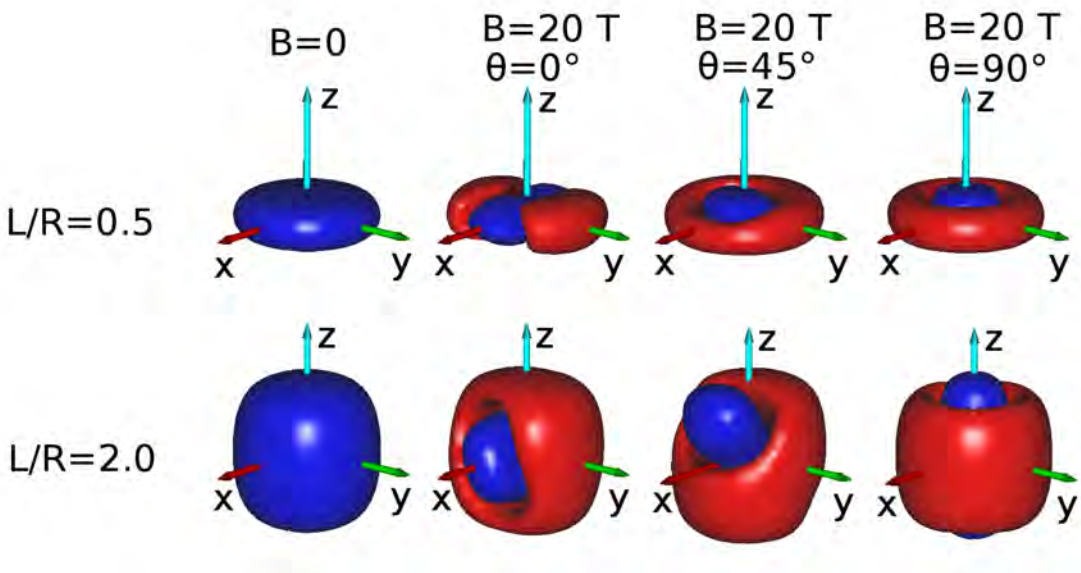

Figure 3.2: The first column corresponds to the three dimensional electron probability density of an impurity free GaAs/$Al_{0.3}Ga_{0.7}As$ cylindrical QD with radius $R = 20$ nm and different aspect ratios in the absence of the magnetic field. The following three columns show suitably chosen isosurfaces of electron probability density differences for non-vanishing magnetic field along various directions.

QD aspect ratio, while on the other hand, the elongation trend is greatly affected. In the absence of the magnetic field, the electron probability density is mainly distributed along the radial direction of a disc-shaped QD ($\rho = 0.5$) due to the strong confinement in the growth direction; whereas, for a rod-shaped QD ($\rho = 2.0$), it extends apparently in all the three directions because it is in weak confinement regime (see the first column of Fig. 3.2). When an experimentally strong tilted magnetic field (for instance, $B = 20$ T and $\theta = 45°$) is applied in a disc shaped QD (see the third column of Fig. 3.2), the electron probability density exhibits an obvious shrinking towards the center of the QD (see the red color) while the elongation is strongly limited by the growth-direction geometric confinement of the QD. The charge density accumulation around the center of the QD is the dominant effect which leads to the decrease (increase) of the mean relative distance between the electron and the top (side) impurity. As a result, the binding energy of top impurity increases dramatically, whereas, that of side impurity obviously decreases. On the contrary, when the dimensions (aspect ratios) of the QD become larger, the elongation trend mediates or even reverses this tendency.

In order to investigate the behaviour of δE_b in different dot sizes subjected to a tilted magnetic field, we also displayed in Fig. 3.1(c), the magnetic shift of the donor binding energy δE_b as a function of the magnetic field strength in a cylindrical QD with aspect ratio $\rho = 1.0$ but with a smaller radius ($R = 10$ nm). In this calculation, three different impurity positions (top, side and center) are considered. At a first glance, we can find

that the binding energy of the surface impurities does not change in the same way as that of the on-center impurity when the magnetic field is enhanced. For instance, δE_b of side impurity slightly decreases with increasing the magnetic field. However, for an on-center donor impurity, it exhibits an apparent increase. This finding is totally different from the case of growth direction magnetic field, which states that the change of the binding energy of off-center impurity is similar to that of an on-center impurity.[61] Furthermore, by comparing the three plots shown in Fig. 3.1, it is found that decrease of the QD size can lead to the decrease of the sensitivity of the magnetic shift of the donor binding energy with respect to the magnetic field strength but can not change its general behaviour.

As expected, the magnetic field orientation also has a significant influence on the binding energy of surface impurities in a cylindrical QD. As indicated from Fig. 3.3(a) and (b), both the top and side impurities show monotonic dependence of the binding energy on the tilted angle, irrespectively of the QD aspect ratios. However, the variation of the magnetic filed orientation from in-plane direction to the growth direction contributes positively to the angle shift of the binding energy of top impurity. While it has a negative influence on the angle shift of the binding energy of side impurity. This can be understood as follows. When the magnetic field is applied along the x-axial direction ($\theta = 0°$), the magnetic field induced confinement is in yoz plane as shown from Eq. (3.4). For this reason, the electron probability density shrinks in the plane perpendicular to the magnetic field direction and mainly elongates along the field direction at this stage (see the density differences shown in the second column of Fig. 3.2). While when the magnetic field is tilted from the in-plane direction, the magnetic field has both longitudinal and transverse components, which correspond to the magnetic field induced confinement in xoy and yoz plane, respectively. Consequently, the electron probability density shrinks toward the center of the QD and the mean relative distance between the electron and side (top) impurity is increased (decreased). Finally, when the magnetic field is applied along the growth direction and the magnetic field induced confinement contributed from the transverse component of the magnetic field is diminished, the electron probability density is distributed apparently along the growth direction of the QD. Therefore, in this situation, the binding energy of top (side) impurity reaches its largest (smallest) value. Furthermore it can be deduced from Fig. 3.2 that the charge depletion (accumulation) is much more sensitive to the magnetic field orientation for the case of larger aspect ratio ($\rho = 2$). This directly indicates that the effect of the magnetic field orientation is more pronounced in a semiconductor QD with large aspect ratios.

As for the behaviour of the angle shift of the donor binding energy, several interesting trends can be observed from Fig. 3.3. As shown by Fig. 3.3(a), the sensitivity of ΔE_b of the top impurity with respect to the variation of the tilted angle appears to be significantly pronounced for the case of disc-shaped QD. However, this sensitivity exhibits an apparent decrease as the aspect ratio of the QD increases. On the contrary, for side impurity (see

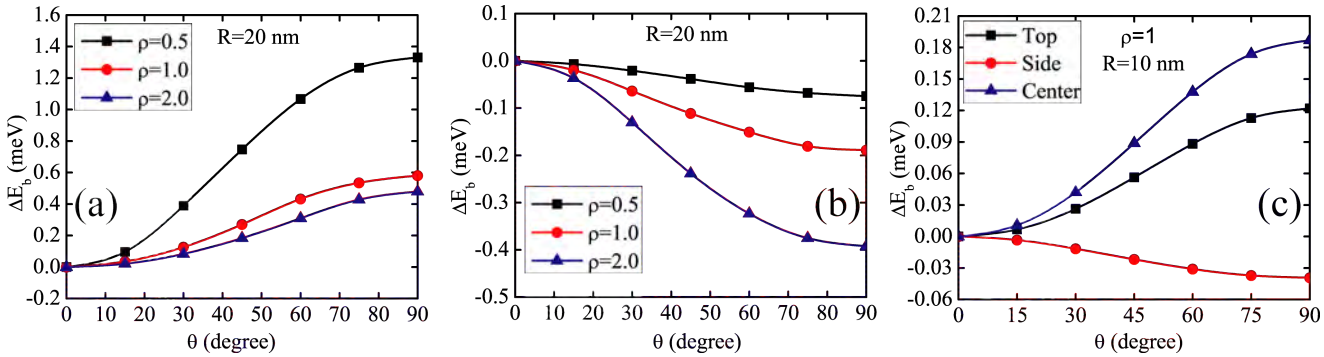

Figure 3.3: Angle shift of the donor binding energy ΔE_b as a function of the tilted angle θ with magnetic field $B = 20$ T. (a) is for different aspect ratios ($R = 20$ nm) and top impurity; (b) is for different aspect ratios ($R = 20$ nm) but side impurity; (c) is for different impurity positions (top, side and center) but for radius $R = 10$ nm and aspect ratio $\rho = 1$.

Fig. 3.3(b)), the sensitivity of ΔE_b is enhanced for a rod-shaped QD and it appears to increase with increasing the aspect ratio, as expected. In order to show the angle shift of the donor binding energy in different dot sizes, we also exhibit in Fig. 3.3(c), the dependence of ΔE_b of top (side or center) impurity on the field orientation in a cylindrical QD with aspect ratio $\rho = 1$ but for a smaller radius ($R = 10$ nm). It is found that the variation of ΔE_b strongly depends on the surface impurity positions and it does not always behave in the similar way as that of an on-center impurity. By comparing the values of ΔE_b in the three plots (see Fig. 3.3), it is not difficult to find that the decrease of the QD size leads to a decreases of the sensitivity of ΔE_b with regard to the tilted angle, but it does not change its general behaviour, which is similar to that of the magnetic shift of the donor binding energy (see the plots exhibited in Fig. 3.1).

3.4 Brief summary

In summary, our results show that QD geometric characteristics (dot sizes and aspect ratios), impurity positions (top, side or center) and the magnetic field intensities and orientations affect significantly the donor binding energy. The magnetic (angle) shift of the donor binding energy is not always enhanced by the presence of a tilted magnetic field. Its sensitivity with respect to the field strength (or tilted angle) can be reduced by decreasing the QD size, but its general behaviour can not be altered. Furthermore, it is found that the angle shift of the donor binding energy is a monotonic function of the tilted angle, irrespectively of the QD sizes and aspect ratios.

4

Combination effects of tilted electric and magnetic fields on donor binding energy in a GaAs/AlGaAs cylindrical quantum dot

*In this chapter, we perform a systematic study on the ground-state binding energy of an on-center donor impurity confined in a $GaAs/Al_{0.3}Ga_{0.7}As$ cylindrical quantum dots, subjected to simultaneously applied electric and magnetic fields. The two fields are tilted with respect to the dot growth direction and they are either parallel or perpendicular to each other. Our results show that when the tilted electric and magnetic fields are parallel, the magnetic shift of the donor binding energy is a monotonic function of the magnetic field strength. On the other hand, when the two fields are perpendicular to each other, the magnetic shift of the donor binding energy varies non-monotonically with respect to the magnetic field strength, exhibiting a minimum value at a critical magnetic field strength. The position of this minimum value and its dependence on the QD size, its aspect ratio and the orientation of the tilted magnetic field is systematically investigated. Moreover, we discuss in detail the competition effects which appear in the presence of the two fields, showing that the critical line which corresponds to zero shift of the donor binding energy can be manipulated by suitably adjusting the QD size, the aspect ratio and the relative orientation of the two fields. The results presented herein are published in Journal of Physics D: Applied Physics **45**, 23102 (2012).*

Contents

4.1 Introduction

A deep understanding of the effects of impurities on electronic states of semiconductor nanostructures is of fundamental importance in semiconductor physics because their presence can dramatically alter the performance of quantum devices.[62] In the past many years, hydrogenic impurity states in semiconductor nanostructures, such as quantum wells (QWs), quantum well-wires (QWWs) and quantum dots (QDs), have been investigated extensively.[44–46,59,63–73] These studies revealed that the binding energy of a hydrogenic impurity confined in these nanostructures can be directly controlled by choosing appropriated materials, geometries, sizes and doping positions. Besides, external perturbations, such as uniform electric and magnetic fields, are effective tools for studying the impurity related properties in semiconductor nanostructures. As it is well known, the presence of a uniform magnetic field, introduces another electronic confinement (magnetic field induced confinement) which superposes its geometric counterpart. Depending on the direction of the magnetic field (parallel or perpendicular to the growth direction), some interesting physical phenomena can take place.[74] Furthermore, the applied electric field induces an asymmetric distribution of the electron probability density which strongly modifies the electronic and optical properties in semiconductor nanostructures. Thus, to investigate the combination effects of the electric and magnetic fields on the binding energy of a hydrogenic impurity in semiconductor nanostructures were of great interest and attracted much attention in the past many years.[50,75–79] However, vast majority of these calculations treat the most straightforward cases, where the two fields are applied parallel to each other and they are either parallel or perpendicular to the growth direction of the semiconductor nanostructures.

Recently, the rapid advance in material growth technology lead to a renewed interest in studies of semiconductor nanostructures subjected to an external electric or magnetic field directed at an angle with respect to the growth direction. The reason for this interest is the fact that such a unique system provides us novel electronic, optical and transport effects (see Ref. 29 and references therein). More specially, Redliński and Jankó[37] have investigated the tilted magnetic field effect on the binding energy of a shallow donor in a CdTe/MgCdTe QW. Wang et al[23] investigated the effects of an arbitrary tilted electric field on the magnetoexciton in a cylidrical QD by means of a variational procedure. Recently, Monozon and Schmelcher[29] developed an analytical approach to the problem of the fundamental and exciton magnetoelectroabsorption in a narrow QW subjected to the tilted electric and magnetic fields (the electric and magnetic field are parallel and are both tilted with respect to the QW growth direction). However, to the best of our knowledge, the combination effects of the tilted electric and magnetic fields (parallel or

perpendicular to each other) on the donor binding energy in semiconductor nanostructures have not been reported anywhere in the literature. On the other hand, as revealed in the previous reports,[37] the tilted magnetic field induces a three dimensional (3D) electron confinement which makes the electron probability density distribute with respect to the center of the cylindrical QD. This in turn causes the increase of the on-center donor binding energy. On the contrary, as the external tilted electric field is applied, the symmetry of the electron probability density distribution at zero electric field breaks and the maximum of the electron probability density moves away from the center of the cylindrical QD to the opposite direction of the tilted electric field. As a result, the decrease of the binding energy of an on-center donor impurity in a QD takes place. As expected, when the two tilted fields are simultaneously applied in a GaAs/AlGaAs cylindrical QD, competition effects appear. A qualitatively understanding of this type of competition effects on the donor binding energy may be very useful for design and application of some commonly used δ-doped GaAs/AlGaAs QD based optoelectronic devices, such as LEDs and LDs. Unfortunately, no related reports have been published. Therefore, in the present work, we perform for the first time calculations of the ground-state binding energy of an on-center donor impurity in a typical GaAs/AlGaAs cylindrical QD under the influence of simultaneously applied tilted electric and magnetic fields. Both fields are applied parallel to the xoz plane and they are both tilted with respect to the QD growth direction. The cases for which the electric field is parallel or perpendicular to the tilted magnetic field are considered in details. The numerical technique we used in the present calculations is the potential morphing method (PMM)[3,47–49,51–53] which has been developed to solve the time independent Schrödinger equation for any arbitrary interaction potential. The emphasis of the present paper is placed on a detailed analysis of competition effects between the simultaneously applied tilted electric and magnetic fields on the binding energy of an on-center donor impurity in a cylindrical QD.

4.2 General theory

In the framework of effective-mass approximation (EMA), a shallow donor impurity embedded in a cylindrical QD is modeled by the Hamiltonian

$$\hat{H} = (\hat{p} + \frac{e}{c}\vec{A}(\vec{r}))\frac{1}{2m_e^*}(\hat{p} + \frac{e}{c}\vec{A}(\vec{r})) + V(\vec{r}) + V_E(\vec{r}) - \frac{e^2}{4\pi\varepsilon_0\varepsilon_r|\vec{r}|}. \tag{4.1}$$

The first term of the Hamiltonian is the operator for the Kinetic energy of a delocalized conduction electron (where e is the absolute value of the electron charge, c is the speed of the light in vacuum, m_e^* is the electron effective mass) in the presence of a tilted magnetic

field which is parallel to the xoz plane with an angle θ to the x-axial direction ($\vec{B} = B(\cos\theta, 0, \sin\theta)$). The vector potential $\vec{A}$ in the commonly used cylindrical gauge is $\vec{A}(\vec{r}) = \frac{1}{2}\vec{B}\times\vec{r} = \frac{1}{2}B(-y\sin\theta, -(z\cos\theta - x\sin\theta), y\cos\theta)$. Substituting the exact expression of the vector potential into Hamiltonian (4.1), the operator for the Kinetic energy of the electron under the influence of a tilted magnetic field $\vec{B}$ (the first term of Hamiltonian (4.1)) is the following

$$\hat{H}_{Kin} = \hat{p}\frac{1}{2m_e^*}\hat{p} + \frac{eB}{2m_e^*c}(\cos\theta\hat{l}_x + \sin\theta\hat{l}_z) + \frac{e^2B^2}{8m_e^*c^2}[y^2 + (z\cos\theta - x\sin\theta)^2], \tag{4.2}$$

where $\hat{l}_i$ ($i = x, z$) is the i-component of the angular momentum operator ($\hat{l}_x = y\hat{p}_z - z\hat{p}_y$, $\hat{l}_z = x\hat{p}_y - y\hat{p}_x$). The second term of Eq. (4.2) represents the interaction between the magnetic field $\vec{B}$ and the orbital angular momentum $\vec{l}$ ($\vec{B}\cdot\vec{l} = B_x\hat{l}_x + B_y\hat{l}_y + B_z\hat{l}_z$, here $B_y = 0$). The third term of Eq. (4.2),

$$V_B(\vec{r}) = \frac{e^2B^2}{8m_e^*c^2}[y^2 + (z\cos\theta - x\sin\theta)^2], \tag{4.3}$$

is the magnetic field induced confinement potential. For in-plane magnetic field ($\theta = 0°$), the magnetic field induced confinement potential is $V_B(\vec{r}) = \frac{e^2B^2}{8m_e^*c^2}(y^2 + z^2)$, which is in yoz plane; while for growth-direction magnetic field ($\theta = 90°$), $V_B(\vec{r}) = \frac{e^2B^2}{8m_e^*c^2}(x^2 + y^2)$, which is in xoy plane. Furthermore, for any $B\neq0$ and $\theta\neq0°$ (or 90°), the magnetic field induced confinement potential $V_B(\vec{r})$ takes the form of Eq. (4.3), which is in both yoz plane (contributed from the transverse component of the titled magnetic field $B_x = Bcos\theta$) and xoy plane (contributed from the longitudinal component of the tilted magnetic field $B_z = Bsin\theta$). $V(\vec{r})$ in Eq. (4.3) is the electron confinement potential in a cylindrical QD, which is the following

$$V(\vec{r}) = V(x, y, z) = \begin{cases} V(x, y), & |z| \leq \frac{L}{2} \\ V_0, & |z| > \frac{L}{2} \end{cases}, \tag{4.4}$$

$$V(x, y) = \begin{cases} 0, & \sqrt{x^2 + y^2} \leq R \\ V_0, & \sqrt{x^2 + y^2} > R \end{cases}, \tag{4.5}$$

where V_0 is the conduction band discontinuity, L and R are the dot height and radius of the cylindrical QD, respectively. The third part of the Eq. (4.4) is the electrostatic potential induced by a tilted electric field applied parallel to the xoz plane but making an angle θ' to the x-axial direction, which is the following

$$V_E(\vec{r}) = eE(x\cos\theta' + z\sin\theta'). \tag{4.6}$$

If the tilted angle $\theta' = \theta$, this means that the electric field is applied parallel to the magnetic field ($\vec{E}\|\vec{B}$). While, when the tilted angle $\theta' = \theta \pm 90°$, this represents that the electric field is applied perpendicular to the magnetic field ($\vec{E}\perp\vec{B}$). The last term of the Eq. (4.1) represents the Coulomb interaction between the electron and the shallow donor impurity located at the center of the cylindrical QD ($\vec{r_i} = (x_i, y_i, z_i) = (0, 0, 0)$, $\vec{r_i}$ is the impurity position vector), and ε is the static dielectric constant.

In the present work, we intend to investigate the ground-state donor binding energy under the combined effects of the simultaneously applied tilted electric and magnetic fields in a cylindrical QD. The ground-sate donor binding energy is defined as a difference between the ground-state energies of the free electron and that of the donor with the same electron spin configuration,[37] which is the following

$$E_b = E_0 - \widetilde{E}, \tag{4.7}$$

where $\widetilde{E}$ is the energy which corresponds to the Hamiltonian in Eq. (4.1) and E_0 is the energy without Coulomb interaction (absence of the last term in Eq. (4.1)). This definition indicates that the interaction between the spin and the external magnetic field ($\mp\frac{1}{2}\mu_B g_e^* \vec{B}\cdot\vec{S}$, μ_B is the Bohr magneton and $\vec{S}$ is the spin operator) does not contribute to the donor binding energy. In order to obtain the ground state energy of the electron (E_0) and the donor ($\widetilde{E}$) as well as corresponding wave functions, PMM, as we described in Chapter 1, is employed. In our calculations, the usual three-dimensional (3D) harmonic oscillator is taken as a reference system and its ground state wave function is selected as the initial wave function (Φ_R). The interaction potential corresponding to the ground-state energy of the electron (E_0) is

$$v_S^e = \frac{eB}{2m_e^* c}(\cos\theta\hat{l}_x + \sin\theta\hat{l}_z) + V(\vec{r}) + V_B(\vec{r}) + V_E(\vec{r}). \tag{4.8}$$

Whereas, the interaction potential corresponding to the ground-state energy of the donor ($\widetilde{E}$) is

$$v_S^d = \frac{eB}{2m_e^* c}(\cos\theta\hat{l}_x + \sin\theta\hat{l}_z) + V(\vec{r}) + V_B(\vec{r}) + V_E(\vec{r}) - \frac{e^2}{4\pi\varepsilon_0\varepsilon_r|r|}. \tag{4.9}$$

It should be noted here that adopting the harmonic oscillator as a reference system does not affect our results because the PMM needs only a known reference system to start the morphing process and finally to give the eigenfunctions and eigenvalues for the unknown system, independently on the choice of the initial reference system.[3,53]

To further understand the magnetic field effect on the donor binding energy in a semiconductor QD subjected to an electric field, the magnetic shift of the donor binding energy is defined as the difference between the binding energy of a donor impurity at magnetic field $B\neq 0$ (a finite magnetic field) and its binding energy at $B = 0$ (zero magnetic field) for a

fixed electric field, which can be given by

$$\delta E_b = E_b(E, \theta'; B{\neq}0, \theta) - E_b(E, \theta'; B = 0, \theta). \tag{4.10}$$

Similarly, in an attempt to understand the competition effects between the tilted electric and magnetic fields on the donor binding energy in a cylindrical QD, the energetic shift of the donor binding energy is defined as the difference between the binding energy of a donor impurity at finite electric and magnetic fields ($E{\neq}0, B{\neq}0$) and its binding energy at zero electric and magnetic fields ($E = 0, B = 0$), which can be given by

$$\Delta E_b = E_b(E{\neq}0, \theta'; B{\neq}0, \theta) - E_b(E = 0, \theta'; B = 0, \theta). \tag{4.11}$$

The negative energetic shift of the donor binding energy ($\Delta E_b < 0$) means essentially the combination effects of the tilted electric and magnetic fields makes the donor binding energy red shift. Conversely, the blue shift of the donor binding energy takes place if the energetic shift of the donor binding energy is positive ($\Delta E_b > 0$).

4.3 Results and discussion

According to the previous theoretical studies on the semiconductor QDs,[70,72,73,77,80] we consider a typical GaAs cylindrical QD, surrounded by large band gap material AlGaAs in both the radial and z-axial directions. The origin is taken at the center of the QD and the z-axial direction is defined as the growth direction (see Fig. 4.1). The physical parameters used in our calculations are $\varepsilon_r = 12.4$ (assume that there is no dielectric mismatch) and $V_0 = 228$ meV. It is well known that the conduction-electron effective mass (m_e^*) depends on the aluminium concentration. Such an effect may contribute to an effective mass discontinuity at the QD interfaces and leads to an enhancement of the donor binding energy. However, in the present calculations, a position independent conduction-electron effective mass ($m_e^* = 0.0667m_0$ (where m_0 is the free electron mass)) is considered as an approximation. These parameters are suitable for GaAs/Al_xGa_{1-x}As heterostructures with an Al concentration $x{\cong}0.3$.

4.3.1 Tilted electric field effect on the magnetic shift

In this section, the tilted electric field effect on the magnetic shift of the binding energy of an on-center donor impurity is calculated as a function of the magnitude of the magnetic

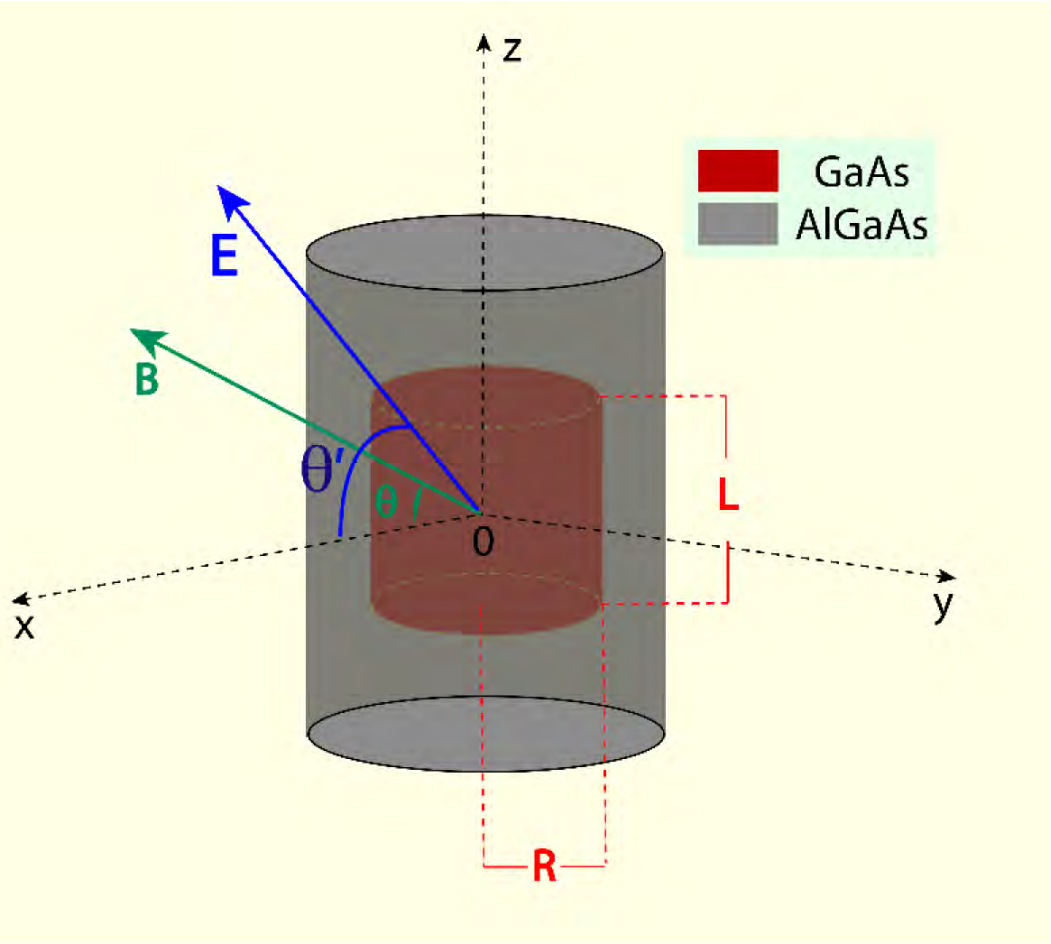

Figure 4.1: Schematic representation of the GaAs/AlGaAs cylindrical QD under investigation with the dot height L and the radius R. The magnetic field ($\vec{B}$) is applied parallel to the xoz plane making an angle θ to the x-axial direction. The electric field ($\vec{E}$) is also applied parallel to the xoz plane but it makes an angle θ' to the x-axial direction.

field for different dot sizes, electric fields (strengths and orientations), orientations of the magnetic field and aspect ratios of the cylindrical QD.

At first we examine the magnetic shift of the donor binding energy δE_b as a function of the magnetic field magnitude in a GaAs/$Al_{0.3}Ga_{0.7}$As cylindrical QD for various electric ($\vec{E}$) and magnetic fields ($\vec{B}$). The electric field is always applied parallel ($\theta' = \theta$) or perpendicular ($\theta' = 90° \pm \theta$) to the magnetic field. The calculations have been performed for two dot sizes ($L = R = 10$ nm and $L = R = 20$ nm). Our results (Fig. 4.2) show that in the absence of the electric field, δE_b increases as the magnetic field increases for any dot size and magnetic field orientation. As expected, for lager dot size (weaker confinement) the variation of δE_b with respect to the magnetic field strength, appears to be significantly more intense (see Fig. 4.2(b) and (c)). Moreover, it is found from Fig. 4.2 that in larger dot (i.e., $L = R = 20$ nm), variation of the magnetic field orientation from in-plane direction (Viogt configuration) to growth direction (Faraday configuration), leads to the decrease of

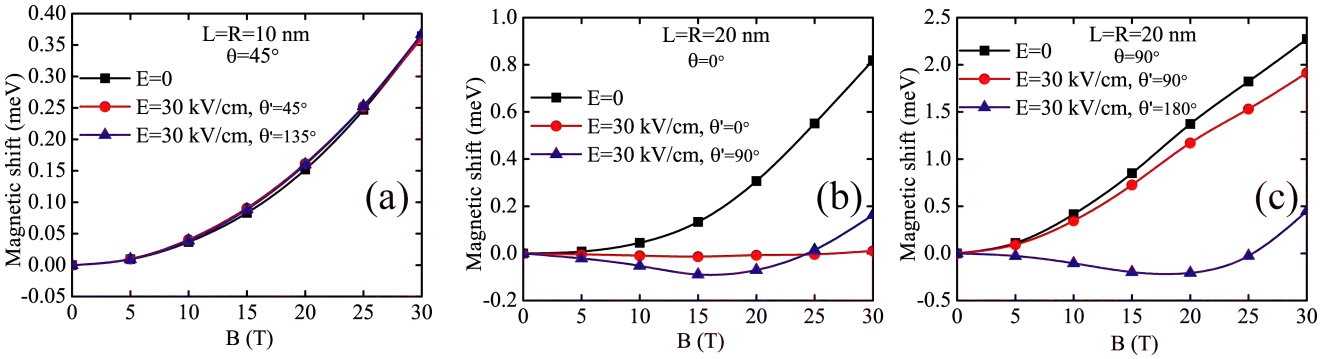

Figure 4.2: Magnetic shift of the donor binding energy δE_b as a function of the magnitude of the magnetic field $\vec{B}$ in a GaAs/$Al_{0.3}Ga_{0.7}As$ cylindrical QD for various electric fields ($\vec{E}$). Here, (a) is for $L = R = 10$ nm and $\theta = 45°$, (b) is for $L = R = 20$ nm and $\theta = 0°$, (c) is for $L = R = 20$ nm but $\theta = 90°$, respectively. The electric field is applied either parallel ($\theta' = \theta$ ($\vec{E}\|\vec{B}$)) or perpendicular ($\theta' = \theta + 90°$ ($\vec{E}\perp\vec{B}$)) to the magnetic field.

the sensitivity of δE_b with respect to the magnetic field strength. For instance, at $B = 30$ T, the magnetic shift of the donor binding energy in Viogt configuration is $\delta E_b = 0.819$ meV; while in the Faraday configuration, $\delta E_b = 2.27$ meV. This is because in the Faraday configuration, the magnetic field induced confinement is more effective due to the very weak confinement in the radial direction ($d = 2R = 2L = 40$ nm, d is the diameter of the cylindrical QD). On the other hand, for the case of the small dot size it becomes clear from Fig. 4.2(a) that the monotonic increase of δE_b is practically independent on the electric field orientation ($\theta' = 45°$ or $\theta' = 135°$). This can be easily understood by the fact that for $L = R = 10$ nm, the QD is in strong confinement regime and the effect of the electric field is marginal. Thus, it can be safely concluded that in the strong confinement regime, the value of the magnetic shift of the donor binding energy is practically not affected by the presence of an electric field.

On the contrary, in weak confinement regime (see Fig. 4.2(b) and (c)), δE_b depends strongly on the relative orientations of the electric and magnetic fields (tilted angle θ and θ'). When the electric field is applied parallel to the magnetic field ($\theta' = \theta$), δE_b increases monotonically with increasing the magnetic field strength in both Viogt ($\theta = 0°$) and Faraday configurations ($\theta = 90°$). Moreover, in Faraday configuration ($\vec{B}\|\vec{z}$), the increase of δE_b is practically more sensitive to the magnetic field strength, as expected. However, when a perpendicular electric field ($\theta' = \theta + 90°$) is applied, δE_b is a non-monotonic function of the magnetic field strength in both Viogt and Faraday configurations. It exhibits a minimum at a critical value B_c. In particular, it is interesting to find from Fig. 4.2(b) that in Viogt configuration, the critical magnetic field is $B_c \approx 16$ T; while in the Faraday configuration (Fig. 4.2(c)), it is $B_c \approx 20$ T. In other words, the critical magnetic field B_c increases when the magnetic field is tilted from the in-plane direction ($\vec{B}\|\vec{x}$) to the growth direction ($\vec{B}\|\vec{z}$).

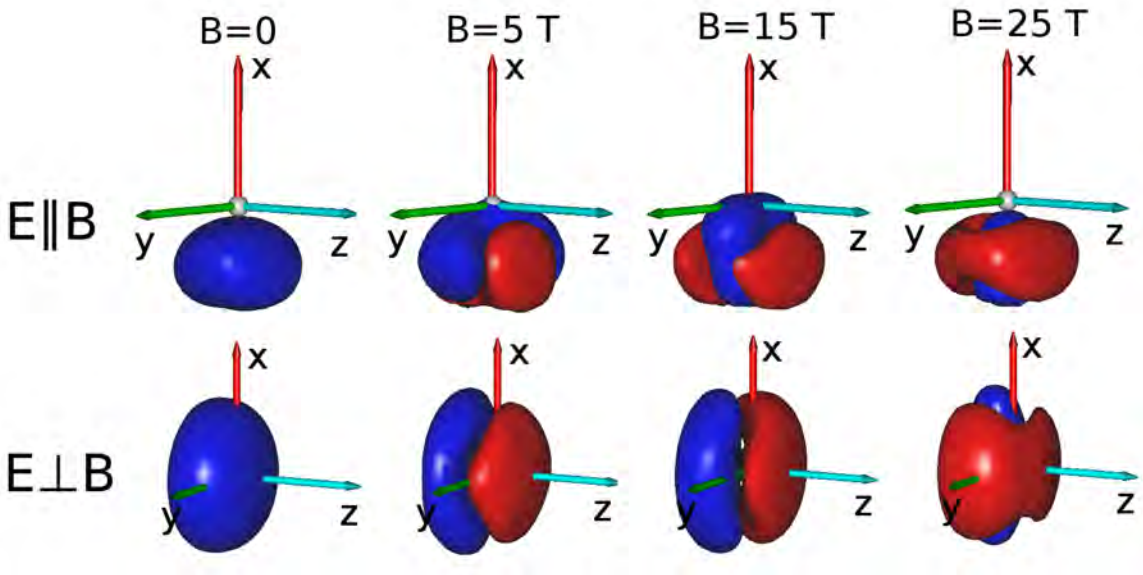

Figure 4.3: The first column corresponds to the three dimensional contour plots of the electron probability density distributions in an impurity free GaAs/$Al_{0.3}Ga_{0.7}$As cylindrical QD with dot height $L = 20$ nm and radius $R = 20$ nm subjected to different tilted electric fields but zero magnetic field. The following three columns show suitably chosen isosurfaces of electron probability density differences, which have been produced by subtracting the density at zero magnetic field from the density which corresponds to a specific magnetic field strength in Viogt configuration ($\vec{B}\|\vec{x}$). The red surfaces correspond to charge depletion areas, while the blue surfaces correspond to charge accumulation areas. The upper panel is corresponding to the case that the electric field is applied parallel ($E = 30$ kV/cm and $\theta' = 0°$) to the magnetic field, whereas, the lower panel is corresponding to the case that the electric field is applied perpendicular ($E = 30$ kV/cm and $\theta' = 90°$) to the magnetic field.

To understand the behaviour of the magnetic shift of the donor binding energy under the influence of parallel (perpendicular) electric and magnetic fields, we create suitable three dimensional (3D) contour plots of the electron probability density (first column of Fig. 4.3), as well as isosurfaces of the electron probability density differences (the last four columns of Fig. 4.3) in an impurity-free QD for different electric and magnetic fields. The electric field is applied either parallel (the upper panel of Fig. 4.3) or perpendicular (the lower panel of Fig. 4.3) to the magnetic field. In particular, each density difference plot has been produced by subtracting the density at zero magnetic field from the density which corresponds to a specific magnetic field strength (the magnetic field is applied along the x-axial direction). This subtraction leads to positive (blue) and negative (red) density areas which indicate the charge movement due to the applied magnetic field. As a result, the red surfaces correspond to charge depletion areas, while the blue surfaces correspond to charge accumulation areas. For the creations of these 3D contour plots, the Gabedit graphical program was used.[60] By observing the first column of Fig. 4.3, it is found that in the absence of the magnetic field, the electric field always moves the electron probability density far away from the QD center to its opposite direction. However, the

density displacement is highly affected by the QD geometric confinement and the electric field effect turns out to be more effective in the weak confinement regime (see the upper contour plot in the first column of Fig. 4.3), as expected.

Before proceeding to explain the density changes that take place due to the applied magnetic field, it would be useful to make a distinction between the two different trends which are introduced by the presence of a magnetic field. At first, the magnetic field induced confinement tends to squeeze the charge density around the axis of the applied magnetic field and secondly it tends to move the charge density towards the center of the QD. Although both effects are due to the cylindrical symmetry of the magnetic induced confinement, their behaviour is differently influenced by the geometric characteristics of the QD and the presence of an extra electric field. As a result, under certain conditions these two trends may be considered separately. This description may prove to be useful for understanding the competition effects between the two fields. For the case of a parallel magnetic field ($\vec{E}\|\vec{x}$,$\vec{B}\|\vec{x}$), we can see from Fig. 4.3, that the charge density is squeezed around the x axis as the field strength increases. It is obvious that for large values of B the magnetic field induced confinement imposes its cylindrical symmetry, while for smaller values of B the geometric confinement leads to less symmetric density distributions. In all cases, the charge density exhibits a small displacement towards the QD center. Consequently the mean relative electron-impurity distance decreases and the binding energy slightly and monotonically increases with increasing the magnetic field strength. However, this monotonic displacement of the charge density does not occur when the electric field is applied perpendicular ($\vec{E}\|\vec{z}$,$\vec{B}\|\vec{x}$) to the magnetic field (see the lower panel of Fig. 4.3). It is found that for magnetic field $B \leq B_c = 15$ T, the charge density moves far from the QD center when the perpendicular magnetic field increases. Conversely, it tends to move toward the QD center when the magnetic field becomes stronger ($B > 15$ T). This can be attributed to the competition effects between the two fields. In particular, although the magnetic field introduces both trends (squeezing and displacing towards the center of the QD) for small values of B ($0 < B < 15$ T) the presence of the electric field inhibits the displacement, allowing only for an asymmetric squeezing of the density. As a result, the mean relative electron-impurity distance increases and the binding energy slightly decreases (see Fig. 4.3(b) and (c)). On the other hand, if the magnetic field becomes stronger ($B > 15$ T), its influence begins to superpose its electric counterpart and the two trends (squeezing and displacing towards the center of the QD) lead to a charge density accumulation closer to the QD center. As a result, the increase of the magnetic field begins to contribute positively to δE_b.

In the Viogt configuration ($\theta = 0°$), we have also examined the dependence of δE_b on the magnetic field strength for various tilted electric fields at aspect ratios $\rho = \frac{L}{R} = 0.5$ (Fig. 4.4(a)) and $\rho = 2.0$ (Fig. 4.4(b)), respectively. Our results (Fig. 4.4(a)) indicate that for $\rho = 0.5$, in the absence of the electric field ($E = 0$), δE_b decreases as the strength of the

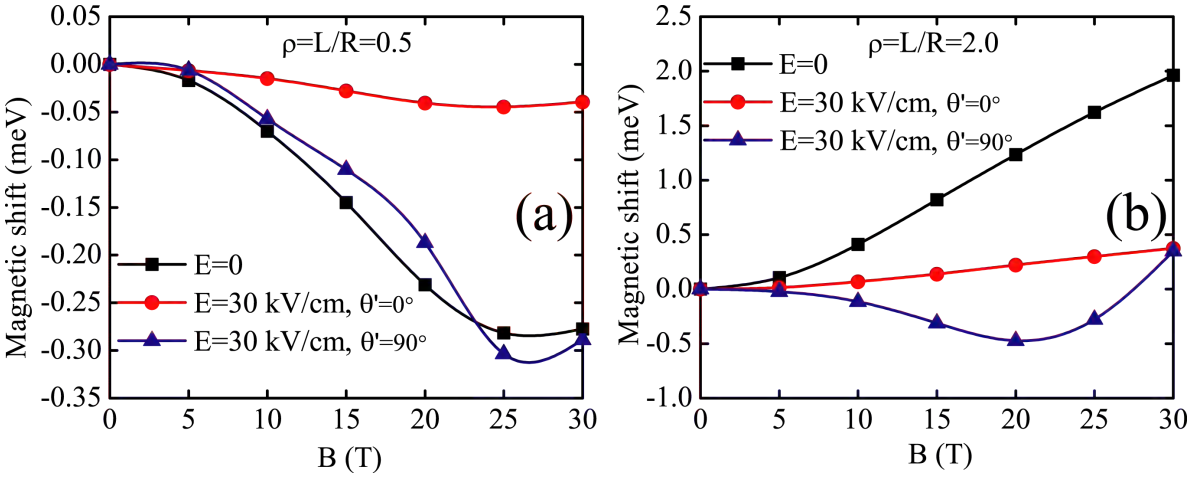

Figure 4.4: Magnetic shift of the donor binding energy δE_b as a function of the magnitude of the tilted magnetic field $\vec{B}$ in a GaAs/$Al_{0.3}Ga_{0.7}$As cylindrical QD with radius $R = 20$ nm for various tilted electric fields $\vec{E}$. The magnetic field is applied along the x-axial direction ($\theta = 0°$). The electric field is applied parallel ($\theta' = \theta$) or perpendicular ($\theta' = \theta + 90°$) to the magnetic field. Here, (a) and (b) are for aspect ratio $\rho = \frac{L}{R} = 0.5$ and 2.0, respectively.

magnetic field increases ($0 < B \leq 25$ T) and then it becomes insensitive to the increased magnetic field (25 T $\leq$ B $\leq$ 30 T). On the other hand, when the aspect ratio goes up to $\rho = \frac{L}{R} = 2.0$ (see Fig. 4.4(b)), δE_b increases monotonically with increasing the magnitude of the magnetic field. This behaviour is related to the variation of the quantum confinement in the z-axial direction which is induced by the change in the aspect ratio. For small aspect ratio ($\rho = \frac{L}{R} = 0.5$), the electron probability density is mainly distributed along the radial direction due to the weaker confinement ($R = 2L = 20$ nm). For magnetic field $0 < B \leq 25$ T, the magnetic field induced confinement (in yoz plane) makes the electron probability density more extend along the radial direction with increasing the magnetic field strength. Thus, the mean relative electron-impurity distance is increased and the donor binding energy is decreased. On the other hand, for $B \geq 25$ T the electron probability density appears to be only slightly affected and consequently the δE_b becomes almost invariant to any further increase of the magnetic field. Conversely, when the aspect ratio increases up to $\rho = \frac{L}{R} = 2.0$, the magnetic field effect is more effective because of the weak confinement in the z-axial direction ($L = 2R = 40$ nm) and it makes the electron probability density move closer to the impurity center as the magnetic field increases. Therefore, the mean relative electron-impurity distance is decreased and the donor binding energy is increased significantly.

It is interesting to find from Fig. 4.4 that in the presence of perpendicular electric field ($\theta' = 90° + \theta$), for any aspect ratio, the magnetic shift of the donor binding energy δE_b exhibits a minimum value at a critical magnetic field $B = B_c$. For aspect ratio $\rho = \frac{L}{R} = 0.5$, $B_c \approx 26$ T; while for aspect ratio $\rho = \frac{L}{R} = 2.0$, it is $B_c \approx 20$ T. In other words, the critical magnetic field B_c decreases with increasing the aspect ratio ρ. Moreover, when the parallel

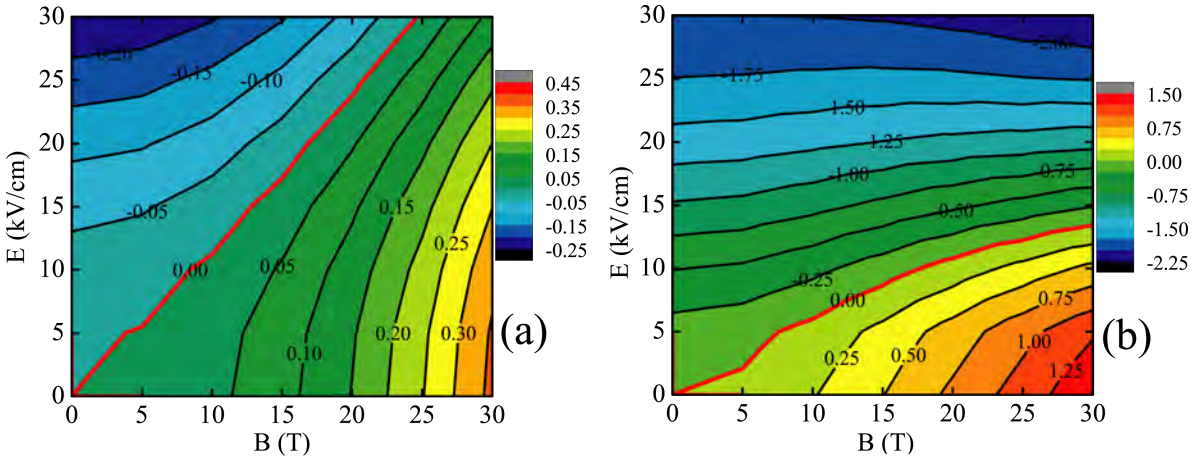

Figure 4.5: Contour plot of the energetic shift of the donor binding energy ΔE_b (in unite of meV) for various electric ($\vec{E}$) and magnetic ($\vec{B}$) fields in a GaAs/$Al_{0.3}Ga_{0.7}$As cylindrical QD. The magnetic field is applied at an angle $\theta = 45°$). The electric field is applied parallel to the magnetic field ($\theta' = \theta = 45°$). Here, (a) and (b) are for $L = R = 10$ nm and $L = R = 20$ nm, respectively.

electric field is applied ($\theta' = \theta$), the magnetic shift of the donor binding energy δE_b decreases slightly with increasing the magnetic field for small aspect ratio (for instance, $\rho = L/R = 0.5$). For large aspect ratio $\rho = L/R = 2.0$, δE_b increases monotonically when the magnetic field is enhanced. This behaviour is associated with the interplay between the applied electric and magnetic fields effect as well as the geometric confinement and it can be understood in the similar way as in Fig. 4.2.

4.3.2 Competition effects between the two fields

As we know from the above section, the magnetic shift of the binding energy exhibits novel behaviour due to the competition effects between the tilted electric and magnetic fields. Thus, in the following part, the energetic shift of the donor binding energy ΔE_b (defined by Eq. (4.11)) in a cylindrical QD subjected to simultaneously applied tilted electric and magnetic fields will be investigated in order to understand in details the competition effects.

Firstly, in an attempt to obtain a qualitatively understanding of the competition effects, we have created a suitable contour plot (Fig. 4.5) of the energetic shift of the donor binding energy ΔE_b for various electric (0 - 30 kV/cm) and magnetic (0 - 30 T) fields. The magnetic field is directed at an angle $\theta = 45°$, while the electric field is applied parallel to it ($\theta' = \theta = 45°$). Here, two different dot sizes ($L = R = 10$ nm and 20 nm) are considered. It is interesting to find from Fig. 4.5 that for any dot size, there is a critical line determined

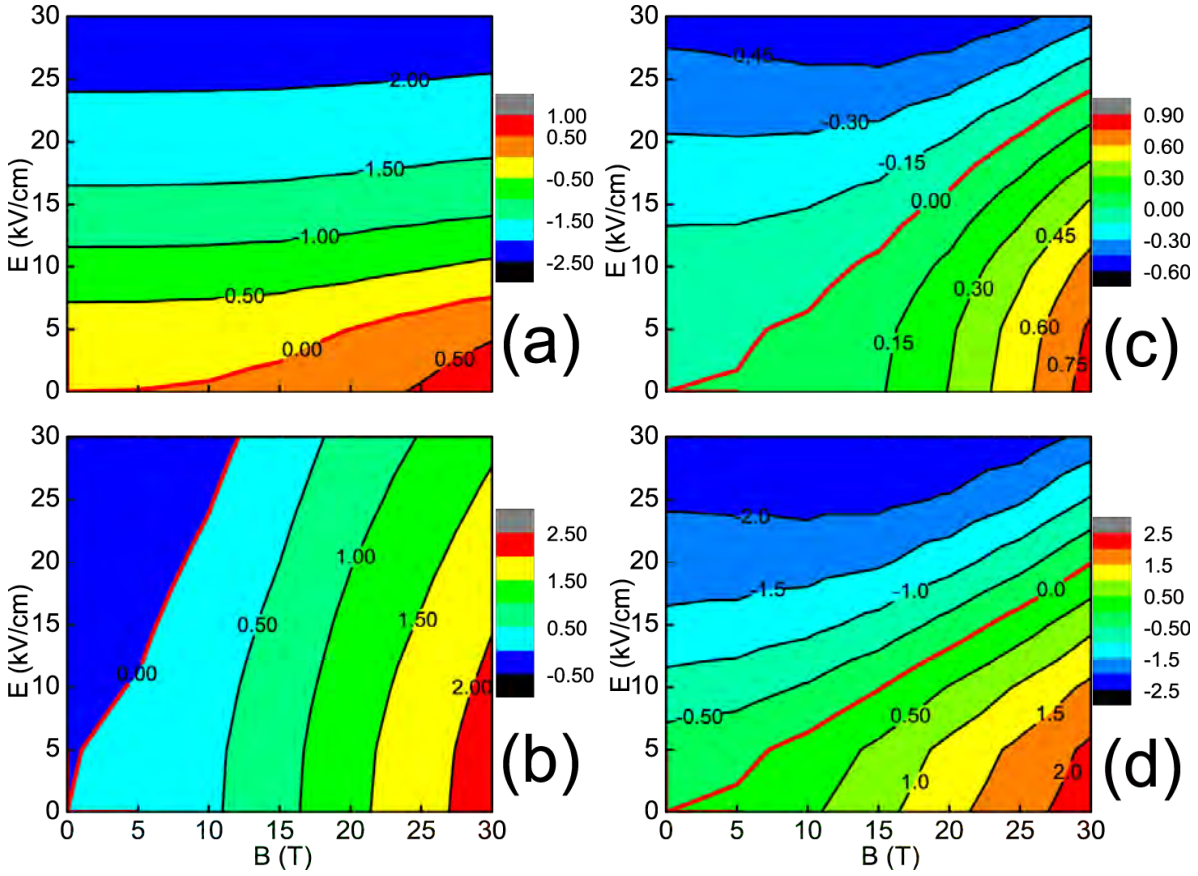

Figure 4.6: Contour plot of the energetic shift of the donor binding energy ΔE_b (in unite of meV) for various electric ($\vec{E}$) and magnetic ($\vec{B}$) fields in a $GaAs/Al_{0.3}Ga_{0.7}As$ cylindrical QD with dot height $L = 20$ nm and radius $R = 20$ nm. Here, (a): $\theta = \theta' = 0°$; (b): $\theta = \theta' = 90°$; (c): $\theta = 0°, \theta' = 90°$; (d) $\theta = 90°, \theta' = 0°$.

by $\Delta E_b = 0$. The region above the critical line satisfying $\Delta E_b > 0$ represents the red shift of the donor binding energy and the region below the critical line described by $\Delta E_b < 0$ shows the blue shift of the donor binding energy. Fig. 4.5 also shows that the critical line corresponding to $\Delta E_b = 0$ is highly dependent on the dot size. Comparing Fig. 4.5(a) and (b), it is found that the critical line moves down when the dot size increases from $L = R = 10$ nm to $L = R = 20$ nm. This means that the energetic shift of the donor binding energy ΔE_b is dominated by the electric field effect for the case of large dot size (i.e., $L = R = 20$ nm).

As verified by the previous discussions, the relative orientation of the tilted electric and magnetic fields plays an important role on the manipulation of the donor binding energy. To clarify the competition effects between the two fields applied in different configurations, we presents the contour plot of the energetic shift of the donor binding energy ΔE_b for various electric (0 - 30 kV/cm) and magnetic (0 - 30 T) fields in Fig. 4.6, where the magnetic field is applied at $\theta = 0°$ ((a) and (c)) or 90° ((b) and (d)) and the electric field is either parallel (left column) or perpendicular (right column) to it. As shown from Fig. 4.6,

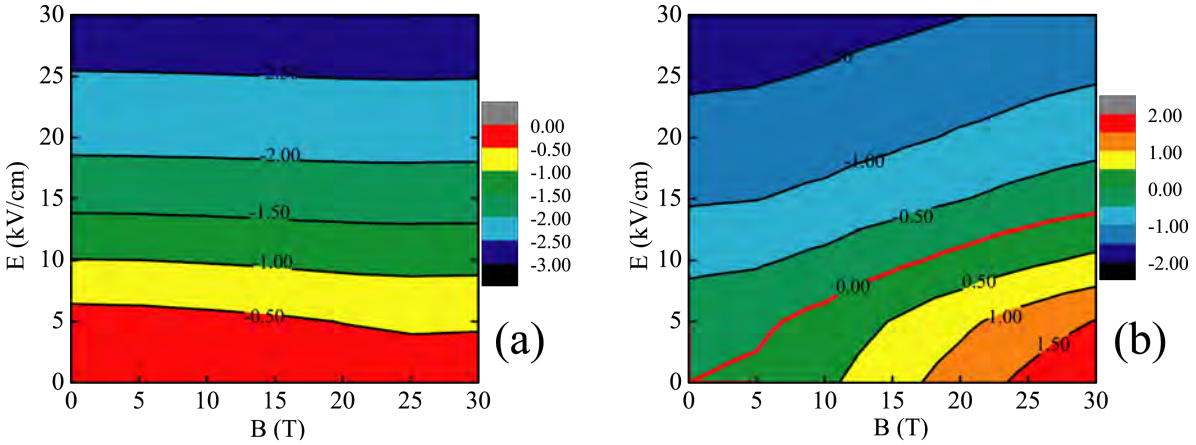

Figure 4.7: Contour plot of the energetic shift of the donor binding energy ΔE_b (in unite of meV) for various electric ($\vec{E}$) and magnetic ($\vec{B}$) fields in a GaAs/$Al_{0.3}Ga_{0.7}$As cylindrical QD with dot height $L = 20$ nm and radius $R = 20$ nm. The tilted $\theta = \theta' = 0°$. Here, (a) and (b) are for aspect ratio $\rho = \frac{L}{R} = 0.5$ and 2.0, respectively.

in the Viogt configuration ($\vec{B}\|\vec{x}$), the critical line goes up when the electric field is tilted from $\theta' = 0°$ (see Fig. 4.6(a)) to $\theta' = 90°$((see Fig. 4.6(c))). Making a comparison between Fig. 4.6(b) and (d), it is easy to discover that this finding is also valid in the Faraday configuration ($\theta = 90°$). The reasons can be understood as follows. When the electric field is tilted from the x-axial direction ($\theta' = 0°$) to the z-axial direction ($\theta' = 90°$), the electric field effect becomes less important due to the stronger confinement in the z-axial direction ($L = d/2 = 20$ nm, $d = 2R$ is the diameter of the cylindrical QD). This directly leads to the shrinking of the region described by $\Delta E_b < 0$ and the critical line goes up.

Similarly, we find from Fig. 4.6 that when the electric field is applied along the x-axial direction ($\theta' = 0°$), the critical line moves up as the magnetic field is tilted from $\theta = 0°$ (see Fig. 4.6(a)) to $\theta = 90°$ (see Fig. 4.6(d)). The same behaviour happens for the case of growth-direction electric field (see Fig. 4.6(b) and (c)). This can be understood analogously as follows. When the magnetic field shifts from the x-axial direction to the z-axial direction, the magnetic filed induced confinement becomes more pronounced due to the weaker confinement in the radial direction ($d = 2R = 2L = 40$ nm). As a result, the region corresponding to $\Delta E_b > 0$ is enlarged and the critical line moves up.

Finally, Fig. 4.7 displays the contour plot of the energetic shift of the donor binding energy ΔE_b for various electric $\vec{E}$ (0 - 30 kV/cm) and magnetic $\vec{B}$ (0 - 30 T) fields in two aspect ratio ($\rho = \frac{L}{R} = 0.5$ and 2.0) configurations, where the electric and magnetic fields are both applied along the x-axial direction. As indicated from Fig. 4.7(a) (aspect ratio $\rho = \frac{L}{R} = 0.5$), ΔE_b is negative for any electric and magnetic field. Furthermore, for small electric field, it decreases slightly with increasing the magnetic field. For large electric field, however, it is insensitive to the increased magnetic field. This is because that for aspect ratio $\rho = 0.5$, both the in-plane electric and magnetic fields move the electron

probability density far from the impurity center. Therefore, the donor binding energy reduces as the applied electric (or magnetic) field increases. Moreover, for very strong electric field (for instance, $E = 25$ kV/cm), the electron probability density distribution is totally dominated by the in-plane electric field and it is insensitive to the increased magnetic field. This directly makes the donor binding energy become invariant with the increased in-plane magnetic field. While when the aspect ratio goes up to $\rho = \frac{L}{R} = 2$ (see Fig. 4.7(b)), the critical line corresponding to $\Delta E_b = 0$ appears. Moreover, comparing Fig. 4.6(a) to Fig. 4.7(b), it is easy to find that the critical line moves up as the aspect ratio increases. This is because when the aspect ratio increases the confinement in the z-axial direction becomes weak and the magnetic field induced confinement in yoz plane becomes significant.

4.4 Brief summary

In summary, using the potential morphing method (PMM) in the framework of the effective-mass approximation (EMA), the combination effects of the tilted electric and magnetic fields on the binding energy of an on-center donor impurity localized in a $GaAs/Al_{0.3}Ga_{0.7}As$ cylindrical QD has been investigated theoretically. The electric and magnetic fields are both tilted with respect to the QD growth direction and they are either parallel or perpendicular to each other. It is found that for small dot size, the magnetic shift of the donor binding energy is insensitive to the orientation of the electric field. However, for large dot size, it strongly depends on the orientation of the electric field. Moreover, our results show that when the tilted electric and magnetic fields are parallel, the magnetic shift of the donor binding energy is a monotonic function of the strength of the magnetic field; while when the applied electric and magnetic fields are perpendicular, it is a non-monotonic function of the magnetic field and it exhibits a minimum at a critical magnetic field. The critical magnetic field increases when the magnetic field is tilted from the in-plane direction to the growth direction. However, it decreases with increasing the aspect ratio of the cylindrical QD. Furthermore, we have systematically discussed the competition effects between the two fields on the donor binding energy. It is found that there is a critical line corresponding to the zero shift of the donor binding energy under the influence of simultaneously applied tilted electric and magnetic fields. Moreover, this critical line is highly dependent on the dot size, relative orientation of the titled electric and magnetic fields as well as the aspect ratio of the cylindrical QD. We believe that the results presented here can be useful for us to directly manipulate the performance of the $GaAs/Al_{0.3}Ga_{0.7}As$ QD-based optoelectronic devices by applying suitable tilted electric and magnetic fields. We also hope that our results can stimulate forthcoming theoretical

and experimental investigations in this research area.

5

Competition effects of static fields on impurity binding energy in a quantum dot in the presence of pressure and temperature

*In this chapter, we study the combination effects of the electric and magnetic fields on the binding energy of an on-center donor impurity in disc-shaped $GaAs/Al_{0.3}Ga_{0.7}As$ quantum dots with emphasis on the competition effects between the two fields under externally applied pressure and temperature. The electric field is applied along the radial direction of the quantum dots, while the magnetic field is applied along the growth direction. Our results show that the two fields exhibit a competition effect on the donor binding energy, leading to an invariant binding energy as in the zero field case at a critical line. This line separates the region corresponding to the red shift of the donor binding energy from the one referring to the blue shift of the binding energy. Comparing to the magnetic field effect, increasing in the QD sizes or applied pressure is found to favour more its electric counterpart, enlarging the region satisfied by the red shift of the donor binding energy. The temperature effect appears to decrease the donor binding energy. However, the competition effects between the two fields retain the same when the temperature varies. The results presented herein are published in Science of Advanced Materials **6**, 586 (2014).*

Contents

5.1 Introduction

Doping of semiconductors by impurity atoms has widespread technological applications in microelectronics and optoelectronics. It provides further means to control the performance of related devices.[6] Donors have been used in some elegant quantum computing proposals that draws upon the vast expertise of the semiconductor device industry.[7] One of the proposals that renewed interest in the quantum mechanics of donors is the Kane qubit[81] in which information is encoded into the nuclear spins of donor atoms in doped silicon electronic devices, and engineers the donor electron wave function by electrodes to manipulate information.

Due to the development of nanoscience and nanotechnology, the study of donor related electronic and optical properties in semiconductor quantum dots (QDs) has been of great interest in the past.[70,73,80,82–86] It has been found that donor related properties in semiconductor QDs depend significantly on the materials, geometries (sizes and shapes), shapes of the confinement potentials and also dopant positions. External perturbations, such as applied electric and magnetic fields, hydrostatic pressure and temperature, also modify significantly the confined states of the donors.[80,87–92] To control and modulate the output of the doped-QDs-based optoelectronic devices, a combined application of these external perturbations in semiconductor QDs, such as a combination of the electric field with the magnetic field, has drawn increasingly attentions recently.[93–99] When the electric and magnetic fields are applied perpendicular to each other in a QD system, as reported in a recent paper[99] of our group, competition effects appear. These competition effects on the donor binding energy have been found to be strongly dependent on the QD geometric characteristics (dot sizes and aspect ratios) and also the strength and orientation of the two fields.[99] When another external perturbation is also simultaneously present in the QD system under the influence of perpendicular electric and magnetic fields, a question, which will arise, is that how a given perturbation influences the competition effects.

In this contribution, we theoretically investigate the combination effects of the electric and magnetic fields on the donor binding energy in disc-shaped QDs with emphasis on the competition effects between the two fields under the externally applied pressure and temperature. The electric field is applied along the radial direction, while the magnetic field is applied perpendicular to it which is along the QD growth direction. The numerical approach we use for the present calculations is the potential morphing method (PMM)[3] in the framework of the effective mass approximation (see Chapter 1), which has been proved to be a robust tool for the calculations of impurity-related electronic and optical properties in a QD system.[58,91,99,100] In the following section, we define our model and explain the general theory.

5.2 Theoretical framework

In the framework of effective mass approximation, an on-center shallow donor impurity in a disc-shaped QD with radius R, under the influence of the electric and magnetic fields, applied pressure and temperature, can be modeled by the Hamiltonian

$$\hat{H} = (\hat{p} + \frac{e}{c}\vec{A}(\vec{r}))\frac{1}{2m_e^*(P,T)}(\hat{p} + \frac{e}{c}\vec{A}(\vec{r})) + V(\vec{r},P,T) + |e|\vec{E}\cdot\vec{r} - \frac{e^2}{4\pi\varepsilon_0\varepsilon_r(P,T)|\vec{r}|}. \quad (5.1)$$

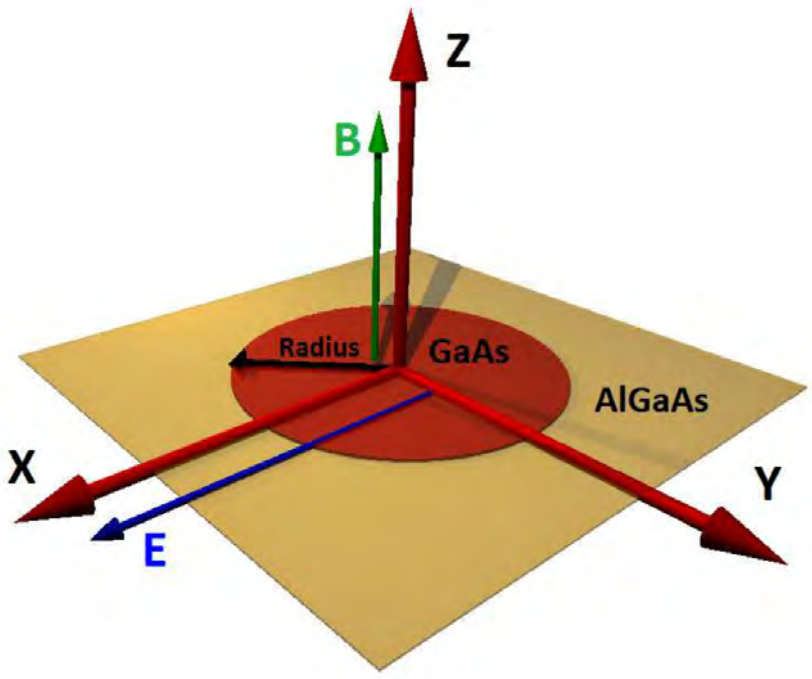

Figure 5.1: Schematic representations of a GaAs/AlGaAs disc-shaped QD under the influence of the applied electric and magnetic fields. The electric field ($\vec{E}$) is applied along the x-axis direction and the magnetic field ($\vec{B}$) is applied perpendicular to it which is along the z-axis direction.

The first term of the Hamiltonian is the Kinetic term of the delocalized conduction electron under the influence of the z-axis magnetic field ($\vec{B} = B\vec{z}$ (see Fig. 5.1), where B is the magnitude of the magnetic field and $\vec{z}$ is the z-axis unit vector). $\vec{A}$ is the vector potential.

In the cylindrical gauge ($\vec{A} = \frac{1}{2}\vec{B}\times\vec{r}$), the operator for the Kinetic energy of the electron (the first term of Eq. (5.1)) is

$$\hat{H}_{Kin} = \hat{p}\frac{1}{2m_e^*(P,T)}\hat{p} + \frac{eB}{2m_e^*(P,T)c}\hat{l}_z + \frac{e^2B^2}{8m_e^*(P,T)c^2}(x^2+y^2), \tag{5.2}$$

where e is the absolute value of the electron charge, c is the speed of the light in vacuum, and $\hat{l}_z$ is the z-component of the angular momentum operator. $m_e^*(P,T)$ is the pressure and temperature dependent electron effective mass, which is given by[101]

$$m_e^*(P,T) = \frac{m_0}{1 + E_P^\Gamma[(\frac{2}{E_g^\Gamma(P,T)}) + (\frac{1}{E_g^\Gamma(P,T)+\Delta_0})]}, \tag{5.3}$$

in which m_0 is the bare mass of the electron, P and T stand for the applied pressure and temperature, respectively, $E_P^\Gamma = 7.51$ eV is an energy related to the momentum matrix element and the spin-orbit splitting for GaAs QD is $\Delta_0 = 0.341$ eV. E_g^Γ is the pressure and temperature dependent energy gap at Γ point in the Brillouin zone for GaAs QD, which is the following[102,103]

$$E_g^\Gamma(P,T) = E_g^\Gamma(0,T) + aP + bP^2, \tag{5.4}$$

where $a = 1.07\times10^{-2}$ eV/kbar, $b = -3.77\times10^{-5}$ eV/kbar^2, and

$$E_g^\Gamma(0,T) = [1.519 - \frac{5.045\times10^{-4}T^2}{T+204}], \tag{5.5}$$

in unit of eV. $V(\vec{r},P,T)$ is the pressure and temperature dependent conduction electron confinement potential, which is given by

$$V(\vec{r},P,T) = V_0(P,T)\Theta(|\vec{r}| - R), \tag{5.6}$$

where Θ is the Heaviside step function and $\vec{r}$ is the position vector with $|\vec{r}| = \sqrt{x^2+y^2}$, where x and y are the Cartesian coordinates, respectively. The pressure and temperature dependent conduction band discontinuity at the interface of the GaAs/AlGaAs heterostructure is

$$V_0(P,T) = Q[E_{Gap}^{Al_xGa_{1-x}As}(P,T) - E_{Gap}^{GaAs}(P,T)], \tag{5.7}$$

where Q is the conduction band offset which is assumed to be pressure independent and taken as Q=60% for GaAs/AlGaAs heterostructure. The pressure and temperature dependent band gap is provided by[104]

$$E_{Gap}^i(P,T) = E_1^i + \beta^i P + \alpha^i T^2/(T+T_1^i), \tag{5.8}$$

where for GaAs (i = GaAs), $E_1 = 1.519$ eV, $\alpha = -5.405\times10^{-4}$ eV/K, $\beta = 10.7\times10^{-3}$ eV/kbar and $T_1 = 204$ K at Γ point, while for $Al_xGa_{1-x}As$ (i = $Al_xGa_{1-x}As$), $E_1 = 1.519 + 1.155x + 0.37x^2$ eV, $\alpha = -5.405\times10^{-4}$ eV/K, $\beta = (10.8 - 3.2x + 3.8x^2)\times10^{-3}$ eV/kbar and $T_1 = 204$ K, respectively.

The third term of Eq. (5.1) is the electrostatic potential induced by the external electric field with strength E, which is applied along the radial direction in our calculations (see Fig. 5.1). ε_0 in the last term is the permittivity in vacuum and $\varepsilon_r(P,T)$ is the pressure and temperature dependent relative dielectric constant, which is[105,106]

$$\varepsilon_r(P,T) = \begin{cases} 12.74\exp[-1.67\times10^{-3}P]\exp[9.4\times10^{-5}(T-75.6)], & 0 < T \leq 200 \\ 13.18\exp[-1.73\times10^{-3}P]\exp[20.4\times10^{-5}(T-300)], & T \geq 200 \end{cases}, \tag{5.9}$$

where T is in unit of Kelvin.

To solve numerically the Schrödinger equation based on Hamiltonian (5.1), PMM is used (see Chapter 1). In our calculations, the usual two-dimensional (2D) harmonic oscillator is chosen as a reference system and its ground-state wave function is selected as the initial wave function. The interaction potential corresponding to the ground-state energy of the electron is

$$V_S^e = \frac{eB}{2m_e^*(P,T)c}\hat{l}_z + \frac{e^2B^2}{8m_e^*(P,T)c^2}(x^2+y^2) + V(\vec{r},P,T) + |e|\vec{E}\cdot\vec{r}, \tag{5.10}$$

whereas, the interaction potential for the ground-state energy of the shallow donor impurity is

$$V_S^i = \frac{eB}{2m_e^*(P,T)c}\hat{l}_z + \frac{e^2B^2}{8m_e^*(P,T)c^2}(x^2+y^2) + V(\vec{r},P,T) + |e|\vec{E}\cdot\vec{r} - \frac{e^2}{4\pi\varepsilon_0\varepsilon_r(P,T)|\vec{r}|}. \tag{5.11}$$

The binding energy of the shallow donor impurity is defined as

$$E_b = E_0 - E_i, \tag{5.12}$$

where E_0 is the electron ground-state energy (without the last term of Eq. (5.1)) and E_i is the impurity ground-state energy (with the last term of Eq. (5.1)). To study the competition effects of the applied electric and magnetic fields, we defined the energetic shift of the donor binding energy as[99]

$$\delta E_b = E_b(F\neq0, B\neq0) - E_b(F=0, B=0). \tag{5.13}$$

5.3 Numerical results and discussion

In what follows, we present our results for the combination effects of the electric and magnetic fields on the binding energy of an on-center donor impurity in GaAs/$Al_{0.3}Ga_{0.7}As$ disc-shaped QDs under externally applied pressure and temperatures. A position independent electron effective mass is used in the present calculations as an approximation and the dielectric mismatch between the dot and barrier materials is not considered.

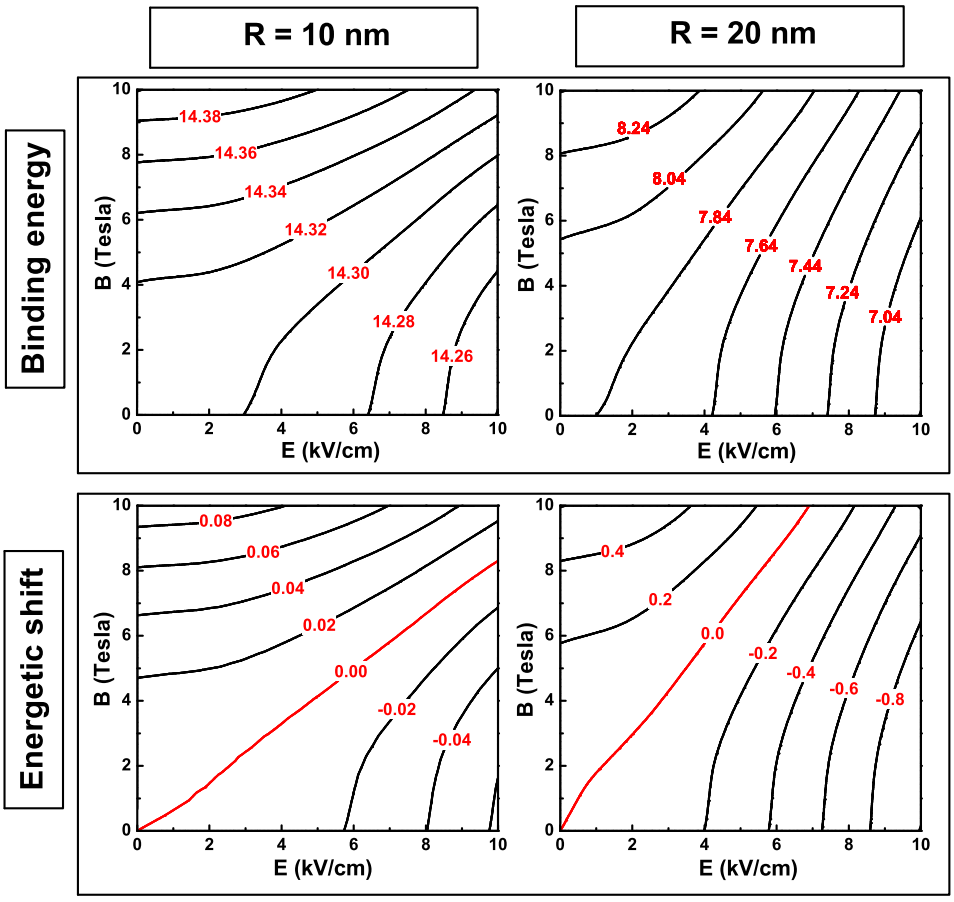

Figure 5.2: Contour plot of the binding energy of an on-center donor impurity E_b (upper panel, in unit of meV) and the energetic shift of the donor binding energy (δE_b) (lower panel, in unit of meV) for various electric (E) and magnetic (B) fields in GaAs/$Al_{0.3}Ga_{0.7}As$ disc-shaped QDs at room temperature (T = 300 K) and zero pressure ($P = 0$). Two dot sizes $R = 10$ nm (left panel) and 20 nm (right panel) are considered, respectively.

As a first step towards the combination effects of the electric and magnetic fields on the binding energy of an on-center donor impurity in disc-shaped QDs, we present several suitable contour plots (see Fig. 5.2) of the donor binding energy and the energetic shift of the donor binding energy for various electric (0 - 10 kV/cm) and magnetic (0 - 10 Tesla) fields. The calculations are performed for two dot sizes (R = 10 nm and 20 nm). The obtained results show that for any magnetic field, the applied electric field tends to decrease the donor binding energy. Whereas, an increase in the magnetic field appears to enhance significantly the binding energy for any electric field. This is due to fact that the electric field pushes the electron density far away from the impurity center, while its magnetic counterpart squeezes the electron probability with respect to the impurity center. When these two fields are simultaneously employed in the QD systems, competition effects appear. A visualization of these effects can be found in the lower panel of Fig. 5.2. It shows that there is a critical line (see the red lines in Fig. 5.2) corresponding to the zero energetic shift of the donor binding energy (δE_b=0) under the influence of the applied electric and magnetic fields, irrespectively of the dot sizes. The area above the critical line which satisfies $\delta E_b > 0$ represents the blue shift of the donor binding energy and the region below the critical line determined by $\delta E_b < 0$ describes the red shift of the donor binding energy.

A red shift of the donor binding energy means essentially that the electric field effect is dominant over its magnetic field counterpart and finally a negative energetic shift of the donor binding energy is exhibited. Conversely, if the magnetic field effect is more pronounced, the energetic shift of the donor binding energy is positive ($\delta E_b > 0$) and a blue shift of the donor binding energy appears. An increase in the dot size leads to a decrease in the donor binding energy but favors both the electric and magnetic field effects. This can be easily conformed by the significantly increased energetic shift of the donor binding energy in QDs within the weak confinement regime in comparison to the ones in the strong confinement regime. When the dot size increases, the applied electric field effect appears to be more pronounced than its magnetic field counterpart. This causes an enlarged region which describes the red shift of the donor binding energy ($\delta E_b < 0$). As a result, the critical line presents a considerable counterclockwise planer rotation as the dot size increases.

For the QDs in the weak confinement regime (R = 20 nm), we also present in Fig. 5.3 the contour plots of the donor binding energy and energetic shift of the donor binding energy for various electric and magnetic fields, where two different pressures are considered. It shows that the applied electric and magnetic fields retain a very similar effect on the donor binding energy in the presence of the pressure as in the zero pressure case (see the plots in the right panel of Fig. 5.2). However, when the pressure increases, the donor binding energy increases at given electric and magnetic fields. This is associated with the modification of the material parameters induced by the applied pressure. The electron

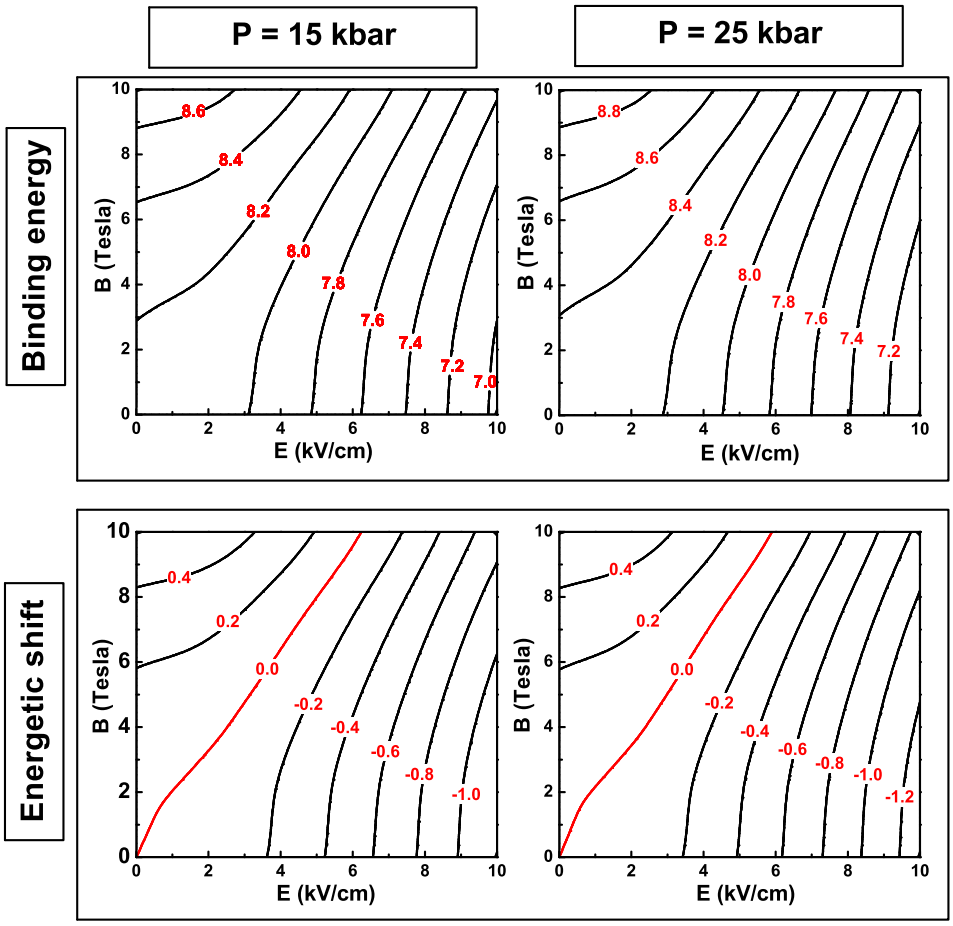

Figure 5.3: Contour plot of the binding energy of an on-center donor impurity E_b (upper panel, in unit of meV) and the energetic shift of the donor binding energy (δE_b) (lower panel, in unit of meV) for various electric (E) and magnetic (B) fields in GaAs/$Al_{0.3}Ga_{0.7}As$ disc-shaped QDs with radius $R = 20$ nm at room temperature (T = 300 K) . Two pressure values ($P = 15$ kbar (left panel)and 25 kbar (right panel)) are considered, respectively.

effective mass increases with increasing the pressure, while the relative dielectric constant and electron confinement potential (V_0) tend to decrease as the pressure increases. The joint effects of the variation of these material parameters leads to an effectively enhanced Rydberg energy with increasing the pressure and finally an increase in the donor binding energy is present.

Fig. 5.3 also shows that for any applied pressure, the critical line determined by the zero energetic shift of the donor binding energy appears (see the red lines in the plots on the lower panel). The presence of the applied pressure turns out to favor more the electric field effect, which causes an increase in the region determined by the red shift of the donor binding energy ($\delta E_b < 0$). Consequently, the critical line experiences a slight counterclockwise rotation when the applied pressure increases.

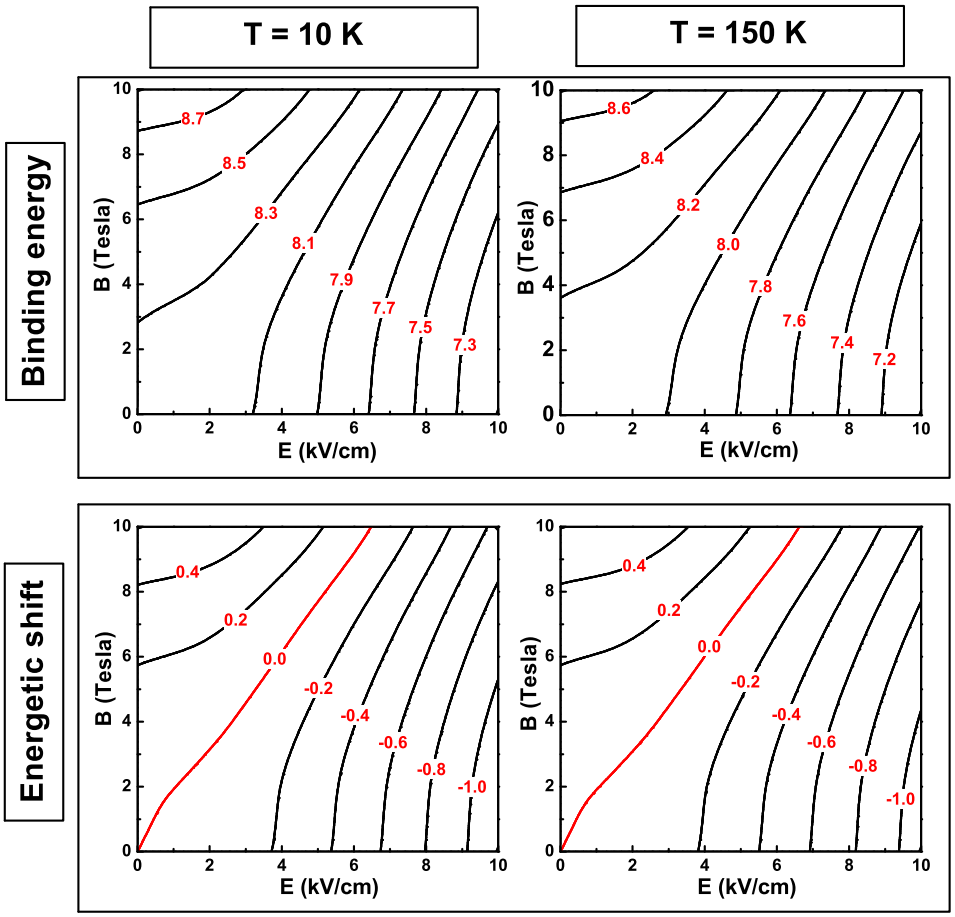

Figure 5.4: Contour plot of the binding energy of an on-center donor impurity E_b (upper panel, in unit of meV) and the energetic shift of the donor binding energy (δE_b) (lower panel, in unit of meV) for various electric (E) and magnetic (B) fields in GaAs/$Al_{0.3}Ga_{0.7}As$ disc-shaped QDs with radius $R = 20$ nm at zero pressure ($P = 0$) . Two temperature values ($T = 10$ K (left panel)and 150 K (right panel)) are considered, respectively.

Finally, in an effort to show the competition effects of the electric and magnetic fields in a disc-shaped QD under the influence of temperature, we display in Fig. 5.4 the contour plots of the donor binding energy and energetic shift of the donor binding energy for various electric and magnetic fields, where two different temperature values are considered. As the first glance of the figure, one could find that increasing the temperature causes a decrease in the donor binding energy for any electric and magnetic fields (see the right plots of Fig. 5.2). This is related to the temperature dependent variation of the material parameters. As indicated explicitly from Eqs. (5.3) and (5.9), an increase in the temperature appears to decrease the electron effective mass and enhance the relative dielectric constant. Consequently, a reduce in the Rydberg energy occurs and the donor binding energy decreases as the temperature increases. Similarly to what Fig. 5.3 shows, the critical line described by $\delta E_b = 0$ appears for any temperature considered. It also

appears from Fig. 5.4 that the presence of the temperature do not have any significant influence on the competition effect of the electric and magnetic fields on the binding energy of an on-center donor impurity in disc-shaped QDs. This can be clearly confirmed by the invariant position of this critical line in Fig. 5.4 (see the plots on the lower panel).

5.4 Brief summary

In summary, we have studied the combination effects of the electric and magnetic fields on the binding energy of an on-center donor impurity in disc-shaped GaAs/$Al_{0.3}Ga_{0.7}As$ quantum dots (QDs), emphasizing on the competition effects between these two fields under various externally applied pressures and temperatures. The electric field is applied along the radial direction, while the magnetic field is applied perpendicular to it, which is along the growth direction of the QD. It is found that the enhanced electric field decreases the donor binding energy, while the simultaneously applied magnetic field exhibits a reversed effect, increasing the binding energy with increasing the field strength. These competition effects between the two fields lead to a critical line in which the donor binding energy keeps invariant as in the zero field case. The position of this line is found to be strongly dependently on the QD sizes. Comparing to the magnetic field effect, an increase in the QD size causes a more pronounced electric field effect which in turn enhances drastically the region corresponding to the red shift of the donor binding energy. The applied pressure exhibits a very similar but weaker effect on the critical line as the QD sizes, favoring more the electric field effect. Although the increased temperature effect turns out to decrease the donor binding energy, it does not have significant influence on the competition effects between the two fields. We believe that the results presented here can be useful for the doped GaAs/AlGaAs QDs based functional devices.

6

Optical susceptibilities in singly charged ZnO colloidal quantum dots embedded in different dielectric matrices

*In this chapter, we derive the analytical expressions for the linear, third-order nonlinear and intensity-dependent susceptibilities in quantum dots (QDs) embedded in a dielectric matrix by using density matrix equations within the two-level system approximation, considering the local field effect due to the presence of dielectric mismatch. Based on the derived expressions, we perform a comparative study of the optical susceptibilities in singly charged Zinc oxide quantum dots embedded in various dielectric matrices. Three commonly adopted matrices are considered. The electronic structure of the system is numerically calculated. In general, our results indicate that the optical susceptibilities are highly affected by the capped matrices. For example, QDs embedded in the matrix with the largest dielectric constant but the smallest energy band gap exhibit the largest linear and nonlinear optical susceptibilities, while that dispersed in a matrix with the largest energy band gap show the highest threshold energy. It is also found that the third-order nonlinear susceptibility exhibits a stronger dependence on the nature of the capped matrix as compared to its linear counterpart. Finally, we find that the total susceptibility in charged QD immersed in a matrix with a higher dielectric constant is more sensitive to the applied radiation intensity. The results presented herein are published in Journal of Applied Physics **113**, 054303 (2013).*

Contents

6.1 Introduction

Zinc oxide (ZnO) is a material with a great variety of technological applications, such as surface acoustic wave devices, piezoelectric transducers, optical waveguides, transparent conductive oxides, chemical and gas sensors, spin functional devices, and ultraviolet (UV) light emitters (Ref. 107 and references therein). Its wide band gap (3.445 eV) makes ZnO a promising material for UV photonic applications, while the high exciton binding energy (around 60 meV) allows efficient excitonic emission, even at room temperature. In addition, ZnO is plentiful, cost-effective, and relatively non-toxic which is desirable for bio-applications such as bio-imaging and cancer detection. Due to the important modifications that appear at the nanoscale, ZnO nanostructures, especially zero dimensional nanoparticles or colloidal quantum dots (QDs) have attracted increasing attention.

As it is well known, chemical synthesis methods are the most common way to grow uniformly dispersed QDs. However, QDs prepared by such methods are relatively unstable and encounter the difficulties in dispersion and preservation. To stabilize the QDs when coupling with devices, matrix passivation is one of the most commonly adopted ways. Besides, immersing semiconductor QDs in polymer or glass matrix by using surface chemistry methods is also a good way of passivating the dangling bond at the QD surface.[108–110] Distinct photoluminescence properties have been demonstrated in such unique systems that can be served as fluorescent materials or active media in tunable lasers to achieve full color emission.[111,112] Due to these reasons, the optical properties of ZnO QDs embedded in organic polymers, such as poly(vinyl alcohol) (PVA), poly(methyl methacrylate) (PMMA) and poly(vinyl pyrrolidone) (PVP),[113–117] and inorganic materials, such as CaF_2, MgO, SiO_2 and BaF_2,[118–122] have been widely studied. However, most of these studies are focused on the experimental synthesis and characterization for possible device application purposes. Theoretical investigations on the electronic and optical properties in colloidal ZnO QDs embedded in different matrices are very recent. Using the atomistic empirical pseudopotential mehthod, Baskoutas and Bester[123] have studied the electronic properties and optical emission polarizations of free-standing ZnO QDs. Dallali et al.[124] have investigated theoretically the energies of exciton and acceptor-bound exciton complex in ZnO QDs embeded in SiO_2 matrix. A theoretical work associated with the intersubband optical properties of ZnO QDs dispersed in SiO_2 matrix has also been reported recently.[125] Though plenty of new insights have been brought by these studies, the influence of the capped matrices on the electronic and optical properties in ZnO colloid QDs is still unknown.

In this contribution, we carried out a theoretical comparative study of the optical susceptibilities[126–128] of charged ZnO colloidal QDs embedded in various dielectric matrices.

Three commonly used matrices, such as PVA, PMMA and SiO_2, have been used in the present calculations. The theoretical approach we are using is the potential morphing method (PMM)[3] (see Chapter 1) in the framework of the effective mass approximation, which has already been applied in the past for the study of optical properties of several nanostructures.[48,49,52,58]

6.2 Calculation details

6.2.1 Calculation of the electronic structure

The Schrödinger equation for an electron confined inside a singly charged ZnO colloidal QD of radius R is

$$\left(\hat{p}\frac{1}{2m_e^*}\hat{p} + V(\vec{r})\right)\psi(\vec{r}) = E\psi(\vec{r}), \tag{6.1}$$

where m_e^* is the effective mass, and $V(\vec{r})$ is the confinement potential which is zero inside and V_0 outside of the QD. V_0 is the conduction-band electron confinement potential at the interface of the QD and the surrounding matrix given by

$$V_0 = V_b + \Sigma, \tag{6.2}$$

where V_b is the finite barrier height and Σ is the self-energy due to the polarization induced by charging the QD. The self-energy is given by[129,130]

$$\Sigma = \frac{1}{8\pi\varepsilon_0}\left(\frac{1}{\varepsilon_{out}} - \frac{1}{\varepsilon_{in}}\right)\frac{e^2}{R} + \delta\Sigma, \tag{6.3}$$

where ε_{in} and ε_{out} are the dielectric constants of the dot material and the surrounding matrix material, respectively. When $\varepsilon_{in} + \varepsilon_{out} \gg 1$, one gets[129]

$$\delta\Sigma \approx 0.466\frac{e^2}{4\pi\varepsilon_0\varepsilon_{in}R}\left(\frac{\varepsilon_{in} - \varepsilon_{out}}{\varepsilon_{in} + \varepsilon_{out}}\right), \tag{6.4}$$

which is usually small but not negligible.[129] This simple model has been successfully applied for the theoretical investigation of the photoabsorption and photoelectric process of charged silicon nanocrystallites embedded in amorphous SiO_2 matrix.[130] To obtain the ground state, the first excited state and the corresponding energies for the Hamiltonian (6.1), which are needed for the calculation of the linear and nonlinear optical properties

below, PMM is employed. The interaction potential involved in the potential morphing process is $v_S = V(\vec{r})$ and the reference system is selected as the usual harmonic oscillator in three dimensions with well-known eigenfunctions. It should be noted here that adopting the harmonic oscillator as a reference system does not affect our results because the PMM needs only a known reference system to start the morphing process and finally to give the eigenfunctions and eigenvalues for the unknown system, independently on the choice of the initial reference system.[3,53,91,99]

6.2.2 Calculation of the susceptibilities

After obtaining the necessary wave functions and eigenenergies, we start to calculate the linear, nonlinear and total susceptibilities of a charged QD embedded in a dielectric matrix. The QD interacts with an electromagnetic field with time-dependent electric field $E(t) = E_0 \cos(\omega t)$, where E_0 is the time-independent electric field amplitude and ω is the angular frequency of the applied electric field. Within the two-level system approximation, the dynamics of the QD system under the interaction of an electromagnetic field is modeled by the Hamiltonian

$$\hat{H} = \hbar\omega_0(|j\rangle\langle j|) - \mu E^{'}(t)(|i\rangle\langle j| + |j\rangle\langle i|), \tag{6.5}$$

where $|i\rangle$ and $|j\rangle$ represent the initial and final states, respectively, μ is the transition matrix element between the initial and final states which is defined as $\mu = \langle i|ez|j\rangle$, where we assume the polarization of electromagnetic radiation is along the z-axis direction. $E^{'}(t) = \frac{E_0}{2\varepsilon_{eff}}(e^{-i\omega t} + e^{i\omega t})$, where ε_{eff} is the effective dielectric constant which considers the local field effect due to the dielectric mismatch, and it is given by $\varepsilon_{eff} = \frac{2\varepsilon_{out}+\varepsilon_{in}}{3\varepsilon_{out}}$.

The density matrix equations, in the rotating wave approximation, for the slowly varying elements of the density matrix are[128,131]

$$\dot{\sigma}(t) = -\frac{1}{T_2}\sigma(t) + i\Omega\Delta(t) + i\delta\sigma(t), \tag{6.6}$$

$$\dot{\Delta}(t) = 2i\Omega\sigma(t) - 2i\Omega\sigma^*(t) - \frac{\Delta(t) - 1}{T_1}. \tag{6.7}$$

Here $\delta = \omega - \omega_0$ is the detuning of applied field from resonance, where $\omega_0 = (E_j - E_i)/\hbar$ with E_i and E_j being the energy eigenvalues of the initial (ground) and final (first excited) states in the charged QD, respectively, $\Delta(t) = \sigma_{ii}(t) - \sigma_{jj}(t)$ with σ_{ij} being the density matrix element, T_1 and T_2 are the population relaxation time and the dephasing time,

respectively, and $\Omega = \frac{\mu E_0}{2\hbar\varepsilon_{eff}}$ is the Rabi frequency which differs from the usual definition by the local field term (ε_{eff}).

From Eqs. (6.6) and (6.7) in steady state we take

$$\sigma = \frac{(i-\delta T_2)T_2\Omega}{1+\delta^2T_2^2+4\Omega^2T_1T_2}. \tag{6.8}$$

Therefore, the susceptibility of the system is given by

$$\chi = \frac{2N\mu}{\varepsilon_0\varepsilon_{eff}E_0}\sigma = \frac{N\mu^2T_2}{\hbar\varepsilon_0\varepsilon_{eff}^2}\frac{i-\delta T_2}{1+\delta^2T_2^2+\frac{\mu^2E_0^2}{\hbar^2\varepsilon_{eff}^2}T_1T_2}, \tag{6.9}$$

where N is the electron volume density in the QD system and ε_0 is the permeability in vacuum.

We define $E_0^s = \frac{\hbar\varepsilon_{eff}}{\mu\sqrt{T_1T_2}}$ which is the saturation electric field strength. By this, we can rewrite Eq. (6.9) as

$$\chi = \frac{N\mu^2T_2}{\hbar\varepsilon_0\varepsilon_{eff}^2}\frac{i-\delta T_2}{1+\delta^2T_2^2+\frac{E_0^2}{(E_0^s)^2}}. \tag{6.10}$$

Assuming the electric field parameter $x = \frac{E_0^2}{(E_0^s)^2} \ll 1$, we can perform a power-series expansion of χ in terms of x, retaining only terms up to the first order. The resultant solution for χ takes the form

$$\chi \simeq \frac{N\mu^2T_2}{\hbar\varepsilon_0\varepsilon_{eff}^2}\left[\frac{i-\delta T_2}{1+\delta^2T_2^2} - \frac{i-\delta T_2}{(1+\delta^2T_2^2)^2}\frac{E_0^2}{(E_0^s)^2}\right]. \tag{6.11}$$

Taking into account $\chi \simeq \chi^{(1)} + \frac{3}{4}\chi^{(3)}E_0^2$, we obtain the linear ($\chi^{(1)}$) and third-order nonlinear ($\chi^{(3)}$) optical susceptibilities as

$$\chi^{(1)} = \frac{N\mu^2T_2}{\hbar\varepsilon_0\varepsilon_{eff}^2}\frac{i-\delta T_2}{1+\delta^2T_2^2}, \tag{6.12}$$

$$\chi^{(3)} = -\frac{4N\mu^4T_1T_2^2}{3\hbar^3\varepsilon_0\varepsilon_{eff}^4}\frac{i-\delta T_2}{(1+\delta^2T_2^2)^2}. \tag{6.13}$$

In the linear regime the real part of susceptibility $\chi^{(1)}$ exhibits a standard dispersive lineshape, while its imaginary counterpart presents a Lorentzian lineshape.

We may also write the total susceptibility as

$$\chi = \chi^{'} + i\chi^{''}, \tag{6.14}$$

where $\chi^{'}$ and $\chi^{''}$ are the real and imaginary part, given by

$$\chi^{'} = \frac{N\mu^2 T_2}{\hbar\varepsilon_0\varepsilon_{eff}^2}\frac{1}{\sqrt{1+\kappa}}\frac{-\frac{\delta T_2}{\sqrt{1+\kappa}}}{1+(\frac{\delta T_2}{\sqrt{1+\kappa}})^2}, \tag{6.15}$$

$$\chi^{''} = \frac{N\mu^2 T_2}{\hbar\varepsilon_0\varepsilon_{eff}^2}\frac{1}{\sqrt{1+\kappa}}\frac{1}{1+(\frac{\delta T_2}{\sqrt{1+\kappa}})^2}, \tag{6.16}$$

respectively, with $\kappa = \frac{\mu^2 E_0^2 T_1 T_2}{\hbar^2 \varepsilon_{eff}^2}$. It turns out that the real ($\chi^{'}$) and imaginary ($\chi^{''}$) parts of total susceptibility still display respectively dispersive and Lorentzian lineshapes, but they are saturated and broadened.

Finally, one may rewrite the Eqs. (6.9) in terms of the incident optical intensity (I) as

$$\chi = \frac{N\mu^2 T_2}{\hbar\varepsilon_0\varepsilon_{eff}^2}\frac{i-\delta T_2}{1+\delta^2 T_2^2+\frac{2\mu^2 I}{cn\varepsilon_0\hbar^2\varepsilon_{eff}^2}T_1 T_2}. \tag{6.17}$$

Here, the relation between the optical intensity and the applied electric field is taken $I = \frac{n\varepsilon_0 c}{2}E_0^2$, where c is the light speed in vacuum, $n = \sqrt{\varepsilon_{in}}$ is the refractive index of the QD material.

6.3 Results and discussion

In the following, we will study the susceptibilities in the singly charged ZnO colloidal QDs, using the formulas presented in Sec.6.2. Three different matrices (i.e., PMMA, PVA and SiO_2) are considered. The relevant material parameters for the present calculations are listed in Tables 6.1 and 6.2, taking $N = 1.7\times10^{17}$ cm^{-3}, T_1=1 ps and T_2=0.14 ps.[132] As have been reported by Baskoutas and Terzis,[48] the height of the finite-depth confinement potential does not depend on the specific semiconductor of the QD, but exclusively depends on the matrix energy band gap by a simple linear relation of the form $V_{conf}=0.08\cdot E_g(M)$, where $E_g(M)$ is the matrix energy band gap. Thus, in the present calculations, we adopted the same relation, using the electron confinement potential $V_b=0.08\cdot E_g(M)$. As an approximation, the values of the electron effective mass are assumed to be the same in QD material (ZnO) and matrix materials[21] with value $m_e^* = 0.265\ m_0$, where m_0 is the electron mass in the free space .

Firstly, we display the real and imaginary part of the linear susceptibility $\chi^{(1)}$ (Fig. 6.1) and third-order nonlinear susceptibility $\chi^{(3)}$ (Fig. 6.2) as a function of the incident photon energy for the three different matrices. As clearly shown in Tables 6.1 and 6.2, different

Table 6.1: Theoretical values of the relative dielectric constant ε_r, the effective dielectric constant ε_{eff} and the local field factor F ($= \frac{1}{\varepsilon_{eff}}$) for three different dielectric matrices (PMMA, PVA and SiO_2). Relative dielectric constant for ZnO is 8.66.[125]

Materials	ε_r[133]	ε_{eff}	F
PMMA	3.4	1.516	0.66
PVA	14	0.873	1.15
SiO_2	3.9	1.407	0.71

Table 6.2: Theoretical values of the energy parameters used in our calculations. Here, E_g is in unit of eV, V_b and V_0 are in unit of meV, R is in unit of nm. The energy band gap, E_g, of ZnO is 3.445 eV[123] and $\Sigma_0 = \frac{1}{4\pi\varepsilon_0}\frac{e^2}{R} = \frac{1.44}{R}$ eV/nm.

Materials	E_g	$V_b = 80\times E_g$	Σ/Σ_0	V_0(R = 2)	V_0(R = 6)
PMMA	5.6[134]	448	+0.113	530	475
PVA	4.98[135]	398	-0.035	373	390
SiO_2	9[136]	720	+0.091	786	742

capped matrices have different dielectric constants and energy band gaps which differ substantially from the QD material. A higher dielectric constant of the capped matrix is related to a smaller self-polarization energy induced by the QD charging, which resultantly leads to a lower or even a negative (e.g., PVA) contribution to the QD confinement potential (see the forth column of Table 6.2). Conversely, it also causes a stronger local field effect in the corresponding charged QD, characterized by a larger local field factor $F = \frac{1}{\varepsilon_{eff}}$ (see

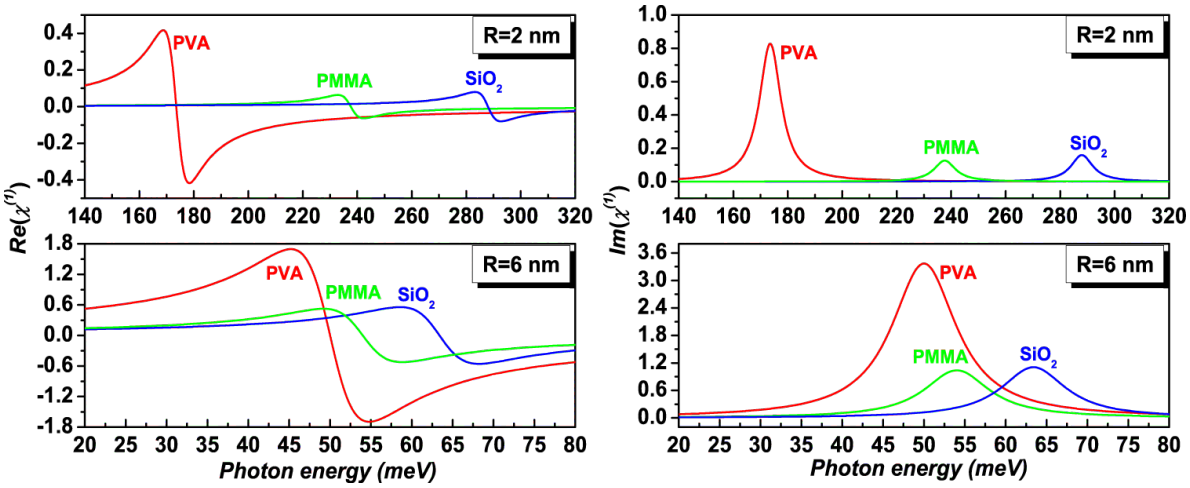

Figure 6.1: The real (left panel) and imaginary (right panel) part of $\chi^{(1)}$ as a function of the photon energy $\hbar\omega$ in singly charged ZnO QDs embedded in three different matrices (PVA (red line), PMMA (green line) and SiO_2 (blue line)). Two dot sizes $R = 2$ nm and 6 nm are considered, separately.

the last column of Table 6.1). However, a lower energy band gap of the capped matrix corresponds to a smaller QD confinement potential (see the last two columns of Table 6.2), consequently leading to a larger dipole transition matrix element. Due to the combination effects of local field and quantum confinement, QD embedded in polymeric matrix PVA which has the largest dielectric constant but the smallest energy band gap exhibits the largest (in absolute value) $\chi^{(1)}$ and $\chi^{(3)}$ (both real and imaginary part). Moreover, these two effects appear to compensate with each other and exhibit a competitive phenomenon in the other two phenomenological QDs. The local field effect turns out to dominate over its quantum confinement counterpart and consequently the susceptibilities in the charged QD capped with PMMA which has smaller energy band gap and dielectric constant exhibit a slightly smaller (absolute) value in comparison to that dispersed in inorganic matrix SiO_2.

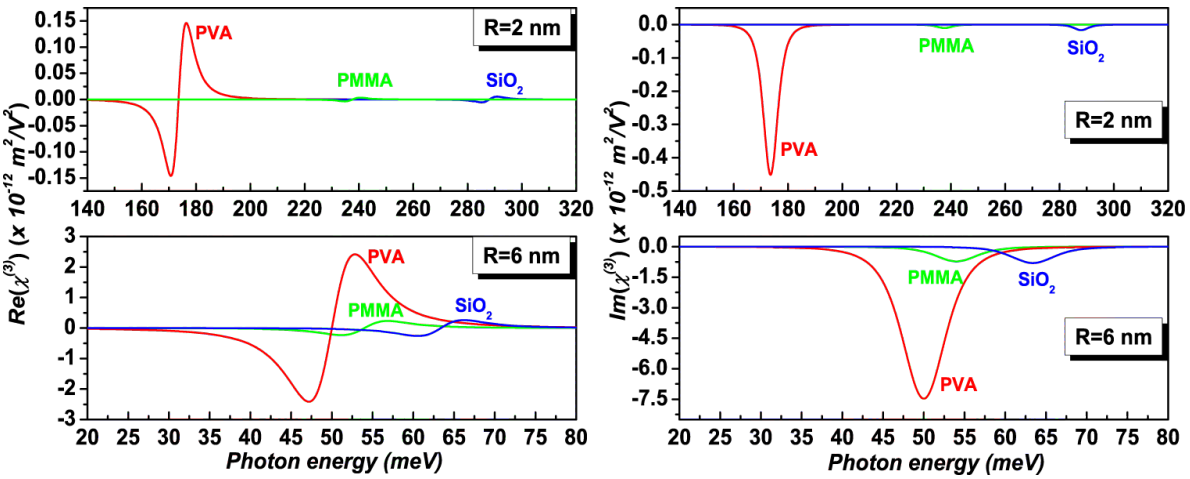

Figure 6.2: The same as Fig. 6.1 but for $\chi^{(3)}$.

Compared to the linear susceptibility (see Fig. 6.1), its third-order nonlinear counterpart appears to be more sensitive to the capped matrices, especially in the strong confinement regime (e.g., R =2 nm). This becomes evident by the top plot in the left panel of Fig. 6.2, where $\chi^{(3)}$ in QDs dispersed in PMMA and SiO_2 is practically marginal, while that in PVA exhibits a relatively large strength. This is also valid for QDs within the weak confinement regime, although $\chi^{(3)}$ in PMMA and SiO_2 capped QDs is substantially enhanced. We relate this to a stronger dependence of $\chi^{(3)}$ on the combined effects of local field and quantum confinement (e.g., $\chi^{(3)} \propto (\frac{\mu}{\varepsilon_{eff}})^4$, while $\chi^{(1)} \propto (\frac{\mu}{\varepsilon_{eff}})^2$).

In the same figures, we also find that the QD size influences significantly the susceptibilities in all the three charged QDs. Both the linear and nonlinear susceptibilities in all the capped QDs are substantially broadened and enhanced as the QD size increases. This can be attributed to the decrease of the quantum confinement effect, which leads to a

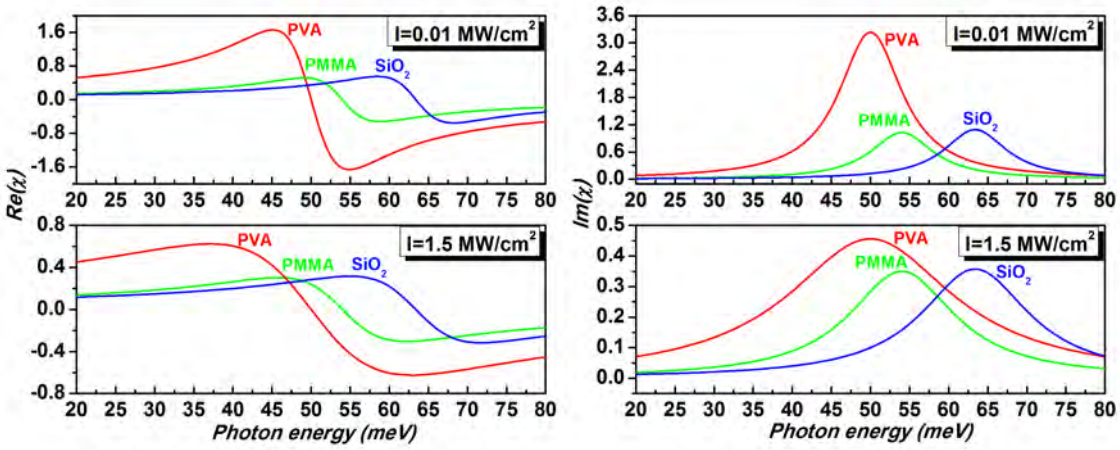

Figure 6.3: The real (left panel) and imaginary (right panel) part of χ as a function of the photon energy $\hbar\omega$ in singly charged ZnO QDs with radius R = 6 nm under various radiation intensities (I = 0.01 and 1.5 MW/cm^2). Three capped matrices, e.g., PVA, PMMA and SiO_2, are considered.

significant increase of the transition matrix elements. This behavior is significantly more pronounced for the case of the nonlinear term. Furthermore, drastic red shifts are observed when the QD size is increased, irrespectively of the capped matrices. Another important feature is that the threshold energies in the three capped QDs are getting closer when the quantum confinement becomes weak. Based on this observation, it becomes clear that the influence of the capped matrices on the threshold energy is significant in small QDs (e.g., R = 2 nm). However, in large QDs (e.g., R = 6 nm), it becomes less important. In addition to this, we find that the QD capped with PVA exhibits a more drastic increase in both $\chi^{(1)}$ and $\chi^{(3)}$ in comparison to the other two charged QDs.

Finally, in an attempt to investigate the influence of the applied intensity on the total susceptibility (Eq. (6.17)), we present in Fig. 6.3 the real and imaginary parts of total optical susceptibility χ under two different radiation intensities. We find that the real and imaginary part of χ exhibit a standard dispersive and Lorentzian lineshape, respectively. This is independent of the capped matrices and applied intensities. However, for the larger intensity χ is substantially decreased in magnitude and strongly broadened in the near resonant region in all the three charged QDs. For all the applied intensities, the PVA capped QDs exhibit the largest χ values, while the PMMA capped QDs exhibit the smallest ones, which also appear to be similar to the intensity-free $\chi^{(1)}$ and $\chi^{(3)}$. Moreover, the decrease of χ with respect to intensity is found to be more pronounced for the case of PVA capping.

6.4 Brief summary

We have studied the linear, third-order nonlinear and intensity-dependent optical susceptibilities of singly charged ZnO QDs embedded in different dielectric matrices. Three commonly used matrices, PVA, PMMA, and SiO_2, are considered for the present calculations. The analytical expressions for these optical susceptibilities are derived by using density matrix equations within the two-level system approximation. We find that QD capped with PVA which has the largest dielectric constant always exhibits the largest linear and third-order nonlinear optical susceptibilities, while that dispersed in amorphous SiO_2 which has the largest band gap energy shows the highest threshold energy, irrespectively of the QD sizes. Increasing the QD sizes leads to the drastic increase in the magnitude of both the linear and nonlinear susceptibilities. Comparing to the linear susceptibility, the third-order nonlinear counterpart appears to be more sensitive to the variation of the capped matrices. Finally, we investigate the influence of the applied radiation intensities on the total susceptibility in all the three different capped QDs. We show that the real and imaginary part of the total susceptibility always exhibit a standard dispersive and Lorentzian lineshape, irrespectively of the applied intensities. However, enhancing the applied intensity leads to a drastic decrease in the (absolute) magnitude of the total susceptibility and a substantially broadening in the near resonance region. Furthermore, the total susceptibility exhibits a stronger dependence on the applied radiation intensity in charged QD capped by a matrix with a relatively high dielectric constant but with a relatively small energy band gap. We believe that our results can be useful and helpful not only in the elucidation of the fundamental physics but also for possible devices application based on ZnO QDs-matrix systems.

7

Linear and nonlinear optical properties of ZnO/ZnS and ZnS/ZnO core shell quantum dots

*In this chapter, we study theoretically the linear, nonlinear and total absorption coefficients and refractive index changes associated with intersubband transitions in ZnO/ZnS core shell quantum dot (CSQD) and ZnS/ZnO inverted core shell quantum dot (ICSQD), emphasizing on the influence of the shell thickness, impurity and dielectric environment. We find that in both impurity-free CSQD and ICSQD, increasing the shell thickness red shifts significantly the threshold energy and enhances drastically the nonlinear absorption coefficients and all the refractive index changes, independently on the dielectric environments. Similar behaviour has also been observed in most of the cases studied when the impurity is displaced from the core center to the shell center. Finally, we find that the nonlinear properties are more sensitive to the external perturbations, while at a weak radiation intensity, the variation of the total quantities is generally dominated by that of the corresponding linear terms. The results presented herein are published in Journal of Applied Physics **114**, 023510 (2013).*

Contents

7.1 Introduction

Zinc oxide (ZnO) and Zinc sulfide (ZnS) quantum dots (QDs) have received considerable attentions due to their wide applications in optoelectronics and spintronic devices, such as light-emitting, laser diodes and electroluminescent devices (see Refs. 137 and 138 and references therein). These QDs can be fabricated successfully by using the well-established chemical synthesis methods, e.g., sol-gel,[139,140] wet chemical approach,[141–143] to mention only a few. However, the synthesized colloidal QDs (generally uncapped) are relatively unstable and encounter the difficulties in dispersion and preservation. Possible existing of the surface states significantly reduces the electron-hole recombination rate, lowering the luminescent quantum yield. Size-dependent photophysical properties can also be obscured.[144] One possible way of overcoming such problems is to further cap the bare QD (core) with an another material (shell), forming a core-shell configuration.

Wurtzite (WZ) ZnO has a relatively smaller band gap (3.445 eV[145]) in comparison to that of WZ ZnS (3.864 eV[146]). Therefore, capping bare ZnO QDs with a thin layer of ZnS forms the conventional ZnO/ZnS core-shell quantum dot (CSQD) structure where the core material has a narrower band gap (ZnO) than the shell material (ZnS). Conversely, ZnS/ZnO inverted core-shell quantum dot[147,148] (ICSQD) will be fabricated if the wider gap ZnS is overcoated with a shell of narrower gap ZnO. ZnO/ZnS CSQDs with dimension in the range of few nanometer to about 30 nanometer have been successfully synthesized by epitaxial growth in solution.[149] Comparing to the bare ZnO QDs, the fabricated CSQDs exhibit enhanced ultraviolet (UV) emission and present type I band alignment. Employing a simple one-step solvent-thermal method, Wang et al.[150] have synthesized ZnS/ZnO ICSQDs. The stability of ICSQDs has been found to be far superior to that of uncapped ZnS QDs, and the corresponding emission quantum yield is higher than that of bare ZnO QDs. A type II band alignment has been demonstrated. Very recently, ZnS/ZnO ICSQDs of size 4 nanometer have been grown by controlled oxidation of ZnS QDs,[151] showing enormous enhancement in UV emission ($\sim$ 10 times). Possible applications of ZnO/ZnS CSQD on drugs and food delivery in blood have also been reported recently.[152,153] In contrast to the multiplicity of experimental work, theoretical work on ZnO/ZnS and ZnS/ZnO CSQD is very scare and limited. Using band-corrected pseudopotential density functional theory calculations, Schrier et al.[154] have studied the band gap, optical absorption, and carrier localization of ZnO/ZnS core/shell nanowires, proposing this heterostructure for photovoltaic applications. McDonald et al.[155] have successfully simulated the biexciton binding and antibinding in CSQD by using a path integral quantum Monte Carlo method. The electronic structure of ZnO/ZnS CSQD has also been theoretically calculated by employing the self-consistent charge density functional tight-binding method.[156] Despite

of considerable new insights brought by these work, no attention has been paid to the linear and nonlinear optical properties in the CSQD and ICSQD systems.

In this contribution, we performed theoretical calculations of the linear, nonlinear, total absorption coefficients and refractive index changes in ZnO/ZnS CSQD and ZnS/ZnO ICSQD. The emphasis of the present paper is placed on the shell thickness, possible doping (or dopant positions), dielectric environment influences on the linear and nonlinear optical properties in both structures. The local field correction due to the dielectric mismatch between the CSQD (or ICSQD) and its surrounding matrix, which has rarely been addressed previously,[130,157] has been taken into account in the present calculations. The electronic structures of the systems are numerically calculated by employing the potential morphing method (PMM) in the framework of effective mass approximation, which has been already successfully applied in the past for the study of optical properties in several nanostructures[48,49,52,58] and very recently for the calculation of optical susceptibilities in ZnO-matrix system.[157]

7.2 Model and theoretical framework

In the framework of effective-mass approximation, a single dopant in a CSQD (or an ICSQD) with inner radius R_1 and outer radius R_2 (see Fig. 7.1) can be modeled by the following Hamiltonian

$$\hat{H} = \hat{p}\frac{1}{2m_e^*}\hat{p} + V_{con}(\vec{r}) + \Sigma(\vec{r}) + V_{Coul}(\vec{r}). \tag{7.1}$$

The first term of the Hamiltonian is the operator for the Kinetic energy of a delocalized conduction electron and m_e^* is the electron effective mass. As justified by the experimental work,[149–151] the conduction bandedge of ZnO in ZnO-ZnS hybrid QDs lies below that of its ZnS counterpart. In accordance with this, the confinement potential (the second term of Eq. (7.1)) in our calculations is taken to be step-like (see Fig. 7.1), which is

$$V_{con}(\vec{r}) = \begin{cases} 0, & |\vec{r}| \leq R_1 \\ V_0, & R_1 \leq |\vec{r}| \leq R_2 \\ \infty, & |\vec{r}| > R_2 \end{cases}, \tag{7.2}$$

for ZnO/ZnS CSQD, while for ZnS/ZnO ICSQD, it is

$$V_{con}(\vec{r}) = \begin{cases} V_0, & |\vec{r}| \leq R_1 \\ 0, & R_1 \leq |\vec{r}| \leq R_2 \\ \infty, & |\vec{r}| > R_2 \end{cases}, \tag{7.3}$$

where V_0 is the electron confinement potential due to the conduction band discontinuity. $\Sigma(\vec{r})$ is the electron self-polarization potential, describing the interaction of the electron and its image charge, which is given by[148,158–160]

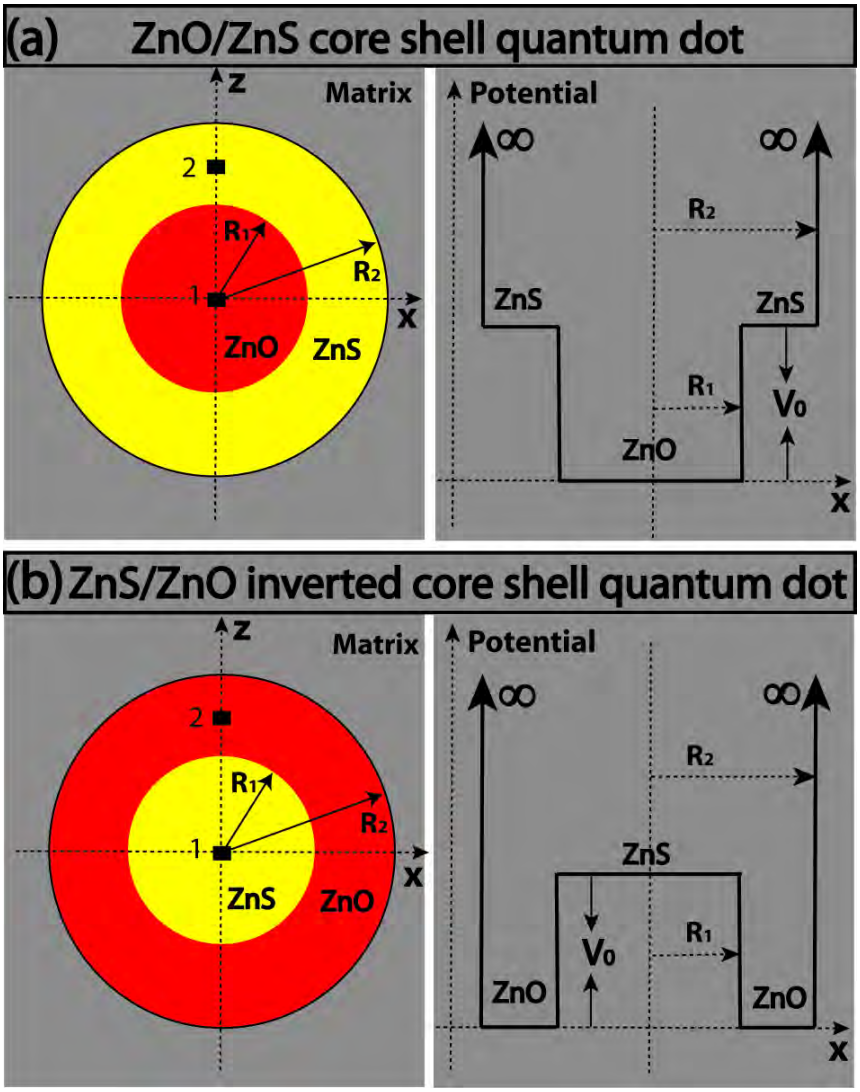

Figure 7.1: Schematic representations (left panel) and conduction band profiles (right panel) of the ZnO/ZnS core shell quantum dot (CSQD) (a) and ZnS/ZnO inverted core-shell quantum dot (ICSQD) (b) with inner radius R_1 and outer radius R_2, embedded in a dielectric matrix. Two impurity positions, 1 (core-center impurity) and 2 (shell-center impurity), considered in our calculations, have been explicitly shown.

$$\Sigma(r) = \frac{e^2}{8\pi\varepsilon_0\varepsilon_{in}R_2}\sum_{k=0}^{\infty}\frac{(k+1)(\varepsilon_{in}-\varepsilon_{out})}{k\varepsilon_{in}+(k+1)\varepsilon_{out}}\frac{r^{2k}}{R_2^{2k}}, \tag{7.4}$$

where ε_0 is the permittivity in vacuum, $\varepsilon_{in} = \sqrt{\varepsilon_c\varepsilon_s}$ with ε_c and ε_s being the relative dielectric constants of the core and shell materials, respectively. ε_{out} is the relative dielectric constant of the surrounding matrix. This self-polarization potential diverges as the electron approaches the dielectric interface ($r \to R_2$). In our calculations, this problem is solved by employing the well-known hard wall boundary conditions (e.g., for $R > R_2$, potential is assumed to be infinite (see Eqs. (7.2) and (7.3))), forcing a null electron density at the interface.

The last term of Eq. (7.1) is the Coulomb potential due to the mutual interaction between the electron and the shallow donor impurity (or the image charge of the donor impurity), depending strongly on the doping positions. For an on-center impurity, it is[148,158–160]

$$V_{Coul}(r) = -\frac{e^2}{4\pi\varepsilon_0\varepsilon_{in}r} - \frac{e^2(\varepsilon_{in}-\varepsilon_{out})}{4\pi\varepsilon_0\varepsilon_{in}\varepsilon_{out}R_2}, \tag{7.5}$$

while for an off-center impurity, it is[148,158–160]

$$V_{Coul}(r) = -\frac{e^2}{4\pi\varepsilon_0\varepsilon_{in}|\vec{r}-\vec{r_i}|} - \frac{e^2}{4\pi\varepsilon_0\varepsilon_{in}R_2}\sum_{k=0}^{\infty}\frac{r_i^k r^k}{R_2^{2k}} \times\frac{(k+1)(\varepsilon_{in}-\varepsilon_{out})}{k\varepsilon_{in}+(k+1)\varepsilon_{out}}P_k(\cos\theta), \tag{7.6}$$

where $\vec{r}$ and $\vec{r_i}$ are the position vectors of the electron and impurity, respectively, with $|\vec{r_i}| = \sqrt{x_i^2+y_i^2+z_i^2}$, where x_i, y_i and z_i are the Cartesian coordinates of the impurity. Without the loss of generality, the impurity in our calculation is placed on the z-axis ($x_i = y_i = 0$, see also Fig. 7.1). $\cos\theta = \frac{\vec{r}\cdot\vec{z_i}}{|\vec{r}|\cdot|\vec{z_i}|}$ for an off-center impurity (located at (0,0,z_i)) and $P_k(\cos\theta)$ is the Legendre polynomial. The first term of Eq. (7.6) describes the direct Coulomb interaction between the electron and the impurity, while the last term accounts for the Coulomb interaction between the electron and the image charge of an off-center impurity. Here, we assume that the Coulomb potential incorporates the effects of the polarization charges induced on the QD surface as a consequence of the dielectric mismatch.[158–160] To truncate the infinite sum in Eqs. (7.4), (7.5) and (7.6), k is taken up to 4500 in our calculations, which ensures the potential values being insensitive to the further increase in k. This model has been successfully used for the investigation of the electronic properties and impurity binding energy in ZnS/CdSe and CdSe/ZnS core-shell nanodots.[148]

In order to solve the Schrödinger equation based on the Hamiltonian (7.1) numerically, potential morphing method (PMM) (see Chapter 1) is employed. In our present calculations,

the usual three-dimensional (3D) harmonic oscillator is chosen as a reference system in order to start the morphing process and its wave functions are selected as the initial wave functions (Φ_R). The interaction potential for an impurity-free system is $V_S(\vec{r}) = V_{con}(\vec{r}) + \Sigma(\vec{r})$, while it is $V_S(\vec{r}) = V_{con}(\vec{r}) + \Sigma(\vec{r}) + V_{Coul}(\vec{r})$ for an impurity-present system. In our PMM, a very dense grid is employed to ensure the accuracy of our results and all calculations are performed with the same grid number. It should be noted here that adopting the harmonic oscillator as a reference system does not affect our results because the PMM needs only a known reference system to start the morphing process and finally to give the eigenfunctions and eigenvalues for the unknown system, independently on the choice of the initial reference system.[3,53,91,99]

After obtaining the necessary eigenenergies and wave functions by using PMM, we start to calculate the linear, nonlinear and total absorption coefficients and refractive index changes associated with the intersubband transitions in the ZnO/ZnS CSQD and ZnS/ZnO ICSQD. Within a two-level system approach, the linear and third-order nonlinear optical absorption coefficients can be obtained by a density matrix approach and a perturbation expansion method, given by[161]

$$\alpha^{(1)}(\omega) = \frac{\omega}{\varepsilon_0 c n_r} \frac{|M_{21}|^2 \sigma_V \hbar\Gamma_{12}}{(E_{12} - \hbar\omega)^2 + (\hbar\Gamma_{12})^2}, \tag{7.7}$$

$$\alpha^{(3)}(\omega, I) = -\frac{2I\omega}{\varepsilon_0^2 n_r^2 c^2} \frac{|M_{21}|^4 \sigma_V \hbar\Gamma_{12}}{[(E_{21} - \hbar\omega)^2 + (\hbar\Gamma_{12})^2]^2}$$
$$\{1 - \frac{|M_{22} - M_{11}|^2}{4|M_{21}|^2} \times \frac{3E_{21}^2 - 4E_{21}\hbar\omega + \hbar^2(\omega^2 - \Gamma_{12}^2)}{E_{21}^2 + (\hbar\Gamma_{12})^2}\}, \tag{7.8}$$

where σ_V is the electron density, $\Gamma_{12} = 1/T_{12}$ is the relaxation rate with T_{12} being the relaxation time, I is the incident optical intensity, $n_r = \sqrt{\varepsilon_{in}}$ is the refractive index, c is the speed of light in vacuum, $E_{21} = E_f - E_i$ is the energy difference between the final (first excited) state and the initial (ground state) state. By assuming that the polarization of electromagnetic radiation is along the z-axis direction, the transition matrix element between these two states is defined by $\mathrm{M}_{ij} = -\frac{\langle f|ez|i\rangle}{\varepsilon_{eff}}$, which takes into account the local field correction due to the dielectric mismatch between the system and its surrounding matrix, differing from the the usual definition by the local field factor $F = \frac{1}{\varepsilon_{eff}} = \frac{3\varepsilon_{out}}{2\varepsilon_{out}+\varepsilon_{in}}$.[157] For a dielectric environment free system ($\varepsilon_{in} = \varepsilon_{out}$), the local field factor equals to 1 and it has no influence on the transition matrix element, recovering the usual situation which has been widely addressed in the published literature. However, if the system is dispersed in a matrix with a lower dielectric constant ($\varepsilon_{in} > \varepsilon_{out}$), e.g., ZnO/ZnS CSQD (or ZnS/ZnO ICSQD) embedded in amorphous SiO_2,[162] the local field factor $F < 1$ and it significantly decreases the transition matrix element. At a very weak radiation intensity,

the total absorption coefficient can be approximated as

$$\alpha(\omega, I) \approx \alpha^{(1)}(\omega) + \alpha^{(3)}(\omega, I). \tag{7.9}$$

The linear and the third order nonlinear refractive index changes are given by[161]

$$\frac{\Delta n^{(1)}(\omega)}{n_r} = \frac{1}{2n_r^2\varepsilon_0}|M_{21}|^2\sigma_V\{\frac{E_{21}-\hbar\omega}{(E_{21}-\hbar\omega^2)^2+(\hbar\Gamma_{12})^2}\}, \tag{7.10}$$

and

$$\begin{aligned}\frac{\Delta n^{(3)}(\omega)}{n_r} = &-\frac{\mu_0 c}{n_r^3\varepsilon_0}\frac{|M_{21}|^4(E_{21}-\hbar\omega)\sigma_V I}{[(E_{21}-\hbar\omega)^2+(\hbar\Gamma_{12})^2]^2}\\ &\times[1-\frac{(M_{22}-M_{11})^2}{4|M_{21}|^2((E_{21})^2+(\hbar\Gamma_{12})^2)(E_{21}-\hbar\omega)}\\ &\{(E_{21}-\hbar\omega)\times[E_{21}(E_{21}-\hbar\omega)-(\hbar\Gamma_{12})^2]-\\ &(\hbar\Gamma_{12})^2(2E_{12}-\hbar\omega)\}],\end{aligned} \tag{7.11}$$

respectively, where μ_0 is the permeability in vacuum and the relative permeability μ_r is taken to be unity in our calculations. In the presence of a weak radiation intensity, the total refractive index change can be defined by

$$\frac{\Delta n(\omega)}{n_r} \approx \frac{\Delta n^{(1)}(\omega)}{n_r} + \frac{\Delta n^{(3)}(\omega)}{n_r}. \tag{7.12}$$

7.3 Results and discussion

In what follows, we will discuss the shell thickness, impurity and dielectric environment influences of the linear and nonlinear optical properties associated with the intersubband transitions in both ZnO/ZnS CSQD (see Sec. 7.3.1) and ZnS/ZnO ICSQD (see Sec. 7.3.2). The parameters used in our calculations are the same as in Ref. 157, taking $\sigma_V = 1.7\times10^{17}$ cm^{-3} , $T_{12} = 1$ ps and $n_r = \sqrt{\varepsilon_{in}} = 2.9629$ with $\varepsilon_r^{ZnO} = 8.66$ and $\varepsilon_r^{ZnS} = 8.9$,[148] where ε_r^{ZnO} and ε_r^{ZnS} are the relative dielectric constants of ZnO and ZnS, respectively. The electron effective mass is assumed to be position-independent, taking the value of the core material (e.g., for ZnO/ZnS CSQD, $m_e = m_e^{ZnO} = 0.265m_0$[145] and for ZnS/ZnO ICSQD, it is $m_e = m_e^{ZnS} = 0.24m_0$,[146] where m_0 is the free electron mass). According to the previous literatures about the linear and nonlinear optical properties in semiconductor nanostructures,[58,157,163–167] the radiation intensity significantly affects the magnitude of

the third order absorption coefficient and refractive index change, leading to a substantial decrease in the magnitude of the total counterparts. However, in the present calculations, we keep the radiation intensity as a constant value I = 0.02 MW/cm^2 and take the inner radius $R_1 = 1.5$ nm, which is slightly larger than the ZnO effective exciton Bohr radius ($a_B^* = 1.4$ nm). Both the systems with ($\varepsilon_{out} = 3.9$, corresponding to disperse the CSQDs into amorphous SiO_2 matrix) and without ($\varepsilon_{out} = \varepsilon_{in} = 8.779$) dielectric environment effect are considered. The strain effects due to the lattice mismatch between the core and shell materials are not considered in the present intersubband (conduction band) calculations.

It should be noted that *ab initio* calculations have been confirmed as a robust tool of describing the band lineups for a great variety of semiconductor heterostructures (for example, see Refs. 168–170). However, to the best of our knowledge, such type of calculations has not yet been performed for WZ ZnO-ZnS hybrid structures, which are addressed herein. Therefore, in our calculations, the conduction band discontinuity is taken as $V_0 = 0.08 \cdot E_g^{ZnS} = 292.8$ meV, where the coefficient 0.08 is empirically derived by fitting to the experimental measurements for a great variety of semiconductor colloidal QDs[48,53] and E_g^{ZnS} is the energy band gap of WZ ZnS. The sensitivity of our results for WZ ZnO/ZnS CSQDs and ZnS/ZnO ICSQDs to the conduction band discontinuity parameter (i.e., see V_0 in Fig. 7.1) will also be discussed in Sec. 7.3.1 and Sec. 7.3.2, respectively.

Before presenting the numerical results, we firstly address several important characteristics of the absorption coefficients and refractive index changes, indicating from the corresponding expressions described in the last section. The peak value of the linear absorption coefficient occurs at the photon energy $\hbar\omega = \sqrt{E_{21}^2 + (\hbar\Gamma_{12})^2}$ and the peak intensity is proportional to $|M_{21}|^2 \cdot \sqrt{E_{21}^2 + (\hbar\Gamma_{12})^2}$. For $\hbar\Gamma_{12} \ll E_{21}$, which is valid for all the cases considered below, the peak value of the linear absorption coefficient turns out to be at the photon energy $\hbar\omega \approx E_{21}$ and the peak intensity is in proportion to $E_{21} \cdot |M_{21}|^2$. For systems with inversion symmetry, e.g., impurity free CSQD and ICSQD systems or these systems doped by a core-center impurity (see Fig. 7.1), the diagonal matrix elements M_{11} and M_{22} vanish, leading to a zero contribution from the last term of Eq. (7.8) to $\alpha^{(3)}$. For $\hbar\Gamma_{12} \ll E_{21}$, although $\alpha^{(3)}$ reaches its peak value at approximately the same photon energy as its linear counterpart, the corresponding peak intensity is more sensitive to the transition matrix element ($\propto E_{21} \cdot |M_{21}|^4$). When this inversion symmetry is broken by the external perturbations, e.g, doping an off-center impurity, nonzero M_{11} and M_{22} appear and the aforementioned dependence will be further corrected by the negative contribution of the anisotropic term (see the term which contains $|\frac{M_{11}-M_{22}}{M_{21}}|$ in Eq. (7.8)).

Concerning to $\frac{\Delta n^{(1)}(\omega)}{n_r}$, it always exhibits a standard dispersive lineshape (e.g., it presents firstly a maximum and then a minimum as the photon energy increases). The maximum and minimum appear at the photon energy $\hbar\omega = E_{21} - \hbar\Gamma_{12}$ and $\hbar\omega = E_{21} + \hbar\Gamma_{12}$,

respectively. They are equivalent in magnitude (in absolute value) which is proportional to $|M_{21}|^2$, independently on the transition energy (E_{21}). Whereas, for $\frac{\Delta n^{(3)}(\omega)}{n_r}$, this standard dispersive lineshape is reversed (e.g, it shows firstly a *minimum* and then a *maximum* as the photon energy increases). Analogously to $\alpha^{(3)}$, $\frac{\Delta n^{(3)}(\omega)}{n_r}$ in a system with an inversion symmetry is fully determined by the first term of Eq. (7.11) due to the vanishing diagonal matrix elements M_{11} and M_{22}. Its global minimum and maximum occur at $\hbar\omega = E_{21} - (\hbar\Gamma_{12})/\sqrt{3}$ and $\hbar\omega = E_{21} + (\hbar\Gamma_{12})/\sqrt{3}$, respectively. The magnitudes of these minimum and maximum are equivalent (in absolute value), exhibiting a stronger exclusive dependence on the transition matrix element (e.g., $\propto |M_{21}|^4$) in comparison to $\frac{\Delta n^{(1)}(\omega)}{n_r}$ (e.g., $\propto |M_{21}|^2$)). However, these relations will also be influenced by the anisotropic term if the system is lack of inversion symmetry (see Eq. (7.11)).

7.3.1 Optical properties in core shell quantum dots

As a first step towards investigating the linear and nonlinear optical properties in impurity free ZnO/ZnS CSQDs, we present in Fig. 7.2 the linear, third order nonlinear and total absorption coefficients and refractive index changes as a function of the photon energy for three different shell thickness values. It shows that increasing the thickness of the capping layer leads to a red shift of the threshold energy. This shift appears to be very sensitive to the initial capping and becomes less significant when the shell layer is relatively thick. In addition to this, varying the shell thickness also significantly enhances all the refractive index changes. This effect favors more the nonlinear term. To capture the physical reasons, we calculated the probability of finding the electron in the shell region for various shell thickness values. The results for the ground and first excited states are shown in Fig. 7.3. It appears that increasing the capping thickness enhances the penetration of the electron wave functions into shell region, irrespectively of the dielectric environment. This movement of the wave functions eventually causes an increase in the transition matrix element M_{21} which is fully responsible for the variation of the refractive index changes. In contrast to the increase in the matrix element, the transition energy experiences a decrease with increasing the capping thickness, which is associated with the observed red shift. The competition effects of these two factors (e.g., $|M_{21}|^2$ and E_{21}) determine the tendency of the peak intensity of the linear absorption coefficients with respect to the shell thickness. In a dielectrically homogeneous system (see the dash dotted lines), the later effect (e.g., E_{21}) is more pronounced and the peak intensity of $\alpha^{(1)}$ decreases with regard to the increased capping thickness. Conversely, when the dielectric inhomogeneity is present (see the solid lines), the former effect ($|M_{21}|^2$) is more effective, finally inducing an increase in the peak intensity of $\alpha^{(1)}$.

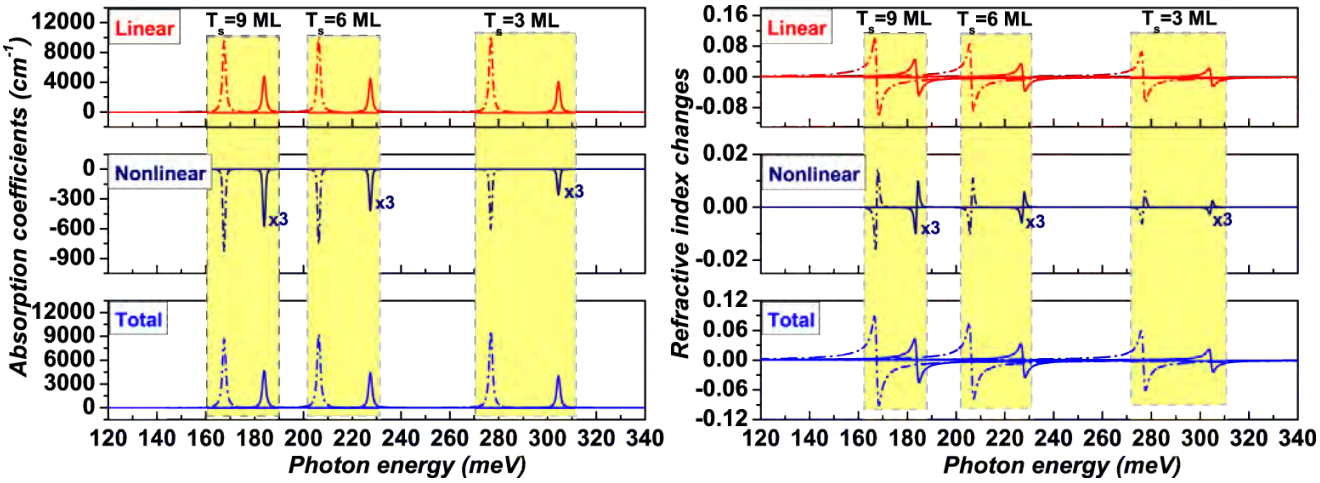

Figure 7.2: Linear (red), third order nonlinear (navy) and total (blue) absorption coefficients (left panel) and refractive index changes (right panel) as a function of the photon energy $\hbar\omega$ for various shell (ZnS) thickness (T_s=$R_2 - R_1$, in unit of monolayer (ML)) values in impurity free ZnO/ZnS CSQDs without ($\varepsilon_{in} = \varepsilon_{out}$, dash dotted lines) and with ($\varepsilon_{in} > \varepsilon_{out}$, solid lines) dielectric environment. Here, the inner radius $R_1 = 1.5$ nm and 1 ML = 0.3117 nm (for ZnS).

Concerning to $\alpha^{(3)}$, its peak intensity exhibits a more straightforward variation, increasing significantly with increasing the shell thickness both with and without the dielectric environment. This is due to the fact that comparing to $\alpha^{(1)}$ ($\propto E_{21} \cdot |M_{21}|^2$), the peak intensity of $\alpha^{(3)}$ ($\propto E_{21} \cdot |M_{21}|^4$) is more sensitive to the variation of the transition matrix element, which contributes positively with the capping thickness as addressed above. Although the change of the nonlinear term is more drastic with increasing the shell thickness, the peak magnitude of total absorption coefficient follows the same variation of the linear term due to its dominant contribution at relatively weak radiation intensity.

In comparison to a dielectrically homogeneous system, all the quantities are substantially reduced if the system is dispersed in a matrix with a lower dielectric constant and considerable blue shift of the threshold energy is observed. This is attributed to the fact that for a phenomenological CSQD, the existence of the dielectric environment (e.g., in our case, $\varepsilon_{in} > \varepsilon_{out}$) induces a self energy which is positive and a short range interaction at the CSQD-matrix interface (see Eq. (7.4)), forcing the electron to move towards the core center. This can be easily justified by the fact the probability of finding the electron of ground state in the shell region becomes smaller in the presence of the dielectric mismatch (see the left panel of Fig. 7.3). Moreover, local field effect, characterizing by the local field factor $F = \frac{1}{\varepsilon_{eff}} = 0.705$, also appears. The combination effects of the charge movement and the local field consequently decrease the transition element, which is related to the reducing in all the refractive index changes. Although the transition energy exhibits an increase by taking into account the dielectric environment effect, the decrease in the matrix element is more significant, leading to the observed variation (decreasing) in all the absorption coefficients.

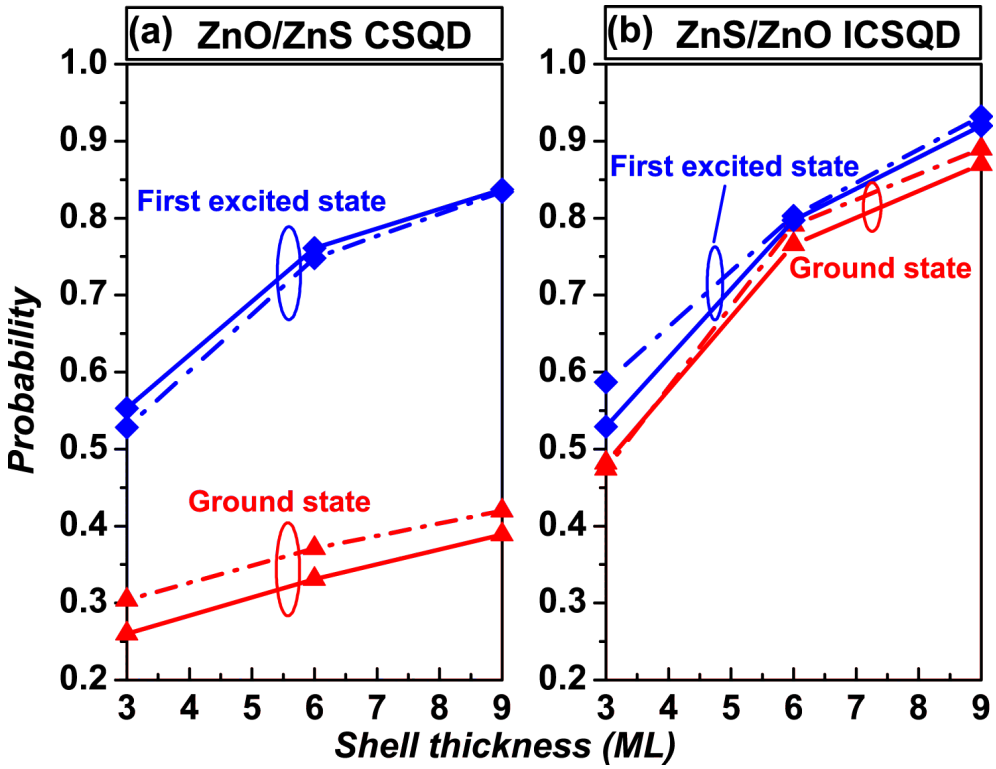

Figure 7.3: Probability of finding the electron of ground-state (red triangles) and first excited state (blue diamonds) in the shell region as a function of the shell thickness (in unit of monolayer (ML)) in ZnO/ZnS CSQDs (left panel) and ZnS/ZnO ICSQDs (right panel) without ($\varepsilon_{in} = \varepsilon_{out} = 8.779$, dash dotted lines) and with dielectric environment ($\varepsilon_{in} > \varepsilon_{out}, \varepsilon_{in} = 8.779, \varepsilon_{out} = 3.9$, solid lines). For the left panel, 1 ML = 0.3117 nm (WZ ZnS), while for the right panel, 1 ML = 0.26025 nm (WZ ZnO).

Possible existence of dopants (or intrinsic hydrogen like defects) is also expected to affect significantly the linear and nonlinear optical properties in a CSQD. From the last section (see Eqs. (7.4), (7.5) and (7.6)), we know that in a dielectrically homogeneous system, the presence of the donor ion induces a well-known electron-ion Coulomb interaction. However, this interaction is further influenced by the effect of the polarization image charges (e.g., positive self-energy and the Coulomb interaction between the electron and the impurity image) when the CSQD is embedded in a matrix with a lower dielectric constant. Although the Coulomb potential is different in these two dielectric environments, the variation of linear and nonlinear optical properties with respect to a core-center doping appears to be very similar. Comparing to the impurity free system (see Fig. 7.2), Fig. 7.4 shows that doping the CSQD at the core center ($z_i = 0$) with a hydrogenic impurity leads to a blue shift of the transition energy and simultaneously a slight decrease (in absolute magnitude) in both the linear and nonlinear absorption coefficients and refractive index changes, irrespectively of the dielectric environment. The physical reason is that the occurrence of impurity center increases the separation of the energy levels of the two states (E_{21}) in both with and without dielectric environment. Conversely, the charge accumulation towards

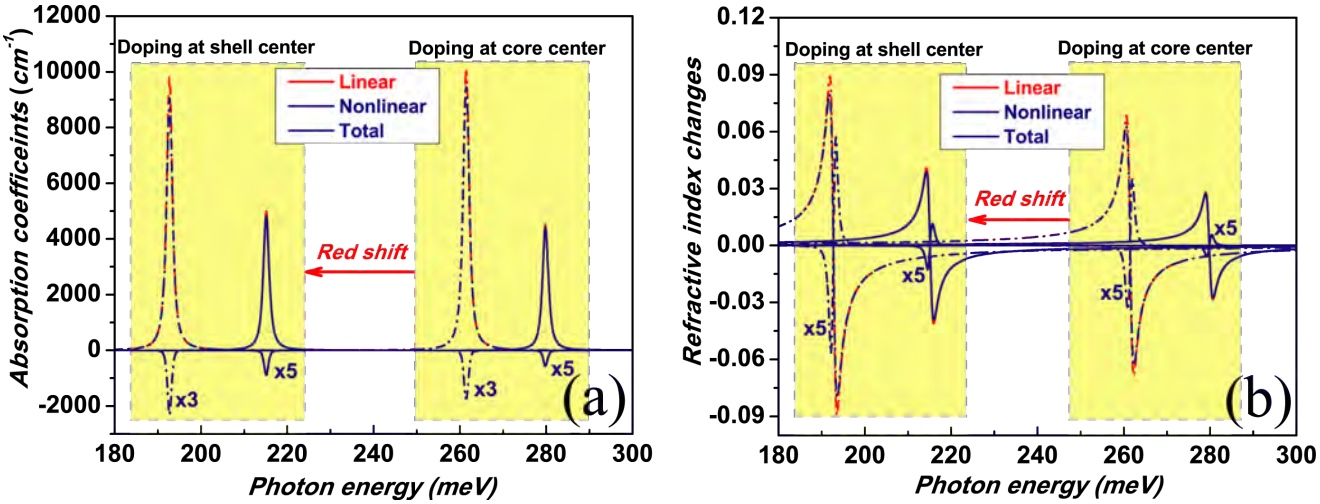

Figure 7.4: Linear (red), third order nonlinear (navy) and total (blue) absorption coefficients (a) and refractive index changes (b) as a function of the photon energy $\hbar\omega$ for various dopant positions in doped ZnO/ZnS CSQDs without (dash dotted lines) and with (solid lines) dielectric environment. Here, the dopants located at the core center ($z_i = 0$) and at the shell center ($z_i = 0.75R_2$) are considered. The inner radius $R_1 = 1.5$ nm and the shell thickness is $T_s = 6$ ML ($R_2 = R_1 + T_s = 3.3702$ nm).

the impurity center (core center) decreases significantly the transition matrix element. These two effects appear to compensate with each other and the influence of latter factor turns out to be more pronounced, causing a decrease of both the linear and nonlinear quantities.

The influence of the variation of the transition matrix element on the peak intensity of the nonlinear absorption coefficient is always dominant over its transition energy counterpart, resulting a similar behaviour in both with and without dielectric environment (it increases with moving the dopant to the shell center). More specially, we found that comparing to the system without dielectric environment, both the absorption coefficients and refractive index changes are substantivally reduced when the system is dispersed in a lower dielectric constant matrix ($\varepsilon_{in} > \varepsilon_{out}$) and blue shift of the threshold energy is observed, as expected.

Finally, in an attempt to investigate the sensitivity of the presented results to the conduction band discontinuity parameter V_0 (see Fig. 7.1), we show in Fig. 7.5 the linear absorption coefficient and refractive index change as a function of the photon energy for various shell thickness values, taking $V_0 = 200$ meV ($\sim 0.052 \cdot E_g^{ZnS}$). It appears that the deviation of the V_0 value from the empirically derived one does not cause any changes in the general tendency of the transition energy E_{21} (decreases) and off-diagonal matrix element M_{21} (increases) with respect to the increase in the shell thickness. This can be confirmed by the appearance of red-shift phenomenon and also the enhancement of the change in the refractive index (in absolute value) shown in Fig. 7.5 with increasing the capping

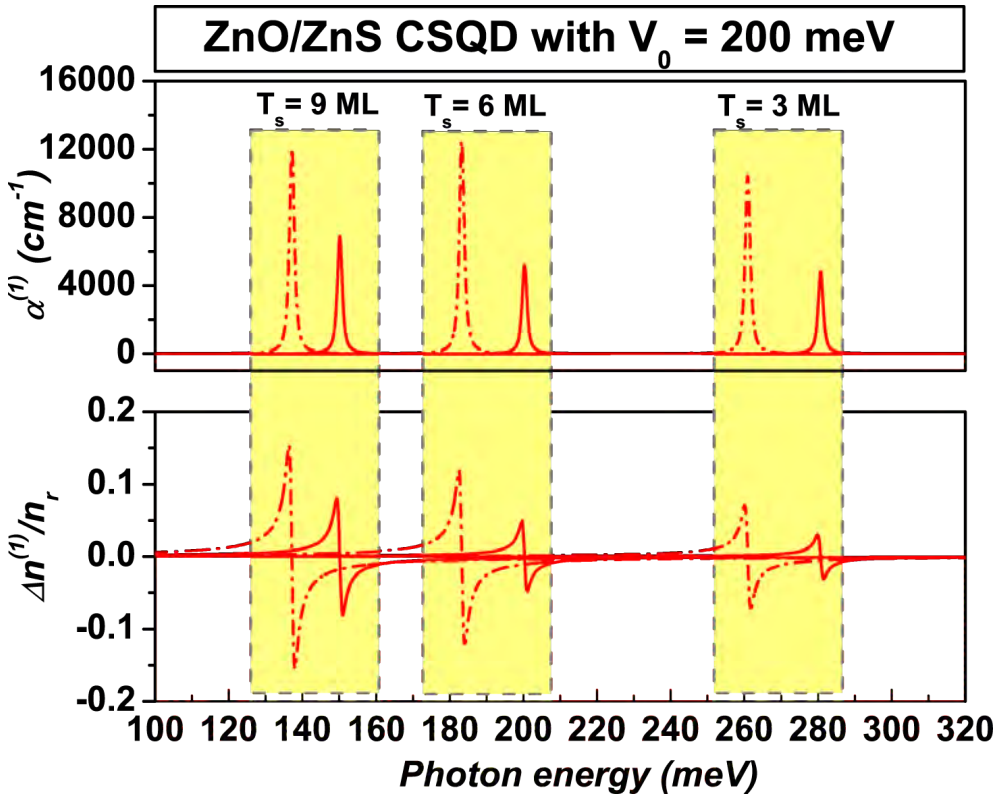

Figure 7.5: Linear absorption coefficient ($\alpha^{(1)}$, upper panel) and refractive index change ($\Delta n^{(1)}/n_r$, lower panel) as a function of the photon energy $\hbar\omega$ for various shell thickness values (in unit of ML) in ZnO/ZnS CSQD without (dash dotted lines) and with (solid lines) dielectric environment, using the conduction band discontinuity parameter $V_0 = 200$ meV.

thickness (very similarly to the ones pictured in Fig. 7.2). However, possible variation in V_0 affects strongly the interplay of the two factors on the peak intensity of the absorption coefficient. This becomes clear by the non-monotonic variation in the absorption coefficient (i.e., first increases (from 3 ML to 6 ML) and then slightly decreases (from 6 ML to 9 ML)) shown in Fig. 7.5, very differently from the ones shown Fig. 7.2 (i.e., the peak intensity decreases monotonically with increasing the shell thickness). In addition to this, the decrease in V_0 results in a smaller resonant peak photon energy in CSQDs both with and without dielectric environment. In the presence of the dielectric environment, the linear and nonlinear optical properties are independent on the variation of V_0, always decreasing the peak intensity and blue-shifting the peak position (see Figs. 7.2 and 7.5).

7.3.2 Optical properties in inverted core shell quantum dots

In the previous subsection, we find that the shell thickness, impurity and possible existence of the dielectric environment significantly influence the linear and nonlinear optical

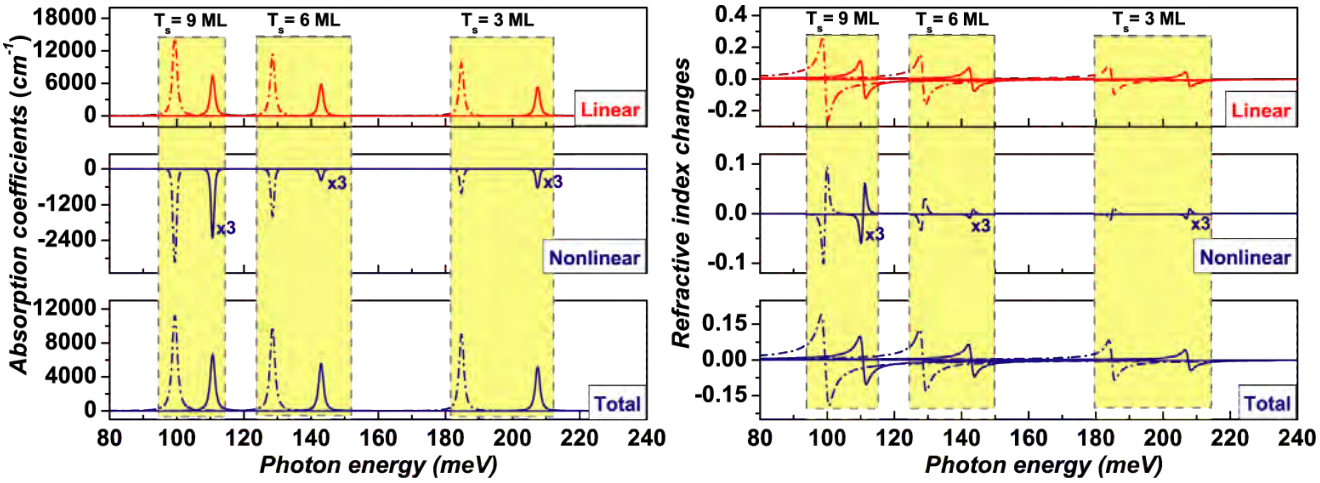

Figure 7.6: The same as in Fig. 7.2 but for ZnS/ZnO *inverted* core-shell quantum dots (ICSQDs). Here, 1 ML = 0. 26025 nm (for ZnO (shell material)).

properties in ZnO/ZnS CSQDs. Comparing to the *conventional* configuration, ZnS/ZnO ICSQDs exhibit very different potential profiles (see Fig. 7.1). Herein, we present the dependence of the absorption coefficients and refractive index changes in the ICSQD on the aforementioned three factors and possible comparison between these two systems (CSQD and ICSQD) is performed.

Following the same procedures in the last subsection, we firstly studied the effect of the shell thickness on the absorption coefficients and refractive index changes in ZnS/ZnO ICSQDs. As shown in Fig. 7.6, increasing the shell thickness leads to an enhancement of all the absorption coefficients and refractive index changes both with and without dielectric environment. This is independent on the variation of the conduction band discontinuity parameter V_0 (see Fig. 7.7), which is different from the case shown in CSQDs by the variation of the linear absorption coefficients with respect to the capping thickness (see Fig. 7.2). The physical reason is attributed to the charge accumulation towards the shell region induced by the increase in the shell thickness (see Fig. 7.3(b)), which is similar to that in the *conventional* systems (see the right panel of Fig. 7.3). The resultant increase in the transition matrix element is the direct reason for the increase in the refractive index changes. However, comparing to the CSQD, the charge movement appears to be comparatively more significant in the ICSQD systems (see Fig. 7.3). Therefore, the positive contribution from the transition matrix element variation completely dominates over the negative contribution from its transition energy counterpart, causing a monotonic increase in the linear absorption coefficient peak intensity. We further found from Fig. 7.6 that the increase in the nonlinear quantities with enhancing the capping layer is significantly more pronounced. Similarly to the CSQD, for a given shell thickness value, all the quantities are drastically reduced by dispersing the ICSQD into a matrix with a lower dielectric constant and a blue shift of the threshold energy appears.

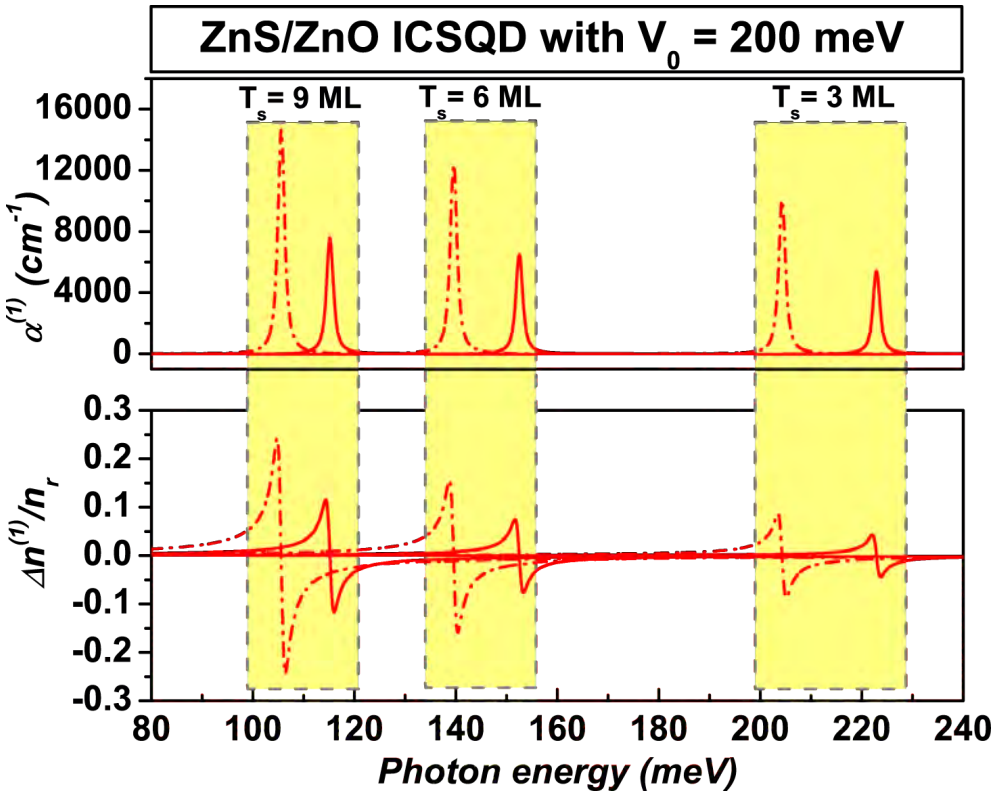

Figure 7.7: The same as in Fig. 7.5 but for ZnS/ZnO inverted core-shell quantum dots (ICSQDs).

In the *unconventional* CSQD structure, Fig. 7.6 shows that enhancing the thickness of the capping layer causes a strong red shift in the threshold energy. This red shift is very sensitive to the initial capping (e.g., from 3 ML to 6 ML) and the sensitivity reduces if the capping layer becomes comparable to the core radius (e.g., from 6 ML to 9 ML), similarly to its *conventional* counterpart (shown in Fig. 7.2). This behaviour appears to be irrespective of the involved conduction band parameter V_0 (see Fig. 7.7). Comparing Fig. 7.6 to Fig. 7.7, we find that for a specific capping thickness, possible variation in V_0 also considerably affects the threshold energy, exhibiting a larger value for a smaller V_0, contrary to the CSQD structure. This is due to the fact that although decreasing the V_0 value results in lowering both the ground state and the first excited state energy levels, the sensitivity of this decrease in these two energy levels turns out to be completely different in the CSQD and ICSQD structures. In ICSQD, the decrease in the ground state energy level with respect to the reducing of V_0 is more significant, leading to a relatively larger transition energy E_{21} for a smaller V_0 value. However, in CSQD, this decrease favors more the energy level of the first excited state, causing a reversed picture.

Finally, we present in Fig. 7.8 the linear, nonlinear and total absorption coefficients and refractive index changes as a function of the photon energy for two doping positions, with and without dielectric environment. It appears that varying the doping position from the core center to the shell center causes a red shift of the threshold energy. However, the

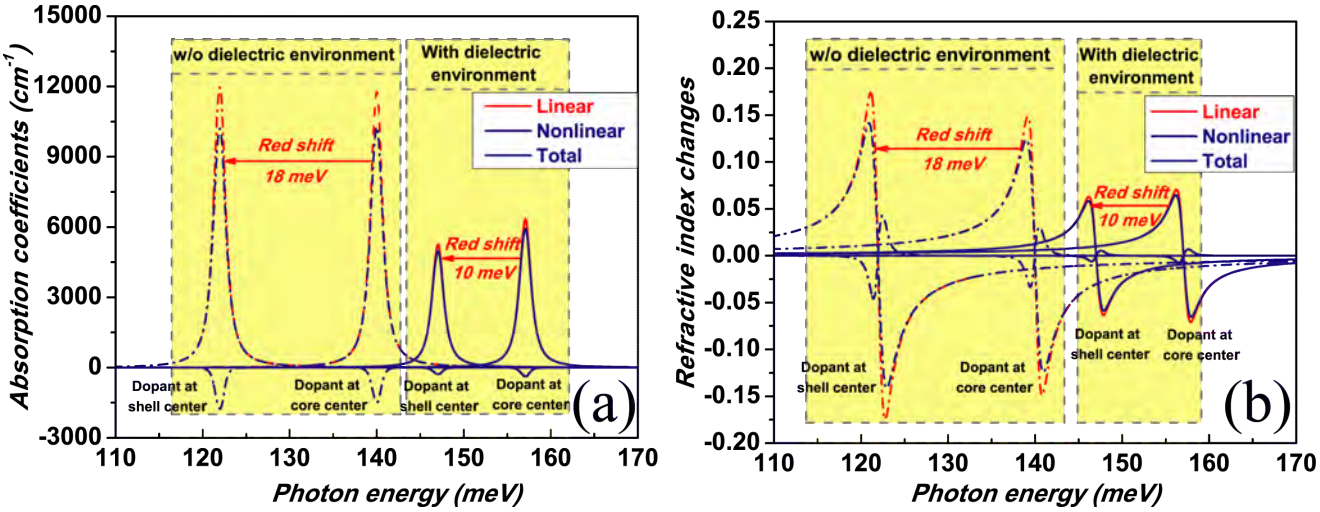

Figure 7.8: The same as in Fig. 7.4 but for ZnS/ZnO inverted core-shell quantum dots (ICSQDs). The inner radius $R_1 = 1.5$ nm and the shell thickness is $T_s = 6$ ML ($R_2 = R_1 + T_s = 3.0615$ nm).

sensitivity of this shift with respect to the impurity locations is reduced by considering the dielectric environment (see Fig. 7.8). Additionally, the peak intensity of the absorption coefficients and the changes in the refractive index are differently influenced by the doping position in the two dielectric environments. In a dielectrically homogeneous system, the displacement of the impurity from the on-center position to an off-center position leads to an increase in the peak intensity of the linear and nonlinear quantities. Similar behaviour has been found in the CSQD and the corresponding physical reasons can be understood analogously. However, when the dielectric environment effect is present, the magnitudes of all the quantities are reduced significantly, very similar to that in the conventional CSQD systems (see Fig. 7.4). In contrast to this consistency, displacing the *on-center* impurity to an *off-center* position in the *unconventional* systems decreases the peak intensity of all the absorption coefficients and reduces all the changes in the refractive index. This is associated with the decrement in both the transition energy (e.g., E_{21}) and matrix element (e.g., $|M_{21}|$).

7.4 Brief summary

In summary, we have performed a theoretical study on the linear, nonlinear and total absorption coefficients and refractive index changes associated with the intersubband transitions in both WZ ZnO/ZnS CSQD and ZnS/ZnO ICSQD. The influence of the shell thickness, impurity and dielectric environment has been addressed. The necessary wave functions and corresponding energy levels are numerically calculated by using potential

morphing method (PMM) in the framework of effective mass approximation. We find that in both CSQD and ICSQD, increasing the shell thickness causes a significant red shift of the threshold energy and enhances drastically the nonlinear absorption coefficients and all the changes in the refractive index. This shift appears to be very sensitive to the initial capping and then becomes insensitive to the further capping if the shell layer becomes comparatively thick. Similar red shift phenomenon has also been observed in the most cases studied when the impurity is displaced from the core-center to the shell-center. In all the cases investigated, further dispersing the systems into a matrix with a lower dielectric environment blue shifts all the peak positions of the absorption coefficients and refractive index changes. However, the corresponding magnitudes (in absolute value) are substantially reduced. In the ICSQD, moving the core center impurity to the shell center position even causes a slight decrease in all the absorption coefficients and refractive index changes. Generally, the nonlinear terms are more sensitive to the external perturbations. However, we found that at a relatively weak radiation intensity, the variation of the total counterparts is completely dominated by the corresponding linear terms.

Our results also highlight prominently the importance of accurate determination of the conduction band discontinuity parameter in WZ ZnO-ZnS hybrid systems. Possible variation of this parameter appears to affect the tendency of the peak intensity of the linear absorption coefficient with respect to the shell thickness in the conventional CSQD structure and also the threshold energy of the absorption coefficient and refractive index change in both CSQD and ICSQD structures. Despite of this, we believe that the present results would be useful not only in the elucidation of the fundamental physics but also for possible devices application based on ZnO/ZnS hybrid systems.

8

Linear and nonlinear optical susceptibilities in a laterally coupled quantum dot quantum ring system

*Linear and nonlinear optical susceptibilities in a laterally coupled quantum-dot-quantum-ring system have been theoretically studied. In general, we find that the structure parameters of the coupled system significantly affect the optical susceptibilities. The enhancement of the coupling effects between the dot and ring is found to increase considerably the optical susceptibilities and redshift drastically the transition energies. Comparing to the linear susceptibility, the nonlinear optical susceptibility is found to be more sensitive to the variation of the structure parameters. A comprehensive analysis of the electron probability density movement with respect to the modification of the structure parameters is provided, which offers a unique perspective of the ground-state localization. The results presented herein are published in Physics Letters A **378**, 2713 (2014).*

Contents

8.1 Introduction

Coupling between semiconductor quantum dots (QDs) forms so-called quantum dot molecules (QDMs). This can be realized either by vertically stacking or by laterally aligning the QDs in the same plane.[171] Comparing to the traditional vertically stacking structure, the degree of external control of individual QD within an array of laterally aligned QDMs is believed to be larger. Laterally coupled QDMs are also found as peculiar candidates for applications in quantum information science because of the potential to couple several QDs scaling to form the first building block of a useful device.[172–174] Due to these reasons, plenty of efforts have been committed to study the optical proprieties of the laterally coupled QDMs.[174–179] On the other hand, quantum rings (QRs) have demonstrated unique electronic, magnetic, and optical properties.[180–182] For example, quantum phase coherence effects on carrier transport, such as Aharonov-Bohm and Aharonov-Casher effects, have been observed in QR structures,[183,184] which have potential applications in quantum information devices.[185] Patterned QR magnetic tunnel junctions have shown superior prospects for very high density magnetic random access memory, recording medium, and other spintronic devices.[186] High performance QR terahertz (THz) photodetectors have been fabricated.[187,188] Due to the relevance in potential device applications,[189–191] the studies of the nonlinear optical properties in semiconductor QRs have received great attention.[192–199] It is found that the potential geometry, size, alloys composition and the external perturbations, such as applied electric and/or magnetic fields, hydrostatic pressure et al. have significant influence on the optical nonlinearities in semiconductor QRs.

In this Chapter, we pay attention to the study of the linear and nonlinear optical susceptibilities in a different geometry of lateral coupling, namely quantum-dot-quantum-ring system (QDQR) in which a QD is surrounded by a QR with a tunneling barrier separating both parts of the system. This system has been justified as a good candidate for the realization of the magnetic field controllable pair of spin qubits which is necessary in quantum computation.[171] However, the optical properties, especially the nonlinear optical properties, have rarely been studied in such a unique system. Furthermore, to the best of our knowledge, the coupling effects, which appear in all types of coupled structures, on the optical nonlinearities are not yet well understood. In the present work, the linear and nonlinear optical susceptibilities in a laterally coupled GaAs QDQR system are theoretically investigated with an emphasis on the coupling effects between the dot and ring on these quantities. The electronic structure calculations are performed via potential morphing method (PMM)[3] (see Chapter 1) in the framework of the effective mass approximation (EMA), which has been successfully employed previously for the study of optical properties in several nanostructures[49,52] and very recently for the calculations of the nonlinear optical

properties in ZnO-based QD systems.[100,157] A detailed visualization of the variation in the electron probability density of the ground-state and first-excited state with respect to the changes in the structure parameters has been provided. The calculations of the linear and nonlinear susceptibilities are realized by using our recently developed analytical expressions for symmetric systems[157] (see Chapter 6). In the following section, we define our model and explain the general theory.

8.2 Theoretical framework

8.2.1 Electronic structure calculations

In the framework of EMA, an electron confined in a GaAs QDQR system can be modeled by the following Hamiltonian:

$$\hat{H} = \hat{p}\frac{1}{2m_e^*}\hat{p} + V(\vec{r}), \tag{8.1}$$

where the first term is the kinetic term in which m_e^* is the electron effective mass and the second term is the confinement potential. Considering the fact that the thickness of the QDQR along the growth direction (e.g., z-axis direction) is much smaller than the radial dimensions, one can decouple the electron motion along the growth direction from that along the in-plane direction and retain the analysis only the first state along the growth direction. For simplicity but without the loss of generality, we consider a two-dimensional QD (with the electron confined in the plane $z = 0$) placed within a QR. Experimentally, local oxidation method with atomic force microscope can be used to realize a variety of nanostructures on metals and semiconductors (cf. Ref. 200 and references therein), including high-quality QDs[201] and QRs.[202] Therefore, the two-dimensional coupled QDQR structure considered herein can be realized by employing this technique to produce both a QD and a QR which coexist on a GaAs-AlGaAs heterostructure. The shape of the confinement potential of an individual part (QD or QR) can be tuned via a suitable choice of gate voltages.[200] Consequently, the QD and QR confinement potentials do not necessarily have the same depths. To model this coupled structure, we employ the following confinement potential:

$$V(\vec{r}) = V(\vec{\rho}) = \min[m_e^*\omega_d^2\rho^2/2 + V_0, m_e^*\omega_r^2(\rho - R)^2/2], \tag{8.2}$$

where $\hbar\omega_d$ and $\hbar\omega_r$ are the confinement energies of the QD and the QR, respectively. The radius of the QR is defined by the sum of oscillator lengths for the QD and QR potential and the barrier thickness (B_T) according to the formula $R = \sqrt{2\hbar/m_e^*\omega_d} + B_T + \sqrt{2\hbar/m_e^*\omega_r}$. V_0 is the depth of the dot confinement with respect to the bottom of the QR potential. A view of the potential profile (detailed in Eq. (8.2)) is pictured in Fig. 8.1 for $\hbar\omega_d = 6$ meV, $\hbar\omega_r = 12$ meV, $V_0 = -5$ meV, and $B_T = 10$ nm. As shown in Fig. 8.1, the potential appears to be parabolic within both the QD and the QR. This strictly cylindrically symmetric potential have been adopted previously for the study of the electron spin and charge switching in a coupled QDQR system.[171] Similar potential has also been used previously for the description of side by side QDs.[203,204]

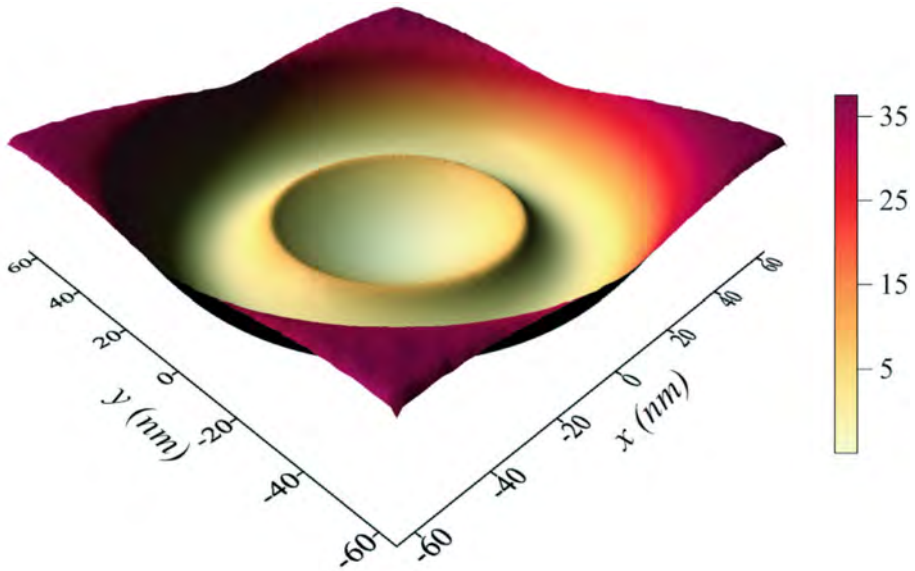

Figure 8.1: Potential profile (in unit of meV) for a laterally coupled GaAs quantum-dot-quantum-ring with the confinement energy of the dot $\hbar\omega_d = 6$ meV, the confinement energy of the ring $\hbar\omega_r = 12$ meV, the depth of the dot confinement V_0 = -5 meV and the barrier thickness $B_T = 10$ nm. The dot oscillator length $l_d = \sqrt{2\hbar/m_e^*\omega_d} = 19.51$ nm and the ring oscillator length $l_r = \sqrt{2\hbar/m_e^*\omega_r} = 13.798$ nm, giving the ring radius $R = 43.31$ nm.

To calculate the eigenenergies and corresponding wave functions of Hamiltonian (8.1), which are necessary for the calculations of optical susceptibilities, we employ potential morphing method.[3,49,52,100,157] The reference system we used to start the morphing procedure is the usual harmonic oscillator in two dimensions with well-known eigenfunctions. The interaction potential is $V_s = V(\vec{r})$, as shown in Eq. (8.2).

8.2.2 Optical susceptibility calculations

Within the two-level system approximation, the linear ($\chi^{(1)}$) and third-order ($\chi^{(3)}$) nonlinear optical susceptibilities are give by[157]

$$\chi^{(1)} = \frac{N\mu^2 T_2}{\hbar\varepsilon_0\varepsilon_{eff}^2}\frac{i-\delta T_2}{1+\delta^2 T_2^2}, \tag{8.3}$$

$$\chi^{(3)} = -\frac{4N\mu^4 T_1 T_2^2}{3\hbar^3\varepsilon_0\varepsilon_{eff}^4}\frac{i-\delta T_2}{(1+\delta^2 T_2^2)^2}. \tag{8.4}$$

where N is the electron volume density in the QDQR system, ε_0 is the permittivity in vacuum, $\delta = \omega - \omega_0$ is the detuning of applied field from resonance, where $\omega_0 = (E_j - E_i)/\hbar$ with E_i and E_j being the energy eigenvalues of the initial (ground) and final (first excited) states which we obtained in the last subsection, respectively. T_1 and T_2 are the population relaxation time and the dephasing time, respectively, μ is the transition matrix element between the initial and final states which is defined as $\mu = -\langle i|ex|j\rangle$, where we assume that the polarization of electromagnetic radiation is along the x-axis direction. $\varepsilon_{eff} = \frac{2\varepsilon_{out}+\varepsilon_{in}}{3\varepsilon_{out}}$ is the local field factor due to the possible existence of the dielectric mismatch, where ε_{in} is the dielectric constant of the QDQR material, and ε_{out} is the dielectric constant of surrounding matrix material. As shown from the Eqs. (8.3) and (8.4), possible existence of the dielectric mismatch ($\varepsilon_{in}\neq\varepsilon_{out}$) has significant influence on the linear and nonlinear optical susceptibilities. This has also been addressed in more details in our previous work regarding to the ZnO-based colloidal QD systems.[100,157] However, we assume that the GaAs coupled QDQR structures studied herein are obtained on a GaAs-$Al_xGa_{1-x}As$ heterostructure with Al concentration $x = 0.3$,[200] and the QDQR material GaAs and the possible barrier material $Al_{0.3}Ga_{0.7}As$ have closely matching dielectric constants (e.g., ε_{in}=ε_{out} and ε_{eff}=1).

8.3 Numerical results and discussion

In the linear regime, two characteristics of the linear and nonlinear optical susceptibilities are of great importance. One is the photon energy at which the susceptibility reaches its peak value, and the other one is the magnitude or the intensity of this peak. The analytical expressions of the linear and nonlinear optical susceptibilities we employ herein offer us the possibility to quantify these two characteristics. As indicated from Eq. (8.3), the real part of the linear susceptibility $\chi^{(1)}$ exhibits a standard dispersive lineshape, presenting

firstly a maximum and then a minimum as the photon energy increases. These maximum and minimum appear at the photon energy $\hbar\omega = E_{21} - \hbar/T_2$ and $E_{21} + \hbar/T_2$, respectively, where E_{21} is the transition energy. They are equivalent in the magnitude and defined by the expression $|\chi^{(1)}_{Real,max}| = N\mu^2 T_2/(2\hbar\varepsilon_0)$. On the other hand, the imaginary part of $\chi^{(1)}$ displays a standard Lorentzian lineshape, presenting a maximum at photon energy $\hbar\omega = E_{21}$. This peak value is determined by $|\chi^{(1)}_{Real,max}| = N\mu^2 T_2/(\hbar\varepsilon_0)$. Comparing to the linear counterpart, the real part of the nonlinear susceptibility $\chi^{(3)}$, as indicated from Eq. (8.4), shows an inverted dispersive lineshape, exhibiting firstly a minimum at $\hbar\omega = E_{21} - \hbar/T_2$ and then a maximum at $\hbar\omega = E_{21} + \hbar/T_2$ when the photon energy increases. The intensities of these extremums are equivalent (in absolute value) which are described by $|\chi^{(3)}_{Real,max}| = 4N\mu^4 T_1 T_2^2/(3\hbar^3\varepsilon_0)$. As concerning the imaginary part of $\chi^{(3)}$, it is negative and presents a maximum (in absolute value) at the photon energy $\hbar\omega = E_{21}$ whose magnitude is determined by $|\chi^{(3)}_{Img,max}| = N\mu^4 T_1 T_2^2/(3\hbar^3\varepsilon_0)$. It should be noted here that the linear susceptibility $\chi^{(1)}$ is a dimensionless quantity, while its nonlinear susceptibility $\chi^{(3)}$ is in unit of m^2/V^2.

As shown above, the peak intensities of the linear and nonlinear optical susceptibilities are dependent on the electron volume density N, the relaxation time T_1, the dephasing time T_2 and the transition matrix element $|\mu|$. However, in what follows, we focus on the study of the influence of the structure parameters of the coupled QDQR system, such as the confinement energy of the ring (or the dot), the depth of the dot confinement relative to the bottom of the QR potential and the tunneling barrier thickness, on the transition energy (i.e., E_{21}) and the peak values of the linear and nonlinear susceptibilities. The relevant parameters used in our calculations for GaAs QDQR systems are: $m_e^* = 0.0667m_0$ (m_0 is the free electron mass), $N = 3{\times}10^{16}$ cm^{-3}[Ref. 199], $T_1 = 1$ ps and $T_2 = 0.2$ ps,[205] respectively. The influence of the volume density N or the dephasing time T_2 on the optical nonlinearities in semiconductor nanostructures have been addressed in the literature and can be found in Refs. 206 and 128.

Firstly, in order to study the dependence of the the linear and nonlinear susceptibilities on the relative strength of the dot and ring confinement, we define a parameter $\gamma = (\hbar\omega_r)/(\hbar\omega_d)$. Large γ corresponds to a narrower (wider) path for the electron to transverse in the ring (dot) part of the QDQR and *vice versa*. The calculations are based on QDQRs with equal depth of the dot and ring (i.e., $V_0 = 0$). We start our calculations with a ring confinement energy $\hbar\omega_r = 3$ meV which is only a half of its dot counterpart ($\gamma = 0.5$, cf. Fig. 8.2). It appears that the ground state is almost purely ring-localized state (see the upper plot of the first column in Fig. 8.3). This can also be justified by its energy, i.e., $E = 1.42$ meV, which is pretty close to the ground state energy of the single-dimensional harmonic oscillator in the radial direction (i.e., $\approx \hbar\omega_r/2 = 1.5$ meV). As γ increases (the ring confinement energy increases), the oscillator length of ring decreases and the wave functions gradually penetrate through the central tunneling barrier into the dot part (cf.

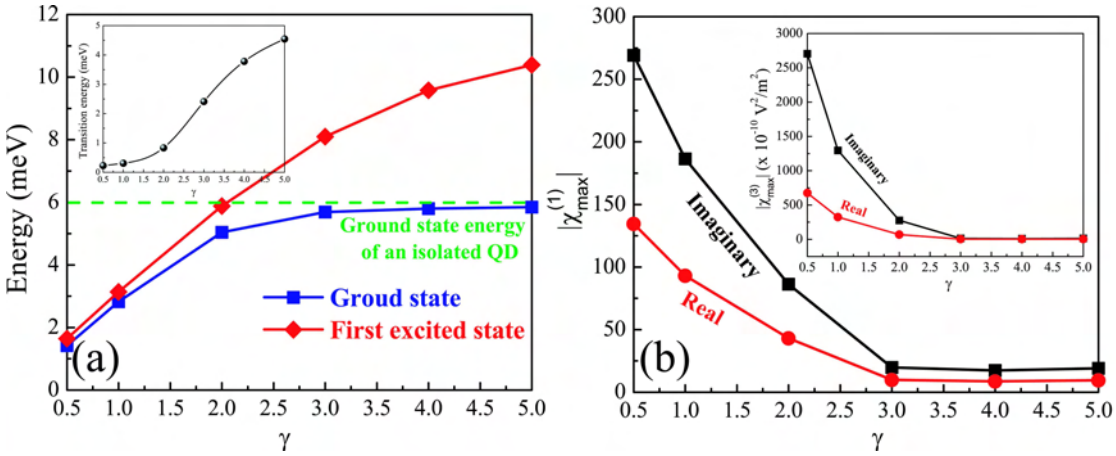

Figure 8.2: (a) The ground-state (blue solid square), first excited state (red solid diamond) energies and transition energy (inset) as a function of γ. (b) The maximum values (in absolute value) of the real (red solid sphere) and imaginary (black solid square) parts of the linear and nonlinear (inset) susceptibilities as a function of γ. Here, $\gamma = (\hbar\omega_r)/(\hbar\omega_d)$ where $\hbar\omega_r$ and $\hbar\omega_d$ are the confinement energies of the dot and ring, respectively. $\hbar\omega_d = 6$ meV, $V_0 = 0$ and $B_T = 10$ nm.

Fig. 8.3). Consequently, both energies of the ground state and the first excited state increase as shown in Fig. 8.2(a). However, comparing to the ground state energy, the energy of the excited state turns out to be more sensitive to the variation of γ. This results in a substantially increase in the transition energy (cf. the inset of Fig. 8.2(a)). For $\hbar\omega_r \geqslant 3\hbar\omega_d = 18$ meV ($\gamma = 3$), we find that the ground state is nearly purely dot-localized state (cf. Fig. 8.3) and its energy approaches to the ground state energy of an isolated QD, i.e., $E = V_0 + \hbar\omega_d = 6$ meV (see the dashed line in Fig. 8.2(a)). As regards the first excited state, the density movement towards the dot part of QDQR appears to be slower in comparison to its ground state counterpart.

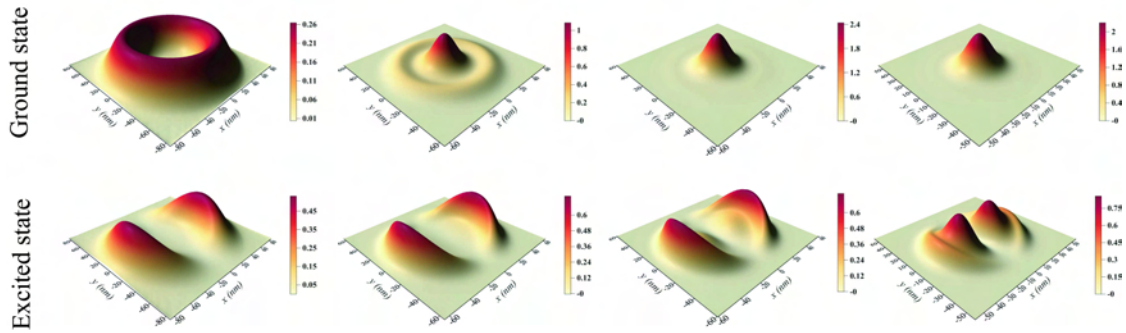

Figure 8.3: Electron probability densities of the ground state (the upper panel) and the first excited state (the lower panel) in QDQRs with various confinement energy values of the ring $\hbar\omega_r$. From the leftmost to the rightmost columns are for $\hbar\omega_r = 3$ meV, 12 meV, 18 meV, 30 meV, respectively. Here, the depth of the dot (V_0), the confinement energy of the dot ($\hbar\omega_d$) and the barrier thickness (B_T) are the same as in Fig. 8.2.

At the meantime, the aforementioned penetration of both the ground-state and first excited-state wave functions into the dot part of the QDQR system also causes a decrease in the transition matrix element $|\mu|$. This in turn leads to a decrease in the maximum values of the real and imaginary parts of both linear and nonlinear susceptibilities (in absolute value, cf. Fig. 8.2(b)). Comparing the linear susceptibility (e.g., $|\chi^{(1)}_{max}|$), the maximum value of its nonlinear counterpart (e.g., $|\chi^{(3)}_{max}|$) is found to be more sensitive to the variation of the relative strength of the dot and ring confinement (as characterized by γ). This is related to the fact that $|\chi^{(3)}_{max}|$ is more dependent on the transition matrix element (e.g., $|\chi^{(3)}_{max}| \propto |M_{21}|^4$, while $|\chi^{(1)}_{max}| \propto |M_{21}|^2$). We further find that for a given quantity (linear or nonlinear susceptibility), the imaginary part exhibits a stronger dependence on γ in comparison to its real analog (cf. Fig. 8.2(b)). All the maximum values appear to be insensitive to the further increase in γ when $\gamma \geq 3$ ($\hbar\omega_r \geq 18$ meV).

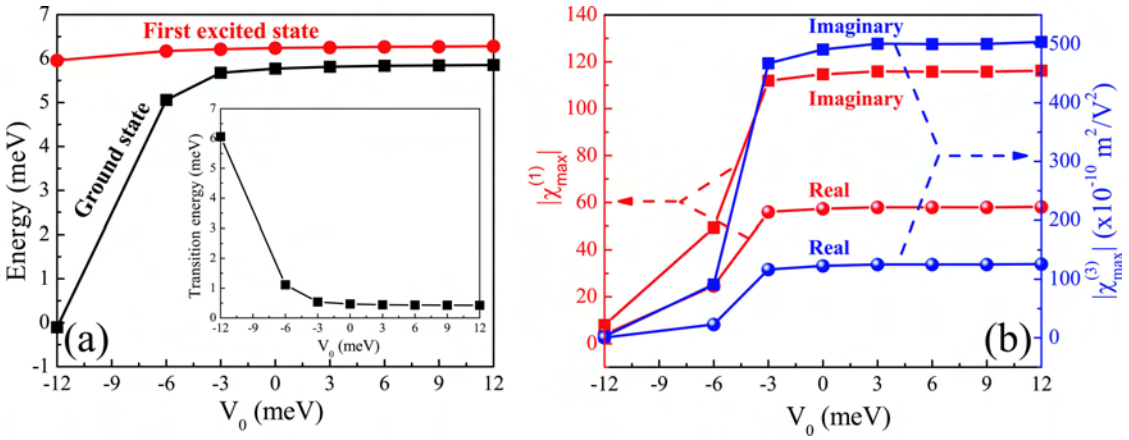

Figure 8.4: (a) The ground-state (black solid square), first excited state (red solid sphere) energies and transition energy (inset) as a function of the depth of dot confinement relative to the bottom of the QR potential V_0. (b) The maximum values (in absolute value) of the real (solid spheres) and imaginary (solid squares) parts of the linear (red lines) and nonlinear (blue lines) susceptibilities as a function of the depth of dot confinement. Here, $B_T = 10$ nm and $\hbar\omega_d = \hbar\omega_r = 12$ meV.

To proceed our calculations, we turn our attention to study the influence of the depth of dot confinement relative to the bottom of the QR potential (e.g., V_0) on the optical susceptibilities in coupled QDQRs with the dot and ring having the same confinement energies (e.g., $\hbar\omega_d = \hbar\omega_r = 12$ meV). For a dot with very deep confinement (e.g., $V_0 = -12$ meV), the ground-state is almost purely dot-localized state with an energy ($= -0.1$ meV) approaching to the ground-state energy of an isolated QD ($\approx V_0 + \hbar\omega_d = 0$ meV, cf. Fig. 8.4(a)). As V_0 increases, both the ground-state and first excited-state wave functions leak gradually from the dot part to the ring part of the QDQR (cf. Fig. 8.5). This causes an increase in both the ground-state and first excited-state energies (cf. Fig. 8.4(a)).

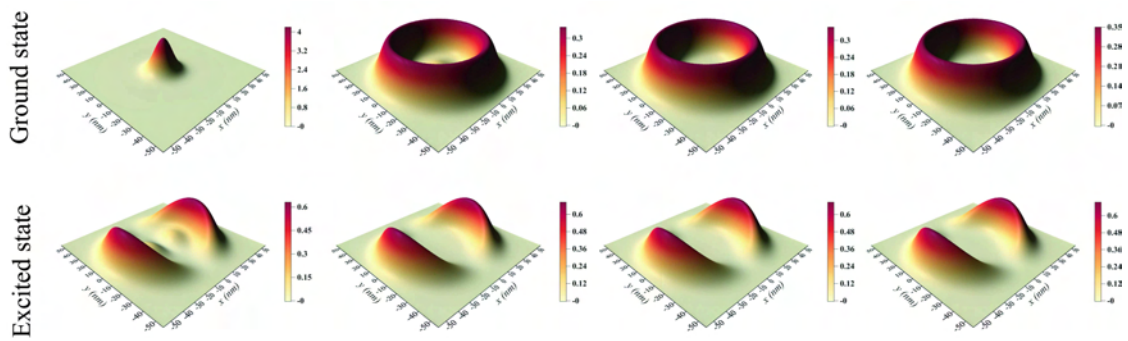

Figure 8.5: Electron probability densities of the ground state (the upper panel) and the first excited state (the lower panel) in QDQRs with various depths of the dot confinement relative to the bottom of the QR potential V_0. From the leftmost to the rightmost columns are for $V_0 = -12$ meV, -3 meV, 3 meV, 12 meV, respectively. Here, the confinement energies of the dot ($\hbar\omega_d$) and the ring ($\hbar\omega_r$), and the barrier thickness (B_T) are the same as in Fig. 8.4.

However, the ground state exhibits a significantly stronger dependence on the increase of V_0, experiencing a quick increase in the corresponding energy as V_0 enhances. Conversely, the variation of V_0 on the first-excited state is practically marginal and only a slight increase in its energy is observed (cf. Fig. 8.4(a)). As a consequence, the transition energy decreases as V_0 increases (see the inset of Fig. 8.4(a)). We further find that for $V_0 \geq -3$ meV which is a quarter of the dot (or ring) confinement energy (in absolute value), both energies (ground-state and first excited state) are insensitive to the further increase in V_0. The ground-state becomes a nearly purely ring-like state (see the upper panel of Fig. 8.5) and its energy approaches to the ground-state energy of the single-dimensional harmonic oscillator in the radial direction ($\approx \frac{1}{2}\hbar\omega_r = 6$ meV, see Fig. 8.4(a)).

The leakage of the wave function from the dot part to the ring part also causes a significant increase in transition matrix element $|\mu|$. This resultantly leads to a considerable enhancement of the maximum values of the linear and nonlinear susceptibilities (both real and imaginary parts, cf. Fig. 8.4(b)). Similarly to what we have found previously, the maximum value of the nonlinear susceptibility, especially that of the imaginary part, appears to be more sensitive to the variation of V_0. For $V_0 \geq -3$ meV, the maximum values of all the quantities are insensitive to the increase in V_0 (see Fig. 8.4(b)).

Finally, we study the coupling effects between the dot and ring on the optical susceptibilities in a laterally coupled QDQR structure. In the strong coupling limit (e.g., $B_T = 5$ nm), the ground state is a dominant dot-localized state, having an energy ($= 0.76$ meV) very close to the ground-state energy of an isolated QD ($\approx V_0 + \hbar\omega_d = 1$ meV, cf. Figs. 8.6(a) and 8.7). As the barrier thickness increases, the ground-state energy increases slightly (cf. Fig. 8.6(a)), while its first excited counterpart appears to be more energetically dependent on the central barrier thickness, experiencing a faster increase in its energy. Consequently, as shown in Fig. 8.6(a), the transition energy is an increasing function of the barrier thickness. For $B_T \geq 25$ nm, both the ground-state and first excited-state energies are insensitive to

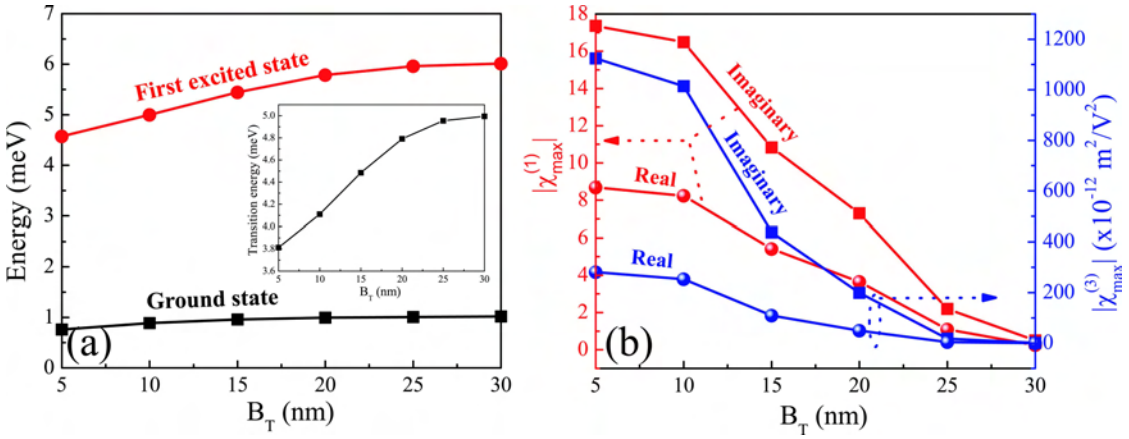

Figure 8.6: (a) The ground-state (black solid square), first excited state (red solid sphere) energies and transition energy (inset) as a function of the barrier thickness B_T. (b) The maximum values (in absolute value) of the real (solid spheres) and imaginary (solid squares) parts of the linear (red lines) and nonlinear (blue lines) susceptibilities as a function of the barrier thickness B_T. Here, $\hbar\omega_d = 6$ meV, $\hbar\omega_r = 12$ meV and $V_0 = -5$ meV.

the further increase in the barrier thickness and a decoupling phenomenon is observed (cf. Figs. 8.6(a)). We also find that the ground-state wave function is more localized towards the dot center (see the upper panel of Fig. 8.7), whereas the first excited state one turns out to move away from the dot center (see the lower panel of Fig. 8.7) when B_T increases. Therefore, the overlap between these two wave functions decreases and the transition matrix element $|\mu|$ reduces considerably as the coupling effects become less significant. This eventually causes a drastic decrement of the maximum values of all the optical susceptibilities (cf. Fig. 8.6(b)). At the meanwhile, we find that in comparison to the linear susceptibility, its nonlinear analogue is more sensitive to the coupling effects, while for a given quantity, the imaginary part demonstrates a stronger dependence on the coupling effects than the real part.

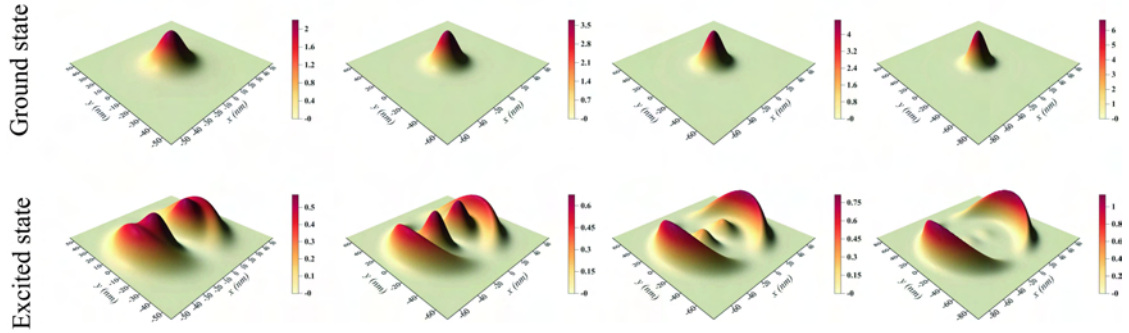

Figure 8.7: Electron probability densities of the ground state (the upper panel) and the first excited state (the lower panel) in QDQRs with various values of central barrier thickness B_T. From the leftmost to the rightmost columns are for $B_T = 5$ nm, 15 nm, 20 nm, 30 nm, respectively. Here, the confinement energies of the dot ($\hbar\omega_d$) and the ring ($\hbar\omega_r$), and the depth of the dot confinement (V_0) are the same as in Fig. 8.6.

8.4 Brief summary

In summary, we have theoretically studied the influence of the structure parameters, such as the relative strength of the dot and ring confinement, the depth of the dot confinement relative to the bottom of the QR potential and the central tunneling barrier thickness, on the linear and nonlinear optical susceptibilities in a laterally coupled quantum-dot-quantum-ring (QDQR) system. A simple model for the potential, which assumes parabolic confinement in both the dot and the ring, is adopted. We employ the potential morphing method (PMM) in the framework of the effective mass approximation for the electronic structure calculations. It is found that the ground electron state can be changed from a nearly pure dot-localized state to a nearly pure ring-localized state or *vice versa* by suitably choosing the structure parameters (e.g., the ring (or dot) confinement energy and/or the depth of the dot confinement). However, this can not be realized by modifying the coupling effects which have a strong influence primarily on the shape and energy of the excited state counterpart. The significant modification appeared in the electronic structure through controlling the structure parameters eventually leads to a considerable influence on the optical susceptibilities in such a coupled structure. A significant blue shift of the transition energy is observed when the relative strength of the dot and ring confinement and/or the central barrier thickness are enhanced. Conversely, a red shift is found when the depth of the dot confinement increases. For the confinement energy of the ring larger than a critical value (around three times of the confinement energy of the dot), all the maximum values of the optical susceptibilities appear to be insensitive to the increase in the confinement energy of the ring. Similar behaviour has also been observed for the variation of the maximum values with respect to the depth of the dot confinement. The enhancement of the coupling effects turns out to have a significantly positive contribution on the linear and nonlinear optical susceptibilities. Finally, we find that the nonlinear optical susceptibility is more sensitive to the modification of the structure parameters in comparison to its linear counterpart, while for a given quantity, its imaginary part always exhibits a stronger dependence on the change in the structure parameters than the real part.

Part II

Pseudopotential Theory

9

Background Theory

The envelope function and effective-mass approximations, which have been discussed and applied in many interesting systems previously, allow many of the most fundamental properties of semiconductor and their nanostructures to be explained. However, it would be worthwhile considering more complex models to bring up more physical insights. In this chapter, we describe the general pseudopotential theory with an emphasis on the plane wave empirical pseudopotential method which we will employ for the calculations of the electronic structure of several realistic systems in the following few chapters. The configuration interaction approach which is used for studying the excitonic effects in these systems is also described.

Contents

9.1 Plane wave expansion

One of the crucial points of any electronic structure method is to select a set of basis functions so that the wave function of the system under consideration can be represented as a linear combination of these basis functions. The choice of the basis functions is generally strongly relevant to the accuracy of the results and also the computational efficiency. In quantum chemistry and/or computational physics, the most widely used basis sets are: (i) Slater (i.e., $\exp(\alpha|\mathbf{r}|)$), (ii) Gaussian (i.e., $\exp(-\alpha\mathbf{r}^2)$), (iii) plane wave. In addition to these widespread basis sets, there are also some other basis sets which are less popular, such as numerical basis sets, discrete variable representations, wavelets, non-orthogonal generalized Wannier functions and so on. In what follows, we will discuss in details about the simplest complete and orthonormal basis set, the plane wave basis set, which is employed in our work.

In principle, the single electron wave function of a crystal $\psi_n(\mathbf{k},\mathbf{r})$ can always be expanded by the plane wave $\exp[i(\mathbf{k}+\mathbf{G})\cdot\mathbf{r}]$, where $\mathbf{k}$ is the wave vector and $\mathbf{G}$ is the reciprocal lattice vector. That is,

$$\psi_n(\mathbf{k},\mathbf{r}) = \frac{1}{\sqrt{N\Omega_c}}\sum_{\mathbf{G}} c_n(\mathbf{k},\mathbf{G})\exp[i(\mathbf{k}+\mathbf{G})\cdot\mathbf{r}], \tag{9.1}$$

where $\frac{1}{\sqrt{N\Omega_c}}$ is the normalization constant and Ω_c is the volume of the primitive cell. For a given expansion, an infinite number of $\mathbf{G}$ is generally needed to ensure the completeness. However, the Fourier coefficients $c_n(\mathbf{k},\mathbf{G})$ decreases with increasing in $\mathbf{G}$. Therefore, the expansion can be reasonably truncated at an energy cutoff E_{cut}, which is $\frac{\hbar^2}{2m}|\mathbf{k}+\mathbf{G}|^2<E_{cut}$.

The advantages of the plane wave basis set are:

1. The convergence with respect to the completeness of the basis set can be easily checked by controlling only one parameter, i.e., E_{cut},

2. Due to the orthonormality of the basis set, the Kinetic term of the single electron Hamiltonian is diagonal in reciprocal space. The wave functions can be effectively transformed between the real space and the reciprocal space by using the fast Fourier transformation (FFT). Consequently, the calculations are significantly speeded up.

3. The basis set is atom position independent. This largely simplifies the calculations of the forces on the atoms and the stresses on the unit cell, which can be done directly via the Hellmann-Feynman theorem without applying Pulay corrections[207] for the site-dependence of the basis set.

9.2 Orthogonalized plane wave method

There is a large number of crystals whose electronic states can be separated into two classes: (i) *inner states (core states)*, which are very localized spatially and very deep in energy; (ii) *outer states (valence and/or conduction states)*, which are spread out spatially and at higher energy. The use of the plane wave expansion of all the electron states fails on the description (with a reasonable number of plane waves) of the strongly localized core states. Herring[208] proposed a solution to this problem: describing the core states by Bloch sums built from localized orbitals and the valence and/or conduction states by plane waves orthogonalized to the core states. Orthogonalized plane waves can be effectively used to describe the itinerant states, since they are atomic-like and very close to the nuclei where the crystal potential is atomic-like, while the plane waves can describe the interstitial regions, where the crystal potential is smooth. This is the so-called orthogonalized plane wave (OPW) method.

We assume that the core wave function $\langle\phi_c(\mathbf{k},\mathbf{r})|$ is the summation of all the core Bloch,

$$|\phi_c(\mathbf{k},\mathbf{r})\rangle = \frac{1}{\sqrt{N}}\sum_{\mathbf{R}}\exp(i\mathbf{k}\cdot\mathbf{R})\varphi_c(\mathbf{r}-\mathbf{R}). \tag{9.2}$$

This wave function is not the eigenfunction of the crystal Hamiltonian $\hat{H}$. However, we *enforce* that it is the eigenfunction of the crystal Hamiltonian $\hat{H}$ and satisfies the following Schrödinger equation

$$\hat{H}|\phi_c(\mathbf{k},\mathbf{r})\rangle = E_c|\phi_c(\mathbf{k},\mathbf{r})\rangle. \tag{9.3}$$

We define the OPW $|\chi_{\mathbf{k}+\mathbf{G}}\rangle$ as

$$|\chi_{\mathbf{k}+\mathbf{G}}\rangle = |\mathbf{k}+\mathbf{G}\rangle - \sum_c |\phi_c(\mathbf{k},\mathbf{r})\rangle\langle\phi_c(\mathbf{k},\mathbf{r})|\mathbf{k}+\mathbf{G}\rangle, \tag{9.4}$$

where $|\mathbf{k}+\mathbf{G}\rangle$ represents the plane waves and the summation in the second term on the right hand side covers all the *inner states*. It can be justified that

$$\langle\phi_c(\mathbf{k},\mathbf{r})|\chi_{\mathbf{k}+\mathbf{G}}\rangle = 0. \tag{9.5}$$

We now expand the crystal wave function $|\psi_{\mathbf{k}}\rangle$ by using the OPWs $|\chi_{\mathbf{k}+\mathbf{G}}\rangle$:

$$|\psi_{\mathbf{k}}\rangle = \sum_{\mathbf{G}} c_{\mathbf{G}}(\mathbf{k})|\chi_{\mathbf{k}+\mathbf{G}}\rangle. \tag{9.6}$$

One can get the following secular equation by using the standard variational procedures on the coefficients of the expansion $c_{\mathbf{G}}(\mathbf{k})$,

$$\mathbf{det}|\langle\chi_{\mathbf{k}+\mathbf{G}'}|\hat{H}|\chi_{\mathbf{k}+\mathbf{G}}\rangle - E_{\mathbf{k}}\langle\chi_{\mathbf{k}+\mathbf{G}'}|\chi_{\mathbf{k}+\mathbf{G}}\rangle| = 0. \tag{9.7}$$

The lowest eigenvalue of (9.7) corresponds to the lowest (valence or conduction) crystal eigenstate. If one uses the expression (9.4), the secular equation (9.7) can be written in an alternative but perfectly equivalent form,

$$\mathbf{det}|\langle\mathbf{k}+\mathbf{G}^{'}|-\nabla^{\mathbf{2}}+V(\mathbf{r})+V^{(rep)}|\mathbf{k}+\mathbf{G}\rangle - E_{\mathbf{k}}\delta_{\mathbf{G}'\mathbf{G}}| = 0, \tag{9.8}$$

where $\hat{H} = -\nabla^{\mathbf{2}} + V(\mathbf{r})$ is the crystal Hamiltonian and the operator $V^{(rep)}$ is defined as,

$$V^{(rep)} = \sum_{c}(E_{\mathbf{k}} - E_c)|\phi_c(\mathbf{k},\mathbf{r})\rangle\langle\phi_c(\mathbf{k},\mathbf{r})|. \tag{9.9}$$

The operator $V^{(rep)}$, as defined in (9.9), is a non-orthodox operator, which is energy-dependent and non-local; qualitatively, it can be interpreted as a repulsive potential produced by the presence of the core states.[209]

In general, the OPW method has reasonable rapid convergence and in the expansion, a number of ten to hundred OPWs are sufficient.[209] As pointed out previously, the core wave function $|\phi_c(\mathbf{k},\mathbf{r})\rangle$ is not the eigenstate of the crystal Hamiltonian. However, in OPW method, this is enforced to be valid. Within this approximation, the calculated energy is systematically smaller than the true energy. This problem essentially leads to a significant limitation of the applications of the OPW method.

9.3 Pseudopotential method

9.3.1 The derivation of the pseudopotential

The concept of pseudopotentials was proposed by Fermi[210] to study high-lying atomic states. Later on, Hellman introduced the pseudopotentials for the calculations of the energy levels of the alkaline molecules and its hydrides.[211] The usage of pseudopotentials did not become wide spread until the late 1950s, when the activity in the area of condensed matter physics began to accelerate. The pseudopotential method is based on the previously discussed OPW method. **The basic idea of the OPW method** is *to exploit the presence*

of the core states for the determination of the valence and conduction energy bands, both in the core regions and outside the core regions. While, **the basic idea of pseudopotential method** is to *get rid of the core states, by replacing the strong crystalline potential with a weak pseudopotential, which is sufficient for the determination of the valence and conduction energy bands.* The pseudo wave functions are required to represent the genuine crystalline wave functions only outside the core regions, without worrying about the smoothing occurring inside the core regions.

In OPW method, the valence and conduction states are obtained solving the secular Eq. (9.8). The effect of the energy-dependent non-local orthogonalization terms in equation (9.8) is to cancel (to large extent) the true all-electron crystal potential $V(\mathbf{r})$ just in the core region, where $V(\mathbf{r})$ is particularly strong. From this, the hope arises that the effective potential (true potential plus orthogonalization terms) in Eq. (9.8) can be mimicked by an appropriate weak pseudopotential $V^{(pseudo)}$, smoother than the true potential $V(\mathbf{r})$ within the core region, and equal to it outside the core region. Following this idea, the pseudopotentials will be introduced as the following.

ψ_C and ψ_V represent respectively the true valence and core wave functions corresponding to the crystal Hamiltonian $\hat{H}$ with eigenvalues E_V and E_C. They satisfy the following Schrödinger equations,

$$\hat{H}|\psi_V\rangle = E_V|\psi_V\rangle, \tag{9.10}$$

and

$$\hat{H}|\psi_C\rangle = E_C|\psi_C\rangle, \tag{9.11}$$

respectively. Similarly to the OPW method, we now define the valence wave function of the crystal,

$$|\psi_V\rangle = |\psi_V^{ps}\rangle + \sum_C \mu_{CV}|\psi_C\rangle. \tag{9.12}$$

Unlikely to the OPW method, the $|\psi_C\rangle$ is the true core wave function. Using the orthogonality condition $\langle\psi_C|\psi_V\rangle = 0$, the coefficient μ_{CV} can be obtained as following,

$$\mu_{CV} = -\langle\psi_C|\psi_V^{ps}\rangle. \tag{9.13}$$

If $|\psi_V^{ps}\rangle$ is applied by the operator $\hat{H} - E_V$, one can get,

$$\begin{aligned}(\hat{H} - E_V)|\psi_V^{ps}\rangle &= (\hat{H} - E_V)(|\psi_V^{ps}\rangle + \sum_C \mu_{CV}|\psi_C\rangle) \\ &= (\hat{H} - E_V)\sum_C |\psi_C\rangle\langle\psi_C|\psi_V^{ps}\rangle \\ &= \sum_C (E_C - E_V)\langle\psi_C|\psi_V^{ps}\rangle.\end{aligned} \tag{9.14}$$

Making some arrangements on the above equation, the following equation can be obtained,

$$[\hat{H} + \sum_{C}(E_V - E_C)|\psi_C\rangle\langle\psi_C| - E_V]|\psi_V^{ps}\rangle = 0. \tag{9.15}$$

If one uses,

$$\hat{H} = \hat{T} + \hat{V}, \tag{9.16}$$

and defines,

$$V^{ps} = \hat{V} + \sum_{C}(E_V - E_C)|\psi_C\rangle\langle\psi_C|, \tag{9.17}$$

The equation (9.15) can be re-written as the following,

$$[\hat{T} + V^{ps}]|\psi_V^{ps}\rangle = E_V|\psi_V^{ps}\rangle, \tag{9.18}$$

where $\hat{T}$ is the Kinetic operator, V^{ps} is the pseudopotential, and (9.18) is the pseudopotential Schrödinger equation.

9.3.2 Basic properties of pseudopotential

As one can see from (9.17), the pseudopotential is made of two terms. One is the positive attractive term $\hat{V}$, and the other one is the negative repulsive term $\sum_C(E_V - E_C)|\psi_C\rangle\langle\psi_C|$. The summation of these two terms leads to a weak and smooth potential. It should be noted here the although $|\psi_V^{ps}\rangle$ is the pseudo wave function, the obtained eigenenergies by solving the corresponding Schrödinger equation (9.18) are not the ***pseudo energies***, but the ***true*** eigenenergyies E_V of the valence states.

The pseudopotential at this point is non-local. It can be written as the following,

$$V^{ps}(\mathbf{r}, \mathbf{r}^{'}) = V_L^{ps}(\mathbf{r})\delta(\mathbf{r} - \mathbf{r}^{'}) + V_{NL}^{ps}(\mathbf{r}, \mathbf{r}^{'}), \tag{9.19}$$

where the first term on the right-hand side of the above equation $V_L^{ps}(\mathbf{r}) = V$, which is local, and the other term $V_{NL}^{ps} = \sum_C(E_V - E_C)|\psi_C\rangle\langle\psi_C|$, which contains the core states and is non-local. The non-local term V_{NL}^{ps} is generally not unique, since $(E_V - E_C)$ can be arbitrarily replaced. This property will be used for the generation of the pseudopotential. There are several ways to construct the pseudopotentials. One of them is the so-called norm-conserving pseudopotentials (NCPPs), which were introduced by Hamann, Schlüter, Chiang[212] in 1979, which are based on the ***ab initio*** atomic calculations. These pseudopotentials have to meet the following conditions:[212] (i) real and pseudo valence eigenvalues agree for a chosen prototype atomic configuration; (ii) real and pseudo atomic wave functions agree beyond a chosen core radius r_c; (iii) the integrals

from 0 to r of the real and pseudo charge densities agree for $r > r_c$ for each valence state (***norm conservation***); (iv) the logarithmic derivatives of the real and pseudo wave functions and their first energy derivatives agree for $r > r_c$. Atoms with strongly oscillating pseudo wave functions generally produce *hard* NCPPs. More plane waves are required in the calculations. However, the transferability of the pseudopotentials is better and can be used in different chemical environments. On the other hand, larger core radius means better softness of the pseudopotential, but worse transferability. The common procedures of generating such type of pseudopotentials can be found in Refs. 212–216. Generally, the NCPPs remain hard for the first row elements (particularly, N, O, F) and for transition metals (particularly, Cr, Mn, Fe, Co, Ni). More plane waves are needed in the relevant calculation, even if only one atom is hard. This leads to large CPU and RAM requirements.

Ultrasoft pseudopotentials (USPPs) are devised to overcome the above mentioned problems. This type of PPs were introduced by Vanderbilt[217] in 1990 in order to allow calculations to be performed with the lowest possible cutoff energy for the plane wave basis set. For this type of pseudopotentials, they must meet the following properties:[217] (i) it takes the form of a sum of a few separable forms; (ii) it becomes local and vanishes outside the core; (iii) the scattering properties and their energy derivatives are, by construction, correct at several energies spanning the range of occupied states, and the transferability can be systematically improved by increasing the number of such energies; (iv) the norm-conserving constraint is removed so that the pseudopotential can be constructed in such a way as to optimize smoothness; (v) the pseudopotential itself becomes involved in the self-consistent screening process, thereby improving transferability with respect to changes in the charge configuration. The procedures of constructing this type of pseudopotentials can be found in Refs. 217, 218.

The previously discussed two ways of constructing pseudopotentials, where the interaction of the valence electrons has been taken into account explicitly, have been very successful in the modern *ab initio* calculations. There is also another way of constructing pseudopotentials which includes of the interaction of not only the valence electrons but of all the electrons, that is, empirical pseudopotential method. The details of this method will be outlined in the following section.

9.3.3 Empirical pseudopotential method

The empirical pseudopotential method (EPM) was developed in 1960's[219–221] to solve the Schrödinger equation of the bulk crystal without knowing exactly the potential experienced

by an electron in the lattice. The pseudopotential Hamiltonian for an electron in the crystal can be written as the following,

$$\hat{H} = -\frac{\hbar^2}{2m_0}\nabla^2 + V(\mathbf{r}), \tag{9.20}$$

where the first term is the Kinetic term and the other term is the effective crystal potential. The first assumption of EPM is that $V(\mathbf{r})$ can be written as a summation of the atom-centered pseudopotentials,

$$V(\mathbf{r}) = \sum_{\alpha,j,n} v_\alpha(\mathbf{r} - \mathbf{R}_n - \mathbf{r}_{\alpha,j}), \tag{9.21}$$

where n is the index for the primitive unit cells, $\mathbf{R}_n$ is the corresponding lattice vector, α represents the atom type, j is the atom index. $\mathbf{r}_{\alpha,j}$ is the basis vector of atom j of type α. We start with the simplest case where the crystal is consisted with only one type of atoms (e.g., Si). $V(\mathbf{r})$ can be expanded in reciprocal lattice vector $\mathbf{G}$ and can be expressed as the product of a structure factor $S(\mathbf{G})$ times a pseudopotential form factor $v(\mathbf{G})$ as in the following equation,

$$V(\mathbf{r}) = \sum_{\mathbf{G}} v(\mathbf{G})S(\mathbf{G}) \exp(i\mathbf{G}\mathbf{r}). \tag{9.22}$$

The structure factor $S(\mathbf{G})$ in the above equation is

$$S(\mathbf{G}) = \frac{1}{n}\sum_j e^{-i\mathbf{G}\mathbf{r}_j}. \tag{9.23}$$

The structure factor only depends on the geometry and the form factor is treated in the EPM as disposable parameters.[222] The cubic semiconductors of the diamond structure (e.g., Si, Ge) have the face-centered cubic (fcc) structure with two atoms per unit cell. We take the origin to be halfway between these two atoms, whose posisions are donated by $\mathbf{r}_1$ and $\mathbf{r}_2$, so that $\mathbf{r}_1 = a_0(\frac{1}{8}, \frac{1}{8}, \frac{1}{8}) = \tau$, and $\mathbf{r}_2 = -\tau$, where a_0 is the length of the unit cube. In this case, the structure factor $S(\mathbf{G})$ in (9.23) is simplified as

$$S(\mathbf{G}) = \cos(\mathbf{G} \cdot \tau). \tag{9.24}$$

It has been proved that for Si and most conventional IV, and III-IV semiconductors the potential $V(\mathbf{G})$ becomes week for reciprocal vectors larger than $|\mathbf{G}|^2 = 11(\frac{2\pi}{a_0})^2$.[223] Therefore, it could be a reasonable approximation to truncate the expansion at this point (e.g., $|\mathbf{G}| \leq 11$ (in unit of $\frac{2\pi}{a_0}$)). The first five reciprocal lattice vectors have squared magnitudes of 0, 3, 4, 8, and 11 (in unit of $(\frac{2\pi}{a_0})^2$), which are corresponding to $\mathbf{G} = \{0,0,0\}, \{1,1,1\}, \{2,0,0\}, \{2,2,0\}, \{3,1,1\}$ (in unit of $\frac{2\pi}{a_0}$), respectively. If one takes a look on the results of $\mathbf{G} \cdot \tau$, it is very easy to find out that only three of these five $\mathbf{G}$ give

non-zero structure factors. They are $\mathbf{G} = \{1,1,1\}, \{2,2,0\}, \{3,1,1\}$. It should be noted here that the structure factor for $\mathbf{G} = \{0,0,0\}$ is kept as zero, since it merely adds a constant value to all the energy levels. If $v(\mathbf{r})$ is assumed to be spherically symmetric and the form factor takes $v(\mathbf{G})$, only three different form factors remain. They are $v(\mathbf{G} = \{1,1,1\})$, $v(\mathbf{G} = \{2,2,0\})$, and $v(\mathbf{G} = \{3,1,1\})$, respectively. These three form factors are then treated as adjustable parameters to reproduce the well-known experimental quantities of the crystal, such as the band structure. Consequently, this method is named as EPM. Initially, this method was used successfully both to obtain very accurate band structures[224–227] for Si and Ge, and also to interpret optical experiments.[228] It was soon extended by Cohen and Bergstresser[223] with great success for the determination of the band structures and pseudopotential form factors for fourteen semiconductors of the diamond and zinc-blende structures. The band structures of most semiconductors can be fitted accurately by using such a procedure giving us the hint that a local potential $V(\mathbf{r})$ can used as a mean field to describe the complex many-body electron interactions in the crystal.[222]

The emphasis of the present Thesis is to investigate the electronic structures of the nanostructures by employing the EPM. However, this requires a continuous form of $v(\mathbf{G})$ rather than few discrete points of $v(\mathbf{G})$ in the traditional EPM.[229,230] The continuous empirical pseudopotential in the reciprocal has been introduced by Wang and Zunger[229] as,

$$v^{EPM}(q) = \frac{a_1(q^2 - a_2)}{a_3 e^{a_4 q^2} - 1}, \tag{9.25}$$

where a_1, a_2, a_3, and a_4 are fitting parameters, or it is introduced by Mäder and Zunger[230] as a linear combination of N Gaussains, i.e.,

$$v^{EPM}(q) = \sum_{i=1}^{N} a_i e^{-c_i(q-b_i)^2}, \tag{9.26}$$

where a_i, b_i, and c_i are the fitting parameters. Using a specific type of continuous empirical pseudopotential, the crystal potential $V(\mathbf{r})$ can be obtained as a superposition of the atomic pseudopotentials as detailed in equation (9.21). Once the crystal potential is calculated, we solve the following Schrödinger equation,

$$\{-\frac{\hbar^2}{2m_0}\nabla^2 + V^{EPM}(\mathbf{r}) + \hat{V}^{SO}\}\psi_i(\mathbf{r}) = \varepsilon_i \psi_i(\mathbf{r}), \tag{9.27}$$

where $\hat{V}^{SO}$ is the non-local spin-orbit operator which is,[222,231,232]

$$\hat{V}^{SO} = \sum_{i\alpha} \hat{V}^{SO}_{\alpha}(\mathbf{R}_i) = \sum_{i\alpha}\sum_{lm} V^{SO}_{l,\alpha}(\mathbf{r} - \mathbf{R}_i)|P_{lm}(\mathbf{R}_i)\rangle \mathbf{L}\cdot\mathbf{S}\langle P_{lm}(\mathbf{R}_i)|, \tag{9.28}$$

where $\sum |P_{lm}(\mathbf{R}_i)\rangle\langle P_{lm}(\mathbf{R}_i)|$ is a projector of angular momentum lm centered at the atomic position $\mathbf{R}_i$, $\mathbf{L}$ is the spatial angular momentum operator, $\mathbf{S}$ is the spin operator with components given by Pauli matrices, and $V_{l,\alpha}^{SO}(\mathbf{r})$ is a potential describing the spin-orbit interaction. The functional form of $V_{l,\alpha}^{SO}(\mathbf{r})$ was set to a Gaussian and only the effect of p states ($l = 1$) was included in the most recent works.[233,234] Practically, this approach leads to only one free spin-orbit parameter for each atom type α. At this point, the free parameters in the pseudopotential and the free parameter in the non-local spin-orbit operator are fitted to reproduce the well-known experimental quantities such as the energy gaps at high symmetry points of the Brillouin zone, the effective masses at different bands at different k points and along different reciprocal space directions, the surface work function, the spin-orbit and/or crystal field parameters.

If the optimized parameters of the pseudopotentials are found for a specific material (e.g., ZnO or ZnS), one can move the attentions to the calculations of the electronic and optical properties of the nanostructures of this material, such as quantum dot (QD), nanorod (NR), and nanowire (NW). The nanostructures are cut from the corresponding bulk material with desired shape or cross section. In this case, the atoms at the surface of the nanostructure have dangling bonds. As is well-known, the existence of these dangling bonds generates electronic states localized at the surface, with energies usually in the gap of the semiconductor.[235,236] These states can have energies close the conduction and valence band edges, and can include an artificial modification of the conduction and valence band states.[237–239] Therefore, they should be eliminated. In the literature, there are two ways to passivate the surface dangling bonds of the nanostructure:

1. embed the structure inside an *artificial ligand* material. This artificial material has the same structure as the nanomaterial except a larger band gap. This way of saturating the surface dangling bonds of the nanostructure has been successfully adopted previously for the study of the electronic and optical properties of wurtzite CdSe QDs.[235,240]

2. passivate the surface dangling bonds with pseudo-hydrogen atom, displacing the energies of the surface states far from the band gap.[241–243]

In our calculations, we prefer the first way. The pseudopotentials of the artificial material are generated in the same way as the nanomaterial. Once all the empirical pseudopotentials of the nanomaterial and the artificial material are obtained, the crystal potential can be calculated according to Eq. (9.21).

9.4 Solve pseudopotential Schrödinger equation

Now, with the crystal potential $V(\mathbf{r})$ specified, the next task is to solve the pseudopotential Schrödinger equation,

$$\{-\frac{\hbar^2}{2m_0}\nabla^2 + V(\mathbf{r})\}\psi(\mathbf{r}) = E\psi(\mathbf{r}). \tag{9.29}$$

Essentially, there are two ways of solving the equations: (i) direct diagonalization method, (ii) folding spectrum method (FSM). In the following two subsections, these two methods will be discussed.

9.4.1 Direct diagonalization method

We expand the unknown wave function $\psi(\mathbf{r})$ by using the plane wave basis set according to the expression (9.1). Substituting $\psi(\mathbf{r})$ with (9.1) and then multiplying both sides $\exp[-i(\mathbf{k}+\mathbf{G}^{'})\cdot\mathbf{r}]$, one can obtain the following equation by making an integration over the crystal,

$$\sum_{\mathbf{G}}\{[(\mathbf{k}+\mathbf{G})^2 - E_n(\mathbf{k})]\delta_{\mathbf{G}\mathbf{G}'} + V(\mathbf{G}^{'}-\mathbf{G})\}c_n(\mathbf{k},\mathbf{G}) = 0, \tag{9.30}$$

where

$$V(\mathbf{G}^{'}-\mathbf{G}) = \frac{1}{N\Omega_c}\int d\mathbf{r}\exp[-(\mathbf{G}^{'}-\mathbf{G})\cdot\mathbf{r}]V(\mathbf{r}), \tag{9.31}$$

is the Fourier coefficient of $V(\mathbf{r})$.

The expression specified in Eq. (9.30) is zero when each term in the sum is identically zero, which implies the following equation,

$$[(\mathbf{k}+\mathbf{G})^2 - E_n(\mathbf{k})]\delta_{\mathbf{G}\mathbf{G}'} + V(\mathbf{G}^{'}-\mathbf{G}) = 0. \tag{9.32}$$

The eigenvalue problem can be written in a familiar form $\mathbf{H}\psi = E\psi$, where $\mathbf{H}$ is a matrix, ψ is a column vector representing the coefficient $c_n(\mathbf{k},\mathbf{G})$, and E is the eigenvalues corresponding to the matrix H. The diagonal matrix elements of matrix $\mathbf{H}$ is $(\mathbf{k}+\mathbf{G})^2$ for $\mathbf{G} = \mathbf{G}^{'}$, while the off diagonal matrix elements are $V(\mathbf{G}^{'}-\mathbf{G})$ for $\mathbf{G} \neq \mathbf{G}^{'}$. The solution to the energy eigenvalues and corresponding eigenvectors can be found by diagonalizing the matrix $\mathbf{H}$, thus giving the name of the method *direct diagonalization method*. In this method, the number of reciprocal lattice vectors $\mathbf{G}$ or $\mathbf{G}^{'}$ employed determines both the matrix size and the accuracy of the results.

9.4.2 Folding spectrum method

In most of the modern electronic structure calculations, people generally solve the effective single-particle Schrödinger equation, $\hat{H}\psi_i = \varepsilon_i\psi_i$, for all the occupied wave functions ($\{\psi_i\}$) and corresponding eigenenergies ($\{\varepsilon_i\}$). This is indeed necessary for the case that for a given problem, the potential $V(\mathbf{r})$ and the atomic positions are not known in advanced and they have to be obtained from the solution of all the occupied states. To achieve this purpose, the conventional variational method is employed, which is to minimize $\langle\psi|\hat{H}|\psi\rangle/\langle\psi|\psi\rangle$ by varying the coefficients of the basis functions, to obtained the lowest eigenenergy and corresponding eigenfunction. To find a higher energy state, one needs to orthogonalize this state to all the energy states below it. The computational efforts required by the above mentioned way scale as approximately N^3 where N is the number of atoms in the system. This way can not be applied for the system containing more than 1000 atoms, depending on the available computational power and level of approximations.

If one's aim is to find very limited states on either side of the gap which determines most of the properties related to excitations, the above mentioned way appears to be very insufficient. In 1994, Wang and Zunger[244] proposed a way of solving the effective single-particle Schrödinger equation around a desired energy, that is, folding spectrum method (FSM). The central idea of the this method is that the eigenfunctions $\{\psi_i\}$ and eigenenergies $\{\varepsilon_i\}$ of the Schrödinger equation, $\hat{H}\psi_i = \varepsilon_i\psi_i$, also satisfy,

$$(\hat{H} - \varepsilon_{ref})^2\psi_i = (\varepsilon_i - \varepsilon_{ref})^2\psi_i. \tag{9.33}$$

The lowest solution of Eq. (9.33) is the eigenstate with ε_i closest to ε_{ref}. By putting the ε_{ref} in the physically interesting range, one transforms an arbitrarily highest eigensolution to the lowest one, obviating the need for orthogonalization.[244] For example, if one places ε_{ref} in the energy band gap of a semiconductor nanostructure, the minimization of $\langle\psi|(\hat{H} - \varepsilon_{ref})^2|\psi\rangle/\langle\psi|\psi\rangle$ results either the highest molecular orbital (HOMO) state or the lowest molecular orbital (LUMO) state, depending on which is closer to ε_{ref}. This method was initially applied for silicon QDs, giving very satisfactory precision of the results.[244] However, the computational efforts involved scale only ***linearly*** with the system's size, thus enabling calculations of band gap properties in mesoscopic systems. For example,[244] for $Si_{1315}H_{460}$ QDs, the actual CPU time consumed for the calculation of the band gap by employing the conventional method (e.g., solving Schrödinger equation, $\hat{H}\psi_i = \varepsilon_i\psi_i$) is approximately two weeks. However, it is only one CPU hour if the FSM is employed.

In our calculations, we generally solve the effective single-particle Schrödinger equation by using the direct diagonalization method for the bulk material since in this case, there are only few atoms in the unit cell and only very limited occupied states have to be

calculated. For example, for wurtzite ZnO, there are only four atoms per unit cell and eight occupied states have to be calculated. By successfully diagonalizing the matrix **H**, we can obtain the locations of the conduction band minimum (CBM) and the valance band maximum (VBM). By choosing the reference energy ε_{ref} close to the VBM (CBM) of the bulk material, we employ the FSM for calculating the target single-particle hole (electron) states at the vicinity of the HOMO (LUMO) state for the corresponding nanostructures. After obtaining the desired single-particle electron and hole states, we are at a position of solving the many-body problem. It should be noted that we assume that the obtained single-particle eigenfunctions and eigenvalues by solving the pseudopotential Schrödinger equation are already fully correlated. Therefore, we do not attempt to solve the many-body problem for the ground-state. A detailed explanation of this assumption can be found in Ref. 222.

9.5 Many-body problem

9.5.1 Configuration interaction

In our calculations, we are mainly interested on the excitonic properties of the nanostructured materials. Once the single-particle electron and hole states are obtained, the excitonic effects are taken into account by employing the configuration interaction (CI) approach. This approach generally appears in *quantum chemistry* to obtain the correlation energy E_{corr} which is defined as,

$$E_{corr} = \varepsilon_0 - E_0, \tag{9.34}$$

where ε_0 is the exact nonrelativistic energy of the system under consideration and E_0 is the Hartree-Fock (HF) energy (E_0) in the limit that the basis set approaches completeness. Since the HF energy is an upper bound to the exact energy, the correlation energy is negative. The CI approach in *quantum chemistry* started from the solution of the Hartree-Fock-Roothaan equation (suppose that the system under consideration has even number of electrons and is adequately represented by a closed-shell restricted HF equation), where one can obtain a set of spin-orbitals. However, in our calculations, we do not start from the HF ground-state, but from the solution of the single-particle pseudopotential Schrödinger equation, where we obtain a set of correlated single-particle electron and hole wave functions and energy levels. It has been justified[245] that the Brillouin's Theorem

which states that the singly-excited determinants $|\Psi_S\rangle$ will not interact with a reference HF determinant $|\Psi_0\rangle$, i.e., $\langle\Psi_S|\Psi_0\rangle = 0$, is still valid.

A set of single-substitution Slater determinant $|\Phi_{v_a}^{c_r}\rangle$ (e.g., singlet excitation) can be constructed from the reference ground state $|\Phi_0\rangle$ by promoting one electron from the valence state ψ_{v_a} with energy ε_{v_a} to the conduction state ψ_{c_r} with energy ε_{c_r}, that is,

$$\begin{aligned}\Phi_0(\mathbf{r}_1,\sigma_1,....,\mathbf{r}_N,\sigma_N) &= \mathcal{A}[\psi_1(\mathbf{r}_1,\sigma_1),...,\psi_{v_a}(\mathbf{r}_{v_a},\sigma_{v_a}),...,\psi_N(\mathbf{r}_N,\sigma_N)],\\ \Phi_{v_a}^{c_r}(\mathbf{r}_1,\sigma_1,....,\mathbf{r}_N,\sigma_N) &= \mathcal{A}[\psi_1(\mathbf{r}_1,\sigma_1),...,\psi_{c_r}(\mathbf{r}_{v_a},\sigma_{v_a}),...,\psi_N(\mathbf{r}_N,\sigma_N)]\end{aligned} \tag{9.35}$$

where N is the number of electrons in the system, $\sigma =\uparrow$ or $\downarrow$ is the spin variable, and $\mathcal{A}$ is the anti-symmetrizing operator. The exciton wave functions Ψ^{α} can be expanded in terms of this determinantal basis set,

$$\Psi^{(\alpha)} = \sum_{v_a=1}^{N_v}\sum_{c_r=1}^{N_c} C_{v_a,c_r}^{(\alpha)}\Phi_{v_a}^{c_r}, \tag{9.36}$$

where N_v and N_c represents the number of hole and electron states included in the expansion of the exciton wave functions, respectively. The hole states are numbered from 1 to N_v in order of *decreasing* energy starting from the highest occupied molecular orbital (HOMO) state, while the electron states are numbered from 1 to N_c with *increasing* energy starting from the lowest unoccupied molecular orbital (LUMO) state. It should be noted here that we are only interested on the single-exciton state, that is, one electron in the conduction band and one hole in the valence band. The doublet excitation, which means promoting two electrons at valence band states ψ_{v_a} and ψ_{v_b} from the reference ground state to the conduction band state ψ_{c_r} and ψ_{c_s}, and higher order excitations (e.g., triplet, quadruplet , ...) are neglected in the expansion (9.36) which can be justified by the fact that the doublet and even higher-order excitations are energetically remote from the ground-state. Since limited number of electron and hole states (e.g., N_v and N_c) are chosen in the expansion of the exciton wave functions, the quality of the basis set $\Phi_{v_a}^{c_r}$ should be checked by comparing the results of the calculations using progressively larger basis sets (e.g., increasing the number of electron and hole states in the expansion).

Once the exciton wave functions are constructed, the following task is to solve the many-body Schrödinger equation, $\hat{H}\Psi = \varepsilon\Psi$. The matrix elements of the many-body Hamiltonian $\hat{H}$ in the basis $\{\Phi_{v_a}^{c_r}\}$ can be written as

$$\hat{\mathbf{H}}_{v_a c_r, v_b c_s} = \langle\Phi_{v_a}^{c_r}|\hat{\mathbf{H}}|\Phi_{v_b}^{c_s}\rangle = (\varepsilon_{c_r} - \varepsilon_{v_a})\delta_{v_a v_b}\delta_{c_r c_s} - J_{v_a c_r, v_b c_s} + K_{v_a c_r, v_b c_s}, \tag{9.37}$$

where J and K are the Coulomb and exchange integrals, respectively, which are given as

following,

$$J_{v_a c_r, v_b c_s} = e^2 \sum_{\sigma_1,\sigma_2} \int\int \frac{\psi^*_{v_b}(\mathbf{r}_1,\sigma_1)\psi^*_{c_r}(\mathbf{r}_2,\sigma_2)\psi_{v_a}(\mathbf{r}_1,\sigma_1)\psi_{c_s}(\mathbf{r}_2,\sigma_2)}{\bar{\varepsilon}|\mathbf{r}_1-\mathbf{r}_2|} d\mathbf{r_1} d\mathbf{r_2},$$
$$K_{v_a c_r, v_b c_s} = e^2 \sum_{\sigma_1,\sigma_2} \int\int \frac{\psi^*_{v_b}(\mathbf{r}_1,\sigma_1)\psi^*_{c_r}(\mathbf{r}_2,\sigma_2)\psi_{c_s}(\mathbf{r}_1,\sigma_1)\psi_{v_a}(\mathbf{r}_2,\sigma_2)}{\bar{\varepsilon}|\mathbf{r}_1-\mathbf{r}_2|} d\mathbf{r_1} d\mathbf{r_2}. \quad (9.38)$$

In the above expressions, $\bar{\varepsilon}$ represents the *microscopic*, position-dependent dielectric constant. The excitonic states of the system under consideration can be obtained by solving the following secular equation,

$$\sum_{v_b=1}^{N_v} \sum_{c_s=1}^{N_c} \hat{\mathbf{H}}_{v_a c_r, v_b c_s} C^{(\alpha)}_{v_b, c_s} = E^{(\alpha)} C^{(\alpha)}_{v_{va} c_r}. \quad (9.39)$$

9.5.2 Screening function

It has been well understood that[246,247] (i) when the size of nanostructure is reduced, the dielectric constant decreases considerably, enhancing significantly the electron-hole Coulomb interaction, (ii) the electron-hole exchange interaction in quantum confinement systems consists of a short-range component and a long-range component. Consequently, the screening of the long range electron-hole exchange interaction has a sizable effect on the extent of the electron-hole exchange splitting in a quantum confinement system. In order to take all these facts into account, we have chosen a position dependent dielectric constant to screen the Coulomb and exchange interactions in the nanostructures under consideration. In equations (9.38), the Coulomb potential can be written as,

$$g(\mathbf{r}_1,\mathbf{r}_2) = \frac{e^2}{\varepsilon(\mathbf{r}_1,\mathbf{r}_2)|\mathbf{r}_1-\mathbf{r}_2|} = e^2 \int \varepsilon^{-1}(\mathbf{r}_1,\mathbf{r}_2)|\mathbf{r}_1-\mathbf{r}_2|^{-1} d\mathbf{r}_1, \quad (9.40)$$

where $\varepsilon^{-1}(\mathbf{r}_1,\mathbf{r}_2)$ is the inverse of the dielectric function. If we assume that $\varepsilon^{-1}(\mathbf{r}_1,\mathbf{r}_2) \approx \varepsilon^{-1}(\mathbf{r}_1-\mathbf{r}_2)$, the Fourier transform of the screened Coulomb potential is given by,

$$g(\mathbf{k}) = \varepsilon^{-1}(\mathbf{k}) \frac{4\pi e^2}{k^2}, \quad (9.41)$$

where $\varepsilon^{-1}(\mathbf{k})$ is the Fourier transform of $\varepsilon^{-1}(\mathbf{r}_1-\mathbf{r}_2)$. We have chosen that $\varepsilon^{-1} = \varepsilon^{-1}_{el} + \varepsilon^{-1}_{ion}$, which consists of an electronic (high frequency) contribution ε^{-1}_{el} and an ionic (low-frequency) contribution ε^{-1}_{ion}, which are approximated here by the Thomas-Fermi model proposed by Resta[248] and by the polaronic model of Haken, respectively. ε^{-1}_{el} and ε^{-1}_{ion} are

diagonal and isotropic in reciprocal space, and they can have the following analytic form,

$$\varepsilon_{el}^{-1}(k) = \frac{k^2 + q^2 \sin(k\rho_\infty)/(\varepsilon_\infty^S k\rho_\infty)}{k^2 + q^2},$$
$$\varepsilon_{ion}^{-1} = (\frac{1}{\varepsilon_0^S} - \frac{1}{\varepsilon_\infty^S})(\frac{1/2}{1+\rho_h^2 k^2} + \frac{1/2}{1+\rho_e^2 k^2}), \tag{9.42}$$

where $q = 2\pi^{-1/2}(3\pi^2 n_0)^{1/3}$ is the Thomas-Fermi wave vector in which n_0 is the electron density, and ρ_∞ is the solution of the equation $\sinh(q\rho_\infty)/(q\rho_\infty) = \varepsilon_\infty^S$, $\rho_{h,e} = (\hbar/2m_{h,e}^*\omega_{LO})^{1/2}$, where $m_{h,e}^*$ represents the hole (h) and electron (e) effective masses, and ω_{LO} is the frequency of the bulk LO photon mode. ε_0^S and ε_∞^S are the macroscopic high-frequency and low-frequency dielectric constants of the system under consideration (e.g., S), respectively.

9.5.3 Absorption spectra

After obtaining the the exciton states by solving equation (9.37), we are interested on the absorption spectra of the nanostructure. The oscillator strength for the absorption from initial state ($|\Psi^{(i)}\rangle$) to the final state ($|\Psi^{(f)}\rangle$) can be given by,[222]

$$\alpha(\omega, T) \propto \sum_{i,f} |M_{if}|^2 P_i(T)\delta(\omega - \omega_{if}), \tag{9.43}$$

where

$$M_{if} = \langle \Psi^{(f)} | \hat{\mathbf{e}} \cdot \mathbf{p} | \Psi^{(i)} \rangle, \tag{9.44}$$

is the optical transition dipole matrix element with the momentum operator $\mathbf{p}$ and the polarization vector of the electromagnetic field $\hat{\mathbf{e}}$,

$$P_i(T) = N \exp\{-[E^{(i)} - E^{(0)}]/k_B T\} \tag{9.45}$$

is the occupation probability of the initial state $|\Psi^{(i)}\rangle$ at temperature T and N is the normalization constant, and the delta function $\delta(\omega - \omega_{if})$ can be replaced by the a Gaussian to take into account the size distribution or by a Lorentzian to account for the intrinsic sources of broadening.

In the following few chapters of the Thesis, we will employ the theory decried herein for the study of the electronic and excitonic properties of the realistic nanostructures, including ZnO colloidal quantum dots, ZnO nanowires and ZnS colloidal quantum dots.

10

Electronic and optical properties of ZnO quantum dots under hydrostatic pressure

*In this chapter, we study the electronic and optical properties of ZnO quantum dots subjected to applied hydrostatic pressure. The optical band gap, Stokes shift and optical emission polarization are investigated as a function of the applied pressure. It is found that the applied pressure causes a linear increase in the optical band gap. The pressure coefficient appears to be highly size-dependent, exhibiting a monotonic increase with increasing dot size. In contrast to this monotonic behaviour, the applied pressure induces a nonmonotonic Stokes shift which presents a minimum value at a critical pressure. The results presented herein are published in Physical Review B **87**, 125302 (2013).*

Contents

10.1 Introduction

Nanostructures and heterostructures made of zinc oxide (ZnO), such as nanowalls,[249] nanotubes,[250] nanorods[251] and quantum dots (QDs),[113,252] have already been used as transparent conductors in solar cells, as components in high-power electronics, UV light emitters, and gas and chemical sensors (see Ref. 253 and references therein). Possible applications of ZnO nanostructures in optoelectronic and spintronic devices, such as laser diodes with polarized output, spin-based memory and logic, have also attracted great attention.[107,137] As an important member of the nanostructure family, zero-dimensional ZnO QDs have become the subject of recent developments. Experimental fabrication of this type of nanostructures has been achieved by using different chemical synthesis methods, such as sol-gel,[139] thermolysis[254] and polyol methods,[113] to mention only a few. From a theoretical point of view, due to the specifics of the wurtzite ZnO material, such as the anisotropy of the valence band, as well as the small dielectric constant and correspondingly strong electron-hole Coulomb interaction, simple one-band effective-mass models fail to deliver predictive results. To have a good interpretation of experimental measurements and optimization of ZnO QDs for possible device applications, an accurate theoretical method able to predict the transition energy and the oscillator strength of optical transitions is required. Accurate atomistic empirical pseudopotential calculations have shown to describe exciton states in CdSe[255] QDs, and very recently in ZnO QDs[145] very well.

On the other hand, high pressure investigations of semiconductor nanostructures such as nanocrystals or QDs have emerged as a focus area in condensed mater physics and material science because of their large impact on the tunable optical properties that may be advantageous for application in optoelectronics, QD lasers, high-density memory, bioengineering, etc.[256–259] Most of the existing theoretical work concerning the hydrostatic pressure effect focused on QDs with zinc-blende structure, such as self-assembled InAs/GaAs[260] or InGaAs/GaAs[261] QDs. Theoretical work associated with the pressure effect in wurtzite ZnO colloidal QDs is very limited.[262] Here, we study the electronic and optical properties of ZnO QDs under externally applied hydrostatic pressure. The single particle orbitals and energies are calculated by the atomistic empirical pseudopotential method using recently derived pseudopotentials,[145] considering the effects of multiband coupling, multivalley coupling, spin-orbit interaction, while the excitonic effects are taken into account by using the configuration interaction approach.[263] The present numerical results cover a variety of optical properties of ZnO QDs under pressure, such as optical band gap, pressure coefficient, Stokes Shift and the optical emission polarization.

10.2 Computational details

10.2.1 Crystal structure of bulk ZnO

ZnO is mostly stablized with hexagonal wurtzite structure with lattice parameters $a = 3.249$ Å, $c = 5.205$ Å, and internal parameter $u = 0.382$. There are four atoms (e.g., two Zn atoms and two O atoms) per unit cell which is shown in Fig. 10.1, where the lattice vectors are given in Table 10.1, the atom positions in Cartesian and fractional coordinates are given in Tables 10.2 and 10.3, respectively.

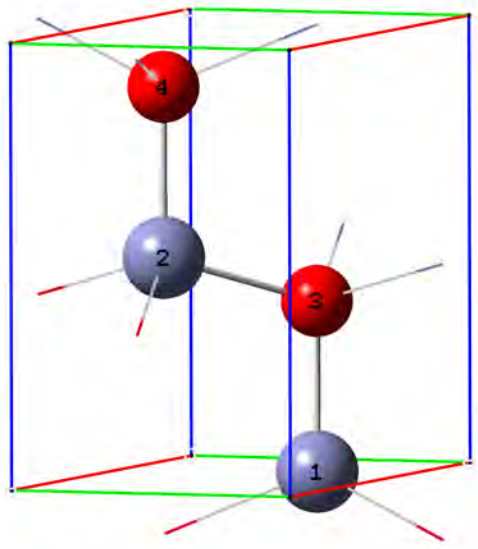

Figure 10.1: Unit cell of wurtzite ZnO. Gray balls represent Zn atoms and red balls represent the O atoms, respectively.

For ideal wurtzite structure, $\frac{c}{a} = 1.6333$ and $u = 0.375$. However, these two parameters for ZnO are $\frac{c}{a} = 1.6019$ and $u = 0.382$ which significantly deviate from the ideal values. These are strongly relevant to the crystal field splitting which appears in the wurtzite structures, which is proportional to the deviation of these two parameters (e.g., $\frac{c}{a}$ and u) from the ideal values. In wurtzite ZnO, there are two types of bond length: one is

Table 10.1: Unit vectors $\mathbf{a}_1$, $\mathbf{a}_2$ and $\mathbf{a}_3$ in wurtzite structure. a and c are the lattice parameters.

	$\hat{\mathbf{x}}$	$\hat{\mathbf{y}}$	$\hat{\mathbf{z}}$
$\mathbf{a}_1$	$\frac{1}{2}a$	$-\frac{\sqrt{3}}{2}a$	0
$\mathbf{a}_2$	$\frac{1}{2}a$	$\frac{\sqrt{3}}{2}a$	0
$\mathbf{a}_3$	0	0	c

Table 10.2: Atom positions in the unit cell in Cartesian coordinates. a, c, u are the structure parameters.

Atom	$\hat{\mathbf{x}}$	$\hat{\mathbf{y}}$	$\hat{\mathbf{z}}$
Zn_1	$\frac{1}{2}a$	$\frac{1}{2\sqrt{3}}a$	0
Zn_2	$\frac{1}{2}a$	$-\frac{1}{2\sqrt{3}}a$	$\frac{1}{2}c$
O_1	$\frac{1}{2}a$	$\frac{1}{2\sqrt{3}}a$	u c
O_2	$\frac{1}{2}a$	$-\frac{1}{2\sqrt{3}}a$	$(\frac{1}{2}+u)c$

$R^{(1)} = uc = 1.988$ Å and the other one $R^{(2)} = \frac{\sqrt{3c^2(1-2u)^2+4a^2}}{2\sqrt{3}} = 1.974$ Å, and two types of angles θ' and θ with

$$\theta' = \arccos\left(\frac{-\sqrt{3}c(1-2u)}{\sqrt{3c^2(1-2u)^2+4a^2}}\right) = 108.13^\circ, \tag{10.1}$$

and

$$\theta = \arccos\left(\frac{3c^2(1-2u)^2-2a^2}{3c^2(1-2u)^2+4a^2}\right) = 110.78^\circ, \tag{10.2}$$

respectively.

Table 10.3: The same as in Table 10.2 but in fractional coordinates.

Atom	$\mathbf{a}_1$	$\mathbf{a}_2$	$\mathbf{a}_3$
Zn_1	1/3	2/3	0
Zn_2	2/3	1/3	$\frac{1}{2}$
O_1	1/3	2/3	u
O_2	2/3	1/3	$\frac{1}{2}+u$

Table 10.4: The pseudopotential parameters a_1, a_2, a_3 and a_4 and spin-orbit interaction parameter λ for Zn and O, which are taken from Ref. 145.

	λ	a_1	a_2	a_3	a_4
Zn	0.00533	-8.561564	0.0062352	-0.001589	0.5521333
O	0.0	-28.419299	4.2557852	-0.0100096	0.95926425

10.2.2 Generate empirical pseudopotentials for ZnO

After knowing the crystal structure of wurtzite ZnO, the following task is to generate reliable empirical pseudopotentials for ZnO. This has been done by Baskoutas and Bester[145] in 2010. Exponential form of the pseudopotential(s), as detailed in (9.25), has been chosen, which has four free parameter a_1, a_2, a_3, and a_4 for each atom type (e.g., Zn and O). These parameters and the spin-orbit interaction parameter λ_α (α = Zn or O) are fitted to reproduce the well-known experimental or theoretical bulk properties, including the energy gap at specific high symmetry points of the Brillouin zone, the effective masses of different bands, the crystal splitting and spin-orbit splitting values. The optimized parameters are given in Table 10.4, which leads to a very good agreement between the calculated results and the existing experimental (or theoretical) results (see Table 10.5). The volume normalized local parts of the Zn and O empirical pseudopotentials are shown in Fig. 10.2.

It has been well proved that in order to accurately capture the pressure effects on the electronic and optical properties of QDs, it is necessary to have empirical pseudopotentials that are explicitly dependent on the strain.[261] We follow the same strategy as Williamson et al,[264] designing the pseudopotentials to further include the stain dependence:

$$v_\alpha(r;\tilde{\varepsilon}) = v_\alpha(r)[1 - \gamma_\alpha \mathbf{Tr}(\tilde{\varepsilon})], \tag{10.3}$$

where α = Zn or O, γ is a fitting parameter to reproduce the pressure coefficient of the bulk material, and $\mathbf{Tr}(\tilde{\varepsilon})$ is the strain tensor, which is calculated through the following equation,

$$V_0/V = [1 + \mathbf{Tr}(\tilde{\varepsilon})]^{-1}, \tag{10.4}$$

where V_0 is the volume of the dot (or unit cell (for bulk material)) at zero pressure, and V is the corresponding volume under pressure. In our calculations, we have chosen $\gamma_O = 0$ and $\gamma_{Zn} = 0.304$, giving a pressure coefficient for bulk ZnO equal to 24.7 meV/GPa, which reproduces exactly the experimental value of 24.7 ± 0.1 meV/GPa.[265] The calculated conduction band minimum (CBM) and the top most three valence band states of bulk

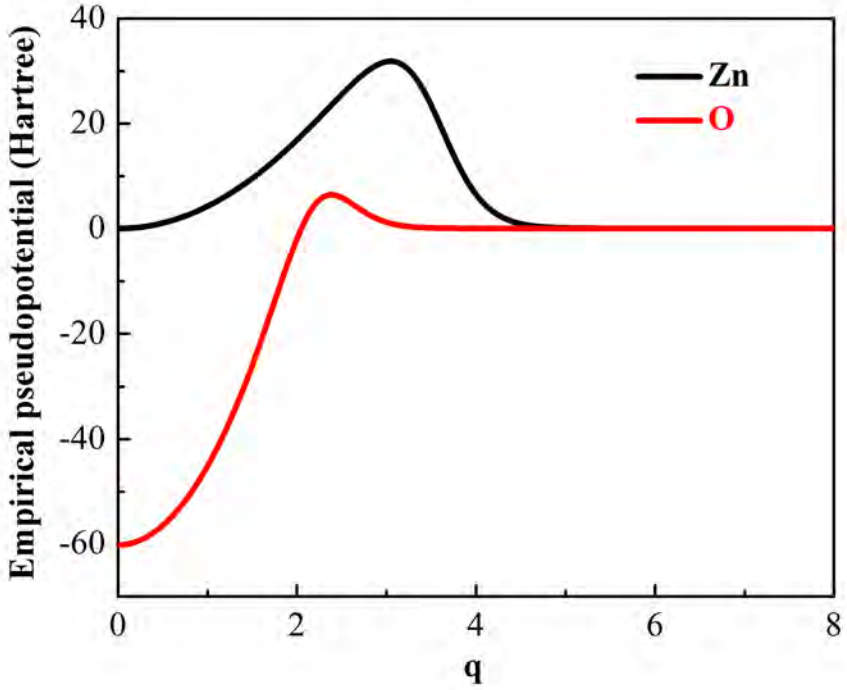

Figure 10.2: Volume normalized local parts of the Zn and O empirical pseudopotentials.

ZnO as a function of the applied pressure are shown in Fig. 10.3. It is found that the energy level of CBM increases with increasing the applied pressure, giving a conduction band deformation potential $a_c = -2.26$ eV. In contrast, all the energy levels of the topmost three valence band states exhibit a decreasing function of the applied pressure. The valence band deformation potential $a_v = 2.27$ eV and the effective deformation potential

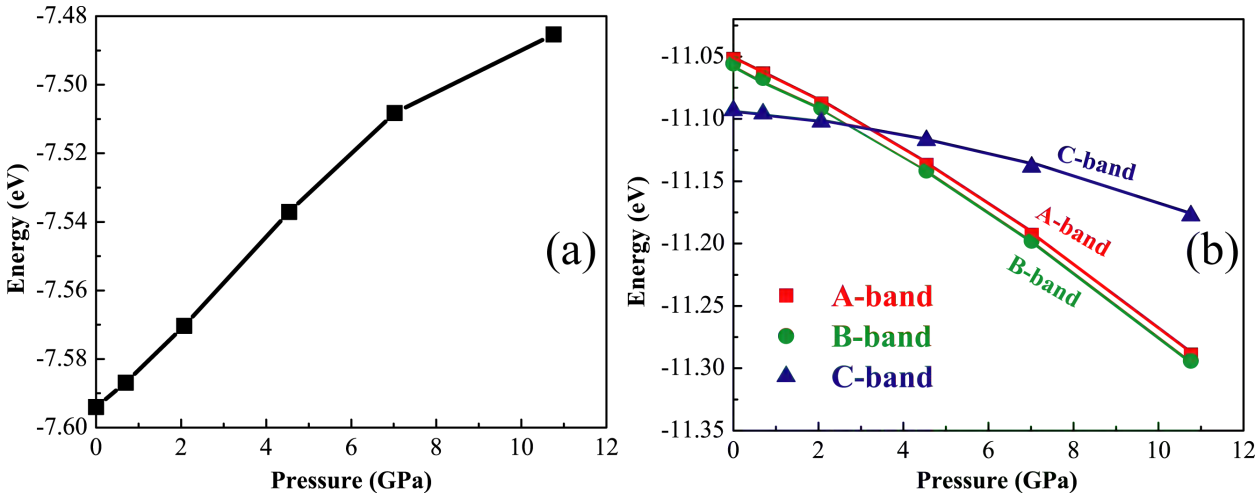

Figure 10.3: The conduction band minimum (a) and the top most three valence band states (b) of bulk ZnO as a function of the applied pressure.

Table 10.5: Compiled reference bulk properties and results calculated from empirical pseudopotential method by using the parameters listed in Table 10.4. The results are taken from Ref. 145.

Properties	Experiments	Theory	EPM
$\varepsilon(\Gamma_{7v}-\Gamma_{3v})$	5.0	3.8, 5.517, 8.92, 5.0	3.454
$\varepsilon(\Gamma_{1c}-\Gamma_{7v})$	3.4449, 3.435, 3.4376	3.44,3.458	3.458
$\varepsilon(\Gamma_{3c}-\Gamma_{1c})$		3.366, 4.394	3.032
$\varepsilon(\Gamma_{6c}-\Gamma_{1c})$		13.21, 7.303, 7.320, 7.3897	8.590
$\varepsilon(H_{3c}-\Gamma_{1c})$		6.44, 5.0, 7.105	4.655
$\varepsilon(K_{2c}-\Gamma_{1c})$		7.25, 6.75, 5.99, 6.831	5.361
$\varepsilon(M_{1c}-\Gamma_{1c})$		5.03, 5.11, 5.017	3.502
$m_e^{\perp}$	0.265	0.177, 0.21, 0.130, 0.211	0.213
$m_e^{\parallel}$	0.265	0.21, 0.137, 0.225	0.239
$m_A^{\perp}$	0.59	0.351, 4.31, 2.5899	0.712
$m_A^{\parallel}$	0.59	1.98, 3.06, 1.091	2.120
$m_B^{\perp}$	0.59	0.30, 0.55, 0.227, 0.5813	0.515
$m_B^{\parallel}$	0.59	2.979, 3.227, 4.330, 3.06, 0.8454	0.572
$m_C^{\perp}$	0.55	0.288, 0.537, 1.12, 0.1769	1.075
$m_C^{\parallel}$	0.31	0.169, 0.330, 0.26, 0.27, 0.2071	0.250
Δ_{so}	-0.0035, -0.0047	-0.0035	-0.0035
Δ_{cr}	0.0404, 0.0408	0.0391, 0.0392	0.040

$a_g = a_c - a_v = -4.53$ eV, which is in very good agreement with the experimental values ~ -3.51 to -3.81 eV, and -3.5 ± 0.4 eV by using different experimental methods.[266,267]

We further find from Fig. 10.3(b) that the bulk A-band and B-band exhibit a stronger dependence on the pressure than the C-band. This indicates that the A-band and B-band of bulk ZnO have larger deformation potentials than the C-band. Consequently, for pressure larger than a critical value (≈ 3.45 GPa), C-band rises above the A-band and B-band and becomes the valence band maximum (VBM). Similar behaviour has been found by Schleife et al[268] in wurtzite ZnO under bilateral strain. The change in the valence band ordering will have strong influence on the nature of the near-band-edge exciton and the optical polarizations in ZnO QDs, which we shall discuss later.

10.2.3 Geometry optimization

The ZnO QDs studied herein are cut from the bulk material and characterized by diameter D. The surface passivation is approximated by a high band gap artificial material, as

practiced successfully previously.[145,240,269] The pressure is created by equally compressing the lattice constants in both the in-plane direction and out-of-band direction. The pressure values are obtained approximately by using the Murnaghan equation of states,[261,264]

$$P = (B/B^{'})[(\frac{V_0}{V})^{B'} - 1], \tag{10.5}$$

where P is the pressure value, V_0 and V have the same meanings as in equation (10.4). B and $B^{'}$ are the bulk modulus and its pressure derivative, respectively. Here, we have used B = 142.4 GPa and $B^{'} = 3.6$ [Ref. 265]. The atom positions of the QD structure is then relaxed to the minimum strain energy by using Keating's valence force field (VFF) for wurtzite materials.[270]

According to the generalized Keating's VFF model, the elastic energy per atom in wurtzite material reads,[270]

$$U_i = \frac{3\alpha}{16r_0^2}\sum_{j=1}^{3}(\mathbf{r}_{ij}^2 - r_0^2)^2 + \frac{3\alpha^{'}}{16r_0^{'2}}(\mathbf{r}_{i4}^2 - r_0^{'2})^2$$
$$+\frac{3\beta}{8r_0^2}\sum_{j=1}^{3}\sum_{k>j}^{3}(\mathbf{r}_{ij}\cdot\mathbf{r}_{ik} - r_0^2\cos\theta_0)^2 + \frac{3\beta^{'}}{8r_0r_0^{'}}\sum_{k=1}^{3}(\mathbf{r}_{i4}\cdot\mathbf{r}_{ik} - r_0r_0^{'}\cos\theta_0^{'})^2, \tag{10.6}$$

where α and $\alpha^{'}$ are the two bonding stretching constants, and β and $\beta^{'}$ are the two bond bending constants, respectively,

$$r_0^{'} = cu, \tag{10.7}$$

$$r_0 = \frac{\sqrt{3c^2\nu^2 + 4a^2}}{2\sqrt{3}}, \tag{10.8}$$

$$\cos\theta_0^{'} = \frac{-\sqrt{3}c\nu}{\sqrt{3c^2\nu^2 + 4a^2}}, \tag{10.9}$$

$$\cos\theta_0 = \frac{3c^2\nu^2 - 2a^2}{3c^2\nu^2 + 4a^2}, \tag{10.10}$$

where $\nu = 1 - 2u$, a, c, u are the structure parameters of wurtzite materials and the corresponding values for wurtzite ZnO are given in subsection (10.2.1). The free parameters α, $\alpha^{'}$, β and $\beta^{'}$ are optimized to reproduce the well-known macroscopic elastic constants c_{ij} of bulk ZnO. To this end, we build the following function,

$$f(\alpha,\alpha^{'},\beta,\beta^{'}) = (c_{11} - c_{11}^{tag})^2 + (c_{33} - c_{33}^{tag})^2 + (c_{12} - c_{12}^{tag})^2$$
$$+(c_{13} - c_{13}^{tag})^2 + (c_{44} - c_{44}^{tag})^2 + (c_{66} - c_{66}^{tag})^2, \tag{10.11}$$

where c^{tag} are the well known elastic constants for bulk ZnO, and

$$c_{11} = \frac{a^2}{2\sqrt{3}c}\frac{(4A^2+13AB+B^2)(8A^{'}u^2+3B^{'}w^2)+162AB(A+B)\nu^2}{(2A+B)[8A^{'}u^2+6(A+2B)\nu^2+3B^{'}w^2]}, \tag{10.12}$$

$$c_{33} = \frac{3\sqrt{3}c^3}{4a^2}\frac{(A+2B)(8A^{'}u^2\nu^2+3B^{'}\nu^4)+16A^{'}B^{'}u^4}{8A^{'}u^2+6(A+2B)\nu^2+3B^{'}w^2}, \tag{10.13}$$

$$c_{12} = \frac{a^2}{2\sqrt{3}c}\frac{(A-B)[(4A-B)(8A^{'}u^2+3B^{'}w^2+54AB\nu^2)]}{(2A+B)[8A^{'}u^2+6(A+2B)\nu^2+3B^{'}w^2]}, \tag{10.14}$$

$$c_{13} = \frac{\sqrt{3}c}{2}\frac{(A-B)(8A^{'}u^2+3B^{'}\nu w)\nu}{8A^{'}u^2+6(A+2B)\nu^2+3B^{'}w^2}, \tag{10.15}$$

$$c_{44} = \frac{\sqrt{3}c}{4}\frac{(2A+B)B^{'}}{(2A+B+B^{'})}, \tag{10.16}$$

$$c_{66} = \frac{c_{11}-c_{12}}{2}, \tag{10.17}$$

where $A = \alpha/r_0^2$, $A^{'} = \alpha^{'}/r_0^{'2}$, $B = \beta/r_0^2$, $B^{'} = \beta^{'}/(r_0 r_0^{'})$, and $w = 1-4u$. In order to obtain the optimized values for α, $\alpha^{'}$, β and $\beta^{'}$, we use the standard conjugate gradient method to minimize the function (10.11). The optimized values are $\alpha = 59.15$ N/m, $\alpha^{'} = 80.23$ N/m, $\beta = 6.88$ N/m and $\beta^{'} = 7.63$ N/m, respectively. The resultant elastic constants c_{ij} and bulk modulus (B) are $c_{11} = 209.7$ GPa, $c_{33} = 211.4$ GPa, $c_{12} = 121.8$ GPa, $c_{13} = 103.8$ GPa, $c_{44} = 41.32$ GPa, $c_{66} = 43.9$ GPa and B = 143.1 GPa, reproducing almost exactly the experimental target values:[265,271] $c_{11}^{tag} = 209.7$ GPa, $c_{33}^{tag} = 210.9$ GPa, $c_{12}^{tag} = 121.1$ GPa, $c_{13}^{tag} = 105.1$ GPa, $c_{44}^{tag} = 42.47$ GPa, $c_{66}^{tag} = 44.3$ GPa and $B^{tag} = 142.4$ GPa. It should be noted that the bulk modulus B is calculated through the following equation,

$$B = \frac{c_{33}(c_{11}+c_{12})-2c_{c_{13}}^2}{c_{11}+c_{12}+2c_{33}-4c_{13}}. \tag{10.18}$$

The positions of the atoms in the compressed QD are then optimized by minimizing the total elastic energy,

$$U = \sum_{i=1}^{N} U_i, \tag{10.19}$$

where N is the total number of atoms in the QD. The optimization procedure is processed by the standard conjugate gradient (CG) method.

10.2.4 Calculations of electronic and optical properties

After performing the geometry optimization, the relaxing atom positions are obtained. The crystal potential is then obtained as a superposition of the atomic pseudopotentials (see Eq. (9.22)). The single-particle electron and hole states are calculated by employing the empirical pseduopotential method as discussed in Section 9.3.3 of Chapter 9. We employ configuration interaction approach, as described in Section 9.5 of Chapter 9, to taking into the excitonic effects. The corresponding many-body Hamiltonian is solved using iterative diagonalization techniques. Our computational limitations allow us to include in the configruation interaction treatment 10 states from the valence band and 10 states from the conduction band. For the screening function needed in the Coulomb integrals we used the phenomenological microscopic, isotropic and uniform model proposed by Resta[248] (see Subsection 9.5.2 of Chapter 9). The optical dipole matrix elements are calculated within the dipole approximation, and the oscillator strength was calculated using Fermi's golden rule (see Subsection 9.5.3 of Chapter 9).

10.3 Results and discussion

10.3.1 Valence band ordering of bulk ZnO

There are two main characteristics of bulk ZnO we would like to address prior to the discussion of our main results later on. One is the crystal field and the other one is the spin-orbit interaction. Without these two characteristics, the top valence band is six fold Γ_{5v} states. The crystal field splits the Γ_{5v} states into four fold Γ_{5v} states and Γ_{1v} states. Further including the spin-orbit interaction leads to the formation of three 2-fold states at the top of the Γ-point of the Brillouin Zone. In the conventional situation, the spin-orbit parameter is positive. The top three valence band states at the Γ point of the Brillouin zone from the top to the bottom are so-called A-band, B-band and C-band, respectively, which are of symmetry Γ_{9v}, Γ_{7v}, and Γ_{7v}, respectively. However, for ZnO, the spin-orbit parameter is negative. The origin of this negative spin-orbit coupling has been discussed initially for cuprous halides and has been attributed to the spin-orbit effect of cation d states. This leads to a situation which is contrary to the conventional situation: the topmost three valence band states from the top to the bottom are named as A-band, B-band and C-band but with symmetry Γ_{7v}, Γ_{9v} and Γ_{7v}, respectively. These states are

corresponding to the A-, B- and C-exciton lines in photoluminescence experiments. Due to the rather small spin-orbit splitting parameter (e.g., $\Delta_{so} = 3.5$ meV), A-band and B-band are nearly degenerate, exhibiting a tiny splitting. Conversely, the separation between A-band (or B-band) and C-band is much larger.

10.3.2 Projection onto bulk technique

To visualize the QD wave functions $|\psi_i^{QD}\rangle$, we employ the projection onto bulk technique.[145] In this technique, we project the QD wave function $|\psi_i^{QD}\rangle$ onto the bulk wurtzite ZnO wave functions with band index n and wave vector $\mathbf{k}$, that is $\psi_{n\mathbf{k}}^{buk}$,

$$|\psi_i^{QD}\rangle = \sum_{n\mathbf{k}} |\psi_{n\mathbf{k}}^{bulk}\rangle\langle\psi_{n\mathbf{k}}^{bulk}|\psi_i^{QD}\rangle, \tag{10.20}$$

where $\sum|\psi_{n\mathbf{k}}^{bulk}\rangle\langle\psi_{n\mathbf{k}}^{bulk}|$ is the projection operator. The expansion coefficients $c_{n\mathbf{k}}^i = \langle\psi_{n\mathbf{k}}^{buk}|\psi_i^{QD}\rangle$ are used to determine the bulk band character of the dot wave function,

$$bbc_n^i = \sum_{\mathbf{k}} c_{n\mathbf{k}}^i c_{n\mathbf{k}}^{i*}. \tag{10.21}$$

By chopping the QD wave functions into bulk cells, and projecting each of them onto bulk states, we obtain space-resolved function $bbc_n^i(x, y, z)$. Summing them over bands leads to the envelope functions,

$$env^i(x, y, z) = \sum_n bbc_n^i(x, y, z). \tag{10.22}$$

One shall see from the above technique, the fast oscillating atomic wave functions of the QD is projected on the bulk wave functions. This leads to the visualization of the symmetry of the envelope function and the parentage of each dot state. This is indeed a very useful tool and we shall see its applications in the coming sections.

10.3.3 Pressue-dependent electronic properties

To determine the electronic and optical properties in ZnO QDs in both the strong and the intermediate confinement regime under externally applied hydrostatic pressure, we considered five different ZnO colloidal QDs with diameters D = 1.7 nm, 2.1 nm, 3.1 nm, 3.6 nm, 5.2 nm, respectively. ZnO QDs with such sizes can be experimentally synthesized by using the well-established colloidal fabrication techniques, leading to a nearly spherical

shape.[113,139] The numbers of atoms for the respective structures are $Zn_{99}O_{111}$, $Zn_{204}O_{210}$, $Zn_{654}O_{654}$, $Zn_{1014}O_{1011}$, and $Zn_{3063}O_{3102}$.

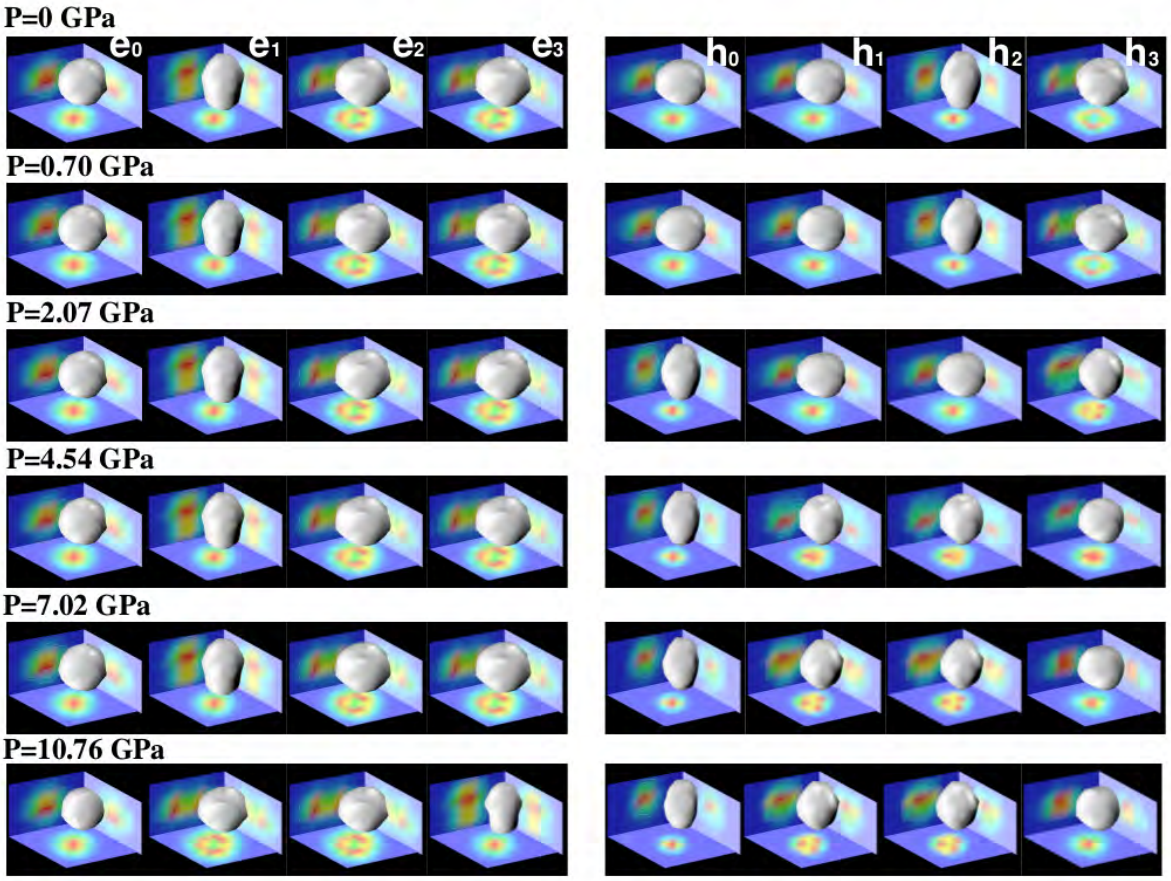

Figure 10.4: Envelope functions for the first four electron ($e_{0,1,2,3}$) and first four hole ($h_{0,1,2,3}$) states in a ZnO QD with diameter D = 1.7 nm for various hydrostatic pressures. The isosurface values are chosen in such a way to enclose 75% of the state densities.

As a first step toward elucidating the electronic structure in ZnO QDs, we project the fast oscillating atomic wave functions onto the bulk ZnO Bloch states (as stated in the above subsection). This gives us access to the envelope functions, which are more convenient to visualize than the fast oscillating real wave functions. However, it should be kept in mind that the energetic for each state is not governed by the envelope function alone, but determined by the full atomic wave function. As the representatives of the electronics of ZnO QDs under hydrostatic pressure in both the strong and intermediate confinement regimes, we present the projected envelope functions of the first four electron states and

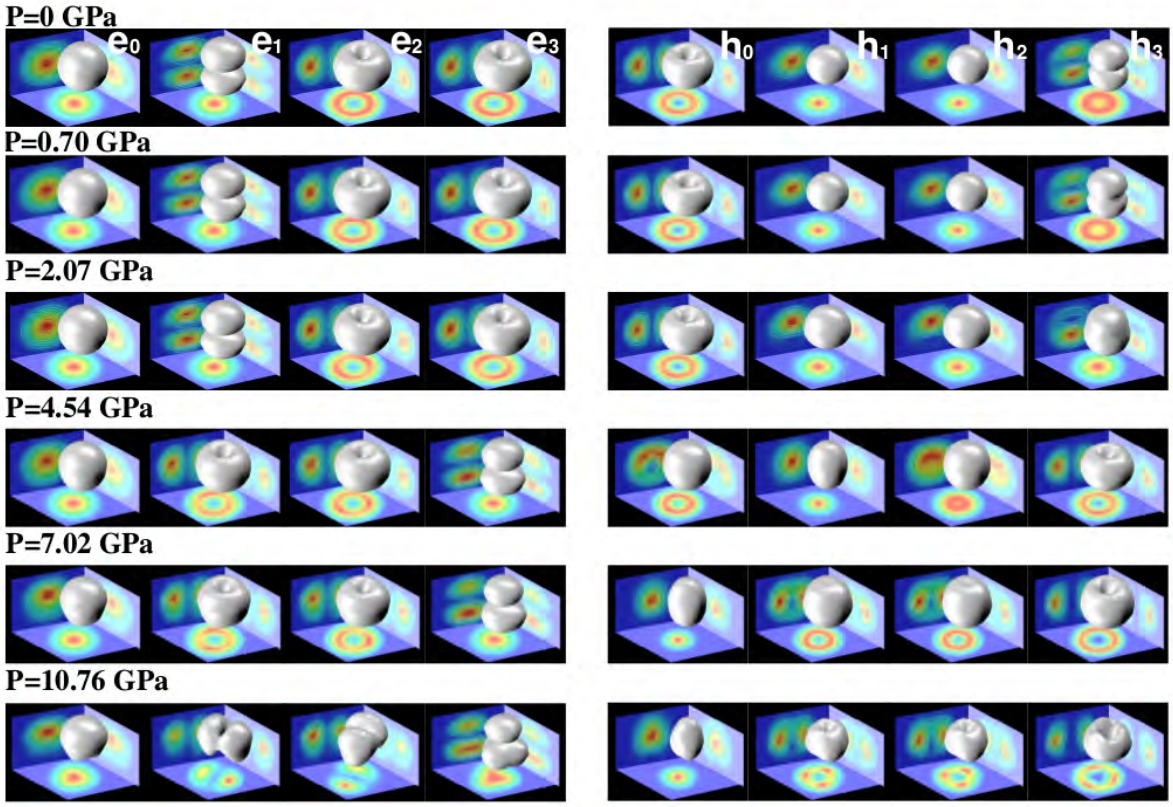

Figure 10.5: Same as Fig. 10.4 but for D = 5.2 nm.

the first four hole states of our smallest and largest structures in Figs. 10.4 and 10.5, respectively. The results are shown for six different hydrostatic pressures. To characterize the symmetry of the wave functions, which is very useful to understand the relevant optical properties discussed in the next subsection, we use the notation ω_ζ where ω represents the number of nodes encountered by moving across a specific direction (xy or z-axis direction), while the subscript ζ indicates the direction in which we find the node(s). The possible value for ω are S, P, D, etc., where S represents the form of the wave function without node (in this case, we neglect the subscript ζ), P with one node etc. This way, we tabulated the characters of the electron and hole envelope functions shown in Figs. 10.4 and 10.5 in Tables 10.6 and 10.7, respectively.

In Fig. 10.6 we plot the Bloch function character of the first four hole states using the projection formalism described in the last subsection. After a combined analysis of the relative contribution from the bulk valence bands with the characters of the hole envelope functions listed in Tables 10.6 and 10.7, we find that in the absence of external pressure, the highest occupied molecular orbital (HOMO, h_0) of our smallest structure (with diameter

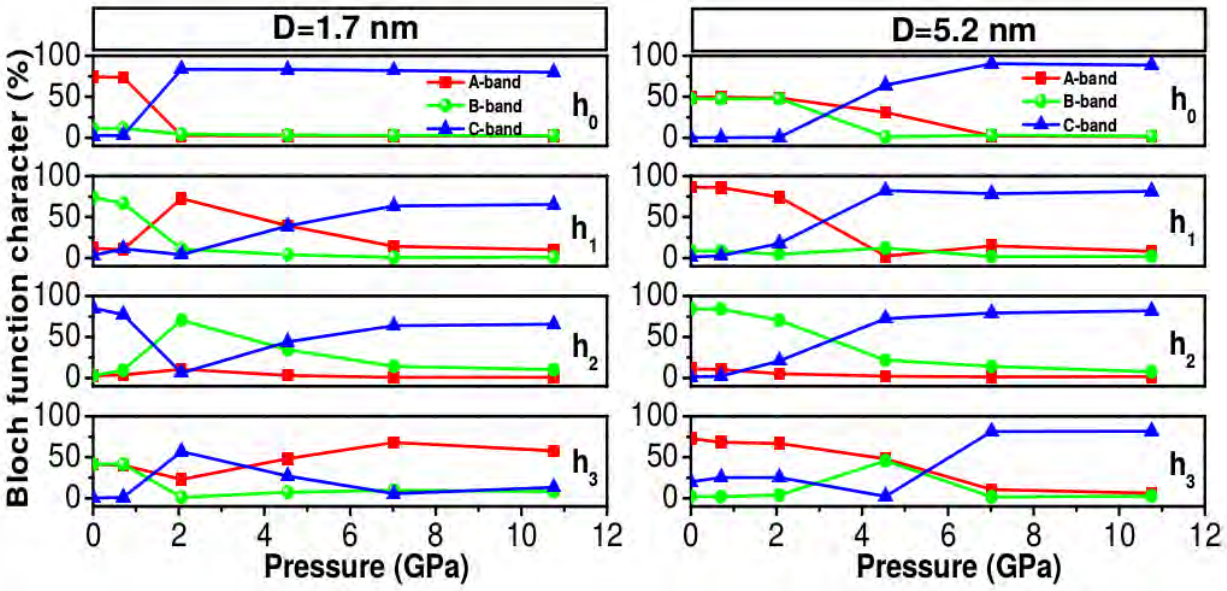

Figure 10.6: Analysis of the Bloch function character of the first four hole states $h_{0,1,2,3}$ in a ZnO QD under various hydrostatic pressures. The left panel corresponds to the QD with diameter D = 1.7 nm, while the right panel corresponds to the QD with diameter D = 5.2 nm. The colors red, green and blue correspond to A-, B- and C- bands, respectively.

D = 1.7 nm) has orbital S character, while it shows a P character in our largest structure (with diameter D = 5.2 nm). This is in agreement with one of the important conclusions of Ref. 145 which demonstrates that the HOMO of ZnO QDs is of orbital P character for structures larger than 2.6 nm in diameter. Under pressure, the orbital character of the HOMO state of our smallest structure appears to be pressure-independent, always exhibiting a conventional S-type character. Conversely, the orbital character of the HOMO state of our largest structure experiences a drastic change in the envelope function character, switching to a more conventional S orbital character for pressures larger than 2.07 GPa. This is due to the pressure effect which modifies the Bloch function parentage from an even mixture of A- and B-band (P $\leq$ 2.07 GPa) to a nearly pure single-C-band (P $>$ 2.07 GPa), as seen in Fig. 10.6 (see the top plot of the right panel). In addition to the HOMO state, the applied pressure significantly modifies the Bloch function characters for the other hole states ($h_{1,2,3}$): they are nearly pure single-band objects for relatively high pressures (e.g., P $>$ 4.54 GPa), originating mainly from bulk Bloch C-band ($\sim$ 75%) and exhibiting P_{xy}-type characters. The only exception is h_3 of our smallest structure which has a dominant bulk Bloch A-band parentage and shows a S-type character for pressures larger than 4.54 GPa. The fact that the P^C_{xy} states at the pressures of 7.02 and 10.76 GPa ($h_{1,2}$ states in Table 10.6) are energetically separated from the P^C_z state can be related to the anisotropic effective masses of the topmost three ZnO valence bands. The C-band effective mass is anisotropic and larger perpendicular to the c-axis ($m^*_{C\perp} = 0.55\ m_0$ and $m^*_{C\parallel} = 0.31\ m_0$, where m_0 is the free electron mass). This favors the orbital P-states with

Table 10.6: Character of the first four envelope functions for electrons and holes in a ZnO QD with diameter D = 1.7 nm under various hydrostatic pressures (in unit of GPa). The superscript (A, B, C) indicates the corresponding hole state parentage (A-band, B-band, C-band) obtained from Fig. 10.6 and the symbol (*) means that the wave function is a mixed state with orbital P-character.

Pressure	e_0	e_1	e_2	e_3	h_0	h_1	h_2	h_3
0	S	P_z	P_{xy}	P_{xy}	S^A	S^B	S^C	P_{xy}^{AB}
0.70	S	P_z	P_{xy}	P_{xy}	S^A	S^B	S^C	P_{xy}^{AB}
2.07	S	P_z	P_{xy}	P_{xy}	S^{C*}	S^{A*}	S^{B*}	S^{C*}
4.54	S	P_z	P_{xy}	P_{xy}	S^{C*}	S^{AC*}	S^{BC*}	S^{ABC*}
7.02	S	P_z	P_{xy}	P_{xy}	S^C	P_{xy}^C	P_{xy}^C	S^A
10.76	S	P_{xy}	P_{xy}	P_z	S^C	P_{xy}^C	P_{xy}^C	S^A

Table 10.7: Same as table 10.6 but for D = 5.2 nm.

Pressure	e_0	e_1	e_2	e_3	h_0	h_1	h_2	h_3
0	S	P_z	P_{xy}	P_{xy}	P_{xy}^{AB}	S^A	S^B	P_z^A
0.70	S	P_z	P_{xy}	P_{xy}	P_{xy}^{AB}	S^A	S^B	P_z^A
2.07	S	P_z	P_{xy}	P_{xy}	P_{xy}^{AB}	S^A	S^B	P_z^A
4.54	S	P_{xy}	P_{xy}	P_z	P_{xy}^{ABC}	S^C	S^C	P_{xy}^{AB}
7.02	S	P_{xy}	P_{xy}	P_z	S^C	P_{xy}^C	P_{xy}^C	P_{xy}^C
10.76	S	P_y	P_x	P_z	S^C	P_{xy}^C	P_{xy}^C	P_{xy}^C

in-plane nodes, P_{xy}, over the ones with nodes along the c-axis, P_z. No such anisotropy exists for the A- and B- bands and the orbital P_{xy} states are not favored over the P_z states. The electron states follow the typical pattern of a single-band object originating from an isotropic band. The lowest four electron states have orbital S and P character, where P_z is slightly favored over P_{xy} at low pressures and vice versa at high pressures.

As mentioned before, the applied hydrostatic pressure strongly modifies the relative contribution of the bulk valence band states to the QD hole states, which causes the changes in the symmetry of the hole envelope functions. In Fig. 10.7, we see that states with dominant A, B-band parentage have a stronger dependence on pressure than the states with dominant C-band parentage. This is associated with the larger deformation potential of A- and B-bands in comparison to that of the C-band. Fig. 10.7 also shows that the C-band states rise above the A- and B-band states at a critical pressure and finally become the energetically favorable states. This critical pressure appears to be highly size-dependent. For our smallest structure, it is $P_1 \approx 1.2$ GPa, while for our largest structure, it is $P_2 \approx 3.3$ GPa.

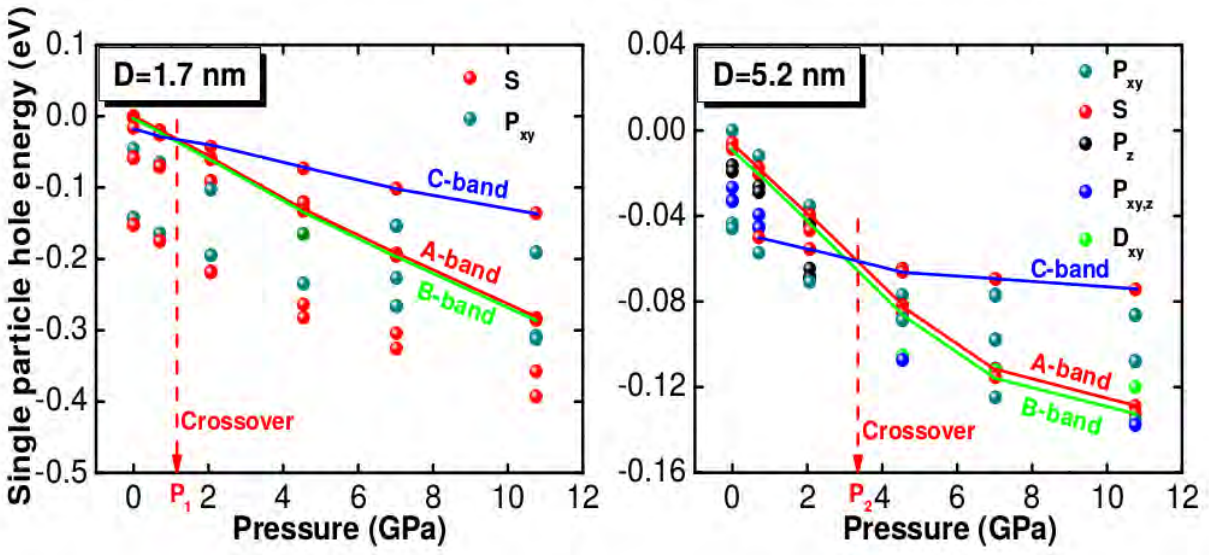

Figure 10.7: Energy of the first ten hole states relative to the HOMO state at zero pressure, in ZnO QDs under various hydrostatic pressures (in unit of GPa). The lines connect states which are of the same symmetry ω_ζ. The red, green, blue lines connect states with dominant A-, B-, C-band character, respectively. Two QD sizes D = 1.7 and 5.2 nm, where D is the diameter of the QD, are considered.

10.3.4 Pressue-dependent optical properties

We first present the optical band gap of ZnO QDs as a function of the applied hydrostatic pressure. The calculations are performed for five different QD sizes which are in the strong or intermediate confinement regime. Two levels of theory: at the single particle (SP) level and at the configuration interaction (CI) level, are employed. Fig. 10.8(a) and (b) show a strong size dependence of the optical band gap and a weaker, nearly linear, pressure dependence. The pressure coefficients (dE/dP) are given in Fig. 10.8(c) for uncorrelated and correlated calculations. Both the single-particle and the excitonic pressure coefficients are strongly size-dependent. Increasing the QD size causes a monotonic increase in the pressure coefficient. A similar behaviour has also been calculated theoretically for CdSe QDs.[272] Furthermore, it is shown from Fig. 10.8(c) that the QD excitonic pressure coefficients obtained in the full CI scheme are substantially smaller than the bulk value (see the dot dashed line) with deviations at small diameters of up to 41%. The single-particle results exceed the bulk limit for QD diameters larger than D = 4.5 nm. This prominently highlights the importance of the higher level of theory accounting for excitonic effects. We also studied in Fig. 10.8(d) the Stokes shift, defined as the energetic difference between the lowest dark exciton state and the first bright exciton state. The Stokes shift displays a nonmonotonic dependence of the applied hydrostatic pressure, exhibiting a minimum value at a critical pressure P_c. This critical pressure is highly size-sensitive. It appear to

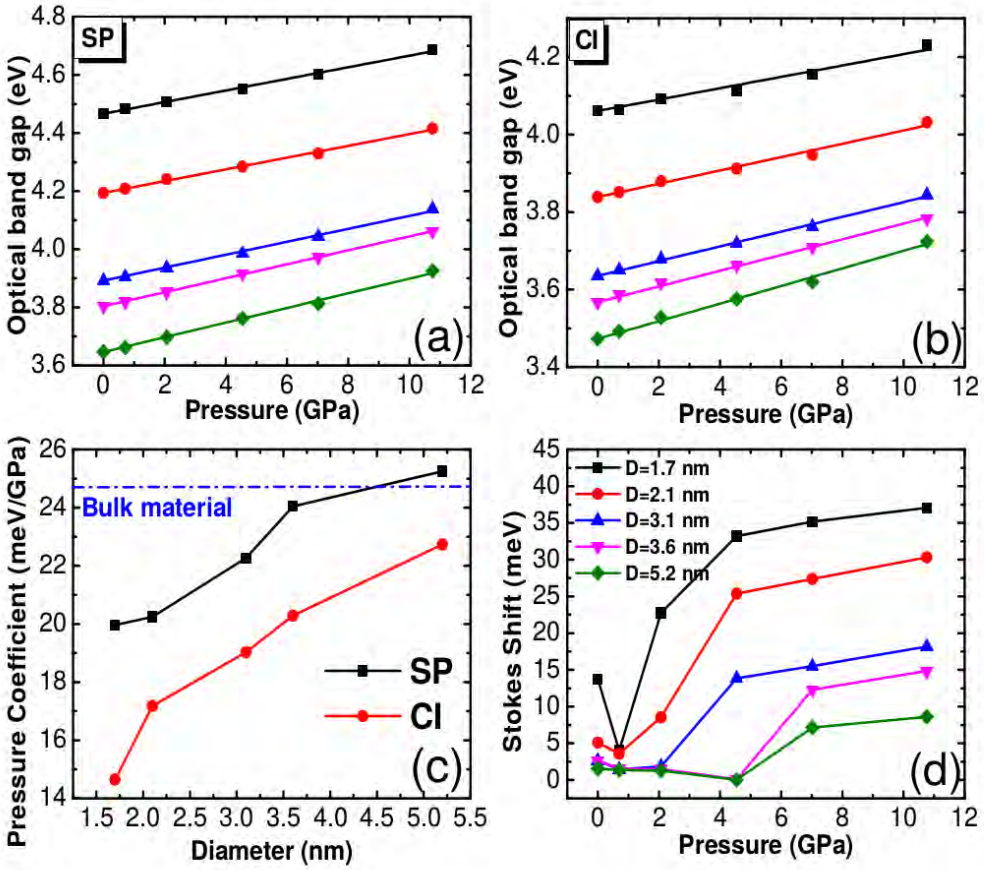

Figure 10.8: Optical band gap of ZnO QDs at the single particle (SP) level (a), and at the CI level (b) as a function of the hydrostatic pressure (symbols). (c) Pressure coefficients at the single particle level (obtained from (a)) and at the CI level (obtained from (b)) versus QD diameter. (d) Stokes shift as a function of the applied hydrostatic pressures. Here, five different QD sizes (D = 1.7 nm, 2.1 nm, 3.1 nm, 3.6 nm and 5.2 nm, where D is the QD diameter) are considered. All the symbols and colors in (a) and (b) are the same as in (d).

be $P_c = 0.7$ GPa for the first two smallest structures, $P_c = 2.07$ GPa for the QD diameter D = 3.1 nm and $P_c = 4.54$ GPa for the other two largest structures.

To clarify the physical reasons for this nonmonotonic behaviour, we take our largest structure as an example and recall the electronic properties of the single electron and hole states presented in the last subsection. For pressures smaller than or equal to the critical value (P = 4.54 GPa), both the first bright and dark exciton states have a dominant contribution from the (0,1) configuration, where both the electron and hole have *S*-type orbital character. In the CI scheme, the lowest exciton state is spin-forbidden. However, when the applied pressure is larger than the critical value (P > 4.54 GPa), the single-particle states which are responsible for the two exciton states show an abrupt change from the configuration (0,1) to (0,0). This level crossing is responsible for the nonmonotonic behavior in Stokes shift. This nonmonotonic behaviour in Stokes shift makes evident that the electron-hole spin-exchange interaction is much stronger in the (0,0) configuration

(C-exciton) and it is enhanced with increasing pressure. Similar behaviour has also been experimentally measured and theoretically calculated in CdSe NRs by systematically varying the height-to-diameter aspect ratio.[273] For larger pressures, Fig. 10.8(d) shows that the Stokes shift is significantly larger than the corresponding value at zero pressure. A larger Stokes shift means a smaller overlap area between absorption and emission spectra, which is desirable in applications such as light-emitting diodes, where reabsorption reduces the total efficiency.[273]

Finally, we calculate in Fig. 10.9 the photoluminescence emission spectrum in the full CI scheme for our smallest and largest structures. We find that the applied pressure induces a strong blue shift in the emission spectrum. This blue shift is more pronounced in the larger QD in accordance with Fig. 10.8(c). In an attempt to indicate explicitly the emission polarization direction, we also present the spectra at each pressure with a vertical line. It is shown that in both, the strong and intermediate confinement regimes, the optical emission polarization exhibits a crossing from in-plane ($\mathbf{E}\perp\vec{c}$) to out-of-plane ($\mathbf{E}\|\vec{c}$) polarization at a critical pressure value. It is $P_c = 0.70$ GPa for our smallest structure and $P_c = 4.54$ GPa for our largest structure. In other words, the emission changes from a normal α-emission ($\mathbf{E}\perp\vec{c}$) to the unusual[274,275] so-called σ- and π-emission ($\mathbf{E}\|\vec{c}$) for pressures larger than the critical pressure. After reaching the crossing, the lowest optically bright exciton state in both confinement regimes has a dominant contribution from the (0,0) configuration,

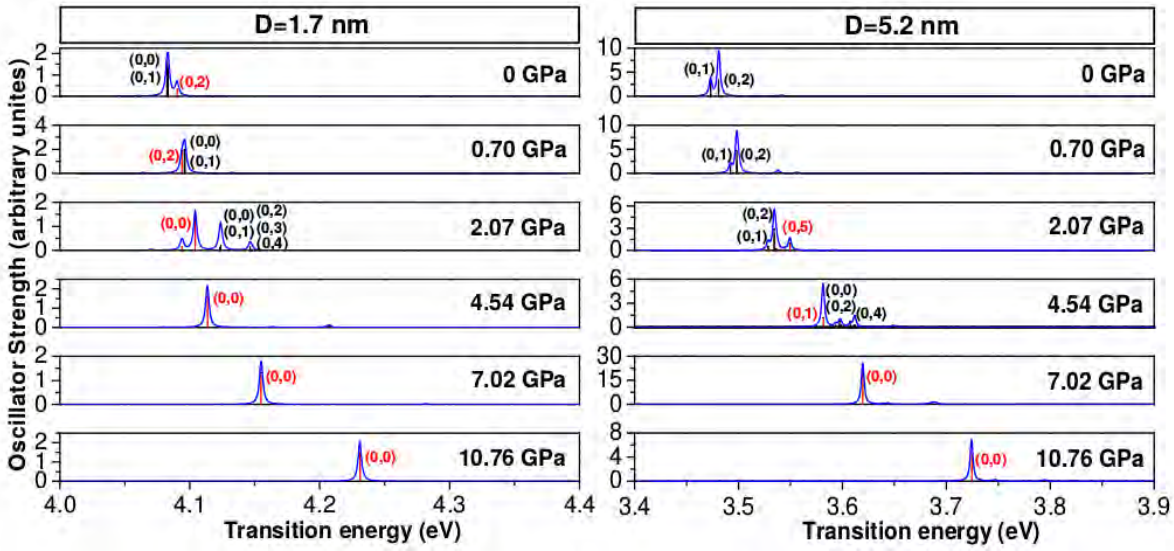

Figure 10.9: Oscillator strength for the emission $|X\rangle$ to $|0\rangle$ at room temperature in ZnO QDs which are obtained by full CI. Transitions polarized along the out-of-plane direction (c-axis) are shown by red vertical lines, while the ones polarized along in-plane direction are shown as black vertical lines. The numbers in bracket refer to the dominant single-particle levels involved in the transitions (e,h). The blue curve represents the total emission spectra. The left panel is corresponding to the QD with diameter $D = 1.7$ nm, while the right panel is corresponding to the QD with diameter $D = 5.2$ nm.

where the single-particle hole state has S-type character, and is derived from the dominant bulk Bloch C-band contribution. Recently, it has been shown that the polarization of the C-exciton along the c-axis ($\mathbf{E}\|\vec{c}$) holds not only for bulk ZnO[276] but also for ZnO nanowires.[277] The possibility to effectively manipulate the optical emission polarization of QDs via pressure should be advantageous in the design of future experiments.

10.4 Brief summary

In summary, we studied the electronic and optical properties of ZnO colloidal QDs as a function of applied hydrostatic pressure. We find that for QD larger than 2.6 nm in diameter, the increased pressure induces a drastic change in the highest occupied molecular orbital from an unconventional P-type character to a normal S-type character. Hole states tend to become single-band objects originating from the Bloch C-band with increasing pressure. We relate this effect to the fact that the hole states with dominant A- and B-band parentage experience a stronger pressure dependence, in comparison to the corresponding C-band states. In other words, the Bloch band hydrostatic deformation potentials are negative and larger in magnitude for the A/B-bands than for the C-band. As a consequence, the C-band states emerge as the HOMO states at high pressure. We show that the crossover between A/B-band and C-band HOMO states is size dependent and occurs at higher pressures for larger QDs. We further find that the P-states derived from the Bloch C-band are energetically split into states with nodes in-plane and nodes along the c-direction. This is attributed to the anisotropy of bulk Bloch C-band which has a heavier in-plane effective mass favoring P states with in-plane nodes. At both single-particle and at the correlated excitonic level, the optical band gap experiences a linear increase with increasing pressure, with a highly size-dependent pressure coefficient. The pressure coefficient is significantly lowered, by as much as 41%, by correlations. Only the correlated results (configuration interaction) can be brought in agreement with experiment. In contrast to the monotonic increase of the optical band gap, the applied hydrostatic pressure causes a non-monotonic Stokes shift with a minimum at a specific pressure. For pressures larger than this critical value, the optical emission polarization changes from in-plane to out-of-plane polarization. We explained this behavior through the drastic change of the single-particle hole state parentage from a dominant bulk Bloch A/B-band (before crossing) to a nearly pure C-band (after crossing). Finally, we find that the critical pressure at which the crossing takes place strongly depends on the QD size, showing larger pressure values for larger QD sizes. After this crossing, the optically bright exciton state has a pure contribution from the (0,0) configuration, where both the electron and hole states have S-type orbital character and the single-particle hole state has a dominant contribution from the bulk Bloch C-band.

11

Near-band-edge exciton polarization change in ZnO nanowires

In this chapter, using the atomistic pseudopotential method complemented by configuration interaction calculations, the electronic and optical properties of ZnO nanowires (NWs) in the presence of quantum confinement effects are studied. Our results indicate that the near-band-edge exciton experiences a crossover from an in-plane polarized A-exciton (for $D \geq 3$ nm) to an out-of-plane polarized C-exciton (for $D < 3$ nm) due to quantum confinement. This transition leads to a non-monotonic variation of Stokes shift, exhibiting a maximum value around the critical diameter of 3 nm. The observed behavior is analyzed by a stepwise inclusion of correlation effects, leading to a comprehensive description of the excitonic fine structure. The results presented herein are published in Physical Chemistry Chemical Physics (2015), DOI: 10.1039/C4CP04551C.

Contents

11.1 Introduction

Zinc oxide (ZnO) nanowires (NWs) have attracted considerable attention as promising candidates for device applications. The wide direct band gap (3.445 eV) and large exciton binding energy (60 meV) of bulk ZnO make them one of the most remarkable optoelectronic materials for nanoscale device applications, such as ultraviolet (UV) lasers,[278] light-emitting diodes[279] (LEDs), field-effect transistors (FETs),[275] and UV photodetectors.[280,281] Their high surface-to-volume ratio and high density of surface states promote the development of a new generation of chemical and biological gas sensors with high sensitivity and fast response.[282,283] Piezoelectric nanogenerators based on ZnO NWs for self-powered systems have also been reported.[284,285] Experimental fabrication of this type of nanostructures has been successfully achieved by using different synthesis methods, such as vapor trapping chemical vapor deposition,[275] thermal evaporation,[286] chemical synthesis by vapour phase transport,[277] to mention only a few. However, the vast majority of the fabricated NWs are so large in diameter (e.g., > 15 nm which is more than 10 times of the exciton Bohr radius of bulk ZnO (≈ 1.4 nm)) that the quantum confinement effects remain absent. A clear picture of the quantum confinement effects on the electronic and optical properties of ZnO NWs remains unknown.

Due to the specific features of wurtzite ZnO, such as anisotropy of the valence band, as well as the small dielectric constant and strong electron-hole Coulomb interaction, a simple one-band effective mass model[287] is not able to deliver predictive results. The incorporation of many-body effects in an effective mass model to probe large nanostructures has been recently achieved.[288,289] Density functional theory (DFT) calculations have been employed to study the piezoelectricity and the band structure,[290] the charged states and the band gap in ZnO NWs (or doped ZnO NWs).[291] This type of calculations are restricted to nonpassivated, small-diameter (e.g., < 3 nm) NWs. Moreover, since in DFT the bulk ZnO band gaps are significantly underestimated (e.g., $\sim$0.63 eV [Ref. 290] by local density approximations (LDA or GGA) (82% underestimated in comparison to the well-known experimental value 3.445 eV), the description of the quantum confinement effects on the electronic and optical properties of ZnO NWs is more than questionable.

In this Chapter, we study the electronic and optical properties of ZnO NWs with diameters up to 6 nm, covering the intermediate and weak confinement regimes. The calculations are performed via the empirical pseudopotential method, using recently derived and well-tested ZnO pseudopotentials from Ref. 145, and the excitonic effects are considered by using the configuration interaction approach.[236] This method has been shown to describe very well the excitonic properties in wurtzite CdSe quantum dots (QDs),[255] and very recently in

ZnO QDs[145,292] and Si NWs.[293] In the following section, we present the computational details.

11.2 Computational details

The empirical pseudopotentials for Zn and O employed herein are are derived and well-tested by Baskoutas and Bester.[145] Both potentials have exponential form and the corresponding parameters are given in Table 10.4. The ZnO NWs are constructed with a cross section as circular as possible, considering the atomistic nature of the structure and extend along the [0001] crystallographic direction, while the lateral surface of the NWs is well passivated by an artificial ligand with the same crystal structure and lattice parameters as ZnO and a higher band gap. Since there is no mismatch between the NW and the passivating material the electric field induced by piezoelectric effects can be safely neglected. The contribution of spontaneous polarization to the internal field is expected not to be significant since the polar direction of the NW coincides with the infinite growth direction. It has been demonstrated by large scale DFT calculations[294] that the internal field even in a polar quasi-one-dimensional nanorod (NR) does not depend strongly on the spontaneous polarization of the underlying lattice.This type of surface passivation has been practiced successfully previously for this material system,[145,240,269] and very recently in Si NWs.[293] It should be noted here that the nature of the surface passivation and morphology may play an important role in the determination of the electronic and optical properties of semiconductor NWs, especially with smaller sizes. However, in our calculations, the emphasis is put on the size effects rather than the surface effects.

The many-body excitonic properties are calculated via configuration interaction (CI), as described in Section 9.5 of Chapter 9. The excitonic wave functions are expanded in terms of single-substitution Slater determinants constructed from the single-particle wave functions of electrons and holes (see Section 9.5.1 of Chapter 9). The corresponding many-body Hamiltonian is solved either in the framework of the single configuration (SC) approximation or in the CI scheme. At the SC level, the intraconfiguration Coulomb and exchange matrix elements are fully included, but the interaction between different configurations is neglected.[236] Consequently, the correlation effects at this level of theory are willingly not accounted for. The interconfiguration coupling is fully included in the CI scheme.[236] It should be noted that our calculations are focused on the near-band-edge low energy excitonic states which are dominantly originated from the transitions at the Γ-point of the Brillouin zone. The band dispersion along the growth direction of the NWs is expected to have only very marginal influence on the results presented herein. It should

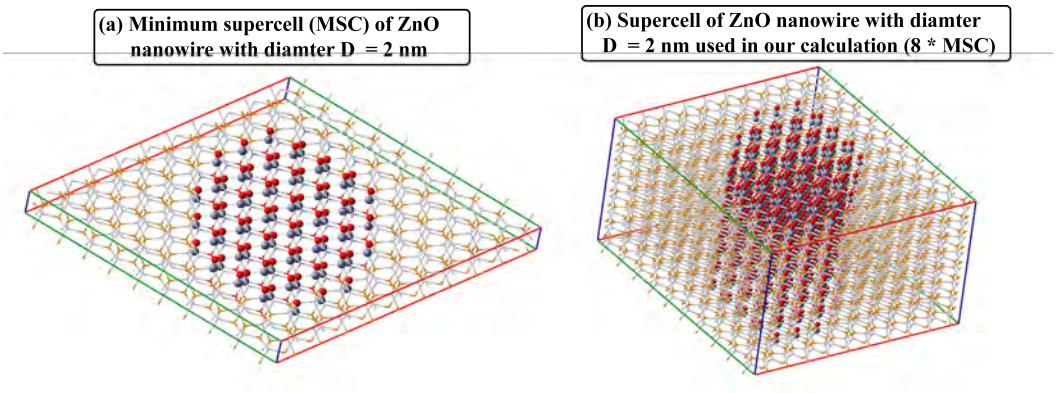

Figure 11.1: (a) Mininum supercell for ZnO nanowire with diameter D = 2 nm. (b) Supercell for ZnO nanowire (e.g., 8 minimum supercells along the growth direction) with diameter D = 2 nm used in our calculations.

be also noted that an infinite wire will exhibit a continuum of states above (below) the LUMO (HOMO) from which we capture only a subset with our finite NW.

There are two ways to capture the electron-hole interaction of excitons,

1. Reciprocal space implementation: use a minimum supercell size in the NW growth direction and increase the k-point sampling;

2. Real space implementation: use a large supercell extended in the NW growth direction and limit the calculation to the Γ point of the Brillouin zone.

In our calculations, we prefer the real space implementation: the NWs are periodically expanded along the growth direction with a length of ∼4.164 nm, which is around three times the exciton Bohr radius in bulk ZnO (∼1.4 nm). The Coulomb and exchange integrals are screened by the position-dependent and size-dependent screening function proposed by Resta (see Section 9.5.2 of Chapter 9), which gives a physically smooth transition from short range (unscreened) to long range (screened).[236,293] An important issue in the calculation of excitonic properties in nanostructures is the treatment of correlations. Our CI treatment exhibits a poor scaling, which limits the number of states that we are able to include in the expansion. A careful convergence test is therefore necessary, especially in the case of a NW, where the confinement in the NW direction is the sole result of the electron-hole interaction. For the convergence test, we choose our smallest ZnO NW with a diameter D = 2 nm. The minimum supercell and the supercell used in our calculations (e.g., 8 minimum supercells along the growth direction) are shown in Fig. 11.1(a) and (b), respectively.

We firstly calculated the corresponding single-particle electron and hole energy levels and the results are shown in Fig. 11.2(a). We find that the single-particle electron states spread in a much larger energy window than its hole states counterparts, e.g., the first five electron states distribute in an energy window of 0.56 eV, while the first fifty hole states

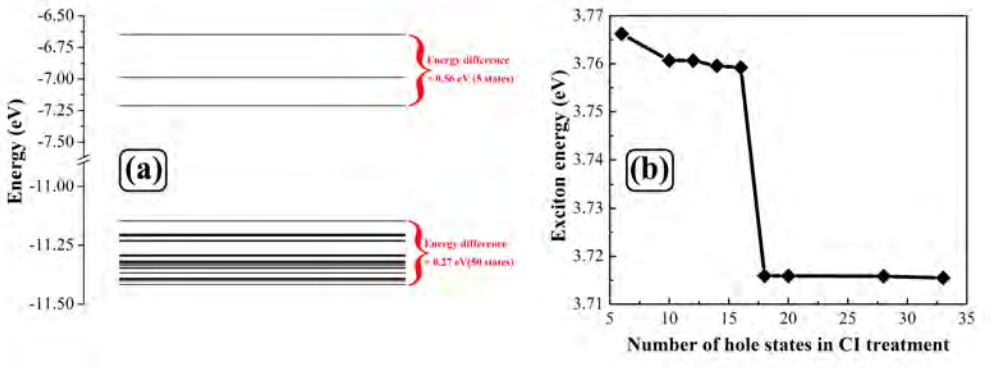

Figure 11.2: (a) Single-particle electron and hole energy levels diagram for our smallest ZnO nanowire (with diameter D = 2 nm). Here, we have plotted the first five electron energy levels and the first fifty hole energy levels. (b) Exciton energy as a function of the number of the hole states in the configuration interaction (CI) treatment for our smallest ZnO nanowire (with diameter D = 2 nm). Here, we include the first five electron states in the CI.

only spread in a energy window of 0.27 eV. Therefore, we include in our configuration interaction (CI) treatment the first five electron states and systematically increase the number of hole states. The exciton energy as a function of the number of hole states is presented in Fig. 11.2(b). As we can see from Fig. 11.2(b), the exciton energy is insensitive to a further increase of the number of hole states when the number of hole states is larger than eighteen. Thus, we include in our CI treatment five states from the conduction band and eighteen states from the valence band. The optical dipole matrix elements are calculated within the dipole approximation, and the oscillator strength was calculated using Fermi's golden rule (see Section 9.5.3 of Chapter 9).

11.3 Numerical results and discussion

11.3.1 Electronic properties of ZnO nanowires

We consider five different ZnO NWs with diameters D = 2, 3, 4, 5, 6 nm. The fast oscillating atomic wave functions are projected onto bulk ZnO Bloch states, which enables us to visualize the envelope functions and quantify the Bloch function parentage of each NW state (see the projection onto bulk technique in Section 10.3.2 of Chapter 10). The envelope functions and Bloch function characters obtained from the projection for the first electron and first four hole states are presented in Fig. 11.3. We use the notation ω to characterize the symmetry of the envelope functions, where ω gives the number of nodes

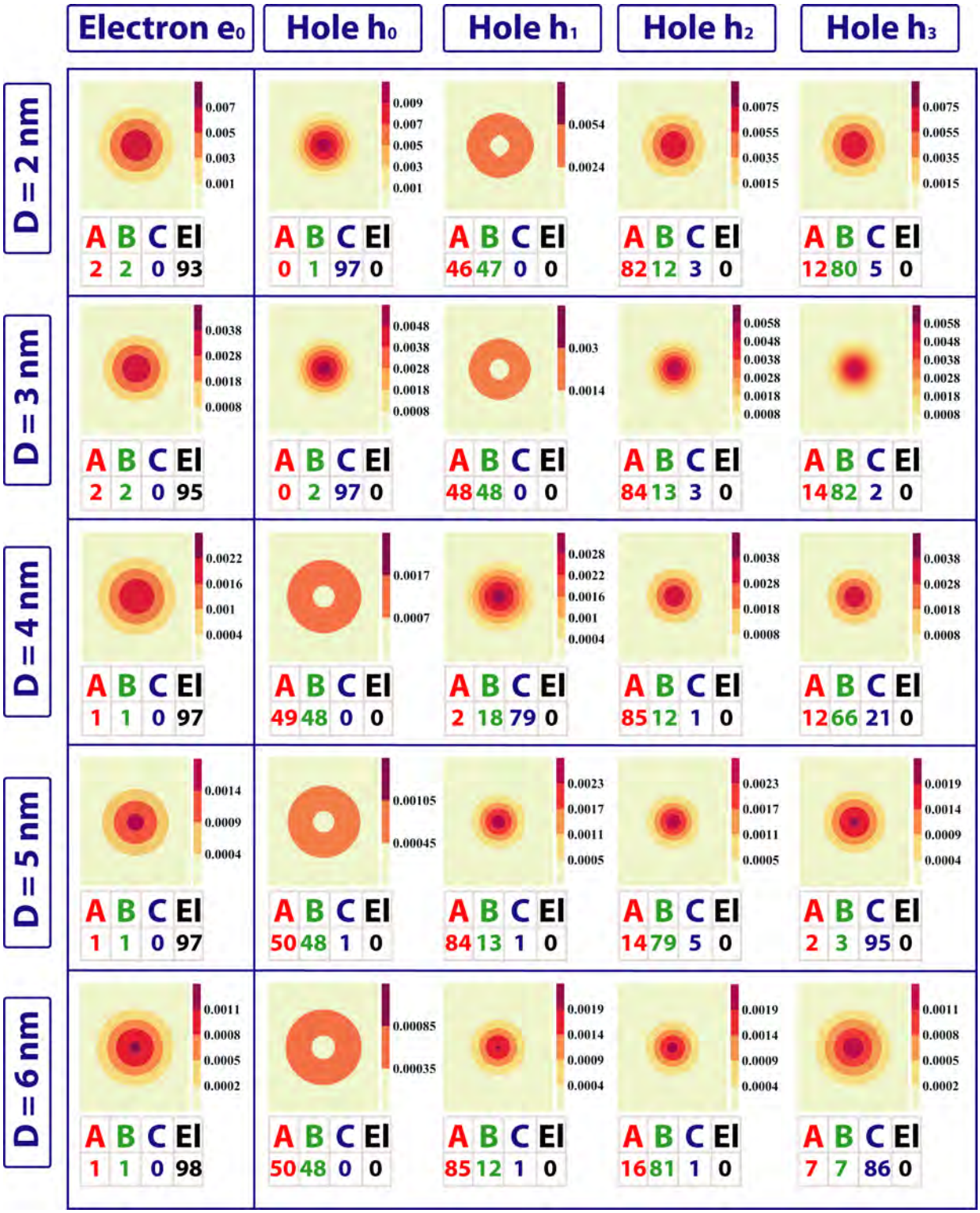

Figure 11.3: Contour plot of the square of the envelope functions (perpendicular to the NW growth direction), extracted from our atomistic wave functions, for the first electron and first four hole states for various ZnO NWs. The parentage of each atomic NW wave function from the topmost three bulk valence band states (labeled as A, B and C) and the lowest bulk conduction band state (labeled as El) is tabulated under each plot in percentage.

Table 11.1: Orbital character of the first four electron and hole envelope functions in ZnO NWs of various diameters (in unit of nm). The superscript (A,B,C) indicates the Bloch function parentage of the corresponding hole state obtained from Fig. 11.3.

Diameter	e_0	e_1	e_2	e_3	h_0	h_1	h_2	h_3
2	S	S	S	P	S^C	$P^{A,B}$	S^A	S^B
3	S	S	S	P	S^C	$P^{A,B}$	S^A	S^B
4	S	P	P	S	$P^{A,B}$	S^C	S^A	S^B
5	S	P	P	S	$P^{A,B}$	S^A	S^B	S^C
6	S	P	P	P	$P^{A,B}$	S^A	S^B	S^C

encountered when the envelope function is projected on a plane which contains both the growth direction vector and the center of the NW. The possible values of ω can be S, P and so forth, where S represents the an envelope function without node, P with one node, etc.. The results for the first four electron and first four hole states are presented in Table 11.1.

It is found that the lowest unoccupied molecular orbital (LUMO) state exhibits an S-like envelope function, derived purely from the lowest bulk conduction band, irrespectively of the variation of the level of quantum confinement. The following two electron states ($e_{1,2}$) appear to be energetically degenerate (see Fig. 11.4(a)), switching from an S-type to a P-type envelope function at a diameter around 3 nm. Furthermore, a P-like envelope function is more preferable for electron states $e_{1,2,3}$ in the presence of very weak quantum confinement effects (i.e., D = 6 nm $\approx 4.3a_B$, where $a_B = 1.4$ nm is the exciton Bohr radius of bulk ZnO).

Concerning the hole states, Fig. 11.3 and Table. 11.3 show that the wave functions with dominant single-band character (either A-, B-, or C-band) have S-type envelope functions, while the ones with an even mixing of bulk Bloch A- and B-bands have P-type envelope functions. The S^A and S^B states are energetically close to each other, whereas they are considerably separated from the S^C states (see Fig. 11.4(b)). This is a consequence of the nature of the topmost three valence bands in bulk ZnO, where the A- and B-bands are very close to each other, being energetically separated from the C-band. The S^C states exhibit a weaker diameter dependence than the S^A and S^B states (see Fig. 11.4(b)). Consequently, the A- and B-band states rise above the C-band states at the critical diameters $D_c^{A/C}$ and $D_c^{B/C}$, respectively, and become energetically more favorable, reproducing the usual electronic structure encountered in bulk ZnO. The critical values are $D_c^{A/C} = 4.2$ nm and $D_c^{B/C} = 4.6$ nm, respectively (see Fig. 11.4(b)). The $P^{A,B}$ states are energetically very close to the S^A and S^B states. The S^C states become the highest occupied molecular orbital (HOMO) states for diameter smaller than a critical value $D_c^{S/P} = 3.8$ nm (see Fig. 11.4(b)). These $P^{A,B}$ states are energetically more sensitive to the NW diameter, crossing over the S^C states at $D = D_c^{S/P}$ and becoming the HOMO states for $D > D_c^{S/P}$. This

diameter dependent change in HOMO state from a conventional electronic state (e.g., with S-type envelope) to an unconventional state (e.g., with P-type envelope) has also been found previously in colloidal ZnO QDs[145] and very recently in GaN NWs,[295] and is being attributed to the nontrivial interplay between symmetry mixing, spin-orbit coupling, and quantum confinement effects on the valence band electronic structure.

11.3.2 Optical properties of ZnO nanowires

First, we present the optical band gap of ZnO NWs for various diameters, which correspond to the intermediate or weak confinement regime (see Fig. 11.4(c)). The calculations are

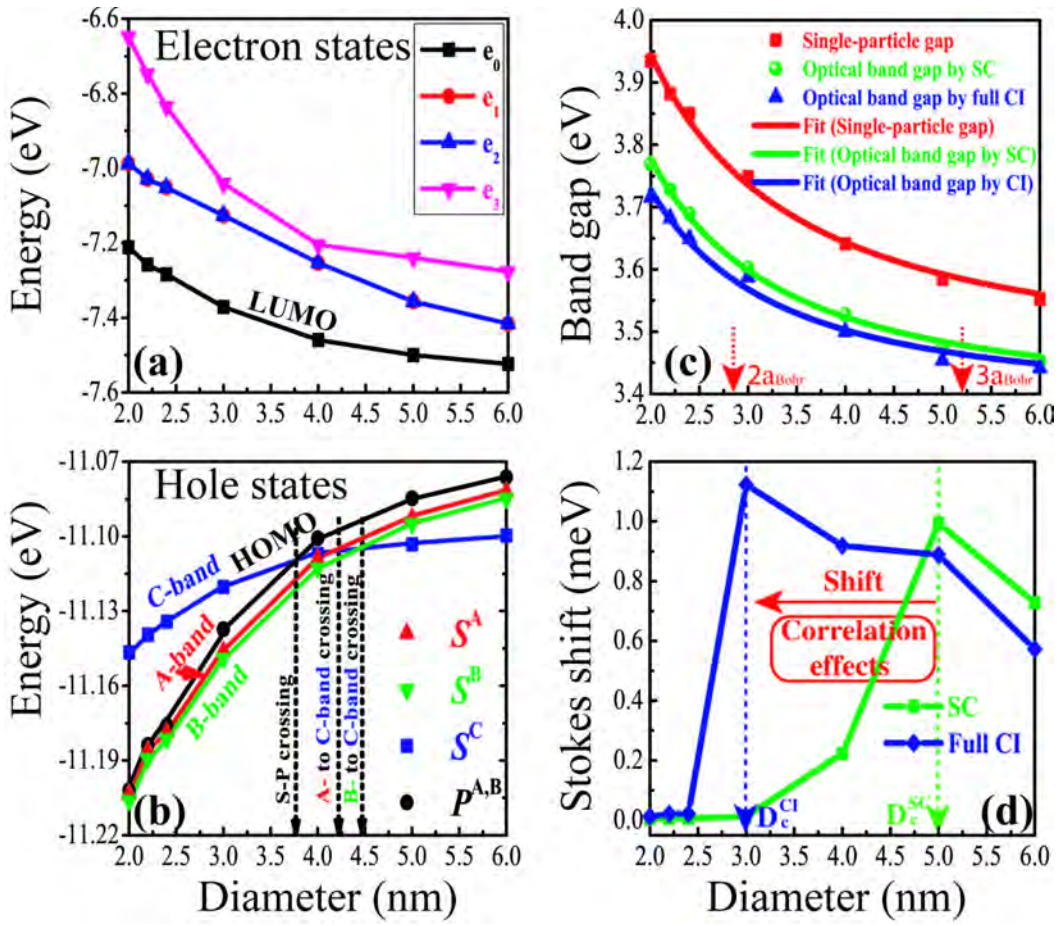

Figure 11.4: Single-particle electron states (a), hole states (b), (c) single-particle gap (red solid squares), optical band gap at SC level (green filled spheres) and optical band gap at the CI level (blue regular triangles), Stokes shift (d), as a function of the NW diameter. In figure (b), the lines connect states of the same symmetry ω. The red, green, blue, and black lines connect states with dominant A-band, B-band, C-band, and an even mixing of A- and B-bands parentage, respectively. In figure (c), each solid line represents a fit according to Eq. (11.1).

performed at three levels of theory, i.e., single-particle (SP) level, SC level, and CI level. Expectedly, the band gap appears to be a decreasing function of the NW diameter at all the three levels (see Fig. 11.4(c)). The size-dependent gaps are best fitted according to

$$\begin{aligned} E_g^{SP} &= E_g^{bulk} + \alpha/D^{\beta}, \\ E_g^{Op,SC} &= E_g^{bulk,op} + \alpha^{'}/D^{\beta^{'}}, \\ E_g^{Op,CI} &= E_g^{bulk,op} + \alpha^{''}/D^{\beta^{''}}, \end{aligned} \tag{11.1}$$

where E_g^{SP}, $E_g^{Op,SC}$, $E_g^{Op,CI}$ are the calculated single-particle gaps, optical band gaps at the SC level, optical band gaps at the CI level, respectively. $E_g^{bulk} = 3.445$ eV [Ref. 269] is the fundamental band gap of bulk ZnO, and $E_g^{bulk,op} = 3.385$ eV is the bulk optical gap. The respective values of the fitting parameters α, β, $\alpha^{'}$, $\beta^{'}$, $\alpha^{''}$, $\beta^{''}$ are 1.26, 1.33, 1.11, 1.5, 0.99, 1.54, where α, $\alpha^{'}$ and $\alpha^{''}$ are in unit of eV $\cdot$ nm, while β, $\beta^{'}$ and $\beta^{''}$ are dimensionless quantities. It is found that the diameter-dependent optical band gap of ZnO NWs (at the CI level), in the presence of quantum confinement effects, scales as $\sim 1/D^{1.539}$, rather than $\sim 1/D$ as predicted by the effective mass approximation.[296] The difference between the single-particle gap and the optical band gap at the CI level gives an exciton binding energy (in meV) which is best fitted by:

$$E_b^X = E_b^{bulk,X} + 310/D^{0.97}, \tag{11.2}$$

where $E_b^{bulk,X} = 60$ meV is the well-known exciton binding energy of bulk ZnO at room temperature. As expected from the quantum confinement effects, the exciton binding energy is significantly enhanced in ZnO NWs in comparison to bulk ZnO ($\sim$ 60 meV at room temperature), giving 111.25 meV at D = 6 nm, 140.99 meV at D = 4 nm and 218.78 meV at D = 2 nm, respectively.

The redshift of the emission spectra with respect to absorption spectra is known as the Stokes shift. It has two possible contributions:[297] (i) a purely electronic shift due to the splitting of exciton states into bright and dark states, which is usually called as *electronic Stokes shift*, and (ii) vibrational (phonon) relaxation due to movement of nuclei to new equilibrium positions in the excited state, which is called as *vibrational Stokes shift*. In general, the vibrational part is very difficult to model[297] since it requires excited state geometry optimization. Moreover, it has been well justified[298,299] that the Stokes shift in III-V and II-VI semiconductor nanostructures is mainly attributed to the (i) contribution. Therefore, in our calculations, the emphasis is put on the *electronic Stokes shift* which for brevity is called as Stokes shift. Its dependence on the NW diameter is shown in Fig. 11.4(d). The results are obtained at two levels of theory: at SC level and at CI level. It is found that the Stokes shift is a *non-monotonic* function of the diameter at both levels, having a maximum at a critical diameter value D_c. This critical values appear to

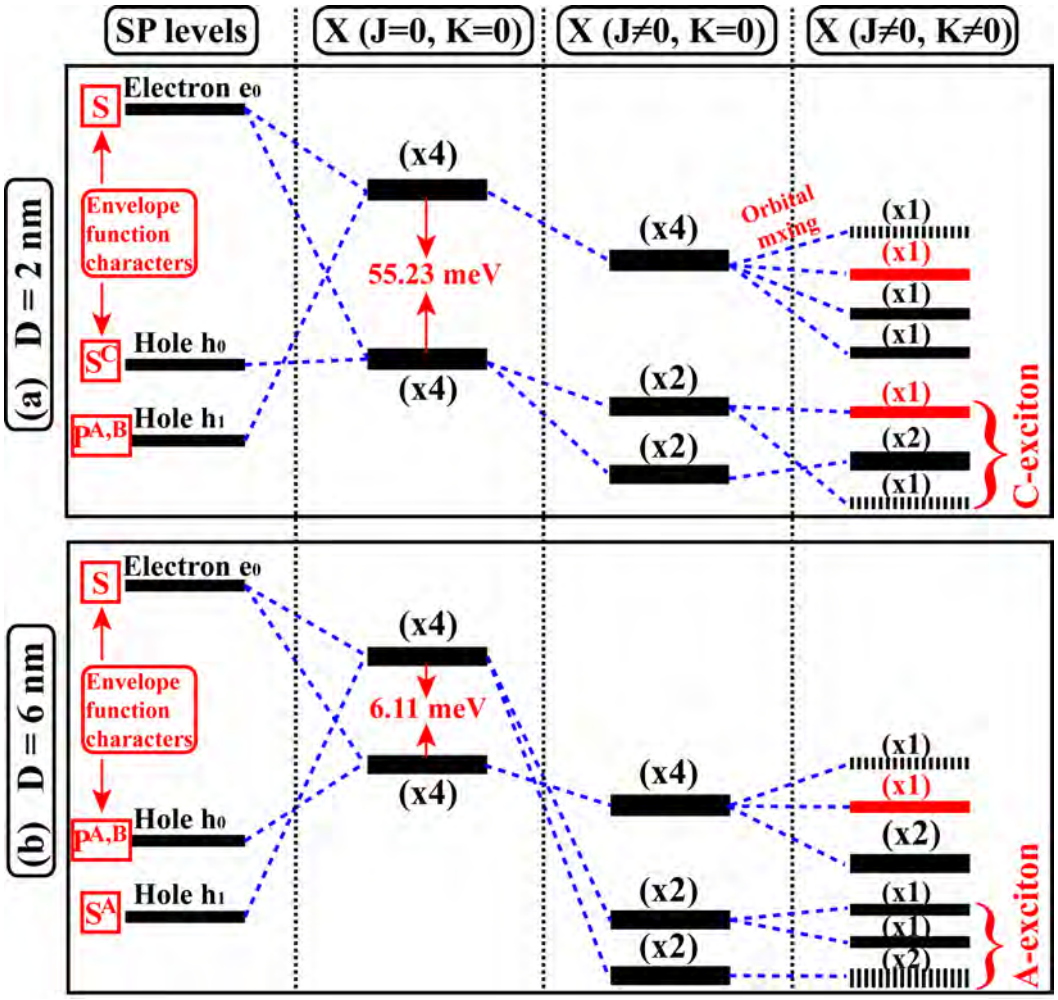

Figure 11.5: Schematic picture of the evolution of the exciton states in ZnO NWs of two different diameters. From the left to the right columns are the single-particle states (column (i)), energy of the uncoupled electron-hole pairs (column (ii)), excitonic states obtained via CI including the Coulomb interaction but neglecting the exchange interaction (column (iii)), final result for the excitonic states including Coulomb, exchange and correlation effects (column (iv)). The numbers in parenthesis indicate the degeneracy of each level. The dark-exciton states, bright-exciton states with in-plane polarization, bright exciton states with out-of-plane polarization are shown in dashed black, solid black and solid red lines, respectively. For columns (ii)-(iv), the lowest total energy is placed at the bottom.

be significantly different at both levels of theory, with $D_c^{SC}\approx$5 nm at SC level, and it is $D_c^{CI}\approx$3 nm at CI level. To understand this behaviour, we take our smallest and largest NWs as examples and present the corresponding near-band-edge exciton pictures in the last column of Fig. 11.5. For $D < D_c$ (top panels in Fig. 11.5), the lowest and first bright exciton states belong to C-exciton at both SC and CI levels (the results at SC level are not shown), being contributed nearly purely (or dominantly) from the configuration where the hole state has an S-type envelope function and derives from bulk Bloch C-band (S^C state). However, for $D \geq D_c$, the two exciton states responsible for the Stokes shift switch to the A-exciton, deriving mainly from the configuration where the hole state has an S-type

envelope function and a dominant bulk Bloch A-band parentage. This diameter-dependent C-exciton to A-exciton transition is responsible for the *non-monotonic* behaviour in Stokes shift.

We find from Fig. 11.5 that the formation of the optically dark and bright states is due to the electron-hole exchange interaction (see the last two columns). The C-exciton consists of one optically dark state and three optically bright states (see the upper panel of Fig. 11.5). The dark state is spin-forbidden and lower in energy. The lowest two bright exciton states are energetically very close to the dark state (i.e., ∼0.013 meV for D = 2 nm (by CI), see Fig. 11.4(d)), being doubly degenerate (with a very small splitting of 0.4 μeV (by CI)) and weakly polarized (with low intensity) along the in-plane direction. The third bright state is energetically far away (i.e., ∼4.01 meV (by CI) to the lowest dark state for D = 2 nm) and is singly degenerate with strong out-of-plane polarization (with high intensity). Concerning the A-exciton (see the lower panel of Fig. 11.5), it consists of two optically dark and two optically bright states. The dark states appear to be degenerate and present the ground state. The two bright exciton states are nearly degenerate with a small splitting of up to 58.25 μeV, being significantly separated from their dark counterparts (e.g., ∼ 0.573 meV for D = 6 nm). These results are in full agreement with the symmetry analysis developed by Hopfield.[300] The Stokes shift originating from different types of exciton is found to exhibit a different diameter-dependence. As shown in Fig. 11.4(d), the Stokes shift derived from C-exciton states is quantitatively much smaller and it increases slightly with increasing diameter. Conversely, the one derived from A-exciton states turns out to be quantitatively much larger and it decreases significantly with respect to the increase in the diameter.

As mentioned previously, the S^A state rises over the S^C state and becomes energetically more favourable for $D > D_c^{A/C} = 4.2$ nm. Therefore, one might expect that the transition between the near-band-edge C-exciton (electron-S—hole-S^C) and A-exciton (electron-S—hole-S^A) takes place around the critical value (≈ 4.2 nm). This is indeed the case if correlation effects are neglected. The maximum of the Stokes shift appears at a critical diameter D_c^{SC}≈5 nm, as shown by the SC results (see Fig. 11.4(d)). However, when the correlation effects are fully considered (see the CI results), the critical value at which the transition occurs shifts to a significantly smaller diameter value (e.g., D_c^{CI} ≈3 nm). This nonmonotonic behaviour in Stokes shift has been found previously in several semiconductor nanostructures, e.g., CdSe nanorods (NRs) [Ref. 273], ZnO NRs [Ref. 269], ZnO QDs under pressure [Ref. 292]. A larger Stokes shift means a smaller overlap area between absorption and emission spectra, which is desirable in applications such as light-emitting diodes, where reabsorption reduces the total efficiency.[273] The transition between different types of excitons have recently been found in GaAs/AlGaAs QDs by applying elastic stress,[301] which is believed to have potential application in quantum technologies.

We also find that the exciton nearly purely derived from a configuration (e, h) where the electron has an S-type envelope function (in LUMO) and the hole has a P-type envelope function does not exhibit the orbitally forbidden, dark ground state (see the lower panel). The exciton ground state appears to be orbitally allowed but spin-forbidden, derived from electron (in LUMO) and hole (in HOMO-1) with both S-type envelope functions, similar to the case of small diameter NWs (see the upper panel of Fig. 11.5). After the detailed analysis of the evaluation of the band-edge exciton states through the stepwise incorporation of Coulomb and exchange interactions (see Fig. 11.5), we find that two combined effects are responsible for this phenomenon:

(i) Increasing the diameter leads to a significant decrease in the energy difference between the two four-fold uncoupled states (see the second column of Fig. 11.5), e.g., the energy difference is 55.23 meV for D = 2 nm, while it is only 6.11 meV for D = 6 nm;

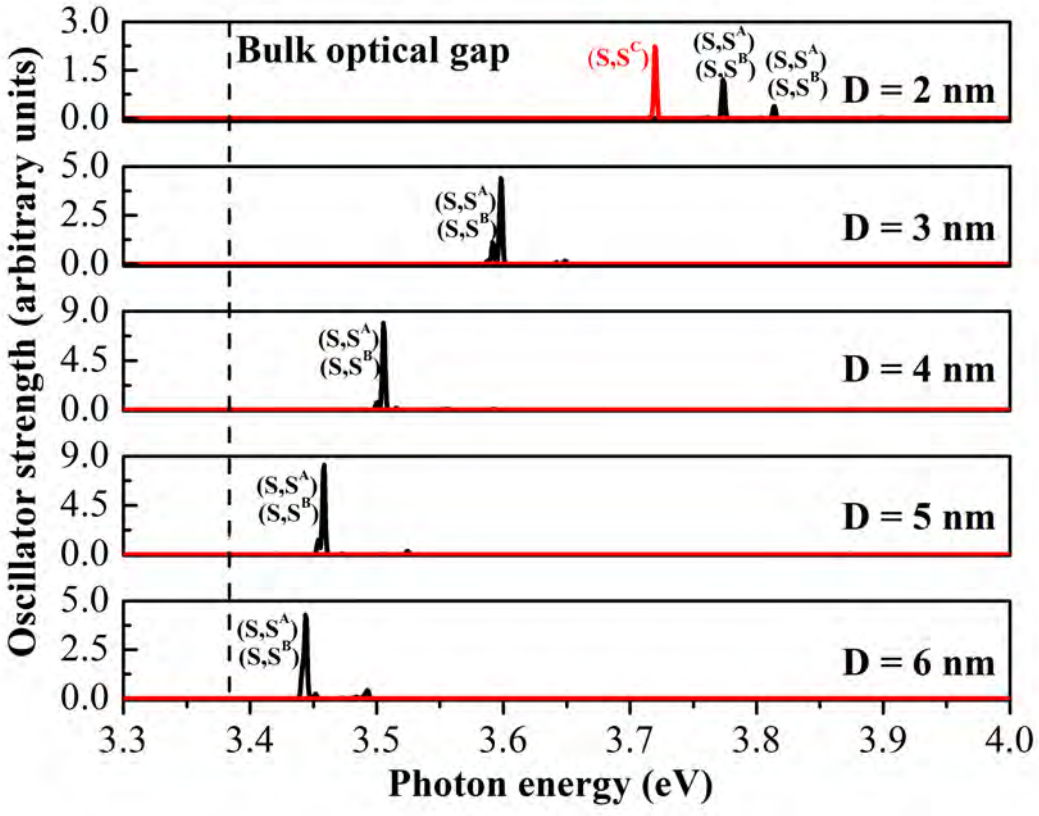

Figure 11.6: Oscillator strength for the absorption $\langle 0|$ to $\langle X|$ in various ZnO NWs at room temperature obtained via CI. Absorptions polarized along the out-of-plane (c axis) and in-plane (perpendicular to the c-axis) directions are shown by red and black vertical lines, respectively. The symbols in parentheses indicate the dominant envelope function characters of the single-particle states (e, h) involved in the emissions, and the parentage of the corresponding hole state is given as superscript.

(ii) The Coulomb interaction is more pronounced for the configuration with both electron and hole having the same envelope function characters (both S-type) than that with electron and hole having different characters (electron: S-type, and hole: P-type), irrespective of the NW diameter. For example, for D = 2 nm, the Coulomb interaction experienced by the configuration (e_0, h_0) $(e_0 - S - h_0 - S)$ is around 218.8 meV, while it is around 213.7 meV for the configuration (e_0, h_1) $(e_0 - S - h_1 - P)$. These two values appear to be 106.6 meV (configuration (e_0, h_0), $(e_0 - S - h_1 - P)$) and 117.9 meV (configuration (e_0, h_1), $(e_0 - S - h_1 - S)$), for D = 6 nm.

This conventional optics from unconventional electronics has also been found previously in ZnO colloidal QDs.[145] Compared to the Coulomb interaction, the influence of the exchange interaction (fourth column of Fig. 11.5) has a significantly smaller magnitude (below 1 meV, depending on the NW diameter) but is important for the optical polarization properties.

Finally, we present in Fig. 11.6 the absorption spectrum at room temperature for various NW diameters. The calculations are performed in the CI scheme. A Gaussian broadening function is adopted with a broadening parameter of 1.2 meV. It is found that increasing the diameter leads to a redshift in the absorption spectrum. This redshift is more pronounced for narrow NWs (with small diameters). Decreasing the NW diameter results in a transition in the optical absorption polarization from an in-plane polarization ($\mathbf{E}\perp\vec{c}$) to an out-of-plane polarization ($\mathbf{E}\parallel\vec{c}$) at a diameter of around 3 nm. This transition between *usual* α-absorption ($\mathbf{E}\perp\vec{c}$) and *unusual* σ and π absorptions ($\mathbf{E}\parallel\vec{c}$) has also been found previously in ZnO QDs under hydrostatic pressures[292] and ZnO NRs by changing the length-to-diameter aspect ratios.[269] Before the transition occurs (e.g., for $D \geq 3$ nm), the near-band-edge optical absorption is dominated by the A- and B-exciton absorptions, which can not be separately resolved experimentally.[277] However, after the transition takes place (e.g., for $D < 3$ nm), the *unusual* C-exciton absorption (σ and π absorptions) becomes active. This type of absorption in ZnO NWs has been recently experimentally achieved by Jacopin *et al.*[277] using a thermal approach. The results we present here offer a new way (e.g., narrowing the NW diameter) to activate the C-exciton absorption in ZnO NWs, which should be very interesting for the design of future experiments in the realm of quantum technology.[301]

11.4 Brief summary

In the present work, we have studied the electronic and optical properties of ZnO NWs as a function of the diameter. We find that the hole states with dominant single-band

(bulk A-, B- or C-band) parentage exhibit S-type envelope functions, while the states with an even mixture of bulk Bloch A- and B-bands present P-type envelope functions. The A-band and B-band states are very close in energy and more sensitive to the NW diameter than the C-band states. Consequently, these states rise over the C-band states at a critical diameters (e.g., $D_c^{A/C} = 4.2$ nm and $D_c^{B/C} = 4.8$ nm) and become energetically more favourable, reproducing the usual electronic structure of bulk ZnO. Comparing to the C-band states, the states with an even mixture of bulk Bloch A- and B-bands parentage exhibit a stronger size-dependence, causing a drastic change in the envelope function character of the highest occupied molecular orbital (HOMO) state from a *conventional* S-like character to an *unconventional* P-like character at diameter around 3.8 nm. The lowest unoccupied molecular orbital (LUMO) state always presents an S-type envelope function, irrespectively of the variation of the quantum confinement effects.

The optical band gap is a decreasing function of the NW diameter and scales as $\sim 1/D^{1.54}$, rather than $\sim 1/D$ as expected from effective mass theory. The exciton binding energy is calculated and the associated scaling law is provided. In contrast to monotonic behaviour in the optical band gap, the Stokes shift displays a non-monotonic function of the diameter, exhibiting a maximum at a critical diameter value around 3 nm. We explain this behaviour through the transition of the near-band-edge exciton from a usual C-exciton to an unusual A-exciton by varying the NW diameters. For NWs larger than the critical diameter, the near-band-edge photoluminescence is dominated by the in-plane polarized A- and B-exciton emissions. For NWs smaller than the critical diameter the out-of-plane polarized C-exciton emission is dominant.

12

New insights in the excitonic emission of ZnS colloidal quantum dots

In this chapter, we have studied the electronic and optical properties of wurtzite ZnS colloidal quantum dots by means of atomistic empirical pseudopotential method complemented by configuration interaction calculations. For this purpose we have developed a new set of reliable pseudopotentials (for Zn and S) which give an accurate and balanced description of ZnS bulk properties. Our results for the size-dependent optical gap are found to be in excellent agreement with the experimental measurements, offering valuable information with regard to the nature of the near-band-edge excitons. In particular, it is found that, not only the first optically allowed exciton is an A-exciton for the full range of dot sizes, but also all the pronounced emission peaks exhibit an in-plane polarization (i.e. A or B excitons). Under normal conditions, the C-exciton emissions which are common in the ZnO analogs are found to be inactive in the lower part of the excitonic spectrum of ZnS colloidal quantum dots. The results presented herein are published in The Journal of Physical Chemistry C ***118****, 10502 (2014).*

Contents

12.1 Introduction

Zinc Sulfide (ZnS), as one of the typical II-VI semiconductor compounds, is an excellent optical material having a wide optical transparency from the ultraviolet (UV) to the far infrared (IR) region.[302,303] It is also widely used for flat panel displays,[304] laser,[305] sensor,[306] cathode ray tube and electroluminescence device[304,307] applications. ZnS usually crystallizes into a cubic zinc-blende (ZB) structure at low temperature which transforms to a more stable hexagonal wurtzite (WZ) structure above 1020 °C under normal pressure.[308,309] Comparing to the ZB counterpart, WZ ZnS exhibits a higher ionization transition rate and therefore has a higher optical gain.[310] The most recent developments are towards nanostructured ZnS, such as nanowires, nanoribbons, nanotubes and quantum dots. Great progresses in the fabrication and characterization of ZnS nanostructures for device application purposes have been committed (see Ref. 311 and references therein). However, several important challenges still remain and await for being explored. One of them is the application of ZnS in transparent and flexible electronics due to the challenge which exists in optimization of nanodevice performances. Although several ways to optimize the performances of ZnS-based devices have been exploited, more work on tuning the conductivity, band gap, surface and optical properties is still quite desired.[311]

From a theoretical standpoint, Density functional theory (DFT) calculations have been widely employed for the study of the bulk ZnS band structure,[312–314] the geometric and the electronic properties of ZnS nanowires, nanotubes, nanosheets.[315] These types of calculations are restricted to nonpassivated and small size nanostructures. Since in DFT the band gap in bulk ZnS are not well-reproduced,[313] the description of the quantum confinement effects in ZnS nanostructures is questionable. Furthermore, effective mass and tight binding models have been applied to interpret the experimental measurements of ZnS QDs with realistic sizes. However, these approaches are either only appropriate for QDs within the weak confinement regime or significantly underestimate the optical band gap.[316]

In this Chapter, we derived a new empirical pseudopotential for wurtzite ZnS, which reproduced well the experimental and/or theoretical bulk properties, such as band gap, critical energy levels, effective masses, crystal-field and spin-orbit splitting. This allows us to calculate electronic and optical properties of wurtzite ZnS QDs with realistic sizes at an atomistic level by means of empirical pseudopotential method and configuration interaction approach. We studied the size-dependent optical band gap, Stokes shift and optical emission polarizations of ZnS colloidal QDs. Our calculated optical band gap is in very good agreement with the experimental work. For the full range of QD sizes

studied, the near-band-edge exciton emission is polarized along the in-plane direction, corresponding to A-exciton emission.

12.2 Computational details

12.2.1 Crystal structure of bulk ZnS

We use the experimental structure parameter for bulk wurtzite ZnS and constructing wurtzite ZnS QDs later on, which are listed in Table 12.1. Similarly to wurzite ZnO, there are four atoms per unit cell, that is, two Zn atoms and two S atoms. The lattice vectors of the unit cell, and the atom positions in the unit cell in Cartesian and fractional coordinates can be obtained from Tables 10.1, 10.2 and 10.3, respectively, by using the above mentioned structure parameters. In wurzite ZnS, there are two types of bond length: one is $R^{(1)} = uc = 2.338$ Å and the other one $R^{(2)} = \frac{\sqrt{3c^2(1-2u)^2+4a^2}}{2\sqrt{3}} = 2.334$ Å, and two types of angles $\theta^{'}$ and θ with

$$\theta^{'} = \arccos\left(\frac{-\sqrt{3}c(1-2u)}{\sqrt{3c^2(1-2u)^2+4a^2}}\right) = 109.44^{\circ}, \tag{12.1}$$

and

$$\theta = \arccos\left(\frac{3c^2(1-2u)^2-2a^2}{3c^2(1-2u)^2+4a^2}\right) = 109.502^{\circ}, \tag{12.2}$$

respectively.

Table 12.1: Structure parameters a, c, u and c/a for wurtzite ZnS.

a (Å)	c (Å)	u	c/a
3.811[241]	6.234[241]	0.375[241]	1.63579[241]

12.2.2 Generate empirical pseudopotentials for ZnS

We follow the atomistic empirical pseudopotential method[145,269,292,317,318] and derive new pseudopotentials for Zn and S. The Hamiltonian has the form

$$\hat{\mathrm{H}} = -\frac{1}{2}\nabla^2 + \sum_{n\alpha}[v_\alpha(\vec{\mathbf{r}} - \vec{\mathbf{R}}_{\alpha n}) + \hat{\mathrm{v}}_\alpha^{SO}], \tag{12.3}$$

where n is an atomic index, α specifies the atom type, and $\hat{\mathrm{v}}_\alpha^{SO}$ is the nonlocal spin-orbit operator, including one parameter λ for each atom type. The screened atomic pseudopotentials v_α (with $\alpha =$ Zn, S) are centered at each atomic position and their superposition generates the crystal potential. In the present work, we employed pseudopotentials with four free parameters, which are defined in reciprocal space, having the analytic form

$$v_\alpha(q) = \frac{\alpha_1(q^2 - \alpha_2)}{\alpha_3 e^{\alpha_4 q^2} - 1}. \tag{12.4}$$

This exponential type of pseudopotential has been successfully adopted previously for the study of electronic and optical properties of wurtzite ZnO nanostructures.[145,269,292,318] The quasicubic model of Hopfield[300] is adopted to obtain the spin-orbit Δ_{so} and crystal-field Δ_{cr} splittings

$$\begin{aligned} E_A(\Gamma_{9v}) &= \frac{1}{2}(\Delta_{so} + \Delta_{cr}), \\ E_{B(C)}(\Gamma_{7v}) &= \pm\frac{1}{2}[(\Delta_{so} + \Delta_{cr})^2 - \frac{8}{3}\Delta_{so}\Delta_{cr}], \end{aligned} \tag{12.5}$$

where E_A, E_B and E_C are the energies of the top three valence bands at Γ point of the Brillouin Zone.

To define the free parameters a_1, a_2, a_3, a_4 and λ, the unknown eigenfunctions of Hamilton (12.3) are expanded by using the plane wave basis set. The plane wave energy cutoff is 8.5 Ryd and the Kinetic energy is not re-scaled. The Schrödinger's equation is solved by using the direct diagonalization method (see Section 9.4.1 of Chapter 9). During the generation procedure, larger weight has been allocated to the quantities close to the conduction band minimum (CBM) and valence band maximum (VBM), while smaller weight has been put on these quantities which are remote from CBM and VBM. This procedure is ended until the known bulk properties of wurtzite ZnS, such as the energy gaps at specific symmetry points of the Brillouin Zone, the perpendicular and parallel effective masses of electron and hole, the spin-orbit, and crystal-field splitting (see Table 12.2), are well-reproduced.

Table 12.2: Compiled reference bulk properties and empirical pseudopotential results (including spin-orbit interaction) using the parameters presented in Table 12.3.

Quantities	Experiment	Theory	Targets	EPM
$E_g(\Gamma_{1c}-\Gamma_{6v})$	3.864,[146] 3.872,[146] 3.75,[319] 3.76,[320] 3.78[321]	1.968,[313] 2.211,[313] 2.260[313]	3.75	3.739
$E_g(\Gamma_{3c}-\Gamma_{1c})$		1.5[322]	1.5	1.59
$E_g(\Gamma_{6c}-\Gamma_{1c})$		4.4[322]	4.4	4.40
$E_g(\mathrm{H}_{3c}-\Gamma_{1c})$		2.7[322]	2.7	2.55
$E_g(\mathrm{K}_{2c}-\Gamma_{1c})$		1.8[322]	1.8	1.526
$E_g(\mathrm{M}_{1c}-\Gamma_{1c})$		1.6[322]	1.6	1.52
$m_e^{\perp}$		0.33,[146] 0.153,[313] 0.199,[313] 0.157[313]	0.33	0.079
$m_e^{\parallel}$	0.24[146]	0.144,[313] 0.142,[313] 0.138[313]	0.24	0.100
$m_A^{\perp}$	0.49[146]	3.838,[313] 1.713,[313] 2.914,[313] 1.470[241]	0.49	1.15
$m_A^{\parallel}$	1.40[146]	1.746,[313] 2.176,[313] 1.785,[313] 1.51[241]	1.40	5.02
$m_B^{\perp}$		0.485,[146] 0.180,[313] 0.198,[313] 0.195[313]	0.485	0.21
$m_B^{\parallel}$		0.53,[146] 0.756,[313] 0.402,[313] 0.621[313]	0.53	0.42
$m_C^{\perp}$		0.75,[146] 0.337,[313] 0.443,[313] 0.303[313]	0.75	1.23
$m_C^{\parallel}$		0.32,[146] 0.183,[313] 0.440,[313] 0.339[313]	0.32	0.27
Δ_{cr}	0.058,[146] 0.055,[146] 0.029[146]	0.052,[313] 0.049,[313] 0.055[313]	0.0580	0.0526
Δ_{so}	0.086,[146] 0.089,[146] 0.092[146]	0.027,[313] 0.025,[313] 0.026[313]	0.086	0.0926

The optimized four free parameters for Zn and S are listed in Table 12.3 and the volume normalized local parts of the Zn and S pseudoptentials are presented in Fig. 12.1(a). Using these pseudopotentials, the computed quantities of bulk wurtzite ZnS are in very good agreement with existing experimental and/or theoretical results (see Table 12.2). The calculated band structure is depicted in Fig. 12.1(b) which reproduces almost exactly the result of Bergstresser and Cohen.[322]

Table 12.3: Empirical pseudopotential parameters $a_{1,2,3,4}$ and spin-orbit parameter λ.

	a_1	a_2	a_3	a_4	λ
Zn	-5.091010	0.000005	-0.011512	0.285308	0.1165
S	-20.220911	3.750462	-0.000227	1.465173	0.0

12.2.3 Input geometry

After deriving the reliable atomic pseudopotentials, we turn our attention to the study of the electronic and optical properties of wurtzite ZnS colloidal QDs. The QDs are cut from the bulk ZnS with a spherical shape, being centered on an Sulfide atom. The surface dangling bonds are passivated by employing a high band gap artificial material, as successfully practised previously.[145,240,269,292,293] The geometry of our smallest QD structure (e.g., with radius R = 1 nm, unpassivated) is displayed in Fig. 12.2(a) and the

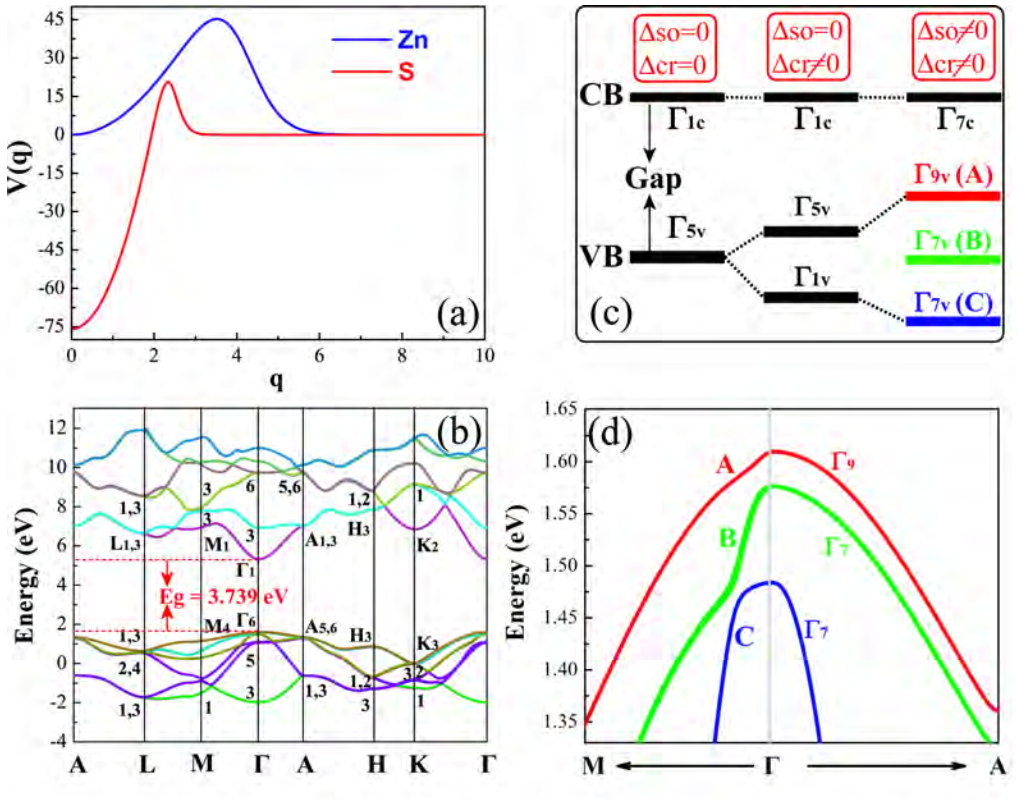

Figure 12.1: (a) Normalized atom pseudopotentials for Zn and S. (b) Band structure of wurtzite ZnS by our empirical pseudopotential methods (EPM) including spin-orbit interaction. (c) Schematic representation of the symmetry evolution of the conduction band minimum (CBM) and valence band maximum (VBM) of bulk ZnS by the crystal-field and/or spin-orbit splitting. (d) Topmost three valence bands around Γ-point of the Brillouin Zone obtained by EPM including spin-orbit splitting.

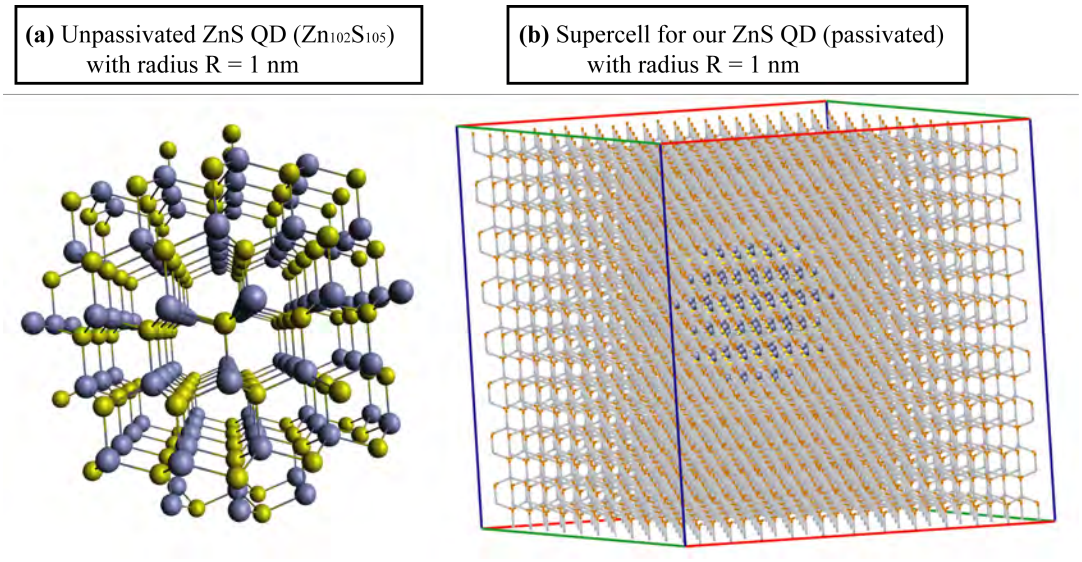

Figure 12.2: (a) Geometry of our $Zn_{102}S_{105}$ quantum dot (Radius R = 1 nm) and (b) its corresponding suppercell used in our calculations. The blue and yellow balls represent the Zn and S atoms, respectively.

corresponding supercell used in our calculations are shown in Fig. 12.2(b).

12.2.4 Calculations of electronic and optical properties

The single-particle electron and hole eigenenergies and wave functions are calculated by the aforementioned empirical pseudopotential method which naturally includes the effects of multiband coupling, multivalley coupling, and spin-orbit interaction. The many-body excitonic properties are calculated via configuration interaction (CI) approach[263] and the excitonic wave functions are expanded in terms of single-substitution Slater determinants constructed from the single-particle wave functions of electrons and holes (see Section 9.5 of Chapter 9). The Coulomb and exchange integrals are screened by the position-dependent and size-dependent screening function proposed by Resta,[248] which gives a smooth transition from short range (unscreened) to long range (screened)[263,293] (see Subsection 9.5.2 of Chapter 9). We include in the CI treatment 4 states from the conduction band and 10 states from the valence band. The optical dipole matrix elements are calculated within the dipole approximation, and the oscillator strength was calculated using Fermi's golden rule (see Subsection 9.5.3 of Chapter 9).

12.3 Results and discussion

12.3.1 Valence band ordering of bulk ZnS

Before presenting our QD results, we briefly describe the valence band structure of bulk ZnS which is relevant to the later discussion. Without crystal-field and spin-orbit splitting, the top valence band of ZnS is six-fold Γ_{5v} state (see Fig. 12.1(c)). This state is split into a four-fold Γ_{5v} state and a two-fold Γ_{1v} state by the crystal field which is a typical characteristic of wurtzite structure. The Γ_{5v} state is a p_x, p_y-like state, while Γ_{1v} state is a p_z-like state. Further inclusion of spin-orbit coupling leads to a splitting of the four-fold Γ_{5v} state into two doubly-degenerate states, which are corresponding to the heavy hole and light hole states, respectively. The two-fold Γ_{1v} state is transferred accordingly to the spin-split-off hole state. For wurtzite ZnS, the spin-orbit parameter is positive, which is pretty similar to wurtzite GaN. In this conventional situation, the top three valence bands, from top to bottom, are the so-called bulk A-, B-, C-bands, respectively, which are of symmetry character Γ_{9v}, Γ_{7v} and Γ_{7v}, respectively (see Fig. 12.1(d)). It should be mentioned that although wurzite ZnS exhibits a normal valence band ordering, the generation of reliable atomistic pseudopotentials appears to be an uneasy task in comparison to its ZnO counterpart which has an abnormal valence band ordering.[145]

12.3.2 Electronic properties of ZnS quantum dots

We have studied wurtzite ZnS colloidal QDs with experimentally achievable sizes, which are defined by radii R = 1 nm, 1.5 nm, 1.75 nm, 2.25 nm, 2.5 nm, respectively. The numbers of atoms for each respective radius are $Zn_{102}S_{105}$, $Zn_{356}S_{359}$, $Zn_{573}S_{575}$, $Zn_{1222}S_{1207}$ and $Zn_{1646}S_{1677}$.

Firstly, we present the electron and hole envelope functions for each dot size in Fig. 12.3. These envelope functions are obtained by employing the projection onto bulk technique[145] which gives us the access to visualize the symmetry of the envelope functions and the parentage of the atomic wave function of each state. We use the notation ω_ζ to describe the symmetry of the envelope functions, where ω donates the number of nodes encountered by moving across the in-plane (xy-direction) or out-of-plane (z-direction) directions, and ζ represents the direction in which we find the node(s). The possible values for ω are S,

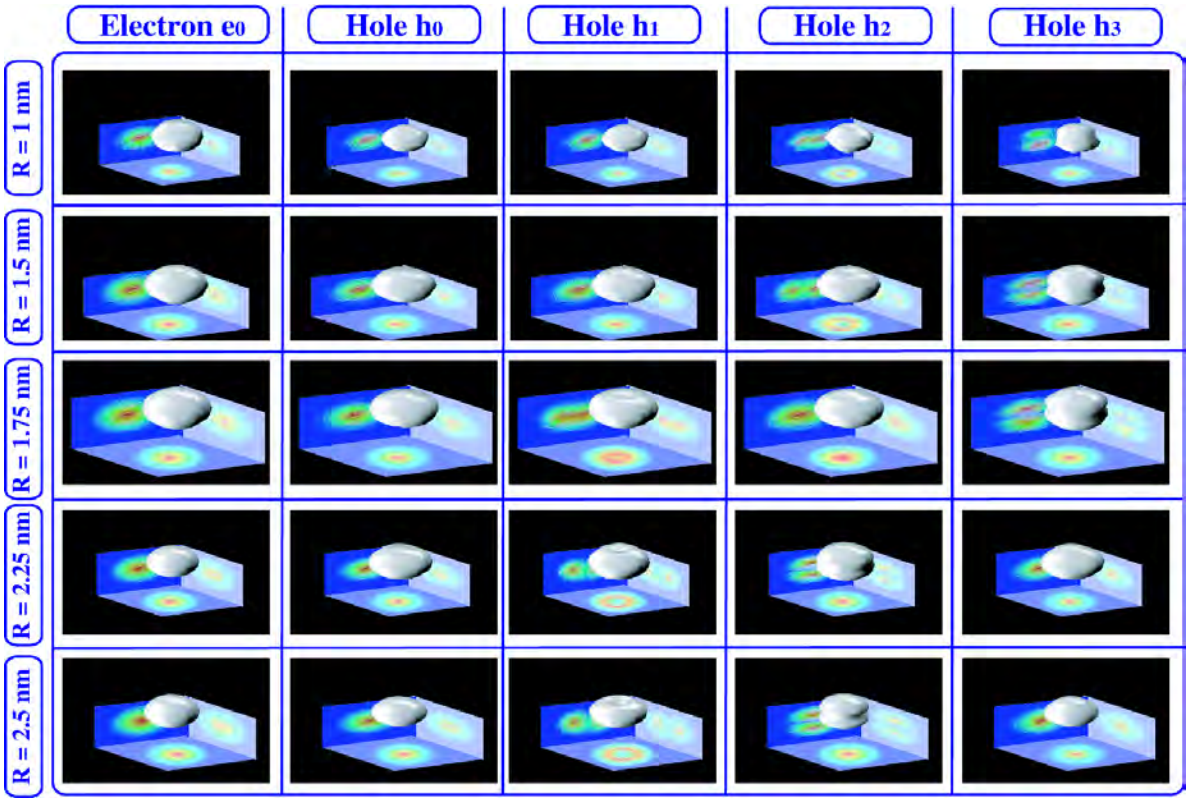

Figure 12.3: The first electron (e_0) and first four hole ($h_{0,1,2,3}$) envelope functions for five different radii.

P, etc., where S indicates the form of the envelope function without a node (in this case, we neglect the subscript ζ), P with one node, etc. Using this notation, the symmetry characters for the first electron and first four hole states are tabulated in Table 12.4. The evolution of the parentage of each hole state with respect to the dot size is pictured in Fig. 12.4.

Table 12.4: Character of the first electron and first four hole envelope functions for various QD radii. The superscript (A and/or B) indicates the corresponding hole state parentage (A-band, B-band or A, B-bands mixing).

Radius (nm)	e_0	h_0	h_1	h_2	h_3
1	S	S^A	S^B	$P_{xy}^{A,B}$	P_z^A
1.5	S	S^A	S^B	$P_{xy}^{A,B}$	P_z^A
1.75	S	S^A	$P_{xy}^{A,B}$	S^B	P_z^A
2.25	S	S^A	$P_{xy}^{A,B}$	P_z^A	S^B
2.5	S	S^A	$P_{xy}^{A,B}$	P_z^A	S^B

We find from Table 12.4 and Fig. 12.4 that the states having S-type characters (S^A or S^B)

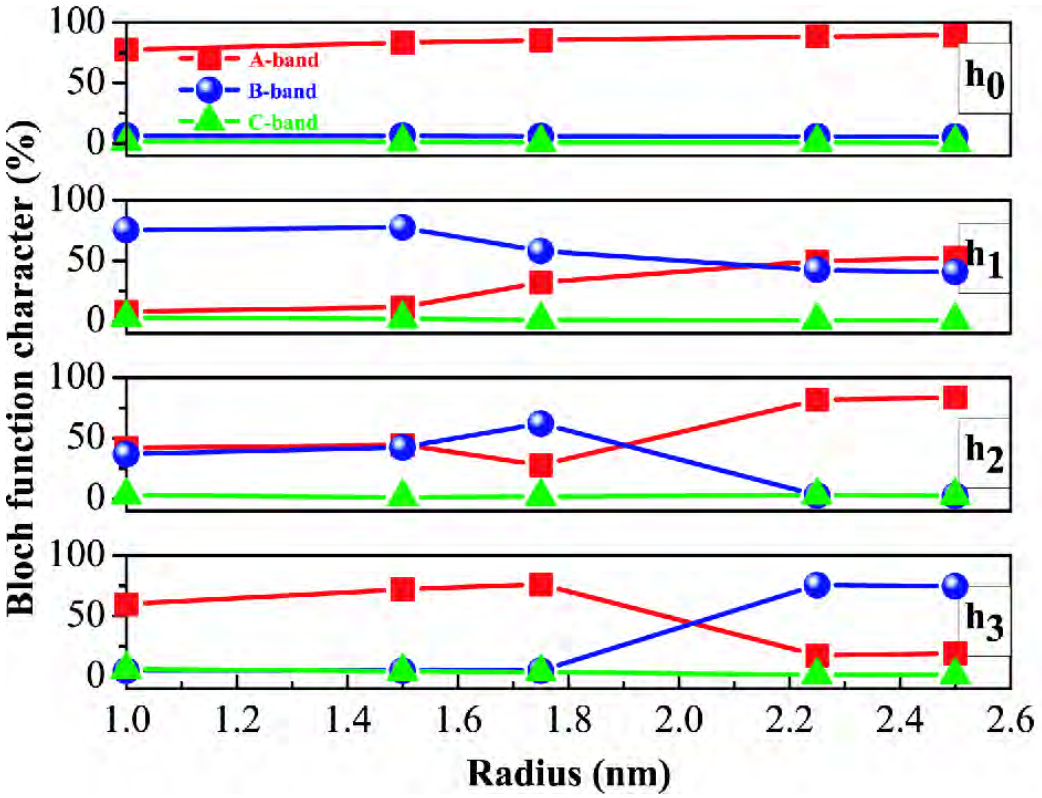

Figure 12.4: Bloch function characters of the first four hole states for various radii. The red, green and blue colors are corresponding to the bulk bloch A-, B- and C-bands, respectively.

are derived mainly from a single-band state (either A-band or B-band). These conventional S^A and S^B states are separated significantly from each other in energy, whereas their energetic dependence on the QD sizes appears to be very similar (see Fig. 12.5). This is a consequence of the nature of topmost valence band structure of bulk ZnS, where A-band and B-band are energetically separated considerably (see Fig. 12.1(c) and (d)). We further find that the states with an even admixture of bulk A- and B-band parentage (e.g., h_1 at $R = 1.75$ nm, 2.25 nm, 2.5 nm) display P_{xy}-type envelope function characters. These $P_{xy}^{A,B}$ characters have also been found previously in wurtzite ZnO nanostructures[145,269,292] and very recently in wurtzite GaN nanowires,[295] being attributed to be one of consequences of the nontrivial interplay between symmetry mixing, spin-orbit coupling and quantum confinement effects on the valence band electronic structure. Comparing to the S-like states, these states appear to be more sensitive to the quantum confinement effects, rising over the S^B state at a critical radius value $R^c = 1.66$ nm and becoming energetically more favourable (see Fig. 12.5).

In addition to the S-type envelope function characters, the states with a dominant bulk Bloch A-band parentage also exhibit P-like characters (e.g., h_3 at $R = 1$ nm, 1.5 nm, 1.75 nm, see Table 12.4) with a node exclusively along the out-of-plane direction. The reason for the fact that the P_{xy}^A-like states are energetically separated from the P_z^A-like states is related to the anisotropic hole effective masses of the bulk A-band, which is larger along

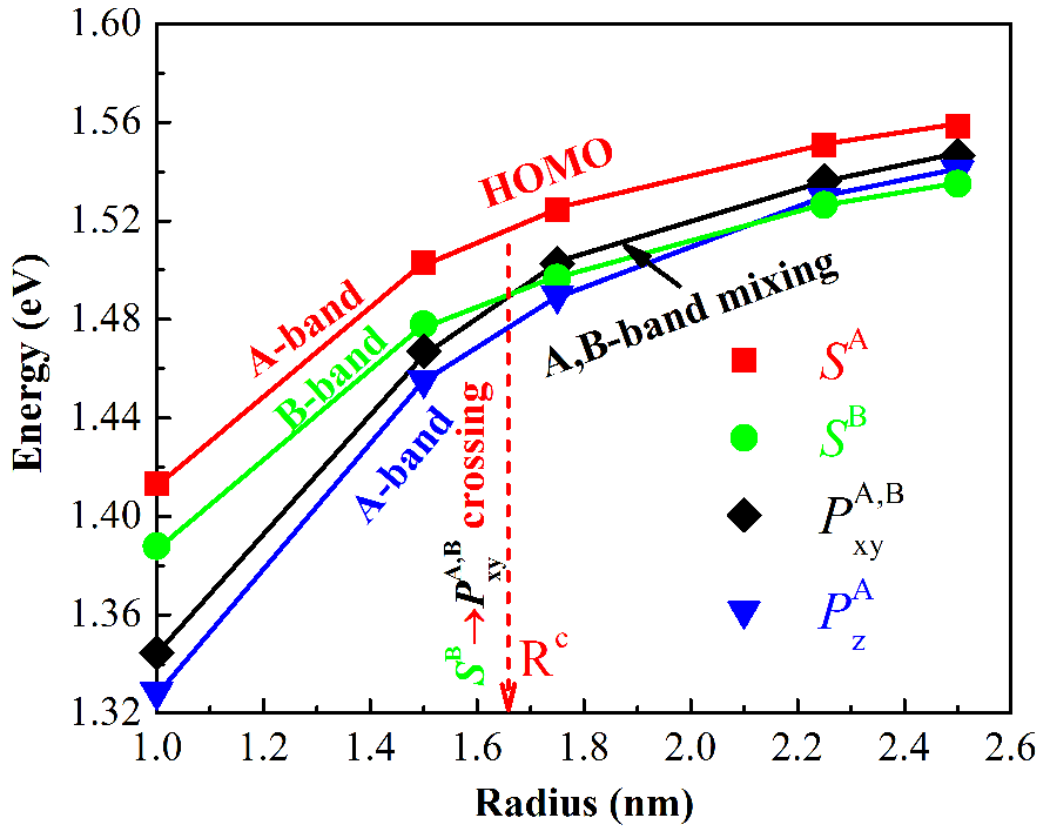

Figure 12.5: Single particle energies of the first four hole states as a function of the QD radius. The lines connected states are of the same symmetry. The red (or blue), green, black lines connect states with dominant A-band, B-band, and an even mixing of A- and B-band parentage, respectively.

the direction parallel to the c-axis ($m^*_{A\parallel} > m^*_{A\perp}$, see Table 12.2). This favours a state with a node along the out-of-plane direction, P^A_z, rather than with a node along the in-plane direction, P^A_{xy}. These P^A_z-like states are energetically very close to the $P^{A,B}_{xy}$ states, showing a similar sensitivity of energy to the variation of the quantum confinement effects (see Fig. 12.5). In contrast to the A-band and/or B-band states, the states with dominant C-band parentage are not energetically very favourable, being remote from HOMO state (e.g., h_9 at $R = 1.5$ nm, not shown in the figures for clarity). The lowest unoccupied molecular orbital (LUMO) state turns out to be a single band object deriving purely from bulk Γ_{7c} band and presenting an S-type envelope function.

12.3.3 Optical properties of ZnS quantum dots

We present the optical band gap of ZnS colloidal QDs with realistic sizes in Fig. 12.6. The necessary material parameters used in our calculations are given in Ref. 323. The

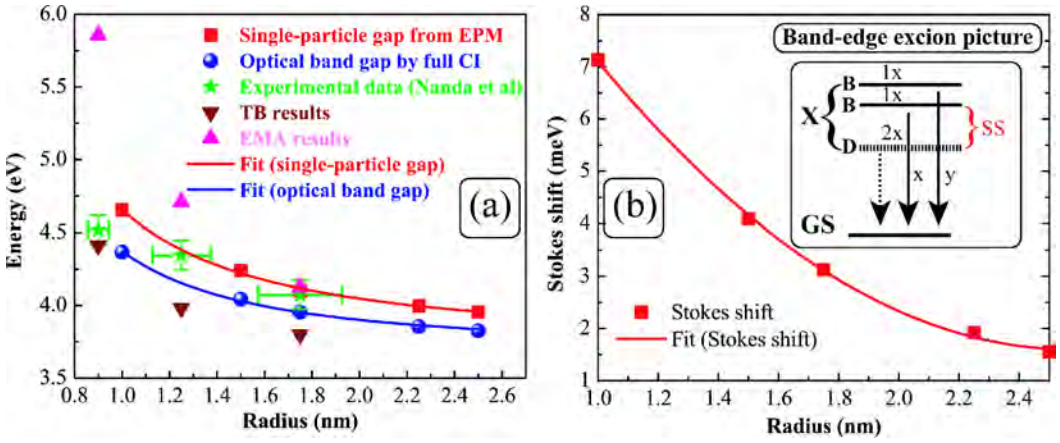

Figure 12.6: (a) Single-particle gap (red boxes) and optical band gap (blue circles) as a function of the QD radius. The green stars with error bars, the wine inverted triangles and pink regular triangles are the experimental results, the values calculated from the effective mass approximation (EMA) and tight-binding (TB) models (Ref. 316), respectively. Each line represents a fit of the band gap energy by $E_g = \alpha + \beta/R^{\gamma}$ where E_g is the band gap energy, R is the QD radius, α, β, γ are the fitting parameters. (b) The Stokes shift (SS, red boxes) as a function of the QD radius. The red solid line donates a parabolic fit of the Stokes shift. The inset shows the near-band-edge exciton picture and corresponding emission polarization directions (x or y). X indicates the near-band-edge exciton (A-exciton) which is consisted of a doubly degenerate (2x) dark (D) state and two non-degenerate (1x) bright (B) states decaying to the ground state (GS).

calculations are performed at single-particle level and configuration interaction (CI) level, respectively. The calculated optical band gap appears to be in very good agreement with the experimental measurements by Nanda et al.[316] for the full range of QD sizes in comparison to the results based on the effective mass model[324,325] and semiempirical tight binding model.[326] The dependence of the band gap on the QD radius is best fitted by $E_g^{SP} = E_g^{bulk} + 0.91/R^{1.61}$ at single-particle (SP) level where $E_g^{bulk} = 3.75$ eV is the fundamental gap of bulk ZnS (see Table 12.2), and $E_g^{CI} = E_g^{bulk,opt} + 0.66/R^{1.79}$ at full CI level in which $E_g^{bulk,opt} = 3.709$ eV is the optical gap of bulk ZnS, respectively. Here E_g is in unit of eV and R is in unit of nm. The exciton binding energy can be obtained by subtracting the SP results from the correlated results (CI results), best fitted by $E_b^X = E_b^{X,bulk} + 240.95/R^{1.81}$ where $E_b^{X,bulk} = 41$ meV is the exciton binding energy of bulk ZnS at room temperature[327] and all the energies are in unit of meV. In an attempt to bridge our findings to other material systems, the scaling law associated with the calculated exciton binding energy can also be written as $E_b^X \backsim 1/R^n$ with $n = 0.919$ which appears to be larger than its counterpart for CdSe colloidal QDs obtained theoretically by Franceschetti and Zunger (i.e., $n = 0.86$ [Ref. 328]) and experimentally by Meulenberg et al. (i.e., $n = 0.72$ [Ref. 329]). We also find that the obtained exciton binding energy exhibits a *sublinear* dependence on the QD radius, which is consistent with the results reported previously for CdSe QDs.[328,329] As expected from the quantum confinement

effects, the exciton binding energy is significantly enhanced in colloidal ZnS QDs in comparison to bulk ZnS, giving 130 meV at $R = 2.5$ nm, 145 meV at $R = 1.75$ nm and 284 meV at $R = 1$ nm, respectively.

The near-band-edge exciton is found to be A-exciton for all the QD sizes, which is contributed nearly purely from HOMO-LUMO transition, where the HOMO state has a S-like symmetry character and derives dominantly from bulk A-band. This type of exciton consists of two optically passive (dark) states and two optically active (bright) states. The formation of these dark-exciton (or bright-exciton) states are originated from the electron-hole exchange interaction.[298,330] The exchange interaction gives rise to the splitting between the singlet and triplet states. The aforementioned two dark-exciton states are orbitally allowed but spin-forbidden (spin-triplet states), being doubly degenerate and energetically favourable. The two bright-exciton states (spin-singlet states) appear to be singly-degenerate and energetically very close to each other, exhibiting in-plane polarizations.

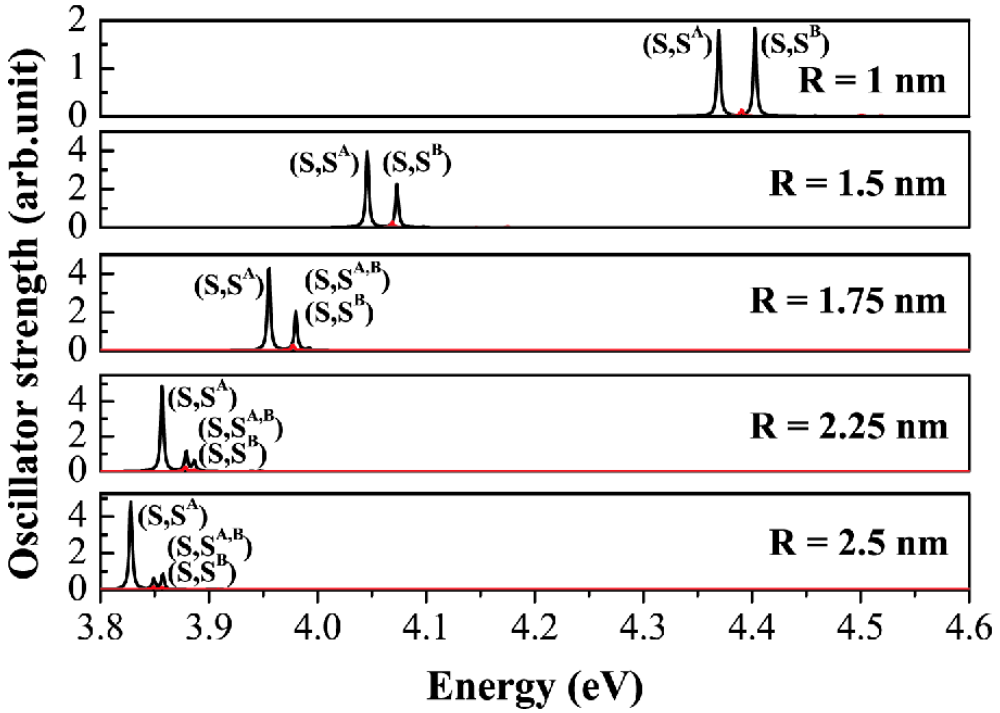

Figure 12.7: Oscillator strength for the emission $|X\rangle$ to $|0\rangle$ for various QD sizes obtained by full CI at room temperature. Emissions polarized along the in-plane and out-of-plane directions are shown in black red lines, respectively. The symbols in parentheses indicate the envelope function characters of the single-particle states (e, h) involved in the emissions (for the hole state, the corresponding parentage has also been shown).

The energetic difference between the first bright-exciton state and the first dark-exciton

state is defined as Stoke shift (SS). The SS is in the scale of 10^{-3} eV, being a decreasing function of the QD sizes (see Fig. 12.6(b)). This is qualitatively consistent with the previous reports[331–333] for wurtzite CdSe and CdS colloidal QDs. The calculated SS is found to be in a similar energy window as that of similarly sized CdSe counterparts ($\sim$ 5 - 20 meV [Ref. 331]). However, it turns out to be quantitatively much smaller than that of CdS analogs ($\sim$ 20 - 70 meV for radius of R = 1 - 2.3 nm [Ref. 333]). This is related to different near-band-edge dark-exciton mechanisms. The lowest dark-exciton state of CdS QDs is orbitally forbidden (electron-S-hole-P),[333] in contrast to that of CdSe[331] and our ZnS QDs with orbitally allowed but spin-forbidden (electron-S-hole-S) ground-state dark-exciton states. The dependence of the our obtained SS on the QD radius within the range studied is best fitted by $E^{SS} = 16.31 - 11.43R + 2.22R^2$, where E^{SS} is in unit of meV (see Fig. 12.6(b)).

Finally, we present in Fig. 12.7 the photoluminescence emission spectrum for various QD sizes, which are obtained by full CI at room temperature. Lorentzian broadening function is employed and the broadening parameter is chosen as 1.5 meV. As expected, increasing the QD sizes leads to a significant redshift in the emission spectrum. This redshift is more pronounced for smaller QDs. For all the QD sizes, the pronounced emissions are polarized exclusively along the in-plane direction ($\mathbf{E}\perp\vec{c}$, α-emission[277]) and attributed to A- and B-exciton emissions. The C-exciton emissions with out-of-plane polarization appear to be not active in ZnS colloidal QDs under normal conditions.

12.4 Brief summary

In conclusion, we have derived a new and reliable empirical pseudopotential for wurtzite ZnS which enables us to study the size-dependent electronic and optical properties of ZnS colloidal quantum dots at an atomistic level. The single-particle states are calculated by employing empirical pseudopotential method and the many-body excitonic effects are considered via configuration interaction approach. We find that the highest occupied molecular orbital (HOMO) states have a dominant bulk Bloch A-band parentage, exhibiting S-like envelope function characters. These S^A states are energetically separated significantly from their counterparts originated mainly from bulk bloch B-band with S-like envelopes. We related this to the nature of the topmost valence band structure of wurtzite ZnS where A-band and B-band are separated considerably in energy. The states with an even admixture of bulk A-band and B-band turn out to have P_{xy}-like characters.

In addition to the S-type symmetry characters, the states with a dominant A-band parentage also exhibit P-like characters but with nodes exclusively along the out-of-plane

direction. This is attributed to the anisotropy of the hole effective masses of the bulk bloch A-band. The calculated optical band gaps are in excellent agreement with the experiments which confirms the accuracy of the present method. We provide scaling laws for the experimentally measurable physical quantities, such as optical band gap and Stokes shift, for the full range of QD sizes. Finally, we find that the near-band-edge exciton is A-exciton and the pronounced exciton emissions are from A-exciton and/or B-exciton emissions with in-plane polarizations. The C-exciton emissions with out-of-plane polarization are found to be not active in ZnS colloidal quantum dots under normal conditions.

Bibliography

[1] A. I. M. Rae. *Quantum Mechanics*. Institute of Physics Publishing, Bristol and Philadelphia, 2002.

[2] T. Kato. *Perturbation Theory for Linear Operators*. Springer-Verlag Berlin Heidelberg New York, 1980.

[3] M. Rieth, W. Schommers, and S. Baskoutas. Exact numerical solution of Schrödinger's equation for a particle in an interaction potential of general shape. *Int. J. Mod. Phys. B*, 16:4081–4092, 2002.

[4] W. Schweizer, P. Faßbinder, R. González-Ferez, M. Braun, S. Kulla, and M. Stehle. Discrete variable and finite element techniques applied to simple atomic systems. *J. Comput. Appl. Math.*, 109:95 – 122, 1999.

[5] J. P. Killingbeck. *Microcomputer Quantum Mechanics*. Adam Hilger Ltd, Bristol.

[6] D. Mocatta, G. Cohen, J. Schattner, O. Millo, E. Rabani, and U. Banin. Heavily doped semiconductor nanocrystal quantum dots. *Science*, 332:77, 2011.

[7] R. Rahman, G. P. Lansbergen, Seung H. Park, J. Verduijn, G. Klimeck, S. Rogge, and Lloyd C. L. Hollenberg. Orbital stark effect and quantum confinement transition of donors in silicon. *Phys. Rev. B*, 80:165314, 2009.

[8] C. Bose. Binding energy of impurity states in spherical quantum dots with parabolic confinement. *J. Appl. Phys*, 83:3089, 1998.

[9] J. L. Movilla and J. Planelles. Off-centering of hydrogenic impurities in quantum dots. *Phys. Rev. B*, 71:075319, 2005.

[10] H. A. Kassim. Study of shallow donor level binding energies confined in a GaAs-$Ga_{1-x}Al_xAs$ spherical quantum dot. *J. Phys: Condens. Matter*, 19:036204, 2007.

[11] G. Wang and P. Zhang. Hydrogenic impurity binding energy in self-assembled GaAs/$Ga_{1-x}Al_xAs$ quantum rings. *J. Appl. Phys.*, 103:063713, 2008.

[12] F. Dujardin, A. Oukerroum, E. Feddi, J. Bosch Bailach, J. Martinez-Pastor, and M. Zazi. Effect of a lateral electric field on an off-center single dopant confined in a thin quantum disk. *J. Appl. Phys.*, 111:034317, 2012.

[13] J. W. Robinson, J. H. Rice, K. H. Lee, J. H. Na, R. A. Taylor, D. G. Hasko, R. A. Oliver, M. J. Kappers, C. J. Humphreys, and G. Andrew D. Briggs. Quantum-confined stark effect in a single InGaN quantum dot under a lateral electric field. *Appl. Phys. Lett.*, 86:213103, 2005.

[14] K. Kowalik, O. Krebs, A. Lemaitre, S. Laurent, P. Senellart, P. Voisin, and J. A. Gaj. Influence of an in-plane electric field on exciton fine structure in InAs-GaAs self-assembled quantum dots. *Appl. Phys. Lett.*, 86:041907, 2005.

[15] T. Nakaoka, S. Kako, and Y. Arakawa. Unconventional quantum-confined stark effect in a single GaN quantum dot. *Phys. Rev. B*, 73:121305, 2006.

[16] B. D. Gerardot, S. Seidl, P. A. Dalgarno, R. J. Warburton, D. Granados, J. M. Garcia, K. Kowalik, O. Krebs, K. Karrai, A. Badolato, and P. M. Petroff. Manipulating exciton fine structure in quantum dots with a lateral electric field. *Appl. Phys. Lett.*, 90:041101, 2007.

[17] S. Ritter, P. Gartner, N. Baer, and F. Jahnke. Anomalous stark effect in semiconductor quantum dots. *Phys. Rev. B*, 76:165302, 2007.

[18] A. Oukerroum, E. Feddi, J. Bosch Bailach, J. Martínez-Pastor, F. Dujardin, and E. Assaid. On the anomalous stark effect in a thin disc-shaped quantum dot. *J. Phys: Condens. Matter.*, 22:375301, 2010.

[19] C. Priester, G. Allan, and M. Lannoo. Validity of the effective-mass approximation for shallow impurity states in narrow superlattices. *Phys. Rev. B*, 28:7194–7200, 1983.

[20] R. Tsu and D. Babić. Doping of a quantum dot. *Appl. Phys. Lett.*, 64:1806, 1994.

[21] S.-S. Li and J.-B. Xia. Binding energy of a hydrogenic donor impurity in a rectangular parallelepiped-shaped quantum dot: Quantum confinement and stark effects. *J. Appl. Phys.*, 101:093716, 2007.

[22] H. Ham and H. N. Spector. Stark effect of electrons in a semiconducting quantum disk. *Physica B*, 381:53 – 56, 2006.

[23] D. Wang, G. Jin, Y. Zhang, and Y.-Q. Ma. Effect of a tilted electric field on the magnetoexciton ground state in a semiconductor quantum dot. *J. Appl. Phys.*, 105:063716, 2009.

[24] W. Thirring. *Quantum Mathematical Physics*. Springer, Heidelberg, 2002.

[25] S. Takaoka, A. Kuriyama, K. Oto, K. Murase, S. Shimomura, S. Hiyamizu, M. Cukr, T. Jungwirth, and L. Smrcka. Far-infrared magneto-absorption of double-layer two-dimensional electron system in tilted magnetic fields. *Physica E*, 6:623, 2000.

[26] T. M. Fromhold, A. A. Krokhin, C. R. Tench, S. Bujkiewicz, P. B. Wilkinson, F. W. Sheard, and L. Eaves. Effects of stochastic webs on chaotic electron transport in semiconductor superlattices. *Phys. Rev. Lett.*, 87:046803, 2001.

[27] G. Yu, D. J. Lockwood, A. J. SpringThorpe, and D. G. Austing. Crossing and anticrossing of spin-split landau levels in an $Al_{1-x}Ga_xAs/GaAs$ parabolic quantum well ferromagnet. *Phys. Rev. B*, 76:085331, 2007.

[28] G. M. Gusev, C. A. Duarte, T. E. Lamas, A. K. Bakarov, and J. C. Portal. Interlayer interference in double wells in a tilted magnetic field. *Phys. Rev. B*, 78:155320, 2008.

[29] B. S. Monozon and P. Schmelcher. Optical absorption by excitons in semiconductor quantum wells in tilted magnetic and electric fields. *Phys. Rev. B*, 82:205313, 2010.

[30] F. Stern. Self-consistent results for n-type Si inversion layers. *Phys. Rev. B*, 5:4891, 1972.

[31] J. C. Maan. *Two Dimensional Systems, Heterostructures, and Superlattices*. Springer-Verlag, Berlin, 1984, page 183.

[32] R. Merlin. Subband-landau-level coupling in tilted magnetic fields: Exact results for parabolic wells. *Solid State Commun.*, 64:99, 1987.

[33] M. A. Brummell, M. A. Hopkins, R. J. Nicholas, J. C. Portal, K. Y. Cheng, and A. Y. Cho. Subband-landau level coupling in a two-dimensional electron gas in tilted magnetic fields. *J. Phys. C*, 19:L107, 1986.

[34] M. K. Bose, C. Majumdar, A. B. Maity, and A. N. Chakravarti. On electron states of quantum wells in ultrathin films of wide-gap semiconductors in an oriented magnetic field. *Phys. Status Solidi B*, 146:525, 1988.

[35] M. K. Bose, C. Majumdar, A. B. Maity, and A. N. Chakravarti. Effect of a tilted magnetic field on the size-quantized levels of quantum wells in ultrathin films of narrow-gap semiconductors. *Phys. Status Solidi B*, 148:165, 1988.

[36] E. Kasapoglu, H. Sari, and I. Sökmen. Binding energy of hydrogenic impurities in a quantum well under the tilted magnetic field. *Solid State Commun.*, 125:429, 2003.

[37] P. Redliński and B. Jankó. Binding energy of shallow donors in a quantum well in the presence of a tilted magnetic field. *Phys. Rev. B*, 71:113309, 2005.

[38] T. Chakraborty and P. Pietiläinen. Fractional quantum hall effect in tilted magnetic fields. *Phys. Rev. B*, 39:7971, 1989.

[39] E. Kasapoglu, H. Sari, and I. Sökmen. Excitonic structure in a quantum well under the tilted magnetic field. *J. Appl. Phys.*, 88:2671, 2000.

[40] A. D. Wieck, J. C. Maan, U. Merkt, J. P. Kotthaus, K. Ploog, and G. Weimann. Intersubband energies in GaAs-$Ga_{1-x}Al_x$as heterojunctions. *Phys. Rev. B*, 35:4145, 1987.

[41] R. Borroff, R. Merlin, R.L. Greene, and J. Comas. Electronic raman scattering in quantum wells: Coupled levels in tilted magnetic fields. *Superlattices Microst.*, 3:493, 1987.

[42] M. Shayegan, T. Sajoto, J. Jo, M. Santos, and H. D. Drew. Electron states of a wide quantum well in a tilted magnetic field. *Phys. Rev. B*, 40:3476, 1989.

[43] R. Borroff, R. Merlin, J. Pamulapati, P. K. Bhattacharya, and C. Tejedor. Raman scattering by coupled intersubband-landau-level excitations in quantum-well structures. *Phys. Rev. B*, 43:2081, 1991.

[44] Y. J. Wang, Y. A. Leem, B. D. McCombe, X.-G. Wu, F. M. Peeters, E. D. Jones, J. R. Reno, X. Y. Lee, and H. W. Jiang. Strong three-level resonant magnetopolaron effect due to the intersubband coupling in heavily modulation-doped GaAs/Al_xGa_{1-x}As single quantum wells at high magnetic fields. *Phys. Rev. B*, 64:161303, 2001.

[45] H. Ham, C. J. Lee, and H. N. Spector. Photoionization cross section of hydrogenic impurities in cylindrical quantum wires: Infinite well model. *J. Appl. Phys.*, 96:335, 2004.

[46] H. Ham and H. N. Spector. Photoionization cross section of hydrogenic impurities in cylindrical quantum wires: Finite well model. *J. Appl. Phys.*, 100:024304, 2006.

[47] S. Baskoutas, A. F. Terzis, and W. Schommers. Size-dependent exciton energy of narrow band gap colloidal quantum dots in the finite depth square-well effective mass approximation. *J. Comput. Theor. Nanos.*, 3:269, 2006.

[48] S. Baskoutas and A. F. Terzis. Size-dependent band gap of colloidal quantum dots. *J. Appl. Phys.*, 99:013708, 2006.

[49] S. Baskoutas and A. F. Terzis. Biexciton luminescence in inas nanorods. *J. Appl. Phys.*, 98:044309, 2005.

[50] S. Baskoutas and A. F. Terzis. Binding energy of hydrogenic impurity states in an inverse parabolic quantum well under static external fields. *Eur. Phys. J. B*, 69:237, 2009.

[51] A. F. Terzis and S. Baskoutas. *Trends in Quantum Dots Research*. Nova Science Publishers, New York, 2005, pages 93–124.

[52] S. Baskoutas, E. Paspalakis, and A. F. Terzis. Effects of excitons in nonlinear optical rectification in semiparabolic quantum dots. *Phys. Rev. B*, 74:153306, 2006.

[53] P. Poulopoulos, S. Baskoutas, S. D. Pappas, C. S. Garoufalis, S. A. Droulias, A. Zamani, and V. Kapaklis. Intense quantum confinement effects in Cu_2O thin films. *J. Phys. Chem. C*, 115:14839, 2011.

[54] S. C. Erwin, L. Zu, M. I. Haftel, A. L. Efros, T. A. Kennedy, and D. J. Norris. Doping semiconductor nanocrystals. *Nature*, 436:91, 2005.

[55] D. J. Norris, A. L. Efros, and S. C. Erwin. Doped nanocrystals. *Science*, 319:1776, 2008.

[56] S. V. Nistor, M. Stefan, L. C. Nistor, E. Goovaerts, and G. V. Tendeloo. Incorporation and localization of substitutional Mn^{2+} ions in cubic ZnS quantum dots. *Phys. Rev. B*, 81:035336, 2010.

[57] S. Kang, J. Li, and T. Y. Shi. Investigation of hydrogenic-donor states confined by spherical quantum dots with B-splines. *J. Phys. B: At. Mol. Opt. Phys.*, 39:3491, 2006.

[58] İ. Karabulut and S. Baskoutas. Linear and nonlinear optical absorption coefficients and refractive index changes in spherical quantum dots: Effects of impurities, electric field, size, and optical intensity. *J. Appl. Phys.*, 103:073512, 2008.

[59] R. Charrour, M. Bouhassoune, M. Fliyou, and A. Nougaoui. Magnetic field effect on the binding energy of a hydrogenic impurity in cylindrical quantum dot. *Physica B*, 293:137, 2000.

[60] A.-R. Allouche. Gabedit—A graphical user interface for computational chemistry softwares. *J. Comput. Chem.*, 32:174, 2011.

[61] Z. Xiao, J. Zhu, and F. He. Magnetic field dependence of the binding energy of a hydrogenic impurity in a spherical quantum dot. *J. Appl. Phys.*, 79:9181, 1996.

[62] T. Ando, Y. Arakawa, K. Foruka, S. Komiyama, and H. Nakashima. *Mesoscopic Physics and Electronics*. Spinger, 1998.

[63] Y.-X. Li, J.-J. Liu, and X.-J. Kong. The effect of a spatially dependent effective mass on hydrogenic impurity binding energy in a finite parabolic quantum well with a magnetic field. *J. Appl. Phys.*, 88:2588, 2000.

[64] C. A. Duque, A. Montes, and A. L. Morales. Binding energy and polarizability in GaAs–(Ga,Al)As quantum-well wires. *Physica B*, 302:84, 2001.

[65] E. Niculescu, A. Gearba, G. Cone, and C. Negutu. Magnetic field dependence of the binding energy of shallow donors in GaAs quantum-well wires. *Superlattices Microst.*, 29:319, 2001.

[66] F. K. Boz and S. Aktas. Magnetic field effect on the binding energy of a hydrogenic impurity in coaxial $GaAs/Al_xGa_{1-x}As$ quantum well wires. *Superlattices Microst.*, 37:281, 2005.

[67] X.-T. An and J.-J. Liu. Hydrogenic impurities in parabolic quantum-well wires in a magnetic field. *J. Appl. Phys*, 99:123713, 2006.

[68] F. J. Betancur, I. D. Mikhailov, and L. E. Oliveira. Shallow donor states in GaAs-(Ga, Al)As quantum dots with different potential shapes. *J. Phys. D*, 31:3391, 1998.

[69] A. Corella-Madueno, R. Rosas, J. L. Marín, and R. Riera. Hydrogenic impurities in spherical quantum dots in a magnetic field. *J. Appl. Phys*, 90:2333, 2001.

[70] S.-S. Li and J.-B. Xia. Electronic structure and binding energy of a hydrogenic impurity in a hierarchically self-assembled GaAs/Al_xGa_{1-x}As quantum dot. *J. Appl. Phys.*, 100:083714, 2006.

[71] M. Barati, G. Rezaei, and M. R. K. Vahdani. Binding energy of a hydrogenic donor impurity in an ellipsoidal finite-potential quantum dot. *Phys. Status Solidi B*, 244:2605, 2007.

[72] L. Jiang, H. Wang, H. Wu, Q. Gong, and S. Feng. External electric field effect on the hydrogenic donor impurity in zinc-blende GaN/AlGaN cylindrical quantum dot. *J. Appl. Phys.*, 105:053710, 2009.

[73] C. Xia, Z. Zeng, and S. Wei. Effects of applied electric field and hydrostatic pressure on donor impurity states in cylindrical GaN/AlN quantum dot. *J. Appl. Phys.*, 107:014305, 2010.

[74] G. Brozak, E. A. de Andrada e Silva, L. J. Sham, F. DeRosa, P. Miceli, S. A. Schwarz, J. P. Harbison, L. T. Florez, and S. J. Allen. Tunneling cyclotron resonance and the renormalized effective mass in semiconductor barriers. *Phys. Rev. Lett.*, 64:471, 1990.

[75] A. John Peter, K. Gnanasekar, and K. Navaneethakrishnan. Combined effects of electric and magnetic fields on confined donor states in a diluted magnetic semiconductor parabolic quantum dot. *Eur. J. Phys. B*, 53:283, 2006.

[76] E. Kasapoglu and I. Sökmen. Shallow donor impurity binding energy in the V-shaped quantum well under the crossed electric and magnetic fields. *Physica E*, 27:198, 2005.

[77] M. G. Barseghyan, A. A. Kirakosyan, and C. A. Duque. Donor-impurity related binding energy and photoinization cross-section in quantum dots: electric and magnetic fields and hydrostatic pressure effects. *Eur. Phys. J. B*, 72:521, 2009.

[78] S. Baskoutas and A. F. Terzis. Binding energy of hydrogenic impurity states in an inverse parabolic quantum well under electric and magnetic fields parallel to the growth direction. *J. Comput. Theor. Nanos.*, 7:492, 2010.

[79] V. N. Mughnetsyan, M. G. Barseghyan, and A. A. Kirakosyan. Binding energy and photoionization cross section of hydrogen-like donor impurity in quantum well-wire in electric and magnetic fields. *Superlattices Microst.*, 44:86, 2008.

[80] S.-S. Li and J.-B. Xia. Binding energy of a hydrogenic donor impurity in a rectangular parallelepiped-shaped quantum dot: Quantum confinement and Stark effects. *J. Appl. Phys.*, 101:093716, 2007.

[81] B. E. Kane. A silicon-based nuclear spin quantum computer. *Nature (London)*, 393:133–137, 1998.

[82] J.-L. Zhu, J. Wu, R. T. Fu, H. Chen, and Y. Kawazoe. Effects of quantum size and potential shape on the spectra of an electron and a donor in quantum dots. *Phys. Rev. B*, 55:1673–1679, 1997.

[83] R. Charrour, M. Bouhassoune, M. Fliyou, D. Bria, and A. Nougaoui. Binding energy of hydrogenic impurities in polar cylindrical quantum dot. *J. Phys.: Condens. Matter.*, 12:4817, 2000.

[84] W. Xie. Binding energy of an off-center hydrogenic donor in a spherical gaussian quantum dot. *Physica B*, 403:2828 – 2831, 2008.

[85] L. Yang and W. Xie. Photoionization cross section of a donor impurity in a two-dimensional anisotropic quantum dot. *Physica B*, 407:3884 – 3887, 2012.

[86] C. Xia, Z. Zeng, and S. Wei. Electron and impurity states in GaN/AlGaN coupled quantum dots: Effects of electric field and hydrostatic pressure. *J. Appl. Phys.*, 108:054307, 2010.

[87] G. M. Huang, Y. M. Liu, and C. G. Bao. Electronic structure of donor states under a strong magnetic field. *Phys. Rev. B*, 71:075302, 2005.

[88] A. John Peter. The effect of hydrostatic pressure on binding energy of impurity states in spherical quantum dots. *Physica E*, 28:225 – 229, 2005.

[89] S. T. Perez-Merchancano, H. Paredes-Gutierrez, and J. Silva-Valencia. Hydrostatic-pressure effects on the donor binding energy in GaAs/(Ga, Al)As quantum dots. *J. Phys.: Condens. Matter.*, 19:026225, 2007.

[90] M. Kirak, S. Yilmaz, M. Sahin, and M. Gencaslan. The electric field effects on the binding energies and the nonlinear optical properties of a donor impurity in a spherical quantum dot. *J. Appl. Phys.*, 109:094309, 2011.

[91] Z. Zeng, C. S. Garoufalis, S. Baskoutas, and A. F. Terzis. Tuning the binding energy of surface impurities in cylindrical GaAs/AlGaAs quantum dots by a tilted magnetic field. *J. Appl. Phys.*, 112:064326, 2012.

[92] A. Sivakami and V. Gayathri. Hydrostatic pressure and temperature dependence of dielectric mismatch effect on the impurity binding energy in a spherical quantum dot. *Superlattice Microst.*, 58:218 – 227, 2013.

[93] V. L. Nguyen, M. T. Nguyen, and T. D. Nguyen. Magnetic field effects on the binding energy of hydrogen impurities in quantum dots with parabolic confinements. *Physica B*, 292:153 – 159, 2000.

[94] S. Sahoo, Y. C. Lin, and Y. K. Ho. Quantum-confined hydrogenic impurity in a spherical quantum dot under the influence of parallel electric and magnetic fields. *Physica E*, 40:3107 – 3114, 2008.

[95] M. G. Barseghyan, A. A. Kirakosyan, and C. A. Duque. Hydrostatic pressure, electric and magnetic field effects on shallow donor impurity states and photoionization cross section in cylindrical $GaAs/Ga_{1-x}Al_xAs$ quantum dots. *Phys. Status Solidi B*, 246:626–629, 2009.

[96] M. G. Barseghyan, A. A. Kirakosyan, and C. A. Duque. Donor-impurity related binding energy and photoinization cross-section in quantum dots: electric and magnetic fields and hydrostatic pressure effects. *Eur. Phys. J. B*, 72:521–529, 2009.

[97] C. Dane, H. Akbas, S. Minez, and A. Guleroglu. Simultaneous effects of electric and magnetic fields in a GaAs/AlAs spherical quantum dot with a hydrogenic impurity. *Physica E*, 42:1901 – 1904, 2010.

[98] G. Rezaei and S. S. Kish. Effects of external electric and magnetic fields, hydrostatic pressure and temperature on the binding energy of a hydrogenic impurity confined in a two-dimensional quantum dot. *Physica E*, 45:56 – 60, 2012.

[99] Z. Zeng, C. S Garoufalis, and S. Baskoutas. Combination effects of tilted electric and magnetic fields on donor binding energy in a GaAs/AlGaAs cylindrical quantum dot. *J. Phys. D: Appl. Phys.*, 45:235102, 2012.

[100] Z. Zeng, C. S. Garoufalis, A. F. Terzis, and S. Baskoutas. Linear and nonlinear optical properties of ZnO/ZnS and ZnS/ZnO core shell quantum dots: Effects of shell thickness, impurity, and dielectric environment. *J. Appl. Phys.*, 114:023510, 2013.

[101] C. A. Moscoso-Moreno, R. Franco, and J. Silva-Valencia. Binding energy of heavy excitons in spherical quantum dots under hydrostatic pressure. *Phys. Status Solidi B*, 246:486–490, 2009.

[102] H. Ehrenreich. Band structure and transport properties of some 3–5 compounds. *J. Appl. Phys.*, 32:2155, 1961.

[103] Benjamin Welber, Manuel Cardona, C. K. Kim, and Sergio Rodriguez. Dependence of the direct energy gap of GaAs on hydrostatic pressure. *Phys. Rev. B*, 12:5729–5738, 1975.

[104] C. A. Duque, S. Y. López, and M. E. Mora-Ramos. Hydrostatic pressure effects on the Γ-X conduction band mixing and the binding energy of a donor impurity in GaAs/$Ga_{1-x}Al_x$As quantum wells. *Phys. Status Solidi B*, 244:1964, 2007.

[105] E. H. Li. Material parameters of ingaasp and inalgaas systems for use in quantum well structures at low and room temperatures. *Physica E*, 5:215, 2000.

[106] H. Odhiambo Oyoko, N. Porras-Montenegro, S. Y. López, and C. A. Duque. Comparative study of the hydrostatic pressure and temperature effects on the impurity-related optical properties in single and double GaAs/$Ga_{1-x}Al_x$As quantum wells. *Phys. Status Solidi C*, 4:298, 2007.

[107] Ü. Özgür, Ya. I. Alivov, C. Liu, A. Teke, M. A. Reshchikov, S. Doğan, V. Avrutin, S.-J. Cho, and H. Morkoç. A comprehensive review of ZnO materials and devices. *J. Appl. Phys.*, 98:041301, 2005.

[108] D. E. Fogg, L. H. Radzilowski, R. Blanski, R. R. Schrock, and E. L. Thomas. Fabrication of quantum dot/polymer composites: phosphine-functionalized block copolymers as passivating hosts for cadmium selenide nanoclusters. *Macromolecules*, 30:417, 1997.

[109] D. E. Fogg, L. H. Radzilowski, B. O. Dabbousi, R. R. Schrock, E. L. Thomas, and M. G. Bawendi. Fabrication of quantum dot-polymer composites: semiconductor nanoclusters in dual-function polymer matrices with electron-transporting and cluster-passivating properties. *Macromolecules*, 30:8433, 1997.

[110] C. B. Murray, D. J. Norris, and M. G. Bawendi. Synthesis and characterization of nearly monodisperse CdE (E = sulfur, selenium, tellurium) semiconductor nanocrystallites. *J. Am. Chem. Soc.*, 115:8706, 1993.

[111] J. Lee, V. C. Sundar, J. R. Heine, M. G. Bawendi, and K. F. Jensen. Full color emission from II-VI semiconductor quantum dot/polymer composites. *Adv. Mater.*, 12:1102, 2000.

[112] S. T. Selvan, C. Bullen, M. Ashokkumar, and P. Mulvaney. Synthesis of tunable, highly luminescent QD-glasses through sol-gel processing. *Adv. Mater.*, 13:985–988, 2001.

[113] N. Bouropoulos, I. Tsiaoussis, P. Poulopoulos, P. Roditis, and S. Baskoutas. ZnO controllable sized quantum dots produced by polyol method: An experimental and theoretical study. *Mat. Lett.*, 62:3533, 2008.

[114] D. I. Son, C. H. You, W. T. Kim, and T. W. Kim. White light-emitting diodes fabricated utilizing hybrid polymer-colloidal ZnO quantum dots. *Nanotechnology*, 20:365206, 2009.

[115] D. I. Son, C. H. You, J. H. Jung, and T. W. Kim. Carrier transport mechanisms of organic bistable devices fabricated utilizing colloidal ZnO quantum dot-polymethylmethacrylate polymer nanocomposites. *Appl. Phys. Lett.*, 97:013304, 2010.

[116] Y. Tu, L. Zhou, Y. Z. Jin, C. Gao, Z. Z. Ye, Y. F. Yang, and Q. L. Wang. Transparent and flexible thin films of ZnO-polystyrene nanocomposite for UV-shielding applications. *J. Mater. Chem.*, 20:1594, 2010.

[117] M. Sudha, S. Senthilkumar, R. Hariharan, A. Suganthi, and M. Rajarajan. Controlled reduction of the deleterious effects of photocatalytic activity of ZnO nanoparticles by PVA capping. *J. Sol-Gel Sci. Technol.*, 61:14, 2012.

[118] Y. C. Liu, H. Y. Xu, R. Mu, D. O. Henderson, Y. M. Lu, J. Y. Zhang, D. Z. Shen, X. W. Fan, and C. W. White. Production, structure, and optical properties of zno nanocrystals embedded in CaF_2 matrix. *Appl. Phys. Lett.*, 83:1210, 2003.

[119] K.-K. Kim, N. Koguchi, Y.-W. Ok, T.-Y. Seong, and S.-J. Park. Fabrication of ZnO quantum dots embedded in an amorphous oxide layer. *Appl. Phys. Lett.*, 84:3810, 2004.

[120] Y.-Q. Li, Y. Yang, C. Q. Sun, and S.-Y. Fu. Significant enhancements in the fluorescence and phosphorescence of ZnO quantum dots/SiO_2 nanocomposites by calcination. *J. Phys. Chem. C*, 112:17397, 2008.

[121] D. Bera, L. Qian, and P. H. Holloway. Time-evolution of photoluminescence properties of ZnO/MgO core/shell quantum dots. *J. Phys. D: Appl. Phys.*, 41:182002, 2008.

[122] N. Hagura, T. Takeuchi, S. Takayama, F. Iskandar, and K. Okuyama. Enhanced photoluminescence of ZnO/SiO_2 nanocomposite particles and the analyses of structure and composition. *J. Lumin.*, 131:138, 2011.

[123] S. Baskoutas and G. Bester. Conventional optics from unconventional electronics in ZnO quantum dots. *J. Phys. Chem. C*, 114:9301–9307, 2010.

[124] L. Dallali, S. Jaziri, J. E. Haskouri, P. Amoras, and J. Martanez-Pastor. Energy of excitons and acceptor exciton complexes to explain the origin of ultraviolet photoluminescence in ZnO quantum dots embedded in a SiO_2 matrix. *Solid State Commun.*, 151:822, 2011.

[125] D. Maikhuri, S. P. Purohit, and K. C. Mathur. Linear and nonlinear intraband optical properties of ZnO quantum dots embedded in SiO_2 matrix. *AIP Advances*, 2:012160, 2012.

[126] S. Sauvage, P. Boucaud, F. Glotin, R. Prazeres, J.-M. Ortega, A. Lemaitre, J.-M. Gerard, and V. Thierry-Mieg. Third-harmonic generation in InAs/GaAs self-assembled quantum dots. *Phys. Rev. B*, 59:9830–9833, 1999.

[127] T. Brunhes, P. Boucaud, S. Sauvage, A. Lemaitre, J.-M. Gerard, F. Glotin, R. Prazeres, and J.-M. Ortega. Infrared second-order optical susceptibility in InAs/GaAs self-assembled quantum dots. *Phys. Rev. B*, 61:5562–5570, 2000.

[128] S. G. Kosionis, A. F. Terzis, C. Simserides, and E. Paspalakis. Linear and nonlinear optical properties of a two-subband system in a symmetric semiconductor quantum well. *J. Appl. Phys.*, 108:034316, 2010.

[129] M. Lannoo, C. Delerue, and G. Allan. Screening in semiconductor nanocrystallites and its consequences for porous silicon. *Phys. Rev. Lett.*, 74:3415–3418, 1995.

[130] Anchala, S. P. Purohit, and K. C. Mathur. Photoabsorption and photoelectric process in Si nanocrystallites. *Appl. Phys. Lett.*, 98:043106, 2011.

[131] R. W. Boyd. *Nonlinear Optics*. Academic Press, San Diego, third edition, 2008, Chap. 6.

[132] F. Yu, L. Zhang, and K. Guo. Exciton effects on the refractive index and optical absorption in wurtzite quantum wells via a fractional-dimensional space approach. *Superlattice Microst*, 50:128 – 138, 2011.

[133] R. Naturalium. *Photoluminescence Intermittency of Semiconductor Quantum Dots in Dielectric Environments*. PhD thesis, von der Fakultät für Naturwissenschaften der Technischen Universität, Germany, 2006.

[134] J. A. Hagen, W. Li, A. J. Steckl, and J. G. Grote. Enhanced emission efficiency in organic light-emitting diodes using deoxyribonucleic acid complex as an electron blocking layer. *Appl. Phys. Lett.*, 88:171109, 2006.

[135] S. Mahendia, A. K. Tomar, R. P. Chahal, P. Goyal, and S. Kumar. Optical and structural properties of poly(vinyl alcohol) films embedded with citrate-stabilized gold nanoparticles. *J. Phys. D: Appl. Phys.*, 44:205105, 2011.

[136] J. Robertson. High dielectric constant oxides. *Eur. Phys. J.-Appl. Phys.*, 28:265–291, 2004.

[137] V. A. Fonoberov and A. A. Balandin. ZnO quantum dots: Physical properties and optoelectronic applications. *J. Nanoelectron. Optoe.*, 1:19–38, 2006.

[138] C. Jiang, W. Zhang, G. Zou, W. Yu, and Y. Qian. Hydrothermal synthesis and characterization of zns microspheres and hollow nanospheres. *Mater. Chem. Phys.*, 103:24–27, 2007.

[139] K.-F. Lin, H.-M. Cheng, H.-C. Hsu, L.-J. Lin, and W.-F. Hsieh. Band gap variation of size-controlled ZnO quantum dots synthesized by sol-gel method. *Chem. Phys. Lett.*, 409:208–211, 2005.

[140] B. Bhattacharjee, D. Ganguli, S. Chaudhuri, and A. K. Pal. Synthesis and optical characterization of sol-gel derived zinc sulphide nanoparticles confined in amorphous silica thin films. *Mater. Chem. Phys.*, 78:372–379, 2003.

[141] M. Navaneethan, J. Archana, K. D. Nisha, Y. Hayakawa, S. Ponnusamy, and C. Muthamizhchelvan. Synthesis of highly size confined ZnS quantum dots and its functional characteristics. *Mater. Lett.*, 68(0):78–81, 2012.

[142] A. L. Donne, S. K. Jana, S. Banerjee, S. Basu, and S. Binetti. Optimized luminescence properties of Mn doped ZnS nanoparticles for photovoltaic applications. *J. Appl. Phys.*, 113:014903, 2013.

[143] X. Xu, C. Xu, J. Dai, J. Hu, F. Li, and S. Zhang. Size dependence of defect-induced room temperature ferromagnetism in undoped ZnO nanoparticles. *J. Phys. Chem. C*, 116:8813–8818, 2012.

[144] K. Rajeshwar, N. R. de Tacconi, and C. R. Chenthamarakshan. Semiconductor-based composite materials: Preparation, properties, and performance. *Chem. Mater.*, 13:2765–2782, 2001.

[145] S. Baskoutas and G. Bester. Conventional optics from unconventional electronics in ZnO quantum dots. *J. Phys. Chem. C*, 114:9301, 2010.

[146] Landolt-Börnstein. *Numerical Data and Functional Relationships in Science and Technology*, volume 22a. Springer, Berlin, 1982.

[147] L. P. Balet, S. A. Ivanov, A. Piryatinski, M. Achermann, and V. I. Klimov. Inverted core/shell nanocrystals continuously tunable between type-I and type-II localization regimes. *Nano Lett.*, 4:1485–1488, 2004.

[148] M. Cristea and E. C. Niculescu. Hydrogenic impurity states in CdSe/ZnS and ZnS/CdSe core-shell nanodots with dielectric mismatch. *Eur. Phys. J. B*, 85:1–13, 2012.

[149] S. Sharma and S. Chawla. Enhanced UV emission in ZnO/ZnS core shell nanoparticles prepared by epitaxial growth in solution. *Electron. Mater. Lett.*, 9:267–271, 2013.

[150] F. Wang, J. Liu, Z. Wang, A.-J. Lin, H. Luo, and X. Yu. Interfacial heterostructure phenomena of highly luminescent ZnS/ZnO quantum dots. *J. Electrochem. Soc.*, 158:H30–H34, 2011.

[151] M. Rajalakshmi, S. Sohila, R. Ramesh, and G.M. Bhalerao. Enhancement of photoluminescence in ZnS/ZnO quantum dots interfacial heterostructures. *Mater. Res. Bull.*, 47(9):2668–2672, 2012.

[152] J. Xiao, M. Wu, G. Kai, F. Wang, H. Cao, and X. Yu. ZnO-ZnS QDs interfacial heterostructure for drug and food delivery application: enhancement of the binding affinities of flavonoid aglycones to bovine serum albumin. *Nanomed. NBM*, 7:850–858, 2011.

[153] J. Xiao, F. Wang, J. Liu, L. Wang, G. Kai, and X. Yu. Effect of ZnO/ZnS QDs heterojunctures on the stilbenes-plasma proteins interactions. *Mol. BioSyst.*, 7:2452–2458, 2011.

[154] J. Schrier, D.S O. Demchenko, L. Wang, and A. P. Alivisatos. Optical properties of ZnO/ZnS and ZnO/ZnTe heterostructures for photovoltaic applications. *Nano Lett.*, 7:2377–2382, 2007.

[155] P. G. McDonald, E. J. Tyrrell, J. Shumway, J. M. Smith, and I. Galbraith. Tuning biexciton binding and antibinding in core/shell quantum dots. *Phys. Rev. B*, 86:125310, 2012.

[156] S. Saha and P. Sarkar. Electronic structure of ZnO/ZnS core/shell quantum dots. *Chem. Phys. Lett.*, 555:191–195, 2013.

[157] Z. Zeng, E. Paspalakis, C. S. Garoufalis, A. F. Terzis, and S. Baskoutas. Optical susceptibilities in singly charged zno colloidal quantum dots embedded in different dielectric matrices. *J. Appl. Phys.*, 113:054303, 2013.

[158] L. Bányai, P. Gilliot, Y. Z. Hu, and S. W. Koch. Surface-polarization instabilities of electron-hole pairs in semiconductor quantum dots. *Phys. Rev. B*, 45:14136–14142, 1992.

[159] G. Allan, C. Delerue, M. Lannoo, and E. Martin. Hydrogenic impurity levels, dielectric constant, and coulomb charging effects in silicon crystallites. *Phys. Rev. B*, 52:11982–11988, 1995.

[160] J. L. Movilla, F. Rajadell, and J. Planelles. Delocalized image surface states in defect-free SiO_2 hollow nanospheres. *J. Appl. Phys.*, 103:014310, 2008.

[161] S. Unlu, I. Karabulut, and H. Safak. Linear and nonlinear intersubband optical absorption coefficients and refractive index changes in a quantum box with finite confining potential. *Physica E*, 33:319–324, 2006.

[162] J. Cao, J. Yang, L. Yang, M. Wei, B. Feng, D. Han, L. Fan, B. Wang, and H. Fu. The effects of doping and shell thickness on the optical and magnetic properties of Mn/Cu/Fe-doped and Co-doped ZnS nanowires/ZnO quantum dots/SiO_2 heterostructures. *J. Appl. Phys.*, 112:014316, 2012.

[163] W. Xie. Linear and nonlinear optical properties of a hydrogenic donor in spherical quantum dots. *Physica B*, 403:4319 – 4322, 2008.

[164] W. Xie. A study of two confined electrons using the woods?saxon potential. *J. Phys.: Condens. Matter.*, 21:115802, 2009.

[165] M. Şahin. Photoionization cross section and intersublevel transitions in a one- and two-electron spherical quantum dot with a hydrogenic impurity. *Phys. Rev. B*, 77:045317, 2008.

[166] M. Şahin. Third-order nonlinear optical properties of a one- and two-electron spherical quantum dot with and without a hydrogenic impurity. *J. Appl. Phys.*, 106:063710, 2009.

[167] İbrahim Karabulut. Effect of coulomb interaction on nonlinear (intensity-dependent) optical processes and intrinsic bistability in a quantum well under the electric and magnetic fields. *J. Appl. Phys.*, 109:053101, 2011.

[168] S.-H. Wei and A. Zunger. Calculated natural band offsets of all II–VI and III–V semiconductors: Chemical trends and the role of cation d orbitals. *Appl. Phys. Lett.*, 72:2011–2013, 1998.

[169] A. Janotti and C. G. Van de Walle. Absolute deformation potentials and band alignment of wurtzite ZnO, MgO, and CdO. *Phys. Rev. B*, 75:121201, 2007.

[170] P. G. Moses, M. Miao, Q. Yan, and C. G. Van de Walle. Hybrid functional investigations of band gaps and band alignments for AlN, GaN, InN, and InGaN. *J. Chem. Phys.*, 134:084703, 2011.

[171] B. Szafran, F. M. Peeters, and S. Bednarek. Electron spin and charge switching in a coupled quantum-dot-quantum ring system. *Phys. Rev. B*, 70:125310, 2004.

[172] J. Wu, X. Hu, J. Lee, E.-S. Kim, and Z. M. Wang. Epitaxially self-assemblied quantum dot pairs. *Adv. Opt. Mat.*, 1:201–214, 2013.

[173] T. Hatano, M. Stopa, and S. Tarucha. Single-electron delocalization in hybrid vertical-lateral double quantum dots. *Science*, 309:268–271, 2005.

[174] J. Peng and G. Bester. Charged excitons and biexcitons in laterally coupled (In,Ga)As quantum dots. *Phys. Rev. B*, 82:235314, 2010.

[175] L. Wang, A. Rastelli, S. Kiravittaya, M. Benyoucef, and O. G. Schmidt. Self-assembled quantum dot molecules. *Adv. Mater.*, 21:2601–2618, 2009.

[176] A. Kwaśniowski and J. Adamowski. Tuning the exchange interaction by an electric field in laterally coupled quantum dots. *J. Phys.: Condens. Matter.*, 21:235601, 2009.

[177] T. Kubo, Y. Tokura, and S. Tarucha. Kondo effects and shot noise enhancement in a laterally coupled double quantum dot. *Phys. Rev. B*, 83:115310, 2011.

[178] M. Royo, J. I. Climente, and J. Planelles. Emission spectrum of quasiresonant laterally coupled quantum dots. *Phys. Rev. B*, 84:235312, 2011.

[179] M. Raith, P. Stano, and J. Fabian. Theory of spin relaxation in two-electron laterally coupled Si/SiGe quantum dots. *Phys. Rev. B*, 86:205321, 2012.

[180] N. A. J. M. Kleemans, I. M. A. Bominaar-Silkens, V. M. Fomin, V. N. Gladilin, D. Granados, A. G. Taboada, J. M. García, P. Offermans, U. Zeitler, P. C. M. Christianen, J. C. Maan, J. T. Devreese, and P. M. Koenraad. Oscillatory persistent currents in self-assembled quantum rings. *Phys. Rev. Lett.*, 99:146808, 2007.

[181] N. A. J. M. Kleemans, J. H. Blokland, A. G. Taboada, H. C. M. van Genuchten, M. Bozkurt, V. M. Fomin, V. N. Gladilin, D. Granados, J. M. García, P. C. M. Christianen, J. C. Maan, J. T. Devreese, and P. M. Koenraad. Excitonic behavior in self-assembled InGs/GaAs quantum rings in high magnetic fields. *Phys. Rev. B*, 80:155318, 2009.

[182] F. Ding, N. Akopian, B. Li, U. Perinetti, A. Govorov, F. M. Peeters, C. C. Bof Bufon, C. Deneke, Y. H. Chen, A. Rastelli, O. G. Schmidt, and V. Zwiller. Gate controlled aharonov-bohm-type oscillations from single neutral excitons in quantum rings. *Phys. Rev. B*, 82:075309, 2010.

[183] M. Zarenia, J. M. Pereira, F. M. Peeters, and G. A. Farias. Electrostatically confined quantum rings in bilayer graphene. *Nano Lett.*, 9:4088–4092, 2009.

[184] A. V. Chaplik. Magnetoexcitons in quantum rings and in antidots. *JETP Lett.*, 62:900, 1995.

[185] M. D. Teodoro, V. L. Campo, V. Lopez-Richard, E. Marega, G. E. Marques, Y. Galvão Gobato, F. Iikawa, M. J. S. P. Brasil, Z. Y. AbuWaar, V. G. Dorogan, Yu. I. Mazur, M. Benamara, and G. J. Salamo. Aharonov-bohm interference in neutral excitons: Effects of built-in electric fields. *Phys. Rev. Lett.*, 104:086401, 2010.

[186] Z. C. Wen, H. X. Wei, and X. F. Han. Patterned nanoring magnetic tunnel junctions. *Appl. Phys. Lett.*, 91:122511, 2007.

[187] J. Wu, Z. Li, D. Shao, M. O. Manasreh, V. P. Kunets, Z. M. Wang, G. J. Salamo, and B. D. Weaver. Multicolor photodetector based on GaAs quantum rings grown by droplet epitaxy. *Appl. Phys. Lett.*, 94:171102, 2009.

[188] S. Bhowmick, G. Huang, W. Guo, C. S. Lee, P. Bhattacharya, G. Ariyawansa, and A. G. U. Perera. High-performance quantum ring detector for the 1-3 terahertz range. *Appl. Phys. Lett.*, 96:231103, 2010.

[189] F. Capasso, K. Mohammed, and A. Y. Cho. Resonant tunneling through double barriers, perpendicular quantum transport phenomena in superlattices, and their device applications. *IEEE J. Quantum Electron.,*, 22:1853–1869, 1986.

[190] D.A.B. Miller. Quantum well optoelectronic switching devices. *Int. J. High Speed Electron. Syst.*, 01:19–46, 1990.

[191] E. Rosencher and B. Vinter. *Optoelectronics*. Cambridge University Press, Cambridge, 2003.

[192] T. Meier, P. Thomas, and S.W. Koch. Linear and nonlinear optical properties of semiconductor nanorings with magnetic field and disorder - influence on excitons and biexcitons. *Eur. Phys. J. B*, 22:249–256, 2001.

[193] S. Liang, W. Xie, H. A. Sarkisyan, A. V. Meliksetyan, and H. Shen. Nonlinear optical properties in a nanoring: quantum size and magnetic field effect. *J. Phys.: Condens. Matter.*, 23:415302, 2011.

[194] S. Liang, W. Xie, H. A. Sarkisyan, A. V. Meliksetyan, and H. Shen. Electronic and optical properties of a nanoring in the presence of external magnetic field. *Superlattices Microstruct.*, 51:868–876, 2012.

[195] H. M. Baghramyan, M. G. Barseghyan, A. A. Kirakosyan, R. L. Restrepo, and C. A. Duque. Linear and nonlinear optical absorption coefficients in GaAs/$Ga_{1-x}Al_xAs$ concentric double quantum rings: Effects of hydrostatic pressure and aluminum concentration. *J. Lumin.*, 134:594–599, 2013.

[196] C. M. Duque, M.E. Mora-Ramos, and C. A. Duque. Properties of the second and third harmonics generation in a quantum disc with inverse square potential. a modeling for nonlinear optical responses of a quantum ring. *J. Lumin.*, 138:53–60, 2013.

[197] R. L. Restrepo, M. G. Barseghyan, M. E. Mora-Ramos, and C. A. Duque. Effects of hydrostatic pressure on the nonlinear optical properties of a donor impurity in a GaAs quantum ring. *Physica E*, 51:48–54, 2013.

[198] W. Xie. The nonlinear optical rectification coefficient of quantum dots and rings with a repulsive scattering center. *J. Lumin.*, 143:27–30, 2013.

[199] H. M. Baghramyan, M. G. Barseghyan, A. A. Kirakosyan, R. L. Restrepo, M. E. Mora-Ramos, and C. A. Duque. Donor impurity-related linear and nonlinear optical absorption coefficients in concentric double quantum rings: Effects of geometry, hydrostatic pressure, and aluminum concentration. *J. Lumin.*, 145:676–683, 2014.

[200] R. Held, S. Luscher, T. Heinzel, K. Ensslin, and W. Wegscheider. Fabricating tunable semiconductor devices with an atomic force microscope. *Appl. Phys. Lett.*, 75:1134–1136, 1999.

[201] S. Lüscher, T. Heinzel, K. Ensslin, W. Wegscheider, and M. Bichler. Signatures of spin pairing in chaotic quantum dots. *Phys. Rev. Lett.*, 86:2118–2121, 2001.

[202] A. Fuhrer, S. Lüscher, T. Ihn, T. Heinzel, K. Ensslin, W. Wegscheider, and M. Bichler. Energy spectra of quantum rings. *Nature*, 413:822–825, 2001.

[203] A. Wensauer, O. Steffens, M. Suhrke, and U. Rössler. Laterally coupled few-electron quantum dots. *Phys. Rev. B*, 62:2605–2613, 2000.

[204] A. Harju, S. Siljamäki, and R. M. Nieminen. Two-electron quantum dot molecule: Composite particles and the spin phase diagram. *Phys. Rev. Lett.*, 88:226804, 2002.

[205] K.-X. Guo and S.-W. Gu. Nonlinear optical rectification in parabolic quantum wells with an applied electric field. *Phys. Rev. B*, 47:16322–16325, 1993.

[206] Y.-B. Yu, S.-N. Zhu, and K.-X. Guo. Exciton effects on the nonlinear optical rectification in one-dimensional quantum dots. *Phys. Lett. A*, 335:175–181, 2005.

[207] P. Pulay. Ab initio calculation of force constants and equilibrium geometries in polyatomic molecules. *Molec. Phys.*, 17:197–204, 1969.

[208] Conyers Herring. A new method for calculating wave functions in crystals. *Phys. Rev.*, 57:1169–1177, 1940.

[209] G. Grosso and G. P. Parravicini. *Solid state physics*. Academic press, 2003.

[210] Enrico Fermi. Sopra lo spostamento per pressione delle righe elevate delle serie spettrali. *Il Nuovo Cimento*, 11:157–166, 1934.

[211] H. Hellmann. A new approximation method in the problem of many electrons. *J. Chem. Phys.*, 3:61–61, 1935.

[212] D. R. Hamann, M. Schlüter, and C. Chiang. Norm-conserving pseudopotentials. *Phys. Rev. Lett.*, 43:1494–1497, 1979.

[213] D. Vanderbilt. Optimally smooth norm-conserving pseudopotentials. *Phys. Rev. B*, 32:8412–8415, 1985.

[214] G. B. Bachelet, D. R. Hamann, and M. Schlüter. Pseudopotentials that work: From H to Pu. *Phys. Rev. B*, 26:4199–4228, 1982.

[215] N. Troullier and J. Martins. A straightforward method for generating soft transferable pseudopotentials. *Solid State Comm.*, 74:613–616, 1990.

[216] G. P. Kerker. Non-singular atomic pseudopotentials for solid state applications. *J. Phys. C: Solid State Phys.*, 13:L189, 1980.

[217] D. Vanderbilt. Soft self-consistent pseudopotentials in a generalized eigenvalue formalism. *Phys. Rev. B*, 41:7892–7895, 1990.

[218] P. E. Blöchl. Generalized separable potentials for electronic-structure calculations. *Phys. Rev. B*, 41:5414–5416, 1990.

[219] J. C. Phillips. Energy-band interpolation scheme based on a pseudopotential. *Phys. Rev.*, 112:685–695, 1958.

[220] J. C. Phillips and L. Kleinman. New method for calculating wave functions in crystals and molecules. *Phys. Rev.*, 116:287–294, 1959.

[221] L. Kleinman and J. C. Phillips. Crystal potential and energy bands of semiconductors. III. self-consistent calculations for silicon. *Phys. Rev.*, 118:1153–1167, 1960.

[222] G. Bester. Electronic excitations in nanostructures: an empirical pseudopotential based approach. *J. Phys.: Condens. Matter*, 21:023202, 2009.

[223] M. L. Cohen and T. K. Bergstresser. Band structures and pseudopotential form factors for fourteen semiconductors of the diamond and zinc-blende structures. *Phys. Rev.*, 141:789–796, 1966.

[224] D. Brust, J. C. Phillips, and F. Bassani. Critical points and ultraviolet reflectivity of semiconductors. *Phys. Rev. Lett.*, 9:94–97, 1962.

[225] D. Brust, M. L. Cohen, and J. C. Phillips. Reflectance and photoemission from Si. *Phys. Rev. Lett.*, 9:389–392, 1962.

[226] F. Bassani and D. Brust. Effect of alloying and pressure on the band structure of germanium and silicon. *Phys. Rev.*, 131:1524–1529, 1963.

[227] D. Brust. Electronic spectra of crystalline germanium and silicon. *Phys. Rev.*, 134:A1337–A1353, 1964.

[228] M. L. Cohen and J. C. Phillips. Spectral analysis of photoemissive yields in Si, Ge, GaAs, GaSb, InAs, and InSb. *Phys. Rev.*, 139:A912–A920, 1965.

[229] L. W. Wang and A. Zunger. Electronic structure pseudopotential calculations of large (.apprx.1000 atoms) Si quantum dots. *J. Phys. Chem.*, 98:2158–2165, 1994.

[230] K. A. Mäder and A. Zunger. Empirical atomic pseudopotentials for AlAs/GaAs superlattices, alloys, and nanostructures. *Phys. Rev. B*, 50:17393–17405, 1994.

[231] G. Weisz. Band structure and fermi surface of white tin. *Phys. Rev.*, 149:504–518, 1966.

[232] M. S. Hybertsen and S. G. Louie. Spin-orbit splitting in semiconductors and insulators from the ab initio pseudopotential. *Phys. Rev. B*, 34:2920–2922, 1986.

[233] A. J. Williamson, L. W. Wang, and A. Zunger. Theoretical interpretation of the experimental electronic structure of lens-shaped self-assembled InAs/GaAs quantum dots. *Phys. Rev. B*, 62:12963–12977, 2000.

[234] G. Bester and A. Zunger. Compositional and size-dependent spectroscopic shifts in charged self-assembled $In_xGa_{1-x}As$/GaAs quantum dots. *Phys. Rev. B*, 68:073309, 2003.

[235] L.-W. Wang and A. Zunger. Pseudopotential calculations of nanoscale CdSe quantum dots. *Phys. Rev. B*, 53:9579–9582, 1996.

[236] A. Franceschetti, H. Fu, L. W. Wang, and A. Zunger. Many-body pseudopotential theory of excitons in InP and CdSe quantum dots. *Phys. Rev. B*, 60:1819, 1999.

[237] A. Puzder, A. J. Williamson, F. A. Reboredo, and G. Galli. Structural stability and optical properties of nanomaterials with reconstructed surfaces. *Phys. Rev. Lett.*, 91:157405, 2003.

[238] A. Puzder, A. J. Williamson, F. Gygi, and G. Galli. Self-healing of CdSe nanocrystals: First-principles calculations. *Phys. Rev. Lett.*, 92:217401, 2004.

[239] A. Puzder, A. J. Williamson, N. Zaitseva, G. Galli, L. Manna, and A. P. Alivisatos. The effect of organic ligand binding on the growth of CdSe nanoparticles probed by ab initio calculations. *Nano Letters*, 4:2361–2365, 2004.

[240] M. Califano, G. Bester, and A. Zunger. Prediction of a shape-induced enhancement in the hole relaxation in nanocrystals. *Nano Lett.*, 3:1197, 2003.

[241] Y.-N. Xu and W. Y. Ching. Electronic, optical, and structural properties of some wurtzite crystals. *Phys. Rev. B*, 48:4335–4351, 1993.

[242] X. Huang, E. Lindgren, and J. R. Chelikowsky. Surface passivation method for semiconductor nanostructures. *Phys. Rev. B*, 71:165328, 2005.

[243] F. A. Reboredo and A. Zunger. Surface-passivation-induced optical changes in Ge quantum dots. *Phys. Rev. B*, 63:235314, 2001.

[244] Lin-Wang Wang and Alex Zunger. Solving Schrödinger's equation around a desired energy: Application to silicon quantum dots. *J. Chem. Phys.*, 100(3):2394–2397, 1994.

[245] C. Delerue and M. Lannoo. *Nanostructures: theory and modelling*. Springer Verlag, Berlin and Heidelberg, 2004.

[246] L.-W. Wang and A. Zunger. Dielectric constants of silicon quantum dots. *Phys. Rev. Lett.*, 73:1039–1042, 1994.

[247] A. Franceschetti, L. W. Wang, H. Fu, and A. Zunger. Short-range versus long-range electron-hole exchange interactions in semiconductor quantum dots. *Phys. Rev. B*, 58:R13367–R13370, 1998.

[248] R. Resta. Thomas-fermi dielectric screening in semiconductors. *Phys. Rev. B*, 16:2717, 1977.

[249] M. Q. Israr, J. R. Sadaf, O. Nur, M. Willander, S. Salman, and B. Danielsson. Chemically fashioned zno nanowalls and their potential application for potentiometric cholesterol biosensor. *Appl. Phys. Lett.*, 98:253705, 2011.

[250] H. Guo, Z. Lin, Z. Feng, L. Lin, and J. Zhou. White-light-emitting diode based on ZnO nanotubes. *J. Phys. Chem. C*, 113:12546, 2009.

[251] S. H. Ko, D. Lee, H. W. Kang, K. H. Nam, J. Y. Yeo, S. J. Hong, C. P. Grigoropoulos, and H. J. Sung. Nanoforest of hydrothermally grown hierarchical ZnO nanowires for a high efficiency dye-sensitized solar cell. *Nano Lett.*, 11:666, 2011.

[252] Q. Qiao, B.H. Li, C.X. Shan, J.S. Liu, J. Yu, X.H. Xie, Z.Z. Zhang, T.B. Ji, Y. Jia, and D.Z. Shen. Light-emitting diodes fabricated from small-size ZnO quantum dots. *Mat. Lett.*, 74:104, 2012.

[253] A. B. Djurisic and Y. H. Leung. Optical properties of ZnO nanostructures. *Small*, 2:944–961, 2006.

[254] M. Salavati-Niasari, F. Davar, and Z. Fereshteh. Synthesis and characterization of ZnO nanocrystals from thermolysis of new precursor. *Chem. Eng. J.*, 146:498 – 502, 2009.

[255] M. Califano, A. Zunger, and A. Franceschetti. Efficient inverse auger recombination at threshold in CdSe nanocrystals. *Nano Letters*, 4:525–531, 2004.

[256] H. Fu and A. Zunger. Quantum-size effects on the pressure-induced direct-to-indirect band-gap transition in InP quantum dots. *Phys. Rev. Lett.*, 80:5397–5400, 1998.

[257] S. J. Chen, Y. C. Liu, C. L. Shao, C. S. Xu, Y. X. Liu, C. Y. Liu, B. P. Zhang, L. Wang, B. B. Liu, and G. T. Zou. Photoluminescence study of ZnO nanotubes under hydrostatic pressure. *Appl. Phys. Lett.*, 88:133127, 2006.

[258] X. Michalet, F. F. Pinaud, L. A. Bentolila, J. M. Tsay, S. Doose, J. J. Li, G. Sundaresan, A. M. Wu, S. S. Gambhir, and S. Weiss. Quantum dots for live cells, in vivo imaging, and diagnostics. *Science*, 307:538–544, 2005.

[259] G. Ouyang, C. Q. Sun, and W. G. Zhu. Atomistic origin and pressure dependence of band gap variation in semiconductor nanocrystals. *J. Phys. Chem. C*, 113:9516–9519, 2009.

[260] J.-W. Luo, S.-S. Li, J.-B. Xia, and L.-W. Wang. Photoluminescence pressure coefficients of InAs/GaAs quantum dots. *Phys. Rev. B*, 71:245315, 2005.

[261] G. A. Narvaez, G. Bester, and A. Zunger. Pressure effects on neutral and charged excitons in self-assembled (In,Ga)As/GaAs quantum dots. *Phys. Rev. B*, 72:041307, 2005.

[262] J. W. Li, L. W. Yang, Z. F. Zhou, Paul K. Chu, X. H. Wang, J. Zhou, L. T. Li, and Chang Q. Sun. Bandgap modulation in ZnO by size, pressure, and temperature. *J. Phys. Chem. C*, 114:13370–13374, 2010.

[263] A. Franceschetti, H. Fu, L. W. Wang, and A. Zunger. Many-body pseudopotential theory of excitons in InP and CdSe quantum dots. *Phys. Rev. B*, 60:1819–1829, 1999.

[264] A. J. Williamson, L. W. Wang, and A. Zunger. Theoretical interpretation of the experimental electronic structure of lens-shaped self-assembled InAs/GaAs quantum dots. *Phys. Rev. B*, 62:12963, 2000.

[265] H. Morkoç and Ü. Özgür. *Zinc Oxide*. Wiley-vch, 2009.

[266] A. Mang, K. Reimann, and St. Rübenacke. Band gaps, crystal-field splitting, spin-orbit coupling, and exciton binding energies in ZnO under hydrostatic pressure. *Solid State Commun.*, 94(4):251–254, 1995.

[267] A. Segura, J. A. Sans, F. J. Manjan, A. Muñoz, and M. J. Herrera-Cabrera. Optical properties and electronic structure of rock-salt ZnO under pressure. *Appl. Phys. Lett.*, 83:278–280, 2003.

[268] A. Schleife, C. Rodl, F. Fuchs, J. Furthmuller, and F. Bechstedt. Strain influence on valence-band ordering and excitons in ZnO: An ab initio study. *Appl. Phys. Lett.*, 91:241915, 2007.

[269] S. Baskoutas and G. Bester. Transition in the optical emission polarization of ZnO nanorods. *J. Phys. Chem. C*, 115:15862, 2011.

[270] D. Camacho and Y. M. Niquet. Application of Keating's valence force field model to non-ideal wurtzite materials. *Physica E*, 42:1361, 2010.

[271] T. B. Bateman. Elastic moduli of single-crystal zinc oxide. *J. Appl. Phys.*, 33:3309–3312, 1962.

[272] C. D. Grant, J. C. Crowhurst, S. Hamel, A. J. Williamson, and N. Zaitseva. Anomalous photoluminescence in CdSe quantum-dot solids at high pressure due to nonuniform stress. *Small*, 4:788–794, 2008.

[273] J. Hu, L.-S. Li, W. Yang, L. Manna, L.-W. Wang, and A. P. Alivisatos. *Science*, 292:2060, 2001.

[274] N. S. Han, H. S. Shim, S. Lee, S. M. Park, M. Y. Choi, and J. K. Song. Light-matter interaction and polarization of single ZnO nanowire lasers. *Phys. Chem. Chem. Phys.*, 14:10556, 2012.

[275] Z. Fan, P. C. Chang, J. G. Lu, E. C. Walter, R. M. Penner, C. H. Lin, and H. P. Lee. Photoluminescence and polarized photodetection of single ZnO nanowires. *Appl. Phys. Lett.*, 85:6128–6130, 2004.

[276] J.E. Rowe, M. Cardona, and F.H. Pollak. Valence band symmetry and deformation potentials of ZnO. *Solid State Commun.*, 6:239–242, 1968.

[277] G. Jacopin, L. Rigutti, A. Bugallo, F. Julien, C. Baratto, E. Comini, M. Ferroni, and M. Tchernycheva. High degree of polarization of the near-band-edge photoluminescence in ZnO nanowires. *Nanoscale Res. Lett.*, 6:501, 2011.

[278] P. Yang, H. Yan, S. Mao, R. Russo, J. Johnson, R. Saykally, N. Morris, J. Pham, R. He, and H.-J. Choi. Controlled growth of ZnO nanowires and their optical properties. *Adv. Funct. Mater.*, 12:323–331, 2002.

[279] C. H. Liu, J. A. Zapien, Y. Yao, X. M. Meng, C. S. Lee, S. S. Fan, Y. Lifshitz, and S. T. Lee. High-density, ordered ultraviolet light-emitting ZnO nanowire arrays. *Adv. Mater.*, 15:838–841, 2003.

[280] H. Kind, H. Yan, B. Messer, M. Law, and P. Yang. Nanowire ultraviolet photodetectors and optical switches. *Adv. Mater.*, 14:158–160, 2002.

[281] K. Keem, H. Kim, G.-T. Kim, J. S. Lee, B. Min, K. Cho, M.-Y. Sung, and S. Kim. Photocurrent in ZnO nanowires grown from Au electrodes. *Appl. Phys. Lett.*, 84:4376–4378, 2004.

[282] Q. Wan, Q. H. Li, Y. J. Chen, T. H. Wang, X. L. He, J. P. Li, and C. L. Lin. Fabrication and ethanol sensing characteristics of zno nanowire gas sensors. *Appl. Phys. Lett.*, 84(18):3654–3656, 2004.

[283] C. Baratto, S. Todros, G. Faglia, E. Comini, G. Sberveglieri, S. Lettieri, L. Santamaria, and P. Maddalena. Luminescence response of ZnO nanowires to gas adsorption. *Sens. Actuator B-Chem.*, 140:461–466, 2009.

[284] Z. L. Wang and J. Song. Piezoelectric nanogenerators based on zinc oxide nanowire arrays. *Science*, 312:242–246, 2006.

[285] G. Zhu, R. Yang, S. Wang, and Z. L. Wang. Flexible high-output nanogenerator based on lateral ZnO nanowire array. *Nano Lett.*, 10:3151–3155, 2010.

[286] Q. Wan, C. L. Lin, X. B. Yu, and T. H. Wang. Room-temperature hydrogen storage characteristics of ZnO nanowires. *Appl. Phys. Lett.*, 84:124–126, 2004.

[287] Y. Gu, Igor L. Kuskovsky, M. Yin, S. O'Brien, and G. F. Neumark. Quantum confinement in ZnO nanorods. *Appl. Phys. Lett.*, 85:3833, 2004.

[288] M. Sahin, S. Nizamoglu, A. E. Kavruk, and H. V. Demir. Self-consistent computation of electronic and optical properties of a single exciton in a spherical quantum dot via matrix diagonalization method. *J. Appl. Phys.*, 106:043704, 2009.

[289] A. W. Long and B. M. Wong. Pamela: An open-source software package for calculating nonlocal exact exchange effects on electron gases in core-shell nanowires. *AIP Adv.*, 2:032173, 2012.

[290] H. J. Xiang, J. Yang, J. G. Hou, and Q. Zhu. Piezoelectricity in ZnO nanowires: A first-principles study. *Appl. Phys. Lett.*, 89:223111, 2006.

[291] Z. Xu, Q.-R. Zheng, and G. Su. Charged states and band-gap narrowing in codoped ZnO nanowires for enhanced photoelectrochemical responses: Density functional first-principles calculations. *Phys. Rev. B*, 85:075402, 2012.

[292] Z. Zeng, C. S. Garoufalis, S. Baskoutas, and G. Bester. Electronic and optical properties of ZnO quantum dots under hydrostatic pressure. *Phys. Rev. B*, 87:125302, 2013.

[293] L. Zhang, J.-W. Luo, A. Franceschetti, and A. Zunger. Excitons and excitonic fine structures in Si nanowires: Prediction of an electronic state crossover with diameter changes. *Phys. Rev. B*, 84:075404, 2011.

[294] P. W. Avraam, N.D. M. Hine, P. Tangney, and P. D. Haynes. Factors influencing the distribution of charge in polar nanocrystals. *Phys. Rev. B*, 83:241402, 2011.

[295] A. Molina-Sanchez, A. Garcia-Cristobal, and G. Bester. Semiempirical pseudopotential approach for nitride-based nanostructures and ab initio based passivation of free surfaces. *Phys. Rev. B*, 86:205430, 2012.

[296] L. E. Brus. Electron–electron and electron-hole interactions in small semiconductor crystallites: The size dependence of the lowest excited electronic state. *J. Chem. Phys.*, 80:4403–4409, 1984.

[297] B. S. Kim, M. A. Islam, L. E. Brus, and I. P. Herman. Interdot interactions and band gap changes in CdSe nanocrystal arrays at elevated pressure. *J. Appl. Phys.*, 89:8127, 2001.

[298] A. Bagga, P. K. Chattopadhyay, and S. Ghosh. Origin of stokes shift in InAs and CdSe quantum dots: Exchange splitting of excitonic states. *Phys. Rev. B*, 74:035341, 2006.

[299] D. O. Demchenko and L.-W. Wang. Optical transitions and nature of stokes shift in spherical CdS quantum dots. *Phys. Rev. B*, 73:155326, 2006.

[300] J. J. Hopfield. Fine structure in the optical absorption edge of anisotropic crystals. *J. Phys. Chem. Solids*, 15:97–107, 1960.

[301] Y. H. Huo, B. J. Witek, S. Kumar, J. R. Cardenas, J. X. Zhang, N. Akopian, R. Singh, E. Zallo, R. Grifone, D. Kriegner, R. Trotta, F. Ding, J. Stangl, V. Zwiller, G. Bester, A. Rastelli, and O. G. Schmidt. A light-hole exciton in a quantum dot. *Nat. Phys.*, 10:46–51, 2014.

[302] T. Hattori, Y. Homma, A. Mitsuishi, and M. Tacke. Indices of refraction of ZnS, ZnSe, ZnTe, CdS, and CdTe in the far infrared. *Opt. Commun.*, 7:229–232, 1973.

[303] L. Thamizhmani, A. K. Azad, J. Dai, and W. Zhang. Far-infrared optical and dielectric response of ZnS measured by terahertz time-domain spectroscopy. *Appl. Phys. Lett.*, 86:131111, 2005.

[304] M Bredol and J Merikhi. ZnS precipitation: morphology control. *J. Mater. Sci.*, 33:471–476, 1998.

[305] Y. Jiang, W.-J. Zhang, J.?S. Jie, X.-M. Meng, J.-A. Zapien, and S.-T. Lee. Homoepitaxial growth and lasing properties of ZnS nanowire and nanoribbon arrays. *Adv. Mater.*, 18:1527–1532, 2006.

[306] P. T. Snee, R. C. Somers, G.Nair, J. P. Zimmer, M. G. Bawendi, and D. G. Nocera. A ratiometric CdSe/ZnS nanocrystal pH sensor. *J. Am. Chem. Soc.*, 128:13320–13321, 2006.

[307] P. Calandra, M. Goffredi, and V. T. Liveri. Study of the growth of ZnS nanoparticles in water/AOT/n-heptane microemulsions by UV-absorption spectroscopy. *Colloids Surf. A*, 160:9–13, 1999.

[308] S. D. Scott and H. L. Barnes. Sphalerite-wurtzite equilibria and stoichiometry. *Geochim. Cosmochim. Acta*, 36:1275 – 1295, 1972.

[309] Qihua Xiong, G. Chen, J. D. Acord, X. Liu, J. J. Zengel, H. R. Gutierrez, J. M. Redwing, L. C. Lew Yan Voon, B. Lassen, and P. C. Eklund. Optical properties of rectangular cross-sectional ZnS nanowires. *Nano Lett.*, 4:1663–1668, 2004.

[310] E. Bellotti, K. F. Brennan, R. Wang, and P. P. Ruden. Calculation of the electron initiated impact ionization transition rate in cubic and hexagonal phase ZnS. *J. Appl. Phys.*, 82:2961–2964, 1997.

[311] X. Wang, H. Huang, B. Liang, Z. Liu, D. Chen, and G. Shen. ZnS nanostructures: Synthesis, properties, and applications. *Critical Rev. Sol. State and Mat. Scien.*, 38:57–90, 2013.

[312] C.-Y. Yeh, S.-H. Wei, and A. Zunger. Relationships between the band gaps of the zinc-blende and wurtzite modifications of semiconductors. *Phys. Rev. B*, 50:2715–2718, 1994.

[313] S. Zh. Karazhanov, P. Ravindran, A. Kjekshus, H. Fjellvåg, U. Grossner, and B. G. Svensson. Coulomb correlation effects in zinc monochalcogenides. *J. Appl. Phys.*, 100:043709, 2006.

[314] S.Zh. Karazhanov, P. Ravindran, A. Kjekhus, H. Fjellvåg, U. Grossner, and B.G. Svensson. Electronic structure and band parameters for ZnX(X = O, S, Se, Te). *J. Cryst. Growth*, 287:162–168, 2006.

[315] X. Zhang, M. Zhao, S. Yan, T. He, W. Li, X. Lin, Z. Xi, Z. Wang, X. Liu, and Y. Xia. First-principles study of ZnS nanostructures: nanotubes, nanowires and nanosheets. *Nanotechnology*, 19:305708, 2008.

[316] J. Nanda, S. Sapra, D. D. Sarma, N. Chandrasekharan, and G. Hodes. Size-selected zinc sulfide nanocrystallites: Synthesis, structure, and optical studies. *Chem. Mater.*, 12:1018–1024, 2000.

[317] L.-W. Wang and A. Zunger. Local-density-derived semiempirical pseudopotentials. *Phys. Rev. B*, 51:17398–17416, 1995.

[318] S. Baskoutas, Z. Zeng, C. S. Garoufalis, and G. Bester. Tuning of the optical emission polarization of ZnO nanorods by an applied hydrostatic pressure. *J. Phys. Chem. C*, 116:26592–26597, 2012.

[319] J. W. Baars. *In proceedings of the international conference on II-VI semiconducting compounds*, Volume 22a. Benjamin, New York, Providence, 1968.

[320] R. E. Drews, E. A. Davis, and A. G. Leiga. Reflectivity spectra of $Cd_{1-x}Zn_xS$ single crystals. *Phys. Rev. Lett.*, 18:1194–1196, 1967.

[321] A. Ebina, E. Fukunaga, and T. Takahashi. Reflectivity spectra of structurally pure wurtzite-type ZnS in ultraviolet and vacuum-ultraviolet regions. *Phys. Rev. B*, 12:687–689, 1975.

[322] T. K. Bergstresser and M. L. Cohen. Electronic structure and optical properties of hexagonal CdSe, CdS, and ZnS. *Phys. Rev.*, 164:1069–1080, 1967.

[323] The macroscopic low-frequency and high-frequency dielectric constant $\varepsilon_0 = 9.6$ and $\varepsilon_\infty = 5.8$, respectively. Thomas-Fermi wave vector $q_{TF} = 0.68$, $\rho_\infty = 5.498$, $\rho_e = 55.96$ and $\rho_h = 16.43$.

[324] A. L. Efros and A. L. Efros. Interband absorption of light in a semiconductor sphere. *Sov. Phys. Semicond.*, 16:772–775, 1982.

[325] L. E. Brus. A simple model for the ionization potential, electron affinity, and aqueous redox potentials of small semiconductor crystallites. *J. Chem. Phys.*, 79:5566–5571, 1983.

[326] P. E. Lippens and M. Lannoo. Calculation of the band gap for small CdS and ZnS crystallites. *Phys. Rev. B*, 39:10935–10942, 1989.

[327] H. C. Ong and R. P. H. Chang. Optical constants of wurtzite ZnS thin films determined by spectroscopic ellipsometry. *Appl. Phys. Lett.*, 79:3612–3614, 2001.

[328] A. Franceschetti and A. Zunger. Direct pseudopotential calculation of exciton coulomb and exchange energies in semiconductor quantum dots. *Phys. Rev. Lett.*, 78:915–918, 1997.

[329] R. W. Meulenberg, J. R.I. Lee, A. Wolcott, J. Z. Zhang, L. J. Terminello, and T. V. Buuren. Determination of the exciton binding energy in CdSe quantum dots. *ACS Nano*, 3:325–330, 2009.

[330] Al. L. Efros, M. Rosen, M. Kuno, M. Nirmal, D. J. Norris, and M. Bawendi. Band-edge exciton in quantum dots of semiconductors with a degenerate valence band: Dark and bright exciton states. *Phys. Rev. B*, 54:4843–4856, 1996.

[331] M. Kuno, J. K. Lee, B. O. Dabbousi, F. V. Mikulec, and M. G. Bawendi. The band edge luminescence of surface modified CdSe nanocrystallites: Probing the luminescing state. *J. Chem. Phys.*, 106:9869–9882, 1997.

[332] J. Li and J.-B. Xia. Hole levels and exciton states in CdS nanocrystals. *Phys. Rev. B*, 62:12613–12616, 2000.

[333] Z. Yu, J. Li, D. B. O'Connor, Wang, and P. F. Barbara. Large resonant stokes shift in CdS nanocrystals. *J. Phys. Chem. B*, 107:5670–5674, 2003.

Part III

Papers

A

Appendix

This appendix includes twelve published papers during my PhD.

Paper I

In which we study the effect of a tilted magnetic field on the binding energy of surface impurities in $Al_{03}Ga_{0.7}As/GaAs$ cylindrical quantum dots ...

Tuning the binding energy of surface impurities in cylindrical GaAs/AlGaAs quantum dots by a tilted magnetic field

Zaiping Zeng,[1] Christos S. Garoufalis,[1,2] Sotirios Baskoutas,[1,a)] and Andreas F. Terzis[3]
[1]*Department of Materials Science, University of Patras, 26504 Patras, Greece*
[2]*Department of Environment Technology and Ecology, Technological Institute of Ionian Islands, 2 Kalvou Sq, 29100 Zakynthos, Greece*
[3]*Department of Physics, University of Patras, 26504 Patras, Greece*

(Received 17 December 2011; accepted 24 August 2012; published online 27 September 2012)

Using the potential morphing method in the framework of the effective-mass approximation, we have studied theoretically the effect of a tilted magnetic field on the binding energy of surface impurities in $GaAs/Al_{0.3}Ga_{0.7}As$ cylindrical quantum dots. It is found that contrary to what was expected based on the existing literature for growth-direction magnetic fields, the presence of a tilted field does not always contribute positively to the binding energy of surface impurities. The shape (aspect ratio) and size of the cylindrical QD as well as the dopant positions at the QD surface play an important role. Furthermore, we find that decrease of the QD size can reduce the sensitivity of the variation of the donor binding energy with respect to the field strength (orientation), but it cannot change its general behaviour. © *2012 American Institute of Physics*. [http://dx.doi.org/10.1063/1.4754824]

I. INTRODUCTION

Rapid advance in material growth technology leads to a renewed interest in studies of semiconductor nanostructures subjected to a magnetic field directed at an angle with respect to the growth direction.[1–5] Investigations of hydrogenic impurity in the above setup are of particular relevance, since the presence of the hydrogenic impurity influences greatly the electronic mobility and optical properties. Furthermore, surface impurities play a crucial role in the design of new materials with desirable properties.[6–8] Up to now, only few reports[5,9,10] were involved with studying the tilted magnetic field effect on the donor impurity states in such unique systems, and all of them were exclusively based on semiconductor quantum well (QW) structures. To the best of our knowledge, there are no reports based on the effective mass approximation (EMA) offering a detailed account of the behaviour of the binding energy of impurities (on-surface or on-center) localized in QDs subjected to a tilted magnetic field. The present work attempts to fill this gap in the literature by providing theoretical predictions based on the potential morphing method (PMM)[11,12] which is employed in the framework of EMA. The emphasis of the present paper is placed on the behaviour of the donor binding energy with respect to the geometric characteristics of the QDs, impurity positions, and magnetic field orientation and intensity.

II. GENERAL THEORY

In the framework of EMA, a shallow donor impurity embedded in a cylindrical QD is modeled by the Hamiltonian

$$\hat{H} = (\hat{p} + \frac{e}{c}\vec{A}(\vec{r}))\frac{1}{2m_e^*}(\hat{p} + \frac{e}{c}\vec{A}(\vec{r})) + V(\vec{r}) - \frac{e^2}{\epsilon|\vec{r} - \vec{r}_i|}. \quad (1)$$

The first term of the Hamiltonian is the operator for the Kinetic energy of a delocalized conduction electron (where e is the absolute value of the electron charge, c is the speed of the light in vacuum, and m_e^* is the electron effective mass) in the presence of a magnetic field B. In our case, the magnetic field is applied parallel to the xoz plane making an angle θ with the x-axial direction (i.e., $\vec{B} = B(\cos\theta, 0, \sin\theta)$). For the uniform magnetic field $\vec{B}$, the commonly used cylindrical gauge is employed, and the vector potential assumes the following form:

$$\vec{A}(\vec{r}) = \frac{1}{2}\vec{B} \times \vec{r} = \frac{1}{2}B(-y\sin\theta, -(z\cos\theta - x\sin\theta), y\cos\theta). \quad (2)$$

By substituting Eq. (2) into Hamiltonian (1), the operator for the Kinetic energy of the electron under the influence of a tilted magnetic field $\vec{B}$ (the first term of Hamiltonian (1)) takes the following form:

$$\hat{H}_{Kin} = \hat{p}\frac{1}{2m_e^*}\hat{p} + \frac{eB}{2m_e^* c}(\cos\theta\hat{l}_x + \sin\theta\hat{l}_z) + \frac{e^2B^2}{8m_e^* c^2}[y^2 + (z\cos\theta - x\sin\theta)^2], \quad (3)$$

where $\hat{l}_i$ $(i = x, z)$ is the i-component of the angular momentum operator $(\hat{l}_x = y\hat{p}_z - z\hat{p}_y, \hat{l}_z = x\hat{p}_y - y\hat{p}_x)$. The second term of Eq. (3) represents the interaction between the external applied tilted magnetic field $\vec{B}$ and the orbital angular momentum $\vec{l}(\vec{B}\cdot\vec{l} = B_x\hat{l}_x + B_y\hat{l}_y + B_z\hat{l}_z$, here $B_y = 0)$. The third term of Eq. (3)

$$V_B(\vec{r}) = \frac{e^2B^2}{8m_e^* c^2}[y^2 + (z\cos\theta - x\sin\theta)^2] \quad (4)$$

corresponds to the magnetic field induced confinement potential. $V(\vec{r})$ in Eq. (1) is the step-like electron confinement

a)Electronic mail: bask@upatras.gr.

potential, which is assumed to be zero inside the QD and V_0 outside the dot. The third part of the Eq. (1) is the Coulomb interaction between the electron and the shallow donor impurity located at $\vec{r}_i = (x_i, y_i, z_i)$; ϵ is the static dielectric constant. In order to obtain the ground state of the Hamiltonian (1), we are using the PMM following the procedure outlined in Ref. 11. The ground-state donor binding energy is

$$E_b = E_0 - \tilde{E}, \tag{5}$$

where $\tilde{E}$ is the energy which corresponds to the Hamiltonian in Eq. (1) and E_0 is the energy without Coulomb interaction (absence of the third term in Eq. (1)). The magnetic shift of the donor binding energy is defined as the difference between the binding energy of a donor impurity at magnetic field $B \neq 0$ and its binding energy at magnetic field $B = 0$ for a fixed tilted angle θ, which is given by[5]

$$\delta E_b = E_b(B \neq 0, \theta) - E_b(B = 0, \theta). \tag{6}$$

Similarly, the angle shift of the donor binding energy is defined as the difference between the binding energy of a donor impurity at tilted angle $\theta \neq 0^\circ$ and its binding energy at tilted angle $\theta = 0^\circ$ and hence is the following:[5]

$$\Delta E_b = E_b(B, \theta \neq 0^\circ) - E_b(B, \theta = 0^\circ). \tag{7}$$

III. NUMERICAL RESULTS AND DISCUSSION

In the following, we will discuss the influence of the QD geometric characteristics (such as dot size and height-to-radius aspect ratio), impurities positions (on-surface or on-center), and magnetic field intensities and orientations on the donor binding energy in a cylindrical QD characterized by the dot radius R and dot height L. Our calculations are based on a typical GaAs cylindrical QD, surrounded by larger band gap material $Al_{0.3}Ga_{0.7}As$ in both the radial and z-axis directions. All the material parameters used in our calculations are the same as in Ref. 12. The cartesian coordinates of the on-center, top, and side impurities, which are considered in the present calculations, are (0,0,0), (0,0,L/2), and (R,0,0), respectively.

As a first step towards studying the effect of a tilted magnetic field on the binding energy of surface impurities in cylindrical $GaAs/Al_{0.3}Ga_{0.7}As$ QDs, we performed calculations for the magnetic shift of the donor binding energy of surface impurities δE_b (top and side impurities) as a function of the magnetic field strength B (see the first two plots of the left column of Fig. 1). This procedure was repeated for height-to-radius aspect ratios $\rho = \frac{L}{R} = 0.5$, 1.0, and 2.0, while the dot's radius was set to $R = 20$ nm. As reported in previous investigations,[13] for a cylindrical QD subjected to the growth direction magnetic field, the binding energy of on-edge impurity (corresponding to the top impurity in our calculations) is totally insensitive to the increase of the magnetic field strength. However, for a tilted magnetic field (for instance, $\theta = 45^\circ$), the binding energy of top impurity, as indicated in Fig. 1, is very sensitive to the magnetic field, and δE_b increases dramatically with increasing the magnetic field for a disc-shaped QD (i.e., $\rho = 0.5$). However, as the aspect ration increases this sensitivity declines and δE_b even becomes negative for the rod-shaped QD ($\rho = 2.0$). On the other hand, for the case of side impurity, the behaviour of δE_b is found to be quite different. For a disc-shaped QD ($\rho = 0.5$), as shown in Fig. 1 (see the second plot of the left column), δE_b is negative and it keeps decreasing dramatically with increasing the magnetic field strength. When the aspect ratio goes up to $\rho = 1$, δE_b is also negative as the field increases, but the sensitivity of the donor binding energy with respect to the field strength is reduced. However, if the aspect ratio keeps increasing and a rod-shaped QD is produced, the enhancement of the magnetic field results in a positive δE_b, which is in contrast to the case of top impurity.

In an effort to explain these novel behaviour of the binding energy of surface impurities and understand the underlying physics, we have created suitable 3D contour plots of the electron probability density (first column of Fig. 2), as well as isosurfaces of the electron probability density differences (the last three columns of Fig. 2) in impurity-free QDs with different aspect ratios and magnetic fields (strength and orientation). In particular, each density difference plot has been produced by subtracting the zero field density from the density which corresponds to a specific field strength and orientation. This subtraction leads to positive (blue) and negative (red) density areas which indicate the charge movement due to the presence of the magnetic field. As a result, the red surfaces correspond to charge depletion areas, while the blue surfaces correspond to charge accumulation areas. For the creations of these 3D contour plots, the Gabedit graphical program[14] was used. By observing these figures, two distinct trends can be identified. The presence of the magnetic field makes the electron probability density shrinks towards the center of the dot and also elongates along the applied field direction. The geometric characteristics of the dot (aspect ratio) have a different influence on these two trends. The shrinking due to the magnetic field induced confinement is not significantly affected by the variation of the QD aspect ratio while, on the other hand, the elongation trend is greatly affected. In the absence of the magnetic field, the electron probability density is mainly distributed along the radial direction of a disc-shaped QD ($\rho = 0.5$) due to the strong confinement in the growth direction, whereas for a rod-shaped QD ($\rho = 2.0$), it extends apparently in all the three directions because it is in the weak confinement regime (see the first column of Fig. 2). When an experimentally strong tilted magnetic field (for instance, $B = 20$ T and $\theta = 45^\circ$) is applied in a disc shaped QD (see the third column of Fig. 2), the electron probability density exhibits an obvious shrinking towards the center of the QD (see the red color) while the elongation is strongly limited by the growth-direction geometric confinement of the QD. The charge density accumulation around the center of the QD is the dominant effect which leads to the decrease (increase) of the mean relative distance between the electron and the top (side) impurity. As a direct result, the binding energy of top impurity increases dramatically, whereas that of side impurity obviously decreases. On the contrary, when the dimensions (aspect

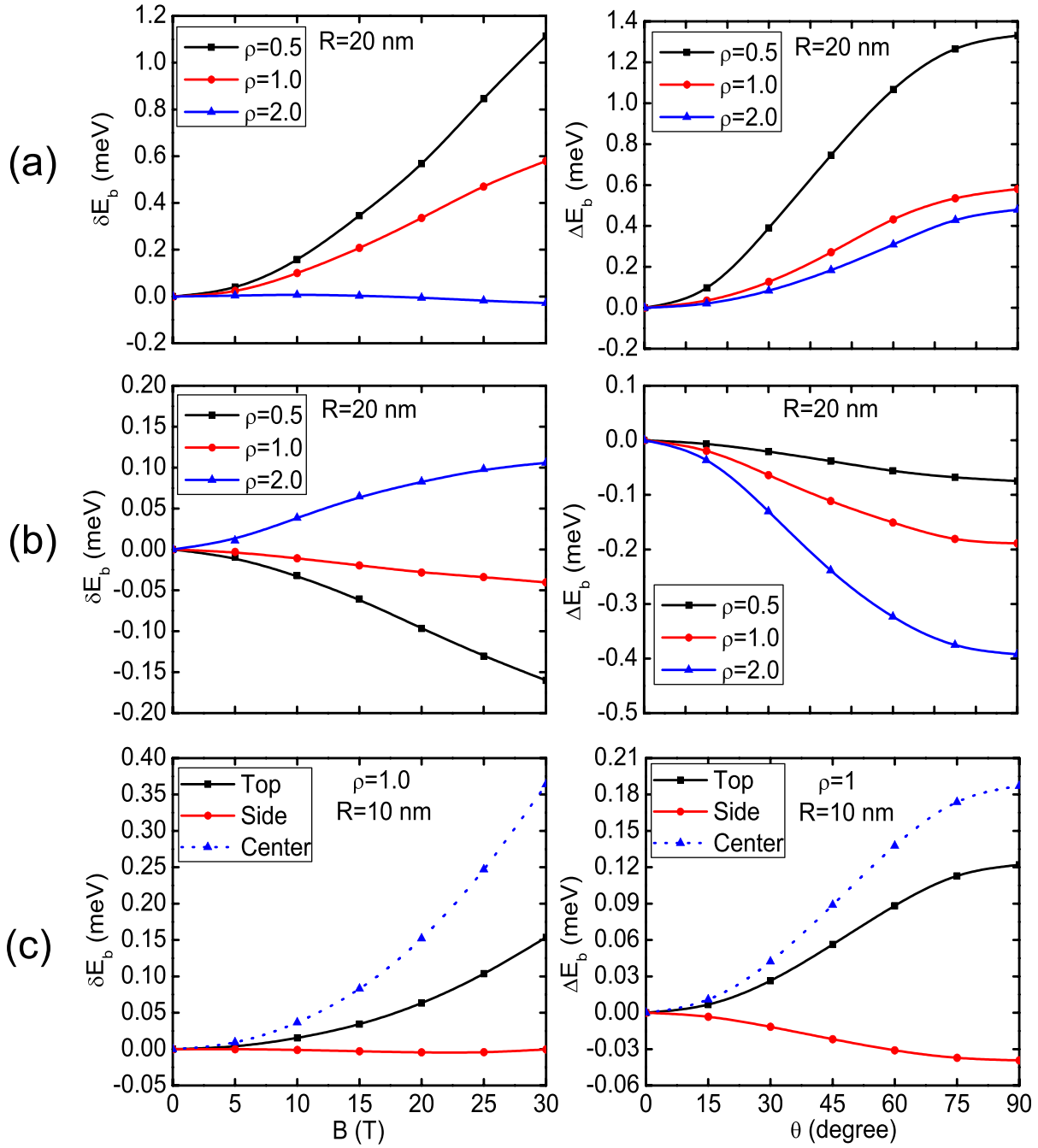

FIG. 1. Left column: magnetic shift of the donor binding energy δE_b as a function of magnetic field B with tilted angle $\theta = 45°$. Right column: angle shift of the donor binding energy ΔE_b as a function of the tilted angle θ with magnetic field $B = 20$ T. (a) is for different aspect ratios ($R = 20$ nm) and top impurity; (b) is for different aspect ratios ($R = 20$ nm) but side impurity; (c) is for different impurity positions (top, side, and center) but for radius $R = 10$ nm and aspect ratio $\rho = 1$.

ratios) of the QD become larger, the elongation trend mediates or even reverses this tendency.

In order to investigate the behaviour of δE_b in different dot sizes subjected to a tilted magnetic field, we also displayed in Fig. 1 (see the last plot of the left column), the magnetic shift of the donor binding energy δE_b as a function of the magnetic field strength in a cylindrical QD with aspect ratio $\rho = 1.0$ but with a smaller radius ($R = 10$ nm). In this calculation, three different impurity positions (top, side, and center) are considered. At a first glance, we can find that the binding energy of the surface impurities does not change in the same way as that of the on-center impurity when the magnetic field is enhanced. For instance, δE_b of side impurity slightly decreases with increasing the magnetic field. However, for an on-center donor impurity, it exhibits an apparent increase. This finding is totally different from the case of growth direction magnetic field, which states that the change of the binding energy of off-center impurity is similar to that of an on-center impurity.[15] Furthermore, by comparing the three plots shown in the left column of Fig. 1, it is found that decrease of the QD size can lead to the decrease of the sensitivity of the magnetic shift of the donor binding

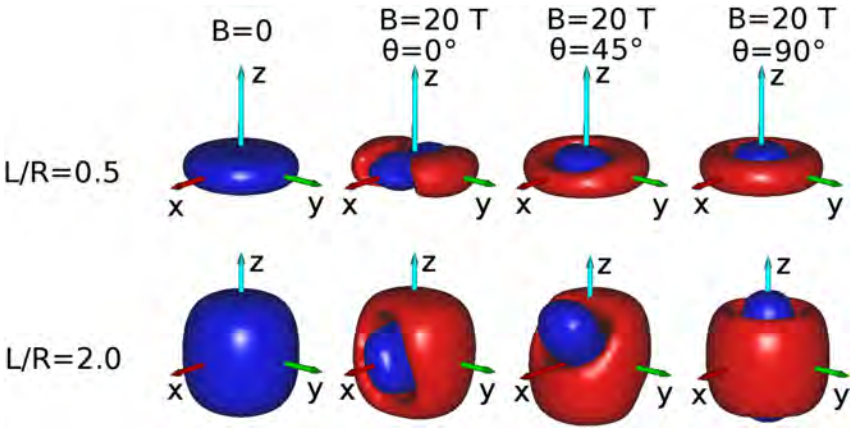

FIG. 2. The first column corresponds to the three dimensional electron probability density of an impurity free $GaAs/Al_{0.3}Ga_{0.7}As$ cylindrical QD with different aspect ratios in the absence of the magnetic field. The following three columns show suitably chosen isosurfaces of electron probability density differences for non-vanishing field along various directions.

energy with respect to the magnetic field strength but can not change its general behaviour.

As expected, the magnetic field orientation also has a significant influence on the binding energy of surface impurities in a cylindrical QD. As indicated from Fig. 1 (see the first two plots of the right column), both the top and side impurities show monotonic dependence of the binding energy on the tilted angle, irrespectively of the QD aspect ratios. However, the variation of the magnetic filed orientation from in-plane direction to the growth direction contributes positively to the angle shift of the binding energy of top impurity, while it has a negative influence on the angle shift of the binding energy of side impurity. This can be understood as follows. When the magnetic field is applied along the x-axial direction ($\theta = 0°$), the magnetic field induced confinement is in yoz plane as shown from Eq. (4). For this reason, the electron probability density shrinks in the plane perpendicular to the magnetic field direction and mainly elongates along the field direction at this stage (see the density differences shown in the second column of Fig. 2). When the magnetic field is tilted from the in-plane direction, the magnetic field has both longitudinal and transverse components, which correspond to the magnetic field induced confinement in xoy and yoz plane, respectively. Consequently, the electron probability density shrinks toward the center of the QD and the mean relative distance between the electron and side (top) impurity is increased (decreased). Finally, when the magnetic field is applied along the growth direction and the magnetic field induced confinement contributed from the transverse component of the magnetic field is diminished, the electron probability density is distributed apparently along the growth direction of the QD. Therefore, in this situation, the binding energy of top (side) impurity reaches its largest (smallest) value. Furthermore it can be deduced from Fig. 2 that the charge depletion (accumulation) is much more sensitive to the magnetic field orientation for the case of larger aspect ratio ($\rho = 2$). This directly indicates that the effect of the magnetic field orientation is more pronounced in a semiconductor QD with large aspect ratios.

As for the behaviour of the angle shift of the donor binding energy, several interesting trends can be observed from Fig. 1. As shown by the first plot of the right column, the sensitivity of ΔE_b of the top impurity with respect to the variation of the tilted angle appears to be significantly pronounced for the case of disc-shaped QD. However, this sensitivity exhibits an apparent decrease as the aspect ratio of the QD increases. On the contrary, for side impurity (see the second plot of the right column in Fig. 1), the sensitivity of ΔE_b is enhanced for a rod-shaped QD, and it appears to increase with increasing the aspect ratio, as expected. In order to show the angle shift of the donor binding energy in different dot sizes, we also exhibit in Fig. 1 (see the last plot of the right column), the dependence of ΔE_b of top (side or center) impurity on the field orientation in a cylindrical QD with aspect ratio $\rho = 1$ but for a smaller radius ($R = 10$ nm). It is found that the variation of ΔE_b strongly depends on the surface impurity positions, and it does not always behave in the similar way as that of an on-center impurity. By comparing the values of ΔE_b in the three plots (see the right column of Fig. 1), it is not difficult to find that the decrease of the QD size leads to a decrease of the sensitivity of ΔE_b with regard to the tilted angle, but it does not change its general behaviour, which is similar to that of the magnetic shift of the donor binding energy (see the plots exhibited in left column of Fig. 1).

In summary, our results show that QD geometric characteristics (dot sizes and aspect ratios), impurity positions (top, side, or center), and the magnetic field intensities and orientations affect significantly the donor binding energy. The magnetic (angle) shift of the donor binding energy is not always enhanced by the presence of a tilted magnetic field. Its sensitivity with respect to the field strength (or tilted angle) can be reduced by decreasing the QD size, but its general behaviour cannot be altered. Furthermore, it is found that the angle shift of the donor binding energy is a monotonic function of the tilted angle, irrespectively of the QD sizes and aspect ratios.

We hope the present work can stimulate forthcoming theoretical, experimental investigations as well as devices applications in this attracting research area.

ACKNOWLEDGMENTS

This research has been co-financed by the European Union (European Regional Development Fund-ERDF) and Greek National Funds through the Operational Program "Regional Operational Programme" of the National Strategic Reference Framework (NSRF)-Research Funding Program:

Support for Research, Technology, and Innovation actions in Region of Western Greece (MIS: 312123, D.237.002). Furthermore, this work is also supported by the Research Project "C. Caratheodory" D. 207 of the Research Committee of the University of Patras.

[1]S. Takaoka, A. Kuriyama, K. Oto, K. Murase, S. Shimomura, S. Hiyamizu, M. Cukr, T. Jungwirth, and L. Smrcka, Physica E **6**, 623 (2000).
[2]T. M. Fromhold, A. A. Krokhin, C. R. Tench, S. Bujkiewicz, P. B. Wilkinson, F. W. Sheard, and L. Eaves, Phys. Rev. Lett. **87**, 046803 (2001).
[3]G. Yu, D. J. Lockwood, A. J. S. Thorpe, and D. G. Austing, Phys. Rev. B **76**, 085331 (2007).
[4]G. M. Gusev, C. A. Duarte, T. E. Lamas, A. K. Bakarov, and J. C. Portal, Phys. Rev. B **78**, 155320 (2008).
[5]B. S. Monozon and P. Schmelcher, Phys. Rev. B **82**, 205313 (2010).
[6]S. Erwin, L. Zu, M. I. Haftel, A. L. Efros, T. A. Kennedy, and D. J. Norris, Nature (London) **436**, 91 (2005).
[7]D. J. Norris, A. L. Efros, and S. C. Erwin, Science **319**, 1776 (2008).
[8]S. V. Nistor, M. Stefan, L. C. Nistor, E. Goovaerts, and G. V. Tendeloo, Phys. Rev. B **81**, 035336 (2010).
[9]E. Kasapoglu, H. Sari, and I. Sökmen, Solid State Commun. **125**, 429 (2003).
[10]P. Redliński and B. Jankó, Phys. Rev. B **71**, 113309 (2005).
[11]M. Rieth, W. Schommers, and S. Baskoutas, Int. J. Mod. Phys. B **16**, 4081 (2002).
[12]S. Baskoutas and A. F. Terzis, Eur. Phys. J. B **69**, 237 (2009).
[13]R. Charrour, M. Bouhassoune, M. Fliyou, and A. Nougaoui, Physica B **293**, 137 (2000).
[14]A. Allouche, J. Comput. Chem. **32**, 174 (2011).
[15]Z. Xiao, J. Zhu, and F. He, J. Appl. Phys. **79**, 9181 (1996).

Paper II

In which we study the donor binding energy distribution with respect to the dopant positions in self-assembled GaAs/AlGaAs quantum dots in the presence of a tilted electric field ...

Physics Letters A 376 (2012) 2712–2716

Contents lists available at SciVerse ScienceDirect

Physics Letters A

www.elsevier.com/locate/pla

Stark effect of donor binding energy in a self-assembled GaAs quantum dot subjected to a tilted electric field

Zaiping Zeng [a], Christos S. Garoufalis [a,b], Sotirios Baskoutas [a,*], Andreas F. Terzis [c]

[a] Materials Science Department, University of Patras, Rio 26504, Greece
[b] Department of Environment Technology and Ecology, Technological Institute of Ionian Islands, 2 Kalvou Sq, 29100 Zakynthos, Greece
[c] Physics Department, University of Patras, 26504 Patras, Greece

ARTICLE INFO

Article history:
Received 13 June 2012
Accepted 28 July 2012
Available online 1 August 2012
Communicated by R. Wu

Keywords:
Donor binding energy
Quantum dot
Electric field

ABSTRACT

We theoretically investigated the donor binding energy distribution with respect to the dopant positions in a self-assembled GaAs/AlGaAs quantum dot (QD) in the presence of a tilted electric field. It is found that there is a critical line in a doping plane, corresponding to zero Stark shift of the donor binding energy. At low electric fields, our work reveals that Stark shift of an on-center donor binding energy is a "purely" quadratic function of the electric field strength, irrespective of QD dimensions and field orientations. This scaling law permits us to indirectly estimate the impurity polarizability in a self-assembled QD.

1. Introduction

Doping semiconductor QDs allows tuning many properties for tailoring quantum devices and it provides further means to control their performance [1]. Moreover, donors have already been used in some elegant quantum computing proposals that draw upon the vast expertise of the semiconductor device industry [2]. Therefore, the binding energy of impurities confined in semiconductor QDs has been extensively studied using different numerical methods and several confining potential shapes [3–7]. In all these reports, only a few impurity positions (on the growth direction or along the radial direction) are considered. Furthermore, application of an external electric field induces the carriers distribution polarization and shifts the energy states. These effects considerably change the energy spectrum of the carriers, which may be used to control and modulate the intensity output of devices. Consequently, this makes the external electric field an effective tool for studying the physical properties of semiconductor nanostructures, both from theoretical and practical points of view. It is well known that when an electric field is applied in a semiconductor QD in which the carriers (electron or hole) are confined in all three directions, the quantum-confined Stark effect appears. Due to this effect, the symmetry of the electron probability density distributions at zero electric field breaks and the maximum of the electron probability density moves away from the QD center to the opposite direction of the applied field. Consequently, the donor binding energy corresponding to the doping positions which are located opposite to applied field direction exhibits "blue" shift. Conversely, "red" shift takes place if the doping positions are distributed along the field direction. Are there any doping positions in the QD at which the donor binding energy keeps invariant (zero shift) under the influence of an applied electric field?

On the other hand, quantum-confined Stark effect on the exciton energy in a semiconductor self-assembled QD has been extensively investigated [8–13], indicating that a shift of the excitonic peak in absorption or photoluminescence (PL) spectra, for small electric field F, has the form $\delta E(F) = E(F \neq 0) - E(F = 0) \approx \alpha^X F - \beta^X F^2$, where α^X and β^X are, respectively, the components of the permanent dipole moment and the polarizability. Especially, if the symmetry of the problem rules out a preferential direction, the Stark shift is an even function of F and the expansion begins with the polarizability term ($\alpha^X = 0$). As is well known, the donor impurity behaves like an exciton with infinite hole effective mass. Therefore, a question which naturally arises is the following: what is the relation connecting the Stark shift of the donor binding energy with the applied electric field in a semiconductor self-assembled QD?

To put a quantitative answer to the questions addressed before, in this Letter, we performed detailed theoretical investigations on the donor binding energy distributions with respect to the dopant positions in a self-assembled GaAs/AlGaAs QD, considering the effect of an applied tilted electric field. The numerical approach we used is potential morphing method [14] (PMM) in the framework of effective-mass approximation. The rest Letter is organized as

* Corresponding author.
E-mail address: bask@upatras.gr (S. Baskoutas).

0375-9601/$ – see front matter
http://dx.doi.org/10.1016/j.physleta.2012.07.032

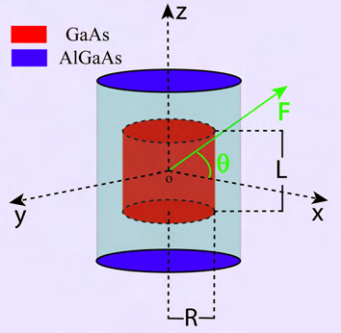

Fig. 1. (Color online.) Schematic representation of the self-assembled GaAs/AlGaAs QD under investigation with the dot height L and the radius R in the presence of a electric field F applied parallel to the xoz plane making an angle θ relative to the x axis.

follows: in Section 2 we define our model and explain the general theory, in Section 3 we present our numerical results and related discussions, and Section 4 is devoted to conclusions.

2. Theoretical model

It is well known that the self-assembled QDs are quasi-two-dimensional structures which strongly confine the carriers (electron or hole) in the growth direction, while the lateral confinement is typically softer. Due to this fact, a GaAs/AlGaAs QD with cylindrical shape is adopted for our model calculations (see Fig. 1). The parameter L referred to the dot height is responsible for the QD growth-direction (z-axial direction) quantum confinement. Whereas the parameter R referred to the dot radius is responsible for the QD lateral quantum confinement.

In the framework of the effective-mass approximation, a shallow donor impurity embedded in a self-assembled QD is modeled by the Hamiltonian

$$\hat{H} = \hat{p}\frac{1}{2m_e^*}\hat{p} + V(\vec{r}) + V_F(\vec{r}) - \frac{e^2}{\epsilon|\vec{r}-\vec{r}_i|}, \tag{1}$$

where m_e^* is the electron effective mass, $V(\vec{r})$ is the electron confinement potential, which is assumed to zero insider the QD and V_0 outside the QD (V_0 is the conduction band discontinuity). $V_F(\vec{r})$ is the electrostatic potential induced by the tiled electric field applied parallel to the xoz plane making an angle θ relative to the x axis (see Fig. 1), which is given by

$$V_F(\vec{r}) = eF(x\cos\theta + z\sin\theta), \tag{2}$$

where e is the absolute value of the electron charge, F is the magnitude of the applied electric field. The last term of Eq. (1) represents the Coulomb interaction between the electron and the shallow donor impurity which is located at $r_i = (x_i, y_i, z_i)$ and ϵ is the static dielectric constant. It should noted here that due to the symmetry consideration, the dopant positions considered in the present calculations are distributed in the xoz plane ($y_i = 0$).

The ground-sate donor binding energy is defined as a difference between the ground-state energies of the free electron and that of the donor, which is the following

$$E_b = E_0 - \widetilde{E}, \tag{3}$$

where $\widetilde{E}$ is the energy which corresponds to the Hamiltonian in Eq. (1) and E_0 is the energy without Coulomb interaction (absence of the last term in Eq. (1)). In order to obtain the ground-state energy of the electron (E_0) and the donor ($\widetilde{E}$) as well as corresponding wavefunctions, PMM is employed. Actually, PMM solves the time-independent Schrödinger equation for an arbitrary interaction potential $v_S(\vec{r})$ starting from a potential $v_R(\vec{r})$ with well-known eigenvalues and eigenfunctions. The essential point is that the transition from potential $v_R(\vec{r})$ to potential $v_S(\vec{r})$ can be performed by means of the time-dependent Schrödinger equation as follows: using the potential $v_R(\vec{r})$ and $v_S(\vec{r})$, we formulate a time-dependent Schrödinger equation [14]

$$\imath\hbar\frac{\partial\Phi(\vec{r},t)}{\partial t} = \left\{-\frac{\hbar^2}{2m}\nabla^2 + \big(1-\sigma(t)\big)v_R(\vec{r}) + \sigma(t)v_S(\vec{r})\right\}\Phi(\vec{r},t), \tag{4}$$

where $\sigma(t)$ has the following property:

$$\sigma(t) = \begin{cases} 0, & t \leqslant t_a, \\ 1, & t \geqslant t_b. \end{cases} \tag{5}$$

For $t_a \leqslant t \leqslant t_b$ (t_a is the morphing starting moment, t_b is the morphing ending moment), the function $\sigma(t)$ should increase monotonically. Moreover, we solve Eq. (4) numerically. After a large number of time steps (so that $t > t_b$), the energy eigenvalue E_S for the potential $v_S(\vec{r})$ is given by

$$E_S = \int d^3r\,\Phi_S^*(\vec{r})\left\{-\frac{\hbar^2}{2m}\nabla^2 + v_S(\vec{r})\right\}\Phi_S(\vec{r}), \tag{6}$$

where Φ_S is the wavefunction of the system under consideration. In the present numerical calculations, the usual three-dimensional (3D) harmonic oscillator is taken as a reference system and its ground-state wavefunction is selected as the initial wavefunction (Φ_R). The interaction potential corresponding to the ground-state energy of the electron (E_0) is

$$v_S^e = V(\vec{r}) + V_F(\vec{r}). \tag{7}$$

Whereas, the interaction potential corresponding to the ground-state energy of the donor ($\widetilde{E}$) is

$$v_S^d = V(\vec{r}) + V_F(\vec{r}) - \frac{e^2}{\epsilon|\vec{r}-\vec{r}_i|}. \tag{8}$$

It should be noted here that adopting the harmonic oscillator as a reference system does not affect our results because the PMM needs only a known reference system to start the morphing process and finally to give the eigenfunctions and eigenvalues for the unknown system, independently on the choice of the initial reference system [14,15].

To further understand the electric field effect on the donor binding energy in a semiconductor QD, the Stark shift of the donor binding energy is defined as the difference between the binding energy of a donor impurity at electric field $F \neq 0$ (a finite electric field) and its binding energy at $F = 0$ (zero electric field), which can be given by

$$\delta E_b = E_b(F \neq 0, \theta) - E_b(F = 0, \theta). \tag{9}$$

The negative Stark shift of the donor binding energy ($\delta E_b < 0$) means essentially the electric field effect makes the donor binding energy "red shift". Conversely, the "blue shift" of the donor binding energy takes place if the Stark shift of the donor binding energy is positive ($\Delta E_b > 0$).

3. Numerical results and discussions

Before presenting the numerical results obtained from our model calculations, it is deserved to discuss the validity of the effective-mass approximation in small systems. As mentioned by several authors [7,16,17], validity of effective-mass approximation

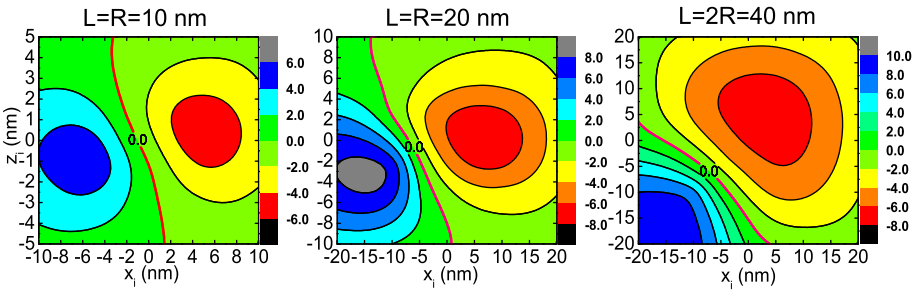

Fig. 2. (Color online.) Contour plots of the Stark shift of the donor binding energy (in unit of meV) for various dopant positions distributed in *xoz* plane of a GaAs/$Al_{0.3}Ga_{0.7}As$ cylindrical QD with different dot configurations subjected to an uniform electric field ($F = 50$ kV/cm, $\theta = 45°$).

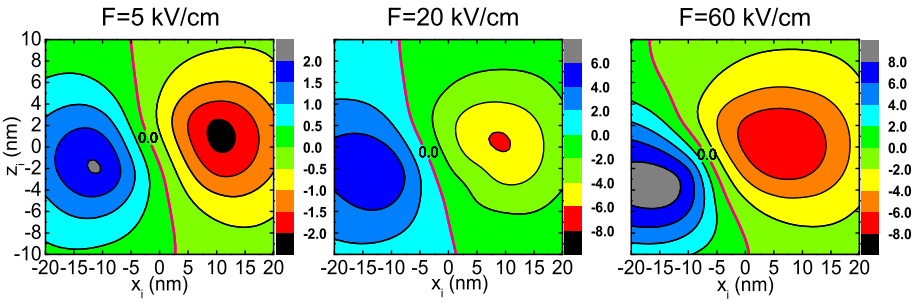

Fig. 3. (Color online.) Contour plots of the Stark shift of the donor binding energy (in unit of meV) for various dopant positions distributed in *xoz* plane of a GaAs/$Al_{0.3}Ga_{0.7}As$ cylindrical QD with dot height $L = 20$ nm and radius $R = 20$ nm, considering different electric field magnitudes at tilted angle $\theta = 45°$.

in semiconductor QD depends on the range of the Bloch function wavevectors necessary to construct the envelope wavefunction for the dot. This range has to be much smaller than the width of the Brillouin zone. For GaAs QD, the effective-mass approximation is valid for the case of dot size larger than 2–3 nm [7]. To insure the validity, the size of the QD in our calculations is much larger than the aforementioned critical dot size value. The physical parameters used in our calculations are $\epsilon = 12.4$ and $V_0 = 228$ meV. As verified by Li and Xia [18], the effective-mass mismatch has considerable influence on the high excited states but it only weakly affects the ground-state donor binding energy and the low excited states. Thus, in our calculations, a position-independent electron effective mass ($m_e^* = 0.0667m_0$) is used as a reasonable approximation. These parameters are suitable for GaAs/$Al_xGa_{1-x}As$ heterostructures with aluminum concentration $x \approx 0.3$.

First of all, in an effort to obtain a quantitative understanding of the dependence of donor binding energy on the dopant positions in the presence of an applied electric field, we create suitable contour plots (Fig. 2) of the Stark shift of the donor binding energy ($\delta E_b = E_b(F \neq 0) - E_b(F = 0)$) for various dopant positions in a cylindrical GaAs QD with different dot configurations. The field strength is $F = 50$ kV/cm and tilted angle $\theta = 45°$. It is interesting to find from Fig. 2 that for any dot configuration, there is a critical line determined by $\delta E_b = 0$. The doping region above the critical line satisfying $\delta E_b < 0$ represents the "red" shift of the donor binding energy and the doping area below the critical line described by $\delta E_b > 0$ shows the "blue" shift of the donor binding energy. By observing these plots, it is found that the critical line exhibits two distinct features. One is horizontal displacement (shift to left/right-hand side) and the other one is planar rotation. Although both of them are due to the applied electric field effect, their behavior is differently influenced by the QD geometric characteristics, such as dot sizes and aspect ratios ($\rho = L/R$). As is observed in Fig. 2, for a specific QD aspect ratio (i.e. $\rho = 1$), the critical line appears to show a left-hand displacement and simultaneously a counterclockwise planar rotation as the dot size increases (see the first two plots). Whereas, if the QD aspect ratio increases (see the last two plots of Fig. 2), a right-hand displacement of the critical line takes place and simultaneously the counterclockwise planar rotation is significantly more intense. Especially, for a weak-confinement cylindrical QD with aspect ratio $\rho = 2$ (see the last plot of Fig. 2), the area corresponding to the "red" shift of the donor binding energy is dominant. The critical line is displaced far from the center of the doping plane and preferably rotated to be perpendicular to the field direction. These novel behavior is attributed to the competition effects between the applied electric field and geometric confinement.

For a self-assembled cylindrical QD with aspect ratio $\rho = 1$ and radius $R = 20$ nm, we have also displayed the contour plots of Stark shift of the donor binding energy for various dopant positions in Fig. 3, in which different field strengths ($\theta = 45°$) are considered. As expected, the critical line corresponding to zero shift of the donor binding energy appears in any field strength configuration. Generally, the enhancement of the applied field causes the enlargement of the doping area corresponding to the "red" shift of the donor binding energy. Particularly, it is found that the increase of the field strength practically has negligible influence on the translational displacement of the critical line. Conversely, it has a significant effect on the planar rotation. As can be seen from Fig. 3, the counterclockwise rotation of the critical line is significantly enhanced as the field strength increases.

In accordance to the previous reports about the tilted electric field effect on the electron [19] and magnetoexciton states [20], the applied field orientation also significantly affects the electron and excitonic properties. At this point, one may expect that the relative orientation of the applied field may also has considerable effect on the Stark shift of the donor binding energy. To check this assumption, in Fig. 4, we displayed several contour plots of the Stark shift of the donor binding energy for various dopant positions in the same QD configuration as in Fig. 3, considering different field orientations. As is observed, the critical line determined by $\delta E_b = 0$ appears for any field orientation. Variation of the field orientation from the in-plane direction ($\vec{F} \parallel \vec{x}$) to the growth direction ($\vec{F} \parallel \vec{z}$) leads to the shrinking of the doping area corresponding to the "red" shift of the donor binding energy. It is also found from Fig. 4 that increasing the titled angle turns out to shift the critical line to

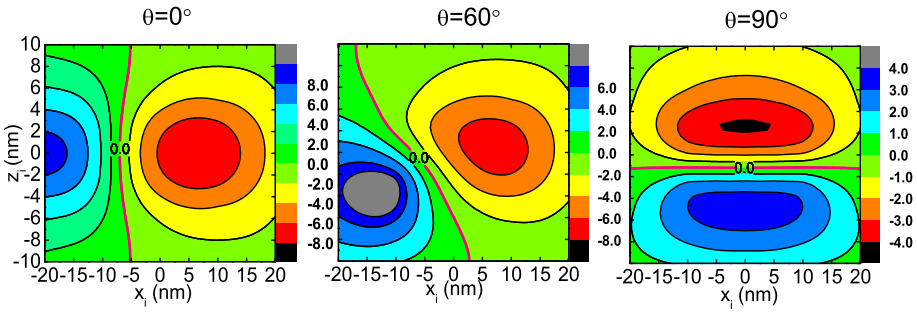

Fig. 4. (Color online.) Contour plots of the Stark shift of the donor binding energy (in unit of meV) for various dopant positions distributed in *xoz* plane of a GaAs/$Al_{0.3}Ga_{0.7}As$ cylindrical QD with dot height $L = 20$ nm and radius $R = 20$ nm, considering different electric field orientations with strength $F = 50$ kV/cm.

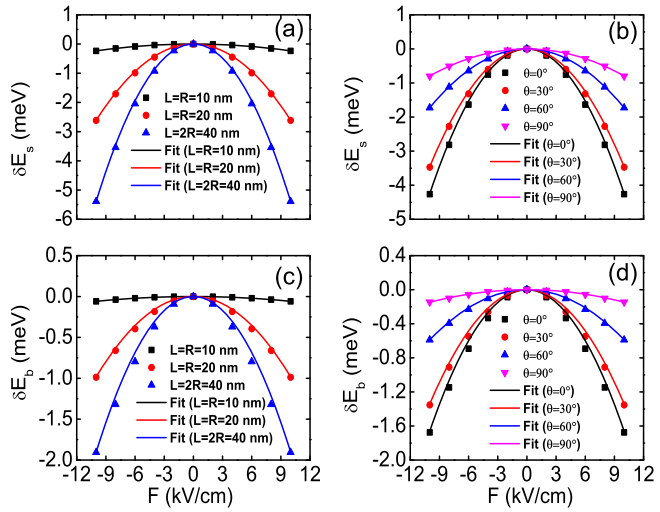

Fig. 5. (Color online.) Variation of the ground-state electron subband energy δE_s ((a) and (b)) and Stark shift of binding energy of an on-center donor impurity δE_b ((c) and (d)) in a self-assembled GaAs/$Al_{0.3}Ga_{0.7}As$ QD as a function of the electric field strength (symbols). In each figure, each solid line represents a fit to a purely quadratic field dependence of the energy variation ($\delta E_i = E_i(F \neq 0) - E_i(F = 0) \approx -\beta^i F^2$ ($i = s$ or b)). (a) and (c) are for different QD configurations and $\theta = 45°$, while (b) and (d) are for different field orientations and $L = R = 20$ nm, respectively.

the right-hand side of the doping plane and simultaneously leads to a counterclockwise planar rotation. Especially, when the field is applied along the growth direction (see the last plot of Fig. 4), the Stark shift of the donor binding energy exhibits obviously axially symmetric distributions (with respect to $x_i = 0$ axis) in the doping plane. Moreover, the critical line corresponding to the zero shift of the donor binding energy is distributed apparently perpendicular to the field direction and vertically but slightly displaced from the center of the doping plane.

Finally, in order to examine whether the aforementioned relation for the field dependence of the Stark shift of the exciton energy is also valid for the Stark shift of the donor binding energy, we firstly present in Fig. 5(a) and (b) the change of the ground-state electron subband energy δE_s ($\delta E_s(F) = E_s(F \neq 0) - E_s(F = 0)$, where E_s is the ground-state electron subband energy) as a function of the applied field strength in a self-assembled GaAs QD, considering different QD configurations (Fig. 5(a)) and field orientations (Fig. 5(b)). As can be seen from Fig. 5(a) and (b), δE_s decreases quadratically with the applied electric field, irrespective of the QD dimensions and the applied field orientations. This finding is in excellent agreement with a general quantum mechanical theorem [21] which states that the ground-state energy is a concave function of any parameter that enters linearly in the Hamiltonian. This is a quite general result, which does not depend on the model Hamiltonian used.

Table 1
Theoretical values of β^s and β^b (in unit of meV cm^2 kV^{-2}) obtained from the fits in Fig. 5(a) and (c), respectively.

QD Configurations	β^s	β^b
$L = R = 10$ nm	$(2.34 \pm 0.003) \times 10^{-3}$	$(0.59 \pm 0.002) \times 10^{-3}$
$L = R = 20$ nm	$(26.1 \pm 0.17) \times 10^{-3}$	$(9.8 \pm 0.15) \times 10^{-3}$
$L = 2R = 40$ nm	$(53.87 \pm 0.4) \times 10^{-3}$	$(19.03 \pm 0.42) \times 10^{-3}$

Table 2
Theoretical values of β^s and β^b (in unit of meV cm^2 kV^{-2}) obtained from the fits in Fig. 5(b) and (d), respectively.

Tilted angle	β^s	β^b
$\theta = 0°$	$(42.52 \pm 0.402) \times 10^{-3}$	$(16.62 \pm 0.37) \times 10^{-3}$
$\theta = 30°$	$(34.62 \pm 0.263) \times 10^{-3}$	$(13.43 \pm 0.24) \times 10^{-3}$
$\theta = 60°$	$(17.26 \pm 0.081) \times 10^{-3}$	$(5.89 \pm 0.07) \times 10^{-3}$
$\theta = 90°$	$(7.94 \pm 0.016) \times 10^{-3}$	$(1.48 \pm 0.02) \times 10^{-3}$

To understand qualitatively the donor binding energy variation under the influence of an applied electric field, we also investigated, in Fig. 5(c) and (d), the Stark shift of the binding energy corresponding to an on-center donor impurity as a function of the field strength for different QD dimensions (Fig. 5(c)) and electric field orientations (Fig. 5(d)). In general, donor's intrinsic dipole moment becomes orientated by the applied electric field, irrespective of dopant positions in a self-assembled QD. Due to an additional separation of the electron and ionized donor impurity (e^-/D^+), the induced dipole moment will also interact with the applied electric field. In total, this results in a change of the donor binding energy as $\delta E_b \approx \alpha^D F - \beta^D F^2$, where the coefficients α^D and β^D donates impurity permanent dipole moment and impurity polarizability, respectively. As can be seen from Fig. 5(c) and (d), it is interesting to find that δE_b decreases ("red shift") quadratically with the applied electric field for any dot configuration and field orientation. This therefore suggests the absence of a permanent dipole moment in each case considered. This result is in good agreement with the symmetry consideration which states that any system with an inversion symmetry does not have a permanent dipole moment ($\alpha^D = 0$). On the other hand, the fits in Fig. 5(c) and (d) also suggest a good way to estimate the impurity poloarizability. As indicated in Tables 1 and 2 (see the third column), the impurity polarizability is in order of 10^{-3} meV cm^2 kV^{-2}, which is comparable with its exciton counterpart as shown in the previous literature [12,13]. After making a comparison between β^s and β^b listed in Tables 1 and 2, it is easy to find that both coefficients are similarly affected by the QD dimensions or the field orientations. Increase of QD dimension results in significantly increase in the two coefficients, while tilting the electric field from the lateral direction to the growth direction turns out to decrease both of them. This is a good reflection of the competition effects between the quantum confinement and applied electric field. More specially, comparing to δE_s, it is found that the applied electric

field effect on δE_b is less effective (β^s is much larger than β^b in each case). This is because of the Coulomb attraction between the electron and the donor impurity which inhibits the displacement of the electron probability density far from the impurity center.

4. Conclusion

In summary, we have studied the Stark shift of the donor binding energy distributions with respect to the dopant positions in a self-assembled GaAs/$Al_{0.3}Ga_{0.7}$As QD subjected to an applied electric field. The electric field is tilted from the QD growth direction. It is found that there is a critical line in the doping plane corresponding to the zero shift of the donor binding energy. The doping area above the critical line shows the "red" shift of the donor binding energy and that below the critical line represents the "blue" shift. The position of the critical line is strongly affected by the QD size, its aspect ratio and the strength and orientation of the applied electric field. Our results also indicate that the variation of the ground-state electron subband energy and the Stark shift of an on-center donor binding energy, for small electric field (0–10 kV/cm in our calculations), are purely quadratic functions of the field strength, irrespective of the QD configurations and the field orientations. More specially, it is found that comparing to the variation of the ground-state electron subband energy under the influence of the applied electric field, the applied field effect on the Stark shift of the on-center donor binding energy is less effective. We believe that the results presented here can be useful for design and application of some commonly used δ-doped self-assembled GaAs/AlGaAs QD based optoelectronic devices. We also hope that our results can stimulate forthcoming theoretical and experimental investigations in this attracting research area.

Acknowledgements

This research has been co-financed by the European Union (European Regional Development Fund – ERDF) and Greek national funds through the Operational Program "Regional Operational Programme" of the National Strategic Reference Framework (NSRF) Research Funding Program: Support for research, technology and innovation actions in Region of Western Greece (MIS: 312123, D.237.002). Furthermore, this work is also supported by the research project "C. Caratheodory" D.207 of the Research Committee of the University of Patras.

References

[1] D. Mocatta, G. Cohen, J. Schattner, O. Millo, E. Rabani, U. Banin, Science 332 (2011) 77.
[2] R. Rahman, G.P. Lansbergen, S.H. Park, J. Verduijn, G. Klimeck, S. Rogge, L.C.L. Hollenberg, Phys. Rev. B 80 (2009) 165314.
[3] C. Bose, J. Appl. Phys. 83 (1998) 3089.
[4] J.L. Movilla, J. Planelles, Phys. Rev. B 71 (2005) 075319.
[5] H.A. Kassim, J. Phys: Condens. Matter 19 (2007) 036204.
[6] G. Wang, P. Zhang, J. Appl. Phys. 103 (2008) 063713.
[7] F. Dujardin, A. Oukerroum, E. Feddi, J.B. Bailach, J. Martinez-Pastor, M. Zazi, J. Appl. Phys. 111 (2012) 034317.
[8] J.W. Robinson, J.H. Rice, K.H. Lee, J.H. Na, R.A. Taylor, D.G. Hasko, R.A. Oliver, M.J. Kappers, C.J. Humphreys, G.A.D. Briggs, Appl. Phys. Lett. 86 (2005) 213103.
[9] K. Kowalik, O. Krebs, A. Lemaitre, S. Laurent, P. Senellart, P. Voisin, J.A. Gaj, Appl. Phys. Lett. 86 (2005) 041907.
[10] T. Nakaoka, S. Kako, Y. Arakawa, Phys. Rev. B 73 (2006) 121305.
[11] B.D. Gerardot, S. Seidl, P.A. Dalgarno, R.J. Warburton, D. Granados, J.M. Garcia, K. Kowalik, O. Krebs, K. Karrai, A. Badolato, P.M. Petroff, Appl. Phys. Lett. 90 (2007) 041101.
[12] S. Ritter, P. Gartner, N. Baer, F. Jahnke, Phys. Rev. B 76 (2007) 165302.
[13] A. Oukerroum, E. Feddi, J.B. Bailach, J. Martínez-Pastor, F. Dujardin, E. Assaid, J. Phys: Condens. Matter 22 (2010) 375301.
[14] M. Rieth, W. Schommers, S. Baskoutas, Int. J. Mod. Phys. B 16 (2002) 4081.
[15] P. Poulopoulos, S. Baskoutas, S.D. Pappas, C.S. Garoufalis, S.A. Droulias, A. Zamani, V. Kapaklis, J. Phys. Chem. C 115 (2011) 14839.
[16] C. Priester, G. Allan, M. Lannoo, Phys. Rev. B 28 (1983) 7194.
[17] R. Tsu, D. Babic, Appl. Phys. Lett. 64 (14) (1994) 1806.
[18] S.-S. Li, J.-B. Xia, J. Appl. Phys. 101 (2007) 093716.
[19] H. Ham, H.N. Spector, Physica B 381 (2006) 53.
[20] D. Wang, G. Jin, Y. Zhang, Y.-Q. Ma, J. Appl. Phys. 105 (2009) 063716.
[21] W. Thirring, Quantum Mathematical Physics, Springer, Heidelberg, 2002.

Paper III

In which we study the combination effects of tilted electric and magnetic fields on the ground-state binding energy of an on-center donor impurity confined in a $GaAs/Al_{0.3}Ga_{0.7}As$ cylindrical quantum dots ...

IOP PUBLISHING JOURNAL OF PHYSICS D: APPLIED PHYSICS

J. Phys. D: Appl. Phys. **45** (2012) 235102 (9pp) doi:10.1088/0022-3727/45/23/235102

Combination effects of tilted electric and magnetic fields on donor binding energy in a GaAs/AlGaAs cylindrical quantum dot

Zaiping Zeng[1], Christos S Garoufalis[1,2] and Sotirios Baskoutas[1]

[1] Materials Science Department, University of Patras, 26504 Patras, Greece
[2] Department of Environment Technology and Ecology, Technological Institute of Ionian Islands, 2 Kalvou Sq, 29100, Zakynthos, Greece

E-mail: bask@upatras.gr

Received 29 February 2012, in final form 21 April 2012
Published 22 May 2012
Online at stacks.iop.org/JPhysD/45/235102

Abstract

We have performed a systematic study on the ground-state binding energy of an on-center donor impurity confined in a GaAs/$Al_{0.3}Ga_{0.7}As$ cylindrical quantum dot (QD), subjected to simultaneously applied electric and magnetic fields. The two fields are tilted with respect to the QD growth direction and they are either parallel or perpendicular to each other. All the calculations are based on the potential morphing method which is employed within the framework of the effective-mass approximation. Our results show that when the tilted electric and magnetic fields are parallel, the magnetic shift of the donor binding energy is a monotonic function of the magnetic field strength. On the other hand, when the two fields are perpendicular to each other, the magnetic shift of the donor binding energy varies nonmonotonically with respect to the magnetic field strength, exhibiting a minimum value at a critical magnetic field strength. The position of this minimum value and its dependence on the QD size, its aspect ratio and the orientation of the tilted magnetic field is systematically investigated. Moreover, we discuss in detail the competition effects which appear in the presence of the two fields, showing that the critical line which corresponds to zero shift of the donor binding energy can be manipulated by suitably adjusting the QD size, the aspect ratio and the relative orientation of the two fields.

(Some figures may appear in colour only in the online journal)

1. Introduction

A deep understanding of the effects of impurities on electronic states of semiconductor nanostructures is of fundamental importance in semiconductor physics because their presence can dramatically alter the performance of quantum devices [1]. In the last few years, hydrogenic impurity states in semiconductor nanostructures, such as quantum wells (QWs), quantum well-wires (QWWs) and quantum dots (QDs), have been investigated extensively [2–16]. These studies revealed that the binding energy of a hydrogenic impurity confined in these nanostructures can be directly controlled by choosing appropriated materials, geometries, sizes and doping positions. Moreover, external perturbations, such as uniform electric and magnetic fields, are effective tools for studying the impurity related properties in semiconductor nanostructures. As is well known, the presence of a uniform magnetic field introduces another electronic confinement (magnetic field induced confinement) which superposes its geometric counterpart. Depending on the direction of the magnetic field (parallel or perpendicular to the growth direction), some interesting physical phenomena can take place [17]. Furthermore, the applied electric field induces an asymmetric distribution of the electron probability density which strongly modifies the electronic and optical properties in semiconductor nanostructures. Thus, to investigate the combination effects of the electric and magnetic fields on the binding energy of a hydrogenic impurity in semiconductor nanostructures was of great interest and has attracted considerable attention in the last few years [18–23]. However, the vast majority of

these calculations treat the most straightforward cases, where the two fields are applied parallel to each other and they are either parallel or perpendicular to the growth direction of the semiconductor nanostructures.

Recently, the rapid advance in material growth technology lead to a renewed interest in studies of semiconductor nanostructures subjected to an external electric or magnetic field directed at an angle with respect to the growth direction. The reason for this interest is the fact that such a unique system provides us with novel electronic, optical and transport effects (see [24] and references therein). More specially, Redliński and Jankó [25] have investigated the tilted magnetic field effect on the binding energy of a shallow donor in a CdTe/MgCdTe QW. Wang *et al* [26] investigated the effects of an arbitrary tilted electric field on the magnetoexciton in a cylindrical QD by means of a variational procedure. Recently, Monozon and Schmelcher [24] developed an analytical approach to the problem of the fundamental and exciton magnetoelectroabsorption in a narrow QW subjected to the tilted electric and magnetic fields (the electric and magnetic field are parallel and are both tilted with respect to the QW growth direction). However, to the best of our knowledge, the combination effects of the tilted electric and magnetic fields (parallel or perpendicular to each other) on the donor binding energy in semiconductor nanostructures have not been reported anywhere in the literature. On the other hand, as revealed in the previous reports [25], the tilted magnetic field induces a three-dimensional (3D) electron confinement which makes the electron probability density distribute with respect to the centre of the cylindrical QD. This in turn causes the increase in the on-centre donor binding energy. In contrast, as the external tilted electric field is applied, the symmetry of the electron probability density distribution at zero electric field breaks and the maximum of the electron probability density moves away from the center of the cylindrical QD to the opposite direction of the tilted electric field. As a result, the decrease in the binding energy of an on-center donor impurity in a QD takes place. As expected, when the two tilted fields are simultaneously applied in a GaAs/AlGaAs cylindrical QD, competition effects appear. More importantly, a qualitatively understanding of these types of competition effects on the donor binding energy may be very useful for design and application of some commonly used δ-doped GaAs/AlGaAs QD-based optoelectronic devices, such as LEDs and LDs. Unfortunately, no related reports have been published. Therefore, in this work, we performed for the first time calculations of the ground-state binding energy of an on-center donor impurity in a typical GaAs/AlGaAs cylindrical QD under the influence of simultaneously applied tilted electric and magnetic fields. Both fields are applied parallel to the xoz plane and they are both tilted with respect to the QD growth direction. The cases for which the electric field is parallel or perpendicular to the tilted magnetic field are considered in detail. The numerical technique we used in the present calculations is the potential morphing method (PMM) [27–33] which has been developed to solve the time-independent Schrödinger equation for any arbitrary interaction potential. The emphasis of this paper is on a detailed analysis of competition effects between the simultaneously applied tilted electric and magnetic fields on the binding energy of an on-center donor impurity in a cylindrical QD.

The rest of the paper is organized as follows. In section 2 we define our model and explain the general theory, in section 3 we present our numerical results and related discussions and section 4 is devoted to conclusions.

2. General theory

Within the framework of effective-mass approximation (EMA), a shallow donor impurity embedded in a cylindrical QD is modelled by the Hamiltonian

$$\hat{H} = (\hat{p} + \frac{e}{c}\vec{A}(\vec{r}))\frac{1}{2m_e^*}(\hat{p} + \frac{e}{c}\vec{A}(\vec{r})) + V(\vec{r}) + V_E(\vec{r}) - \frac{e^2}{\epsilon|\vec{r}|}. \tag{1}$$

The first term of the Hamiltonian is the operator for the kinetic energy of a delocalized conduction electron (where e is the absolute value of the electron charge, c is the speed of the light in vacuum, m_e^* is the electron effective mass) in the presence of a tilted magnetic field which is parallel to the xoz plane with an angle θ to the x-axial direction ($\vec{B} = B(\cos\theta, 0, \sin\theta)$). The vector potential $\vec{A}$ in the commonly used cylindrical gauge is $\vec{A}(\vec{r}) = \frac{1}{2}\vec{B}\times\vec{r} = \frac{1}{2}B(-y\sin\theta, -(z\cos\theta - x\sin\theta), y\cos\theta)$. Substituting the exact expression of the vector potential into Hamiltonian (1), the operator for the kinetic energy of the electron under the influence of a tilted magnetic field $\vec{B}$ (the first term of Hamiltonian (1)) is the following:

$$\hat{H}_{\mathrm{Kin}} = \hat{p}\frac{1}{2m_e^*}\hat{p} + \frac{eB}{2m_e^*c}(\cos\theta\hat{l}_x + \sin\theta\hat{l}_z) + \frac{e^2B^2}{8m_e^*c^2}[y^2 + (z\cos\theta - x\sin\theta)^2], \tag{2}$$

where $\hat{l}_i$ ($i = x, z$) is the i-component of the angular momentum operator ($\hat{l}_x = y\hat{p}_z - z\hat{p}_y$, $\hat{l}_z = x\hat{p}_y - y\hat{p}_x$). The second term of equation (2) represents the interaction between the external applied titled magnetic field $\vec{B}$ and the orbital angular momentum $\vec{l}$ ($\vec{B}\cdot\vec{l} = B_x\hat{l}_x + B_y\hat{l}_y + B_z\hat{l}_z$, here $B_y = 0$). The third term of equation (2),

$$V_B(\vec{r}) = \frac{e^2B^2}{8m_e^*c^2}[y^2 + (z\cos\theta - x\sin\theta)^2], \tag{3}$$

is the magnetic field induced confinement potential. For in-plane magnetic field ($\theta = 0^\circ$), the magnetic field induced confinement potential is $V_B(\vec{r}) = \frac{e^2B^2}{8m_e^*c^2}(y^2 + z^2)$, which is in the yoz plane; while for growth-direction magnetic field ($\theta = 90^\circ$), $V_B(\vec{r}) = \frac{e^2B^2}{8m_e^*c^2}(x^2 + y^2)$, which is in the xoy plane. Furthermore, for any $B\neq0$ and $\theta\neq0^\circ$ (or 90°), the magnetic field induced confinement potential $V_B(\vec{r})$ takes the form of equation (3), which is in both the yoz plane (contributed from the transverse component of the titled magnetic field $B_x = B\cos\theta$) and xoy plane (contributed from the longitudinal component of the tilted magnetic field $B_z = B\sin\theta$). $V(\vec{r})$

in equation (1) is the electron confinement potential in a cylindrical QD, which is the following:

$$V(\vec{r}) = V(x, y, z) = \begin{cases} V(x, y), & |z| \leqslant \frac{L}{2} \\ V_0, & |z| > \frac{L}{2}, \end{cases} \tag{4}$$

$$V(x, y) = \begin{cases} 0, & \sqrt{x^2 + y^2} \leqslant R \\ V_0, & \sqrt{x^2 + y^2} > R, \end{cases} \tag{5}$$

where V_0 is the conduction band discontinuity, L and R are the dot height and radius of the cylindrical QD, respectively. The third part of equation (1) is the electrostatic potential induced by a tilted electric field applied parallel to the xoz plane but making an angle θ' to the x-axial direction, which is the following:

$$V_E(\vec{r}) = eE(x\cos\theta' + z\sin\theta'). \tag{6}$$

If the tilted angle $\theta' = \theta$, this means that the tilted electric field is applied parallel to the tilted magnetic field ($\vec{E} \| \vec{B}$). While, when the tilted angle $\theta' = \theta \pm 90^\circ$, this represents the tilted electric field is applied perpendicular to the tilted magnetic field ($\vec{E} \perp \vec{B}$). The last term of equation (1) represents the Coulomb interaction between the electron and the shallow donor impurity located at the center of the cylindrical QD ($\vec{r}_i = (x_i, y_i, z_i) = (0, 0, 0)$, $\vec{r}_i$ is the impurity position vector); ϵ is the static dielectric constant.

In this paper, we intend to investigate the ground-state donor binding energy under the combined effects of the simultaneously applied tilted electric and magnetic fields in a cylindrical QD. The ground-sate donor binding energy is defined as a difference between the ground-state energies of the free electron and that of the donor with the same electron spin configuration [25], which is the following:

$$E_\mathrm{b} = E_0 - \widetilde{E}, \tag{7}$$

where $\widetilde{E}$ is the energy which corresponds to the Hamiltonian in equation (1) and E_0 is the energy without Coulomb interaction (the absence of the last term in equation (1)). This definition indicates that the interaction between the spin and the external magnetic field ($\mp\frac{1}{2}\mu_\mathrm{B} g_\mathrm{e}^* \vec{B} \cdot \vec{S}$, μ_B is the Bohr magneton and $\vec{S}$ is the spin operator) does not contribute to the donor binding energy. In order to obtain the ground-state energy of the electron (E_0) and the donor ($\widetilde{E}$) as well as corresponding wavefunctions, PMM is employed. Actually, PMM solves the time-independent Schrödinger equation for an arbitrary interaction potential $v_S(\vec{r})$ starting from a potential $v_R(\vec{r})$ with well-known eigenvalues and eigenfunctions. The essential point is that the transition from potential $v_R(\vec{r})$ to potential $v_S(\vec{r})$ can be performed by means of the time-dependent Schrödinger equation as follows: using the potential $v_R(\vec{r})$ and $v_S(\vec{r})$, we formulate a time-dependent Schrödinger equation [30]

$$\imath\hbar\frac{\partial\Phi(\vec{r}, t)}{\partial t} = \left\{-\frac{\hbar^2}{2m}\nabla^2 + (1 - \sigma(t))v_R(\vec{r}) + \sigma(t)v_S(\vec{r})\right\} \times \Phi(\vec{r}, t), \tag{8}$$

where $\sigma(t)$ has the following property:

$$\sigma(t) = \begin{cases} 0, & t \leqslant t_a \\ 1, & t \geqslant t_b \end{cases}. \tag{9}$$

For $t_a \leqslant t \leqslant t_b$ (t_a is the morphing starting moment, t_b is the morphing ending moment), the function $\sigma(t)$ should increase monotonically. Moreover, we solve equation (8) numerically. After a large number of time steps (so that $t > t_b$), the energy eigenvalue E_S for the potential $v_S(\vec{r})$ is given by

$$E_S = \int d^3r\,\Phi_S^*(\vec{r})\left\{-\frac{\hbar^2}{2m}\nabla^2 + v_S(\vec{r})\right\}\Phi_S(\vec{r}), \tag{10}$$

where Φ_S is the wavefunction of the system under consideration. In the present numerical calculations, the usual 3D harmonic oscillator is taken as a reference system and its ground-state wavefunction is selected as the initial wavefunction (Φ_R). The interaction potential corresponding to the ground-state energy of the electron (E_0) is

$$v_S^\mathrm{e} = \frac{eB}{2m_\mathrm{e}^* c}(\cos\theta\hat{l}_x + \sin\theta\hat{l}_z) + V(\vec{r}) + V_B(\vec{r}) + V_E(\vec{r}). \tag{11}$$

Whereas, the interaction potential corresponding to the ground-state energy of the donor ($\widetilde{E}$) is

$$v_S^\mathrm{d} = \frac{eB}{2m_\mathrm{e}^* c}(\cos\theta\hat{l}_x + \sin\theta\hat{l}_z) + V(\vec{r}) + V_B(\vec{r}) + V_E(\vec{r}) - \frac{e^2}{\epsilon|r|}. \tag{12}$$

It should be noted here that adopting the harmonic oscillator as a reference system does not affect our results because the PMM needs only a known reference system to start the morphing process and finally to give the eigenfunctions and eigenvalues for the unknown system, independently on the choice of the initial reference system [30, 33].

To further understand the magnetic field effect on the donor binding energy in a semiconductor QD subjected to an applied electric field, the magnetic shift of the donor binding energy is defined as the difference between the binding energy of a donor impurity at magnetic field $B \neq 0$ (a finite magnetic field) and its binding energy at $B = 0$ (zero magnetic field) for a fixed electric field, which can be given by

$$\delta E_\mathrm{b} = E_\mathrm{b}(E, \theta'; B \neq 0, \theta) - E_\mathrm{b}(E, \theta'; B = 0, \theta). \tag{13}$$

Similarly, in an attempt to understand the competition effects between the tilted electric and magnetic fields on the donor binding energy in a cylindrical QD, the energetic shift of the donor binding energy is defined as the difference between the binding energy of a donor impurity at finite electric and magnetic fields ($E \neq 0$, $B \neq 0$) and its binding energy at zero electric and magnetic fields ($E = 0$, $B = 0$), which can be given by

$$\Delta E_\mathrm{b} = E_\mathrm{b}(E \neq 0, \theta'; B \neq 0, \theta) - E_\mathrm{b}(E = 0, \theta'; B = 0, \theta). \tag{14}$$

The negative energetic shift of the donor binding energy ($\Delta E_\mathrm{b} < 0$) means essentially the combination effects of the tilted electric and magnetic fields make the donor binding energy 'red shift'. Conversely, the 'blue shift' of the donor binding energy takes place if the energetic shift of the donor binding energy is positive ($\Delta E_\mathrm{b} > 0$).

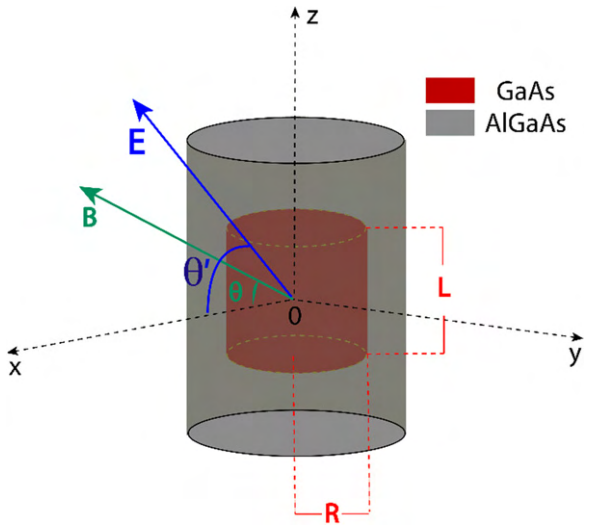

Figure 1. Schematic representation of the GaAs/AlGaAs cylindrical QD under investigation with the dot height L and the radius R. The magnetic field ($\vec{B}$) is applied parallel to the xoz plane making an angle θ to the x-axial direction. The electric field ($\vec{E}$) is also applied parallel to the xoz plane but it makes an angle θ' to the x-axial direction.

3. Numerical results and discussion

According to the previous theoretical studies on the semiconductor QD [13, 15, 16, 20, 34], we consider a typical GaAs cylindrical QD, surrounded by large band gap material AlGaAs in both the radial and z-axial directions. The origin is taken at the center of the QD and the z-axial direction is defined as the growth direction (see figure 1). The physical parameters used in our calculations are $\epsilon = 12.4$ (assume that there is no dielectric mismatch) and $V_0 = 228$ meV. It is well known that the conduction-electron effective mass (m_e^*) depends on the aluminium concentration. Such an effect may contribute to an effective-mass discontinuity at the QD interfaces and leads to an enhancement of the donor binding energy. However, in the present calculations, a position-independent conduction-electron effective mass ($m_e^* = 0.0667m_0$ (where m_0 is the free electron mass)) is considered as an approximation. These parameters are suitable for GaAs/Al_xGa_{1-x}As heterostructures with an Al concentration $x \cong 0.3$.

3.1. Tilted electric field effect on the magnetic shift of the donor binding energy in a GaAs/$Al_{0.3}Ga_{0.7}$As cylindrical QD

In this section, the tilted electric field effect on the magnetic shift of the binding energy of an on-center donor impurity has been calculated as a function of the magnitude of the applied magnetic field for different dot sizes, electric fields (strengths and orientations), orientations of the magnetic field and aspect ratios of the cylindrical QD.

At first, we examine the magnetic shift of the donor binding energy δE_b as a function of the magnetic field magnitude in a GaAs/$Al_{0.3}Ga_{0.7}$As cylindrical QD for various electric ($\vec{E}$) and magnetic fields ($\vec{B}$). The electric field is always applied parallel ($\theta' = \theta$) or perpendicularly ($\theta' = 90^\circ \pm \theta$) to the magnetic field. The calculations have been performed for two dot sizes ($L = R = 10$ nm and $L = R = 20$ nm). Our results (figure 2) show that in the absence of the electric field, δE_b increases as the magnetic field increases for any dot size and magnetic field orientation. As expected, for lager dot size (weaker confinement) the variation of δE_b with respect to the magnetic field strength appears to be significantly more intense (see figures 2(b) and (c)). Moreover, it is found

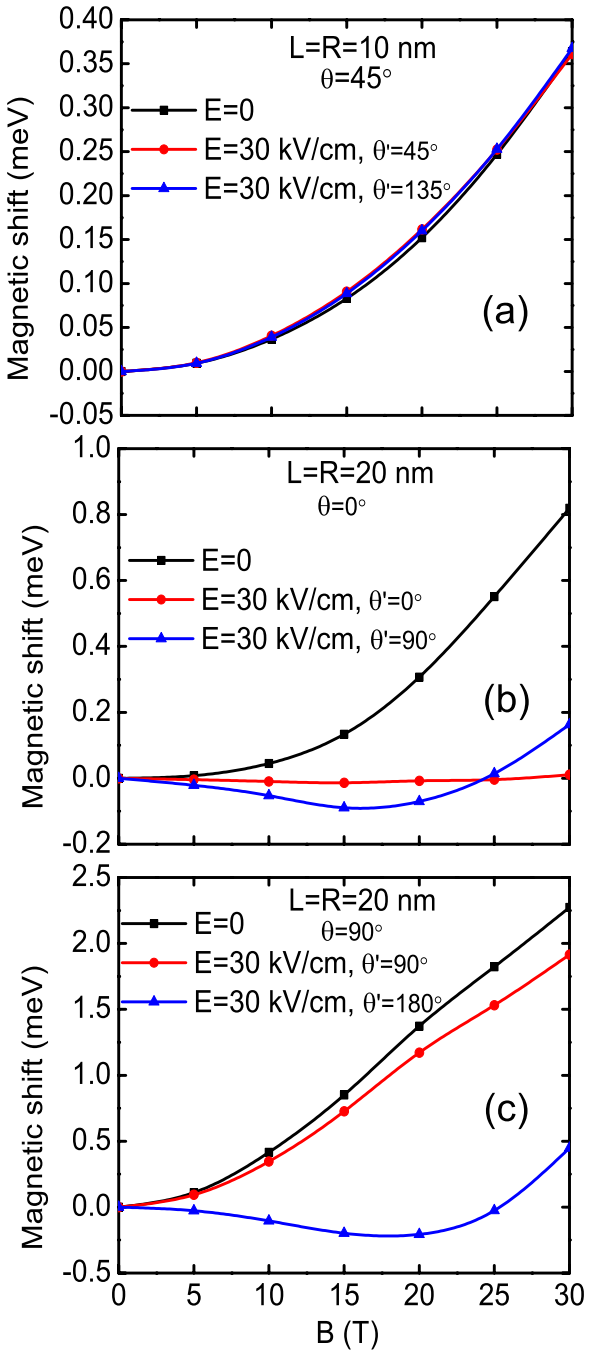

Figure 2. Magnetic shift of the donor binding energy δE_b as a function of the magnitude of the tilted magnetic field $\vec{B}$ in a GaAs/$Al_{0.3}Ga_{0.7}$As cylindrical QD for various tilted electric fields ($\vec{E}$). Here, (a) is for $L = R = 10$ nm and $\theta = 45^\circ$, (b) is for $L = R = 20$ nm and $\theta = 0^\circ$, (c) is for $L = R = 10$ nm but $\theta = 90^\circ$, respectively. The electric field is applied either parallel ($\theta' = \theta$ ($\vec{E} \| \vec{B}$)) or perpendicularly ($\theta' = \theta + 90^\circ$ ($\vec{E} \perp \vec{B}$)) to the tilted magnetic field.

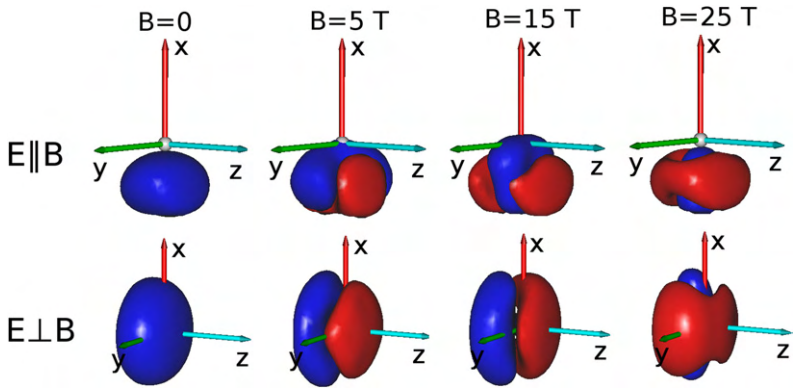

Figure 3. The first column corresponds to the 3D contour plots of the electron probability density distributions in an impurity-free GaAs/$Al_{0.3}Ga_{0.7}$As cylindrical QD with dot height $L = 20$ nm and radius $R = 20$ nm subjected to different tilted electric fields but zero magnetic field. The following three columns show suitably chosen isosurfaces of electron probability density differences, which have been produced by subtracting the density at zero magnetic field from the density which corresponds to a specific magnetic field strength in the Voigt configuration ($\vec{B}\|\vec{x}$). The red surfaces correspond to charge depletion areas, while the blue surfaces correspond to charge accumulation areas. The upper panel is corresponding to the case where the electric field is applied parallel ($E = 30\,\mathrm{kV\,cm^{-1}}$ and $\theta' = 0^\circ$) to the magnetic field, whereas, the lower panel is corresponding to the case where the electric field is applied perpendicularly ($E = 30\,\mathrm{kV\,cm^{-1}}$ and $\theta' = 90^\circ$) to the magnetic field.

from figure 2 that in a larger dot (i.e. $L = R = 20$ nm), variation of the magnetic field orientation from the in-plane direction (Voigt configuration) to the growth direction (Faraday configuration) leads to the decrease of the sensitivity of δE_b with respect to the magnetic field strength. For instance, at $B = 30$ T, the magnetic shift of the donor binding energy in the Voigt configuration is $\delta E_b = 0.819$ meV; while in the Faraday configuration, $\delta E_b = 2.27$ meV. This is because in the Faraday configuration, the magnetic field induced confinement is more effective due to the very weak confinement in the radial direction ($d = 2R = 2L = 40$ nm, d is the diameter of the cylindrical QD). On the other hand, for the case of the small dot size it becomes clear from figure 2(a) that the monotonic increase in δE_b is practically independent on the electric field orientation ($\theta' = 45^\circ$ or $\theta' = 135^\circ$). This can be easily understood by the fact that for $L = R = 10$ nm, the QD is in strong confinement regime and the effect of the electric field is marginal. Thus, it can be safely concluded that for the strong confinement regime, the value of the magnetic shift of the donor binding energy is practically not affected by the presence of an electric field.

In contrast, in the weak confinement regime (see figure 2(b) and (c)), δE_b depends strongly on the relative orientations of the electric and magnetic fields (tilted angle θ and θ'). When the electric field is applied parallel to the magnetic field ($\theta' = \theta$), δE_b increases monotonically with increasing magnetic field strength in both Voigt ($\theta = 0^\circ$) and Faraday configurations ($\theta = 90^\circ$). Moreover, in Faraday configuration ($\vec{B}\|\vec{z}$), the increase in δE_b is practically more sensitive to the magnetic field strength, as expected. However, when a perpendicular electric field ($\theta' = \theta + 90^\circ$) is applied, δE_b is a 'nonmononic' function of the magnetic field strength in both Voigt and Faraday configurations. It exhibits a minimum at a critical value B_c. In particular, it is interesting to find from figure 2(b) that in the Voigt configuration, the critical magnetic field is $B_c \approx 16$ T; while in the Faraday configuration (figure 2(c)), it is $B_c \approx 20$ T. In other words, the critical magnetic field B_c increases when the magnetic field is tilted from the in-plane direction ($\vec{B}\|\vec{x}$) to the growth direction ($\vec{B}\|\vec{z}$).

To understand the behaviour of the magnetic shift of the donor binding energy under the influence of parallel (perpendicular) electric and magnetic fields, we create suitable 3D contour plots of the electron probability density (first column of figure 3), as well as isosurfaces of the electron probability density differences (the last four columns of figure 3) in an impurity-free QD for different electric and magnetic fields. The electric field is applied either parallel (the upper panel of figure 3) or perpendicularly (the lower panel of figure 3) to the magnetic field. In particular, each density difference plot has been produced by subtracting the density at zero magnetic field from the density which corresponds to a specific magnetic field strength (the magnetic field is applied along the x-axial direction). This subtraction leads to positive (blue) and negative (red) density areas which indicate the charge movement due to the applied magnetic field. As a result, the red surfaces correspond to charge depletion areas, while the blue surfaces correspond to charge accumulation areas. For the creations of these 3D contour plots, the Gabedit graphical program was used [35]. By observing the first column of figure 3, it is found that in the absence of the magnetic field, the electric field always moves the electron probability density far away from the QD center to its opposite direction. However, the density displacement is highly affected by the QD geometric confinement and the electric field effect turns out to be more effective in the weak confinement regime (see the upper contour plot in the first column of figure 3), as expected.

Before proceeding to explain the density changes that take place due to the applied magnetic field, it would be useful to make a distinction between the two different trends which are introduced by the presence of a magnetic field. At first, the magnetic field induced confinement tends to squeeze the charge density around the axis of the applied magnetic field and secondly it tends to move the charge density towards

the center of the QD. Although both effects are due to the cylindrical symmetry of the magnetic induced confinement, their behaviour is differently influenced by the geometric characteristics of the QD and the presence of an extra electric field. As a result, under certain conditions these two trends may be considered separately. This description may prove to be useful for understanding the competition effects between the two fields. For the case of a parallel magnetic field ($\vec{E}\|\vec{x},\vec{B}\|\vec{x}$), we can see from figure 3 that the charge density is squeezed around the x-axis as the field strength increases. It is obvious that for large values of B the magnetic field induced confinement imposes its cylindrical symmetry, while for smaller values of B the geometric confinement leads to less symmetric density distributions. In all cases, the charge density exhibits a small displacement towards the QD center. Consequently the mean relative electron-impurity distance decreases and the binding energy slightly and monotonically increases with increasing magnetic field strength. However, this monotonic displacement of the charge density does not occur when the electric field is applied perpendicularly ($\vec{E}\|\vec{z}$, $\vec{B}\|\vec{x}$) to the magnetic field (see the lower panel of figure 3). It is found that for magnetic field $B \leqslant B_c = 15\,\mathrm{T}$, the charge density moves far from the QD center when the perpendicular magnetic field increases. Conversely, it tends to move towards the QD center when the magnetic field becomes stronger ($B > 15\,\mathrm{T}$). This can be attributed to the competition effects between the two fields. In particular, although the magnetic field introduces both trends (squeezing and displacing towards the center of the QD) for small values of B ($0 < B < 15\,\mathrm{T}$) the presence of the electric field inhibits the displacement, allowing only for an asymmetric squeezing of the density. As a result, the mean relative electron-impurity distance increases and the binding energy slightly decreases (see figures 2(b) and (c)). On the other hand, If the magnetic field becomes stronger ($B > 15\,\mathrm{T}$), its influence begins to superpose its electric counterpart and the two trends (squeezing and displacing towards the center of the QD) lead to a charge density accumulation closer to the QD center. As a result, the increase in the magnetic field begins to contribute positively to δE_b.

In the Voigt configuration ($\theta = 0^\circ$), we have also examined the dependence of δE_b on the magnetic field strength for various tilted electric fields at aspect ratios $\rho = \frac{L}{R} = 0.5$ (figure 4(a)) and $\rho = 2.0$ (figure 4(b)), respectively. Our results (figure 4(a)) indicate that for $\rho = 0.5$, in the absence of the electric field ($E = 0$), δE_b decreases as the strength of the magnetic field increases ($0 < B \leqslant 25$) and then it becomes insensitive to the increased magnetic field ($25\,\mathrm{T} \leqslant B \leqslant 30\,\mathrm{T}$). On the other hand, when the aspect ratio goes up to $\rho = \frac{L}{R} = 2.0$ (see figure 4(b)), δE_b increases monotonically with increasing magnitude of the magnetic field. This behaviour is related to the variation of the quantum confinement in the z-axial direction which is induced by the change in the aspect ratio. For small aspect ratio ($\rho = \frac{L}{R} = 0.5$), the electron probability density is mainly distributed along the radial direction due to the weaker confinement ($R = 2L = 20\,\mathrm{nm}$). For magnetic field $0 < B \leqslant 25\,\mathrm{T}$, the magnetic field induced confinement (in the yoz plane) makes the electron probability density extend more along the radial direction with increasing magnetic field strength. Thus, the mean relative electron-impurity distance is increased and the donor binding energy is decreased. On the other hand, for $B \geqslant 25\,\mathrm{T}$ the electron probability density appears to be only slightly affected and consequently the δE_b becomes almost invariant to any further increase in the magnetic field. Conversely, when the aspect ratio increases up to $\rho = \frac{L}{R} = 2.0$, the magnetic field effect is more effective because of the weak confinement in the z-axial direction ($L = 2R = 40\,\mathrm{nm}$) and it makes the electron probability density move closer to the impurity center as the magnetic field increases. Therefore, the mean relative electron-impurity distance is decreased and the donor binding energy is increased significantly.

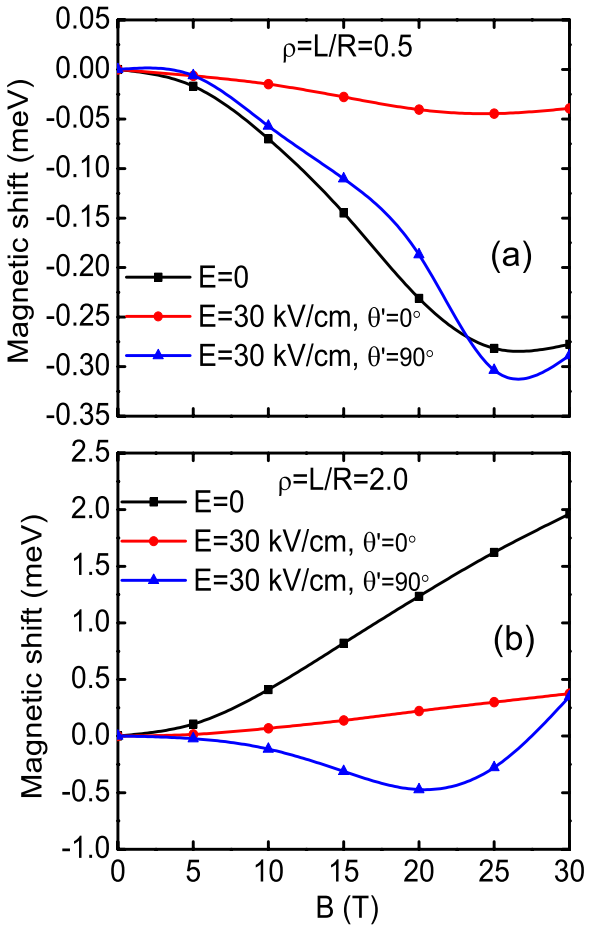

Figure 4. Magnetic shift of the donor binding energy δE_b as a function of the magnitude of the tilted magnetic field $\vec{B}$ in a GaAs/$Al_{0.3}Ga_{0.7}$As cylindrical QD with radius $R = 20\,\mathrm{nm}$ for various tilted electric fields $\vec{E}$. The magnetic field is applied along the x-axial direction ($\theta = 0^\circ$). The electric field is applied parallel ($\theta' = \theta$) or perpendicularly ($\theta' = \theta + 90^\circ$) to the magnetic field. Here, (a) and (b) are for aspect ratio $\rho = \frac{L}{R} = 0.5$ and 2.0, respectively.

It is interesting to find from figure 4 that in the presence of perpendicular electric field ($\theta' = 90^\circ + \theta$), for any aspect ratio, the magnetic shift of the donor binding energy δE_b exhibits a minimum value at a critical magnetic field $B = B_c$. For aspect ratio $\rho = \frac{L}{R} = 0.5$, $B_c \approx 26\,\mathrm{T}$; while for aspect ratio $\rho = \frac{L}{R} = 2.0$, it is $B_c \approx 20\,\mathrm{T}$. In other words, the

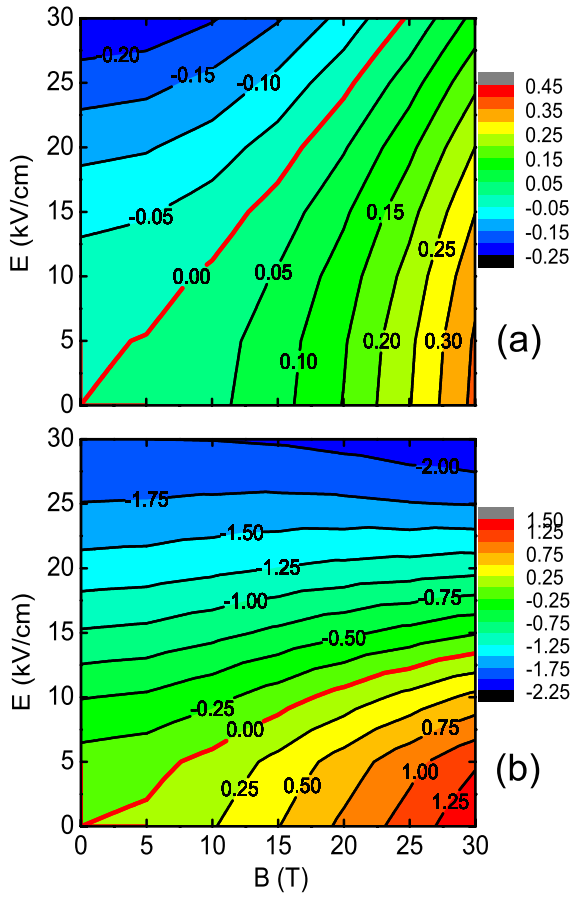

Figure 5. Contour plot of the energetic shift of the donor binding energy ΔE_b (in unite of meV) for various electric ($\vec{E}$) and magnetic ($\vec{B}$) fields in a GaAs/$Al_{0.3}Ga_{0.7}$As cylindrical QD. The magnetic field is applied at an angle $\theta = 45^\circ$). The electric field is applied parallel to the magnetic field ($\theta' = \theta = 45^\circ$). Here, ($a$) and ($b$) are for $L = R = 10$ nm and $L = R = 20$ nm, respectively.

critical magnetic field B_c decreases with increasing aspect ratio ρ. Moreover, when the parallel electric field is applied ($\theta' = \theta$), the magnetic shift of the donor binding energy δE_b decreases slightly with increasing magnetic field for small aspect ratio (for instance, $\rho = L/R = 0.5$). For large aspect ratio $\rho = L/R = 2.0$, δE_b increases monotonically when the magnetic field is enhanced. This behaviour is associated with the interplay between the applied electric and magnetic fields effect as well as the geometric confinement and it can be understood in a similar way as in figure 2.

3.2. Energetic shift of the donor binding energy under the influence of simultaneously applied tilted electric and magnetic fields in a cylindrical QD

As we know from the above section, the magnetic shift of the binding energy exhibits novel behaviour due to the competition effects between the tilted electric and magnetic fields. Thus, in the following part, the energetic shift of the donor binding energy ΔE_b (defined by equation (11)) in a cylindrical QD subjected to simultaneously applied tilted electric and magnetic fields will be investigated in order to understand in detail the competition effects.

Firstly, in an attempt to obtain a qualitative understanding of the competition effects, we have created a suitable contour plot (figure 5) of the energetic shift of the donor binding energy ΔE_b for various electric (0–30 kV cm^{-1}) and magnetic (0–30 T) fields. The magnetic field is directed at an angle $\theta = 45^\circ$, while the electric field is applied parallel to it ($\theta' = \theta = 45^\circ$). Here, two different dot sizes ($L = R = 10$ nm and 20 nm) are considered. It is interesting to find from figure 5 that for any dot size, there is a critical line determined by $\Delta E_b = 0$. The region above the critical line satisfying $\Delta E_b < 0$ represents the 'red shift' of the donor binding energy and the region below the critical line described by $\Delta E_b > 0$ shows the 'blue shift' of the donor binding energy. Figure 5 also shows that the critical line corresponding to $\Delta E_b = 0$ is highly dependent on the dot size. Comparing figures 5(a) and (b), it is found that the critical line moves down when the dot size increases from $L = R = 10$ nm to $L = R = 20$ nm. This means that the energetic shift of the donor binding energy ΔE_b is dominated by the electric field effect for the case of large dot size (i.e. $L = R = 20$ nm).

As verified by the previous discussions, the relative orientation of the tilted electric and magnetic fields plays an important role on the manipulation of the donor binding energy. To clarify the competition effects between the two fields applied in different configurations, we present the contour plot of the energetic shift of the donor binding energy ΔE_b for various electric (0–30 kV cm^{-1}) and magnetic (0–30 T) fields in figure 6, where the magnetic field is applied at $\theta = 0^\circ$ ((a) and (c)) or 90° ((b) and (d)) and the electric field is either parallel (left column) or perpendicular (right column) to it. As shown from figure 6, in the Voigt configuration ($\vec{B} \| \vec{x}$), the critical line goes up when the electric field is tilted from $\theta' = 0^\circ$ (see figure 6(a)) to $\theta' = 90^\circ$ (see figure 6(c)). Making a comparison between figures 6(b) and (d), it is easy to discover that this finding is also valid in the Faraday configuration ($\theta = 90^\circ$). The reasons can be understood as follows. When the electric field is tilted from the x-axial direction ($\theta' = 0^\circ$) to the z-axial direction ($\theta' = 90^\circ$), the electric field effect becomes less important due to the stronger confinement in the z-axial direction ($L = d/2 = 20$ nm, $d = 2R$ is the diameter of the cylindrical QD). This directly leads to the shrinking of the region described by $\Delta E_b < 0$ and the critical line goes up.

Similarly, we find from figure 6 that when the electric field is applied along the x-axial direction ($\theta' = 0^\circ$), the critical line moves up as the magnetic field is tilted from $\theta = 0^\circ$ (see figure 6(a)) to $\theta = 90^\circ$ (see figure 6(d)). The same behaviour happens for the case of growth-direction electric field (see figures 6(b) and (c)). This can be understood analogously as follows. When the magnetic field shifts from the x-axial direction to the z-axial direction, the magnetic field induced confinement becomes more pronounced due to the weaker confinement in the radial direction ($d = 2R = 2L = 40$ nm). As a result, the region corresponding to $\Delta E_b > 0$ is enlarged and the critical line moves up.

Finally, figure 7 displays the contour plot of the energetic shift of the donor binding energy ΔE_b for various electric $\vec{E}$ (0–30 kV cm^{-1}) and magnetic $\vec{B}$ (0–30 T) fields in two aspect ratio ($\rho = \frac{L}{R} = 0.5$ and 2.0) configurations, where the electric field and magnetic field are both applied along

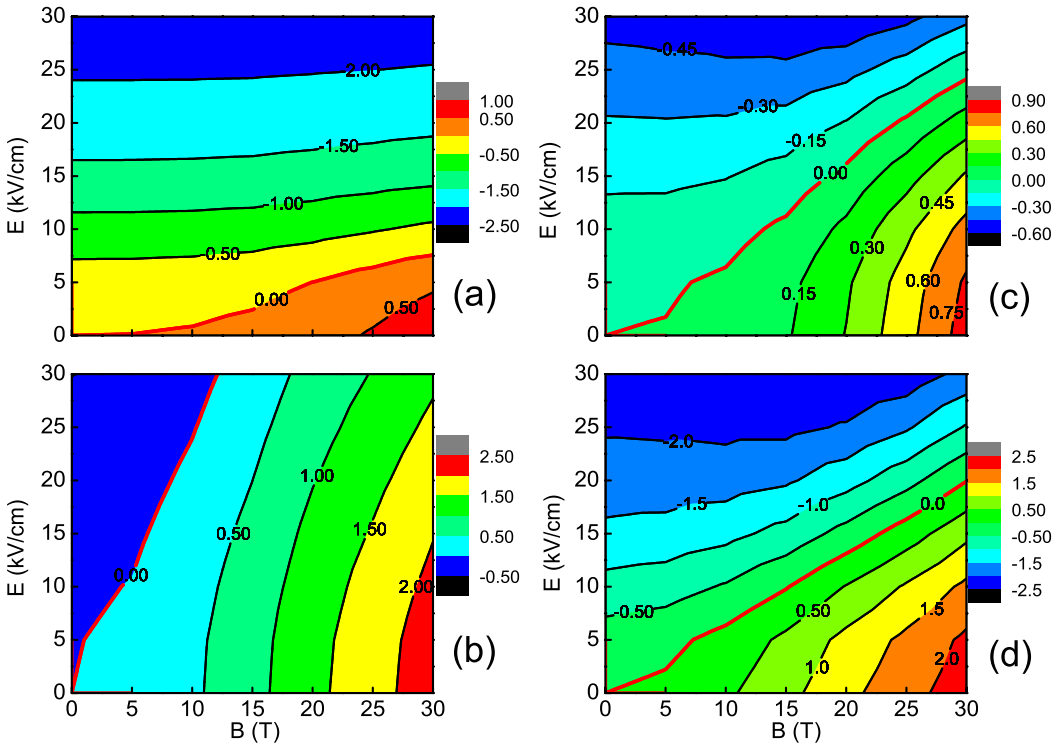

Figure 6. Contour plot of the energetic shift of the donor binding energy ΔE_b (in unite of meV) for various electric ($\vec{E}$) and magnetic ($\vec{B}$) fields in a GaAs/$Al_{0.3}Ga_{0.7}$As cylindrical QD with dot height $L = 20$ nm and radius $R = 20$ nm. Here, (*a*) $\theta = \theta' = 0^\circ$; (*b*) $\theta = \theta' = 90^\circ$; (*c*) $\theta = 0^\circ, \theta' = 90^\circ$; (*d*) $\theta = 90^\circ, \theta' = 0^\circ$.

the x-axial direction. As indicated from figure 7(*a*) (aspect ratio $\rho = \frac{L}{R} = 0.5$), ΔE_b is negative for any electric and magnetic field. Furthermore, for small electric field, it decreases slightly with increasing magnetic field. For large electric field, however, it is insensitive to the increased magnetic field. This is because for aspect ratio $\rho = 0.5$, both the in-plane electric and magnetic fields move the electron probability density far from the impurity center. Therefore, the donor binding energy reduces as the applied electric (or magnetic) field increases. Moreover, for very strong electric field (for instance, $E = 25\,\mathrm{kV\,cm^{-1}}$), the electron probability density distribution is totally dominated by the in-plane electric field and it is insensitive to the increased magnetic field. This directly makes the donor binding energy become invariant with the increased in-plane magnetic field.

When the aspect ratio goes up to $\rho = \frac{L}{R} = 2$ (see figure 7(*b*)), the critical line corresponding to $\Delta E_b = 0$ appears. Moreover, comparing figure 6(*a*) with figure 7(*b*), it is easy to find that the critical line moves up as the aspect ratio increases. This is because when the aspect ratio increases the confinement in the z-axial direction becomes weak and the magnetic field induced confinement in the yoz plane becomes significant.

4. Conclusions

In summary, using the potential morphing method (PMM) with the framework of the effective-mass approximation (EMA), the combination effects of the tilted electric and magnetic fields on the binding energy of an on-center donor impurity localized in a GaAs/$Al_{0.3}Ga_{0.7}$As cylindrical QD have been investigated theoretically. The electric and magnetic fields are both tilted with respect to the QD growth direction and they are either parallel or perpendicular to each other. It is found that for small dot size, the magnetic shift of the donor binding energy is insensitive to the orientation of the electric field. However, for large dot size, it strongly depends on the orientation of the electric field. Moreover, our results show that when the tilted electric and magnetic fields are parallel, the magnetic shift of the donor binding energy is a monotonic function of the strength of the magnetic field; while when the applied electric and magnetic fields are perpendicular, it is a nonmonotonic function of the magnetic field and it exhibits a minimum at a critical magnetic field. The critical magnetic field increases when the magnetic field is tilted from the in-plane direction to the growth direction. However, it decreases with increasing aspect ratio of the cylindrical QD. Furthermore, we have systematically discussed the competition effects between the two fields on the donor binding energy. It is found that there is a critical line corresponding to the zero shift of the donor binding energy under the influence of simultaneously applied tilted electric and magnetic fields. Moreover, this critical line is highly dependent on the dot size, relative orientation of the titled electric and magnetic fields as well as the aspect ratio of the cylindrical QD. We would like to point out that the present numerical results are only valid for the on-center donor impurity in a cylindrical QD subjected to tilted electric and magnetic fields. It is well known that surface impurities play an important role during the doping process of the semiconductor nanocrystals [36–38]. Thus, theoretical predictions of the behaviour of off-center impurities, especially

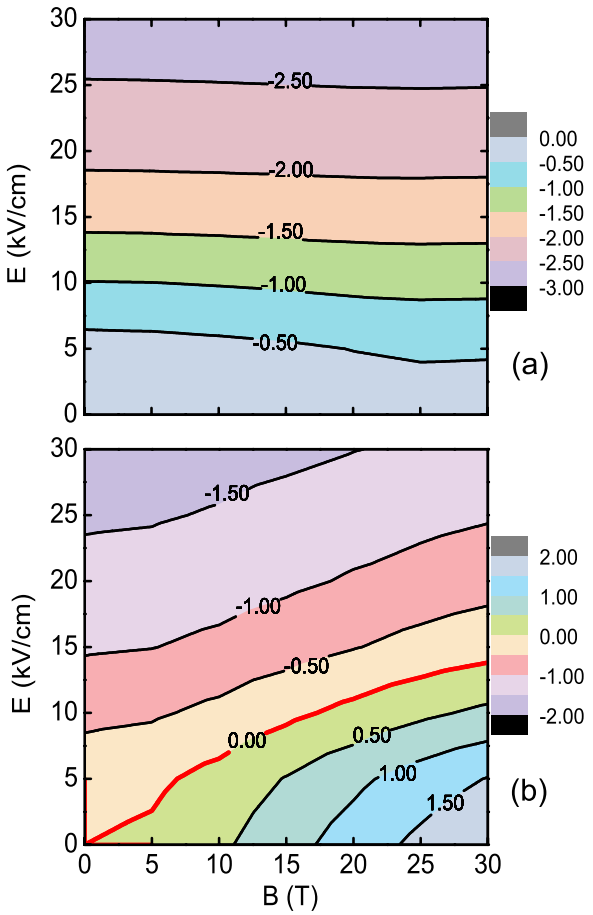

Figure 7. Contour plot of the energetic shift of the donor binding energy ΔE_b (in unite of meV) for various electric ($\vec{E}$) and magnetic ($\vec{B}$) fields in a GaAs/$Al_{0.3}Ga_{0.7}$As cylindrical QD with dot height $L = 20$ nm and radius $R = 20$ nm. The tilted $\theta = \theta' = 0^\circ$. Here, ($a$) and ($b$) are for aspect ratio $\rho = \frac{L}{R} = 0.5$ and 2.0, respectively.

the surface impurities under the influence of tilted electric or magnetic fields deserve to be carried out in detail in the near future. We believe that the results presented here can be useful for us to directly manipulate the performance of the GaAs/$Al_{0.3}Ga_{0.7}$As QD-based optoelectronic devices by applying suitable tilted electric and magnetic fields. We also hope that our results can stimulate forthcoming theoretical and experimental investigations in this attracting research area.

Acknowledgments

This research has been co-financed by the European Union (European Regional Development Fund-ERDF) and Greek national funds through the Operational Program 'Regional Operational Programme' of the National Strategic Reference Framework (NSRF)-Research Funding Program: support for research, technology and innovation actions in Region of Western Greece (MIS: 312123, D.237.002). Furthermore, this work is also supported by the research project 'C. Caratheodory' D. 207 of the Research Committee of the University of Patras.

References

[1] Ando T, Arakawa Y, Foruka K, Komiyama S and Nakashima H 1998 *Mesoscopic Physics and Electronics* (Berlin: Spinger)
[2] Li Y X, Liu J J and Kong X J 2000 *J. Appl. Phys.* **88** 2588
[3] Wang Y J, Leem Y A, McCombe B D, Wu X G, Peeters F M, Jones E D, Reno J R, Lee X Y and Jiang H W 2001 *Phys. Rev.* B **64** 161303
[4] Duque C, Montes A and Morales A 2001 *Physica* B **302** 84
[5] Niculescu E, Gearba A, Cone G and Negutu C 2001 *Superlatt. Microstruct.* **29** 319
[6] Ham H, Lee C J and Spector H N 2004 *J. Appl. Phys.* **96** 335
[7] Ham H and Spector H N 2006 *J. Appl. Phys.* **100** 024304
[8] Boz F K and Aktas S 2005 *Superlatt. Microstruct.* **37** 281
[9] An X T and Liu J J 2006 *J. Appl. Phys* **99** 123713
[10] Betancur F J, Mikhailov I D and Oliveira L E 1998 *J. Phys. D: Appl. Phys.* **31** 3391
[11] Charrour R, Bouhassoune M, Fliyou M and Nougaoui A 2000 *Physica* B **293** 137
[12] Corella-Madueno A, Rosas R, Marín J L and Riera R 2001 *J. Appl. Phys* **90** 2333
[13] Li S S and Xia J B 2006 *J. Appl. Phys.* **100** 083714
[14] Barati M, Rezaei G and Vahdani M R K 2007 *Phys. Status Solidi* b **244** 2605
[15] Jiang L, Wang H, Wu H, Gong Q and Feng S 2009 *J. Appl. Phys.* **105** 053710
[16] Xia C X, Zeng Z P and Wei S Y 2010 *J. Appl. Phys.* **107** 014305
[17] Brozak G, de Andrada e Silva E A, Sham L J, DeRosa F, Miceli P, Schwarz S A, Harbison J P, Florez L T and Allen S J 1990 *Phys. Rev. Lett.* **64** 471
[18] John Peter A, Gnanasekar K and Navaneethakrishnan K 2006 *Eur. J. Phys.* B **53** 283
[19] Kasapoglu E and Sökmen I 2005 *Physica* E **27** 198
[20] Barseghyan M G, Kirakosyan A A and Duque C A 2009 *Eur. Phys. J.* B **72** 521
[21] Baskoutas S and Terzis A F 2010 *J. Comput. Theor. Nanosci.* **7** 492
[22] Baskoutas S and Terzis A F 2009 *Eur. Phys. J.* B **69** 237
[23] Mughnetsyan V, Barseghyan M and Kirakosyan A 2008 *Superlatt. Microstruct.* **44** 86
[24] Monozon B S and Schmelcher P 2010 *Phys. Rev.* B **82** 205313
[25] Redliński P and Jankó B 2005 *Phys. Rev.* B **71** 113309
[26] Wang D, Jin G, Zhang Y and Ma Y Q 2009 *J. Appl. Phys.* **105** 063716
[27] Baskoutas S, Terzis A F and Schommers W 2006 *J. Comput. Theor. Nanosci.* **3** 269
[28] Baskoutas S and Terzis A F 2006 *J. Appl. Phys.* **99** 013708
[29] Baskoutas S and Terzis A F 2005 *J. Appl. Phys.* **98** 044309
[30] Rieth M, Schommers W and Baskoutas S 2002 *Int. J. Mod. Phys.* B **16** 4081
[31] Terzis A F and Baskoutas S 2005 (New York: Nova Science Publishers) pp 93–124
[32] Baskoutas S, Paspalakis E and Terzis A F 2006 *Phys. Rev.* B **74** 153306
[33] Poulopoulos P, Baskoutas S, Pappas S D, Garoufalis C S, Droulias S A, Zamani A and Kapaklis V 2011 *J. Phys. Chem.* C **115** 14839
[34] Li S S and Xia J B 2007 *J. Appl. Phys.* **101** 093716
[35] Allouche A 2011 *J. Comput. Chem.* **32** 174
[36] Erwin S C, Zu L, Haftel M I, Efros A L, Kennedy T A and Norris D J 2005 *Nature* **436** 91
[37] Norris D J, Efros A L and Erwin S C 2008 *Science* **319** 1776
[38] Nistor S V, Stefan M, Nistor L C, Goovaerts E and Tendeloo G V 2010 *Phys. Rev.* B **81** 035336

Paper IV

In which we study the electronic and optical properties of ZnO nanorods as a function of an externally applied hydrostatic pressure ...

THE JOURNAL OF PHYSICAL CHEMISTRY C

Article

pubs.acs.org/JPCC

Tuning of the Optical Emission Polarization of ZnO Nanorods by an Applied Hydrostatic Pressure

Sotirios Baskoutas,*[,†] Zaiping Zeng,[†] Christos S. Garoufalis,[†,§] and Gabriel Bester*[,‡]

[†]Materials Science Department, University of Patras, 26504 Patras, Greece

[‡]Max-Planck-Institut für Festkörperforschung, D-70569 Stuttgart, Germany

ABSTRACT: In the present work, we have performed a systematic theoretical study of the electronic and optical properties of ZnO nanorods as a function of an externally applied hydrostatic pressure. Our calculations are based on the empirical pseudopotential method and configuration interaction to consider the excitonic effects. The optical emission polarization is found to exhibit a transition between in-plane and out-of-plane polarization with increasing pressure. The critical value of the hydrostatic pressure at which the crossover takes place appears to depend strongly on the nanorod's radius. In particular, when the nanorod's radius is smaller than the ZnO exciton Bohr radius, the necessary pressure to reach the crossover point is significantly smaller than the pressure required for a nanorod with radius larger than the exciton Bohr radius. For large pressures, the lowest exciton state is a nearly pure state (0,0), where electron and hole have dominant S-orbital character and the hole has a nearly pure parentage from the bulk Bloch C-band.

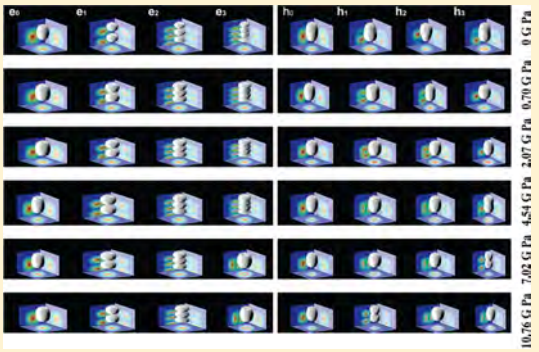

INTRODUCTION

Zinc oxide (ZnO) has emerged as a very promising material for electronic and optoelectronic applications,[1] and it forms a rich variety of nanostructures, such as quantum dots,[2,3] nanowires,[4] nanorods,[5] nanotubes,[6] and nanowalls.[7] It can function in a variety of practical applications from optoelectronic devices, e.g., ultraviolet (UV) sensor[8] and light-emitting diodes (LEDs), to the recently suggested growth of ZnO nanorods (NRs) on graphene for photovoltaic[9] and for biosensor[10] applications. Thanks to the spatial separation of photogenerated carriers, UV photodetectors with a very high photoconductive gain based on ZnO nanowires (NWs) have been demonstrated.[11] It has been shown that the photodetection properties of ZnO NWs depend on the incident light polarization, and when the incident light is parallel to the c-axis of the NW, photocurrent takes its maximum value.[12] Furthermore, as has been proved experimentally, the band-edge UV emission of light along the c-axis of vertically aligned ZnO NWs has a larger intensity in comparison to that parallel to the substrate.[13] For laser applications, the electric field $\mathbf{E}$ (or optical emission polarization) and the wavevector $\mathbf{k}$ must be perpendicular ($\mathbf{E}\perp\vec{c}$) and parallel ($\mathbf{k}\parallel\vec{c}$) to the c-axis of the ZnO NW (α-emission)[14−16] to maximize the light−matter interaction and minimize mirror losses.[16] In our previous work on ZnO NRs,[17] we found a sharp crossover for the optical emission polarization from an in-plane polarized luminescence ($\mathbf{E}\perp\vec{c}$) to an out-of-plane ($\mathbf{E}\parallel\vec{c}$) polarization at a length-to-diameter aspect ratio of around 3. This means the emission of ZnO NRs with aspect ratio larger than 3 has a pure contribution from the so-called σ- and π-emission rather than a normal α-emission. This practically offers us an efficient way to manipulate the optical polarization in ZnO NRs by suitably choosing their sizes and shapes (length-to-diameter aspect ratio). Another way to control the emission properties is via hydrostatic pressure. Such experiments have focused on nanowires,[18] nanosheets,[19] nanotubes,[20] microrods,[21] and nanocrystallites.[22] No attention has been paid to the pressure-dependent optical properties of ZnO NRs. We now investigate the effect of external hydrostatic pressure on the optical emission polarization of ZnO NRs with our recently derived atomistic empirical pseudopotentials.[23] Our calculations include the effects of multiband coupling, multivalley coupling, spin−orbit interaction, and excitonic correlation via configuration interaction. We discuss the pressure dependence of the optical band gap at three levels of theory: at the single particle (SP) level, at the single configuration (SC) level including electron−hole exchange interaction, and at the correlated configuration interaction (CI) level. We find that the optical band gap increases monotonically with increasing pressure for nearly spherical NRs; however, it is a non-monotonic function of the pressure for elongated NRs. The applied pressure induces a sharp transition of the optical emission polarization between the in-plane and an out-of-plane polarization for all the shapes of NRs.

Received: July 23, 2012
Revised: November 22, 2012
Published: November 29, 2012

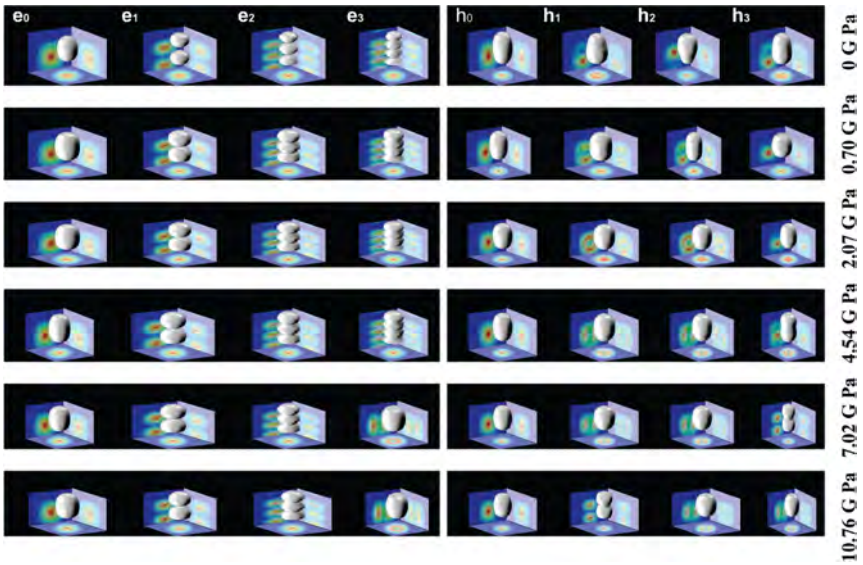

Figure 1. Envelope functions for the first four electron ($e_{0,1,2,3}$) and first four hole ($h_{0,1,2,3}$) states for different hydrostatic pressures and L = 5 nm and D = 2.2 nm. The white isosurfaces enclose 75% of the state density.

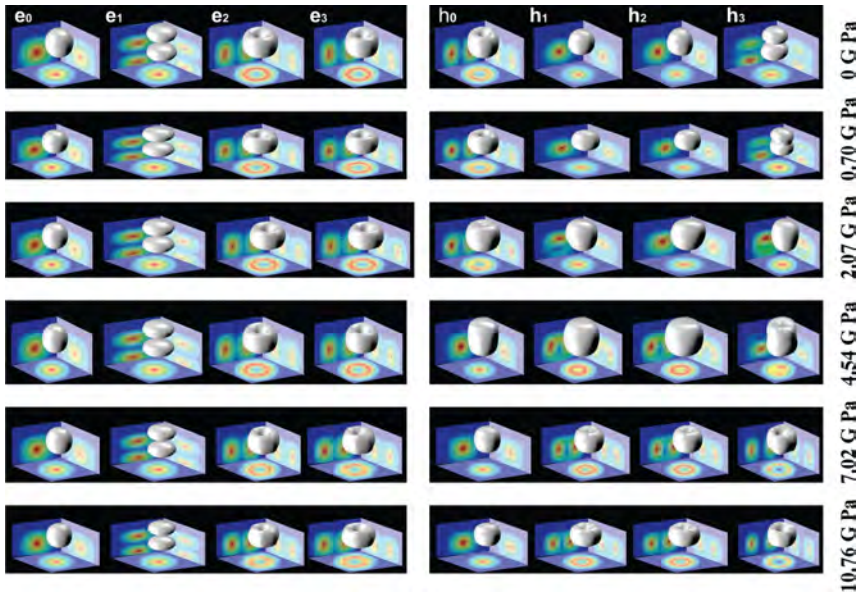

Figure 2. Envelope functions for the first four electron ($e_{0,1,2,3}$) and first four hole ($h_{0,1,2,3}$) states for different hydrostatic pressures and L = 5 nm and D = 4 nm. The white isosurfaces enclose 75% of the state density.

METHODS

The single-particle eigenstates for both conduction and valence bands are obtained using the plane-wave empirical pseudopotential method[24] and our recently derived ZnO pseudopotentials. The adopted Hamiltonian for the single-particle states has the form

$$\hat{H} = -\frac{1}{2}\nabla^2 + \sum_{n\alpha} [v_\alpha(\vec{r} - \vec{R}_{\alpha n}) + \hat{v}_\alpha^{SO}] \quad (1)$$

where n is an atomic index; α specifies the atom type; and $\hat{v}_\alpha^{SO}$ is the nonlocal spin−orbit operator. The screened atomic pseudopotentials v_α (with α = Zn,O) are centered at each atomic position, and their superposition generates the crystal potential. The pseudopotentials v_α incorporate the dependence on the local hydrostatic strain Tr(ε) via the relationship[25]

$$v_\alpha(r; \varepsilon) = v_\alpha^{eq}(r; 0)[1 + \gamma_\alpha \mathrm{Tr}(\varepsilon)] \quad (2)$$

where γ_α is a fitting parameter. The form and the parameters of the zero strain potential, which are optimized to reproduce the known band structure and the bulk properties of ZnO, are given in ref 24. In our calculations, the fitting parameter γ_α has the value 0.304 and gives a pressure coefficient[26] for bulk ZnO equal to 24.7 meV/GPa, which reproduces exactly the experimental value 24.7 ± 0.1 meV/GPa.[27] The surface passivation is approximated by a high band gap artificial material, as practiced successfully previously.[17,23,28] The structure was relaxed with Keating's VFF model for wurtzite

dx.doi.org/10.1021/jp307269d | J. Phys. Chem. C 2012, 116, 26592−26597

Table 1. Character of the First Four Envelope Functions for Electrons and Holes for L = 5 nm, D = 2.2 nm, and Various Hydrostatic Pressures[a]

pressure (GPa)	e_0	e_1	e_2	e_3	h_0	h_1	h_2	h_3
0	(S,S)	(S,P)	(S,D)	(S,F)	(S,S)	(P,S)	(S,S)	(P,S)
0.70	(S,S)	(S,P)	(S,D)	(S,F)	(S,P)	(S,S)	(S,S)	(S,S)
2.07	(S,S)	(S,P)	(S,D)	(S,F)	(S,S)	(S,P)	(S,P)	(S,P)
4.54	(S,S)	(S,P)	(S,D)	(S,F)	(S,S)	(P,S)	(P,S)	(P,S)
7.02	(S,S)	(S,P)	(S,D)	(P,S)	(S,S)	(P,S)	(P,S)	(S,P)
10.76	(S,S)	(S,P)	(S,D)	(P,S)	(S,S)	(S,P)	(P,S)	(P,S)

[a]The given orbital character represents the dominant contribution; significant mixing is present, especially for the hole states.

Table 2. Same as Table 1 but for a NR with L = 5 nm and D = 4 nm

pressure (GPa)	e_0	e_1	e_2	e_3	h_0	h_1	h_2	h_3
0	(S,S)	(S,P)	(P,S)	(P,S)	(P,S)	(S,S)	(S,S)	(S,P)
0.70	(S,S)	(S,P)	(P,S)	(P,S)	(P,S)	(S,S)	(S,S)	(S,P)
2.07	(S,S)	(S,P)	(P,S)	(P,S)	(P,S)	(S,S)	(S,S)	(S,S)
4.54	(S,S)	(S,P)	(P,S)	(P,S)	(S,S)	(P,S)	(P,S)	(S,S)
7.02	(S,S)	(S,P)	(P,S)	(P,S)	(S,S)	(P,S)	(P,S)	(D,S)
10.76	(S,S)	(S,P)	(P,S)	(P,S)	(S,S)	(P,S)	(P,S)	(D,S)

materials.[29] The corresponding envelope functions of the single-particle states in both valence and conduction bands are obtained by projecting the fast oscillating atomic wave functions onto the Bloch states at each unit cell (according to eq 6 of ref 24). This effectively smears out the atomic oscillations and leads to an envelope function that can be displayed with clarity.[17,23] This procedure also allows us to obtain the Bloch function character of each NR state and attribute them A-, B-, or C-band (or a mixture of them) parentage. The excitonic wave functions are expanded in terms of single-substitution Slater determinants constructed from the single-particle wave functions of electrons and holes. The corresponding many-body Hamiltonian is solved in the framework of CI[30] as well as in the SC approximation. As this level of theory, the intraconfiguration Coulomb and exchange matrix elements are fully included, but the interaction between different configurations is neglected.[30] At the SC level, correlations are neglected, and our analysis includes 10 states from the valence band and 10 states from the conduction band. For the screened Coulomb interaction we used the phenomenological isotropic and uniform model proposed by Resta.[31] The optical dipole matrix elements are calculated within the dipole approximation, and the oscillator strength was calculated using Fermi's golden rule. A review of this method can be found in ref 32.

RESULTS AND DISCUSSION

Electronic Properties. We define four different ZnO NRs and more specifically three NRs with diameter D = 2.2 nm and lengths L = 2.2 nm ($Zn_{378}O_{336}$), L = 5 nm ($Zn_{840}O_{798}$), and L = 8 nm ($Zn_{1302}O_{1260}$) and one with D = 4 nm and L = 5 nm ($Zn_{2820}O_{2679}$).

The results for the projected envelope functions of the first four electron states $e_{0,1,2,3}$ and first four hole states $h_{0,1,2,3}$ for L = 5 nm D = 2.2 nm and L = 5 nm D = 4 nm are given in Figures 1 and 2, respectively, for different hydrostatic pressures. To characterize the symmetry of the wave functions, we use the notation (ω,ζ) where the indices ω and ζ represent the number of nodes encountered by moving across the xy plane and along the z-direction, respectively (for more details see ref 10). The

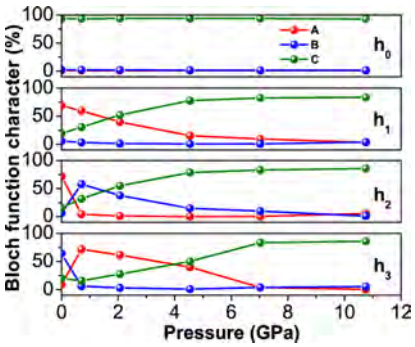

Figure 3. Analysis of the Bloch function character of the first four hole states $h_{0,1,2,3}$ for different hydrostatic pressures, with L = 5 nm and D = 2.2 nm. The colors red, blue, and green correspond to A-, B-, and C-bands, respectively.

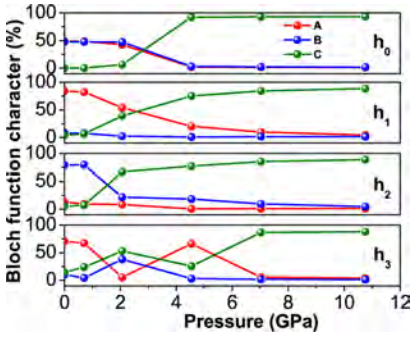

Figure 4. Same as Figure 3 but for a NR with L = 5 nm and D = 4 nm.

results are summarized in Table 1 for L = 5 nm and D = 2.2 nm and in Table 2 for L = 5 nm and D = 4.4 nm.

From Table 1, we can see that all the electron wave functions have the form (S,ζ), as expected from a truly 1D single band system.[17] Only e_3 for pressures greater than or equal to 7.02 GPa develops an in-plane node. The situation is different for the NR with L = 5 nm and D = 4 nm, where e_0 and e_1 have the form (S,ζ) and e_2 and e_3 develop an in-plane node which is very similar to the case of spherical QDs.[23]

dx.doi.org/10.1021/jp307269d | J. Phys. Chem. C 2012, 116, 26592−26597

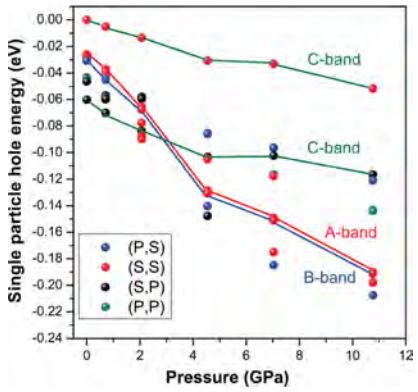

Figure 5. Energy of the first ten hole states versus hydrostatic pressure for ZnO NRs with L = 5 nm and D = 2.2 nm. The lines connect states with the same envelope function symmetry (ω,ζ) and the same strongly dominant (A,B,C)-band character.

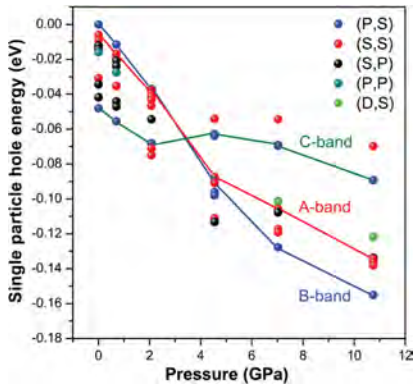

Figure 6. Same as Figure 5 but of a NR with L = 5 nm and D = 4 nm.

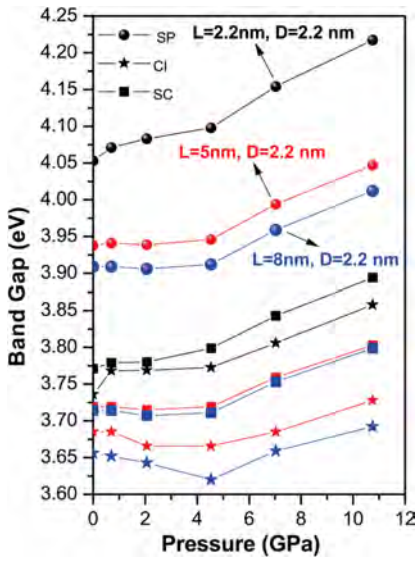

Figure 7. Optical band gap at the SP level (filled circles), in the SC approximation including exchange (squares) and using full CI (solid stars) for various hydrostatic pressures and (*i*) L = 2.2 nm and D = 2.2 nm (black line and symbols); (*ii*) L = 5 nm and D = 2.2 nm (red lines and symbols); and (*iii*) L = 8 nm and D = 2.2 nm (blue lines and symbols).

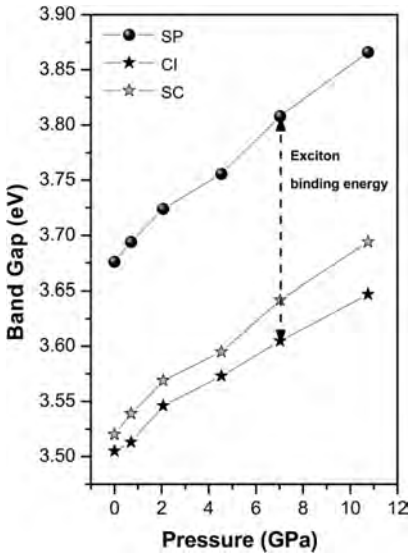

Figure 8. Optical band gap at the SP level (filled circles), in the SC approximation including exchange (open stars) and using full CI (solid stars) for various hydrostatic pressures and L = 5 nm and D = 4 nm.

The situation for the hole states is more complicated, and we analyze them by projection onto bulk ZnO bands (see eq 5 of ref 24 for details). The results are given in Figures 3 and 4 for the first four hole states of NRs with L = 5 nm and D = 2.2 nm and D = 4 nm, respectively, where the contribution of the A-, B-, and C-bands is given in percent. From Figures 3 and 4, we notice that with increasing pressure all the first four hole states acquire nearly pure C-band Bloch function character. Hydrostatic pressure therefore effectively favors hole states with C-band character, in a similar fashion that elongations along the *c*-direction favor holes with C-band character.[17] For the nearly spherical NR (Figures 2 and 4) the ground state hole for pressures below 4 GPa have P-envelope function character (P,S) and have an even mixture of A- and B-band Bloch function parentage. When the pressure is increased above 4 GPa, the state switches to a more conventional S-envelope state with C-band Bloch function parentage. For pressures above 6 GPa, all the first four hole states, for all our shapes, are nearly pure single C-band hole states. The associated envelope wave functions are therefore expected to follow the situation we observe for electrons. However, Figure 2 and especially Figure 1 show that electron and hole states are very different, even in the simple situation of high pressure when the holes are single-band objects. This is due to the very different effective masses of electrons and holes. The electrons are relatively light (m_e = 0.265 m_0, where m_0 is the free electron mass) and isotropic ($m_{e\|}$ = $m_{e\perp}$). This leads to a situation where the states with P envelope functions with a node in-plane (we label these as (P,S), e.g., e_2 at zero pressure in Figure 2) and with a node along the *c*-axis (labeled as (S,P), e.g., e_1 at zero pressure in Figure 2) have a similar energy. In other words, the effective mass, and associated kinetic energy, does not favor one type of node (along or perpendicular to the *c*-axis). This situation is different for holes. These holes are relatively heavy and anisotropic with $m_{h\|}$ = 0.31m_0 and $m_{h\perp}$ = 0.55m_0. The formation of nodes perpendicular to the *c*-axis ($\perp$) is therefore favored over the formation of nodes along the *c*-axis ($\|$). The states (P,S) are therefore preferred over the states (S,P), as can be seen on the right-bottom of Figure 2 where no nodes along

dx.doi.org/10.1021/jp307269d | J. Phys. Chem. C 2012, 116, 26592−26597

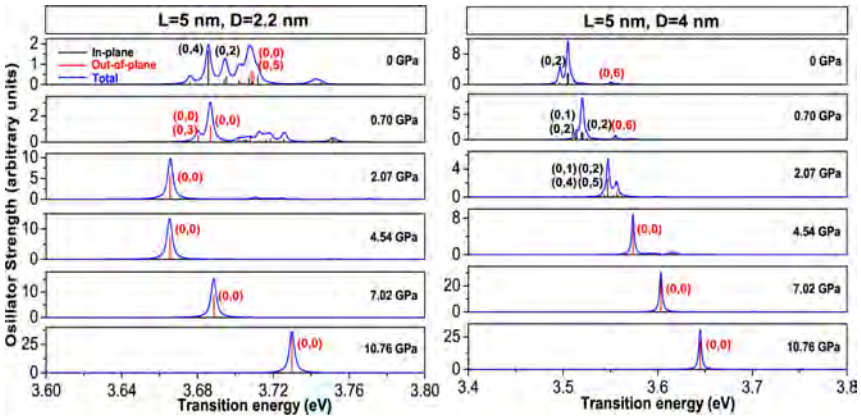

Figure 9. Oscillator strengths for the emission $|X\rangle$ to $|0\rangle$ at room temperature in L = 5 nm, D = 2.2 nm (left panel) and L = 5 nm, D = 4 nm (right panel) calculated at the CI level. Emission polarized along the out-of-plane direction (c-axis) is shown in red, while that polarized in-plane is shown in black. The numbers in brackets refer to the dominant single-particle levels involved in the transitions (e,h). The blue curve is the total emission spectrum where a Lorentz line shape with a broadening of 1.5 meV has been used.

the c-axis are present and h_3 is a state with in-plane D-character. This is however only true for nearly spherical structures. When the NRs are increasingly elongated along the c-direction, the formation of nodes along this direction becomes increasingly favorable as well. This can be seen on the right-bottom part of Figure 1. The effect of the hydrostatic pressure on the envelope functions of the holes can be seen in the hole panels (right) of Figure 1 for 7.02 and 11.76 GPa. All of the states are nearly pure C-band hole states. The P envelope state with a node along the c-direction becomes more favorable (moves from h_3 to h_1) for higher pressure. Pressure favors nodes along the c-direction, although energetically this effect is rather small; i.e., the states $h_{1,2,3}$ are close in energy (see Figure 5).

In Figures 5 and 6, we study the pressure dependence of the first ten hole-state eigenvalues for L = 5 nm, D = 2.2 nm and L = 5 nm, D = 4 nm, respectively, and connect the states according to their symmetry. As we can see, the A- and B-bands are more sensitive to the pressure in comparison to the C-band. On the other hand, the C-band states rise above the other states for pressures greater than 3.0 GPa (Figure 5) and 3.5 GPa (Figure 6).

Optical Properties. While the literature on ZnO NRs in the intermediate and weak confinement is extensive,[5,33,34] the literature on ZnO NRs with radii smaller than or equal to the exciton Bohr radius (1.4 nm) and showing quantum confinement effects is limited.[35−38] The optical band gap for different pressures at three different levels of theory—at the single particle (SP) level (filled circles), at the SC level including electron−hole exchange interaction (squares), and at the correlated CI level (solid stars) for D = 2.2 nm and L = 2.2 nm, 5 and 8 nm are given in Figure 7. As we can see for aspect ratio ρ = 1 (L = 2.2 nm, D = 2.2 nm) with increasing pressure the optical band gap increases at all three levels of theory. The situation is different for the other aspect ratios (ρ = 2.27 and 3.63) where the optical band gap, at the three levels of theory, increases only for pressures larger than 4.54 GPa. For pressures smaller than 4.54 GPa, the optical band gap at the SP level is essentially constant, and at the SC and CI levels the optical band gap even decreases if pressure increases. As is also evident, the difference between the values of the optical band gap between SC and CI levels, which define the correlation effects, becomes larger with increasing pressure and also increasing aspect ratio.

In Figure 8 we depict the behavior of the optical band gap at the SP, SC, and CI levels as a function of pressure for L = 5 nm and D = 4 nm, showing an increasing band gap with increasing pressure, at all three levels of theory. The pressure coefficients are 17.4 meV/GPa (SP), 15.7 meV/GPa (SC), and 13.9 meV/GPa (CI). Finally we show in Figure 9 the emission spectra at the CI level and analyze the results in terms of dominant configurations. The lowest exciton is polarized along the out-of-plane direction (c-polarized) when the pressure reaches a critical value. This critical value is highly dependent on the length-to-diameter aspect ratio and is P_c = 0.70 GPa for large-aspect-ratio NRs, while it is P_c = 4.54 GPa for small-aspect ratios. In both cases, the lowest exciton state is a pure (0,0) state where both electron and hole have (S,S) symmetry and the hole has a dominant parentage from the bulk C-band. This result is in agreement with the theoretical results for ZnO NWs obtained by k·p theory which states that the X_c exciton is strongly polarized parallel to the c-axis.[39] The emission which is treated by line spectrum in Figure 9 (black or red vertical lines) is just to indicate explicitly the polarization direction. To be compared more easily with future experiments, some Lorentz line shape has been added (blue curves of Figure 9).

CONCLUSIONS

In the present work, we have studied the electronic and optical properties of ZnO NRs as a function of the applied hydrostatic pressure within the atomistic empirical pseudopotential framework and configuration interaction. We analyze the hole states according to their envelope function symmetry and their Bloch function character using a projection technique. We find that: (i) The hole states with a mixed parentage of A- and B-bands are more sensitive to pressure than hole states with C-Bloch-band parentage. (ii) For increasing pressure until 4 GPa the optical band gap remains constant, for nearly spherical NRs, and even decreases for elongated NRs. For larger pressures, the band gap increases for all our structures. (iii) The effects of correlations increase with increasing pressure. (iv) We obtain a large difference between the electron and hole envelope functions, even when the holes have a nearly single-C-Bloch band character. This is due to the anisotropic hole effective mass of the C-Bloch band in ZnO. Envelope functions with nodes perpendicular to the c-axis are more favorable than nodes

dx.doi.org/10.1021/jp307269d | J. Phys. Chem. C 2012, 116, 26592−26597

parallel to the *c*-axis. The electron effective mass is, however, isotropic, and there is nearly no preference for the existence of nodes parallel or perpendicular to the *c*-axis. (v) The ground state hole in nearly spherical NRs has *P*-type envelope function. This situation can only occur when the Bloch function character of this state is mixed. In our case, the hole state has a Bloch function made of an even mixture of A and B Bloch bands. (vi) Pressure favors envelope functions with nodes along the c-direction. (vii) Pressure favors the C-band, over the A, B-bands, so that at high pressures the hole states become single-C-band like. In this case the envelope function of the ground state hole has the conventional *S* angular momentum. (viii) Accordingly, the optical polarization exhibits a transition between in-plane ($\mathbf{E}\perp\vec{c}$) to out-of-plane ($\mathbf{E}\|\vec{c}$) with increasing pressure. This indicates the possibility to effectively manipulate the optical emission polarization of NRs via pressure, which should be very attractive for the design of future experiments.

AUTHOR INFORMATION

Corresponding Author

*E-mail: bask@upatras.gr; g.bester@fkf.mpg.de.

Present Address

[§]Department of Environment Technology and Ecology, Technological Institute of Ionian Islands, 2 Kalvou Sq, 29100, Zakynthos, Greece.

Notes

The authors declare no competing financial interest.

ACKNOWLEDGMENTS

This research has been cofinanced by the European Union (European Regional Development Fund-ERDF) and Greek national funds through the Operational Program "Regional Operational Programme" of the National Strategic Reference Framework (NSRF)-Research Funding Program: Support for research, technology and innovation actions in Region of Western Greece (MIS: 312123, D.237.002). Furthermore, this work is also supported by the research project "C. Caratheodory" D. 207 of the Research Committee of the University of Patras.

REFERENCES

(1) Özgür, U.; Alivov, Y. I.; Liu, C.; Teke, A.; Reshchikov, M. A.; Doğan, S.; Avrutin, V.; Cho, S.-J.; Morkoç, H. *J. Appl. Phys.* **2005**, *98*, 041301.

(2) Qiao, Q.; Li, B.; Shan, C.; Liu, J.; Yu, J.; Xie, X.; Zhang, Z.; Ji, T.; Jia, Y.; Shen, D. *Mater. Lett.* **2012**, *74*, 104.

(3) Bouropoulos, N.; Tsiaoussis, I.; Poulopoulos, P.; Roditis, P.; Baskoutas, S. *Mater. Lett.* **2008**, *62*, 3533.

(4) Fan, J.; Güell, F.; Fábrega, C.; Fairbrother, A.; Andreu, T.; López, A. M.; Morante, J. R.; Cabot, A. *J. Phys. Chem. C* **2012**, *116*, 19496.

(5) (a) Ko, S. H.; Lee, D.; Kang, H. W.; Nam, K. H.; Yeo, J. Y.; Hong, S. J.; Grigoropoulos, C. P.; Sung, H. J. *Nano Lett.* **2011**, *11*, 666. (b) Kinadjian, N.; Achard, M.-F.; Julián-López, B.; Maugey, M.; Poulin, P.; Prouzet, E.; Backov, R. *Adv. Funct. Mater.* **2012**, *22*, 3994.

(6) Guo, H.; Lin, Z.; Feng, Z.; Lin, L.; Zhou, J. *J. Phys. Chem. C* **2009**, *113*, 12546.

(7) Israr, M. Q.; Sadaf, J. R.; Nur, O.; Willander, M.; Salman, S.; Danielsson, B. *Appl. Phys. Lett.* **2011**, *98*, 253705.

(8) Gimenez, A. J.; Yanez-Limon, J. M.; Seminario, J. M. *J. Phys. Chem. C* **2011**, *115*, 282.

(9) Yin, Z.; Wu, S.; Zhou, X.; Huang, X.; Zhang, Q.; Boey, F.; Zhang, H. *Small* **2010**, *6*, 307−312.

(10) Dar, G.; Umar, A.; Zaidi, S. A.; Baskoutas, S.; Kim, S.; Abaker, M.; Al-Hajry, A.; Al-Sayari, S. *Sci. Adv. Mater.* **2011**, *3*, 901−906.

(11) Soci, C.; Zhang, A.; Xiang, B.; Dayeh, S. A.; Aplin, D. P. R.; Park, J.; Bao, X. Y.; Lo, Y. H.; Wang, D. *Nano Lett.* **2007**, *7*, 1003.

(12) Fan, Z.; chun Chang, P.; Lu, J. G.; Walter, E. C.; Penner, R. M.; hung Lin, C.; Lee, H. P. *Appl. Phys. Lett.* **2004**, *85*, 6128.

(13) Hsu, N. E.; Hung, W. K.; Chen, Y. F. *J. Appl. Phys.* **2004**, *96*, 4671.

(14) Maslov, A. V.; Ning, C. Z. *Appl. Phys. Lett.* **2003**, *83*, 1237.

(15) Li, H.-Y.; Rühle, S.; Khedoe, R.; Koenderink, A. F.; Vanmaekelbergh, D. *Nano Lett.* **2009**, *9*, 3515.

(16) Han, N. S.; Shim, H. S.; Lee, S.; Park, S. M.; Choi, M. Y.; Song, J. K. *Phys. Chem. Chem. Phys.* **2012**, *14*, 10556.

(17) Baskoutas, S.; Bester, G. *J. Phys. Chem. C* **2011**, *115*, 15862.

(18) Shan, W.; Walukiewicz, W.; Ager, J. W., III; Yu, K. M.; Zhang, Y.; Mao, S. S.; Kling, R.; Kirchner, C.; Waag, A. *Appl. Phys. Lett.* **2005**, *86*, 153117.

(19) Chen, S. J.; Liu, Y. C.; Shao, C. L.; Xu, C. S.; Liu, Y. X.; Wang, L.; Liu, B. B.; Zou, G. T. *J. Appl. Phys.* **2005**, *98*, 106106.

(20) Chen, S. J.; Liu, Y. C.; Shao, C. L.; Xu, C. S.; Liu, Y. X.; Liu, C. Y.; Zhang, B. P.; Wang, L.; Liu, B. B.; Zou, G. T. *Appl. Phys. Lett.* **2006**, *88*, 133127.

(21) Su, F. H.; Wang, W. J.; Ding, K.; Li, G. H.; Liu, Y.; Joly, A. G.; Chen, W. *J. Phys. Chem. Solids* **2006**, *67*, 2376.

(22) Huso, J.; Morrison, J. L.; Hoeck, H.; Chen, X.-B.; Bergman, L.; Jokela, S. J.; McCluskey, M. D.; Zheleva, T. *Appl. Phys. Lett.* **2006**, *89*, 171909.

(23) Baskoutas, S.; Bester, G. *J. Phys. Chem. C* **2010**, *114*, 9301.

(24) Wang, L.-W.; Zunger, A. *J. Chem. Phys.* **1994**, *100*, 2394.

(25) Williamson, A. J.; Wang, L. W.; Zunger, A. *Phys. Rev. B* **2000**, *62*, 12963.

(26) For the determination of pressure, we have used eq 3 of ref 18, where ZnO bulk modulus B = 142.4 GPa and its pressure derivative B' = 3.6.[27]

(27) Morkoç, H.; Özgür, U. *Zinc Oxide*; Wiley-vch: New York, 2009.

(28) Califano, M.; Bester, G.; Zunger, A. *Nano Lett.* **2003**, *3*, 1197.

(29) Camacho, D.; Niquet, Y. M. *Physica E* **2010**, *42*, 1361.

(30) Franceschetti, A.; Fu, H.; Wang, L. W.; Zunger, A. *Phys. Rev. B* **1999**, *60*, 1819.

(31) Resta, R. *Phys. Rev. B* **1977**, *16*, 2717.

(32) Bester, G. *J. Phys: Condens. Matter* **2009**, *21*, 023202.

(33) Chrissanthopoulos, A.; Baskoutas, S.; Bouropoulos, N.; Dracopoulos, V.; Poulopoulos, P.; Yannopoulos, S. *Photonics Nanostruct.* **2011**, *9*, 132.

(34) Ng, A. M.-C.; Djurisic, A. B.; Tam, K.-H.; Kwok, W.-M.; Chan, W.-K.; Tam, W. Y.; Phillips, D. L.; Cheah, K.-W. *Adv. Funct. Mater.* **2008**, *18*, 566.

(35) Greyson, E.; Babayan, Y.; Odom, T. *Adv. Mater.* **2004**, *16*, 1348.

(36) Yin, M.; Gu, Y.; Kuskovsky, I. L.; Andelman, T.; Zhu, Y.; Neumark, G. F.; O'Brien, S. *J. Am. Chem. Soc.* **2004**, *126*, 6206.

(37) Gu, Y.; Kuskovsky, I. L.; Yin, M.; O'Brien, S.; Neumark, G. F. *Appl. Phys. Lett.* **2004**, *85*, 3833.

(38) Hu, Y.; Mei, T.; Guo, J.; White, T. *Inorg. Chem.* **2007**, *46*, 11031.

(39) Jacopin, G.; Rigutti, L.; Bugallo, A.; Julien, F.; Baratto, C.; Comini, E.; Ferroni, M.; Tchernycheva, M. *Nanoscale Res. Lett.* **2011**, *6*, 501.

Paper V

In which we study the quantum confinement effects in SnS nanocrystals in collaboration with the experimentalists from Iran ...

J Nanopart Res (2013) 15:1388
DOI 10.1007/s11051-012-1388-1

RESEARCH PAPER

Strong quantum confinement effects in SnS nanocrystals produced by ultrasound-assisted method

Yashar Azizian-Kalandaragh · Ali Khodayari · Zaiping Zeng · Christos S. Garoufalis · Sotirios Baskoutas · Lionel Cervera Gontard

Received: 3 June 2012 / Accepted: 21 December 2012 / Published online: 5 January 2013

Abstract Nanocrystalline SnS powder has been prepared using tin chloride ($SnCl_2$) as a tin ion source and sodium sulfide (Na_2S) as a sulfur ion source with the help of ultrasound irradiation at room temperature. The as-synthesized SnS nanoparticles were quantitatively analyzed and characterized in terms of their morphological, structural, and optical properties. The detailed structural and optical properties confirmed the orthorhombic SnS structure and a strongly blue shifted direct band gap (1.74 eV), for synthesized nanoparticles. The measured band gap energy of SnS nanoparticles is in a fairly good agreement with the results of theoretical calculations of exciton energy based on the potential morphing method in the Hartree–Fock approximation.

Keywords Quantum confinement effect · SnS · Semiconductor nanoparticles · X-ray diffraction · Potential morphing method · Ultrasound irradiation

Y. Azizian-Kalandaragh (✉)
Department of Physics, University of Mohaghegh Ardabili, P.O. Box 179, Ardabil, Iran
e-mail: yashar.a.k@gmail.com; azizian@uma.ac.ir

A. Khodayari
Department of Chemistry, University of Mohaghegh Ardabili, P.O. Box 179, Ardabil, Iran

Z. Zeng · C. S. Garoufalis · S. Baskoutas
Materials Science Department, University of Patras, 26504 Patras, Greece

C. S. Garoufalis
Department of Environment Technology and Ecology, Technological Institute of Ionian Islands, 2 Kalvou Sq, 29100 Zakynthos, Greece

L. C. Gontard
Instituto de Ciencia de Materiales de Sevilla (CSIC), 41092 Sevilla, Spain

Introduction

Quantum confinement effect in semiconductor nanomaterials has been of special interest during the last decades. Quantum confined semiconductor nanocrystals, which exhibit properties different from bulk materials, are a new class of materials that hold considerable attention for numerous applications in the field of optoelectronics. Modification of molecular design and morphology of such nanostructures provides a powerful approach to control their electronic and optical properties. Reduction in the size of particles to nanometer ranges changes the degree of confinement of charge carriers, which affect the electronic and optical properties of semiconductor materials (Alivisatos 1996; Henglein 1989; Liu et al. 2006; Ögüt et al. 1997; Rama Krishna and Friesner 1991; Trindade et al. 2001). These unique characteristics of semiconductor nanostructured materials originate from the quantum confinement effects. From

theoretical point of view, as the radius of particle approaches the exciton Bohr radius of a given material, quantization of the energy bands become apparent and a blue shift in the exciton transition energy can be observed (Baskoutas and Terzis 2006; Wang and Herron 1990). Among the extensively studied IV–VI semiconductor materials, tin sulfide is very important narrow gap material because of its low toxicity and wide applications as an absorber layer in solar cells, near infrared materials, holographic recording media, and solar control devices (Liu et al. 2010; Rudel 2003; Winship 1998). It is important and necessary to study the band gap changes in semiconductor nanostructures in order to gain a better understanding for their relevant properties. Also, band gap engineering of the semiconductor nanostructures by the control of nanostructure sizes is important. Experimental studies showed that semiconductor SnS exhibit p and n type conduction and has both a direct optical gap located at 1.3 eV and indirect optical band gap located at 1.1 eV (Bashkirov et al. 2011; Ning et al. 2010; Yue et al. 2009). In order to obtain nanostructured SnS, the following methods are used: spray pyrolysis of the water solution (Reddy et al. 1999; Thangaraju and Kaliannan 2000), vacuum evaporation (Johson et al. 1999), chemical vapor deposition (Ortiz et al. 1996; Price et al. 2000), chemical bath deposition (Engelken et al. 1987; Tanusevski 2003), electro deposition and electrochemical deposition (Chazali et al. 1998; Takeuchi et al. 2003), chemical synthesis (Gou et al. 2005), microwave assisted synthesis (Chen et al. 2004), mild solution route (Li et al. 2002), modified solution dispersion method (Zhao et al. 2004), two gas process (Reddy and Reddy 2002), solvothermal process (Panda et al. 2006; Paul and Agarwal 2007; Paul et al. 2008; Qian et al. 1999), successive ionic layer adsorption and reaction (SILAR) method (Ghosh et al. 2008), hydrothermal synthesis (Biswas et al. 2007), and molecular beam epitaxy (Nozaki et al. 2005).

Generally, most of the above-mentioned methods require high temperature as well as the use of highly sensitive toxic solvents. Our attempt is to obtain high quality materials under normal laboratory conditions, using safer precursors by applying ultrasonic waves. Previously ultrasonic waves have been used for the preparation of nanomaterials (Azizian-Kalandaragh et al. 2009; Azizian-Kalandaragh and Khodayari 2010a, b; Bhattacharyya and Gedanken 2008; Goharshadi et al. 2009; Suslick 1990; Suslick et al. 1990; Wang et al. 2002; Zhu et al. 2008).

Ultrasonic waves have been shown to cause physical and chemical effects such as fragmentation to small particles and acceleration of reactions, which may be used for the preparation of new materials with desirable properties.

During sonication, ultrasonic longitudinal waves are radiated through the solution causing alternating high and low pressure regions in the liquid medium. Millions of microscopic bubbles form and grow in the low-pressure stage, and subsequently collapse in the high-pressure stage.

Hot spots that are localized regions of extremely high temperatures as high as 5,000 K, and pressures of up to $\sim$1,800 atm can occur from the collapsing bubbles, and cooling rates can often exceed $\sim 10^{10}$ K s^{-1}. The energy released from this process, known as cavitation, would lead to enhanced chemical reactivity and accelerated reaction rates (Suslick 1988).

In this paper we report the preparation of SnS nanocrystals with the help of ultrasonic irradiation. We have chosen this method because of its many advantages, such as easier composition control, low toxicity, better homogeneity, low processing temperature, easier fabrication of large numbers of nanoparticles, lower cost, and possibility of using high purity starting materials. In this paper we also report the morphological, optical, and structural properties of SnS nanocrystals. As our results indicate, the absorption edge is shifted toward the lower wavelength side (i.e., blue shift) and direct energy gap of SnS nanocrystals is estimated to 1.74 eV. The results are compared to theoretical calculations based on the potential morphing method (PMM) (Rieth et al. 2002) in the Hartree–Fock approximation (Baskoutas 2005a, b; Baskoutas et al. 2006a, b; Baskoutas and Terzis 2006; Poulopoulos et al. 2011). This method, based on the adiabatic theorem of quantum mechanics which states that if the Hamiltonian of the system varies slowly with time then the nth eigenstate of the initial Hamiltonian will be carried into the nth eigenstate of the final Hamiltonian, solves the Schrödinger equation for any arbitrary interaction potential. In the present case, the PMM based results exhibit a fairly good agreement with the experimental data. This combined experimental and theoretical work provides a better insight on the quantum confinement effects in SnS nanoscaled systems.

Experimental details

Materials and instruments

Sodium sulfide hydrate was obtained from Sigma-Aldrich, triethanolamine (TEA) was obtained from Rankem; tin (II) chloride dihydrate, polyvinyl alcohol (PVA), and absolute ethanol were obtained from Merck. All the reagents were used as-received without purification.

X-ray diffraction (XRD) analysis of drop-coated films on an ordinary glass substrate from the SnS nanocrystals was carried out on a Philips X' Pert Pro with CuKα radiation. The optical properties of sample were monitored on a Carry 5 UV-Visible spectrophotometer (model Varian). Scanning electron microscopy (SEM) measurements were performed on a LEO 1430VP instrument operated at an accelerating voltage of 15 kV. The elemental analyses of the products were obtained by energy dispersive X-ray analysis (EDAX) on the same LEO 1430VP instrument with accelerating voltage of 15 kV. Samples for SEM and EDAX studies were prepared by placing drops of the SnS nanostructured suspension on gold- and palladium-coated SEM stage. Transmission electron microscopy (TEM) images of the sample were taken on a Philips CN10, TEM performing at an accelerating voltage of 100 kV.

Preparation of SnS nanocrystals

In a typical procedure, for preparation of 0.2 M solution of tin chloride, 0.90 g of tin chloride powder was dissolved in 20 ml TEA, then 0.31 g of sodium sulfide was dissolved in 20 ml distilled water (0.2 M). These two solutions were mixed and were put in a 100 ml round bottom flask. The pH value of the mixture was 12. The mixture solutions were kept under high intensity ultrasonic transductor at room temperature for 2 h. During irradiation 5 ml of aqueous solutions of PVA (1 %) were added to the mixture. At the end of the reaction, a great amount of black precipitates were obtained. After cooled to room temperature, the precipitates were centrifuged, washed by distilled water and absolute ethanol in sequence, and dried in vacuum. Plenty of SnS nanoparticles have been prepared using this method and the yield of this preparation is high in comparison with most of chemical preparation methods. The final products were collected for characterizations. The products were characterized by XRD, SEM, TEM, EDAX, and UV-Visible spectroscopy.

The formation mechanism of SnS nanocrystals with the reaction equation can be expressed as follows:

$$\mathrm{SnCl_2 \cdot 2H_2O + Na_2S \cdot \ xH_2O \rightarrow \ SnS \ + \ 2NaCl \ + \ xH_2O}$$

The role of PVA is to stabilize the nanostructures preventing them from coagulation.

Theory

In the effective mass approximation the Hamiltonian for the electron hole system can be written as (Baskoutas 2005a, b; Baskoutas et al. 2006a, b; Baskoutas and Terzis 2006; Poulopoulos et al. 2011)

$$H = -\frac{\hbar^2}{2m_e^*}\nabla_e^2 - \frac{\hbar^2}{2m_h^*}\nabla_h^2 + V_0^e(r_e) + V_0^h(r_h) - \frac{e^2}{\varepsilon}\frac{1}{r_{eh}} \quad (1)$$

where m_e^* (m_h^*) is the effective electron (hole) band mass, ε is the effective dielectric constant, r_{eh} is the electron—hole distance in three dimensions, and $V_0^{e(h)}$ is the finite depth well confinement potential of electron (hole). As in our previous work (Poulopoulos et al. 2011; Baskoutas et al. 2006a, b) we will also use here a reliable expression for the dielectric constant ε developed by Hanken (1956) and used by several authors for example Nanda et al. (2004); Pellegrini et al. (2005) and which has the following form

$$\frac{1}{\varepsilon(R_0)} = \frac{1}{\varepsilon_\infty} - \left[\frac{1}{\varepsilon_\infty} - \frac{1}{\varepsilon_0}\right]\left[1 - \frac{\exp\left(-R_0/\rho_e\right) + \exp\left(-R_0/\rho_h\right)}{2}\right] \quad (2)$$

where R_0 is the mean distance between the electron and hole (Nanda et al. 2004; Pellegrini et al. 2005) and approximately takes the values (Nanda et al. 2004) $0.69932R$ or R (Baskoutas et al. 2006a, b), where R is the radius of the cluster and represents half of the confining parameter which is the diameter of the

nanocrystal. ε_0 and ε_∞ are the static and optical dielectric constants, respectively, and $\rho_{e,h}$ are given as follows

$$\rho_{e,h} = \left(\frac{\hbar}{2m^*_{e,h}\omega_{LO}}\right)^{1/2} \tag{3}$$

where ω_{LO} is the frequency of LO phonons.

As regards the height of the finite depth well confining potentials $V_0^{e(h)}$ for electrons and holes, we have shown in our previous study (Baskoutas and Terzis 2006) that is independent of the nanostructured semiconductor material and depends exclusively on the matrix energy band gap $E_g(M)$ by a simple linear relation of the form $V_0 = 0.08 \cdot E_g(M)$. Assuming also that the confining potential has the same value for both electron and hole, we set for our thin film system

$$V_0^e(r_e) = V_0^h(r_h) = \begin{cases} 0 & r < R \\ 0.08 \cdot E_g(M) & r \geq R \end{cases} \tag{4}$$

where R is the radius of the nanocrystal.

The Hartree–Fock equations are solved in an iterative manner until self consistency is achieved. In each iteration the PMM (Baskoutas 2005a, b; Baskoutas et al. 2006a, b; Baskoutas and Terzis 2006; Poulopoulos et al. 2011) is employed as a subroutine for the calculation of the corresponding energies and wavefunctions and thus the Hartree–Fock potential for the next iteration. Actually, PMM solves the time-independent Schrödinger equation for an arbitrary interaction potential $v_S(\vec{r})$ starting from a potential $v_R(\vec{r})$ with well-known eigenvalues and eigenfunctions. The essential point is that the transition from potential $v_R(\vec{r})$ to the potential $v_S(\vec{r})$ by means of the time-dependent Schrödinger equations as follows: using the potential $v_R(\vec{r})$ and $v_S(\vec{r})$, we formulate a time-dependent Schrödinger equation (Rieth et al. 2002)

$$i\hbar\frac{\partial\Phi(\vec{r},t)}{\partial t} = \left\{-\frac{\hbar^2}{2m}\nabla^2 + (1-\sigma(t))v_R(\vec{r}) + \sigma(t)v_s(\vec{r})\right\}\Phi(\vec{r},t), \tag{5}$$

where σ(t) has the following property:

$$\sigma(t) = \begin{cases} 0, & t \leq t_a \\ 1, & t \geq t_b \end{cases}. \tag{6}$$

For $t_a \leq t \leq t_b$ ($t_a$is the morphing starting moment, $t_b$is the morphing ending moment). The function $\sigma(t)$ should increase monotonically. Moreover, we solve equation (5) numerically. After a large number of time steps (so that $t > t_b$), the energy eigenvalue E_S for the potential $v_S(\vec{r})$ is given by

$$E_S = \int d^3r\Phi_S^*(\vec{r})\left\{-\frac{\hbar^2}{2m}\nabla^2 + v_S(\vec{r})\right\}\Phi_S(\vec{r}), \tag{7}$$

where Φ_S is the wave function of the system under consideration. In the present calculations, the reference system for PMM is set to be the three-dimensional harmonic oscillator with the well-known eigenfunctions (Greiner 1989)

$$\Phi_{nlm}(r,\theta,\varphi) = r^l e^{-\frac{m\omega}{2\hbar}r^2}{}_1F_1\left(-n, l+3/2, \lambda r^2\right)Y_{lm}(\theta,\varphi) \tag{8}$$

where ${}_1F_1(-n, l+3/2, \lambda r^2)$ is the hypergeometric function (Greiner 1989). The interaction potential is

$$v_S(\vec{r}) = v_{HF}(\vec{r}) + v_C(\vec{r}), \tag{9}$$

where $v_{HF}(\vec{r})$ is the Hartree–Fock potential for the electron (or hole), while $v_C(\vec{r})$ is the electron (or hole) confinement potential which is given explicitly in Eq. (4). It should be noted here that adopting the harmonic oscillator as a reference system does not affect our results because the PMM needs only a known reference system to start the morphing process and finally to give the eigenfunctions and eigenvalues for the unknown system, independently from the choice of the initial reference system (Rieth et al. 2002).

When the procedure reaches a self consistent solution, then the exciton energy is calculated by the sum of the corresponding electron and hole energies

$$E(X) = \tilde{E}_e + \tilde{E}_h \tag{10}$$

and the effective band gap is given by (Baskoutas 2005a, b; Baskoutas et al. 2006a, b; Baskoutas and Terzis 2006; Poulopoulos et al. 2011)

$$E_B = E_g + E(X) \tag{11}$$

where E_g is the bulk band gap energy.

Results and discussion

The quantitative analysis of the as-prepared product was carried out using the EDAX technique. Figure 1 shows typical EDAX spectrum and details of relative analysis for SnS nanocrystals. The spectrum illustrates

the actual distribution of Sn and S of the prepared sample separately. It is evident from the analysis that the product contains Sn and S materials with a same average atomic percentage ratio (1:1). Note that non-labeled peaks in EDAX spectrum comes from the Au–Pd sputter coating and glass stage.

The morphology of the as-prepared products was studied by SEM. The SEM image (Fig. 2) show that the product consists of very small spherical SnS nanocrystallites aggregated in the form of polydispersive nanoclusters with sizes smaller than 100 nm. It is very hard to discuss about nanoparticles size using SEM images, but from images it is clear that the sizes are in the order of very small nanoparticles.

In order to further elucidate the morphology and the size of nanoparticles, TEM image was taken and is shown in Fig. 3. Comparison of TEM and SEM images confirms the formation of very small spherical SnS nanoparticles, most of which aggregated together in the form of polydispersive nanoclusters.

The particle size distribution was also measured from the bright-field TEM image shown in Fig. 4. The detection and measurement of the nanoparticles (segmentation) on this type of samples is difficult because thickness changes locally, and diffraction from different crystal orientations introduce large contrast variations. First, the image was preprocessed by adjusting the contrast and brightness to minimize the speckle contrast of the background due to the carbon film used to support the sample. Second, the SnS

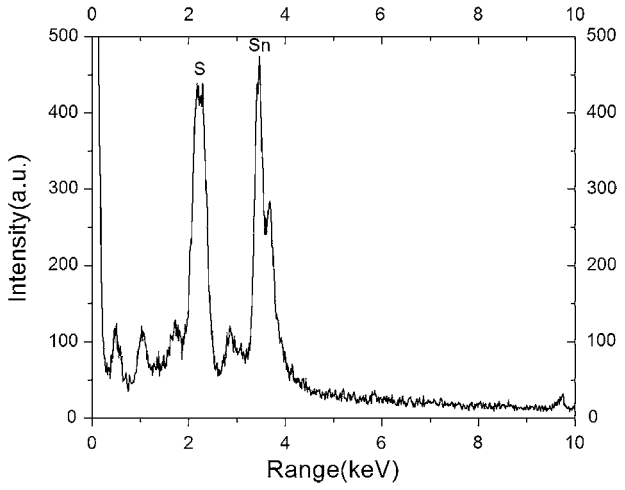

Fig. 1 EDAX spectrum of the as-prepared SnS nanocrystals

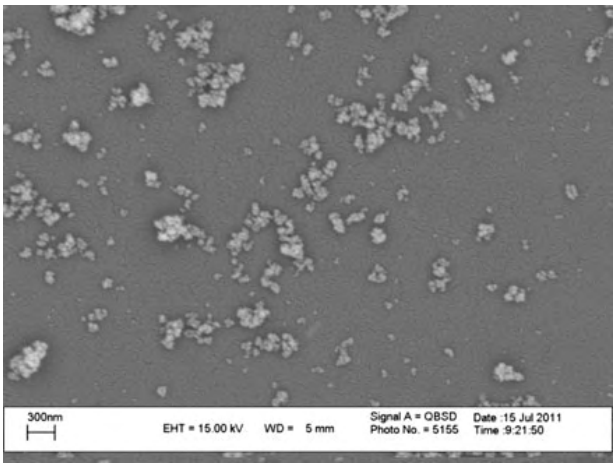

Fig. 2 SEM image of the as-prepared SnS nanocrystals

nanoparticles were segmented using a semiautomatic procedure which combines interactive segmentation with adaptative thresholding, obtaining an mean particle diameter of 3.2 nm with a standard deviation of 1.9 nm (Gontard et al. 2011).

Figure 5 show the XRD pattern of the as-prepared SnS nanocrystals. Several peaks corresponding to diffraction of orthorhombic SnS appear clearly in the

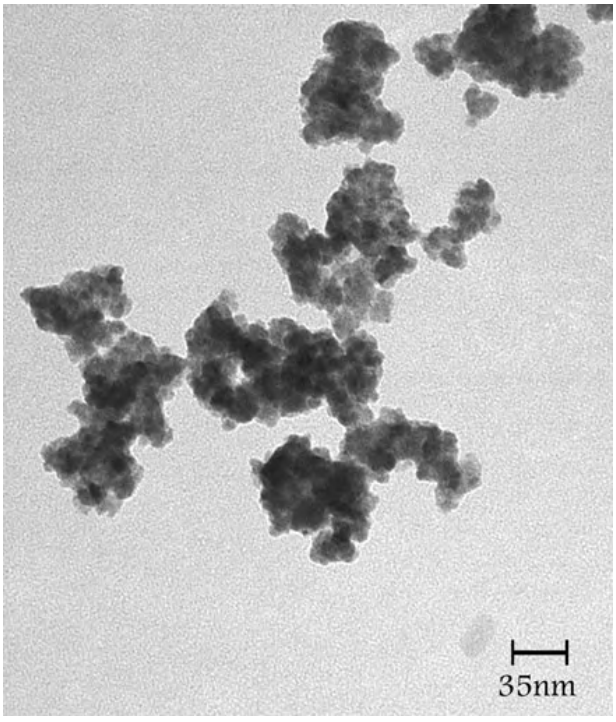

Fig. 3 Typical TEM image of SnS nanocrystals

figure. This clearly proves polycrystalline nature of the as-prepared product in which the appeared peaks are very consistent with the values in the standard card of SnS phase (JCPDS No. 39-0354).The broadness of the peaks indicates that the size of structure is reasonably nanocrystalline in nature. The crystallite size of SnS nanoparticles was calculated using Debye–Scherrer formula (Guinier 1963) $D = \frac{0.9\lambda}{\beta \cos(\theta)}$. Here, D is the coherent length, λ the wave length of X-ray radiation, β the full-width at half-maxima (FWHM) of the prominent peak, and θ is the angle of diffraction. So the corresponding crystallite size of nanoparticles

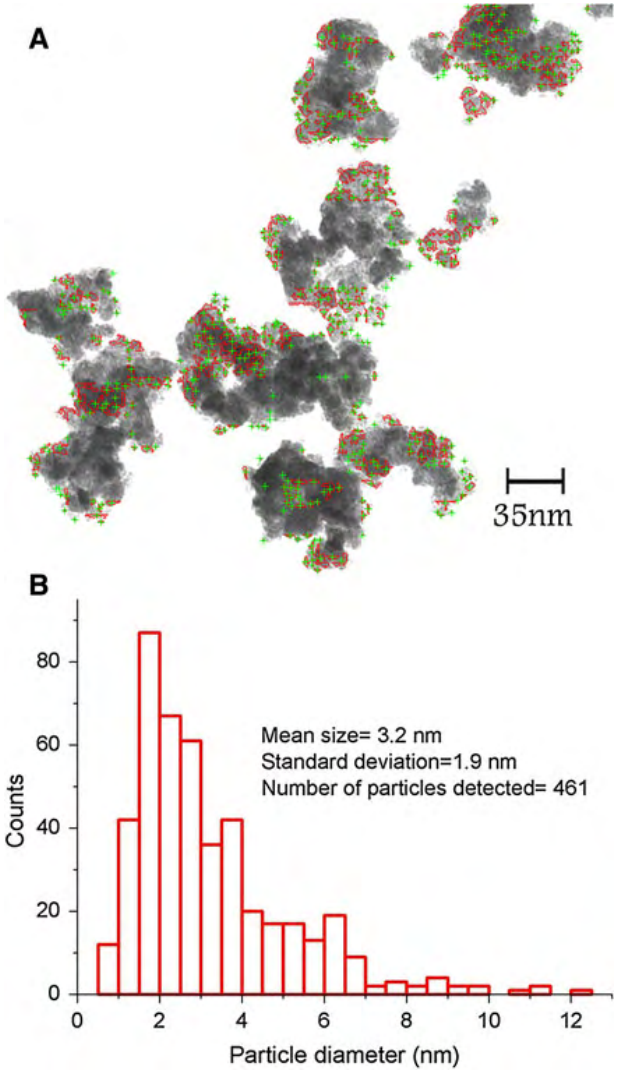

Fig. 4 **a** Image on which an over layer of the boundaries and center of masses of the segmented particles has been added to the original bright-field TEM image shown in Fig. 3. Adaptative thresholding with 80 × 80 divisions and a kernel size of 5 pixels was used. **b** Histogram of the size distribution of the nanoparticles and several statistical parameters

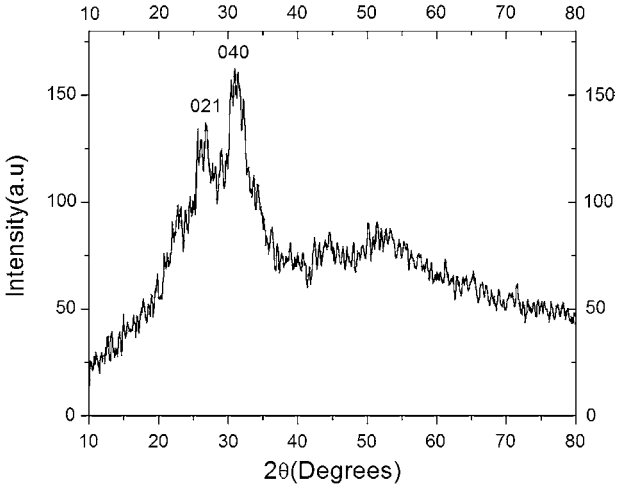

Fig. 5 XRD pattern of the as-prepared SnS nanocrystals

obtained are smaller than 4 nm in the case of broadened peaks.

Figure 6 shows the plot of $(\alpha hv)^2$ versus photon energy (hv) of the SnS nanocrystals and also absorption spectrum of the as-prepared SnS nanocrystals. Investigations prove that the absorption reduces rapidly with the increase of wavelength. These values were used to determine absorption coefficientα. The absorption coefficient α of SnS nanocrystals was calculated from the average absorption index A as $\alpha = \frac{4\pi A}{\lambda}$ (Suslick 1988). The optical energy gap of the SnS nanocrystal was evaluated using the relation $\alpha = \frac{A\left(hv - E_g\right)^n}{hv}$ where A is an energy independent constant and n characterizes the transition process (El-Nahass et al. 2002).

The curve has a good straight line fit with higher energy range above the absorption edge, indicating a direct optical transition edge. Based on Fig. 6, the direct energy gap of the sample has been calculated as 1.74 eV which is blue shifted in comparison to the bulk band gap.

Now in order to investigate the above system theoretically with PMM we assume that the matrix is PVA with $E_g(M) = 4.98$ eV (Mahendia et al. 2011) and we use the following material parameters for SnS: $m_e^* = 0.5\ m_0$ (Vidal et al. 2012), $m_h^* = 0.109\ m_0$ (Reddy and Reddy 2006), where m_0 is the electron mass, $\varepsilon_0 = 32$ (Chandrasekhar et al. 1977) and $\varepsilon_\infty = 16$ (Chandrasekhar et al. 1977) and $\hbar\omega_{LO} = 71$ meV (Chandrasekhar et al. 1977) and$E_g(\text{bulk}) = 1.296$ eV

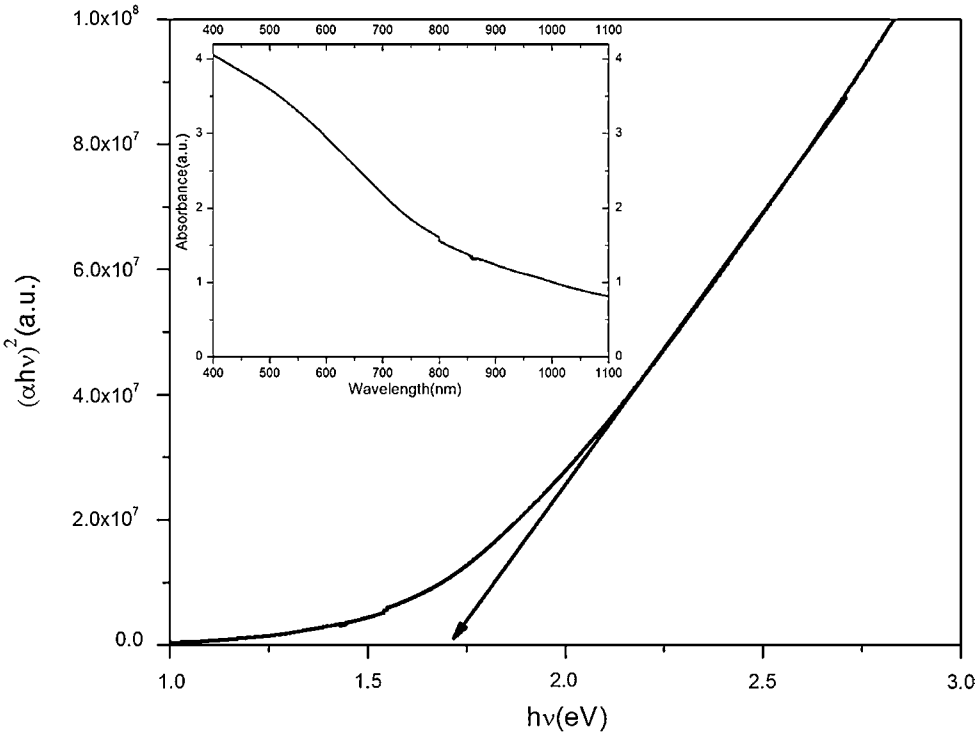

Fig. 6 Plot of $(\alpha h\nu)^2$ versus and Uv–Visible absorption spectrum of the as-prepared SnS nanocrystals

(Parenteau and Carlone, 1990). The effective band gap is calculated according to the relation (11) and the theoretical results are depicted in Fig. 7. The size of the nanocrystals which can be estimated from the curve of Fig. 7 is 4 nm (corresponding to the energy value 1.74 eV) and is in a fairly good agreement with the size which is obtained from the Debye–Scherrer formula and TEM image analysis.

Conclusion

In conclusion, for the first time, using a novel, very simple and not expensive procedure, SnS nanocrystals have been synthesized via ultrasonic waves at normal laboratory conditions. The as-synthesized SnS nanocrystals were quantitatively analyzed and characterized in terms of their morphological, structural, and optical properties. The SnS nanocrystals appear strongly blue shifted with direct band gap energy value of 1.74 eV. Comparison with the theoretical curve of the exciton energy versus the particle size, which is obtained with the PMM method in the Hartree–Fock approximation, shows a fairly good agreement indicating that the observed blue shift is attributed clearly to the effect of the quantum confinement.

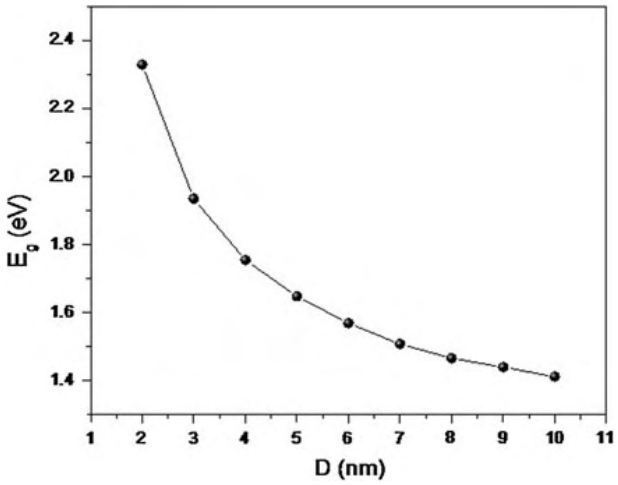

Fig. 7 Theoretical curve of the optical band gap as a function of the nanocrystal radius (with PMM in the Hartree–Fock approximation)

Acknowledgments The support by the University of Mohaghegh Ardabili, Ardabil, Iran, to carry out this study is gratefully acknowledged. The authors (S. Baskoutas, Z. Zeng and Ch. S. Garoufalis) acknowledge the European Union (European Regional Development Fund-ERDF) and Greek national funds through the Operational Program "Regional Operational Programme" of the National Strategic Reference

Framework (NSRF)-Research Funding Program: Support for research, technology and innovation actions in Region of Western Greece (MIS: 312123, D.237.002) for financial supports.

References

Alivisatos AP (1996) Perspectives on the physical chemistry of semiconductor nanocrystals. J Phys Chem 100:13226–13239

Azizian-Kalandaragh Y, Khodayari A (2010a) Ultrasound-assisted preparation of CdSe nanocrystals in the presence of Polyvinyl alcohol as a capping agent. Mater Sci Semicond Process 13:225–230

Azizian-Kalandaragh Y, Khodayari A (2010b) Aqueous synthesis and characterization of nearly monodispersed ZnS nanocrystals. Phys Status Solidi A 207(9):2144–2148

Azizian-Kalandaragh Y, Khodayari A, Behboudnia M (2009) Ultrasound-assisted synthesis of ZnO semiconductor nanostructures. Mater Sci Semicond Process 12:142–145

Bashkirov SA, Gremenok VF, Ivanov VA (2011) Physical properties of SnS thin films fabricated by hot wall deposition. Fizika i Tekhnika Poluprovodnikov 45:765–769

Baskoutas S (2005a) Excitons and charged excitons in InAs nanorods. Chem Phys Lett 404:107–111

Baskoutas S (2005b) Novel formulation of the Hartree–Fock approximation: effective band gap calculation of InAs nanorods. Phys Lett A 341:303–307

Baskoutas S, Terzis AF (2006) Size-dependent band gap of colloidal quantum dots. J Appl Phys 99:013708

Baskoutas S, Poulopoulos P, Karoutsos V, Angelakeris M, Flevaris NK (2006a) Strong quantum confinement effects in thin zinc selenide films. Chem Phys Lett 417:461–464

Baskoutas S, Terzis AF, Schommers W (2006b) Size-Dependent exciton energy of narrow band gap colloidal quantum dots in the finite depth square-well effective mass approximation. J Comp Theor Nanosci 3:269–271

Bhattacharyya S, Gedanken A (2008) A template-free, sonochemical route to porous ZnO nano-disks. Microporous Mesoporous Mater 110:553–559

Biswas S, Kar S, Chaudhuri S (2007) Thioglycolic acid (TGA) assisted hydrothermal synthesis of SnS nanorods and nanosheets. Appl Surf Sci 253:9259–9266

Chandrasekhar HR, Humphreys RG, Zwick U, Cardona M (1977) Infrared and Raman spectra of the IV-VI compounds SnS and SnSe. Phys Rev B 15:2177–2183

Chazali A, Zainal Z, Hussein MZ, Kassim A (1998) Cathodic electrodeposition of SnS in the presence of EDTA in aqueous media. Sol Energy Mater Sol Cells 55:237–249

Chen D, Shen G, Tang K, Lei S, Zheng H, Qian Y (2004) Microwave-assisted polyol synthesis of nanoscale SnS_x ($x = 1, 2$) flakes. J Cryst Growth 260:469–474

El-Nahass MM, Zeyada HM, Aziz MS, El-Ghamaz NA (2002) Optical properties of thermally evaporated SnS thin films. Opt Mater 20:159–170

Engelken RD, McCloud HE, Lee C, Slayton M, Ghoreishi H (1987) Low temperature chemical precipitation and vapor deposition of Sn_x S thin films. J Electrochem Soc 134:2696–2707

Ghosh B, Das M, Banerjee P, Das S (2008) Fabrication and optical properties of SnS thin films by SILAR method. Appl Surf Sci 254:6436–6440

Goharshadi EK, Ding Y, Jorabchi MN, Nancarrow P (2009) Ultrasound-assisted green synthesis of nanocrystalline ZnO in the ionic liquid [hmim][NTf_2]. Ultraso Sonochem 16:120–123

Gontard LC, Ozkaya D, Dunin-Borkowski R (2011) A simple algorithm for measuring particle size distributions on an uneven background from TEM images. Ultramicroscopy 111:101–106

Gou XL, Chen J, Shen PW (2005) Synthesis, characterization and application of SnS_x ($x = 1, 2$) nanoparticles. Mater Chem Phys 93:557–566

Greiner W (1989) Quantum mechanics: an introduction. Springer, Berlin

Guinier A (1963) X-Ray diffraction. In: Crystals, imperfect crystals, and amorphous bodies, Freeman, Sanfrancisco

Hanken H (1956) Nuovo Cim 3:1230

Henglein A (1989) Small-particle research: physicochemical properties of extremely small colloidal metal and semiconductor particles. Chem Rev 89:1861–1873

Johson JB, Jones H, Latham BS, Parker JD, Engelken RD, Barber C (1999) Optimization of photoconductivity in vacuum-evaporated tin sulfide thin films. Semicond Sci Technol 14:501–507

Li Q, Ding Y, Wu H, Liu X, Qian Y (2002) Fabrication of layered nanocrystallites SnS and β-SnS2 via a mild solution route. Mater Res Bull 37:925–932

Liu Y, Xu Y, Li JP, Zhang B, Wu D, Sun YH (2006) Synthesis of CdS_xSe_{1-x} nanorods via a solvothermal route. Mater Res Bull 41:99–109

Liu H, Liu Y, Wang Z, He P (2010) Facile synthesis of monodisperse, size-tunable SnS nanoparticles potentially for solar cell energy conversion. Nanotechnology 21:105707

Mahendia S, Tomar AK, Chahal RP, Goyal P, Kumar S (2011) Optical and structural properties of poly(vinyl alcohol) films embedded with citrate-stabilized gold nanoparticles. J. Phys. D 44:205105

Nanda KK, Kruis FE, Fissan H (2004) Effective mass approximation for two extreme semiconductors: band gap of PbS and CuBr nanoparticles. J Appl Phys 95:5035–5043

Ning J, Men K, Xiao G, Wang L, Dai Q, Zou B, Liu B, Zou G (2010) Facile synthesis of IV–VI SnS nanocrystals with shape and size control: nanoparticles, nanoflowers and amorphous nanosheets. Nanoscale 2:1699–1703

Nozaki H, Onoda M, Dekita M, Kosuda K, Wada T (2005) Variation of lattice dimensions in epitaxial SnS films on MgO(001). J Solid State Chem 178:245–252

Ögüt S, Chelikowsky JR, Louie SG (1997) Quantum confinement and optical gaps in Si nanocrystals. Phys Rev Lett 79:1770–1773

Ortiz A, Alonso JC, Garcia M, Toriz J (1996) Tin sulphide films deposited by plasma-enhanced chemical vapour deposition. Semicond Sci Technol 11:243–247

Panda SK, Gorai S, Chaudhuri S (2006) Shape selective solvothermal synthesis of SnS: role of ethylenediamine–water solvent system. Mater Sci Eng B 129:265–269

Parenteau M, Carlone C (1990) Influence of temperature and pressure on the electronic transitions in SnS and SnSe semiconductors. Phys Rev B 41:5227–5234

Paul GS, Agarwal P (2007). Structural and stability studies of SnS nanoflakes synthesized by solvothermal process for solar photovoltaic applications. IEEE Conference Proceedings, pp. 884–886

Paul GS, Gogoi P, Agarwal P (2008) Structural and stability studies of CdS and SnS nanostructures synthesized by various routes. J Non-Cryst Solids 354:2195–2199

Pellegrini G, Mattei G, Mazzoldi P (2005) Finite depth square well model: applicability and limitations. J Appl Phys 97:073706–073713

Poulopoulos P, Baskoutas S, Pappas SD, Garoufalis CS, Droulias SA, Zamani A, Kapaklis V (2011) Intense quantum confinement effects in Cu_2O thin films. J Phys Chem C 115:14839–14843

Price LS, Parkin IP, Field MN, Hardy AME, Clark RJH, Hibbert TG, Molloy KC (2000) Atmospheric pressure chemical vapour deposition of tin(II) sulfide films on glass substrates from $Bun_3SnO_2CCF_3$ with hydrogen sulfide. J Mater Chem 10:527–530

Qian XF, Zhang XM, Wang C, Wang WZ, Xie Y, Qian YT (1999) Solvent–thermal preparation of nanocrystalline tin chalcogenide. J Phys Chem Solids 60:415–417

Rama Krishna MV, Friesner RA (1991) Quantum confinement effects in semiconductor clusters. J Chem Phys 95:8309–8322

Reddy KTR, Reddy PP (2002) Structural studies on SnS films grown by a two-stage process. Mater Lett 56:108–111

Reddy NK, Reddy KTR (2006) Optical behaviour of sprayed tin sulphide thin films. Mat Res Bull 41:414–422

Reddy NK, Reddy KTR, Fisher G, Best R, Dutta PK (1999) The structural behaviour of layers of SnS grown by spray pyrolysis. J Phys D 32:988–990

Rieth M, Schommers W, Baskoutas S (2002) Exact numerical solution of Schrödinger's equation for a particle in an interaction potential of general shape. Int J Mod Phys B 16:4081

Rudel H (2003) Case study: bioavailability of tin and tin compounds. Ecotoxicol Environ Saf 56:180–189

Suslick KS (1988) Ultrasound: its chemical, physical, and biological effects. VCH, New York

Suslick KS (1990) Sonochemistry. Science 247:1439–1445

Suslick K, Doktycz S, Flint E (1990) On the origin of sonoluminescence and sonochemistry. Ultrasonics 28:280–290

Takeuchi K, Ichimura M, Arai E, Yamazaki Y (2003) SnS thin films fabricated by pulsed and normal electrochemical deposition. Sol Energy Mater Sol Cells 75:427–432

Tanusevski A (2003) Optical and photoelectric properties of SnS thin films prepared by chemical bath deposition. Semicond Sci Technol 18:501

Thangaraju B, Kaliannan P (2000) Spray pyrolytic deposition and characterization of SnS and SnS_2 thin films. J Phys D 33:1054–1059

Trindade T, O'Brien P, Pickett NL (2001) Nanocrystalline semiconductors: synthesis, properties, and perspectives. Chem Mater 13:3843–3858

Vidal J, Lany S, d'Avezac M, Zunger A, Zakutayev A, Francis J, Tate J (2012) Band-structure, optical properties, and defect physics of the photovoltaic semiconductor SnS. Appl Phys Lett 100:032104–032107

Wang Y, Herron N (1990) Quantum size effects on the exciton energy of CdS clusters. Phys Rev B 42:7253–7255

Wang H, Zhang JR, Zhao XN, Xu S, Zhu JJ (2002) Preparation of copper monosulfide and nickel monosulfide nanoparticles by sonochemical method. Mater Lett 55:253–258

Winship KA (1998) Toxicity of tin and its compounds. Adverse Drug React Acute Poisoning Rev 7:19–38

Yue GH, Peng DL, Yan PX, Wang LS, Wang W, Luo XH (2009) Structure and optical properties of SnS thin film prepared by pulse electrodeposition. J Alloy Compd 468:254–257

Zhao Y, Zhang Z, Dang H, Liu W (2004) Synthesis of tin sulfide nanoparticles by a modified solution dispersion method. Mater Sci Eng B 113:175–178

Zhu L, Meng J, Cao X (2008) Sonochemical synthesis of monodispersed $KY_3F_{10}:eu^{3+}$ nanospheres with bimodal size distribution. Mater Lett 62:3007–3009

Paper VI

In which we study the linear, nonlinear, and intensity-dependent total optical susceptibilities in singly charged ZnO colloidal quantum dots embedded in different dielectric matrices ...

JOURNAL OF APPLIED PHYSICS **113**, 054303 (2013)

Optical susceptibilities in singly charged ZnO colloidal quantum dots embedded in different dielectric matrices

Zaiping Zeng,[1] Emmanuel Paspalakis,[1] Christos S. Garoufalis,[1,2] Andreas F. Terzis,[3] and Sotirios Baskoutas[1,a)]

[1]*Materials Science Department, University of Patras, 26504 Patras, Greece*
[2]*Department of Environment Technology and Ecology, Technological Institute of Ionian Islands, 2 Kalvou Sq, 29100 Zakynthos, Greece*
[3]*Physics Department, University of Patras, 26504 Patras, Greece*

(Received 3 January 2013; accepted 8 January 2013; published online 1 February 2013)

Within the two-level system approximation, analytical expressions for the linear, third-order nonlinear and intensity-dependent susceptibilities in quantum dots (QDs) embedded in a dielectric matrix are developed by using density matrix equations, considering the local field effect due to the presence of dielectric mismatch. Based on the derived expressions, we perform a comparative study of the optical susceptibilities in singly charged zinc oxide QDs embedded in various dielectric matrices. Three commonly adopted matrices are considered. The electronic structure of the system is numerically calculated. In general, our results indicate that the optical susceptibilities are highly affected by the capped matrices. For example, QDs embedded in the matrix with the largest dielectric constant but the smallest energy band gap exhibit the largest linear and nonlinear optical susceptibilities, while that dispersed in a matrix with the largest energy band gap show the highest threshold energy. It is also found that the third-order nonlinear susceptibility exhibits a stronger dependence on the nature of the capped matrix as compared to its linear counterpart. Finally, we find that the total susceptibility in charged QD immersed in a matrix with a higher dielectric constant is more sensitive to the applied radiation intensity. © *2013 American Institute of Physics*. [http://dx.doi.org/10.1063/1.4789363]

I. INTRODUCTION

Zinc oxide (ZnO) is a material with a great variety of technological applications, such as surface acoustic wave devices, piezoelectric transducers, optical waveguides, transparent conductive oxides, chemical and gas sensors, spin functional devices, and ultraviolet (UV) light emitters (Ref. 1 and references therein). Its wide band gap (3.445 eV) makes ZnO a promising material for UV photonic applications, while the high exciton binding energy (around 60 meV) allows efficient excitonic emission, even at room temperature. In addition, ZnO is plentiful, cost-effective, and relatively non-toxic which is desirable for bio-applications such as bio-imaging and cancer detection. Due to the important modifications that appear at the nanoscale, ZnO nanostructures, especially zero dimensional nanoparticles or colloidal quantum dots (QDs) have attracted increasing attention.

As it is well known, chemical synthesis methods are the most common way to grow uniformly dispersed QDs. However, QDs prepared by such methods are relatively unstable and encounter the difficulties in dispersion and preservation. To stabilize the QDs when coupling with devices, matrix passivation is one of the most commonly adopted ways. Besides, immersing semiconductor QDs in polymer or glass matrix by using surface chemistry methods is also a good way of passivating the dangling bond at the QD surface.[2,3] Distinct photoluminescence properties have been demonstrated in such unique systems that can be served as fluorescent materials or active media in tunable lasers to achieve full color emission.[4,5] Due to these reasons, the optical properties of ZnO QDs embedded in organic polymers, such as poly(vinyl alcohol) (PVA), poly(methyl methacrylate) (PMMA) and poly (vinyl pyrrolidone) (PVP),[6–9] and inorganic materials, such as CaF_2, MgO, SiO_2 and BaF_2,[10–14] have been widely studied. However, most of these studies are focused on the experimental synthesis and characterization for possible device application purposes. Theoretical investigations on the electronic and optical properties in colloidal ZnO QDs embedded in different matrices are very recent. Using the atomistic empirical pseudopotential method, Baskoutas and Bester[15] have studied the electronic properties and optical emission polarizations of free-standing ZnO QDs. Dallali *et al.*[16] have investigated theoretically the energies of exciton and acceptor-bound exciton complex in ZnO QDs embedded in SiO_2 matrix. A theoretical work associated with the intersubband optical properties of ZnO QDs dispersed in SiO_2 matrix has also been reported recently.[17] Though plenty of new insights have been brought by these studies, the influence of the capped matrices on the electronic and optical properties in ZnO colloid QDs is still unknown.

In this contribution, we carried out a theoretical comparative study of the optical susceptibilities[18–20] of charged ZnO colloidal QDs embedded in various dielectric matrices. Three commonly used matrices, such as PVA, PMMA, and SiO_2, have been used in the present calculations. The theoretical approach we are using is the potential morphing method (PMM)[21] in the framework of the effective mass approximation, which has already been applied in the past

a)Electronic mail: bask@upatras.gr.

for the study of optical properties of several nanostructures.[22–25] The rest of the paper is organized as follows: in Sec. II, we define our model and explain the general theory. In Sec. III, we present numerical results and related discussions, and Sec. IV is devoted to conclusions.

II. DETAILS OF THE CALCULATIONS

A. Calculation of the electronic structure

The Schrödinger equation for an electron confined inside a singly charged ZnO colloidal QD of radius R is

$$\left(\hat{p}\frac{1}{2m_e^*}\hat{p} + V(\vec{r})\right)\psi(\vec{r}) = E\psi(\vec{r}), \tag{1}$$

where m_e^* is the effective mass, and $V(\vec{r})$ is the confinement potential which is zero inside and V_0 outside of the QD. V_0 is the conduction-band electron confinement potential at the interface of the QD and the surrounding matrix given by

$$V_0 = V_b + \Sigma, \tag{2}$$

where V_b is the finite barrier height and Σ is the self-energy due to the polarization induced by charging the QD. The self-energy is given by[26,27]

$$\Sigma = \frac{1}{8\pi\epsilon_0}\left(\frac{1}{\epsilon_{out}} - \frac{1}{\epsilon_{in}}\right)\frac{e^2}{R} + \delta\Sigma, \tag{3}$$

where ϵ_{in} and ϵ_{out} are the dielectric constants of the dot material and the surrounding matrix material, respectively. When $\epsilon_{in} + \epsilon_{out} \gg 1$, one gets[26]

$$\delta\Sigma \approx 0.466\frac{e^2}{4\pi\epsilon_0\epsilon_{in}R}\left(\frac{\epsilon_{in} - \epsilon_{out}}{\epsilon_{in} + \epsilon_{out}}\right), \tag{4}$$

which is usually small but not negligible.[26] This simple model has been successfully applied for the theoretical investigation of the photoabsorption and photoelectric process of charged silicon nanocrystallites embedded in amorphous SiO_2 matrix.[27] To obtain the ground state, the first excited state and the corresponding energies for the Hamiltonian (1), which are needed for the calculation of the linear and nonlinear optical properties below, PMM is employed. A detailed review of this methodology can be found in Ref. 21. The interaction potential involved in the potential morphing process is $v_S = V(\vec{r})$ and the reference system is selected as the usual harmonic oscillator in three dimensions with well-known eigenfunctions. It should be noted here that adopting the harmonic oscillator as a reference system does not affect our results because the PMM needs only a known reference system to start the morphing process and finally to give the eigenfunctions and eigenvalues for the unknown system, independently on the choice of the initial reference system.[21,28–30]

B. Calculation of the susceptibilities

After obtaining the necessary wave functions and eigenenergies, we start to calculate the linear, nonlinear, and total susceptibilities of a charged QD embedded inside a dielectric matrix. The QD interacts with an electromagnetic field with time-dependent electric field $E(t) = E_0\cos(\omega t)$, where E_0 is the time-independent electric field amplitude and ω is the angular frequency of the applied electric field. Within the two-level system approximation, the dynamics of the QD system under the interaction of an electromagnetic field is modeled by the Hamiltonian,

$$\hat{H} = \hbar\omega_0(|j\rangle\langle j|) - \mu E'(t)(|i\rangle\langle j| + |j\rangle\langle i|), \tag{5}$$

where $|i\rangle$ and $|j\rangle$ represent the initial and final states, respectively, μ is the transition matrix element between the initial and final states which is defined as $\mu = -\langle i|ez|j\rangle$, where we assume the polarization of electromagnetic radiation is along the z-axis direction. $E'(t) = \frac{E_0}{2\epsilon_{eff}}(e^{-i\omega t} + e^{i\omega t})$, where ϵ_{eff} is the effective dielectric constant which considers the local field effect due to the dielectric mismatch, and it is given by $\epsilon_{eff} = \frac{2\epsilon_{out}+\epsilon_{in}}{3\epsilon_{out}}$.

The density matrix equations, in the rotating wave approximation, for the slowly varying elements of the density matrix are[20,31]

$$\dot{\sigma}(t) = -\frac{1}{T_2}\sigma(t) + i\Omega\Delta(t) + i\delta\sigma(t), \tag{6}$$

$$\dot{\Delta}(t) = 2i\Omega\sigma(t) - 2i\Omega\sigma^*(t) - \frac{\Delta(t) - 1}{T_1}. \tag{7}$$

Here $\delta = \omega - \omega_0$ is the detuning of applied field from resonance, where $\omega_0 = (E_j - E_i)/\hbar$ with E_i and E_j being the energy eigenvalues of the initial (ground) state and final (first excited) state in the charged QD, respectively, $\Delta(t) = \sigma_{ii}(t) - \sigma_{jj}(t)$ with σ_{ij} being the density matrix element, T_1 and T_2 are the population relaxation time and the dephasing time, respectively, and $\Omega = \frac{\mu E_0}{2\hbar\epsilon_{eff}}$ is the Rabi frequency which differs from the usual definition by the local field term (ϵ_{eff}).

From Eqs. (6) and (7) in steady state, we take

$$\sigma = \frac{(i - \delta T_2)T_2\Omega}{1 + \delta^2T_2^2 + 4\Omega^2T_1T_2}. \tag{8}$$

Therefore, the susceptibility of the system is given by

$$\chi = \frac{2N\mu}{\epsilon_0\epsilon_{eff}E_0}\sigma = \frac{N\mu^2T_2}{\hbar\epsilon_0\epsilon_{eff}^2}\frac{i - \delta T_2}{1 + \delta^2T_2^2 + \frac{\mu^2E_0^2}{\hbar^2\epsilon_{eff}^2}T_1T_2}, \tag{9}$$

where N is the electron volume density in the QD system and ϵ_0 is the permeability in vacuum.

We define $E_0^s = \frac{\hbar\epsilon_{eff}}{\mu\sqrt{T_1T_2}}$ which is the saturation electric field strength. By this, we can rewrite Eq. (9) as

$$\chi = \frac{N\mu^2T_2}{\hbar\epsilon_0\epsilon_{eff}^2}\frac{i - \delta T_2}{1 + \delta^2T_2^2 + \frac{E_0^2}{(E_0^s)^2}}. \tag{10}$$

Assuming the electric field parameter $x = \frac{E_0^2}{(E_0^s)^2} \ll 1$, we can perform a power-series expansion of χ in terms of x,

retaining only terms up to the first order. The resultant solution for χ takes the form,

$$\chi \simeq \frac{N\mu^2 T_2}{\hbar\epsilon_0\epsilon_{eff}^2}\left[\frac{i-\delta T_2}{1+\delta^2 T_2^2} - \frac{i-\delta T_2}{(1+\delta^2 T_2^2)^2}\frac{E_0^2}{(E_0^s)^2}\right]. \tag{11}$$

Taking into account $\chi \simeq \chi^{(1)} + \frac{3}{4}\chi^{(3)}E_0^2$, we obtain the linear ($\chi^{(1)}$) and third-order nonlinear ($\chi^{(3)}$) optical susceptibilities as

$$\chi^{(1)} = \frac{N\mu^2 T_2}{\hbar\epsilon_0\epsilon_{eff}^2}\frac{i-\delta T_2}{1+\delta^2 T_2^2}, \tag{12}$$

$$\chi^{(3)} = -\frac{4N\mu^4 T_1 T_2^2}{3\hbar^3\epsilon_0\epsilon_{eff}^4}\frac{i-\delta T_2}{(1+\delta^2 T_2^2)^2}. \tag{13}$$

In the linear regime, the real part of susceptibility $\chi^{(1)}$ exhibits a standard dispersive lineshape, while its imaginary counterpart presents a Lorentzian lineshape.

We may also write the total susceptibility as

$$\chi = \chi' + i\chi'', \tag{14}$$

where χ' and χ'' are the real and imaginary part, given by

$$\chi' = \frac{N\mu^2 T_2}{\hbar\epsilon_0\epsilon_{eff}^2}\frac{1}{\sqrt{1+\kappa}}\frac{-\frac{\delta T_2}{\sqrt{1+\kappa}}}{1+\left(\frac{\delta T_2}{\sqrt{1+\kappa}}\right)^2}, \tag{15}$$

$$\chi'' = \frac{N\mu^2 T_2}{\hbar\epsilon_0\epsilon_{eff}^2}\frac{1}{\sqrt{1+\kappa}}\frac{1}{1+\left(\frac{\delta T_2}{\sqrt{1+\kappa}}\right)^2}, \tag{16}$$

respectively, with $\kappa = \frac{\mu^2 E_0^2 T_1 T_2}{\hbar^2\epsilon_{eff}^2}$. It turns out that the real (χ') and imaginary (χ'') parts of total susceptibility still display, respectively, dispersive and Lorentzian lineshapes, but they are saturated and broadened.

Finally, one may rewrite the Eq. (9) in terms of the incident optical intensity (I) as

$$\chi = \frac{N\mu^2 T_2}{\hbar\epsilon_0\epsilon_{eff}^2}\frac{i-\delta T_2}{1+\delta^2 T_2^2 + \frac{2\mu^2 I}{cn\epsilon_0\hbar^2\epsilon_{eff}^2}T_1 T_2}. \tag{17}$$

Here, the relation between the optical intensity and the applied electric field is taken $I = \frac{n\epsilon_0 c}{2}E_0^2$, where c is the light speed in vacuum, $n = \sqrt{\epsilon_{in}}$ is the refractive index of the QD material.

III. NUMERICAL RESULTS AND DISCUSSION

In the following, we will study the susceptibilities in the singly charged ZnO colloidal QDs, using the formulas presented in Sec. II. Three different matrices (i.e., PMMA, PVA, and SiO_2) are considered. The relevant material parameters for the present calculations are listed in Tables I and II, taking $N = 1.7\times10^{17}\,\mathrm{cm}^{-3}$, $T_1 = 1$ ps, and $T_2 = 0.14$ ps.[32] As have been reported by Baskoutas and Terzis,[24] the height of the finite-depth confinement potential does not depend on the specific semiconductor of the QD, but exclusively depends on the matrix energy band gap by a simple linear relation of the form

TABLE I. Theoretical values of the relative dielectric constant ϵ_r, the effective dielectric constant ϵ_{eff} and the local field factor $F\,(=\frac{1}{\epsilon_{eff}})$ for three different dielectric matrices (PMMA, PVA, and SiO_2). Relative dielectric constant for ZnO is 8.66.[17]

Materials	ϵ_r (Ref. 34)	ϵ_{eff}	F
PMMA	3.4	1.516	0.66
PVA	14	0.873	1.15
SiO_2	3.9	1.407	0.71

$V_{conf} = 0.08\cdot E_g(M)$, where $E_g(M)$ is the matrix energy band gap. Thus, in the present calculations, we adopted the same relation, using the electron confinement potential $V_b = 0.08\times E_g(M)$. As an approximation, the values of the electron effective mass are assumed to be the same in QD material (ZnO) and matrix materials[33] with value $m_e^* = 0.265\,m_0$, where m_0 is the electron mass in the free space.

First, we display the real and imaginary part of the linear susceptibility $\chi^{(1)}$ (Fig. 1) and third-order nonlinear susceptibility $\chi^{(3)}$ (Fig. 2) as a function of the incident photon energy for the three different matrices. As clearly shown in Tables I and II, different capped matrices have different dielectric constants and energy band gaps which differ substantially from the QD material. A higher dielectric constant of the capped matrix is related to a smaller self-polarization energy induced by the QD charging, which resultantly leads to a lower or even a negative (e.g., PVA) contribution to the QD confinement potential (see the fourth column of Table II). Conversely, it also causes a stronger local field effect in the corresponding charged QD, characterized by a larger local field factor $F = \frac{1}{\epsilon_{eff}}$ (see the last column of Table I). However, a lower energy band gap of the capped matrix corresponds to a smaller QD confinement potential (see the last two columns of Table II), consequently leading to a larger dipole transition matrix element. Due to the combination effects of local field and quantum confinement, QD embedded in polymeric matrix PVA which has the largest dielectric constant but the smallest energy band gap exhibits the largest (in absolute value) $\chi^{(1)}$ and $\chi^{(3)}$ (both real and imaginary part). Moreover, these two effects appear to compensate with each other and exhibit a competitive phenomenon in the other two phenomenological QDs. The local field effect turns out to dominate over its quantum confinement counterpart and consequently the susceptibilities in the charged QD capped with PMMA which has smaller energy band gap and dielectric constant exhibit a slightly smaller (absolute) value in comparison to that dispersed in inorganic matrix SiO_2.

Compared to the linear susceptibility (see Fig. 1), its third-order nonlinear counterpart appears to be more sensitive to the capped matrices, especially in the strong confinement regime (e.g., R = 2 nm). This becomes evident by the top plot in the left panel of Fig. 2, where $\chi^{(3)}$ in QDs dispersed in PMMA and SiO_2 is practically marginal, while that in PVA exhibits a relatively large strength. This is also valid for QDs within the weak confinement regime, although $\chi^{(3)}$ in PMMA and SiO_2 capped QDs is substantially enhanced. We relate this to a stronger dependence of $\chi^{(3)}$ on the

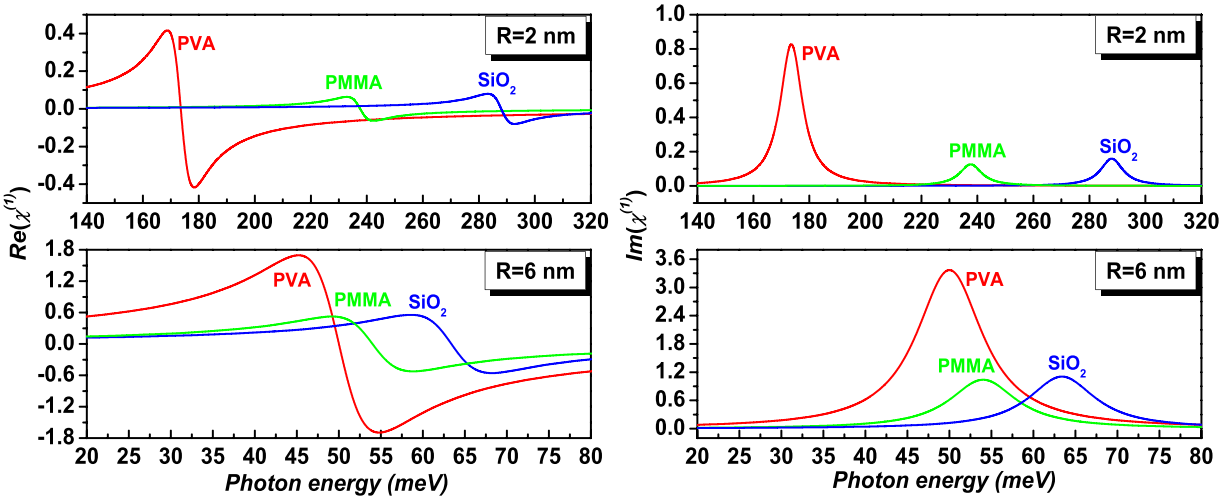

FIG. 1. The real (left panel) and imaginary (right panel) part of $\chi^{(1)}$ as a function of the photon energy $\hbar\omega$ in singly charged ZnO QDs embedded in three different matrices (PVA (red line), PMMA (green line), and SiO_2 (blue line)). Two dot sizes $R = 2$ nm and 6 nm are considered, separately.

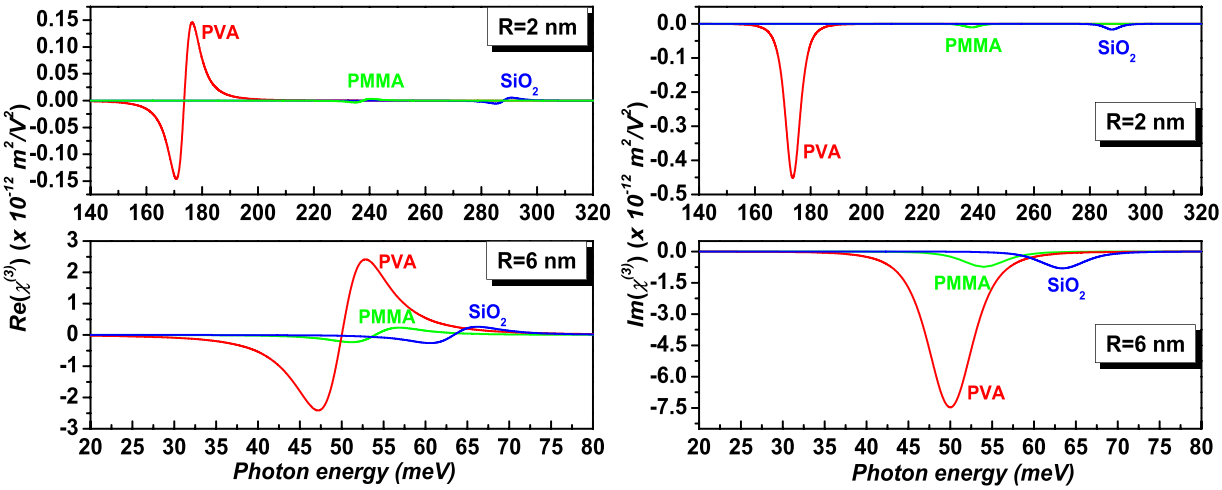

FIG. 2. The same as Fig. 1 but for $\chi^{(3)}$.

combined effects of local field and quantum confinement (e.g., $\chi^{(3)} \propto (\frac{\mu}{\epsilon_{eff}})^4$, while $\chi^{(1)} \propto (\frac{\mu}{\epsilon_{eff}})^2$).

In the same figures, we also find that the QD size influences significantly the susceptibilities in all the three charged QDs. Both the linear and nonlinear susceptibilities in all the capped QDs are substantially broadened and enhanced as the QD size increases. This can be attributed to the decrease of the quantum confinement effect, which leads to a significant increase of the transition matrix elements. This behavior is significantly more pronounced for the case of the nonlinear term. Furthermore, drastic red shifts are observed when the QD size is increased, irrespectively of the capped matrices. Another important feature is that the threshold energies in the three capped QDs are getting closer when the quantum confinement becomes weak. Based on this observation, it becomes clear that the influence of the capped matrices on the threshold energy is significant in small QDs (e.g., R = 2 nm). However, in large QDs (e.g., R = 6 nm), it becomes less important. In addition to this, we find that the QD capped with PVA exhibits a more drastic increase in both $\chi^{(1)}$ and $\chi^{(3)}$ in comparison to the other two charged QDs.

Finally, in an attempt to investigate the influence of the applied intensity on the total susceptibility (Eq. (17)), we present in Fig. 3 the real and imaginary parts of total optical susceptibility χ under two different radiation intensities. We find that the real and imaginary part of χ exhibit a standard dispersive and Lorentzian lineshape, respectively. This is independent of the capped matrices and applied intensities.

TABLE II. Theoretical values of the energy parameters used in our calculations. The energy band gap, E_g, of ZnO is 3.445 eV (Ref. 15) and $\Sigma_0 = \frac{1}{4\pi\epsilon_0}\frac{e^2}{R} = \frac{1.44}{R}$ eV.

Materials	E_g (eV)	$V_b = 0.08E_g$ (meV)	Σ/Σ_0	V_0 (meV), R = 2 nm	V_0 (meV), R = 6 nm
PMMA	5.6 (Ref. 35)	448	+0.113	530	475
PVA	4.98 (Ref. 36)	398	−0.035	373	390
SiO_2	9 (Ref. 37)	720	+0.091	786	742

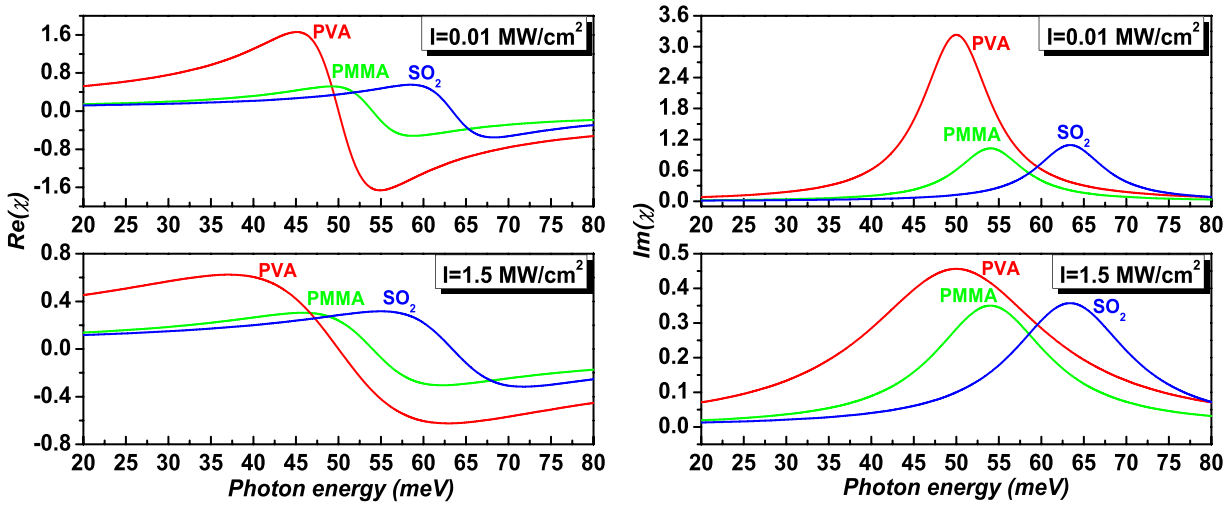

FIG. 3. The real (left panel) and imaginary (right panel) part of χ as a function of the photon energy $\hbar\omega$ in singly charged ZnO QDs with radius R = 6 nm under various radiation intensities (I = 0.01 and 1.5 MW/cm^2). Three capped matrices, e.g., PVA, PMMA, and SiO_2, are considered.

However, for the larger intensity, χ is substantially decreased in magnitude and strongly broadened in the near resonant region in all the three charged QDs. For all the applied intensities, the PVA capped QDs exhibit the largest χ values, while the PMMA capped QDs exhibit the smallest ones, which also appear to be similar to the intensity-free $\chi^{(1)}$ and $\chi^{(3)}$. Moreover, the decrease of χ with respect to intensity is found to be more pronounced for the case of PVA capping.

IV. CONCLUSIONS

In this work, we have studied the linear, third-order nonlinear, and intensity-dependent optical susceptibilities of singly charged ZnO QDs embedded in different dielectric matrices. Three commonly used matrices, PVA, PMMA, and SiO_2, are considered for the present calculations. The analytical expressions for these optical susceptibilities are derived by using density matrix equations within the two-level system approximation. We find that QD capped with PVA which has the largest dielectric constant always exhibits the largest linear and third-order nonlinear optical susceptibilities, while that dispersed in amorphous SiO_2 which has the largest band gap energy shows the highest threshold energy, irrespectively of the QD sizes. Increasing the QD sizes leads to the drastic increase in the magnitude of both the linear and nonlinear susceptibilities. Comparing to the linear susceptibility, the third-order nonlinear counterpart appears to be more sensitive to the variation of the capped matrices. Finally, we investigate the influence of the applied radiation intensities on the total susceptibility in all the three different capped QDs. We show that the real and imaginary part of the total susceptibility always exhibit a standard dispersive and Lorentzian lineshape, irrespectively of the applied intensities. However, enhancing the applied intensity leads to a drastic decrease in the (absolute) magnitude of the total susceptibility and a substantially broadening in the near resonance region. Furthermore, the total susceptibility exhibits a stronger dependence on the applied radiation intensity in charged QD capped by a matrix with a relatively high dielectric constant but with a relatively small energy band gap.

We believe that our results can be useful and helpful not only in the elucidation of the fundamental physics but also for possible devices application based on ZnO QDs-matrix systems.

ACKNOWLEDGMENTS

This research has been co-financed by the European Union (European Social Fund—ESF) and Greek national funds through the Operational Program "Education and Lifelong Learning" of the National Strategic Reference Framework (NSRF)—Research Funding Program: Thales, investing in knowledge society through the European Social Fund.

[1]Ü. Özgür, Y. I. Alivov, C. Liu, A. Teke, M. A. Reshchikov, S. Doğan, V. Avrutin, S.-J. Cho, and H. Morkoç, J. Appl. Phys. **98**, 041301 (2005).
[2]D. E. Fogg, L. H. Radzilowski, R. Blanski, R. R. Schrock, and E. L. Thomas, Macromolecules **30**, 417 (1997); D. E. Fogg, L. H. Radzilowski, B. O. Dabbousi, R. R. Schrock, E. L. Thomas, and M. G. Bawendi, *ibid.* **30**, 8433 (1997).
[3]C. B. Murray, D. J. Norris, and M. G. Bawendi, J. Am. Chem. Soc. **115**, 8706 (1993).
[4]J. Lee, V. C. Sundar, J. R. Heine, M. G. Bawendi, and K. F. Jensen, Adv. Mater. **12**, 1102 (2000).
[5]S. T. Selvan, C. Bullen, M. Ashok Kumar, and P. Mulvaney, Adv. Mater. **13**, 985 (2001).
[6]N. Bouropoulos, I. Tsiaoussis, P. Poulopoulos, P. Roditis, and S. Baskoutas, Mater. Lett. **62**, 3533 (2008).
[7]D. I. Son, C. H. You, W. T. Kim, and T. W. Kim, Nanotechnology **20**, 365206 (2009); D. I. Son, C. H. You, J. H. Jung, and T. W. Kim, Appl. Phys. Lett. **97**, 013304 (2010).
[8]Y. Tu, L. Zhou, Y. Z. Jin, C. Gao, Z. Z. Ye, Y. F. Yang, and Q. L. Wang, J. Mater. Chem. **20**, 1594 (2010).
[9]M. Sudha, S. Senthilkumar, R. Hariharan, A. Suganthi, and M. Rajarajan, J. Sol-Gel Sci. Technol. **61**, 14 (2012).
[10]Y. C. Liu, H. Y. Xu, R. Mu, D. O. Henderson, Y. M. Lu, J. Y. Zhang, D. Z. Shen, X. W. Fan, and C. W. White, Appl. Phys. Lett. **83**, 1210 (2003).
[11]K.-K. Kim, N. Koguchi, Y.-W. Ok, T.-Y. Seong, and S.-J. Park, Appl. Phys. Lett. **84**, 3810 (2004).
[12]Y.-Q. Li, Y. Yang, C. Q. Sun, and S.-Y. Fu, J. Phys. Chem. C **112**, 17397 (2008).

[13]D. Bera, L. Qian, and P. H. Holloway, J. Phys. D: Appl. Phys. **41**, 182002 (2008).
[14]N. Hagura, T. Takeuchi, S. Takayama, F. Iskandar, and K. Okuyama, J. Lumin. **131**, 138 (2011).
[15]S. Baskoutas and G. Bester, J. Phys. Chem. C **114**, 9301 (2010).
[16]L. Dallali, S. Jaziri, J. el Haskouri, P. Amorós, and J. Martínez-Pastor, Solid State Commun. **151**, 822 (2011).
[17]D. Maikhuri, S. P. Purohit, and K. C. Mathur, AIP Adv. **2**, 012160 (2012).
[18]S. Sauvage, P. Boucaud, F. Glotin, R. Prazeres, J.-M. Ortega, A. Lemaitre, J.-M. Gerard, and V. Thierry-Mieg, Phys. Rev. B **59**, 9830 (1999).
[19]T. Brunhes, P. Boucaud, S. Sauvage, A. Lemaitre, J.-M. Gerard, F. Glotin, R. Prazeres, and J.-M. Ortega, Phys. Rev. B **61**, 5562 (2000).
[20]S. G. Kosionis, A. F. Terzis, C. Simserides, and E. Paspalakis, J. Appl. Phys. **108**, 034316 (2010).
[21]M. Rieth, W. Schommers, and S. Baskoutas, Int. J. Mod. Phys. B **16**, 4081 (2002).
[22]I. Karabulut and S. Baskoutas, J. Appl. Phys. **103**, 073512 (2008).
[23]S. Baskoutas and A. F. Terzis, J. Appl. Phys. **98**, 044309 (2005).
[24]S. Baskoutas and A. F. Terzis, J. Appl. Phys. **99**, 013708 (2006).
[25]S. Baskoutas, E. Paspalakis, and A. F. Terzis, Phys. Rev. B **74**, 153306 (2006).
[26]M. Lannoo, C. Delerue, and G. Allan, Phys. Rev. Lett. **74**, 3415 (1995).
[27]Anchala, S. P. Purohit, and K. C. Mathur, Appl. Phys. Lett. **98**, 043106 (2011).
[28]P. Poulopoulos, S. Baskoutas, S. D. Pappas, C. S. Garoufalis, S. A. Droulias, A. Zamani, and V. Kapaklis, J. Phys. Chem. C **115**, 14839 (2011).
[29]Z. Zeng, C. S. Garoufalis, S. Baskoutas, and A. F. Terzis, J. Appl. Phys. **112**, 064326 (2012).
[30]Z. Zeng, C. S. Garoufalis, and S. Baskoutas, J. Phys. D: Appl. Phys. **45**, 235102 (2012).
[31]R. W. Boyd, *Nonlinear Optics*, 3rd ed. (Academic, San Diego, 2008), Chap. 6.
[32]F. Yu, L. Zhang, and K. Guo, Superlattice Microstruct. **50**, 128 (2011).
[33]S.-S. Li and J.-B. Xia, J. Appl. Phys. **101**, 093716 (2007).
[34]A. Issac, "Photoluminescence intermittency of semiconductor quantum dots in dielectric environments," doctoral thesis (von der Fakultät für Naturwissenschaften der Technischen Universität, Germany, 2006), p. 66.
[35]J. A. Hagen, W. Li, A. J. Steckl, and J. G. Grote, Appl. Phys. Lett. **88**, 171109 (2006).
[36]S. Mahendia, A. K. Tomar, R. P. Chahal, P. Goyal, and S. Kumar, J. Phys. D: Appl. Phys. **44**, 205105 (2011).
[37]J. Robertson, Eur. Phys. J.-Appl. Phys. **28**, 265 (2004).

Paper VII

In which we study the electronic and optical properties of ZnO quantum dots subjected to externally applied hydrostatic pressure ...

Electronic and optical properties of ZnO quantum dots under hydrostatic pressure

Zaiping Zeng,[1] Christos S. Garoufalis,[1,2] Sotirios Baskoutas,[1,*] and Gabriel Bester[3,†]
[1]*Materials Science Department, University of Patras, 26504 Patras, Greece*
[2]*Department of Environment Technology and Ecology, Technological Institute of Ionian Islands, 2 Kalvou Square, 29100 Zakynthos, Greece*
[3]*Max-Planck-Institut für Festkörperforschung, D-70569 Stuttgart, Germany*
(Received 2 January 2013; published 6 March 2013)

In the present work, we studied the electronic and optical properties of ZnO quantum dots (QDs) subjected to externally applied hydrostatic pressure. Our single-particle calculations are based on the empirical pseudopotential method and the excitonic effects are considered by employing the configuration interaction approach. The optical band gap, Stokes shift, and optical emission polarization have been investigated as a function of the applied pressure. It is found that the applied pressure causes a linear increase in the optical band gap. The pressure coefficient appears to be highly size dependent, exhibiting a monotonic increase with increasing QD size. In contrast to this monotonic behavior, the applied pressure induces a nonmonotonic Stokes shift which presents a minimum value at a critical pressure. For pressures larger than this critical value, the optical emission polarization exhibits a sharp transition from in-plane to out-of-plane polarization. Finally, it is found that the critical pressure at which the crossing takes place strongly depends on the QD size, showing larger values for larger QD sizes. Beyond this crossing point, the lowest optically bright exciton state mainly originates from one Slater determinant, where both the single-particle electron and hole states have an *S*-type envelope function and the hole state originates mainly from the bulk Bloch C band.

DOI: 10.1103/PhysRevB.87.125302 PACS number(s): 78.67.Hc, 73.21.La, 73.22.Dj, 73.22.Lp

I. INTRODUCTION

Nanostructures and heterostructures made of zinc oxide (ZnO), such as nanowalls,[1] nanotubes,[2] nanorods,[3] and quantum dots (QDs),[4] have already been used as transparent conductors in solar cells and as components in high-power electronics, UV light emitters, and gas and chemical sensors (see Ref. 5 and references therein). Possible applications of ZnO nanostructures in optoelectronic and spintronic devices, such as laser diodes with polarized output, and spin-based memory and logic, have also attracted great attention.[6,7] As an important member of the nanostructure family, zero-dimensional ZnO QDs have become the subject of recent developments. Experimental fabrication of this type of nanostructure has been achieved by using different chemical synthesis methods, such as sol-gel,[8] thermolysis,[9] and polyol methods,[4] to mention only a few. From a theoretical point of view, due to the specifics of the wurtzite ZnO material, such as the anisotropy of the valence band, as well as the small dielectric constant and correspondingly strong electron-hole Coulomb interaction, simple one-band effective-mass models fail to deliver predictive results. To have a good interpretation of experimental measurements and optimization of ZnO QDs for possible device applications, an accurate theoretical method able to predict the transition energy and the oscillator strength of optical transitions is required. Accurate atomistic empirical pseudopotential calculations have been shown to describe exciton states in CdSe QDs (Ref. 10), and very recently in ZnO QDs,[11] very well.

On the other hand, high-pressure investigations of semiconductor nanostructures such as nanocrystals or QDs have emerged as a focus area in condensed-matter physics and material science because of their large impact on the tunable optical properties that may be advantageous for application in optoelectronics, QD lasers, high-density memory, bioengineering, etc.[12–15] Most of the existing theoretical work concerning the hydrostatic pressure effect focused on QDs with zinc-blende structure, such as self-assembled InAs/GaAs (Ref. 16) or InGaAs/GaAs (Ref. 17) QDs. Theoretical work associated with the pressure effect in wurtzite ZnO colloidal QDs is very limited.[18] Here, we study the electronic and optical properties of ZnO QDs under externally applied hydrostatic pressure. The single-particle orbitals and energies are calculated by the atomistic empirical pseudopotential method using recently derived pseudopotentials,[11] considering the effects of multiband coupling, multivalley coupling, and spin-orbit interaction, while the excitonic effects are taken into account by using the configuration interaction approach.[19] The present numerical results cover a variety of optical properties of ZnO QDs under pressure, such as the optical band gap, the pressure coefficient, the Stokes shift, and the optical emission polarization.

In the following section, we outline the computational details. Thereafter, in Sec. III numerical results and related discussions are presented. Sec. IV is devoted to conclusions.

II. COMPUTATIONAL DETAILS

The single-particle energies and eigenstates for both conduction and valence bands are obtained by the plane-wave empirical pseudopotential method,[20] using our recently derived ZnO pseudopotentials.[11] The adopted Hamiltonian for the single-particle states has the form

$$\widehat{\mathrm{H}} = -\frac{1}{2}\nabla^2 + \sum_{n\alpha}\left[v_\alpha(|\vec{r} - \vec{R}_{\alpha n}|;\epsilon) + \widehat{\mathrm{v}}_\alpha^{\mathrm{SO}}\right], \qquad (1)$$

where n is an atomic index, α specifies the atom type, and $\widehat{\mathrm{v}}_\alpha^{\mathrm{SO}}$ is the nonlocal spin-orbit operator. The screened atomic pseudopotentials v_α (with $\alpha = \mathrm{Zn}$, O) are centered at each atomic position and their superposition generates the crystal potential. These pseudopotentials v_α incorporate

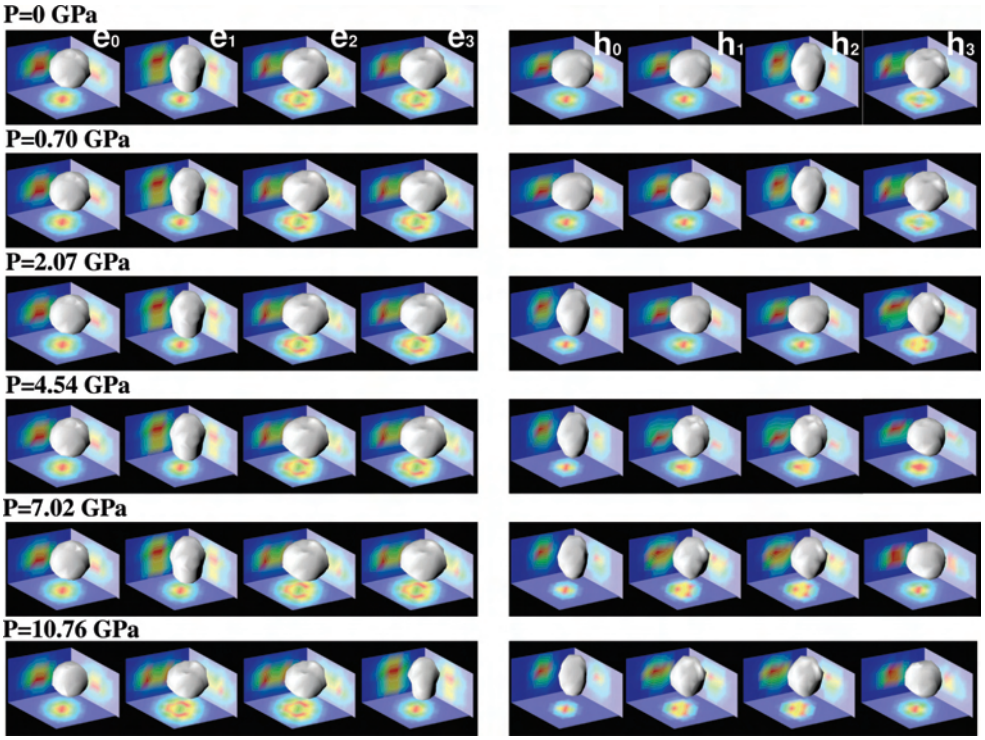

FIG. 1. (Color online) Envelope functions for the first four electron ($e_{0,1,2,3}$) and first four hole ($h_{0,1,2,3}$) states in a ZnO QD with diameter D = 1.7 nm for various hydrostatic pressures. The isosurface values are chosen in such a way to enclose 75% of the state densities.

the dependence on the local hydrostatic strain Tr(ϵ) via the relationship[21]

$$v_\alpha(r;\epsilon) = v_\alpha^{\mathrm{eq}}(r;0)[1 + \gamma_\alpha \mathrm{Tr}(\epsilon)], \qquad (2)$$

where γ_α is a fitting parameter. The form and the parameters of the zero strain potential, which are optimized to reproduce the known band structure and the bulk properties of ZnO, are given in Ref. 11. In our calculations, the fitting parameter γ_α has the value 0.304, giving a pressure coefficient for bulk ZnO equal to 24.7 meV/GPa, which is in very good agreement with the experimental value of 24.7 $\pm$ 0.1 meV/GPa.[22] This also gives the conduction and valence band deformation potentials[17]

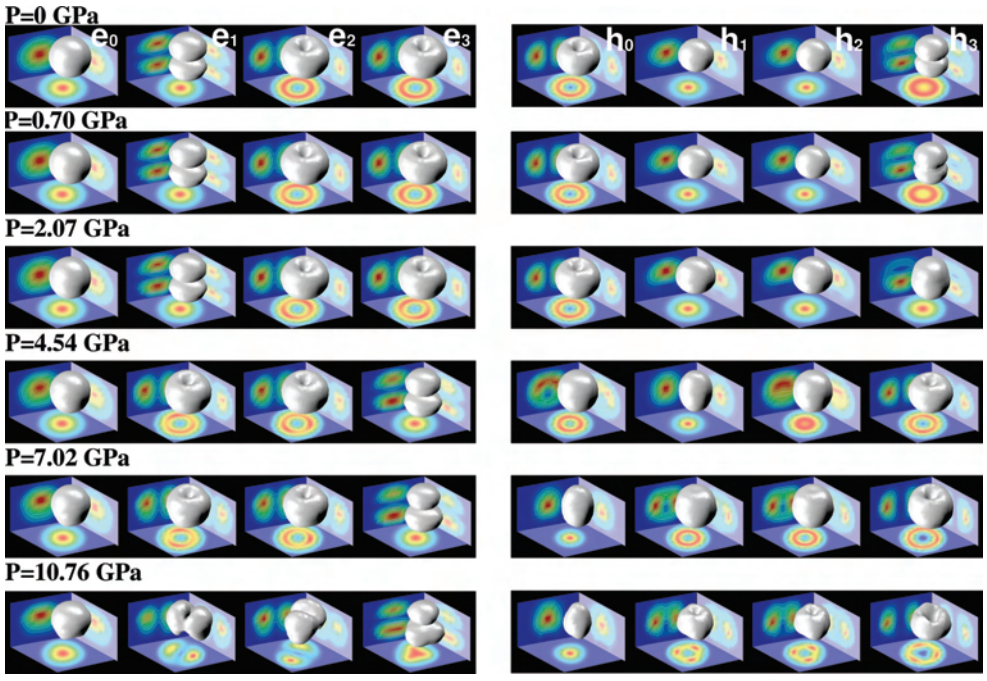

FIG. 2. (Color online) Same as Fig. 1 but for D = 5.2 nm.

$a_c = -4.65$ eV and $a_v = -2.54$ eV, respectively, resulting in a (relative) band-gap deformation potential $a_g = -2.11$ eV, which agrees fairly well with the results predicted by the local-density approximation (LDA) and the LDA $+U$ (Ref. 23): $a_g = -1.7$ eV (LDA) and $a_g = -2.9$ eV (LDA $+U$). The experimental value of the effective deformation potential for bulk ZnO is ~ -3.51 to -3.81 eV, and -3.5 ± 0.4 eV obtained by different experimental methods.[24,25] The pressure values used in our calculations are determined approximately by using the Murnaghan equation of state[17,26]

$$P = (B/B')[(V_0/V)^{B'} - 1], \tag{3}$$

taking for the wurtzite ZnO bulk modulus $B = 142.4$ GPa and for the pressure derivative $B' = dB/dP = 3.6$.[22]

The surface passivation is approximated by a high-band-gap artificial material, as practiced successfully previously.[11,27,28] The structure was relaxed with Keating's valence force field (VFF) model for wurtzite materials.[29] It should be noted that the VFF relaxed structures exhibit a qualitatively correct variation of c/a and u internal parameters with respect to pressure (i.e., c/a decreases while u increases when the pressure increases[30,31]). The corresponding envelope functions of the single-particle states in both valence and conduction bands are obtained by projecting the fast-oscillating atomic wave functions onto the Bloch states of each unit cell [according to Eq. (6) of Ref. 11]. This effectively smears out the atomic oscillations and leads to an envelope function that can be displayed with clarity.[11,27] This procedure also allows us to obtain the Bloch function character of each QD state and analyze them in terms of their Bloch function parentage: A, B, or C band (or a mixture of them). The excitonic wave functions are expanded in terms of single-substitution Slater determinants constructed from the single-particle wave functions of electrons and holes. The corresponding many-body Hamiltonian is solved using iterative diagonalization techniques. Our computational limitations allow us to include in the configuration interaction (CI) treatment ten states from the valence band and ten states from the conduction band. For the screening function needed in the Coulomb integrals we used the phenomenological microscopic, isotropic, and uniform model proposed by Resta.[32] The optical dipole matrix elements are calculated within the dipole approximation, and the oscillator strength was calculated using Fermi's golden rule. A review of this method can be found in Ref. 33.

III. RESULTS AND DISCUSSION

A. Pressure-dependent electronic properties

To determine the electronic and optical properties in ZnO QDs in both the strong and the intermediate confinement regime under externally applied hydrostatic pressure, we considered five different ZnO colloidal QDs with diameters $D = 1.7$, 2.1, 3.1, 3.6, and 5.2 nm, respectively. ZnO QDs with such sizes can be experimentally synthesized by using the well-established colloidal fabrication techniques, leading to a nearly spherical shape.[4,8] The numbers of atoms for the respective structures are $Zn_{99}O_{111}$, $Zn_{204}O_{210}$, $Zn_{654}O_{654}$, $Zn_{1014}O_{1011}$, and $Zn_{3063}O_{3102}$.

TABLE I. Character of the first four envelope functions for electrons and holes in a ZnO QD with diameter $D = 1.7$ nm under various hydrostatic pressures (in unit of GPa). The superscript (A, B, C) indicates the corresponding hole-state parentage (A, B, or C band) obtained from Fig. 3 and the asterisk means that the wave function is a mixed state with orbital P character.

Pressure	e_0	e_1	e_2	e_3	h_0	h_1	h_2	h_3
0	S	P_z	P_{xy}	P_{xy}	S^{A}	S^{B}	S^{C}	P_{xy}^{AB}
0.70	S	P_z	P_{xy}	P_{xy}	S^{A}	S^{B}	S^{C}	P_{xy}^{AB}
2.07	S	P_z	P_{xy}	P_{xy}	$S^{\mathrm{C}*}$	$S^{\mathrm{A}*}$	$S^{\mathrm{B}*}$	$S^{\mathrm{C}*}$
4.54	S	P_z	P_{xy}	P_{xy}	$S^{\mathrm{C}*}$	$S^{\mathrm{AC}*}$	$S^{\mathrm{BC}*}$	$S^{\mathrm{ABC}*}$
7.02	S	P_z	P_{xy}	P_{xy}	S^{C}	P_{xy}^{C}	P_{xy}^{C}	S^{A}
10.76	S	P_{xy}	P_{xy}	P_z	S^{C}	P_{xy}^{C}	P_{xy}^{C}	S^{A}

As a first step toward elucidating the electronic structure in ZnO QDs, we project the fast-oscillating atomic wave functions onto the bulk ZnO Bloch states (as stated in Sec. II). This gives us access to the envelope functions, which are more convenient to visualize than the fast-oscillating real wave functions. However, it should be kept in mind that the energetics for each state is not governed by the envelope function alone, but determined by the full atomic wave function. As the representatives of the electronics of ZnO QDs under hydrostatic pressure in both the strong and intermediate confinement regimes, we present the projected envelope functions of the first four electron states and the first four hole states of our smallest and largest structures in Figs. 1 and 2, respectively. The figures show results for six different hydrostatic pressures. To characterize the symmetry of the wave functions, which is very useful to understand the relevant optical properties discussed in the next section, we use the notation ω_ζ, where ω represents the number of nodes encountered by moving across a specific direction (xy or z-axis direction), while the subscript ζ indicates the direction in which we find the node(s). The possible value for ω are S, P, D, etc., where S represents the form of the wave function without node (in this case, we neglect the subscript ζ), P with one node, etc. This way, we tabulated the characters of the electron and hole envelope functions shown in Figs. 1 and 2 in Tables I and II, respectively.

In Fig. 3 we plot the Bloch function character of the first four hole states using the projection formalism described in Sec. II. After a combined analysis of the relative contribution from the bulk valence bands with the characters of the hole envelope functions listed in Tables I and II, we find that, in the absence of external pressure, the highest occupied molecular orbital

TABLE II. Same as Table I but for $D = 5.2$ nm.

Pressure	e_0	e_1	e_2	e_3	h_0	h_1	h_2	h_3
0	S	P_z	P_{xy}	P_{xy}	P_{xy}^{AB}	S^{A}	S^{B}	P_z^{A}
0.70	S	P_z	P_{xy}	P_{xy}	P_{xy}^{AB}	S^{A}	S^{B}	P_z^{A}
2.07	S	P_z	P_{xy}	P_{xy}	P_{xy}^{AB}	S^{A}	S^{B}	P_z^{A}
4.54	S	P_{xy}	P_{xy}	P_z	P_{xy}^{ABC}	S^{C}	S^{C}	P_{xy}^{AB}
7.02	S	P_{xy}	P_{xy}	P_z	S^{C}	P_{xy}^{C}	P_{xy}^{C}	P_{xy}^{C}
10.76	S	P_y	P_x	P_z	S^{C}	P_{xy}^{C}	P_{xy}^{C}	P_{xy}^{C}

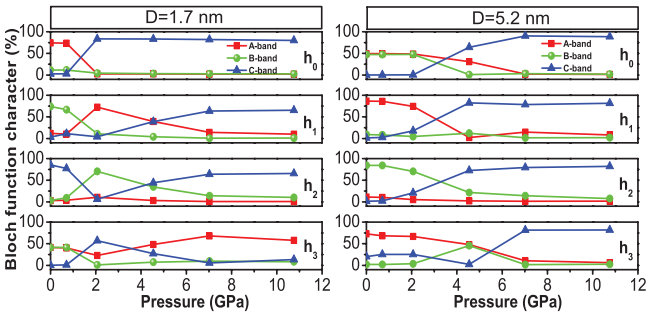

FIG. 3. (Color online) Analysis of the Bloch function character of the first four hole states $h_{0,1,2,3}$ in a ZnO QD under various hydrostatic pressures. The left-hand panel corresponds to the QD with diameter $D = 1.7$ nm, while the right-hand panel corresponds to the QD with diameter $D = 5.2$ nm. The colors red, green, and blue correspond to A, B, and C bands, respectively.

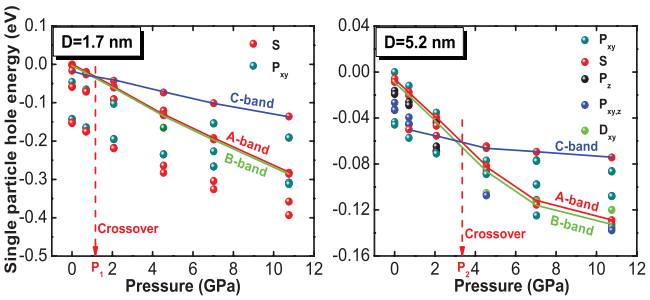

FIG. 4. (Color online) Energy of the first ten hole states relative to the HOMO state at zero pressure, in ZnO QDs under various hydrostatic pressures (in units of GPa). The lines connect states which are of the same symmetry ω_ζ. The red, green, and blue lines connect states with dominant A-, B-, and C-band character, respectively. Two QD sizes, $D = 1.7$ and 5.2 nm, where D is the diameter of the QD, are considered.

(HOMO, h_0) of our smallest structure (with diameter $D = 1.7$ nm) has orbital S character, while it shows a P character in our largest structure (with diameter $D = 5.2$ nm). This is in agreement with one of the important conclusions of Ref. 11 which demonstrates that the HOMO of ZnO QDs is of orbital P character for structures larger than 2.6 nm in diameter. Under pressure, the orbital character of the HOMO state of our smallest structure appears to be pressure independent, always exhibiting a conventional S-type character. Conversely, the orbital character of the HOMO state of our largest structure experiences a drastic change in the envelope function character, switching to a more conventional S orbital character for pressures larger than 2.07 GPa. This is due to the pressure effect which modifies the Bloch function parentage from an even mixture of A and B bands ($P \leqslant 2.07$ GPa) to a nearly pure single C band ($P > 2.07$ GPa), as seen in Fig. 3 (see the top plot of the right-hand panel). In addition to the HOMO state, the applied pressure significantly modifies the Bloch function characters for the other hole states ($h_{1,2,3}$): they are nearly pure single-band objects for relatively high pressures (e.g., $P > 4.54$ GPa), originating mainly from the bulk Bloch C band (∼75%) and exhibiting P_{xy}-type characters. The only exception is h_3 of our smallest structure, which has a dominant bulk Bloch A-band parentage and shows an S-type character for pressures larger than 4.54 GPa. The fact that the P^{C}_{xy} states at the pressures of 7.02 and 10.76 GPa ($h_{1,2}$ states in Table I) are energetically separated from the P^{C}_{z} state can be related to the anisotropic effective masses of the topmost three ZnO valence bands. The C-band effective mass is anisotropic and larger perpendicular to the c axis ($m^*_{\mathrm{C}\perp} = 0.55m_0$ and $m^*_{\mathrm{C}\parallel} = 0.31m_0$, where m_0 is the free electron mass). This favors the orbital P states with in-plane nodes, P_{xy}, over the ones with nodes along the c axis, P_z. No such anisotropy exists for the A and B bands, and the orbital P_{xy} states are not favored over the P_z states. The electron states follow the typical pattern of a single-band object originating from an isotropic band. The lowest four electron states have orbital S and P character, where P_z is slightly favored over P_{xy} at low pressures and vice versa at high pressures.

As mentioned before, the applied hydrostatic pressure strongly modifies the relative contribution of the bulk valence band states to the QD hole states, which causes the changes in the symmetry of the hole envelope functions. In Fig. 4, we see that states with dominant A- and B-band parentage have a stronger dependence on pressure than the states with dominant C-band parentage. This is associated with the larger deformation potential of A and B bands in comparison to that of the C band. Figure 4 also shows that the C-band states rise above the A- and B-band states at a critical pressure and finally become the energetically favorable states. This critical pressure appears to be highly size dependent. For our smallest structure, it is $P_1 \approx 1.2$ GPa, while for our largest structure, it is $P_2 \approx 3.3$ GPa.

B. Pressure-dependent optical properties

We first present the optical band gap of ZnO QDs as a function of the applied hydrostatic pressure. The calculations are performed for five different QD sizes which are in the strong or intermediate confinement regime. Two levels of theory, at the single-particle (SP) level and at the CI level, are employed. Figures 5(a) and 5(b) show a strong size dependence of the optical band gap and a weaker, nearly linear, pressure dependence. The pressure coefficients (dE/dP) are given in Fig. 5(c) for uncorrelated and correlated calculations. Both the single-particle and the excitonic pressure coefficients are strongly size dependent. Increasing the QD size causes a monotonic increase in the pressure coefficient. A similar behavior has also been calculated theoretically for CdSe QDs.[34] Furthermore, it is shown from Fig. 5(c) that the QD excitonic pressure coefficients obtained in the full CI scheme are substantially smaller than the bulk value (see the dot-dashed line), with deviations at small diameters of up to 41%. The single-particle results exceed the bulk limit for QD diameters larger than $D = 4.5$ nm. This prominently highlights the importance of the higher level of theory accounting for excitonic effects. We also studied in Fig. 5(d) the Stokes shift, defined as the energetic difference between the lowest dark exciton state and the first bright exciton state. The Stokes shift displays a nonmonotonic dependence of the applied hydrostatic pressure, exhibiting a minimum value at a critical pressure P_c. This critical pressure is highly size sensitive. It appears to be $P_c = 0.7$ GPa for the first two smallest structures, $P_c = 2.07$ GPa for the QD diameter

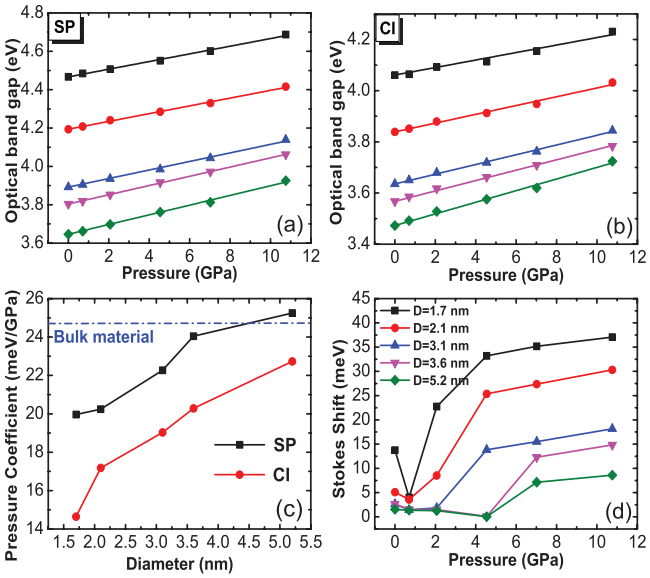

FIG. 5. (Color online) Optical band gap of ZnO QDs at (a) the single-particle (SP) level and (b) the CI level as a function of the hydrostatic pressure (symbols). (c) Pressure coefficients at the single-particle level [obtained from (a) and at the CI level [obtained from (b)] versus QD diameter. (d) Stokes shift as a function of the applied hydrostatic pressures. Here, five different QD sizes ($D = 1.7$, 2.1, 3.1, 3.6, and 5.2 nm, where D is the QD diameter) are considered. All the symbols and colors in (a) and (b) are the same as in (d).

$D = 3.1$ nm, and $P_c = 4.54$ GPa for the other two largest structures.

To clarify the physical reasons for this nonmonotonic behavior, we take our largest structure as an example and recall the electronic properties of the single electron and hole states presented in the previous section. For pressures smaller than or equal to the critical value ($P = 4.54$ GPa), both the first bright and dark exciton states have a dominant contribution from the $(0,1)$ configuration, where both the electron and the hole have S-type orbital character. In the CI scheme, the lowest exciton state is spin forbidden. However, when the applied pressure is larger than the critical value ($P > 4.54$ GPa), the single-particle states which are responsible for the two exciton states show an abrupt change from the configuration $(0,1)$ to the configuration $(0,0)$. This level crossing is responsible for the nonmonotonic behavior in the Stokes shift. This nonmonotonic behavior in the Stokes shift makes evident that the electron-hole spin-exchange interaction is much stronger in the $(0,0)$ configuration (C exciton) and it is enhanced with increasing pressure. Similar behavior has also been experimentally measured and theoretically calculated in CdSe nanorods by systematically varying the height-to-diameter aspect ratio.[35] For larger pressures, Fig. 5(d) shows that the Stokes shift is significantly larger than the corresponding value at zero pressure. A larger Stokes shift means a smaller overlap area between absorption and emission spectra, which is desirable in applications such as light-emitting diodes, where reabsorption reduces the total efficiency.[35]

Finally, we calculate in Fig. 6 the photoluminescence emission spectrum in the full CI scheme for our smallest and largest structures. We find that the applied pressure induces a strong blueshift in the emission spectrum. This blueshift is more pronounced in the larger QD in accordance with Fig. 5(c). In an attempt to indicate explicitly the emission polarization direction, we also present the spectra at each pressure with a vertical line. It is shown that, in both the strong and intermediate confinement regimes, the optical emission polarization exhibits a crossing from in-plane ($\mathbf{E}\perp\vec{c}$) to out-of-plane ($\mathbf{E}\parallel\vec{c}$) polarization at a critical pressure value. It is $P_c = 0.70$ GPa for our smallest structure and $P_c = 4.54$ GPa for our largest structure. In other words, the emission changes from a normal α emission ($\mathbf{E}\perp\vec{c}$) to the unusual[36,37] so-called σ and π emissions ($\mathbf{E}\parallel\vec{c}$) for pressures larger than the critical pressure. After reaching the crossing, the lowest optically bright exciton state in both confinement regimes has a dominant contribution from the $(0,0)$ configuration, where the single-particle hole state has S-type character and is derived

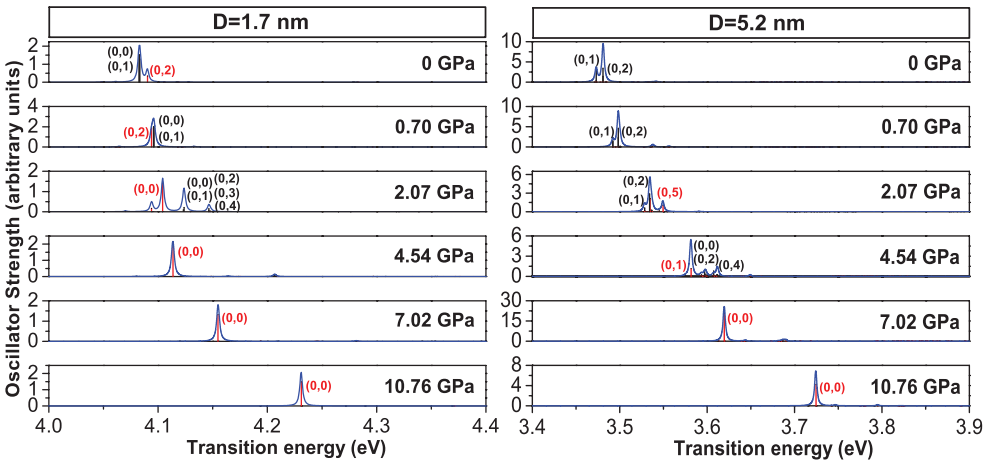

FIG. 6. (Color online) Oscillator strength for the emission $|X\rangle$ to $|0\rangle$ at room temperature in ZnO QDs, which are obtained by full CI. Transitions polarized along the out-of-plane direction (c axis) are shown by red vertical lines, while the ones polarized along the in-plane direction are shown as black vertical lines. The numbers in parentheses refer to the dominant single-particle levels involved in the transitions (e,h). The blue curve represents the total emission spectra. The left-hand panel corresponds to the QD with diameter $D = 1.7$ nm, while the right-hand panel corresponds to the QD with diameter $D = 5.2$ nm.

from the dominant bulk Bloch C-band contribution. Recently, it has been shown that the polarization of the C exciton along the c axis ($\mathbf{E}\|\vec{c}$) holds not only for bulk ZnO (Ref. 38) but also for ZnO nanowires.[39] The possibility to effectively manipulate the optical emission polarization of QDs via pressure should be advantageous in the design of future experiments.

IV. CONCLUSIONS

In summary, we studied the electronic and optical properties of ZnO colloidal QDs as a function of applied hydrostatic pressure. We find that for QD larger than 2.6 nm in diameter, the increased pressure induces a drastic change in the highest occupied molecular orbital from an unconventional P-type character to a normal S-type character. Hole states tend to become single-band objects originating from the Bloch C band with increasing pressure. We relate this effect to the fact that the hole states with dominant A- and B-band parentage experience a stronger pressure dependence, in comparison to the corresponding C-band states. In other words, the Bloch band hydrostatic deformation potentials are negative and larger in magnitude for the A or B bands than for the C band. As a consequence, the C-band states emerge as the HOMO states at high pressure. We show that the crossover between A- or B-band and C-band HOMO states is size dependent and occurs at higher pressures for larger QDs. We further find that the P states derived from the Bloch C band are energetically split into states with nodes in plane and nodes along the c direction. This is attributed to the anisotropy of the bulk Bloch C band, which has a heavier in-plane effective mass favoring P states with in-plane nodes. At both the single-particle level and the correlated excitonic level, the optical band gap experiences a linear increase with increasing pressure, with a highly size-dependent pressure coefficient. The pressure coefficient is significantly lowered, by as much as 41%, by correlations. Only the correlated results (configuration interaction) can be brought into agreement with experiment. In contrast to the monotonic increase of the optical band gap, the applied hydrostatic pressure causes a nonmonotonic Stokes shift with a minimum at a specific pressure. For pressures larger than this critical value, the optical emission polarization changes from in-plane to out-of-plane polarization. We explained this behavior through the drastic change of the single-particle hole state parentage from a dominant bulk Bloch A or B band (before crossing) to a nearly pure C band (after crossing). Finally, we find that the critical pressure at which the crossing takes place strongly depends on the QD size, showing larger pressure values for larger QD sizes. After this crossing, the optically bright exciton state has a pure contribution from the (0,0) configuration, where both the electron and hole states have S-type orbital character and the single-particle hole state has a dominant contribution from the bulk Bloch C band.

ACKNOWLEDGMENTS

This research has been cofinanced by the European Union [European Social Fund (ESF)] and by Greek national funds through the Operational Program "Education and Lifelong Learning" of the National Strategic Reference Framework (NSRF)—Research Funding Program: Thales, investing in knowledge society through the ESF.

*Corresponding author: bask@upatras.gr
†Corresponding author: G.Bester@fkf.mpg.de

[1] M. Q. Israr, J. R. Sadaf, O. Nur, M. Willander, S. Salman, and B. Danielsson, Appl. Phys. Lett. **98**, 253705 (2011).
[2] H. Guo, Z. Lin, Z. Feng, L. Lin, and J. Zhou, J. Phys. Chem. C **113**, 12546 (2009).
[3] S. H. Ko, D. Lee, H. W. Kang, K. H. Nam, J. Y. Yeo, S. J. Hong, C. P. Grigoropoulos, and H. J. Sung, Nano Lett. **11**, 666 (2011).
[4] N. Bouropoulos, I. Tsiaoussis, P. Poulopoulos, P. Roditis, and S. Baskoutas, Mater. Lett. **62**, 3533 (2008); Q. Qiao, B. Li, C. Shan, J. Liu, J. Yu, X. Xie, Z. Zhang, T. Ji, Y. Jia, and D. Shen, *ibid.* **74**, 104 (2012).
[5] A. Djurisic and Y. H. Leung, Small **2**, 944 (2006).
[6] U. Özgür, Y. I. Alivov, C. Liu, A. Teke, M. A. Reshchikov, S. Doğan, V. Avrutin, S.-J. Cho, and H. Morkoç, J. Appl. Phys. **98**, 041301 (2005).
[7] V. A. Fonoberov and A. A. Balandin, J. Nanoelectron. Optoelectron. **1**, 19 (2006).
[8] K.-F. Lin, H.-M. Cheng, H.-C. Hsu, L.-J. Lin, and W.-F. Hsieh, Chem. Phys. Lett. **409**, 208 (2005).
[9] M. Salavati-Niasari, F. Davar, and Z. Fereshteh, Chem. Eng. J. **146**, 498 (2009).
[10] M. Califano, A. Zunger, and A. Franceschetti, Nano Lett. **4**, 525 (2004).
[11] S. Baskoutas and G. Bester, J. Phys. Chem. C **114**, 9301 (2010).
[12] H. Fu and A. Zunger, Phys. Rev. Lett. **80**, 5397 (1998).
[13] S. J. Chen, Y. C. Liu, C. L. Shao, C. S. Xu, Y. X. Liu, C. Y. Liu, B. P. Zhang, L. Wang, B. B. Liu, and G. T. Zou, Appl. Phys. Lett. **88**, 133127 (2006).
[14] X. Michalet, F. F. Pinaud, L. A. Bentolila, J. M. Tsay, S. Doose, J. J. Li, G. Sundaresan, A. M. Wu, S. S. Gambhir, and S. Weiss, Science **307**, 538 (2005).
[15] G. Ouyang, C. Q. Sun, and W. G. Zhu, J. Phys. Chem. C **113**, 9516 (2009).
[16] J.-W. Luo, S.-S. Li, J.-B. Xia, and L.-W. Wang, Phys. Rev. B **71**, 245315 (2005).
[17] G. A. Narvaez, G. Bester, and A. Zunger, Phys. Rev. B **72**, 041307 (2005).
[18] J. W. Li, L. W. Yang, Z. F. Zhou, P. K. Chu, X. H. Wang, J. Zhou, L. T. Li, and C. Q. Sun, J. Phys. Chem. C **114**, 13370 (2010).
[19] A. Franceschetti, H. Fu, L. W. Wang, and A. Zunger, Phys. Rev. B **60**, 1819 (1999).
[20] L.-W. Wang and A. Zunger, J. Chem. Phys. **100**, 2394 (1994).
[21] A. J. Williamson, L. W. Wang, and A. Zunger, Phys. Rev. B **62**, 12963 (2000).
[22] H. Morkoç and U. Özgür, *Zinc Oxide* (Wiley-VCH, Weinheim, 2009).
[23] A. Janotti and C. G. Van de Walle, Phys. Rev. B **75**, 121201 (2007).

[24]A. Mang, K. Reimann, and S. Rübenacke, Solid State Commun. **94**, 251 (1995).
[25]A. Segura, J. A. Sans, F. J. Manjón, A. Muñoz, and M. J. Herrera-Cabrera, Appl. Phys. Lett. **83**, 278 (2003).
[26]B. Welber, M. Cardona, C. K. Kim, and S. Rodriguez, Phys. Rev. B **12**, 5729 (1975).
[27]S. Baskoutas and G. Bester, J. Phys. Chem. C **115**, 15862 (2011).
[28]M. Califano, G. Bester, and A. Zunger, Nano Lett. **3**, 1197 (2003).
[29]D. Camacho and Y. M. Niquet, Physica E **42**, 1361 (2010).
[30]L. Wang, H. Liu, J. Qian, W. Yang, and Y. Zhao, J. Phys. Chem. C **116**, 2074 (2012).
[31]Z. Dong, K. K. Zhuravlev, S. A. Morin, L. Li, S. Jin, and Y. Song, J. Phys. Chem. C **116**, 2102 (2012).
[32]R. Resta, Phys. Rev. B **16**, 2717 (1977).
[33]G. Bester, J. Phys: Condens. Matter **21**, 023202 (2009).
[34]C. D. Grant, J. C. Crowhurst, S. Hamel, A. J. Williamson, and N. Zaitseva, Small **4**, 788 (2008).
[35]J. Hu, L.-s. Li, W. Yang, L. Manna, L.-w. Wang, and A. P. Alivisatos, Science **292**, 2060 (2001).
[36]N. S. Han, H. S. Shim, S. Lee, S. M. Park, M. Y. Choi, and J. K. Song, Phys. Chem. Chem. Phys. **14**, 10556 (2012).
[37]Z. Fan, P. chun Chang, J. G. Lu, E. C. Walter, R. M. Penner, C. hung Lin, and H. P. Lee, Appl. Phys. Lett. **85**, 6128 (2004).
[38]J. Rowe, M. Cardona, and F. Pollak, Solid State Commun. **6**, 239 (1968).
[39]G. Jacopin, L. Rigutti, A. Bugallo, F. Julien, C. Baratto, E. Comini, M. Ferroni, and M. Tchernycheva, Nanoscale Res. Lett. **6**, 501 (2011).

Paper VIII

In which we study the linear, nonlinear, and total absorption coefficients and refractive index changes associated with intersubband transitions in ZnO/ZnS core shell quantum dots and ZnS/ZnO inverted core shell quantum dots ...

JOURNAL OF APPLIED PHYSICS **114**, 023510 (2013)

Linear and nonlinear optical properties of ZnO/ZnS and ZnS/ZnO core shell quantum dots: Effects of shell thickness, impurity, and dielectric environment

Zaiping Zeng,[1] Christos S. Garoufalis,[1,2] Andreas F. Terzis,[3] and Sotirios Baskoutas[1,a)]
[1]*Department of Materials Science, University of Patras, 26504 Patras, Greece*
[2]*Department of Environment Technology and Ecology, Technological Institute of Ionian Islands, 2 Kalvou Sq, 29100 Zakynthos, Greece*
[3]*Department of Physics, University of Patras, 26504 Patras, Greece*

(Received 30 March 2013; accepted 18 June 2013; published online 11 July 2013)

In the present work, we investigated theoretically the linear, nonlinear, and total absorption coefficients and refractive index changes associated with intersubband transitions in ZnO/ZnS core shell quantum dot (CSQD) and ZnS/ZnO *inverted* CSQD (ICSQD), emphasizing on the influence of the shell thickness, impurity, and dielectric environment. The effect of the polarization charges due to the possible existence of the dielectric mismatch between the system and its surrounding matrix is considered. The electronic structures are numerically calculated by employing the potential morphing method in the framework of effective mass approximation. We find that in both impurity-free CSQD and ICSQD, increasing the shell thickness red shifts significantly the threshold energy and enhances drastically the nonlinear absorption coefficients and all the refractive index changes, independently on the dielectric environments. Similar behaviour has also been observed in most of the cases studied when the impurity is displaced from the core center to the shell center. In contrast, comparing to a dielectrically homogeneous system, dispersing the systems into a matrix with a lower dielectric constant blue shifts all the peak positions of the absorption coefficients and refractive index changes. However, the corresponding magnitudes (in absolute value) are substantially reduced. Finally, we find that the nonlinear properties are more sensitive to the external perturbations, while at a weak radiation intensity, the variation of the total quantities is generally dominated by that of the corresponding linear terms. © *2013 AIP Publishing LLC*. [http://dx.doi.org/10.1063/1.4813094]

I. INTRODUCTION

Zinc oxide (ZnO) and Zinc sulfide (ZnS) quantum dots (QDs) have received considerable attentions due to their wide applications in optoelectronics and spintronic devices, such as light-emitting, laser diodes, and electroluminescent devices (see Refs. 1 and 2, and references therein). These QDs can be fabricated successfully by using the well-established chemical synthesis methods, e.g., sol-gel,[3,4] wet chemical approach,[5,6] to mention only a few. However, the synthesized colloidal QDs (generally uncapped) are relatively unstable and encounter the difficulties in dispersion and preservation. Possible existing of the surface states significantly reduces the electron-hole recombination rate, lowering the luminescent quantum yield. Size-dependent photophysical properties can also be obscured.[7] One possible way of overcoming such problems is to further cap the bare QD (core) with an another material (shell), forming a core-shell configuration.

Wurtzite (WZ) ZnO has a relatively smaller band gap (3.445 eV (Ref. 8)) in comparison to that of WZ ZnS (3.864 eV (Ref. 9)). Therefore, capping bare ZnO QDs with a thin layer of ZnS forms the "conventional" ZnO/ZnS core-shell quantum dot (CSQD) structure where the core material has a narrower band gap (ZnO) than the shell material (ZnS). Conversely, ZnS/ZnO "inverted" core-shell quantum dot[10,11] (ICSQD) will be fabricated if the wider gap ZnS is overcoated with a shell of narrower gap ZnO. ZnO/ZnS CSQDs with dimension in the range of few nanometers to about 30 nm have been successfully synthesized by epitaxial growth in solution.[12] Comparing to the bare ZnO QDs, the fabricated CSQDs exhibit enhanced ultraviolet (UV) emission and present type I band alignment. Employing a simple one-step solvent-thermal method, Wang *et al.*[13] have synthesized ZnS/ZnO ICSQDs. The stability of ICSQDs has been found to be far superior to that of uncapped ZnS QDs, and the corresponding emission quantum yield is higher than that of bare ZnO QDs. A type II band alignment has been demonstrated. Very recently, ZnS/ZnO ICSQDs of size 4 nm have been grown by controlled oxidation of ZnS QDs,[14] showing enormous enhancement in UV emission (~10 times). Possible applications of ZnO/ZnS CSQD on drugs and food delivery in blood have also been reported recently.[15] In contrast to the multiplicity of experimental work, theoretical work on ZnO/ZnS and ZnS/ZnO CSQD is very scare and limited. Using band-corrected pseudopotential density functional theory calculations, Schrier *et al.*[16] have studied the band gap, optical absorption, and carrier localization of ZnO/ZnS core/shell nanowires, proposing this heterostructure for photovoltaic applications. McDonald *et al.*[17] have successfully simulated the biexciton binding and antibinding in CSQD by using a path integral quantum Monte Carlo method. The electronic structure of ZnO/ZnS CSQD has also been

a)Electronic mail: bask@upatras.gr

theoretically calculated by employing the self-consistent charge density functional tight-binding method.[18] Despite of considerable new insights brought by these work, no attention has been paid to the linear and nonlinear optical properties in the CSQD and ICSQD systems.

In this contribution, we performed theoretical calculations of the linear, nonlinear, total absorption coefficients, and refractive index changes in ZnO/ZnS CSQD and ZnS/ZnO ICSQD. The emphasis of the present paper is placed on the shell thickness, possible doping (or dopant positions), dielectric environment influences on the linear and nonlinear optical properties in both structures. The local field correction due to the dielectric mismatch between the CSQD (or ICSQD) and its surrounding matrix, which has rarely been addressed previously,[19,20] has been taken into account in the present calculations. The electronic structures of the systems are numerically calculated by employing the potential morphing method (PMM) in the framework of effective mass approximation, which has been already successfully applied in the past for the study of optical properties in several nanostructures[21–23] and very recently for the calculation of optical susceptibilities in ZnO-matrix system.[20] The rest of the paper is organized as follows: in Sec. II, we define our model and explain the general theory. In Sec. III, we present numerical results and discussions, and the conclusions are given in Sec. IV.

II. THEORETICAL FRAMEWORK

In the framework of effective-mass approximation, a single dopant in a CSQD (or an ICSQD) with inner radius R_1 and outer radius R_2 (see Fig. 1) can be modeled by the following Hamiltonian:

$$\hat{H} = \hat{p}\frac{1}{2m_e^*}\hat{p} + V_{con}(\vec{r}) + \Sigma(\vec{r}) + V_{Coul}(\vec{r}). \tag{1}$$

The first term of the Hamiltonian is the operator for the Kinetic energy of a delocalized conduction electron and m_e^* is the electron effective mass. As justified by the experimental work,[12–14] the conduction band edge of ZnO in ZnO-ZnS hybrid QDs lies below that of its ZnS counterpart. Regarding this, the confinement potential (the second term of Eq. (1)) in our calculations is taken to be step-like (see Fig. 1), which is

$$V_{con}(\vec{r}) = \begin{cases} 0, & |\vec{r}| \le R_1 \\ V_0, & R_1 \le |\vec{r}| \le R_2 \\ \infty, & |\vec{r}| > R_2, \end{cases} \tag{2}$$

for ZnO/ZnS CSQD, while for ZnS/ZnO ICSQD, it is

$$V_{con}(\vec{r}) = \begin{cases} V_0, & |\vec{r}| \le R_1 \\ 0, & R_1 \le |\vec{r}| \le R_2 \\ \infty, & |\vec{r}| > R_2, \end{cases} \tag{3}$$

where V_0 is the electron confinement potential due to the conduction band discontinuity. $\Sigma(\vec{r})$ is the electron self-polarization potential, describing the interaction of the electron and its image charge, which is given by[11,24–26]

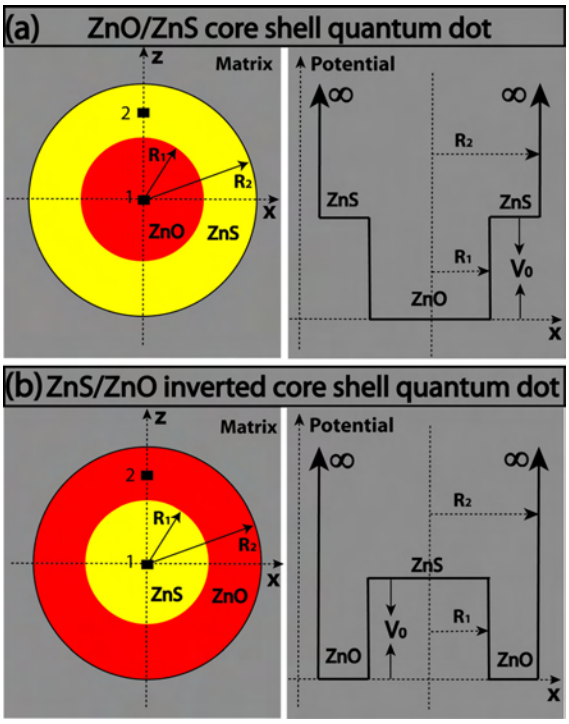

FIG. 1. Schematic representations (left panel) and conduction band profiles (right panel) of the ZnO/ZnS CSQD (a) and ZnS/ZnO ICSQD (b) with inner radius R_1 and outer radius R_2, embedded in a dielectric matrix. Two impurity positions, 1 (core-center impurity) and 2 (shell-center impurity), considered in our calculations, have been explicitly shown.

$$\Sigma(r) = \frac{e^2}{8\pi\epsilon_0\epsilon_{in}R_2}\sum_{k=0}^{\infty}\frac{(k+1)(\epsilon_{in}-\epsilon_{out})}{k\epsilon_{in}+(k+1)\epsilon_{out}}\frac{r^{2k}}{R_2^{2k}}, \tag{4}$$

where ϵ_0 is the permittivity in vacuum, $\epsilon_{in} = \sqrt{\epsilon_c\epsilon_s}$ with ϵ_c and ϵ_s being the relative dielectric constants of the core and shell materials, respectively. ϵ_{out} is the relative dielectric constant of the surrounding matrix. This self-polarization potential diverges as the electron approaches the dielectric interface ($r \to R_2$). In our calculations, this problem is solved by employing the well-known "hard wall" boundary conditions (e.g., for $R > R_2$, potential is assumed to be infinite (see Eqs. (2) and (3))), forcing a null electron density at the interface.

The last term of Eq. (1) is the Coulomb potential due to the mutual interaction between the electron and the shallow donor impurity (or the image charge of the donor impurity), depending strongly on the doping positions. For an on-center impurity, it is[11,24–26]

$$V_{Coul}(r) = -\frac{e^2}{4\pi\epsilon_0\epsilon_{in}r} - \frac{e^2(\epsilon_{in}-\epsilon_{out})}{4\pi\epsilon_0\epsilon_{in}\epsilon_{out}R_2}, \tag{5}$$

while for an off-center impurity, it is[11,24–26]

$$V_{Coul}(r) = -\frac{e^2}{4\pi\epsilon_0\epsilon_{in}|\vec{r}-\vec{r}_i|} - \frac{e^2}{4\pi\epsilon_0\epsilon_{in}R_2}\sum_{k=0}^{\infty}\frac{r_i^k r^k}{R_2^{2k}} \times \frac{(k+1)(\epsilon_{in}-\epsilon_{out})}{k\epsilon_{in}+(k+1)\epsilon_{out}}P_k(\cos\theta), \tag{6}$$

where $\vec{r}$ and $\vec{r_i}$ are the position vectors of the electron and impurity, respectively, with $|\vec{r_i}| = \sqrt{x_i^2 + y_i^2 + z_i^2}$, where x_i, y_i, and z_i are the Cartesian coordinates of the impurity. Without the loss of generality, the impurity in our calculation is placed on the z-axis ($x_i = y_i = 0$, see also Fig. 1). $\cos\theta = \frac{\vec{r}\cdot\vec{z_i}}{|\vec{r}|\cdot|\vec{z_i}|}$ for an off-center impurity (located at $(0,0,z_i)$) and $P_k(\cos\theta)$ is the Legendre polynomial. The first term of Eq. (6) describes the direct Coulomb interaction between the electron and the impurity, while the last term accounts for the Coulomb interaction between the electron and the image charge of an off-center impurity. Here, we assume that the Coulomb potential incorporates the effects of the polarization charges induced on the QD surface as a consequence of the dielectric mismatch.[24–26] To truncate the infinite sum in Eqs. (4)–(6), k is taken up to 4500 in our calculations, which ensures the potential values being insensitive to the further increase in k. This model has been successfully used for the investigation of the electronic properties and impurity binding energy in ZnS/CdSe and CdSe/ZnS core-shell nanodots.[11]

In order to solve the Schrödinger equation based on the Hamiltonian (1) numerically, PMM is employed. A detailed description of this method can be found in Ref. 27. In our present calculations, the usual three-dimensional (3D) harmonic oscillator is chosen as a reference system in order to start the morphing process and its wave functions are selected as the initial wave functions (Φ_R). The interaction potential for an impurity-free system is $V_S(\vec{r}) = V_{con}(\vec{r}) + \Sigma(\vec{r})$, while it is $V_S(\vec{r}) = V_{con}(\vec{r}) + \Sigma(\vec{r}) + V_{Coul}(\vec{r})$ for an impurity-present system. In our PMM, a very dense grid is employed to ensure the accuracy of our results and all calculations are performed with the same grid number. It should be noted here that adopting the harmonic oscillator as a reference system does not affect our results because the PMM needs only a known reference system to start the morphing process and finally to give the eigenfunctions and eigenvalues for the unknown system, independently on the choice of the initial reference system.[27–29]

After obtaining the necessary eigenenergies and wave functions by using PMM, we start to calculate the linear, nonlinear, and total absorption coefficients and refractive index changes associated with the intersubband transitions in the ZnO/ZnS CSQD and ZnS/ZnO ICSQD. Within a two-level system approach, the linear and third-order nonlinear optical absorption coefficients can be obtained by a density matrix approach and a perturbation expansion method, given by[30]

$$\alpha^{(1)}(\omega) = \frac{\omega}{\epsilon_0 c n_r} \frac{|M_{21}|^2 \sigma_V \hbar\Gamma_{12}}{(E_{12} - \hbar\omega)^2 + (\hbar\Gamma_{12})^2}, \tag{7}$$

$$\alpha^{(3)}(\omega, I) = -\frac{2I\omega}{\epsilon_0^2 n_r^2 c^2} \frac{|M_{21}|^4 \sigma_V \hbar\Gamma_{12}}{[(E_{21} - \hbar\omega)^2 + (\hbar\Gamma_{12})^2]^2} \left\{ 1 - \frac{|M_{22} - M_{11}|^2}{4|M_{21}|^2} \times \frac{3E_{21}^2 - 4E_{21}\hbar\omega + \hbar^2(\omega^2 - \Gamma_{12}^2)}{E_{21}^2 + (\hbar\Gamma_{12})^2} \right\}, \tag{8}$$

where σ_V is the electron density, $\Gamma_{12} = 1/T_{12}$ is the relaxation rate with T_{12} being the relaxation time, I is the incident optical intensity, $n_r = \sqrt{\epsilon_{in}}$ is the refractive index, c is the speed of light in vacuum, and $E_{21} = E_f - E_i$ is the energy difference between the final (first excited) state and the initial (ground state) state. By assuming that the polarization of electromagnetic radiation is along the z-axis direction, the transition matrix element between these two states is defined by $M_{ij} = -\frac{\langle f|ez|i\rangle}{\epsilon_{eff}}$, which takes into account the local field correction due to the dielectric mismatch between the system and its surrounding matrix, differing from the usual definition by the local field factor $F = \frac{1}{\epsilon_{eff}} = \frac{3\epsilon_{out}}{2\epsilon_{out}+\epsilon_{in}}$.[20] For a dielectric environment free system ($\epsilon_{in} = \epsilon_{out}$), the local field factor equals to 1 and it has no influence on the transition matrix element, recovering the usual situation which has been widely addressed in the published literature. However, if the system is dispersed in a matrix with a lower dielectric constant ($\epsilon_{in} > \epsilon_{out}$), e.g., ZnO/ZnS CSQD (or ZnS/ZnO ICSQD) embedded in amorphous SiO_2,[31] the local field factor $F < 1$ and it significantly decreases the transition matrix element. At a very weak radiation intensity, the total absorption coefficient can be approximated as

$$\alpha(\omega, I) \approx \alpha^{(1)}(\omega) + \alpha^{(3)}(\omega, I). \tag{9}$$

The linear and the third order nonlinear refractive index changes are given by[30]

$$\frac{\Delta n^{(1)}(\omega)}{n_r} = \frac{1}{2n_r^2\epsilon_0} |M_{21}|^2 \sigma_V \left\{ \frac{E_{21} - \hbar\omega}{(E_{21} - \hbar\omega^2)^2 + (\hbar\Gamma_{12})^2} \right\} \tag{10}$$

and

$$\frac{\Delta n^{(3)}(\omega)}{n_r} = -\frac{\mu_0 c}{n_r^3 \epsilon_0} \frac{|M_{21}|^4 (E_{21} - \hbar\omega)\sigma_V I}{[(E_{21} - \hbar\omega)^2 + (\hbar\Gamma_{12})^2]^2} \left[1 - \frac{(M_{22} - M_{11})^2}{4|M_{21}|^2((E_{21})^2 + (\hbar\Gamma_{12})^2)(E_{21} - \hbar\omega)} \times \{(E_{21} - \hbar\omega) \times [E_{21}(E_{21} - \hbar\omega) - (\hbar\Gamma_{12})^2] - (\hbar\Gamma_{12})^2(2E_{12} - \hbar\omega)\} \right], \tag{11}$$

respectively, where μ_0 is the permeability in vacuum and the relative permeability μ_r is taken to be unity in our calculations. In the presence of a weak radiation intensity, the total refractive index change can be defined by

$$\frac{\Delta n(\omega)}{n_r} \approx \frac{\Delta n^{(1)}(\omega)}{n_r} + \frac{\Delta n^{(3)}(\omega)}{n_r}. \quad (12)$$

III. NUMERICAL RESULTS AND DISCUSSION

In what follows, we will discuss the shell thickness, impurity, and dielectric environment influences of the linear and nonlinear optical properties associated with the intersubband transitions in both ZnO/ZnS CSQD (see Sec. III A) and ZnS/ZnO ICSQD (see Sec. III B). The parameters used in our calculations are the same as in Ref. 20, taking $\sigma_V = 17 \times 10^{17}\,\mathrm{cm}^{-3}$, $T_{12} = 1$ ps, and $n_r = \sqrt{\epsilon_{in}} = 2.9629$ with $\epsilon_r^{ZnO} = 8.66$ and $\epsilon_r^{ZnS} = 8.9$,[11] where ϵ_r^{ZnO} and ϵ_r^{ZnS} are the relative dielectric constants of ZnO and ZnS, respectively. The electron effective mass is assumed to be position-independent, taking the value of the core material (e.g., for ZnO/ZnS CSQD, $m_e = m_e^{ZnO} = 0.265 m_0$ (Ref. 8) and for ZnS/ZnO ICSQD, it is $m_e = m_e^{ZnS} = 0.24 m_0$,[9] where m_0 is the free electron mass). According to the previous literatures about the linear and nonlinear optical properties in semiconductor nanostructures,[20,23,32–34] the radiation intensity significantly affects the magnitude of the third order absorption coefficient and refractive index change, leading to a substantial decrease in the magnitude of the total counterparts. However, in the present calculations, we keep the radiation intensity as a constant value $I = 0.02\,\mathrm{MW/cm}^2$ and take the inner radius $R_1 = 1.5$ nm, which is slightly larger than the ZnO effective exciton Bohr radius ($a_B^* = 1.4$ nm). Both the systems with ($\epsilon_{out} = 3.9$, corresponding to disperse the CSQDs into amorphous SiO_2 matrix) and without ($\epsilon_{out} = \epsilon_{in} = 8.779$) dielectric environment effect are considered. The strain effects due to the lattice mismatch between the core and shell materials are not considered in the present intersubband (conduction band) calculations.

It should be noted that *ab initio* calculations have been confirmed as a robust tool of describing the band lineups for a great variety of semiconductor heterostructures (for example, see Refs. 35–37). However, to the best of our knowledge, such type of calculations has not yet been performed for WZ ZnO-ZnS hybrid structures, which are addressed herein. Therefore, in our calculations, the conduction band discontinuity is taken as $V_0 = 0.08 \cdot E_g^{ZnS} = 292.8$ meV, where the coefficient 0.08 is empirically derived by fitting to the experimental measurements for a great variety of semiconductor colloidal QDs[29] and E_g^{ZnS} is the energy band gap of WZ ZnS. The sensitivity of our results for WZ ZnO/ZnS CSQDs and ZnS/ZnO ICSQDs to the conduction band discontinuity parameter (i.e., see V_0 in Fig. 1) will also be discussed in Secs. III A and III B, respectively.

Before presenting the numerical results, we first address several important characteristics of the absorption coefficients and refractive index changes, indicating from the corresponding expressions described in the last section. The peak value of the linear absorption coefficient occurs at the photon energy $\hbar\omega = \sqrt{E_{21}^2 + (\hbar\Gamma_{12})^2}$ and the peak intensity is proportional to $|M_{21}|^2 \cdot \sqrt{E_{21}^2 + (\hbar\Gamma_{12})^2}$. For $\hbar\Gamma_{12} \ll E_{21}$, which is valid for all the cases considered below, the peak value of the linear absorption coefficient turns out to be at the photon energy $\hbar\omega \approx E_{21}$ and the peak intensity is in proportion to $E_{21} \cdot |M_{21}|^2$. For systems with inversion symmetry, e.g., impurity free CSQD and ICSQD systems or these systems doped by a core-center impurity (see Fig. 1), the diagonal matrix elements M_{11} and M_{22} vanish, leading to a zero contribution from the last term of Eq. (8) to $\alpha^{(3)}$. For $\hbar\Gamma_{12} \ll E_{21}$, although $\alpha^{(3)}$ reaches its peak value at approximately the same photon energy as its linear counterpart, the corresponding peak intensity is more sensitive to the transition matrix element ($\propto E_{21} \cdot |M_{21}|^4$). When this inversion symmetry is broken by the external perturbations, e.g., doping an off-center impurity, nonzero M_{11} and M_{22} appear and the aforementioned dependence will be further corrected by the negative contribution of the anisotropic term (see the term which contains $|\frac{M_{11}-M_{22}}{M_{21}}|$ in Eq. (8)).

Concerning to $\frac{\Delta n^{(1)}(\omega)}{n_r}$, it always exhibits a standard dispersive lineshape (e.g., it presents first a maximum and then a minimum as the photon energy increases). The maximum and minimum appear at the photon energy $\hbar\omega = E_{21} - \hbar\Gamma_{12}$ and $\hbar\omega = E_{21} + \hbar\Gamma_{12}$, respectively. They are equivalent in magnitude (in absolute value) which is proportional to $|M_{21}|^2$, independently on the transition energy (E_{21}). Whereas, for $\frac{\Delta n^{(3)}(\omega)}{n_r}$, this standard dispersive lineshape is reversed (e.g., it shows firstly a *minimum* and then a *maximum* as the photon energy increases). Analogously to $\alpha^{(3)}$, $\frac{\Delta n^{(3)}(\omega)}{n_r}$ in a system with an inversion symmetry is fully determined by the first term of Eq. (11) due to the vanishing diagonal matrix elements M_{11} and M_{22}. Its global minimum and maximum occur at $\hbar\omega = E_{21} - (\hbar\Gamma_{12})/\sqrt{3}$ and $\hbar\omega = E_{21} + (\hbar\Gamma_{12})/\sqrt{3}$, respectively. The magnitudes of these minimum and maximum are equivalent (in absolute value), exhibiting a stronger exclusive dependence on the transition matrix element (e.g., $\propto |M_{21}|^4$) in comparison to $\frac{\Delta n^{(1)}(\omega)}{n_r}$ (e.g., $\propto |M_{21}|^2$)). However, these relations will also be influenced by the anisotropic term if the system is lack of inversion symmetry (see Eq. (11)).

A. Optical absorption coefficients and refractive index changes in ZnO/ZnS core-shell quantum dots

As a first step towards investigating the linear and nonlinear optical properties in impurity free ZnO/ZnS CSQDs, we present in Fig. 2 the linear, third order nonlinear, and total absorption coefficients and refractive index changes as a function of the photon energy for three different shell thickness values. It shows that increasing the thickness of the capping layer leads to a red shift of the threshold energy. This shift appears to be very sensitive to the initial capping and becomes less significant when the shell layer is relatively thick. In addition to this, varying the shell thickness also significantly enhances all the refractive index changes. This effect favors more the nonlinear term. To capture the

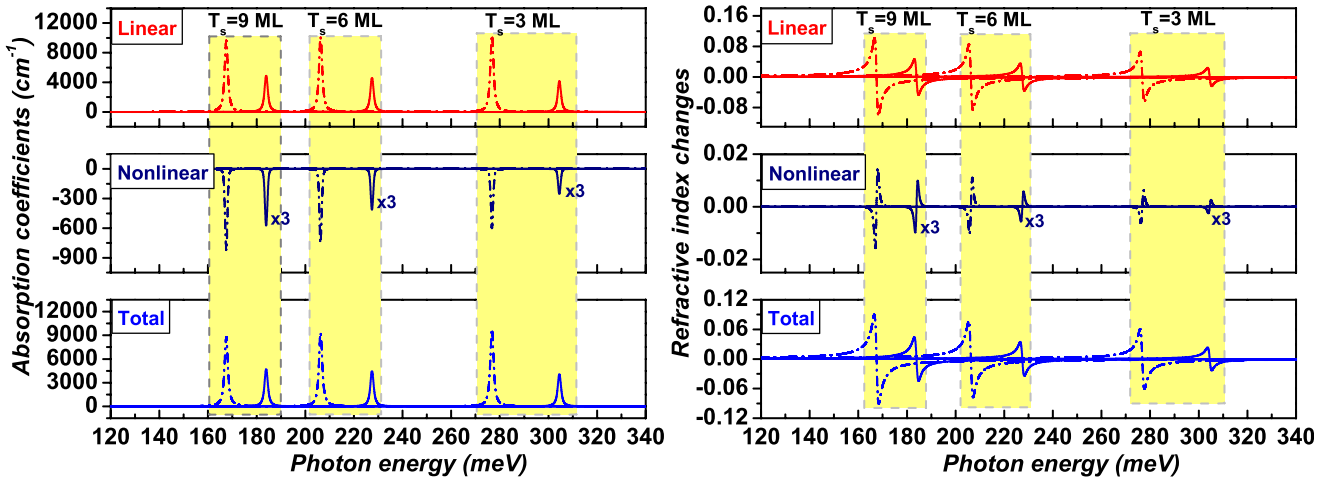

FIG. 2. Linear (red), third order nonlinear (navy), and total (blue) absorption coefficients (left panel) and refractive index changes (right panel) as a function of the photon energy $\hbar\omega$ for various shell (ZnS) thickness ($T_s = R_2 - R_1$, in unit of ML) values in impurity free ZnO/ZnS CSQDs without ($\epsilon_{in} = \epsilon_{out}$, dashed dotted lines) and with ($\epsilon_{in} > \epsilon_{out}$, solid lines) dielectric environment. Here, the inner radius $R_1 = 1.5$ nm and 1 ML = 0.3117 nm (for ZnS).

physical reasons, we calculated the probability of finding the electron in the shell region for various shell thickness values. The results for the ground and first excited states are shown in Fig. 3. It appears that increasing the capping thickness enhances the penetration of the electron wave functions into shell region, irrespectively of the dielectric environment. This movement of the wave functions eventually causes an increase in the transition matrix element M_{21} which is fully responsible for the variation of the refractive index changes. In contrast to the increase in the matrix element, the transition energy experiences a decrease with increasing the capping thickness, which is associated with the observed red shift. The competition effects of these two factors (e.g., $|M_{21}|^2$ and E_{21}) determine the tendency of the peak intensity of the linear absorption coefficients with respect to the shell thickness. In a dielectrically homogeneous system (see the dash dotted lines), the later effect (e.g., E_{21}) is more pronounced and the peak intensity of $\alpha^{(1)}$ decreases with regard to the increased capping thickness. Conversely, when the dielectric inhomogeneity is present (see the solid lines), the former effect ($|M_{21}|^2$) is more effective, finally inducing an increase in the peak intensity of $\alpha^{(1)}$.

Concerning to $\alpha^{(3)}$, its peak intensity exhibits a more straightforward variation, increasing significantly with increasing the shell thickness both with and without the dielectric environment. This is due to the fact that comparing to $\alpha^{(1)}(\propto E_{21}\cdot|M_{21}|^2)$, the peak intensity of $\alpha^{(3)}$ $(\propto E_{21}\cdot|M_{21}|^4)$ is more sensitive to the variation of the transition matrix element, which contributes positively with the capping thickness as addressed above. Although the change of the nonlinear term is more drastic with increasing the shell thickness, the peak magnitude of total absorption coefficient follows the same variation of the linear term due to its dominant contribution at relatively weak radiation intensity.

In comparison to a dielectrically homogeneous system, all the quantities are substantially reduced if the system is dispersed in a matrix with a lower dielectric constant and considerable blue shift of the threshold energy is observed. This is attributed to the fact that for a phenomenological CSQD, the existence of the dielectric environment (e.g., in our case, $\epsilon_{in} > \epsilon_{out}$) induces a self energy which is positive and a short range interaction at the CSQD-matrix interface (see Eq. (4)), forcing the electron to move towards the core center. This can be easily justified by the fact the probability of finding the electron of ground state in the shell region becomes smaller in the presence of the dielectric mismatch (see the left panel of Fig. 3). Moreover, local field effect, characterizing by the local field factor $F = \frac{1}{\epsilon_{eff}} = 0.705$, also appears. The combination effects of the charge movement and the local field consequently decrease the transition element, which is related to the reducing in all the refractive index changes. Although the transition energy exhibits an increase by taking into account the dielectric environment effect, the decrease in the matrix element is more significant,

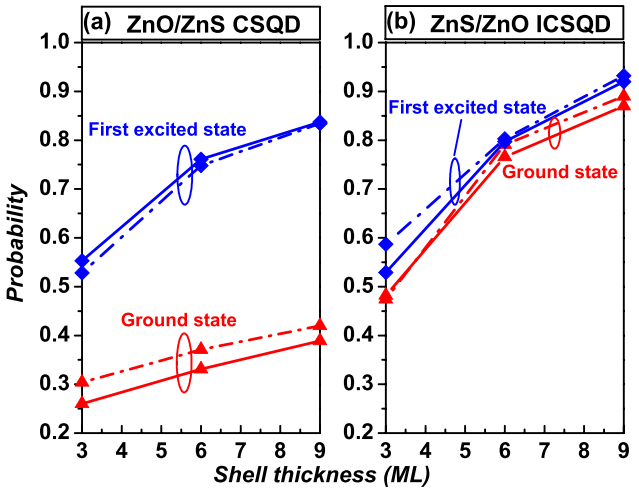

FIG. 3. Probability of finding the electron of ground-state (red triangles) and first excited state (blue diamonds) in the shell region as a function of the shell thickness (in unit of ML) in ZnO/ZnS CSQDs (left panel) and ZnS/ZnO ICSQDs (right panel) without ($\epsilon_{in} = \epsilon_{out} = 8.779$, dashed dotted lines) and with dielectric environment ($\epsilon_{in} > \epsilon_{out}, \epsilon_{in} = 8.779, \epsilon_{out} = 3.9$, solid lines). For the left panel, 1 ML = 0.3117 nm (WZ ZnS), while for the right panel, 1 ML = 0.26025 nm (WZ ZnO).

leading to the observed variation (decreasing) in all the absorption coefficients.

Possible existence of dopants (or intrinsic hydrogen like defects) is also expected to affect significantly the linear and nonlinear optical properties in a CSQD. From the last section (see Eqs. (4)–(6)), we know that in a dielectrically homogeneous system, the presence of the donor ion induces a well-known electron-ion Coulomb interaction. However, this interaction is further influenced by the effect of the polarization image charges (e.g., positive self-energy and the Coulomb interaction between the electron and the impurity image) when the CSQD is embedded in a matrix with a lower dielectric constant. Although the Coulomb potential is different in these two dielectric environments, the variation of linear and nonlinear optical properties with respect to a core-center doping appears to be very similar. Comparing to the impurity free system (see Fig. 2), Fig. 3 shows that doping the CSQD at the core center ($z_i = 0$) with a hydrogenic impurity leads to a blue shift of the transition energy and simultaneously a slight decrease (in absolute magnitude) in both the linear and nonlinear absorption coefficients and refractive index changes, irrespectively of the dielectric environment. The physical reason is that the occurrence of impurity center increases the separation of the energy levels of the two states (E_{21}) in both with and without dielectric environment. Conversely, the charge accumulation towards the impurity center (core center) decreases significantly the transition matrix element. These two effects appear to compensate with each other and the influence of latter factor turns out to be more pronounced, causing a decrease of both the linear and nonlinear quantities.

Varying the doping position from the core center to the shell center breaks the inversion symmetry of the system, causing an increment in the off-diagonal transition matrix element M_{21} and the appearance of a non-zero anisotropic value ($|\frac{M_{11}-M_{22}}{M_{21}}|$), as we addressed before. The increase in M_{21} is dominant and leads to the enhancement of all the refractive index changes. On the other hand, moving the on-center impurity towards an off-center position also results in a decrease in the transition energy which is responsible for the red shift exhibited in Fig. 3. However, the variation of these two effects (M_{21} and E_{21}) with respect to the change of the doping position is different in the two dielectric environments. For a dielectrically homogeneous system, the transition energy is smaller and its variation is more effective. Consequently, the peak intensity of the linear absorption coefficient decreases with moving the impurity to shell center (see the dash dotted lines in the upper plot of Fig. 4). By contrast, in a dielectrically inhomogeneous system, the transition energy is larger due to the incorporation of the self-image effects and its variation with respect to the doping position is less efficient in comparison to its matrix element counterpart. The peak intensity of linear absorption coefficient resultantly experiences an increase.

The influence of the variation of the transition matrix element on the peak intensity of the nonlinear absorption coefficient is always dominant over its transition energy counterpart, resulting a similar behaviour in both with and without dielectric environment (it increases with moving the dopant to the shell center). More specially, we found that comparing to the system without dielectric environment, both the absorption coefficients and refractive index changes are substantially reduced when the system is dispersed in a lower dielectric constant matrix ($\epsilon_{in} > \epsilon_{out}$) and blue shift of the threshold energy is observed, as expected.

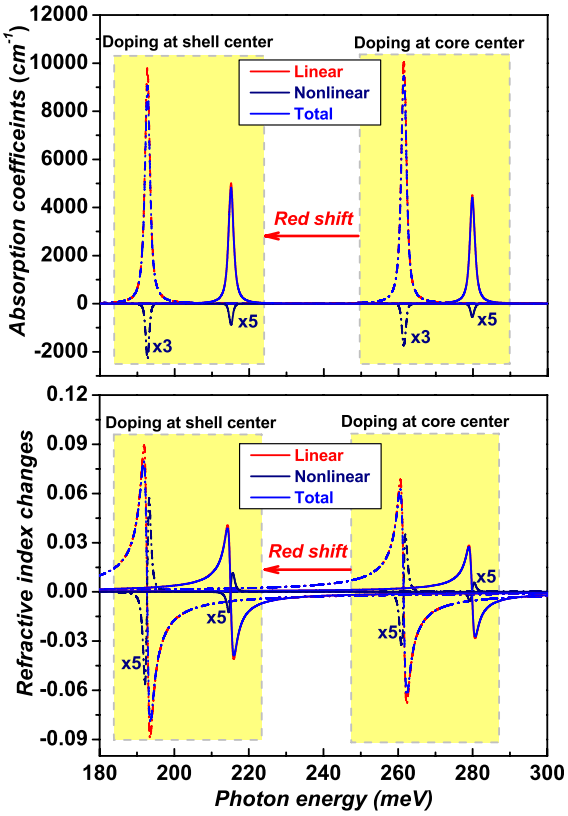

FIG. 4. Linear (red), third order nonlinear (navy), and total (blue) absorption coefficients (upper panel) and refractive index changes (lower panel) as a function of the photon energy $\hbar\omega$ for various dopant positions in doped ZnO/ZnS CSQDs without (dashed dotted lines) and with (solid lines) dielectric environment. Here, the dopants located at the core center ($z_i = 0$) and at the shell center ($z_i = 0.75R_2$) are considered. The inner radius $R_1 = 1.5$ nm and the shell thickness is $T_s = 6$ ML ($R_2 = R_1 + T_s = 3.3702$ nm).

Finally, in an attempt to investigate the sensitivity of the presented results to the conduction band discontinuity parameter V_0 (see Fig. 1), we show in Fig. 5 the linear absorption coefficient and refractive index change as a function of the photon energy for various shell thickness values, taking $V_0 = 200$ meV ($\sim 0.052 \cdot E_g^{ZnS}$). It appears that the deviation of the V_0 value from the empirically derived one does not cause any changes in the general tendency of the transition energy E_{21} (decreases) and off-diagonal matrix element M_{21} (increases) with respect to the increase in the shell thickness. This can be confirmed by the appearance of red-shift phenomenon and also the enhancement of the change in the refractive index (in absolute value) shown in Fig. 5 with increasing the capping thickness (very similarly to the ones pictured in Fig. 2). However, possible variation in V_0 affects strongly the interplay of the two factors on the peak intensity of the absorption coefficient. This becomes clear by the non-monotonic variation in the absorption coefficient (i.e., first increases (from 3 Monolayer (ML) to 6 ML) and then

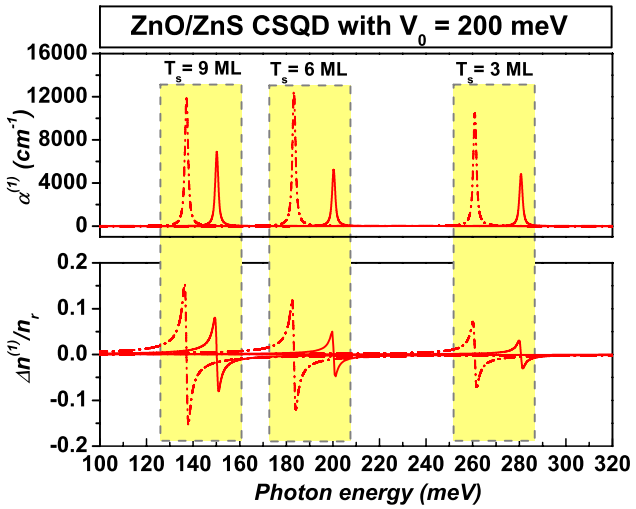

FIG. 5. Linear absorption coefficient ($\alpha^{(1)}$, upper panel) and refractive index change ($\Delta n^{(1)}/n_r$, lower panel) as a function of the photon energy $\hbar\omega$ for various shell thickness values (in unit of ML) in ZnO/ZnS CSQD without (dashed dotted lines) and with (solid lines) dielectric environment, using the conduction band discontinuity parameter $V_0 = 200$ meV.

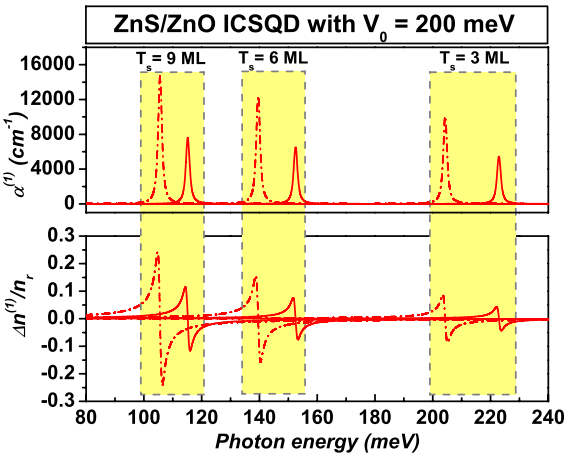

FIG. 7. The same as in Fig. 5 but for ZnS/ZnO ICSQDs.

slightly decreases (from 6 ML to 9 ML)) shown in Fig. 5, very differently from the ones shown in Fig. 2 (i.e., the peak intensity decreases monotonically with increasing the shell thickness). In addition to this, the decrease in V_0 results in a smaller resonant peak photon energy in CSQDs both with and without dielectric environment. In the presence of the dielectric environment, the linear and nonlinear optical properties are independent on the variation of V_0, always decreasing the peak intensity and blue-shifting the peak position (see Figs. 2 and 5).

B. Optical absorption coefficients and refractive index changes in ZnS/ZnO *inverted* core-shell quantum dots

In Subsection III A, we find that the shell thickness, impurity and possible existence of the dielectric environment significantly influence the linear and nonlinear optical properties in ZnO/ZnS CSQDs. Comparing to the *conventional* configuration, ZnS/ZnO ICSQDs exhibit very different potential profiles (see Fig. 1). Herein, we present the dependence of the absorption coefficients and refractive index changes in the ICSQD on the aforementioned three factors and possible comparison between these two systems (CSQD and ICSQD) is performed.

Following the same procedures in the last subsection, we first studied the effect of the shell thickness on the absorption coefficients and refractive index changes in ZnS/ZnO ICSQDs. As shown in Fig. 6, increasing the shell thickness leads to an enhancement of all the absorption coefficients and refractive index changes both with and without dielectric environment. This is independent on the variation of the conduction band discontinuity parameter V_0 (see Fig. 7), which is different from the case shown in CSQDs by the variation of the linear absorption coefficients with respect to the capping thickness (see Fig. 2). The physical reason is attributed to the charge accumulation towards the shell region induced by the increase in the shell thickness (see the right panel of Fig. 3), which is similar to that in the *conventional* systems (see the right panel of Fig. 3). The resultant increase in the transition matrix element is the direct reason for the increase in the refractive index changes. However, comparing to the CSQD, the charge movement appears to be

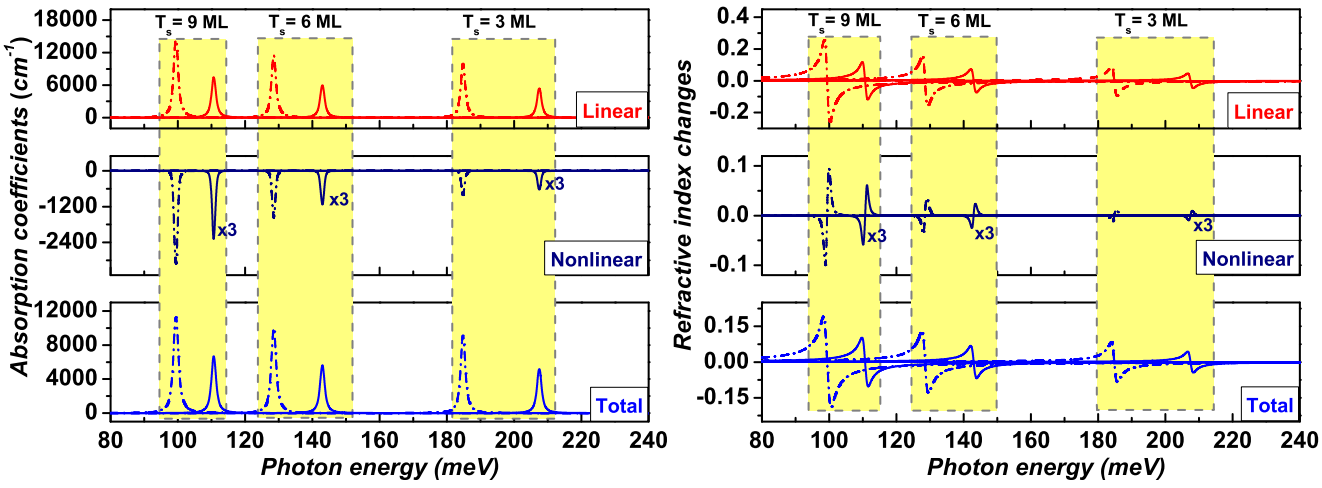

FIG. 6. The same as in Fig. 2 but for ZnS/ZnO ICSQDs. Here, 1 ML = 0. 26025 nm (for ZnO (shell material)).

comparatively more significant in the ICSQD systems (see the two plots in Fig. 3). Therefore, the positive contribution from the transition matrix element variation completely dominates over the negative contribution from its transition energy counterpart, causing a monotonic increase in the linear absorption coefficient peak intensity. We further found from Fig. 6 that the increase in the nonlinear quantities with enhancing the capping layer is significantly more pronounced. Similarly to the CSQD, for a given shell thickness value, all the quantities are drastically reduced by dispersing the ICSQD into a matrix with a lower dielectric constant and a blue shift of the threshold energy appears.

In the *unconventional* CSQD structure, Fig. 6 shows that enhancing the thickness of the capping layer causes a strong red shift in the threshold energy. This red shift is very sensitive to the initial capping (e.g., from 3 ML to 6 ML) and the sensitivity reduces if the capping layer becomes comparable to the core radius (e.g., from 6 ML to 9 ML), similarly to its *conventional* counterpart (shown in Fig. 2). This behaviour appears to be irrespective of the involved conduction band parameter V_0 (see Fig. 7). Comparing Fig. 6 to Fig. 7, we find that for a specific capping thickness, possible variation in V_0 also considerably affects the threshold energy, exhibiting a larger value for a smaller V_0, contrary to the CSQD structure. This is due to the fact that although decreasing the V_0 value results in lowering both the ground state and the first excited state energy levels, the sensitivity of this decrease in these two energy levels turns out to be completely different in the CSQD and ICSQD structures. In ICSQD, the decrease in the ground state energy level with respect to the reducing of V_0 is more significant, leading to a relatively larger transition energy E_{21} for a smaller V_0 value. However, in CSQD, this decrease favors more the energy level of the first excited state, causing a reversed picture.

Finally, we present in Fig. 8 the linear, nonlinear and total absorption coefficients and refractive index changes as a function of the photon energy for two doping positions, with and without dielectric environment. It appears that varying the doping position from the core center to the shell center causes a red shift of the threshold energy. However, the sensitivity of this shift with respect to the impurity locations is reduced by considering the dielectric environment (see Fig. 8). Additionally, the peak intensity of the absorption coefficients and the changes in the refractive index are differently influenced by the doping position in the two dielectric environments. In a dielectrically homogeneous system, the displacement of the impurity from the on-center position to an off-center position leads to an increase in the peak intensity of the linear and nonlinear quantities. Similar behaviour has been found in the CSQD and the corresponding physical reasons can be understood analogously. However, when the dielectric environment effect is present, the magnitudes of all the quantities are reduced significantly, very similar to that in the conventional CSQD systems (see Fig. 4). In contrast to this consistency, displacing the *on-center* impurity to an *off-center* position in the *unconventional* systems decreases the peak intensity of all the absorption coefficients and reduces all the changes in the refractive

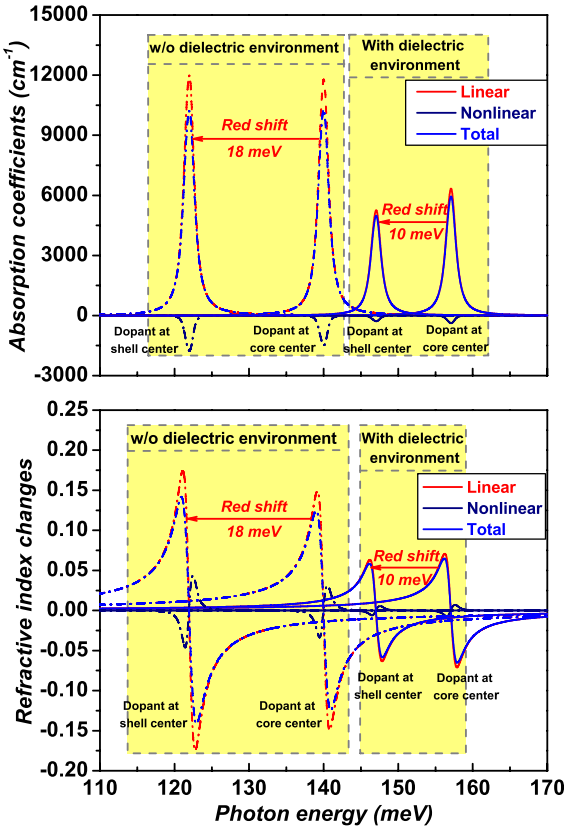

FIG. 8. The same as in Fig. 4 but for ZnS/ZnO ICSQDs. The inner radius $R_1 = 1.5$ nm and the shell thickness is $T_s = 6\text{ML}(R_2 = R_1 + T_s = 3.0615\,\text{nm})$.

index. This is associated with the decrement in both the transition energy (e.g., E_{21}) and matrix element (e.g., $|M_{21}|$).

IV. CONCLUSION

In summary, we have performed a theoretical study on the linear, nonlinear and total absorption coefficients and refractive index changes associated with the intersubband transitions in both WZ ZnO/ZnS CSQD and ZnS/ZnO ICSQD. The influence of the shell thickness, impurity, and dielectric environment has been addressed. The necessary wave functions and corresponding energy levels are numerically calculated by using PMM in the framework of effective mass approximation. We find that in both CSQD and ICSQD, increasing the shell thickness causes a significant red shift of the threshold energy and enhances drastically the nonlinear absorption coefficients and all the changes in the refractive index. This shift appears to be very sensitive to the initial capping and then becomes insensitive to the further capping if the shell layer becomes comparatively thick. Similar red shift phenomenon has also been observed in the most cases studied when the impurity is displaced from the core-center to the shell-center. In all the cases investigated, further dispersing the systems into a matrix with a lower dielectric environment blue shifts all the peak positions of the absorption coefficients and refractive index changes. However, the corresponding magnitudes (in absolute value) are substantially reduced. In the ICSQD, moving the core center impurity to the shell center position even causes a slight decrease

in all the absorption coefficients and refractive index changes. Generally, the nonlinear terms are more sensitive to the external perturbations. However, we found that at a relatively weak radiation intensity, the variation of the total counterparts is completely dominated by the corresponding linear terms.

Our results also highlight prominently the importance of accurate determination of the conduction band discontinuity parameter in WZ ZnO-ZnS hybrid systems. Possible variation of this parameter appears to affect the tendency of the peak intensity of the linear absorption coefficient with respect to the shell thickness in the conventional CSQD structure and also the threshold energy of the absorption coefficient and refractive index change in both CSQD and ICSQD structures. Despite of this, we believe that the present results would be useful not only in the elucidation of the fundamental physics but also for possible devices application based on ZnO/ZnS hybrid systems.

ACKNOWLEDGMENTS

This research has been co-financed by the European Union (European Social Fund-ESF) and Greek national funds through the Operational Program "Education and Lifelong Learning" of the National Strategic Reference Framework (NSRF)-Research Funding Program: Thales, investing in knowledge society through the European Social Fund.

[1]V. A. Fonoberov and A. A. Balandin, J. Nanoelectron. Optoelectron. **1**, 19 (2006).
[2]C. Jiang, W. Zhang, G. Zou, W. Yu, and Y. Qian, Mater. Chem. Phys. **103**, 24 (2007).
[3]K.-F. Lin, H.-M. Cheng, H.-C. Hsu, L.-J. Lin, and W.-F. Hsieh, Chem. Phys. Lett. **409**, 208 (2005).
[4]B. Bhattacharjee, D. Ganguli, S. Chaudhuri, and A. Pal, Mater. Chem. Phys. **78**, 372 (2003).
[5]M. Navaneethan, J. Archana, K. Nisha, Y. Hayakawa, S. Ponnusamy, and C. Muthamizhchelvan, Mater. Lett. **68**, 78 (2012); A. L. Donne, S. K. Jana, S. Banerjee, S. Basu, and S. Binetti, J. Appl. Phys. **113**, 014903 (2013).
[6]X. Xu, C. Xu, J. Dai, J. Hu, F. Li, and S. Zhang, J. Phys. Chem. C **116**, 8813 (2012).
[7]K. Rajeshwar, N. R. de Tacconi, and C. R. Chenthamarakshan, Chem. Mater. **13**, 2765 (2001).
[8]S. Baskoutas and G. Bester, J. Phys. Chem. C **114**, 9301 (2010).
[9]Landolt-Börnstein, *Numerical Data and Functional Relationships in Science and Technology*, edited by O. Madelung and M. Schulz (Springer, Berlin, 1982), Vol. 22a.
[10]L. P. Balet, S. A. Ivanov, A. Piryatinski, M. Achermann, and V. I. Klimov, Nano Lett. **4**, 1485 (2004).
[11]M. Cristea and E. Niculescu, Eur. Phys. J. B **85**, 1 (2012).
[12]S. Sharma and S. Chawla, Electron. Mater. Lett. **9**, 267 (2013).
[13]F. Wang, J. Liu, Z. Wang, A.-J. Lin, H. Luo, and X. Yu, J. Electrochem. Soc. **158**, H30 (2011).
[14]M. Rajalakshmi, S. Sohila, R. Ramesh, and G. Bhalerao, Mater. Res. Bull. **47**, 2668 (2012).
[15]J. Xiao, M. Wu, G. Kai, F. Wang, H. Cao, and X. Yu, Nanomedicine **7**, 850 (2011); J. Xiao, F. Wang, J. Liu, L. Wang, G. Kai, and X. Yu, Mol. BioSyst. **7**, 2452 (2011).
[16]J. Schrier, D. O. Demchenko, L. Wang, and A. P. Alivisatos, Nano Lett. **7**, 2377 (2007).
[17]P. G. McDonald, E. J. Tyrrell, J. Shumway, J. M. Smith, and I. Galbraith, Phys. Rev. B **86**, 125310 (2012).
[18]S. Saha and P. Sarkar, Chem. Phys. Lett. **555**, 191 (2013).
[19]Anchala, S. P. Purohit, and K. C. Mathur, Appl. Phys. Lett. **98**, 043106 (2011).
[20]Z. Zeng, E. Paspalakis, C. S. Garoufalis, A. F. Terzis, and S. Baskoutas, J. Appl. Phys. **113**, 054303 (2013).
[21]S. Baskoutas and A. F. Terzis, J. Appl. Phys. **98**, 044309 (2005); **99**, 013708 (2006).
[22]S. Baskoutas, E. Paspalakis, and A. F. Terzis, Phys. Rev. B **74**, 153306 (2006).
[23]İ. Karabulut and S. Baskoutas, J. Appl. Phys. **103**, 073512 (2008).
[24]L. Bányai, P. Gilliot, Y. Z. Hu, and S. W. Koch, Phys. Rev. B **45**, 14136 (1992).
[25]G. Allan, C. Delerue, M. Lannoo, and E. Martin, Phys. Rev. B **52**, 11982 (1995).
[26]J. L. Movilla, F. Rajadell, and J. Planelles, J. Appl. Phys. **103**, 014310 (2008).
[27]M. Rieth, W. Schommers, and S. Baskoutas, Int. J. Mod. Phys. B **16**, 4081 (2002).
[28]Z. Zeng, C. S. Garoufalis, S. Baskoutas, and A. F. Terzis, J. Appl. Phys. **112**, 064326 (2012); Z. Zeng, C. S. Garoufalis, and S. Baskoutas, J. Phys. D: Appl. Phys. **45**, 235102 (2012).
[29]P. Poulopoulos, S. Baskoutas, S. D. Pappas, C. S. Garoufalis, S. A. Droulias, A. Zamani, and V. Kapaklis, J. Phys. Chem. C **115**, 14839 (2011).
[30]S. Unlu, I. Karabulut, and H. Safak, Physica E **33**, 319 (2006).
[31]J. Cao, J. Yang, L. Yang, M. Wei, B. Feng, D. Han, L. Fan, B. Wang, and H. Fu, J. Appl. Phys. **112**, 014316 (2012).
[32]W. Xie, Physica B **403**, 4319 (2008); J. Phys.: Condens. Matter **21**, 115802 (2009).
[33]M. Şahin, Phys. Rev. B **77**, 045317 (2008); J. Appl. Phys. **106**, 063710 (2009).
[34]İ. Karabulut, J. Appl. Phys. **109**, 053101 (2011).
[35]S.-H. Wei and A. Zunger, Appl. Phys. Lett. **72**, 2011 (1998).
[36]A. Janotti and C. G. Van de Walle, Phys. Rev. B **75**, 121201 (2007).
[37]P. G. Moses, M. Miao, Q. Yan, and C. G. V. de Walle, J. Chem. Phys. **134**, 084703 (2011).

Paper IX

In which we study the combination effects of the electric and magnetic fields on the binding energy of an on-center donor impurity in disc-shaped $GaAs/Al_{0.3}Ga_{0.7}As$ quantum dots ...

AMERICAN SCIENTIFIC PUBLISHERS

Science of Advanced Materials
Vol. 6, pp. 586–591, 2014
(www.aspbs.com/sam)

ARTICLE

Competition Effects of Electric and Magnetic Fields on Impurity Binding Energy in a Disc-Shaped Quantum Dot in the Presence of Pressure and Temperature

Zaiping Zeng, George Gorgolis, Christos S. Garoufalis, and Sotirios Baskoutas*

Materials Science Department, University of Patras, 26504 Patras, Greece

ABSTRACT

We have theoretically studied the combination effects of the electric and magnetic fields on the binding energy of an on-center donor impurity in disc-shaped GaAs/$Al_{0.3}Ga_{0.7}As$ quantum dots (QDs) with emphasis on the competition effects between the two fields under externally applied pressure and temperature. The electric field is applied along the radial direction of the QD, while the magnetic field is applied along the growth direction. The numerical method we employed in the present calculations is the potential morphing method in the framework of the effective mass approximation. Our results show that the two fields exhibit a competition effect on the donor binding energy, leading to an invariant binding energy as in the zero field case at a critical line. This line separates the region corresponding to the "red shift" of the donor binding energy from the one referring to the "blue shift" of the binding energy. Comparing to the magnetic field effect, increasing in the QD sizes or applied pressure is found to favour more its electric counterpart, enlarging the region satisfied by the "red shift" of the donor binding energy. The temperature effect appears to decrease the donor binding energy. However, the competition effects between the two fields retain the same when the temperature varies.

KEYWORDS: Quantum Dot, Impurity, Electric and Magnetic Fields.

1. INTRODUCTION

Doping of semiconductors by impurity atoms has widespread technological applications in microelectronics and optoelectronics. It provides further means to control the performance of related devices.[1] Donors have been used in some elegant quantum computing proposals that draws upon the vast expertise of the semiconductor device industry.[2] One of the proposals that renewed interest in the quantum mechanics of donors is the Kane qubit[3] in which information is encoded into the nuclear spins of donor atoms in doped silicon electronic devices, and engineers the donor electron wave function by electrodes to manipulate information.

Due to the development of nanoscience and nanotechnology, the study of donor related electronic and optical properties in semiconductor quantum dots (QDs) has been of great interest in the past.[4–8] It has been found that donor related properties in semiconductor QDs depend significantly on the materials, geometries (sizes and shapes), shapes of the confinement potentials and also dopant positions. External perturbations, such as applied electric and magnetic fields, hydrostatic pressure and temperature, also modify significantly the confined states of the donors.[6,9–14] To control and modulate the output of the doped-QDs-based optoelectronic devices, a combined application of these external perturbations in semiconductor QDs, such as a combination of the electric field with the magnetic field, has drawn increasingly attentions recently.[15–20] When the electric and magnetic fields are applied perpendicular to each other in a QD system, as reported in a recent paper[20] of our group, competition effects appear. These competition effects on the donor binding energy have been found to be strongly dependent on the QD geometric characteristics (dot sizes and aspect ratios) and also the strength and orientation of the two fields.[20] When another external perturbation is also simultaneously present in the QD system under the influence of perpendicular electric and magnetic fields, a question, which will arise, is that how a given perturbation influences the competition effects.

*Author to whom correspondence should be addressed.
Email: bask@upatras.gr
Received: 2 August 2013
Accepted: 2 October 2013

In this contribution, we theoretically investigate the combination effects of the electric and magnetic fields on the donor binding energy in disc-shaped QDs with emphasis on the competition effects between the two fields under the externally applied pressure and temperature. The electric field is applied along the radial direction, while the magnetic field is applied perpendicular to it which is along the QD growth direction. The numerical approach we use for the present calculations is the potential morphing method (PMM)[21] in the framework of the effective mass approximation, which has been proved to be a robust tool for the calculations of impurity-related electronic and optical properties in a QD system.[13,20,22,23] The rest of the paper is organized as follows: in Section 2, we define our model and explain the general theory. In Section 3, we present numerical results and discussions, and the conclusions are given in Section 4.

2. THEORETICAL FRAMEWORK

In the framework of effective mass approximation, an on-center shallow donor impurity in a disc-shaped QD with radius R, under the influence of the electric and magnetic fields, applied pressure and temperature, can be modeled by the Hamiltonian

$$\hat{H} = \left(\hat{p} + \frac{e}{c}\vec{A}(\vec{r})\right)\frac{1}{2m_e^*(P,T)}\left(\hat{p} + \frac{e}{c}\vec{A}(\vec{r})\right) + V(\vec{r},P,T) + |e|\vec{E}\cdot\vec{r} - \frac{e^2}{4\pi\epsilon_0\epsilon_r(P,T)|\vec{r}|} \quad (1)$$

The first term of the Hamiltonian is the Kinetic term of the delocalized conduction electron under the influence of the z-axis magnetic field ($\vec{B} = B\vec{z}$ (see Fig. 1), where B is the magnitude of the magnetic field and $\vec{z}$ is the z-axis unit vector). $\vec{A}$ is the vector potential. In the cylindrical gauge ($\vec{A} = (1/2)\vec{B}\times\vec{r}$), the operator for the Kinetic energy of the electron (the first term of Eq. (1)) is

$$\hat{H}_{Kin} = \hat{p}\frac{1}{2m_e^*(P,T)}\hat{p} + \frac{eB}{2m_e^*(P,T)c}\hat{l}_z + \frac{e^2B^2}{8m_e^*(P,T)c^2}(x^2+y^2)$$

where e is the absolute value of the electron charge, c is the speed of the light in vacuum, and $\hat{l}_z$ is the z-component of the angular momentum operator. $m_e^*(P,T)$ is the pressure and temperature dependent electron effective mass, which is given by[24]

$$m_e^*(P,T) = \frac{m_0}{1 + E_P^\Gamma[(2/(E_g^\Gamma(P,T))) + (1/(E_g^\Gamma(P,T)+\Delta_0))]} \quad (2)$$

in which m_0 is the bare mass of the electron, P and T stand for the applied pressure and temperature, respectively, $E_P^\Gamma = 7.51$ eV is an energy related to the momentum matrix element and the spin-orbit splitting for GaAs QD is $\Delta_0 = 0.341$ eV. E_g^Γ is the pressure and temperature dependent energy gap at Γ point in the Brillouin zone for GaAs QD, which is the following[25,26]

$$E_g^\Gamma(P,T) = E_g^\Gamma(0,T) + aP + bP^2 \quad (3)$$

where $a = 1.07\times10^{-2}$ eV/kbar, $b = -3.77\times10^{-5}$ eV/kbar^2, and

$$E_g^\Gamma(0,T) = \left[1.519 - \frac{5.045\times10^{-4}T^2}{T+204}\right] \quad (4)$$

in unit of eV. $V(\vec{r},P,T)$ is the pressure and temperature dependent conduction electron confinement potential, which is given by

$$V(\vec{r},P,T) = V_0(P,T)\Theta(|\vec{r}|-R) \quad (5)$$

where Θ is the Heaviside step function and $\vec{r}$ is the position vector with $|\vec{r}| = \sqrt{x^2+y^2}$, where x and y are the Cartesian coordinates, respectively. The pressure and temperature dependent conduction band discontinuity at the interface of the GaAs/AlGaAs heterostructure is

$$V_0(P,T) = Q[E_{Gap}^{Al_xGa_{1-x}As}(P,T) - E_{Gap}^{GaAs}(P,T)] \quad (6)$$

where Q is the conduction band offset which is assumed to be pressure independent and taken as $Q = 60\%$ for GaAs/AlGaAs heterostructure. The pressure and temperature dependent band gap is provided by[27]

$$E_{Gap}^i(P,T) = E_1^i + \beta^i P + \alpha^i T^2/(T+T_1^i) \quad (7)$$

where for GaAs (i = GaAs), $E_1 = 1.519$ eV, $\alpha = -5.405\times10^{-4}$ eV/K, $\beta = 10.7\times10^{-3}$ eV/kbar and $T_1 = 204$ K at Γ point, while for $Al_xGa_{1-x}As$ ($i = Al_xGa_{1-x}As$), $E_1 = 1.519 + 1.155x + 0.37x^2$ eV, $\alpha = -5.405\times10^{-4}$ eV/K,

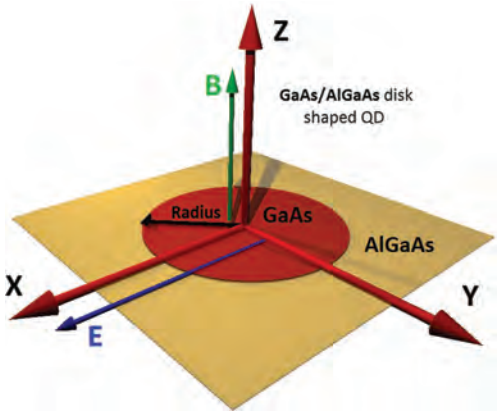

Fig. 1. Schematic representations of a GaAs/AlGaAs disc-shaped QD under the influence of the applied electric and magnetic fields. The electric field ($\vec{E}$) is applied along the x-axis direction and the magnetic field ($\vec{B}$) is applied perpendicular to it which is along the z-axis direction.

$\beta = (10.8 - 3.2x + 3.8x^2) \times 10^{-3}$ eV/kbar and $T_1 = 204$ K, respectively.

The third term of Eq. (1) is the electrostatic potential induced by the external electric field with strength E, which is applied along the radial direction in our calculations (see Fig. 1). ϵ_0 in the last term is the permittivity in vacuum and $\epsilon_r(P,T)$ is the pressure and temperature dependent relative dielectric constant, which is[28,29]

$$\epsilon_r(P,T) = \begin{cases} 12.74\exp[-1.67\times10^{-3}P] \\ \quad \cdot \exp[9.4\times10^{-5}(T-75.6)], & 0 < T \leq 200 \\ 13.18\exp[-1.73\times10^{-3}P] \\ \quad \cdot \exp[20.4\times10^{-5}(T-300)], & T \geq 200 \end{cases} \quad (8)$$

where T is in unit of Kelvin.

To solve numerically the Schrödinger equation based on Hamiltonian (1), PMM is used. A detailed review of this method can be found in Ref. [21]. In our calculations, the usual two-dimensional (2D) harmonic oscillator is chosen as a reference system and its ground-state wave function is selected as the initial wave function. The interaction potential corresponding to the ground-state energy of the electron is

$$V_S^e = \frac{eB}{2m_e^*(P,T)c}\hat{l}_z + \frac{e^2B^2}{8m_e^*(P,T)c^2}(x^2+y^2) + V(\vec{r},P,T) + |e|\vec{E}\cdot\vec{r} \quad (9)$$

whereas, the interaction potential for the ground-state energy of the shallow donor impurity is

$$V_S^i = \frac{eB}{2m_e^*(P,T)c}\hat{l}_z + \frac{e^2B^2}{8m_e^*(P,T)c^2}(x^2+y^2) + V(\vec{r},P,T) + |e|\vec{E}\cdot\vec{r} - \frac{e^2}{4\pi\epsilon_0\epsilon_r(P,T)|\vec{r}|} \quad (10)$$

The binding energy of the shallow donor impurity is defined as

$$E_b = E_0 - E_i \quad (11)$$

where E_0 is the electron ground-state energy (without the last term of Eq. (1)) and E_i is the impurity ground-state energy (with the last term of Eq. (1)). To study the competition effects of the applied electric and magnetic

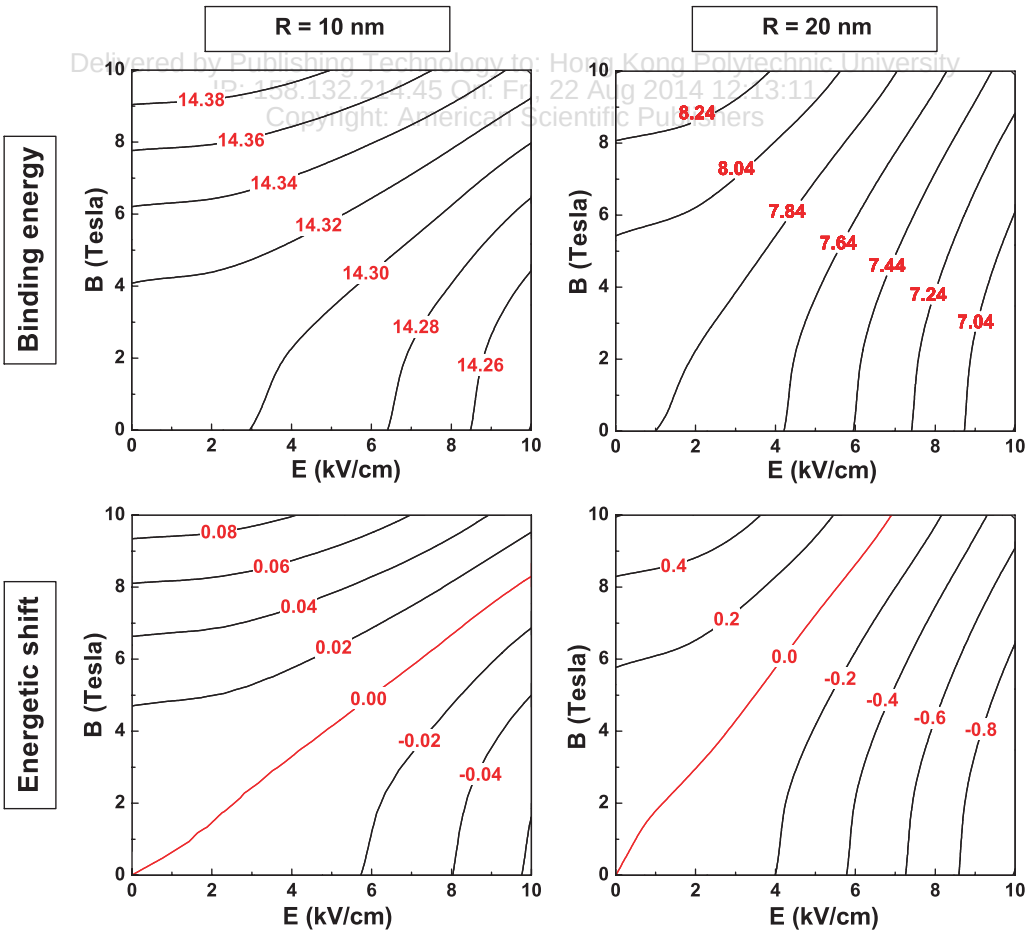

Fig. 2. Contour plot of the binding energy of an on-center donor impurity E_b (upper panel, in unit of meV) and the energetic shift of the donor binding energy (δE_b) (lower panel, in unit of meV) for various electric (E) and magnetic (B) fields in GaAs/$Al_{0.3}Ga_{0.7}As$ disc-shaped QDs at room temperature ($T = 300$ K) and zero pressure ($P = 0$). Two dot sizes $R = 10$ nm (left panel) and 20 nm (right panel) are considered, respectively.

fields, we defined the energetic shift of the donor binding energy as[20]

$$\delta E_b = E_b(F\neq 0, B\neq 0) - E_b(F=0, B=0) \qquad (12)$$

3. NUMERICAL RESULTS AND DISCUSSION

In what follows, we present our results for the combination effects of the electric and magnetic fields on the binding energy of an on-center donor impurity in GaAs/$Al_{0.3}Ga_{0.7}As$ disc-shaped QDs under externally applied pressure and temperatures. A position independent electron effective mass is used in the present calculations as an approximation and the dielectric mismatch between the dot and barrier materials is not considered.

As a first step towards the combination effects of the electric and magnetic fields on the binding energy of an on-center donor impurity in disc-shaped QDs, we present several suitable contour plots (see Fig. 2) of the donor binding energy and the energetic shift of the donor binding energy for various electric (0–10 kV/cm) and magnetic (0–10 Tesla) fields. The calculations are performed for two dot sizes ($R = 10$ nm and 20 nm). The obtained results show that for any magnetic field, the applied electric field tends to decrease the donor binding energy. Whereas, an increase in the magnetic field appears to enhance significantly the binding energy for any electric field. This is due to fact that the electric field pushes the electron density far away from the impurity center, while its magnetic counterpart squeezes the electron probability with respect to the impurity center. When these two fields are simultaneously employed in the QD systems, competition effects appear. A visualization of these effects can be found in the lower panel of Figure 2. It shows that there is a critical line (see the red lines in Fig. 2) corresponding to the zero energetic shift of the donor binding energy ($\delta E_b = 0$) under the influence of the applied electric and magnetic fields, irrespectively of the dot sizes. The area above the critical line which satisfies $\delta E_b > 0$ represents the "blue shift" of the donor binding energy and the region below the critical line determined by $\delta E_b < 0$ describes the "red shift" of the donor binding energy.

A "red shift" of the donor binding energy means essentially that the electric field effect is dominant over its magnetic field counterpart and finally a negative energetic shift of the donor binding energy is exhibited. Conversely, if the magnetic field effect is more pronounced,

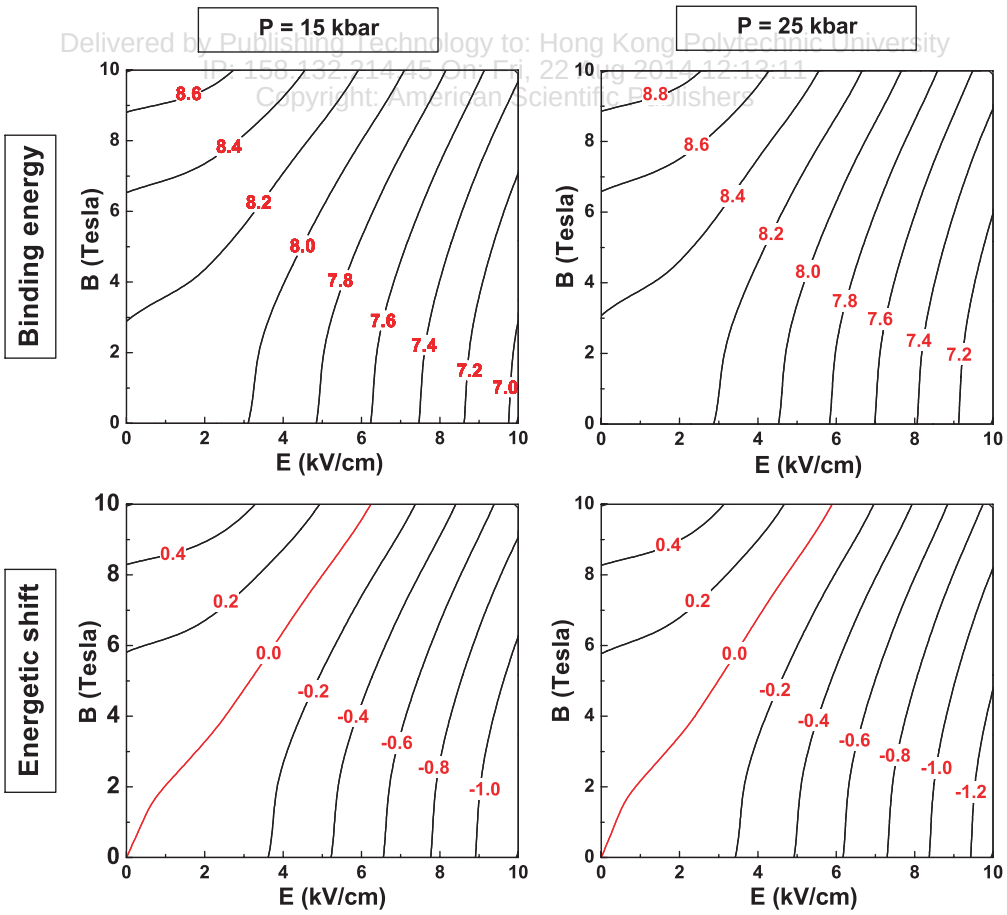

Fig. 3. Contour plot of the binding energy of an on-center donor impurity E_b (upper panel, in unit of meV) and the energetic shift of the donor binding energy (δE_b) (lower panel, in unit of meV) for various electric (E) and magnetic (B) fields in GaAs/$Al_{0.3}Ga_{0.7}As$ disc-shaped QDs with radius $R = 20$ nm at room temperature ($T = 300$ K). Two pressure values ($P = 15$ kbar (left panel) and 25 kbar (right panel)) are considered, respectively.

the energetic shift of the donor binding energy is positive ($\delta E_b > 0$) and a "blue shift" of the donor binding energy appears. An increase in the dot size leads to a decrease in the donor binding energy but favors both the electric and magnetic field effects. This can be easily conformed by the significantly increased energetic shift of the donor binding energy in QDs within the weak confinement regime in comparison to the ones in the strong confinement regime. When the dot size increases, the applied electric field effect appears to be more pronounced than its magnetic field counterpart. This causes an enlarged region which describes the "red shift" of the donor binding energy ($\delta E_b < 0$). As a result, the critical line presents a considerable counterclockwise planer rotation as the dot size increases.

For the QDs in the weak confinement regime ($R = 20$ nm), we also present in Figure 3 the contour plots of the donor binding energy and energetic shift of the donor binding energy for various electric and magnetic fields, where two different pressures are considered. It shows that the applied electric and magnetic fields retain a very similar effect on the donor binding energy in the presence of the pressure as in the zero pressure case (see the plots in the right panel of Fig. 2). However, when the pressure increases, the donor binding energy increases at given electric and magnetic fields. This is associated with the modification of the material parameters induced by the applied pressure. The electron effective mass increases with increasing the pressure, while the relative dielectric constant and electron confinement potential (V_0) tend to decrease as the pressure increases. The joint effects of the variation of these material parameters leads to an effectively enhanced Rydberg energy with increasing the pressure and finally an increase in the donor binding energy is present.

Figure 3 also shows that for any applied pressure, the critical line determined by the zero energetic shift of the donor binding energy appears (see the red lines in the plots on the lower panel). The presence of the applied pressure turns out to favor more the electric field effect, which causes an increase in the region determined by the "red shift" of the donor binding energy ($\delta E_b < 0$). Consequently, the critical line experiences a slight counterclockwise rotation when the applied pressure increases.

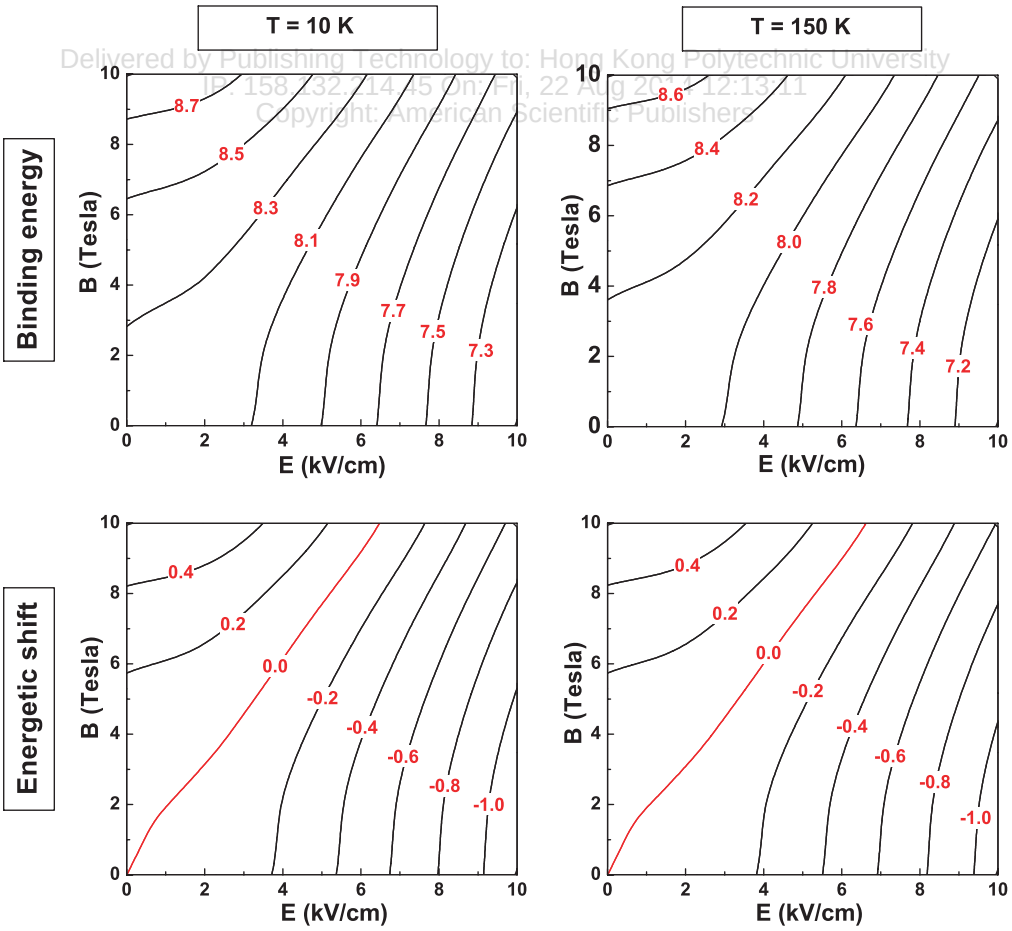

Fig. 4. Contour plot of the binding energy of an on-center donor impurity E_b (upper panel, in unit of meV) and the energetic shift of the donor binding energy (δE_b) (lower panel, in unit of meV) for various electric (E) and magnetic (B) fields in GaAs/$Al_{0.3}Ga_{0.7}As$ disc-shaped QDs with radius $R = 20$ nm at zero pressure ($P = 0$). Two temperature values ($T = 10$ K (left panel)and 150 K (right panel)) are considered, respectively.

Finally, in an effort to show the competition effects of the electric and magnetic fields in a disc-shaped QD under the influence of temperature, we display in Figure 4 the contour plots of the donor binding energy and energetic shift of the donor binding energy for various electric and magnetic fields, where two different temperature values are considered. As the first glance of the figure, one could find that increasing the temperature causes a decrease in the donor binding energy for any electric and magnetic fields (see the right plots of Fig. 2). This is related to the temperature dependent variation of the material parameters. As indicated explicitly from Eqs. (2) and (8), an increase in the temperature appears to decrease the electron effective mass and enhance the relative dielectric constant. Consequently, a reduce in the Rydberg energy occurs and the donor binding energy decreases as the temperature increases. Similarly to what Figure 3 shows, the critical line described by $\delta E_b = 0$ appears for any temperature considered. It also appears from Figure 4 that the presence of the temperature do not have any significant influence on the competition effect of the electric and magnetic fields on the binding energy of an on-center donor impurity in disc-shaped QDs. This can be clearly confirmed by the invariant position of this critical line in Figure 4 (see the plots on the lower panel).

4. CONCLUSIONS

In summary, we have studied the combination effects of the electric and magnetic fields on the binding energy of an on-center donor impurity in disc-shaped $GaAs/Al_{0.3}Ga_{0.7}As$ quantum dots (QDs), emphasizing on the competition effects between these two fields under various externally applied pressures and temperatures. The electric field is applied along the radial direction, while the magnetic field is applied perpendicular to it, which is along the growth direction of the QD. It is found that the enhanced electric field decreases the donor binding energy, while the simultaneously applied magnetic field exhibits a reversed effect, increasing the binding energy with increasing the field strength. These competition effects between the two fields lead to a critical line in which the donor binding energy keeps invariant as in the zero field case. The position of this line is found to be strongly dependently on the QD sizes. Comparing to the magnetic field effect, an increase in the QD size causes a more pronounced electric field effect which in turn enhances drastically the region corresponding to the "red shift" of the donor binding energy. The applied pressure exhibits a very similar but weaker effect on the critical line as the QD sizes, favoring more the electric field effect. Although the increased temperature effect turns out to decrease the donor binding energy, it does not have significant influence on the competition effects between the two fields. We believe that the results presented here can be useful for the doped GaAs/AlGaAs QDs based functional devices.

Acknowledgments: This research has been co-financed by the European Union (European Regional Development Fund-ERDF) and Greek national funds through the Operational Program "Regional Operational Programme" of the National Strategic Reference Framework (NSRF)-Research Funding Program: Support for research, technology and innovation actions in Region of Western Greece (MIS: 312123, D.237.002). Furthermore, this work is also supported by the research project "C. Caratheodory" D. 207 of the Research Committee of the University of Patras.

References and Notes

1. D. Mocatta, G. Cohen, J. Schattner, O. Millo, E. Rabani, and U. Banin, *Science* 332, 77 (**2011**).
2. R. Rahman, G. P. Lansbergen, S. H. Park, J. Verduijn, G. Klimeck, S. Rogge, and L. C. L. Hollenberg, *Phys. Rev. B* 80, 165314 (**2009**).
3. B. E. Kane, *Nature (London)* 393, 133 (**1998**).
4. J.-L. Zhu, J. Wu, R. T. Fu, H. Chen, and Y. Kawazoe, *Phys. Rev. B* 55, 1673 (**1997**).
5. R. Charrour, M. Bouhassoune, M. Fliyou, D. Bria, and A. Nougaoui, *J. Phys.: Condens. Matter.* 12, 4817 (**2000**).
6. S.-S. Li and J.-B. Xia, *J. Appl. Phys.* 100, 083714 (**2006**); *J. Appl. Phys.* 101, 093716 (**2007**).
7. W. Xie, *Physica B* 403, 2828 (**2008**); L. Yang and W. Xie, *Physica B* 407, 3884 (**2012**).
8. C. Xia, Z. Zeng, and S. Wei, *J. Appl. Phys.* 107, 014305 (**2010**); *J. Appl. Phys.* 108, 054307 (**2010**).
9. G. M. Huang, Y. M. Liu, and C. G. Bao, *Phys. Rev. B* 71, 075302 (**2005**).
10. A. J. Peter, *Physica E* 28, 225 (**2005**).
11. S. T. Perez-Merchancano, H. Paredes-Gutierrez, and J. Silva-Valencia, *J. Phys.: Condens. Matter.* 19, 026225 (**2007**).
12. M. Kirak, S. Yilmaz, M. Sahin, and M. Gencaslan, *J. Appl. Phys.* 109, 094309 (**2011**).
13. Z. Zeng, C. S. Garoufalis, S. Baskoutas, and A. F. Terzis, *J. Appl. Phys.* 112, 064326 (**2012**).
14. A. Sivakami and V. Gayathri, *Superlattice Microst.* 58, 218 (**2013**).
15. V. Nguyen, M. Nguyen, and T. Nguyen, *Physica B* 292, 153 (**2000**).
16. S. Sahoo, Y. Lin, and Y. Ho, *Physica E* 40, 3107 (**2008**).
17. M. G. Barseghyan, A. A. Kirakosyan, and C. A. Duque, *Phys. Status Solidi B* 246, 626 (**2009**); *Eur. Phys. J. B* 72, 521 (**2009**).
18. C. Dane, H. Akbas, S. Minez, and A. Guleroglu, *Physica E* 42, 1901 (**2010**).
19. G. Rezaei and S. S. Kish, *Physica E* 45, 56 (**2012**).
20. Z. Zeng, C. S. Garoufalis, and S. Baskoutas, *J. Phys. D: Appl. Phys.* 45, 235102 (**2012**).
21. M. Rieth, W. Schommers, and S. Baskoutas, *Int. J. Mod. Phys. B* 16, 4081 (**2002**).
22. İbrahim Karabulut and S. Baskoutas, *J. Appl. Phys.* 103, 073512 (**2008**).
23. Z. Zeng, C. S. Garoufalis, A. F. Terzis, and S. Baskoutas, *J. Appl. Phys.* 114, 023510 (**2013**).
24. C. A. Moscoso-Moreno, R. Franco, and J. Silva-Valencia, *Phys. Status Solidi B* 246, 486 (**2009**).
25. H. Ehrenreich, *J. Appl. Phys.* 32, 2155 (**1961**).
26. B. Welber, M. Cardona, C. K. Kim, and S. Rodriguez, *Phys. Rev. B* 12, 5729 (**1975**).
27. C. A. Duque, S. Y. López, and M. E. Mora-Ramos, *Phys. Status Solidi B* 244, 1964 (**2007**).
28. E. Li, *Physica E* 5, 215 (**2000**).
29. H. Odhiambo Oyoko, N. Porras-Montenegro, S. Y. López, and C. A. Duque, *Phys. Status Solidi C* 4, 298 (**2007**).

Paper X

In which we study the electronic and optical properties of wurtzite ZnS colloidal quantum dots ...

THE JOURNAL OF PHYSICAL CHEMISTRY C

Article

pubs.acs.org/JPCC

New Insights in the Excitonic Emission of ZnS Colloidal Quantum Dots

Zaiping Zeng, Christos S. Garoufalis, and Sotirios Baskoutas*

Materials Science Department, University of Patras, 26504 Patras, Greece

ABSTRACT: We have studied the electronic and optical properties of wurtzite ZnS colloidal quantum dots by means of atomistic empirical pseudopotential method complemented by configuration interaction calculations. For this purpose, we have developed a new set of reliable pseudopotentials (for Zn and S) which give an accurate and balanced description of ZnS bulk properties. Our results for the size-dependent optical gap are found to be in excellent agreement with the experimental measurements, offering valuable information with regard to the nature of the near-band-edge excitons. In particular, it is found that not only the first optically allowed exciton is an A-exciton for the full range of dot sizes but also all the pronounced emission peaks exhibit an in-plane polarization (i.e., A or B excitons). Under normal conditions, the C-exciton emissions which are common in the ZnO analogues are found to be inactive in the lower part of the excitonic spectrum of ZnS colloidal quantum dots.

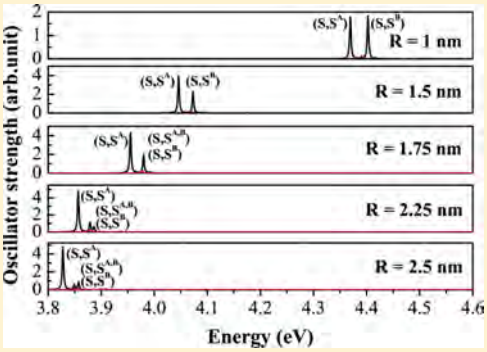

INTRODUCTION

Zinc sulfide (ZnS), as one of the typical II−VI semiconductor compounds, is an excellent optical material having a wide optical transparency from the ultraviolet (UV) to the far-infrared (IR) region.[1,2] It is also widely used for flat panel displays,[3] laser,[4] sensor,[5] cathode ray tube, and electroluminescence device[3,6] applications. ZnS usually crystallizes into a cubic zinc-blende (ZB) structure at low temperature which transforms to a more stable hexagonal wurtzite (WZ) structure above 1020 °C under normal pressure.[7,8] Comparing to the ZB counterpart, WZ ZnS exhibits a higher ionization transition rate, and therefore, has a higher optical gain.[9] The most recent developments are toward nanostructured ZnS, such as nanowires, nanoribbons, nanotubes, and quantum dots (QD). Great progress in the fabrication and characterization of ZnS nanostructures for device application purposes has been made (see ref 10 and references therein). However, several important challenges still remain and await for being explored. One of them is the application of ZnS in transparent and flexible electronics because of the challenge which exists in optimization of nanodevice performances. Although several ways to optimize the performances of ZnS-based devices have been exploited, more work on tuning the conductivity, band gap, and surface and optical properties is still quite desired.[10]

From a theoretical standpoint, density functional theory (DFT) calculations have been widely employed for the study of the bulk ZnS band structure[11−13] and the geometric and the electronic properties of ZnS nanowires, nanotubes, and nanosheets.[14] These types of calculations are restricted to nonpassivated and small-size nanostructures. Because in DFT the band gap in bulk ZnS is not well-reproduced,[12] the description of the quantum confinement effects in ZnS nanostructures is questionable. Furthermore, effective mass and tight-binding models have been applied to interpret the experimental measurements of ZnS QDs with realistic sizes. However, these approaches are either only appropriate for QDs within the weak confinement regime or significantly underestimate the optical band gap.[15]

In this contribution, we derived a new empirical pseudopotential for wurtzite ZnS, which reproduced well the experimental and theoretical bulk properties, such as band gap, critical energy levels, effective masses, crystal field, and spin−orbit splitting. This allows us to calculate electronic and optical properties of wurtzite ZnS QDs with realistic sizes at an atomistic level by means of an empirical pseudopotential method and configuration interaction approach. We studied the size-dependent optical band gap, Stokes shift, and optical emission polarizations of ZnS colloidal QDs. Our calculated optical band gap is in very good agreement with the experimental work. For the full range of QD sizes studied, the near-band-edge exciton emission is polarized along the in-plane direction, corresponding to A-exciton emission.

METHOD

We follow the atomistic empirical pseudopotential method[16−20] and derive new pseudopotentials for Zn and S. The Hamiltonian has the form

$$\hat{H} = -\frac{1}{2}\nabla^2 + \sum_{n\alpha}[v_\alpha(\vec{r} - \vec{R}_{an}) + \hat{v}_\alpha^{SO}] \quad (1)$$

Received: March 10, 2014
Revised: April 22, 2014
Published: April 24, 2014

where n is an atomic index, α specifies the atom type, and $\hat{v}_\alpha^{SO}$ is the nonlocal spin−orbit operator, including one parameter λ for each atom type. This method has been reviewed in more detail in ref 21. The screened atomic pseudopotentials v_α (with α = Zn, S) are centered at each atomic position, and their superposition generates the crystal potential. In the present work, we employed pseudopotentials with four free parameters, which are defined in reciprocal space, having the analytic form

$$v_\alpha(q) = \frac{\alpha_1(q^2 - \alpha_2)}{\alpha_3 e^{\alpha^4 q^2} - 1} \tag{2}$$

This exponential type of pseudopotential has been successfully adopted previously for the study of electronic and optical properties of wurtzite ZnO nanostructures.[17−20] The quasicubic model of Hopfield[22] is adopted to obtain the spin−orbit Δ_{so} and crystal-field Δ_{cr} splittings

$$E_A(\Gamma_{9v}) = \frac{1}{2}(\Delta_{so} + \Delta_{cr})$$

$$E_{B(C)}(\Gamma_{7v}) = \pm\frac{1}{2}\left[(\Delta_{so} + \Delta_{cr})^2 - \frac{8}{3}\Delta_{so}\Delta_{cr}\right] \tag{3}$$

where E_A, E_B, and E_C are the energies of the top three valence bands at Γ point of the Brillouin zone.

We used the experimental structure parameters of bulk wurtzite ZnS, which are listed in Table 1, to generate the atomic pseudopotentials. The plane wave energy cutoff is 8.5 Ryd, and the kinetic energy is not rescaled. During the generation procedure, larger weight has been allocated to the quantities close to the conduction band minimum (CBM) and the valence band maximum (VBM), while smaller weight has been put on the quantities which are remote from CBM and VBM. This procedure stops until the known bulk properties of wurtzite ZnS, such as the energy gaps at specific symmetry points of the Brillouin zone, the perpendicular and parallel effective masses of electron and hole, the spin−orbit, and the crystal-field splitting (see Table 2), are well-reproduced.

Table 1. Structure Parameters *a*, *c*, *u*, and *c*/*a* for Wurtzite ZnS

a (Å)	c (Å)	u	c/a
3.811[23]	6.234[23]	0.375[23]	1.63579[23]

The optimized four free parameters for Zn and S are listed in Table 3, and the volume normalized local parts of the Zn and S pseudopotentials are presented in Figure 1a. Using these pseudopotentials, the computed quantities of bulk wurtzite ZnS are in very good agreement with existing experimental and theoretical results (see Table 2). The calculated band structure is depicted in Figure 1b which reproduces almost exactly the result of Bergstresser and Cohen.[28]

Table 3. Empirical Pseudopotential Parameters $a_{1,2,3,4}$ and Spin−Orbit Parameter λ

	a_1	a_2	a_3	a_4	λ
Zn	−5.091 010	0.000 005	−0.011 512	0.285 308	0.1165
S	−20.220 911	3.750 462	−0.000 227	1.465 173	0.0

After deriving the reliable atomic pseudopotentials, we turn our attention to the study of the electronic and optical properties of wurtzite ZnS colloidal QDs. The QDs are cut from the bulk ZnS with a spherical shape, being centered on a sulfide atom. The surface-dangling bonds are passivated by employing a high band gap artificial material, as successfully practiced previously.[17,18,20,29,30] The single-particle electron and hole eigenenergies and wave functions are calculated by the aforementioned empirical pseudopotential method which naturally includes the effects of multiband coupling, multivalley coupling, and spin−orbit interaction. The many-body excitonic properties are calculated via configuration interaction (CI) approach,[31] and the excitonic wave functions are expanded in terms of single-substitution Slater determinants constructed from the single-particle wave functions of electrons and holes. The Coulomb and exchange integrals are screened by the position-dependent and size-dependent screening function proposed by Resta,[32] which gives a smooth transition from short-range (unscreened) to long-range (screened).[30,31] We include in the CI treatment 4 states from the conduction band and 12 states from the valence band. The optical dipole matrix elements are calculated within the dipole approximation, and the oscillator strength is calculated using Fermi's golden rule.

Table 2. Compiled Reference Bulk Properties and Empirical Pseudopotential Results (Including Spin−Orbit Interaction) Using the Parameters Presented in Table 3

quantities	experiment	theory	targets	EPM
$E_g(\Gamma_{1c} - \Gamma_{6v})$	3.864,[24] 3.872,[24] 3.75,[25] 3.76,[26] 3.78[27]	1.968,[12] 2.211,[12] 2.260[12]	3.75	3.739
$E_g(\Gamma_{3c} - \Gamma_{1c})$		1.5[28]	1.5	1.59
$E_g(\Gamma_{6c} - \Gamma_{1c})$		4.4[28]	4.4	4.40
$E_g(H_{3c} - \Gamma_{1c})$		2.7[28]	2.7	2.55
$E_g(K_{2c} - \Gamma_{1c})$		1.8[28]	1.8	1.526
$E_g(M_{1c} - \Gamma_{1c})$		1.6[28]	1.6	1.52
$m_e^\perp$		0.33,[24] 0.153,[12] 0.199,[12] 0.157[12]	0.33	0.079
$m_e^\parallel$	0.24[24]	0.144,[12] 0.142,[12] 0.138[12]	0.24	0.100
$m_A^\perp$	0.49[24]	3.838,[12] 1.713,[12] 2.914,[12] 1.470[23]	0.49	1.15
$m_A^\parallel$	1.40[24]	1.746,[12] 2.176,[12] 1.785,[12] 1.51[23]	1.40	5.02
$m_B^\perp$		0.485,[24] 0.180,[12] 0.198,[12] 0.195[12]	0.485	0.21
$m_B^\parallel$		0.53,[24] 0.756,[12] 0.402,[12] 0.621[12]	0.53	0.42
$m_C^\perp$		0.75,[24] 0.337,[12] 0.443,[12] 0.303[12]	0.75	1.23
$m_C^\parallel$		0.32,[24] 0.183,[12] 0.440,[12] 0.339[12]	0.32	0.27
Δ_{cr}	0.058,[24] 0.055,[24] 0.029[24]	0.052,[12] 0.049,[12] 0.055[12]	0.0580	0.0526
Δ_{so}	0.086,[24] 0.089,[24] 0.092[24]	0.027,[12] 0.025,[12] 0.026[12]	0.086	0.0926

dx.doi.org/10.1021/jp5024108 | J. Phys. Chem. C 2014, 118, 10502−10508

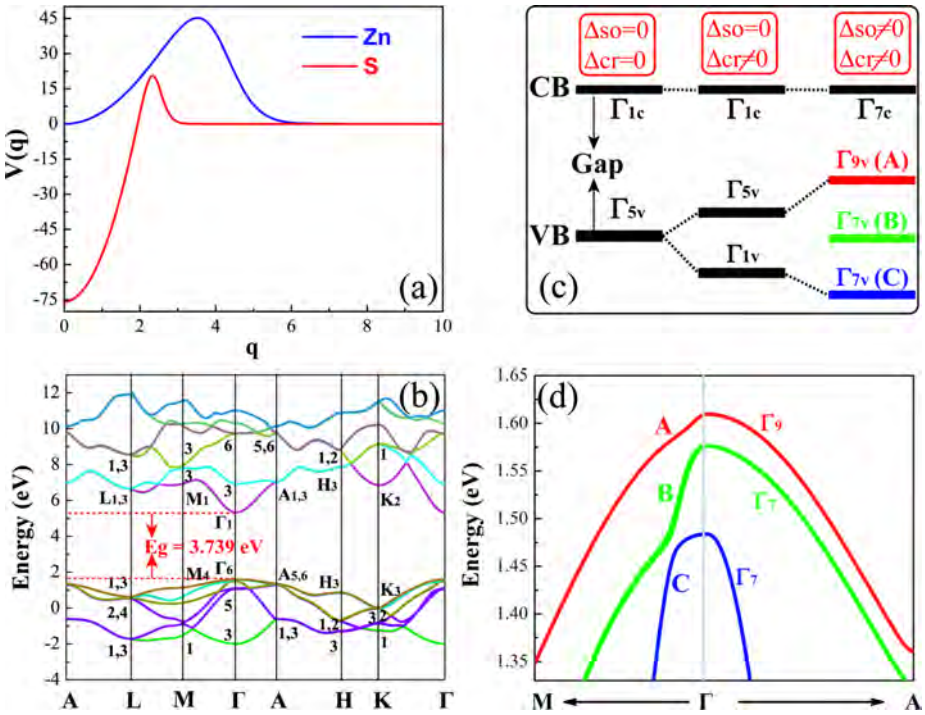

Figure 1. (a) Normalized atom pseudopotentials for Zn and S. (b) Band structure of wurtzite ZnS by our empirical pseudopotential methods (EPM) including spin−orbit interaction. (c) Schematic representation of the symmetry evolution of the conduction band minimum (CBM) and valence band maximum (VBM) of bulk ZnS by the crystal-field and spin−orbit splitting. (d) Topmost three valence bands around Γ-point of the Brillouin zone obtained by EPM including spin−orbit splitting.

NUMERICAL RESULTS AND DISCUSSION

Valence Band Ordering of Bulk Zinc Sulfide. Before presenting our QD results, we briefly describe the valence band structure of bulk ZnS, which is relevant to the later discussion. Without crystal-field and spin−orbit splitting, the top valence band of ZnS is 6-fold Γ_{5v} state (see Figure 1c). This state is split into a 4-fold Γ_{5v} state and a 2-fold Γ_{1v} state by the crystal field which is a typical characteristic of wurtzite structure. The Γ_{5v} state is a p_x, p_y-like state, while Γ_{1v} state is a p_z-like state. Further inclusion of spin−orbit coupling leads to a formation of three 2-fold states at the top of the Γ-point of the Brillouin zone. For wurtzite ZnS, the spin−orbit parameter is positive, which is pretty similar to wurtzite GaN. In this conventional situation, the top three valence states, from top to bottom, are the so-called bulk A-, B-, and C-bands, respectively, which are of symmetry character Γ_{9v}, Γ_{7v}, and Γ_{7v}, respectively (see Figure 1d). These states correspond to the A-, B-, and C-exciton lines in photoluminescence experiments.[33] Although wurzite ZnS exhibits a normal valence band ordering, the generation of reliable atomistic pseudopotentials appears to be an uneasy task in comparison to its ZnO counterpart which has an abnormal valence band ordering.[17]

Electronic Properties of Zinc Sulfide Quantum Dots. We have studied wurtzite ZnS colloidal QDs with experimentally achievable sizes, which are defined by radii R = 1, 1.5, 1.75, 2.25, and 2.5 nm, respectively. The numbers of atoms for each respective radius are $Zn_{102}S_{105}$, $Zn_{356}S_{359}$, $Zn_{573}S_{575}$, $Zn_{1222}S_{1207}$, and $Zn_{1646}S_{1677}$. The geometry of our smallest QD structure is displayed in Figure 2.

First, we present the electron and hole envelope functions for each dot size in Figure 3. These envelope functions are obtained by employing a projection onto bulk technique,[17]

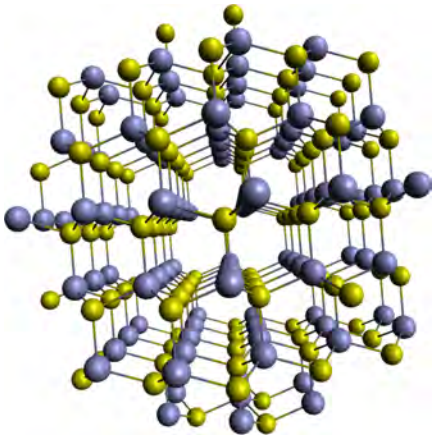

Figure 2. Geometry of our $Zn_{102}S_{105}$ quantum dot. The blue and yellow balls represent the Zn and S atoms, respectively.

which gives us the access to visualize the symmetry of the envelope functions and the parentage of the atomic wave function of each state. We use the notation ω_ζ to describe the symmetry of the envelope functions, where ω denotes the number of nodes encountered by moving across the in-plane (xy-direction) or out-of-plane (z-direction) directions, and ζ represents the direction in which we find the nodes. The possible values for ω are S, P, and so forth, where S indicates the form of the envelope function without a node (in this case, we neglect the subscript ζ), P with one node, and so forth. Using this notation, the symmetry characters for the first electron and the first four hole states are tabulated in Table 4.

dx.doi.org/10.1021/jp5024108 | J. Phys. Chem. C 2014, 118, 10502−10508

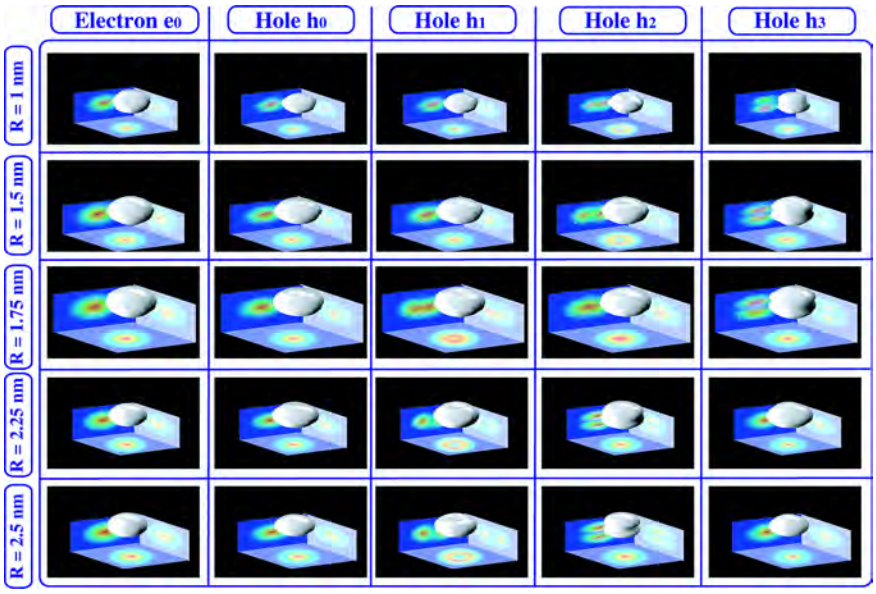

Figure 3. The first electron (e_0) and the first four hole ($h_{0,1,2,3}$) envelope functions for five different radii.

The evolution of the parentage of each hole state with respect to the dot size is pictured in Figure 4.

Table 4. Character of the First Electron and the First Four Hole Envelope Functions for Various QD Radii[a]

radius (nm)	e_0	h_0	h_1	h_2	h_3
1	S	S^A	S^B	$P^{A,B}_{xy}$	P^A_z
1.5	S	S^A	S^B	$P^{A,B}_{xy}$	P^A_z
1.75	S	S^A	$P^{A,B}_{xy}$	S^B	P^A_z
2.25	S	S^A	$P^{A,B}_{xy}$	P^A_z	S^B
2.5	S	S^A	$P^{A,B}_{xy}$	P^A_z	S^B

[a]The superscript (A or B) indicates the corresponding hole state parentage (A-band, B-band, or A, B-bands mixing).

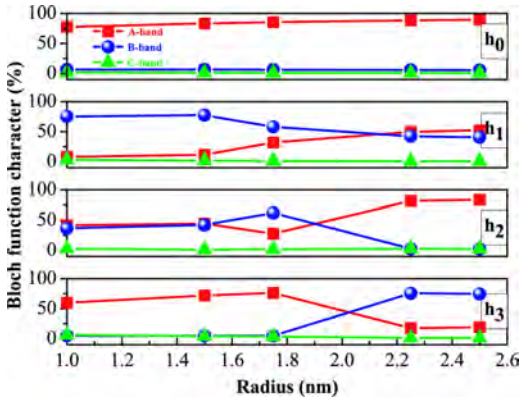

Figure 4. Bloch function characters of the first four hole states for various radii. The red, green, and blue colors correspond to the bulk bloch A-, B-, and C-bands, respectively.

We find from Table 4 and Figure 4 that the states having S-type characters (S^A or S^B) are derived mainly from a single-band state (either A-band or B-band). These conventional S^A and S^B states are separated significantly from each other in energy, whereas their energetic dependence on the QD sizes appears to be very similar (see Figure 5). This is a consequence of the nature of the topmost valence band structure of bulk

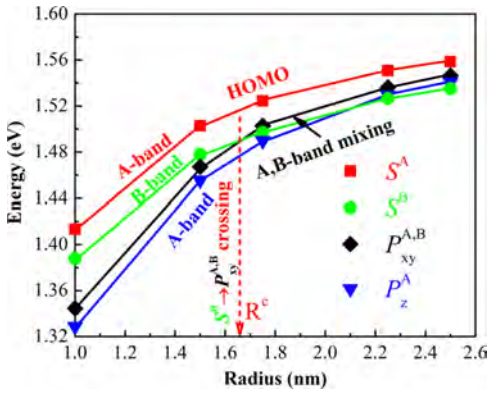

Figure 5. Single particle energies of the first four hole states as a function of the QD radius. The lines connect states that are of the same symmetry. The red (or blue), green, and black lines connect states with dominant A-band, B-band, and an even mixing of A- and B-band parentage, respectively.

ZnS, where A-band and B-band are energetically separated considerably (see Figure 1c and d). We further find that the states with an even admixture of bulk A- and B-band parentage (e.g., h_1 at R = 1.75, 2.25, and 2.5 nm) display P_{xy}-type envelope function characters. These $P^{A,B}_{xy}$ characters have also been found previously in wurtzite ZnO nanostructures[17,18,20] and very recently in wurtzite GaN nanowires,[34] being attributed to one of the consequences of the nontrivial interplay between symmetry mixing, spin−orbit coupling, and quantum confinement effects on the valence band electronic structure. Comparing to the S-like states, these states appear to be more sensitive to the quantum confinement effects, rising over the S^B state at a critical radius value R^c = 1.66 nm and becoming energetically more favorable (see Figure 5).

In addition to the S-type envelope function characters, the states with a dominant bulk Bloch A-band parentage also

dx.doi.org/10.1021/jp5024108 | J. Phys. Chem. C 2014, 118, 10502−10508

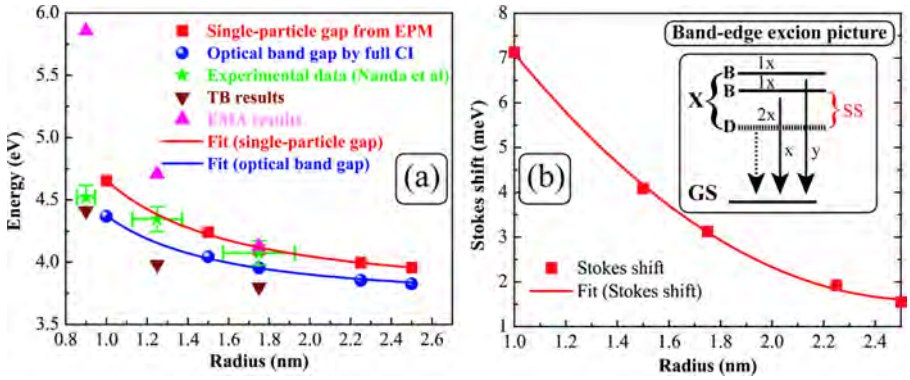

Figure 6. (a) Single-particle gap (red boxes) and optical band gap (blue circles) as a function of the QD radius. The green stars with error bars, the wine inverted triangles, and the pink regular triangles are the experimental results and the values calculated from the effective mass approximation (EMA) and the tight-binding (TB) models[15], respectively. Each line represents a fit of the band gap energy by $E_g = \alpha + \beta/R^{\gamma}$ where E_g is the band gap energy; R is the QD radius; and α, β, and γ are the fitting parameters. (b) The Stokes shift (SS, red boxes) as a function of the QD radius. The red solid line denotes a parabolic fit of the Stokes shift. The inset shows the near-band-edge exciton picture and corresponding emission polarization directions (x or y). X indicates the near-band-edge exciton (A-exciton) which consists of a doubly degenerate (2×) dark (D) state and two nondegenerate (1×) bright (B) states decaying to the ground state (GS).

exhibit P-like characters (e.g., h_3 at R = 1, 1.5, and 1.75 nm, see Table 4) with a node exclusively along the out-of-plane direction. The reason for the fact that the P^A_{xy}-like states are energetically separated from the P^A_z-like states is related to the anisotropic hole effective masses of the bulk A-band, which is larger along the direction parallel to the c-axis ($m^*_{A\|} > m^*_{A\perp}$, see Table 2). This favors a state with a node along the out-of-plane direction, P^A_z, rather than with a node along the in-plane direction, P^A_{xy}. These P^A_z-like states are energetically very close to the $P^{A,B}_{xy}$ states, showing a similar sensitivity of energy to the variation of the quantum confinement effects (see Figure 5). In contrast to the A-band and B-band states, the states with dominant C-band parentage are not energetically very favorable, being remote from the highest occupied molecular orbital (HOMO) state (e.g., h_9 at R = 1.5 nm, not shown in the figures for clarity). The lowest unoccupied molecular orbital (LUMO) state turns out to be a single band object deriving purely from bulk Γ_{7c} band and presenting an S-type envelope function.

Optical Properties of Zinc Sulfide Quantum Dots. We present the optical band gap of ZnS colloidal QDs with realistic sizes in Figure 6. The necessary material parameters used in our calculations are given in ref 35. The calculations are performed at single-particle level and configuration interaction (CI) level. The calculated optical band gap appears to be in very good agreement with the experimental measurements by Nanda et al.[15] for the full range of QD sizes in comparison to the results based on the effective mass model[36,37] and the semiempirical tight binding model.[38] The dependence of the band gap on the QD radius is best fitted by $E_g^{SP} = E_g^{bulk} + 0.91/R^{1.61}$ at single-particle (SP) level in which E_g^{bulk} = 3.75 eV is the fundamental gap of bulk ZnS (see Table 2) and by $E_g^{CI} = E_g^{bulk,opt} + 0.66/R^{1.79}$ at full CI level in which $E_g^{bulk,opt}$ = 3.709 eV is the optical gap of bulk ZnS. Here, E_g is in the unit of eV and R is in the unit of nm. The exciton binding energy can be obtained by subtracting the SP results from the correlated results (CI results), best fitted by $E_b^X = E_b^{X,bulk} + 240.95/R^{1.81}$ where $E_b^{X,bulk}$ = 41 meV is the exciton binding energy of bulk ZnS at room temperature[39] and where all the energies are in the unit of meV. In an attempt to bridge our findings to other material systems, the scaling law associated with the calculated exciton binding energy can also be written as $E_b^X \sim 1/R^n$ with n = 0.919, which appears to be larger than its counterpart for CdSe colloidal QDs obtained theoretically by Franceschetti and Zunger (i.e., n = 0.86[40]) and experimentally by Meulenberg et al. (i.e., n = 0.72[41]). We also find that the obtained exciton binding energy exhibits a sublinear dependence on the QD radius, which is consistent with the results reported previously for CdSe QDs.[40,41] As expected from the quantum confinement effects, the exciton binding energy is significantly enhanced in colloidal ZnS QDs in comparison to bulk ZnS, giving 130 meV at R = 2.5 nm, 145 meV at R = 1.75 nm, and 284 meV at R = 1 nm.

The near-band-edge exciton is found to be A-exciton for all the QD sizes, which is contributed nearly purely from HOMO−LUMO transition, where the HOMO state has an S-like symmetry character and derives dominantly from bulk A-band. This type of exciton consists of two optically passive (dark) states and two optically active (bright) states (see Figure 6b). The formation of these dark-exciton (or bright-exciton) states originates from the electron-hole exchange interaction.[42,43] The exchange interaction gives rise to the splitting between the singlet and triplet states. The aforementioned two dark-exciton states are orbitally allowed but are spin-forbidden (spin-triplet states), being doubly degenerate and energetically favorable. The two bright-exciton states (spin-singlet states) appear to be singly degenerate and energetically very close to each other, exhibiting in-plane polarizations. The energetic difference between the first bright-exciton state and the first dark-exciton state is defined as Stokes shift (SS). The SS is in the scale of 10^{-3} eV, being a decreasing function of the QD sizes (see Figure 6b). This is qualitatively consistent with the previous reports[44−46] for wurtzite CdSe and CdS colloidal QDs. The calculated SS is found to be in a similar energy window as that of similarly sized CdSe counterparts (~5−20 meV[44]). However, it turns out to be quantitatively much smaller than that of CdS analogues (~20−70 meV for radius of R = 1−2.3 nm[46]). This is related to different near-band-edge dark-exciton mechanisms. The lowest dark-exciton state of CdS QDs is orbitally forbidden (electron-S-hole-P),[46] which is in contrast to that of CdSe[44] and our ZnS QDs with orbitally allowed but spin-forbidden (electron-S-hole-S) ground-state dark-exciton states. The dependence of our obtained SS on the

dx.doi.org/10.1021/jp5024108 | J. Phys. Chem. C 2014, 118, 10502−10508

QD radius within the range studied is best fitted by $E^{SS} = 16.31-11.43R + 2.22R^2$, where E^{SS} is in the unit of meV (see Figure 6b).

Finally, we present in Figure 7 the photoluminescence emission spectrum for various QD sizes, which are obtained by full CI at room temperature. Lorentzian broadening function is employed, and the broadening parameter is chosen as 1.5 meV. As expected, increasing the QD sizes leads to a significant redshift in the emission spectrum. This redshift is more pronounced for smaller QDs. For all the QD sizes, the pronounced emissions are polarized exclusively along the in-plane direction ($\mathbf{E}\perp\vec{c}$, α-emission[47]) and are attributed to A- and B-exciton emissions. The C-exciton emissions with out-of-plane polarization appear to be not active in ZnS colloidal QDs under normal conditions.

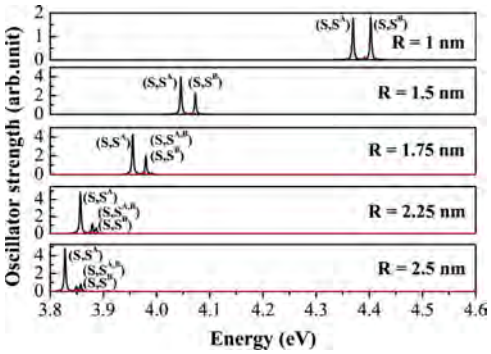

Figure 7. Oscillator strength for the emission $|X\rangle$ to $|0\rangle$ for various QD sizes obtained by full CI at room temperature. Emissions polarized along the in-plane and out-of-plane directions are shown in black and red lines, respectively. The symbols in parentheses indicate the envelope function characters of the single-particle states (e, h) involved in the emissions (for the hole state, the corresponding parentage has also been shown).

CONCLUSIONS

In conclusion, we have derived a new and reliable empirical pseudopotential for wurtzite ZnS which enables us to study the size-dependent electronic and optical properties of ZnS colloidal quantum dots at an atomistic level. The single-particle states are calculated by employing an empirical pseudopotential method, and the many-body excitonic effects are considered via configuration interaction approach. We find that the highest occupied molecular orbital (HOMO) states have a dominant bulk Bloch A-band parentage, exhibiting S-like envelope function characters. These S^A states are energetically separated significantly from their counterparts originated mainly from bulk bloch B-band with S-like envelopes. We related this to the nature of the topmost valence band structure of wurtzite ZnS where A-band and B-band are separated considerably in energy. The states with an even admixture of bulk A-band and B-band turn out to have P_{xy}-like characters.

In addition to the S-type symmetry characters, the states with a dominant A-band parentage also exhibit P-like characters but with nodes exclusively along the out-of-plane direction. This is attributed to the anisotropy of the hole effective masses of the bulk bloch A-band. The calculated optical band gaps are in excellent agreement with the experiments which confirms the accuracy of the present method. We provide scaling laws for the experimentally measurable physical quantities, such as optical band gap and Stokes shift, for the full range of QD sizes. Finally, we find that the near-band-edge exciton is A-exciton and that the pronounced exciton emissions are from A-exciton or B-exciton emissions with in-plane polarizations. The C-exciton emissions with out-of-plane polarization are found to be not active in ZnS colloidal quantum dots under normal conditions.

AUTHOR INFORMATION

Corresponding Author

*E-mail: bask@upatras.gr.

Notes

The authors declare no competing financial interest.

ACKNOWLEDGMENTS

This research has been cofinanced by the European Union (European Social Fund-ESF) and Greek national funds through the Operational Program "Education and Lifelong Learning" of the National Strategic Reference Framework (NSRF)-Research Funding Program: Thales, investing in knowledge society through the European Social Fund.

REFERENCES

(1) Hattori, T.; Homma, Y.; Mitsuishi, A.; Tacke, M. Indices of refraction of ZnS, ZnSe, ZnTe, CdS, and CdTe in the far infrared. *Opt. Commun.* **1973**, *7*, 229−232.

(2) Thamizhmani, L.; Azad, A. K.; Dai, J.; Zhang, W. Far-infrared optical and dielectric response of ZnS measured by terahertz time-domain spectroscopy. *Appl. Phys. Lett.* **2005**, *86*, 131111.

(3) Bredol, M.; Merikhi, J. ZnS precipitation: morphology control. *J. Mater. Sci.* **1998**, *33*, 471−476.

(4) Jiang, Y.; Zhang, W.; Jie, J.; Meng, X.; Zapien, J.; Lee, S.-T. Homoepitaxial Growth and Lasing Properties of ZnS Nanowire and Nanoribbon Arrays. *Adv. Mater.* **2006**, *18*, 1527−1532.

(5) Snee, P. T.; Somers, R. C.; Nair, G.; Zimmer, J. P.; Bawendi, M. G.; Nocera, D. G. A Ratiometric CdSe/ZnS Nanocrystal pH Sensor. *J. Am. Chem. Soc.* **2006**, *128*, 13320−13321.

(6) Calandra, P.; Goffredi, M.; Liveri, V. Study of the growth of ZnS nanoparticles in water/AOT/n-heptane microemulsions by UV-absorption spectroscopy. *Colloids Surf., A* **1999**, *160*, 9−13.

(7) Scott, S.; Barnes, H. Sphalerite-wurtzite equilibria and stoichiometry. *Geochim. Cosmochim. Acta* **1972**, *36*, 1275−1295.

(8) Xiong, Q.; Chen, G.; Acord, J. D.; Liu, X.; Zengel, J. J.; Gutierrez, H. R.; Redwing, J. M.; Lew Yan Voon, L. C.; Lassen, B.; Eklund, P. C. Optical Properties of Rectangular Cross-sectional ZnS Nanowires. *Nano Lett.* **2004**, *4*, 1663−1668.

(9) Bellotti, E.; Brennan, K. F.; Wang, R.; Ruden, P. P. Calculation of the electron initiated impact ionization transition rate in cubic and hexagonal phase ZnS. *J. Appl. Phys.* **1997**, *82*, 2961−2964.

(10) Wang, X.; Huang, H.; Liang, B.; Liu, Z.; Chen, D.; Shen, G. ZnS Nanostructures: Synthesis, Properties, and Applications. *Crit. Rev. Solid State Mater. Sci.* **2013**, *38*, 57−90.

(11) Yeh, C.-Y.; Wei, S.-H.; Zunger, A. Relationships between the band gaps of the zinc-blende and wurtzite modifications of semiconductors. *Phys. Rev. B* **1994**, *50*, 2715−2718.

(12) Karazhanov, S. Z.; Ravindran, P.; Kjekshus, A.; Fjellvåg, H.; Grossner, U.; Svensson, B. G. Coulomb correlation effects in zinc monochalcogenides. *J. Appl. Phys.* **2006**, *100*, 043709.

(13) Karazhanov, S.; Ravindran, P.; Kjekhus, A.; Fjellvåg, H.; Grossner, U.; Svensson, B. Electronic structure and band parameters for ZnX(X = O, S, Se, Te). *J. Cryst. Growth* **2006**, *287*, 162−168.

(14) Zhang, X.; Zhao, M.; Yan, S.; He, T.; Li, W.; Lin, X.; Xi, Z.; Wang, Z.; Liu, X.; Xia, Y. First-principles study of ZnS nanostructures: nanotubes, nanowires and nanosheets. *Nanotechnology* **2008**, *19*, 305708.

(15) Nanda, J.; Sapra, S.; Sarma, D. D.; Chandrasekharan, N.; Hodes, G. Size-Selected Zinc Sulfide Nanocrystallites: Synthesis, Structure, and Optical Studies. *Chem. Mater.* **2000**, *12*, 1018−1024.
(16) Wang, L.-W.; Zunger, A. Local-density-derived semiempirical pseudopotentials. *Phys. Rev. B* **1995**, *51*, 17398−17416.
(17) Baskoutas, S.; Bester, G. Conventional Optics from Unconventional Electronics in ZnO Quantum Dots. *J. Phys. Chem. C* **2010**, *114*, 9301.
(18) Baskoutas, S.; Bester, G. Transition in the Optical Emission Polarization of ZnO Nanorods. *J. Phys. Chem. C* **2011**, *115*, 15862−15867.
(19) Baskoutas, S.; Zeng, Z.; Garoufalis, C. S.; Bester, G. Tuning of the Optical Emission Polarization of ZnO Nanorods by an Applied Hydrostatic Pressure. *J. Phys. Chem. C* **2012**, *116*, 26592−26597.
(20) Zeng, Z.; Garoufalis, C. S.; Baskoutas, S.; Bester, G. Electronic and optical properties of ZnO quantum dots under hydrostatic pressure. *Phys. Rev. B* **2013**, *87*, 125302.
(21) Bester, G. Electronic excitations in nanostructures: an empirical pseudopotential based approach. *J. Phys.: Condens. Matter* **2009**, *21*, 023202.
(22) Hopfdeld, J. Fine structure in the optical absorption edge of anisotropic crystals. *J. Phys. Chem. Solids* **1960**, *15*, 97−107.
(23) Xu, Y.-N.; Ching, W. Y. Electronic, optical, and structural properties of some wurtzite crystals. *Phys. Rev. B* **1993**, *48*, 4335−4351.
(24) *Landolt-Börnstein: Numerical Data and Functional Relationships in Science and Technology*; Madelung, O., Schulz, M., Eds.; Springer: Berlin, 1982; Vol. *22a*.
(25) Baars, J. W. In *Proceedings of the international conference on II-VI semiconducting compounds*; Thomas, D. G., Ed.; Benjamin: New York, Providence, 1968; Vol. *22a*, p 631.
(26) Drews, R. E.; Davis, E. A.; Leiga, A. G. Reflectivity Spectra of Cd1 − *x*Zn*x*S Single Crystals. *Phys. Rev. Lett.* **1967**, *18*, 1194−1196.
(27) Ebina, A.; Fukunaga, E.; Takahashi, T. Reflectivity spectra of structurally pure wurtzite-type ZnS in ultraviolet and vacuum-ultraviolet regions. *Phys. Rev. B* **1975**, *12*, 687−689.
(28) Bergstresser, T. K.; Cohen, M. L. Electronic Structure and Optical Properties of Hexagonal CdSe, CdS, and ZnS. *Phys. Rev.* **1967**, *164*, 1069−1080.
(29) Califano, M.; Bester, G.; Zunger, A. Prediction of a Shape-Induced Enhancement in the Hole Relaxation in Nanocrystals. *Nano Lett.* **2003**, *3*, 1197.
(30) Zhang, L.; Luo, J.-W.; Franceschetti, A.; Zunger, A. Excitons and excitonic fine structures in Si nanowires: Prediction of an electronic state crossover with diameter changes. *Phys. Rev. B* **2011**, *84*, 075404.
(31) Franceschetti, A.; Fu, H.; Wang, L. W.; Zunger, A. Many-body pseudopotential theory of excitons in InP and CdSe quantum dots. *Phys. Rev. B* **1999**, *60*, 1819−1829.
(32) Resta, R. Thomas-Fermi dielectric screening in semiconductors. *Phys. Rev. B* **1977**, *16*, 2717.
(33) Mang, A.; Reimann, K.; Rübenacke, St. Band gaps, crystal-field splitting, spin-orbit coupling, and exciton binding energies in ZnO under hydrostatic pressure. *Solid State Commun.* **1995**, *94*, 251−254.
(34) Molina-Sanchez, A.; Garcia-Cristobal, A.; Bester, G. Semi-empirical pseudopotential approach for nitride-based nanostructures and *ab initio* based passivation of free surfaces. *Phys. Rev. B* **2012**, *86*, 205430.
(35) The macroscopic low-frequency and high-frequency dielectric constant ϵ_0 = 9.6 and ϵ_∞ = 5.8, respectively. Thomas-Fermi wave vector q_{TF} = 0.68, ρ_∞ = 5.498, ρ_e = 55.96, and ρ_h = 16.43.
(36) Efros, A. L.; Efros, A. L. Interband absorption of light in a semiconductor sphere. *Sov. Phys. Semicond.* **1982**, *16*, 772−775.
(37) Brus, L. E. A simple model for the ionization potential, electron affinity, and aqueous redox potentials of small semiconductor crystallites. *J. Chem. Phys.* **1983**, *79*, 5566−5571.
(38) Lippens, P. E.; Lannoo, M. Calculation of the band gap for small CdS and ZnS crystallites. *Phys. Rev. B* **1989**, *39*, 10935−10942.
(39) Ong, H. C.; Chang, R. P. H. Optical constants of wurtzite ZnS thin films determined by spectroscopic ellipsometry. *Appl. Phys. Lett.* **2001**, *79*, 3612−3614.
(40) Franceschetti, A.; Zunger, A. Direct Pseudopotential Calculation of Exciton Coulomb and Exchange Energies in Semiconductor Quantum Dots. *Phys. Rev. Lett.* **1997**, *78*, 915−918.
(41) Meulenberg, R. W.; Lee, J. R.; Wolcott, A.; Zhang, J. Z.; Terminello, L. J.; van Buuren, T. Determination of the Exciton Binding Energy in CdSe Quantum Dots. *ACS Nano* **2009**, *3*, 325−330.
(42) Efros, A. L.; Rosen, M.; Kuno, M.; Nirmal, M.; Norris, D. J.; Bawendi, M. Band-edge exciton in quantum dots of semiconductors with a degenerate valence band: Dark and bright exciton states. *Phys. Rev. B* **1996**, *54*, 4843−4856.
(43) Bagga, A.; Chattopadhyay, P. K.; Ghosh, S. Origin of Stokes shift in InAs and CdSe quantum dots: Exchange splitting of excitonic states. *Phys. Rev. B* **2006**, *74*, 035341.
(44) Kuno, M.; Lee, J. K.; Dabbousi, B. O.; Mikulec, F. V.; Bawendi, M. G. The band edge luminescence of surface modified CdSe nanocrystallites: Probing the luminescing state. *J. Chem. Phys.* **1997**, *106*, 9869−9882.
(45) Li, J.; Xia, J.-B. Hole levels and exciton states in CdS nanocrystals. *Phys. Rev. B* **2000**, *62*, 12613−12616.
(46) Yu, Z.; Li, J.; O'Connor, D. B.; Lin-Wang; Barbara, P. F. Large Resonant Stokes Shift in CdS Nanocrystals. *J. Phys. Chem. B* **2003**, *107*, 5670−5674.
(47) Jacopin, G.; Rigutti, L.; Bugallo, A.; Julien, F.; Baratto, C.; Comini, E.; Ferroni, M.; Tchernycheva, M. High degree of polarization of the near-band-edge photoluminescence in ZnO nanowires. *Nanoscale Res. Lett.* **2011**, *6*, 501.

Paper XI

In which we study the linear and nonlinear optical susceptibilities in a laterally coupled quantum-dot-quantum-ring system ...

Physics Letters A 378 (2014) 2713–2718

Contents lists available at ScienceDirect

Physics Letters A

www.elsevier.com/locate/pla

Linear and nonlinear optical susceptibilities in a laterally coupled quantum-dot–quantum-ring system

Zaiping Zeng, Christos S. Garoufalis, Sotirios Baskoutas *

Materials Science Department, University of Patras, Rio, 26504, Greece

ARTICLE INFO

Article history:
Received 28 May 2014
Received in revised form 26 June 2014
Accepted 23 July 2014
Available online 28 July 2014
Communicated by R. Wu

Keywords:
Optical susceptibilities
Quantum dot
Quantum ring

ABSTRACT

Linear and nonlinear optical susceptibilities in a laterally coupled quantum-dot–quantum-ring system have been theoretically studied. In general, we find that the structure parameters of the coupled system significantly affect the optical susceptibilities. The enhancement of the coupling effects between the dot and ring is found to increase considerably the optical susceptibilities and redshift drastically the transition energies. Comparing to the linear susceptibility, the nonlinear optical susceptibility is found to be more sensitive to the variation of the structure parameters. A comprehensive analysis of the electron probability density movement with respect to the modification of the structure parameters is provided, which offers a unique perspective of the ground-state localization.

1. Introduction

Coupling between semiconductor quantum dots (QDs) forms so-called quantum dot molecules (QDMs). This can be realized either by vertically stacking or by laterally aligning the QDs in the same plane [1]. Comparing to the traditional vertically stacking structure, the degree of external control of individual QD within an array of laterally aligned QDMs is believed to be larger. Laterally coupled QDMs are also found as peculiar candidates for applications in quantum information science because of the potential to couple several QDs "scaling" to form the first building block of a useful device [2–4]. Due to these reasons, plenty of efforts have been committed to study the optical proprieties of the laterally coupled QDMs [4–9]. On the other hand, quantum rings (QRs) have demonstrated unique electronic, magnetic, and optical properties [10–12]. For example, quantum phase coherence effects on carrier transport, such as Aharonov–Bohm and Aharonov–Casher effects, have been observed in QR structures [13,14], which have potential applications in quantum information devices [15]. Patterned QR magnetic tunnel junctions have shown superior prospects for very high density magnetic random access memory, recording medium, and other spintronic devices [16]. High performance QR terahertz (THz) photodetectors have been fabricated [17,18]. Due to the relevance in potential device applications [19–21], the studies of the nonlinear optical properties in semiconductor QRs have received great attention [22–29]. It is found that the potential geometry, size, alloys composition and the external perturbations, such as applied electric and/or magnetic fields, hydrostatic pressure etc. have significant influence on the optical nonlinearities in semiconductor QRs.

In this contribution, we pay attention to the study of the linear and nonlinear optical susceptibilities in a different geometry of lateral coupling, namely quantum-dot–quantum-ring system (QDQR) in which a QD is surrounded by QR with a tunneling barrier separating both parts of the system. This system has been justified as a good candidate for the realization of the magnetic field controllable pair of spin qubits which is necessary in quantum computation [1]. However, the optical properties, especially the nonlinear optical properties, have rarely been studied in such a unique system. Furthermore, to the best of our knowledge, the coupling effects, which appear in all types of coupled structures, on the optical nonlinearities are not yet well understood. In the present work, the linear and nonlinear optical susceptibilities in a laterally coupled GaAs QDQR system have been theoretically investigated with an emphasis on the coupling effects between the dot and ring on these quantities. The electronic structure calculations are performed via potential morphing method (PMM) [30] in the framework of the effective mass approximation (EMA), which has been successfully employed previously for the study of optical properties in several nanostructures [31,32] and very recently for the calculations of the nonlinear optical properties in ZnO-based QD systems [33,34]. A detailed visualization of the variation in the electron probability density of the ground-state and first-excited state with respect to the changes in the structure parameters has been provided. The calculations of the linear and nonlinear susceptibilities are realized by using our recently developed analytical

* Corresponding author.
E-mail address: bask@upatras.gr (S. Baskoutas).

http://dx.doi.org/10.1016/j.physleta.2014.07.036
0375-9601/

expressions for symmetric systems [33]. The rest of the paper is organized as follows: in Section 2, we define our model and explain the general theory. In Section 3, we present numerical results and related discussions, and Section 4 is devoted to conclusions.

2. Theoretical framework

2.1. Electronic structure calculations

In the framework of EMA, an electron confined in a GaAs QDQR system can be modeled by the following Hamiltonian:

$$\hat{H} = \hat{p}\frac{1}{2m_e^*}\hat{p} + V(\vec{r}), \tag{1}$$

where the first term is the kinetic term in which m_e^* is the electron effective mass and the second term is the confinement potential. Considering the fact that the thickness of the QDQR along the growth direction (e.g., z-axis direction) is much smaller than the radial dimensions, one can decouple the electron motion along the growth direction from that along the in-plane direction and retain the analysis only the first state along the growth direction. For simplicity but without the loss of generality, we consider a two-dimensional QD (with the electron confined in the plane $z = 0$) placed within a QR. Experimentally, local oxidation method with atomic force microscope can be used to realize a variety of nanostructures on metals and semiconductors (cf. Ref. [35] and references therein), including high-quality QDs [36] and QRs [37]. Therefore, the two-dimensional coupled QDQR structure considered herein can be realized by employing this technique to produce both a QD and a QR which coexist on a GaAs–AlGaAs heterostructure. The shape of the confinement potential of an individual part (QD or QR) can be tuned via a suitable choice of gate voltages [35]. Consequently, the QD and QR confinement potentials do not necessarily have the same depths. To model this coupled structure, we employ the following confinement potential:

$$V(\vec{r}) = V(\vec{\rho}) = \min\left[m_e^*\omega_d^2\rho^2/2 + V_0, m_e^*\omega_r^2(\rho - R)^2/2\right], \tag{2}$$

where $\hbar\omega_d$ and $\hbar\omega_r$ are the confinement energies of the QD and the QR, respectively. The radius of the QR is defined by the sum of oscillator lengths for the QD and the QR potential and the barrier thickness (B_T) according to the formula $R = \sqrt{2\hbar/m_e^*\omega_d} + B_T + \sqrt{2\hbar/m_e^*\omega_r}$. V_0 is the depth of the dot confinement with respect to the bottom of the QR potential. A view of the potential profile (detailed in Eq. (2)) is pictured in Fig. 1 for $\hbar\omega_d = 6$ meV, $\hbar\omega_r = 12$ meV, $V_0 = -5$ meV, and $B_T = 10$ nm. As shown in Fig. 1, the potential appears to be parabolic within both the QD and the QR. This strictly cylindrically symmetric potential have been adopted previously for the study of the electron spin and charge switching in a coupled QDQR system [1]. Similar potential has also been used previously for the description of side by side QDs [38,39].

To calculate the eigenenergies and corresponding wave functions of Hamiltonian (1), which are necessary for the calculations of optical susceptibilities, we employ potential morphing method [30–34]. A detailed description of this method can be found in Ref. [30]. The reference system we used to start the morphing procedure is the usual harmonic oscillator in two dimensions with well-known eigenfunctions. The interaction potential is $V_s = V(\vec{r})$, as shown in Eq. (2).

2.2. Optical susceptibility calculations

Within the two-level system approximation, the linear ($\chi^{(1)}$) and third-order ($\chi^{(3)}$) nonlinear optical susceptibilities are give by [33]

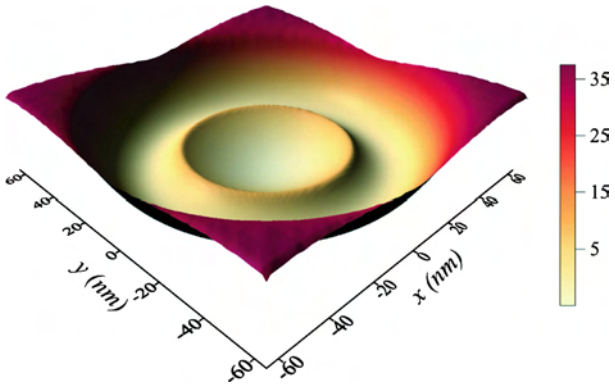

Fig. 1. (Color online.) Potential profile (in unit of meV) for a laterally coupled GaAs quantum-dot–quantum-ring with the confinement energy of the dot $\hbar\omega_d = 6$ meV, the confinement energy of the ring $\hbar\omega_r = 12$ meV, the depth of the dot confinement $V_0 = -5$ meV and the barrier thickness $B_T = 10$ nm. The dot oscillator length $l_d = \sqrt{2\hbar/m_e^*\omega_d} = 19.51$ nm and the ring oscillator length $l_r = \sqrt{2\hbar/m_e^*\omega_r} = 13.798$ nm, giving the ring radius $R = 43.31$ nm.

$$\chi^{(1)} = \frac{N\mu^2 T_2}{\hbar\epsilon_0\epsilon_{eff}^2}\frac{i - \delta T_2}{1 + \delta^2 T_2^2}, \tag{3}$$

$$\chi^{(3)} = -\frac{4N\mu^4 T_1 T_2^2}{3\hbar^3\epsilon_0\epsilon_{eff}^4}\frac{i - \delta T_2}{(1 + \delta^2 T_2^2)^2}, \tag{4}$$

where N is the electron volume density in the QDQR system, ϵ_0 is the permittivity in vacuum, $\delta = \omega - \omega_0$ is the detuning of applied field from resonance, where $\omega_0 = (E_j - E_i)/\hbar$ with E_i and E_j being the energy eigenvalues of the initial (ground) and final (first excited) states which we obtained in the last subsection, respectively. T_1 and T_2 are the population relaxation time and the dephasing time, respectively, μ is the transition matrix element between the initial and final states which is defined as $\mu = -\langle i|ex|j\rangle$, where we assume that the polarization of electromagnetic radiation is along the x-axis direction. $\epsilon_{eff} = \frac{2\epsilon_{out}+\epsilon_{in}}{3\epsilon_{out}}$ is the local field factor due to the possible existence of the dielectric mismatch, where ϵ_{in} is the dielectric constant of the QDQR material, and ϵ_{out} is the dielectric constant of surrounding matrix material. As shown from Eqs. (3) and (4), possible existence of the dielectric mismatch ($\epsilon_{in} \neq \epsilon_{out}$) has significant influence on the linear and nonlinear optical susceptibilities. This has also been addressed in more details in our previous work regarding to the ZnO-based colloidal QD systems [33,34]. However, we assume that the GaAs coupled QDQR structures studied herein are obtained on a GaAs–$Al_xGa_{1-x}As$ heterostructure with Al concentration $x = 0.3$ [35], and the QDQR material GaAs and the possible barrier material $Al_{0.3}Ga_{0.7}As$ have closely matching dielectric constants (e.g., $\epsilon_{in} = \epsilon_{out}$ and $\epsilon_{eff} = 1$).

3. Numerical results and discussion

In the linear regime, two characteristics of the linear and nonlinear optical susceptibilities are of great importance. One is the photon energy at which the susceptibility reaches its peak value, and the other one is the magnitude or the intensity of this peak. The analytical expressions of the linear and nonlinear optical susceptibilities we employ herein offer us the possibility to quantify these two characteristics. As indicated from Eq. (3), the real part of the linear susceptibility $\chi^{(1)}$ exhibits a standard dispersive lineshape, presenting firstly a maximum and then a minimum as the photon energy increases. These maximum and minimum appear at the photon energy $\hbar\omega = E_{21} - \hbar/T_2$ and $E_{21} + \hbar/T_2$, respectively, where E_{21} is the transition energy. They are equivalent in the magnitude and defined by the expression $|\chi^{(1)}_{Real,max}| = N\mu^2 T_2/(2\hbar\epsilon_0)$. On the other hand, the imaginary part of $\chi^{(1)}$ displays a stan-

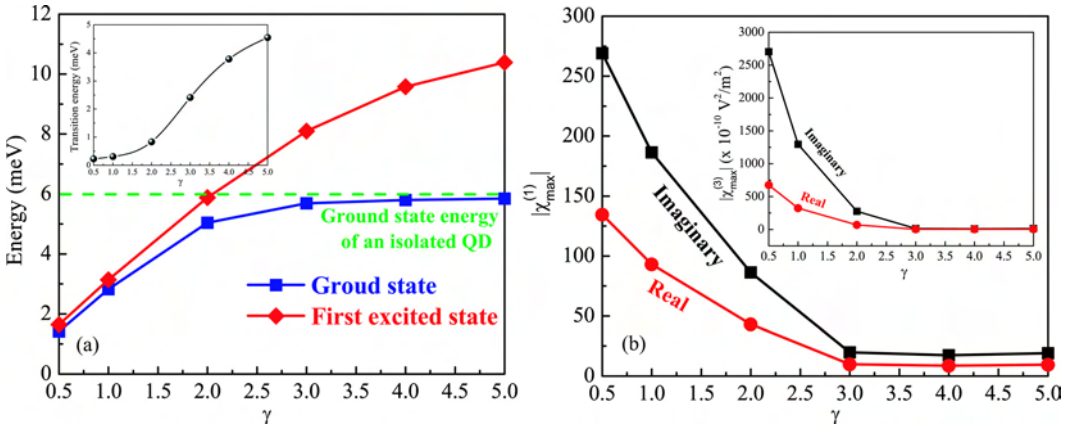

Fig. 2. (Color online.) (a) The ground-state (blue solid square), first excited state (red solid diamond) energies and transition energy (inset) as a function of γ. (b) The maximum values (in absolute value) of the real (red solid sphere) and imaginary (black solid square) parts of the linear and nonlinear (inset) susceptibilities as a function of γ. Here, $\gamma = (\hbar\omega_r)/(\hbar\omega_d)$ where $\hbar\omega_r$ and $\hbar\omega_d$ are the confinement energies of the dot and ring, respectively. $\hbar\omega_d = 6$ meV, $V_0 = 0$ and $B_T = 10$ nm.

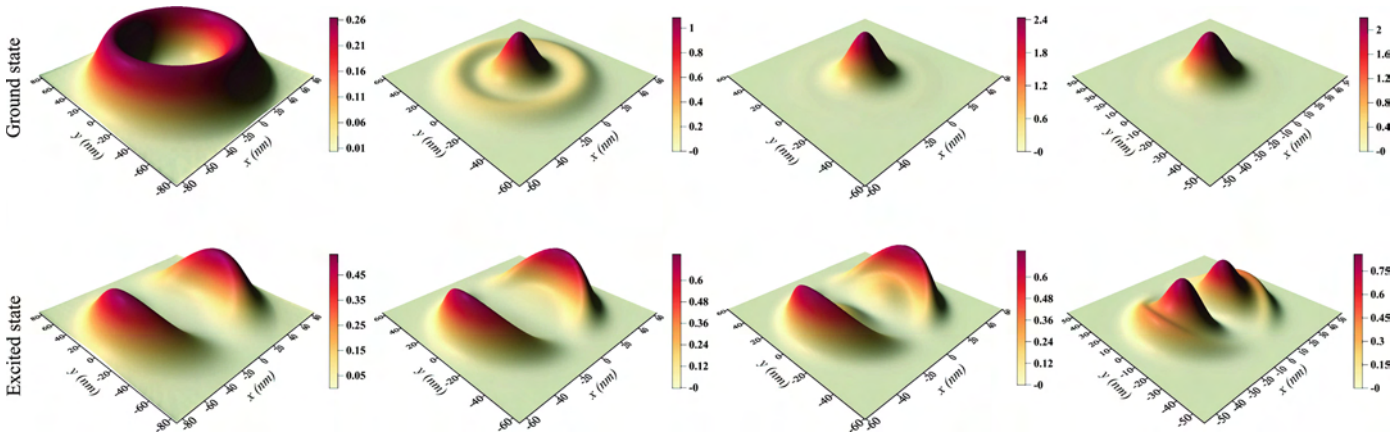

Fig. 3. (Color online.) Electron probability densities of the ground state (the upper panel) and the first excited state (the lower panel) in QDQRs with various confinement energy values of the ring $\hbar\omega_r$. From the leftmost to the rightmost columns are for $\hbar\omega_r = 3$ meV, 12 meV, 18 meV, 30 meV, respectively. Here, the depth of the dot (V_0), the confinement energy of the dot ($\hbar\omega_d$) and the barrier thickness (B_T) are the same as in Fig. 2.

dard Lorentzian lineshape, presenting a maximum at photon energy $\hbar\omega = E_{21}$. This peak value is determined by $|\chi^{(1)}_{Real,max}| = N\mu^2 T_2/(\hbar\epsilon_0)$. Comparing to the linear counterpart, the real part of the nonlinear susceptibility $\chi^{(3)}$, as indicated from Eq. (4), shows an "inverted" dispersive lineshape, exhibiting firstly a minimum at $\hbar\omega = E_{21} - \hbar/T_2$ and then a maximum at $\hbar\omega = E_{21} + \hbar/T_2$ when the photon energy increases. The intensities of these extremums are equivalent (in absolute value) which are described by $|\chi^{(3)}_{Real,max}| = 4N\mu^4 T_1 T_2^2/(3\hbar^3\epsilon_0)$. As concerning the imaginary part of $\chi^{(3)}$, it is negative and presents a maximum (in absolute value) at the photon energy $\hbar\omega = E_{21}$ whose magnitude is determined by $|\chi^{(3)}_{Img,max}| = N\mu^4 T_1 T_2^2/(3\hbar^3\epsilon_0)$. It should be noted here that the linear susceptibility $\chi^{(1)}$ is a dimensionless quantity, while its nonlinear susceptibility $\chi^{(3)}$ is in unit of m^2/V^2.

As shown above, the peak intensities of the linear and nonlinear optical susceptibilities are dependent on the electron volume density N, the relaxation time T_1, the dephasing time T_2 and the transition matrix element $|\mu|$. However, in what follows, we focus on the study of the influence of the structure parameters of the coupled QDQR system, such as the confinement energy of the ring (or the dot), the depth of the dot confinement relative to the bottom of the QR potential and the tunneling barrier thickness, on the transition energy (i.e., E_{21}) and the peak values of the linear and nonlinear susceptibilities. The relevant parameters used in our calculations for GaAs QDQR systems are: $m_e^* = 0.0667m_0$ (m_0 is the free electron mass), $N = 3\times10^{16}$ cm^{-3} (Ref. [29]), $T_1 = 1$ ps and $T_2 = 0.2$ ps [40], respectively. The influence of the volume density N or the dephasing time T_2 on the optical nonlinearities in semiconductor nanostructures have been addressed in the literature and can be found in Refs. [41] and [42].

Firstly, in order to study the dependence of the linear and nonlinear susceptibilities on the relative strength of the dot and ring confinement, we define a parameter $\gamma = (\hbar\omega_r)/(\hbar\omega_d)$. Large γ corresponds to a narrower (wider) path for the electron to transverse in the ring (dot) part of the QDQR and *vice versa*. The calculations are based on QDQRs with equal depth of the dot and ring (i.e., $V_0 = 0$). We start our calculations with a ring confinement energy $\hbar\omega_r = 3$ meV which is only a half of its dot counterpart ($\gamma = 0.5$, cf. Fig. 2). It appears that the ground state is almost purely ring-localized state (see the upper plot of the first column in Fig. 3). This can also be justified by its energy, i.e., $E = 1.42$ meV, which is pretty close to the ground state energy of the single-dimensional harmonic oscillator in the radial direction (i.e., $\approx \hbar\omega_r/2 = 1.5$ meV). As γ increases (the ring confinement energy increases), the oscillator length of ring decreases and the wave functions gradually penetrate through the central tunneling barrier into the dot part (cf. Fig. 3). Consequently, both energies of the ground state and the first excited state increase as shown in Fig. 2(a). However, comparing to the ground state energy, the energy of the excited state turns out to be more sensitive to the variation of γ. This results in a substantially increase in the transition energy (cf. the inset of Fig. 2(a)). For $\hbar\omega_r \geqslant 3\hbar\omega_d = 18$ meV ($\gamma = 3$), we find that the ground state is nearly purely dot-

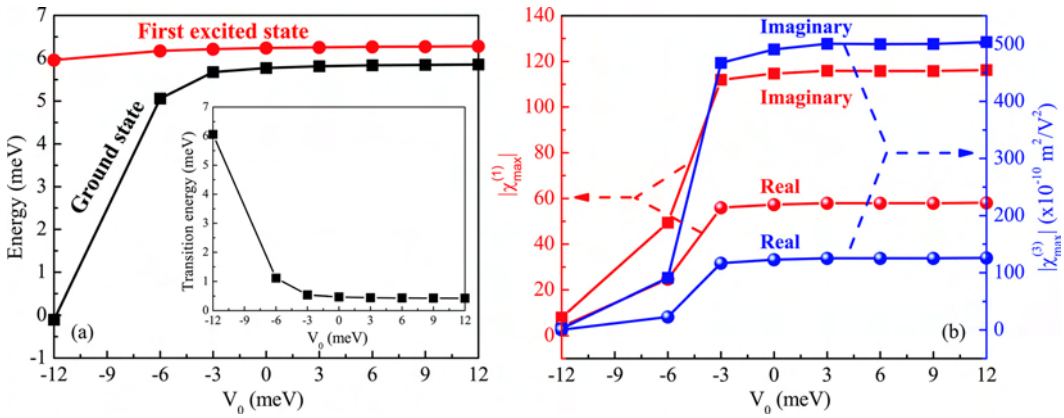

Fig. 4. (Color online.) (a) The ground-state (black solid square), first excited state (red solid sphere) energies and transition energy (inset) as a function of the depth of dot confinement relative to the bottom of the QR potential V_0. (b) The maximum values (in absolute value) of the real (solid spheres) and imaginary (solid squares) parts of the linear (red lines) and nonlinear (blue lines) susceptibilities as a function of the depth of dot confinement. Here, $B_T = 10$ nm and $\hbar\omega_d = \hbar\omega_r = 12$ meV.

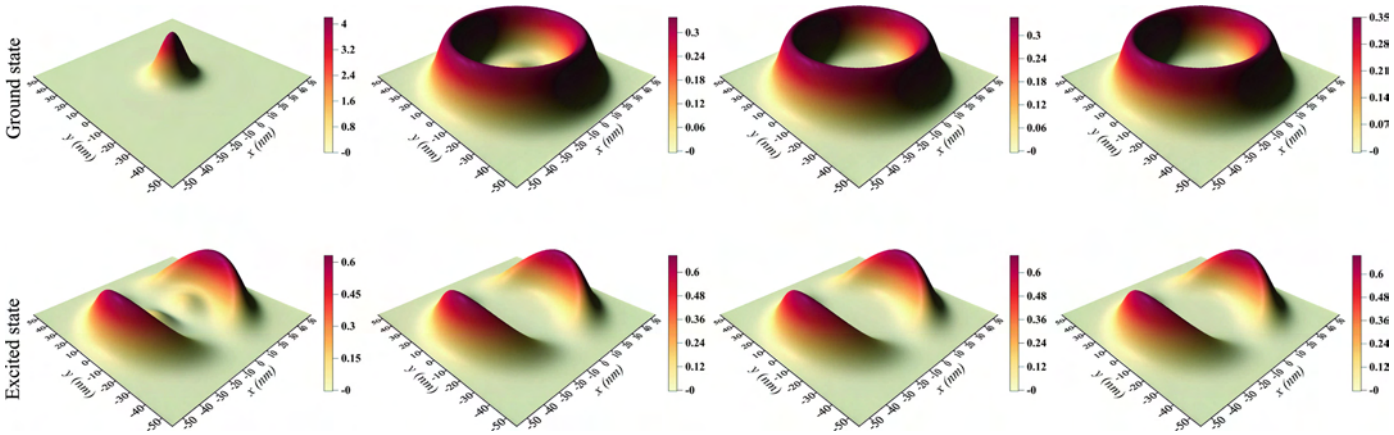

Fig. 5. (Color online.) Electron probability densities of the ground state (the upper panel) and the first excited state (the lower panel) in QDQRs with various depths of the dot confinement relative to the bottom of the QR potential V_0. From the leftmost to the rightmost columns are for $V_0 = -12$ meV, -3 meV, 3 meV, 12 meV, respectively. Here, the confinement energies of the dot ($\hbar\omega_d$) and the ring ($\hbar\omega_r$), and the barrier thickness (B_T) are the same as in Fig. 4.

localized state (cf. Fig. 3) and its energy approaches to the ground state energy of an isolated QD, i.e., $E = V_0 + \hbar\omega_d = 6$ meV (see the dashed line in Fig. 2(a)). As regards the first excited state, the density movement towards the dot part of QDQR appears to be slower in comparison to its ground state counterpart.

At the meantime, the aforementioned penetration of both the ground-state and the first excited-state wave functions into the dot part of the QDQR system also causes a decrease in the transition matrix element $|\mu|$. This in turn leads to a decrease in the maximum values of the real and imaginary parts of both linear and nonlinear susceptibilities (in absolute value, cf. Fig. 2(b)). Comparing the linear susceptibility (e.g., $|\chi^{(1)}_{max}|$), the maximum value of its nonlinear counterpart (e.g., $|\chi^{(3)}_{max}|$) is found to be more sensitive to the variation of the relative strength of the dot and ring confinement (as characterized by γ). This is related to the fact that $|\chi^{(3)}_{max}|$ is more dependent on the transition matrix element (e.g., $|\chi^{(3)}_{max}| \propto |M_{21}|^4$, while $|\chi^{(1)}_{max}| \propto |M_{21}|^2$). We further find that for a given quantity (linear or nonlinear susceptibility), the imaginary part exhibits a stronger dependence on γ in comparison to its real analog (cf. Fig. 2(b)). All the maximum values appear to be insensitive to the further increase in γ when $\gamma \geq 3$ ($\hbar\omega_r \geq 18$ meV).

To proceed our calculations, we turn our attention to study the influence of the depth of dot confinement relative to the bottom of the QR potential (e.g., V_0) on the optical susceptibilities in coupled QDQR systems with the dot and ring having the same confinement energies (e.g., $\hbar\omega_d = \hbar\omega_r = 12$ meV). For a dot with very deep confinement (e.g., $V_0 = -12$ meV), the ground-state is almost purely dot-localized state with an energy ($= -0.1$ meV) approaching to the ground-state energy of an isolated QD ($\approx V_0 + \hbar\omega_d = 0$ meV, cf. Fig. 4(a)). As V_0 increases, both the ground-state and first excited-state wave functions leak gradually from the dot part to the ring part of the QDQR (cf. Fig. 5). This causes an increase in both the ground-state and first excited-state energies (cf. Fig. 4(a)). However, the ground state exhibits a significantly stronger dependence on the increase of V_0, experiencing a quick increase in the corresponding energy as V_0 enhances. Conversely, the variation of V_0 on the first-excited state is practically marginal and only a slight increase in its energy is observed (cf. Fig. 4(a)). As a consequence, the transition energy decreases as V_0 increases (see the inset of Fig. 4(a)). We further find that for $V_0 \geq -3$ meV which is a quarter of the dot (or ring) confinement energy (in absolute value), both energies (ground-state and first excited state) are insensitive to the further increase in V_0. The ground-state becomes a nearly purely ring-like state (see the upper panel of Fig. 5) and its energy approaches to the ground-state energy of the single-dimensional harmonic oscillator in the radial direction ($\approx \frac{1}{2}\hbar\omega_r = 6$ meV, see Fig. 4(a)).

The leakage of the wave function from the dot part to the ring part also causes a significant increase in transition matrix element $|\mu|$. This resultantly leads to a considerable enhancement of the maximum values of the linear and nonlinear susceptibilities (both real and imaginary parts, cf. Fig. 4(b)). Similarly to what we have found previously, the maximum value of the nonlinear susceptibility, especially that of the imaginary part, appears to be

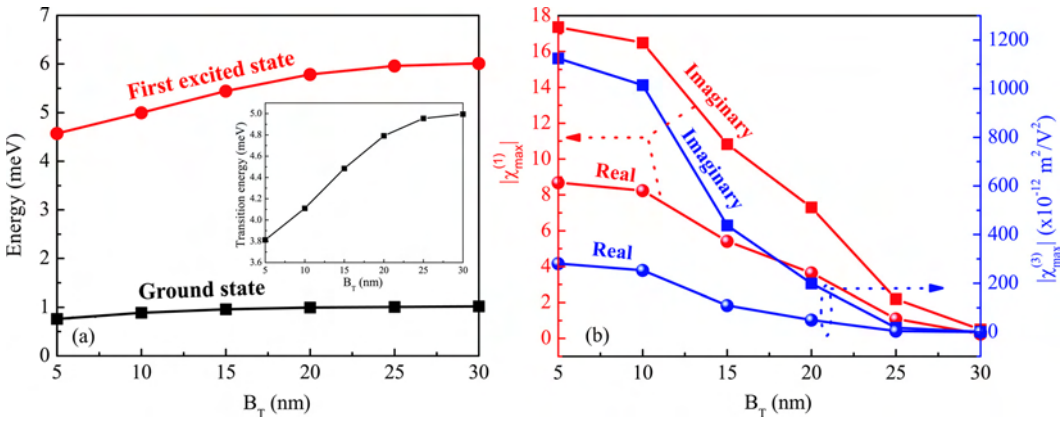

Fig. 6. (Color online.) (a) The ground-state (black solid square), first excited state (red solid sphere) energies and transition energy (inset) as a function of the barrier thickness B_T. (b) The maximum values (in absolute value) of the real (solid spheres) and imaginary (solid squares) parts of the linear (red lines) and nonlinear (blue lines) susceptibilities as a function of the barrier thickness B_T. Here, $\hbar\omega_d = 6$ meV, $\hbar\omega_r = 12$ meV and $V_0 = -5$ meV.

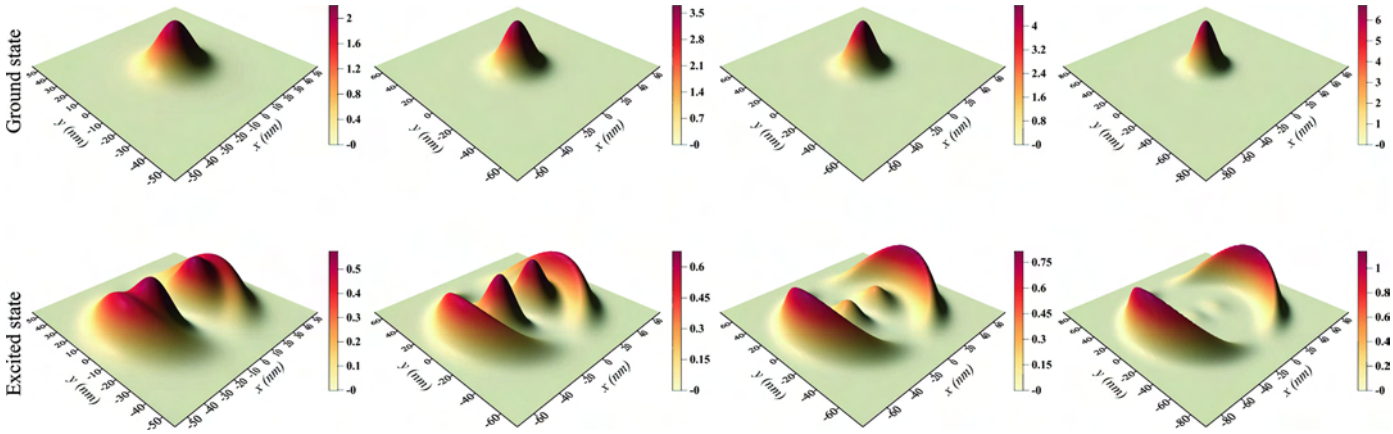

Fig. 7. (Color online.) Electron probability densities of the ground state (the upper panel) and the first excited state (the lower panel) in QDQRs with various values of central barrier thickness B_T. From the leftmost to the rightmost columns are for $B_T = 5$ nm, 15 nm, 20 nm, 30 nm, respectively. Here, the confinement energies of the dot ($\hbar\omega_d$) and the ring ($\hbar\omega_r$), and the depth of the dot confinement (V_0) are the same as in Fig. 6.

more sensitive to the variation of V_0. For $V_0 \geq -3$ meV, the maximum values of all the quantities are insensitive to the increase in V_0 (see Fig. 4(b)).

Finally, we study the coupling effects between the dot and ring (e.g., the barrier thickness B_T) on the optical susceptibilities in a laterally coupled QDQR system. In the strong coupling limit (e.g., $B_T = 5$ nm), the ground state is a dominant dot-localized state, having an energy ($= 0.76$ meV) very close to the ground-state energy of an isolated QD ($\approx V_0 + \hbar\omega_d = 1$ meV, cf. Figs. 6(a) and 7). As the barrier thickness increases, the ground-state energy increases slightly (cf. Fig. 6(a)), while its first excited counterpart appears to be more energetically dependent on the central barrier thickness, experiencing a faster increase in its energy. Consequently, as shown in Fig. 6(a), the transition energy is an increasing function of the barrier thickness. For $B_T \geq 25$ nm, both the ground-state and excited-state energies are insensitive to the further increase in the barrier thickness and a decoupling phenomenon is observed (cf. Fig. 6(a)). We also find that the ground-state wave function is more localized towards the dot center (see the upper panel of Fig. 7), whereas the first excited state one turns out to move away from the dot center (see the lower panel of Fig. 7) when B_T increases. Therefore, the overlap between these two wave functions decreases and the transition matrix element $|\mu|$ reduces considerably as the coupling effects become less significant. This eventually causes a drastic decrement of the maximum values of all the optical susceptibilities (cf. Fig. 6(b)). At the meanwhile, we find that in comparison to the linear susceptibility, its nonlinear analog is more sensitive to the coupling effects, while for a given quantity, the imaginary part demonstrates a stronger dependence on the coupling effects than the real part.

4. Conclusion

In summary, we have theoretically studied the influence of the structure parameters, such as the relative strength of the dot and ring confinement, the depth of the dot confinement relative to the bottom of the QR potential and the central tunneling barrier thickness, on the linear and nonlinear optical susceptibilities in a laterally coupled quantum-dot–quantum-ring (QDQR) system. A simple model for the potential, which assumes parabolic confinement in both the dot and the ring, is adopted. We employ the potential morphing method (PMM) in the framework of the effective mass approximation for the electronic structure calculations. It is found that the ground electron state can be changed from a nearly pure dot-localized state to a nearly pure ring-localized state or *vice versa* by suitably choosing the structure parameters (e.g., the ring (or dot) confinement energy and/or the depth of the dot confinement relative to the bottom of the QR potential). However, this cannot be realized by modifying the coupling effects (e.g., the barrier thickness) which have a strong influence primarily on the shape and energy of the excited state counterpart. The significant modification appeared in the electronic structure through controlling the structure parameters eventually leads to a considerable influence on the optical susceptibilities in such a coupled structure. A sig-

nificant blue shift of the transition energy is observed when the relative strength of the dot and ring confinement and/or the central barrier thickness are enhanced. Conversely, a red shift is found when the depth of the dot confinement increases. For the confinement energy of the ring larger than a critical value (around three times of the confinement energy of the dot), all the maximum values of the optical susceptibilities appear to be insensitive to the increase in the confinement energy of the ring. Similar behavior has also been observed for the variation of the maximum values with respect to the depth of the dot confinement relative to the bottom of the QR potential. The enhancement of the coupling effects turns out to have a significantly positive contribution on the linear and nonlinear optical susceptibilities. Finally, we find that the nonlinear optical susceptibility is more sensitive to the modification of the structure parameters in comparison to its linear counterpart, while for a given quantity, its imaginary part always exhibits a stronger dependence on the change in the structure parameters than the real part.

Acknowledgements

This research has been co-financed by the European Union (European Social Fund-ESF) and Greek national funds through the Operational Program "Education and Lifelong Learning" of the National Strategic Reference Framework (NSRF)-Research Funding Program: Thales (MIS 380252), investing in knowledge society through the European Social Fund.

References

[1] B. Szafran, F.M. Peeters, S. Bednarek, Electron spin and charge switching in a coupled quantum-dot–quantum ring system, Phys. Rev. B 70 (2004) 125310.
[2] J. Wu, X. Hu, J. Lee, E.-S. Kim, Z.M. Wang, Epitaxially self-assemblied quantum dot pairs, Adv. Opt. Mat. 1 (2013) 201–214.
[3] T. Hatano, M. Stopa, S. Tarucha, Single-electron delocalization in hybrid vertical–lateral double quantum dots, Science 309 (2005) 268–271.
[4] J. Peng, G. Bester, Charged excitons and biexcitons in laterally coupled (In, Ga)As quantum dots, Phys. Rev. B 82 (2010) 235314.
[5] L. Wang, A. Rastelli, S. Kiravittaya, M. Benyoucef, O.G. Schmidt, Self-assembled quantum dot molecules, Adv. Mater. 21 (25–26) (2009) 2601–2618.
[6] A. Kwaśniowski, J. Adamowski, Tuning the exchange interaction by an electric field in laterally coupled quantum dots, J. Phys. Condens. Matter 21 (2009) 235601.
[7] T. Kubo, Y. Tokura, S. Tarucha, Kondo effects and shot noise enhancement in a laterally coupled double quantum dot, Phys. Rev. B 83 (2011) 115310.
[8] M. Royo, J.I. Climente, J. Planelles, Emission spectrum of quasiresonant laterally coupled quantum dots, Phys. Rev. B 84 (2011) 235312.
[9] M. Raith, P. Stano, J. Fabian, Theory of spin relaxation in two-electron laterally coupled Si/SiGe quantum dots, Phys. Rev. B 86 (2012) 205321.
[10] N.A.J.M. Kleemans, I.M.A. Bominaar-Silkens, V.M. Fomin, V.N. Gladilin, D. Granados, A.G. Taboada, J.M. García, P. Offermans, U. Zeitler, P.C.M. Christianen, J.C. Maan, J.T. Devreese, P.M. Koenraad, Oscillatory persistent currents in self-assembled quantum rings, Phys. Rev. Lett. 99 (2007) 146808.
[11] N.A.J.M. Kleemans, J.H. Blokland, A.G. Taboada, H.C.M. van Genuchten, M. Bozkurt, V.M. Fomin, V.N. Gladilin, D. Granados, J.M. García, P.C.M. Christianen, J.C. Maan, J.T. Devreese, P.M. Koenraad, Excitonic behavior in self-assembled InAs/GaAs quantum rings in high magnetic fields, Phys. Rev. B 80 (2009) 155318.
[12] F. Ding, N. Akopian, B. Li, U. Perinetti, A. Govorov, F.M. Peeters, C.C. Bof Bufon, C. Deneke, Y.H. Chen, A. Rastelli, O.G. Schmidt, V. Zwiller, Gate controlled Aharonov–Bohm-type oscillations from single neutral excitons in quantum rings, Phys. Rev. B 82 (2010) 075309.
[13] M. Zarenia, J.M. Pereira, F.M. Peeters, G.A. Farias, Electrostatically confined quantum rings in bilayer graphene, Nano Lett. 9 (12) (2009) 4088–4092.
[14] A.V. Chaplik, Magnetoexcitons in quantum rings and in antidots, JETP Lett. 62 (1995) 900.
[15] M.D. Teodoro, V.L. Campo, V. Lopez-Richard, E. Marega, G.E. Marques, Y.G.A. Gobato, F. Iikawa, M.J.S.P. Brasil, Z.Y. AbuWaar, V.G. Dorogan, Y.I. Mazur, M. Benamara, G.J. Salamo, Aharonov–Bohm interference in neutral excitons: effects of built-in electric fields, Phys. Rev. Lett. 104 (2010) 086401.
[16] Z.C. Wen, H.X. Wei, X.F. Han, Patterned nanoring magnetic tunnel junctions, Appl. Phys. Lett. 91 (2007) 122511.
[17] J. Wu, Z. Li, D. Shao, M.O. Manasreh, V.P. Kunets, Z.M. Wang, G.J. Salamo, B.D. Weaver, Multicolor photodetector based on GaAs quantum rings grown by droplet epitaxy, Appl. Phys. Lett. 94 (17) (2009) 171102.
[18] S. Bhowmick, G. Huang, W. Guo, C.S. Lee, P. Bhattacharya, G. Ariyawansa, A.G.U. Perera, High-performance quantum ring detector for the 1–3 terahertz range, Appl. Phys. Lett. 96 (2010) 231103.
[19] F. Capasso, K. Mohammed, A.Y. Cho, Resonant tunneling through double barriers, perpendicular quantum transport phenomena in superlattices, and their device applications, IEEE J. Quantum Electron. 22 (1986) 1853–1869.
[20] D. Miller, Quantum well optoelectronic switching devices, Int. J. High Speed Electron. Syst. 01 (1990) 19–46.
[21] E. Rosencher, B. Vinter, Optoelectronics, Cambridge University Press, Cambridge, 2003.
[22] T. Meier, P. Thomas, S. Koch, Linear and nonlinear optical properties of semiconductor nanorings with magnetic field and disorder — influence on excitons and biexcitons, Eur. Phys. J. B 22 (2) (2001) 249–256.
[23] S. Liang, W. Xie, H.A. Sarkisyan, A.V. Meliksetyan, H. Shen, Nonlinear optical properties in a nanoring: quantum size and magnetic field effect, J. Phys. Condens. Matter 23 (41) (2011) 415302.
[24] S. Liang, W. Xie, H. Sarkisyan, A. Meliksetyan, H. Shen, Electronic and optical properties of a nanoring in the presence of external magnetic field, Superlattices Microstruct. 51 (6) (2012) 868–876.
[25] H.M. Baghramyan, M.G. Barseghyan, A.A. Kirakosyan, R.L. Restrepo, C.A. Duque, Linear and nonlinear optical absorption coefficients in GaAs/$Ga_{1-x}Al_xAs$ concentric double quantum rings: effects of hydrostatic pressure and aluminum concentration, J. Lumin. 134 (2013) 594–599.
[26] C.M. Duque, M. Mora-Ramos, C.A. Duque, Properties of the second and third harmonics generation in a quantum disc with inverse square potential. A modeling for nonlinear optical responses of a quantum ring, J. Lumin. 138 (2013) 53–60.
[27] R.L. Restrepo, M.G. Barseghyan, M.E. Mora-Ramos, C.A. Duque, Effects of hydrostatic pressure on the nonlinear optical properties of a donor impurity in a GaAs quantum ring, Physica E 51 (2013) 48–54.
[28] W. Xie, The nonlinear optical rectification coefficient of quantum dots and rings with a repulsive scattering center, J. Lumin. 143 (2013) 27–30.
[29] H.M. Baghramyan, M.G. Barseghyan, A.A. Kirakosyan, R.L. Restrepo, M.E. Mora-Ramos, C.A. Duque, Donor impurity-related linear and nonlinear optical absorption coefficients in concentric double quantum rings: effects of geometry, hydrostatic pressure, and aluminum concentration, J. Lumin. 145 (2014) 676–683.
[30] M. Rieth, W. Schommers, S. Baskoutas, Exact numerical solution of Schrödinger's equation for a particle in an interaction potential of general shape, Int. J. Mod. Phys. B 16 (2002) 4081–4092.
[31] S. Baskoutas, A.F. Terzis, Biexciton luminescence in InAs nanorods, J. Appl. Phys. 98 (2005) 044309.
[32] S. Baskoutas, E. Paspalakis, A.F. Terzis, Effects of excitons in nonlinear optical rectification in semiparabolic quantum dots, Phys. Rev. B 74 (2006) 153306.
[33] Z. Zeng, E. Paspalakis, C.S. Garoufalis, A.F. Terzis, S. Baskoutas, Optical susceptibilities in singly charged ZnO colloidal quantum dots embedded in different dielectric matrices, J. Appl. Phys. 113 (2013) 054303.
[34] Z. Zeng, C.S. Garoufalis, A.F. Terzis, S. Baskoutas, Linear and nonlinear optical properties of ZnO/ZnS and ZnS/ZnO core shell quantum dots: effects of shell thickness, impurity, and dielectric environment, J. Appl. Phys. 114 (2013) 023510.
[35] R. Held, S. Luscher, T. Heinzel, K. Ensslin, W. Wegscheider, Fabricating tunable semiconductor devices with an atomic force microscope, Appl. Phys. Lett. 75 (1999) 1134–1136.
[36] S. Lüscher, T. Heinzel, K. Ensslin, W. Wegscheider, M. Bichler, Signatures of spin pairing in chaotic quantum dots, Phys. Rev. Lett. 86 (2001) 2118–2121.
[37] A. Fuhrer, S. Lüscher, T. Ihn, T. Heinzel, K. Ensslin, W. Wegscheider, M. Bichler, Energy spectra of quantum rings, Nature 413 (2001) 822–825.
[38] A. Wensauer, O. Steffens, M. Suhrke, U. Rössler, Laterally coupled few-electron quantum dots, Phys. Rev. B 62 (2000) 2605–2613.
[39] A. Harju, S. Siljamäki, R.M. Nieminen, Two-electron quantum dot molecule: composite particles and the spin phase diagram, Phys. Rev. Lett. 88 (2002) 226804.
[40] K.-X. Guo, S.-W. Gu, Nonlinear optical rectification in parabolic quantum wells with an applied electric field, Phys. Rev. B 47 (1993) 16322–16325.
[41] Y.-B. Yu, S.-N. Zhu, K.-X. Guo, Exciton effects on the nonlinear optical rectification in one-dimensional quantum dots, Phys. Lett. A 335 (2005) 175–181.
[42] S.G. Kosionis, A.F. Terzis, C. Simserides, E. Paspalakis, Linear and nonlinear optical properties of a two-subband system in a symmetric semiconductor quantum well, J. Appl. Phys. 108 (3) (2010) 034316.

Paper XII

In which we study the electronic and optical properties of ZnO nanowires in the presence of quantum confinement effects ...

PCCP

PAPER

View Article Online
View Journal

Cite this: DOI: 10.1039/c4cp04551c

Near-band-edge exciton polarization change in ZnO nanowires†

Zaiping Zeng,[a] Alexia Petoni,[a] Christos S. Garoufalis,[a] Sotirios Baskoutas*[a] and Gabriel Bester*[b]

Received 10th October 2014,
Accepted 5th November 2014

DOI: 10.1039/c4cp04551c

www.rsc.org/pccp

Using the atomistic pseudopotential method complemented by configuration interaction calculations, we have studied the electronic and optical properties of ZnO nanowires (NWs) in the presence of quantum confinement effects. Our results indicate that the near-band-edge exciton experiences a crossover from an in-plane polarized A-exciton (for $D \geq 3$ nm) to an out-of-plane polarized C-exciton (for $D < 3$ nm) due to quantum confinement. This transition leads to a non-monotonic variation of Stokes shift, exhibiting a maximum value around the critical diameter of 3 nm. The observed behavior is analyzed by a stepwise inclusion of correlation effects, leading to a comprehensive description of the excitonic fine structure.

1 Introduction

Zinc oxide (ZnO) nanowires (NWs) have attracted considerable attention as promising candidates for device applications. The wide direct band gap (3.445 eV) and the large exciton binding energy (60 meV) of bulk ZnO make them one of the most remarkable optoelectronic materials for nanoscale device applications, such as ultraviolet (UV) lasers,[1,2] light-emitting diodes[3] (LEDs), field-effect transistors (FETs),[4,5] and UV photodetectors.[6,7] Their high surface-to-volume ratio and high density of surface states promote the development of a new generation of chemical and biological gas sensors with high sensitivity and fast response.[8,9] Piezoelectric nanogenerators based on ZnO NWs for self-powered systems have also been reported.[10,11] Experimental fabrication of these types of nanostructures has been successfully achieved by using different synthesis methods, such as vapor trapping chemical vapor deposition,[4] thermal evaporation,[12] chemical synthesis by vapour phase transport,[13] and vapor–liquid–solid method,[14] to mention only a few. However, the vast majority of the fabricated NWs are so large in diameter (*e.g.*, >15 nm which is more than 10 times of the exciton Bohr radius of bulk ZnO (≈1.4 nm)) that the quantum confinement effects remain absent. A clear picture of the quantum confinement effects on the electronic and optical properties of ZnO NWs is still unknown.

Due to the specific features of wurtzite ZnO, such as anisotropy of the valence band, as well as the small dielectric constant and strong electron–hole Coulomb interaction, a simple one-band effective mass model[15] is not able to deliver predictive results. The incorporation of many-body effects in an effective mass model to probe large nanostructures has recently been achieved.[16,17] Density functional theory (DFT) calculations have been employed to study the piezoelectricity and the band structure,[18] the charged states and the band gap in ZnO NWs (or doped ZnO NWs).[19] These types of calculations are restricted to nonpassivated, small-diameter (*e.g.*, <3 nm) NWs. Moreover, since in DFT the bulk ZnO band gaps are significantly underestimated, *e.g.*, ∼0.63 eV (ref. 18) by local density approximations (LDA or GGA) (82% underestimated in comparison to the well-known experimental value of 3.445 eV), the quantum confinement effects on the electronic and optical properties of ZnO NWs are often not well described.

In this contribution, we study the electronic and optical properties of ZnO NWs with diameters up to 6 nm, covering the intermediate and weak confinement regimes. The calculations are performed *via* the empirical pseudopotential method, using the recently derived and well-tested ZnO pseudopotentials from ref. 20, and the excitonic effects are considered by using the configuration interaction approach.[21] This method has been shown to describe very well the excitonic properties in wurtzite CdSe quantum dots (QDs),[22] and very recently in ZnO QDs[20,23] and Si NWs.[24]

2 Computational details

The single-particle electronic energies and wave functions are calculated using the plane-wave empirical pseudopotential method[25] and our recently derived and well-tested ZnO

[a] *Materials Science Department, University of Patras, 26504 Patras, Greece. E-mail: bask@upatras.gr*
[b] *Institut für Physikalische Chemie, Universität Hamburg, Grindelallee 117, 20146 Hamburg, Germany. E-mail: gabriel.bester@uni-hamburg.de*

† Electronic supplementary information (ESI) available: Convergence test results. See DOI: 10.1039/c4cp04551c

pseudopotentials.[20] The Hamiltonian for the single-particle states has the form

$$\hat{H} = -\frac{1}{2}\nabla^2 + \sum_{n\alpha}\left[v_\alpha\left(\vec{r} - \vec{R}_{\alpha n}\right) + \hat{v}_\alpha^{\mathrm{SO}}\right], \quad (1)$$

where n is the atomic index, α specifies the atom type and $\hat{v}_\alpha^{\mathrm{SO}}$ is the non-local spin–orbit operator. The screened atomic pseudopotentials v_α (with α = Zn, O) are centered at each atomic position and their superposition generates the crystal potential. $v_\alpha(\vec{r} - \vec{R}_{\alpha n})$ and $\hat{v}_\alpha^{\mathrm{SO}}$ are fitted to accurately reproduce the well-known properties of bulk ZnO (*e.g.*, band gaps, critical energy levels, effective masses, and spin–orbit splittings), and the parameters are given in ref. 20. This approach naturally includes the effects of multiband coupling, multivalley coupling, and spin–orbit interaction.

The ZnO NWs are constructed with a cross-section as circular as possible, considering the atomistic nature of the structure. The supercells are extended and periodically repeated along the [0001] crystallographic direction, while the lateral surface of the NWs is well passivated by an artificial ligand with the same crystal structure and lattice parameters as ZnO and a higher band gap. Since there is no mismatch between the NWs and the passivating material the electric field induced by piezoelectric effects can be safely neglected. The contribution of spontaneous polarization to the internal field is expected not to be significant since the polar direction of the NW coincides with the infinite growth direction. It has been demonstrated by large scale DFT calculations[26] that the internal field even in a polar quasi-one-dimensional nanorod (NR) does not depend strongly on the spontaneous polarization of the underlying lattice. This type of surface passivation has been practiced successfully previously for this material system,[20,27,28] and very recently in Si NWs.[24] It should be noted here that the nature of the surface passivation and morphology may play an important role in the determination of the electronic and optical properties of semiconductor NWs, especially with smaller sizes. However, in our calculations, the emphasis is placed on the size effects rather than the surface effects.

The many-body excitonic properties are calculated *via* configuration interaction (CI).[21] The excitonic wave functions are expanded in terms of single-substitution Slater determinants constructed from the single-particle wave functions of electrons and holes. The corresponding many-body Hamiltonian is solved either in the framework of the single configuration (SC) approximation or in the CI scheme. At the SC level, the intraconfiguration Coulomb and exchange matrix elements are fully included, but the interaction between different configurations is neglected.[21] Consequently, the correlation effects at this level of theory are willingly not accounted for. The interconfiguration coupling is fully included in the CI scheme.[21] To capture the electron–hole interaction of excitons, the NWs are periodically expanded along the growth direction with a length of ∼4.164 nm, which is around three times the exciton Bohr radius in bulk ZnO (∼1.4 nm). The Coulomb and exchange integrals are screened by the position-dependent and size-dependent screening function proposed by Resta,[29] which gives a physically smooth transition from a short range (unscreened) to a long range (screened).[21,24] According to the results of the convergence test (see the ESI†), we include in the CI treatment eighteen states from the valence band and five states from the conduction band (not counting the spin degree of freedom), which ensures that the conduction and valence band states are in a similar energy window. The optical dipole matrix elements are calculated within the dipole approximation, and the oscillator strength was calculated using Fermi's golden rule. A review of this method can be found in ref. 30. It should be noted that our calculations are focused on the near-band-edge low energy excitonic states which are dominantly originated from the transitions at the Γ-point of the Brillouin zone. The band dispersion along the growth direction of the NWs is expected to have only very marginal influence on the results presented herein. It should also be noted that an infinite wire will exhibit a continuum of states above (below) the LUMO (HOMO) from which we capture only a subset with our finite NW.

3 Numerical results and discussion

3.1 Electronic properties of ZnO nanowires

In an attempt to determine the electronic properties of ZnO NWs in both the intermediate and weak confinement regimes, we consider five different ZnO NWs with diameters D = 2, 3, 4, 5, and 6 nm. The fast oscillating atomic wave functions are projected onto the bulk ZnO Bloch states, which enables us to visualize the envelope functions and quantify the Bloch function parentage of each NW state (*i.e.*, to identify the contribution from each bulk Bloch state).[20] The envelope functions and Bloch function characters obtained from the projection of the first electron and first four hole states are presented in Fig. 1. We use the notation ω to characterize the symmetry of the envelope functions, where ω gives the number of nodes encountered when the envelope function is projected on a plane which contains both the growth direction vector and the center of the NW. The possible values of ω can be S, P and so forth, where S represents an envelope function without a node, P with one node, *etc.* The results obtained for the first four electron and first four hole states are presented in Table 1.

It is found that the lowest unoccupied molecular orbital (LUMO) state exhibits an S-like envelope function, derived purely from the lowest bulk conduction band, irrespective of the variation of the level of quantum confinement. The following two electron states ($e_{1,2}$) appear to be energetically degenerate (see Fig. 2(a)), switching from an S-type to a P-type envelope function at a diameter around 3 nm. Furthermore, a P-like envelope function is more preferable for electron states $e_{1,2,3}$ in the presence of very weak quantum confinement effects (*i.e.*, D = 6 nm ≈ $4.3a_B$, where a_B = 1.4 nm is the exciton Bohr radius of bulk ZnO).

Concerning the hole states, Fig. 1 and Table 1 show that the wave functions with dominant single-band character (either A-, B-, or C-band) have S-type envelope functions, while the ones with an even mixing of bulk Bloch A- and B-bands have P-type envelope functions. The S^A and S^B states are energetically close to each other, whereas they are considerably separated from the S^C states (see Fig. 2(b)). This is a consequence of the nature of

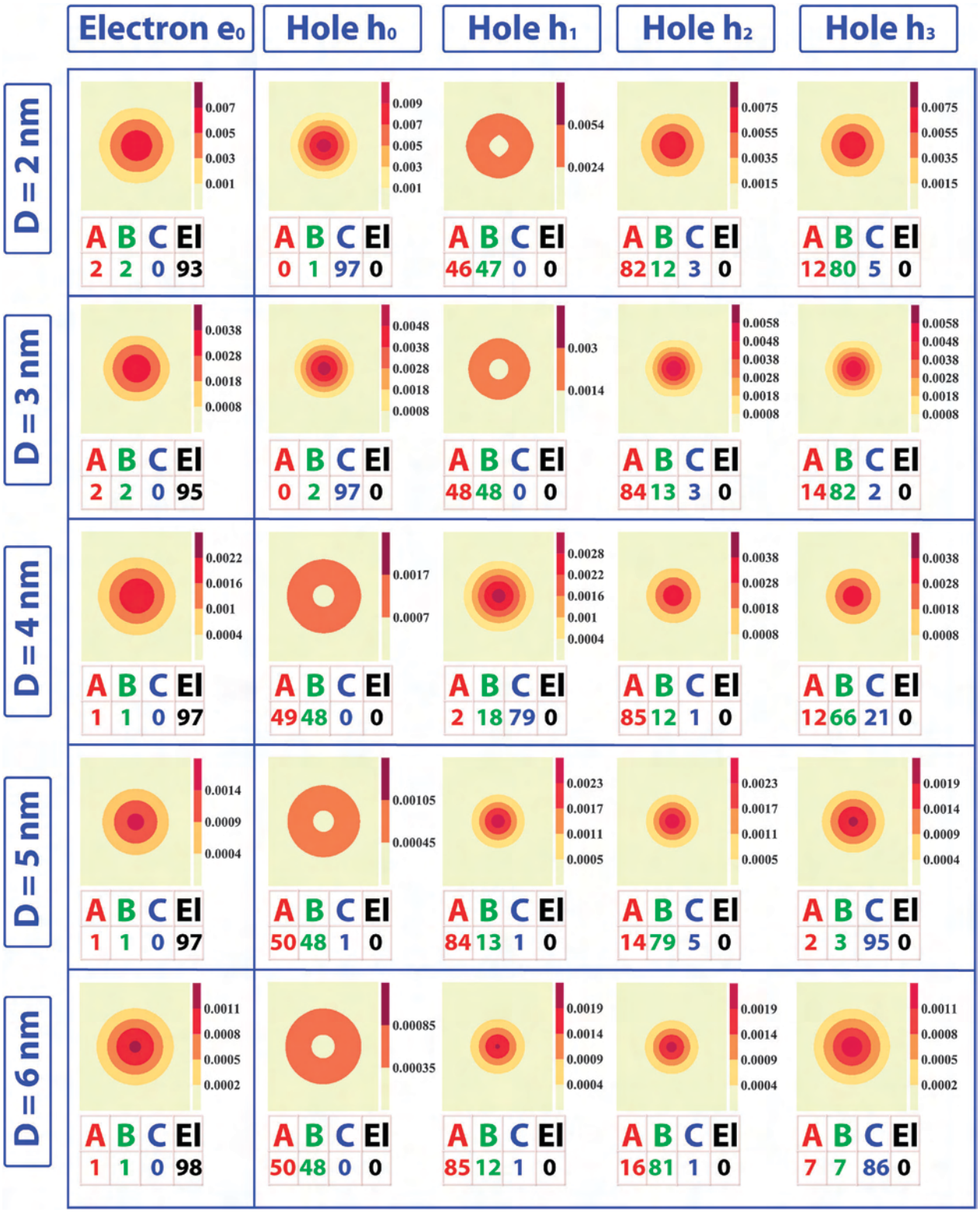

Fig. 1 Contour plot of the square of the envelope functions (perpendicular to the growth direction of NWs), extracted from our atomistic wave functions, for the first electron and first four hole states for various ZnO NWs. The parentage of each atomic NW wave function from the topmost three bulk valence band states (labeled as A–C) and the lowest bulk conduction band state (labeled as El) is tabulated under each plot in percentage.

the topmost three valence bands in bulk ZnO, where the A- and B-bands are very close to each other, being energetically separated from the C-band. The S^C states exhibit a weaker diameter dependence than the S^A and S^B states (see Fig. 2(b)). Consequently, the A- and B-band states rise above the C-band states at the critical diameters $D_c^{A/C}$ and $D_c^{B/C}$, respectively, and become

Table 1 Orbital character of the first four electron and hole envelope functions in ZnO NWs of various diameters (in units of nm). The superscripts (A, B, and C) indicate the Bloch function parentage of the corresponding hole state obtained from Fig. 1

Diameter	e_0	e_1	e_2	e_3	h_0	h_1	h_2	h_3
2	S	S	S	P	S^C	$P^{A,B}$	S^A	S^B
3	S	S	S	P	S^C	$P^{A,B}$	S^A	S^B
4	S	P	P	S	$P^{A,B}$	S^C	S^A	S^B
5	S	P	P	S	$P^{A,B}$	S^A	S^B	S^C
6	S	P	P	P	$P^{A,B}$	S^A	S^B	S^C

energetically more favorable, reproducing the usual electronic structure encountered in bulk ZnO. The critical values are $D_c^{A/C}$ = 4.2 nm and $D_c^{B/C}$ = 4.6 nm, respectively, (see Fig. 2(b)). The $P^{A,B}$ states are energetically very close to the S^A and S^B states. The S^C states become the highest occupied molecular orbital (HOMO) states for the diameter smaller than a critical value $D_c^{S/P}$ = 3.8 nm (see Fig. 2(b)). These $P^{A,B}$ states are energetically more sensitive to the NW diameter, crossing over the S^C states at $D = D_c^{S/P}$ and becoming the HOMO states for $D > D_c^{S/P}$. This diameter dependent change in the HOMO state from a conventional electronic state (*e.g.*, with S-type envelope) to an unconventional state (*e.g.*, with P-type envelope) has also been found previously in colloidal ZnO QDs[20] and very recently in GaN NWs,[31] and is being attributed to the nontrivial interplay between symmetry mixing, spin–orbit coupling, and quantum confinement effects on the valence band electronic structure.

3.2 Optical properties of ZnO nanowires

First, we present the optical band gap of ZnO NWs for various diameters, which correspond to the intermediate or weak confinement regime (see Fig. 2(c)). The calculations are performed at three levels of theory, *i.e.*, single-particle (SP) level, SC level, and CI level. Expectedly, the band gap appears to be a decreasing function of the NW diameter at all the three levels (see Fig. 2(c)). The size-dependent gaps are best fitted according to

$$E_g^{SP} = E_g^{bulk} + \alpha/D^{\beta},$$
$$E_g^{Op,SC} = E_g^{bulk,op} + \alpha'/D^{\beta'},$$
$$E_g^{Op,CI} = E_g^{bulk,op} + \alpha''/D^{\beta''}, \quad (2)$$

where E_g^{SP}, $E_g^{Op,SC}$, and $E_g^{Op,CI}$ are the calculated single-particle gaps, optical band gaps at the SC level, and optical band gaps at the CI level, respectively. E_g^{bulk} = 3.445 eV (ref. 27) is the fundamental band gap of bulk ZnO and $E_g^{bulk,op}$ = 3.385 eV is

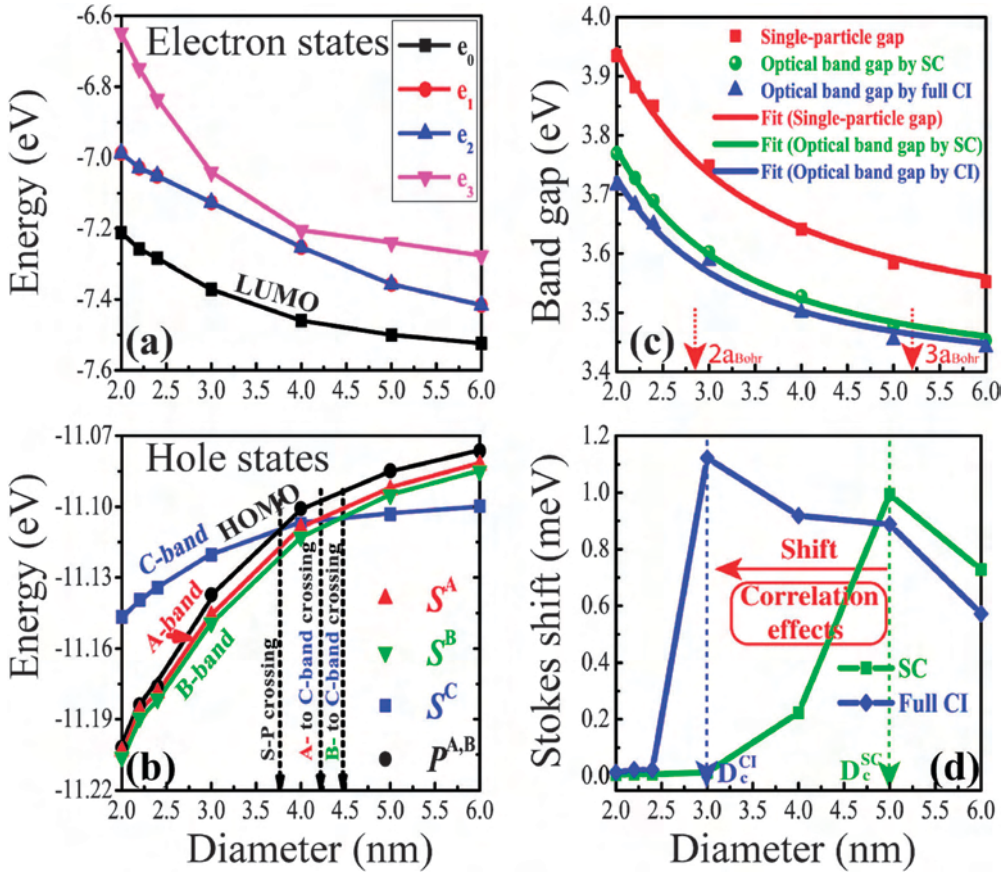

Fig. 2 Single-particle electron states (a), hole states (b), (c) single-particle gap (red solid squares), optical band gap at the SC level (green filled spheres) and optical band gap at the CI level (blue regular triangles), Stokes shift (d), as a function of the NW diameter. In figure (b), the lines connect the states of the same symmetry ω. The red, green, blue, and black lines connect states with the dominant A-band, B-band, and C-band, and an even mixing of A- and B-band parentage, respectively. In figure (c), each solid line represents a fit according to eqn (2).

the bulk optical gap. The respective values of the fitting parameters α, β, α', β', α'', and β'' are 1.26, 1.33, 1.11, 1.5, 0.99, and 1.54, where α, α' and α'' are in units of eV nm, while β, β' and β'' are dimensionless quantities. It is found that the diameter-dependent optical band gap of ZnO NWs (at the CI level), in the presence of quantum confinement effects, scales as $\sim 1/D^{1.54}$, rather than $\sim 1/D$ as predicted by the effective mass approximation.[32] The difference between the single-particle gap and the optical band gap at the CI level gives an exciton binding energy (in meV) which is best fitted by:

$$E_b^X = E_b^{bulk,X} + 310/D^{0.97}, \quad (3)$$

where $E_b^{bulk,X} = 60$ meV is the well-known exciton binding energy of bulk ZnO at room temperature. As expected from the quantum confinement effects, the exciton binding energy is significantly enhanced in ZnO NWs in comparison to bulk ZnO ($\sim$60 meV at room temperature), giving 111.25 meV at $D = 6$ nm, 140.99 meV at $D = 4$ nm and 218.78 meV at $D = 2$ nm, respectively.

The redshift of the emission spectra with respect to absorption spectra is known as the Stokes shift. It has two possible contributions:[33] (i) a purely electronic shift due to the splitting of exciton states into "bright" and "dark" states, which is usually called *electronic Stokes shift*, and (ii) vibrational (phonon) relaxation due to the movement of nuclei to new equilibrium positions in the excited state, which is called *vibrational Stokes shift*. In general, the vibrational part is very difficult to model[33] since it requires excited state geometry optimization. Moreover, it has been well justified[34,35] that the Stokes shift in III–V and II–VI semiconductor nanostructures is mainly attributed to the (i) contribution. Therefore, in our calculations, the emphasis is placed on the *electronic Stokes shift* which for brevity is called Stokes shift. Its dependence on the NW diameter is shown in Fig. 2(d). The results are obtained at two levels of theory: at the SC level and the CI level. It is found that the Stokes shift is a *non-monotonic* function of the diameter at both levels, having a maximum at a critical diameter value D_c. This critical values appear to be significantly different at both levels of theory, with $D_c^{SC} \approx 5$ nm at the SC level, and it is $D_c^{CI} \approx 3$ nm at the CI level. To understand this behaviour, we take our smallest and largest NWs as examples and present the corresponding near-band-edge exciton pictures in the last column of Fig. 3. For $D < D_c$ (top panels in Fig. 3), the lowest and first bright exciton states belong to the C-exciton at both SC and CI levels (the results at the SC level are not shown), being contributed nearly purely (or dominantly) from the configuration where the hole state has an S-type envelope function and is derived from the bulk Bloch C-band (S^C state). However, for $D \geq D_c$, the two exciton states responsible for the Stokes shift switch to the A-exciton, derived mainly from the configuration where the hole state has an S-type envelope function and a dominant bulk Bloch A-band parentage. This diameter-dependent C-exciton to A-exciton transition is responsible for the *non-monotonic* behaviour in Stokes shift.

We find from Fig. 3 that the formation of the optically dark and bright states is due to the electron–hole exchange interaction (see the last two columns). The C-exciton consists of one optically dark state and three optically bright states (see the upper panel of Fig. 3). The dark state is spin-forbidden and lower in energy. The lowest two bright exciton states are energetically very close to the dark state (*i.e.*, $\sim$0.013 meV for $D = 2$ nm (by CI), see Fig. 2(d)), being doubly degenerate (with a very small splitting of 0.4 μeV (by CI)) and weakly polarized (with low intensity) along the in-plane direction. The third bright state is energetically far away (*i.e.*, $\sim$4.01 meV (by CI) to the lowest dark state for $D = 2$ nm) and is singly degenerate with strong out-of-plane polarization (with high intensity). Concerning the A-exciton (see the lower panel of Fig. 3), it consists of two optically dark and two optically bright states. The dark states appear to be degenerate and present the ground state. The two bright exciton states are nearly degenerate with a small splitting of up to 58.25 μeV, being significantly separated from their dark counterparts (*e.g.*, $\sim$0.573 meV for $D = 6$ nm). These results are in full agreement with the symmetry analysis developed by Hopfield.[36] The Stokes shift originating from different types of excitons is found to exhibit a different diameter-dependence. As shown in Fig. 2(d), the Stokes shift derived from C-exciton states is quantitatively much smaller and it increases slightly with an increase in the diameter. Conversely, the one derived from A-exciton states turns out to be quantitatively much larger and it decreases significantly with respect to the increase in the diameter.

As mentioned previously, the S^A state rises over the S^C state and becomes energetically more favourable for $D > D_c^{A/C} = 4.2$ nm.

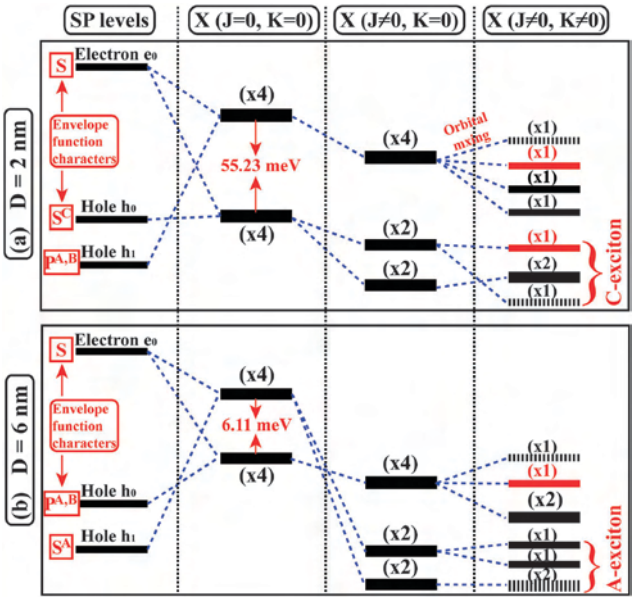

Fig. 3 Schematic picture of the evolution of the exciton states in ZnO NWs of two different diameters. Columns from the left to the right are the single-particle states (column (i)), energy of the uncoupled electron–hole pairs (column (ii)), excitonic states obtained *via* CI including the Coulomb interaction but neglecting the exchange interaction (column (iii)), and the final result obtained for the excitonic states including the Coulomb, exchange and correlation effects (column (iv)). The numbers in parenthesis indicate the degeneracy of each level. The dark-exciton states, bright-exciton states with in-plane polarization, and bright exciton states with out-of-plane polarization are shown in dashed black, solid black and solid red lines, respectively. For columns (ii)–(iv), the lowest total energy is placed at the bottom.

Therefore, one might expect that the transition between the near-band-edge C-exciton (electron-S–hole-S^C) and A-exciton (electron-S–hole-S^A) takes place around the critical value ($\approx$4.2 nm). This is indeed the case if correlation effects are neglected. The maximum of the Stokes shift appears at a critical diameter $D_c^{SC} \approx 5$ nm, as shown by the SC results (see Fig. 2(d)). However, when the correlation effects are fully considered (see the CI results), the critical value at which the transition occurs shifts to a significantly smaller diameter value (*e.g.*, $D_c^{CI} \approx 3$ nm). This nonmonotonic behaviour in Stokes shift has been found previously in several semiconductor nanostructures, *e.g.*, CdSe NRs,[37] ZnO NRs,[27] and ZnO QDs under pressure.[23] A larger Stokes shift means a smaller overlap area between absorption and emission spectra, which is desirable in applications such as light-emitting diodes, where reabsorption reduces the total efficiency.[37] The transition between different types of excitons has recently been found in GaAs/AlGaAs QDs by applying elastic stress,[38] which is believed to have potential applications in quantum technologies.

We also find that the exciton nearly purely derived from a configuration (e,h) where the electron has an S-type envelope function (in LUMO) and the hole has a P-type envelope function does not exhibit the orbitally forbidden, dark ground state (see the lower panel). The exciton ground state appears to be orbitally allowed but spin-forbidden, and derived from electrons (in LUMO) and holes (in HOMO−1) with both S-type envelope functions, similar to the case of small diameter NWs (see the upper panel of Fig. 3). After the detailed analysis of the evaluation of the band-edge exciton states, (see Fig. 3) through the stepwise incorporation of Coulomb and exchange interactions, we find that two combined effects are responsible for this phenomenon:

(i) Increasing the diameter leads to a significant decrease in the energy difference between the two four-fold uncoupled states (see the second column in Fig. 3), *e.g.*, the energy difference is 55.23 meV for D = 2 nm, while it is only 6.11 meV for D = 6 nm.

(ii) The Coulomb interaction is more pronounced for the configuration with both electrons and holes having the same envelope function characters (both S-type) than that with electrons and holes having different characters (electrons: S-type, and holes: P-type), irrespective of the NW diameter. For example, for D = 2 nm, the Coulomb interaction experienced by the configuration (e_0,h_0) (e_0–S–h_0–S) is around 218.8 meV, while it is around 213.7 meV for the configuration (e_0,h_1) (e_0–S–h_1–P). These two values appear to be 106.6 meV (configuration (e_0,h_0), (e_0–S–h_1–P)) and 117.9 meV (configuration (e_0,h_1), (e_0–S–h_1–S)), for D = 6 nm.

This conventional optics from the unconventional electronics has also been found previously in ZnO colloidal QDs.[20] Compared to the Coulomb interaction, the influence of the exchange interaction (fourth column in Fig. 3) has a significantly smaller magnitude (below 1 meV, depending on the NW diameter) but is important for the optical polarization properties.

Finally, we present in Fig. 4 the absorption spectrum at room temperature for various NW diameters. The calculations are performed in the CI scheme. A Gaussian broadening function is adopted with a broadening parameter of 1.2 meV. It is found that

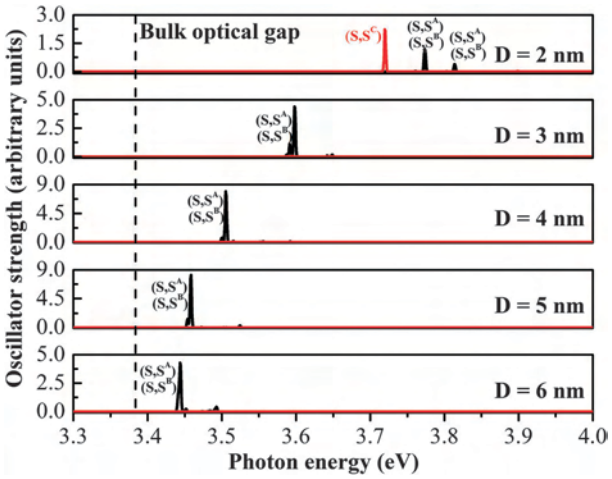

Fig. 4 Oscillator strength for absorption $\langle 0|$ to $\langle X|$ in various ZnO NWs at room temperature obtained *via* CI. Absorptions polarized along the out-of-plane (*c* axis) and in-plane (perpendicular to the *c*-axis) directions are shown by red and black vertical lines, respectively. The symbols in parentheses indicate the dominant envelope function characters of the single-particle states (e,h) involved in the absorptions, and the parentage of the corresponding hole state is given as the superscript.

increasing the diameter leads to a redshift in the absorption spectrum. This redshift is more pronounced for narrow NWs (with small diameters). Decreasing the NW diameter results in a transition in the optical absorption polarization from an in-plane polarization ($\mathbf{E} \perp \vec{c}$) to an out-of-plane polarization ($\mathbf{E} \parallel \vec{c}$) at a diameter of around 3 nm. This transition between the *usual* α-absorption ($\mathbf{E} \perp \vec{c}$) and the *unusual* σ and π absorptions ($\mathbf{E} \parallel \vec{c}$) has also been found previously in ZnO QDs under hydrostatic pressures[23] and ZnO NRs by changing the length-to-diameter aspect ratios.[27] Before the transition occurs (*e.g.*, for $D \geq 3$ nm), the near-band-edge optical absorption is dominated by the A- and B-exciton absorptions, which cannot be separately resolved experimentally.[13] However, after the transition takes place (*e.g.*, for $D < 3$ nm), the *unusual* C-exciton absorption (σ and π absorptions) becomes active. This type of absorption in ZnO NWs has recently been experimentally achieved by Jacopin *et al.*[13] using a thermal approach. The results we present here offer a new way (*e.g.*, narrowing the NW diameter) to activate the C-exciton absorption in ZnO NWs, which should be very interesting for the design of future experiments in the realm of quantum technology.[38]

4 Conclusions

In the present work, we have studied the electronic and optical properties of ZnO NWs as a function of the diameter. We find that the hole states with a dominant single-band (bulk A-, B- or C-band) parentage exhibit S-type envelope functions, while the states with an even mixture of bulk Bloch A- and B-bands present P-type envelope functions. The A- and B-band states are very close in energy and more sensitive to the NW diameter than the C-band states. Consequently, these states rise over the C-band states at critical diameters (*e.g.*, $D_c^{A/C}$ = 4.2 nm and

$D_c^{B/C}$ = 4.8 nm) and become energetically more favourable, reproducing the usual electronic structure of bulk ZnO. Compared to the C-band states, the states with an even mixture of bulk Bloch A- and B-band parentage exhibit a stronger size-dependence, causing a drastic change in the envelope function character of the highest occupied molecular orbital (HOMO) state from a *conventional* S-like character to an *unconventional* P-like character at a diameter around 3.8 nm. The lowest unoccupied molecular orbital (LUMO) state always presents an S-type envelope function, irrespective of the variation of the quantum confinement effects.

The optical band gap is a decreasing function of the NW diameter and scales as $\sim 1/D^{1.54}$, rather than $\sim 1/D$ as expected from effective mass theory. The exciton binding energy is calculated and the associated scaling law is provided. In contrast to monotonic behaviour in the optical band gap, the Stokes shift displays a non-monotonic function of the diameter, exhibiting a maximum at a critical diameter value around 3 nm. We explain this behaviour through the transition of the near-band-edge exciton from a usual C-exciton to an unusual A-exciton by varying the NW diameters. For NWs larger than the critical diameter, the near-band-edge optical absorption is dominated by the in-plane polarized A- and B-exciton absorptions. For NWs smaller than the critical diameter the out-of-plane polarized C-exciton absorption is dominant.

Acknowledgements

This research was co-financed by the European Union (European Social Fund-ESF) and Greek national funds through the Operational Program "Education and Lifelong Learning" of the National Strategic Reference Framework (NSRF)-Research Funding Program: Thales, investing in knowledge society through the European Social Fund.

References

1 P. Yang, H. Yan, S. Mao, R. Russo, J. Johnson, R. Saykally, N. Morris, J. Pham, R. He and H.-J. Choi, *Adv. Funct. Mater.*, 2002, **12**, 323–331.
2 X.-Y. Liu, C.-X. Shan, S.-P. Wang, Z.-Z. Zhang and D.-Z. Shen, *Nanoscale*, 2012, **4**, 2843–2846.
3 C. Liu, J. Zapien, Y. Yao, X. Meng, C. Lee, S. Fan, Y. Lifshitz and S. Lee, *Adv. Mater.*, 2003, **15**, 838–841.
4 Z. Fan, P.-C. Chang, J. G. Lu, E. C. Walter, R. M. Penner, C.-H. Lin and H. P. Lee, *Appl. Phys. Lett.*, 2004, **85**, 6128–6130.
5 Y. T. Lee, S. R. Ali Raza, P. J. Jeon, R. Ha, H.-J. Choi and S. Im, *Nanoscale*, 2013, **5**, 4181–4185.
6 H. Kind, H. Yan, B. Messer, M. Law and P. Yang, *Adv. Mater.*, 2002, **14**, 158–160.
7 K. Keem, H. Kim, G.-T. Kim, J. S. Lee, B. Min, K. Cho, M.-Y. Sung and S. Kim, *Appl. Phys. Lett.*, 2004, **84**, 4376–4378.
8 Q. Wan, Q. H. Li, Y. J. Chen, T. H. Wang, X. L. He, J. P. Li and C. L. Lin, *Appl. Phys. Lett.*, 2004, **84**, 3654–3656.
9 C. Baratto, S. Todros, G. Faglia, E. Comini, G. Sberveglieri, S. Lettieri, L. Santamaria and P. Maddalena, *Sens. Actuators, B*, 2009, **140**, 461–466.
10 Z. L. Wang and J. Song, *Science*, 2006, **312**, 242–246.
11 G. Zhu, R. Yang, S. Wang and Z. L. Wang, *Nano Lett.*, 2010, **10**, 3151–3155.
12 Q. Wan, C. L. Lin, X. B. Yu and T. H. Wang, *Appl. Phys. Lett.*, 2004, **84**, 124–126.
13 G. Jacopin, L. Rigutti, A. Bugallo, F. Julien, C. Baratto, E. Comini, M. Ferroni and M. Tchernycheva, *Nanoscale Res. Lett.*, 2011, **6**, 501.
14 F.-H. Chu, C.-W. Huang, C.-L. Hsin, C.-W. Wang, S.-Y. Yu, P.-H. Yeh and W.-W. Wu, *Nanoscale*, 2012, **4**, 1471–1475.
15 Y. Gu, I. L. Kuskovsky, M. Yin, S. O'Brien and G. F. Neumark, *Appl. Phys. Lett.*, 2004, **85**, 3833–3835.
16 M. Sahin, S. Nizamoglu, A. E. Kavruk and H. V. Demir, *J. Appl. Phys.*, 2009, **106**, 043704.
17 A. W. Long and B. M. Wong, *AIP Adv.*, 2012, **2**, 032173.
18 H. J. Xiang, J. Yang, J. G. Hou and Q. Zhu, *Appl. Phys. Lett.*, 2006, **89**, 223111.
19 Z. Xu, Q.-R. Zheng and G. Su, *Phys. Rev. B: Condens. Matter Mater. Phys.*, 2012, **85**, 075402.
20 S. Baskoutas and G. Bester, *J. Phys. Chem. C*, 2010, **114**, 9301.
21 A. Franceschetti, H. Fu, L. W. Wang and A. Zunger, *Phys. Rev. B: Condens. Matter Mater. Phys.*, 1999, **60**, 1819–1829.
22 M. Califano, A. Zunger and A. Franceschetti, *Nano Lett.*, 2004, **4**, 525–531.
23 Z. Zeng, C. S. Garoufalis, S. Baskoutas and G. Bester, *Phys. Rev. B: Condens. Matter Mater. Phys.*, 2013, **87**, 125302.
24 L. Zhang, J.-W. Luo, A. Franceschetti and A. Zunger, *Phys. Rev. B: Condens. Matter Mater. Phys.*, 2011, **84**, 075404.
25 L.-W. Wang and A. Zunger, *J. Chem. Phys.*, 1994, **100**, 2394–2397.
26 P. W. Avraam, N. D. M. Hine, P. Tangney and P. D. Haynes, *Phys. Rev. B: Condens. Matter Mater. Phys.*, 2011, **83**, 241402.
27 S. Baskoutas and G. Bester, *J. Phys. Chem. C*, 2011, **115**, 15862–15867.
28 M. Califano, G. Bester and A. Zunger, *Nano Lett.*, 2003, **3**, 1197–1202.
29 R. Resta, *Phys. Rev. B: Solid State*, 1977, **16**, 2717.
30 G. Bester, *J. Phys.: Condens. Matter*, 2009, **21**, 023202.
31 A. Molina-Sanchez, A. Garcia-Cristobal and G. Bester, *Phys. Rev. B: Condens. Matter Mater. Phys.*, 2012, **86**, 205430.
32 L. E. Brus, *J. Chem. Phys.*, 1984, **80**, 4403–4409.
33 B. S. Kim, M. A. Islam, L. E. Brus and I. P. Herman, *J. Appl. Phys.*, 2001, **89**, 8127.
34 A. Bagga, P. K. Chattopadhyay and S. Ghosh, *Phys. Rev. B: Condens. Matter Mater. Phys.*, 2006, **74**, 035341.
35 D. O. Demchenko and L.-W. Wang, *Phys. Rev. B: Condens. Matter Mater. Phys.*, 2006, **73**, 155326.
36 J. Hopfield, *J. Phys. Chem. Solids*, 1960, **15**, 97–107.
37 J. Hu, L.-S. Li, W. Yang, L. Manna, L.-W. Wang and A. P. Alivisatos, *Science*, 2001, **292**, 2060–2063.
38 Y. H. Huo, B. J. Witek, S. Kumar, J. R. Cardenas, J. X. Zhang, N. Akopian, R. Singh, E. Zallo, R. Grifone, D. Kriegner, R. Trotta, F. Ding, J. Stangl, V. Zwiller, G. Bester, A. Rastelli and O. G. Schmidt, *Nat. Phys.*, 2014, **10**, 46–51.

Electronic Supplementary Material (ESI) for Physical Chemistry Chemical Physics.

Supplementary Information: Near-band-edge exciton polarization change in ZnO nanowires

Zaiping Zeng,[a] Alexia Petoni,[a] Christos S. Garoufalis,[a] Sotirios Baskoutas*[a] and Gabriel Bester‡[b]

Convergence test

An important issue in the calculation of excitonic properties in nanostructures is the treatment of correlations. Our configuration interaction (CI) treatment exhibits a poor scaling, which limits the number of states that we are able to include in the expansion. A careful convergence test is therefore necessary, especially in the case of a NW, where the confinement in the NW direction is the sole result of the electron-hole interaction. The approach followed in this work is to use a large supercell extended in the NW direction, in order to fully include the physical extent of the exciton state, and limit the calculation to the Γ point of the Brillouin zone. An alternative and equivalent approach is to use a minimum supercell size in the NW direction and introduce k-point sampling.

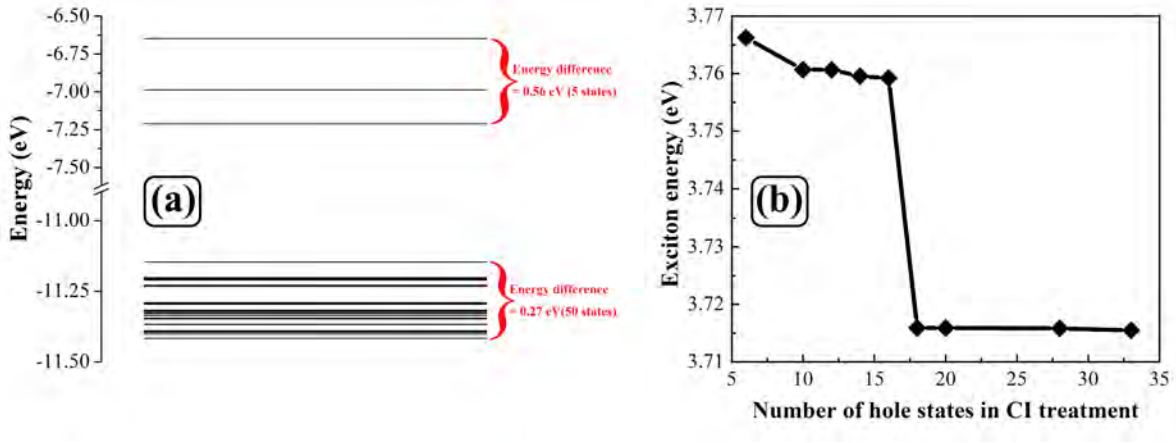

Fig. 1 (a) Single-particle electron and hole energy levels diagram for our smallest ZnO nanowire (with diameter D = 2 nm). Here, we have plotted the first five electron energy levels and the first fifty hole energy levels. (b) Exciton energy as a function of the number of the hole states in the configuration interaction (CI) treatment for our smallest ZnO nanowire (with diameter D = 2 nm). Here, we include the first five electron states in the CI.

For the convergence test, we choose our smallest ZnO nanowire with a diameter D = 2 nm, and plot the corresponding single-particle electron and hole energy levels (see Fig. 1(a)). We find that the single-particle electron states spread in a much larger energy window than its hole states counterparts, e.g., the first five

[a] *Materials Science Department, University of Patras, 26504 Patras, Greece*
[b] *Institut für Physikalische Chemie, Universität Hamburg, Grindelallee 117, 20146 Hamburg, Germany*
* Corresponding author: bask@upatras.gr
‡ Corresponding author: gabriel.bester@uni-hamburg.de

electron states distribute in an energy window of 0.56 eV, while the first fifty hole states only spread in a energy window of 0.27 eV. Therefore, we include in our CI treatment the first five electron states and systematically increase the number of hole states. The exciton energy as a function of the number of hole states is presented in Fig. 1(b). As we can see from Fig. 1(b), the exciton energy is insensitive to a further increase of the number of hole states when the number of hole states is larger than eighteen. Thus, we include in our CI treatment five states from the conduction band and eighteen states from the valence band.